The Topochemical Reduction of Some Complex Iridium Oxides

James Murrell

Exeter College

August 2024



A thesis submitted to the Board of the Faculty of Physical Sciences in partial fulfilment of the requirements for the degree of Doctor of Philosophy

The Topochemical Reduction of Some Complex Iridium Oxides

The work presented in this thesis focuses on the topochemical reduction of Ir-containing oxides with perovskite-type structures to form novel anion-deficient and mixed-anion phases.

Reactions between $n = 1$ Ruddlesden-Popper $La_xSr_{4-x}CoIrO_8$ ($0 \leq x \leq 2$) phases and LiH yields the formation of a series of oxyhydride phases, which represent the first oxyhydrides containing a 5d transition metal. For the Sr-rich members of the series ($x = 0$, 0.5), the extent of oxide-to-hydride exchange is limited by the stability of the overall Ruddlesden-Popper framework and, therefore, the temperature at which the reaction can be performed. Meanwhile, the extent of anion exchange in the remaining members of the series is limited by the formation of the Co^{I}/Ir^{III} oxidation state combination, as reduction of octahedrally-coordinated iridium below Ir^{III} would require occupation of a strongly antibonding e_g orbital.

Similarly, reaction of $LaSr_3NiIrO_8$ with LiH yields the formation of $LaSr_3NiIrO_{5.4}H_{2.6}$, which contains nickel as $Ni^{I/II}$ and iridium as Ir^{III}. Whilst iridium is present in its lowest energetically accessible oxidation state, it is not possible to fully reduce nickel to Ni^{I} without the onset of non-topochemical decomposition. In an attempt to prepare an analogous anion-deficient phase, $LaSr_3NiIrO_8$ was reacted with a Zr getter, which yielded $LaSr_3NiIrO_{6.4}$. This adopts an infinite-chain type structure, which contains Ir^{II} that is likely to be disproportionated into Ir^{I} and Ir^{III}.

Reaction of Sr_4MnIrO_8 with CaH_2 and LiH yields the oxyhydride phases, $Sr_4MnIrO_{6.58}H_{1.42}$ and $Sr_4MnIrO_{5.32}H_{2.68}$, respectively. Whilst the hydride ions are exclusively located at the equatorial positions in $Sr_4MnIrO_{6.58}H_{1.42}$, consistent with the other phases discussed in this thesis, hydride ions are also located at the axial positions in $Sr_4MnIrO_{5.32}H_{2.68}$. This is attributed to a combination of factors, including the strong Jahn-Teller effect associated with Mn^{III}, the tendency for hydride ions to adopt *cis*-arrangements with respect to each other and the preference for iridium to adopt highly symmetric coordination environments.

To explore the reactivity of other Ir-containing phases with LiH, reactions were performed using the 6H-hexagonal perovskite phase, $Ba_3CoIr_2O_9$, and the double perovskite $La_xSr_{2-x}CoIrO_6$ ($x = 0$, 1) phases. This yielded the oxyhydride phases, $Ba_3CoIr_2O_{6.2}H_{2.8}$ and $La_xSr_{2-x}CoIrO_{4.4}H_{1.6}$, in which the extent of anion exchange is limited by the stability of the perovskite frameworks, rather than the obtainment of the Co^{I}/Ir^{III} oxidation state combination. Whilst the $La_xSr_{2-x}CoIrO_{4.4}H_{1.6}$ phases adopt anion-disordered arrangements, $Ba_3CoIr_2O_{6.2}H_{2.8}$ adopts a partially anion-ordered arrangement, in which the hydride ions are preferentially located at the corner-sharing sites and adopt a *trans*-arrangement with respect to each other to optimise the π-bonding interactions.

To investigate the reactivity of the $La_xSr_{2-x}CoIrO_6$ phases further, they were heated in the presence of a Zr getter. This led to the formation of $La_xSr_{2-x}CoIrO_4$ infinite-layer phases, which occurs via $La_xSr_{2-x}CoIrO_5$ intermediates. Below 135−140 K, Sr_2CoIrO_4 adopts a 'type I' antiferromagnetic state at the cobalt sites, with very little ordering at the iridium sites. Meanwhile, $LaSrCoIrO_4$ adopts a magnetic structure based on C-type antiferromagnetic ordering with a possible incommensurate modulation that could arise from spin canting.

Finally, the effect of ball-milling on the reactivity of the perovskite phase, La_2CoRhO_6, was investigated. Whilst ball-milling showed no enhancement in reactivity for the reaction between La_2CoRhO_6 and NaH, reaction of the ball-milled sample with LiH allowed a greater extent of oxide-to-hydride exchange to be achieved. This was attributed to the fact that the oxyhydride product arising from the reaction with LiH is intrinsically highly strained, so ball-milling destabilises the starting material to a greater extent than the oxyhydride product.

Declaration

The work described in this thesis was carried out at the Inorganic Chemistry Laboratory at the University of Oxford between October 2020 and August 2024 under the supervision of Professor Michael A. Hayward. All the work presented in this thesis is my own, except where I have either acknowledged help from a named person or given reference to a published source. None of the work has been submitted by the author for any degree at any other university.

James Murrell
August 2024

Acknowledgements

Firstly, I would like to thank Prof. Mike Hayward for giving me the opportunity to join his group. Over the past four years, your enthusiasm and support has been invaluable to me, and I am very grateful for everything that I have learnt whilst being here. In addition, I would like to thank my second supervisor, Prof. Stephen Blundell, for his help with the muon spectroscopy and for all the helpful discussions. I also acknowledge the OxICFM CDT for their generous funding, which has made this PhD possible.

I am extremely grateful to Prof. Hiroshi Kageyama for allowing me to spend 2 months in his group at Kyoto University. I really appreciated the opportunity to learn about high-pressure and thin-film synthesis, and was also inspired by your group's approach to doing research. I would like to thank everyone from the group for being so friendly and hospitable; I am especially grateful to Tong and Cédric for being so welcoming when I arrived, and to Namba for providing me with so much help and support despite being busy finishing his thesis.

There are a huge number of people who have assisted with my project. I would like to thank Dr Benjamin Huddart for collecting the muon spin-rotation data, Dr Ashok Menon in Warwick for collecting the XAS data and Dr Robert Jacobs for maintaining the TGA instruments. In addition, I would like to thank Dr Simon Cassidy, not only for all his work looking after the X-ray diffractometers and SQUID instruments, but also for always being willing to help and for the opportunities he has given me to learn about the instruments and perform synchrotron measurements. I am also extremely grateful to all the instrument scientists at the WISH, POLARIS, GEM, D2B, D20, I11 and B18 beamlines, who have helped with the measurements in this project.

Most of all, I would like to thank all the members of the Hayward and Clarke groups; having the opportunity to work with you has been the highlight of my PhD. I'm especially grateful to Ella for her endless support, guidance and friendship throughout my PhD. I'd also like to thank: Xabi, Suraj, Subhadip and Zheying for being so welcoming and helpful; Riju, Anni, Romain and Zizhen for helping me to get through the last few months; and Rachel for being the best desk-buddy. I'll miss all the pub trips, squash/volleyball games, coffee breaks, running sessions, hotpots, office chats and Gloucester Green lunches.

I would like to thank all my housemates during my time in Oxford (Kam, Helen, Maya, Charlie, Matt, Fran, Matthew and Emmie). I've really enjoyed the time I've spent living with you (even the month of Covid isolation), and will miss you all a lot. Finally, I would like to thank all my friends (both in and out of Oxford) for their encouragement and helping to keep my project in perspective, and my family for all their support.

Table of Contents

The Topochemical Reduction of Some Complex Iridium Oxides I
Declaration III
Acknowledgements V
Table of Contents VII
Chapter 1 – Introduction 1
1.1 Transition metal oxides 1
1.1.1 Perovskite structure 1
1.1.2 Double perovskite structure 3
1.1.3 Hexagonal perovskite structures 5
1.1.4 Ruddlesden-Popper structures 6
1.2 Magnetic properties of transition metal oxides 7
1.2.1 Diamagnetism 8
1.2.2 Paramagnetism 9
1.2.3 Magnetic superexchange 10
1.2.4 Types of magnetic order 12
1.2.4.1 Ferromagnetism 12
1.2.4.2 Antiferromagnetism 13
1.2.4.3 Spin glasses 13
1.2.4.4 Superparamagnetism 14
1.3 Electronic properties of transition metal oxides 15
1.3.1 Ligand field theory 15
1.3.2 Band theory and the Hubbard model 16
1.3.3 Spin-orbit coupling 18
1.4 Topochemical reduction of transition metal oxides 19
1.4.1 Topochemically reduced anion deficient phases 19
1.4.2 Oxyhydride phases 21
1.5 Motivation of this work 23
Chapter 2 – Experimental methods and techniques 25
2.1 Ceramic synthesis 25
2.2 Topochemical reduction 25
2.2.1 Binary metal hydride reactions 26
2.2.2 Zirconium getter reactions 27
2.3 Powder diffraction 28
2.3.1 Powder X-ray diffraction 30

2.3.1.1 Panalytical Empyrean diffractometer 30
2.3.1.2 Bruker D8 Advance Eco diffractometer 31
2.3.1.3 Synchrotron powder X-ray diffraction 31
2.3.2 Neutron powder diffraction 32
2.3.2.1 ISIS neutron and muon source 33
2.3.2.2 Institut Laue-Langevin 34
2.4 Rietveld refinement 34
2.4.1 Sample contribution to diffraction peak broadening 36
2.4.1.1 Crystallite domain size broadening 37
2.4.1.2 Microstructural strain broadening 37
2.4.2 Magnetic form factors of iridium 38
2.5 Pawley refinement 38
2.6 X-ray absorption spectroscopy 39
2.7 Thermogravimetric analysis 40
2.8 SQUID magnetometry 41
2.8.1 Ferrosubtraction technique 42
2.9 Muon spin rotation spectroscopy 43
2.10 Iodometric titration 45
2.11 Thin-film synthesis and characterisation 45
2.11.1 Pulsed laser deposition 45
2.11.2 X-ray diffraction 46
2.11.3 SQUID magnetometry 47
2.11.4 Transport measurements 48
Chapter 3 – Topochemical reduction of $La_xSr_{4-x}CoIrO_8$ ($0 \leq x \leq 2$) phases using LiH 49
3.1 Introduction 49
3.2 Experimental 49
3.2.1 Synthesis of $La_xSr_{4-x}CoIrO_8$ ($0 \leq x \leq 2$) phases 49
3.2.2 Exploration of the reactivity of $La_xSr_{4-x}CoIrO_8$ phases with LiH 50
3.2.3 Synthesis of $La_xSr_{4-x}CoIrO_{8-y}H_y$ ($0 \leq x \leq 2$) phases 51
3.2.3.1 Synthesis of $Sr_4CoIrO_{6.5}H_{1.5}$ 51
3.2.3.2 Synthesis of $La_{0.5}Sr_{3.5}CoIrO_{5.5}H_{2.5}$ 51
3.2.3.3 Synthesis of $LaSr_3CoIrO_5H_3$ 51
3.2.3.4 Synthesis of $La_{1.5}Sr_{2.5}CoIrO_{8-y}H_y$ 51
3.2.3.5 Synthesis of $La_2Sr_2CoIrO_{8-y}H_y$ 52
3.2.4 Washing of $La_xSr_{4-x}CoIrO_{8-y}H_y$ ($0 \leq x \leq 2$) phases 52
3.3 Structural characterisation 52

3.3.1 Structural characterisation of $La_xSr_{4-x}CoIrO_8$ ($0 \leq x \leq 2$) phases 52
3.3.2 Structural characterisation of $Sr_4CoIrO_{6.5}H_{1.5}$ 53
3.3.2.1 Thermogravimetric analysis 53
3.3.2.2 Neutron powder diffraction 54
3.3.3 Structural characterisation of $La_{0.5}Sr_{3.5}CoIrO_{5.5}H_{2.5}$ 58
3.3.3.1 Thermogravimetric analysis 58
3.3.3.2 Neutron powder diffraction 59
3.3.4 Structural characterisation of $LaSr_3CoIrO_5H_3$ 62
3.3.4.1 Thermogravimetric analysis 62
3.3.4.2 Neutron powder diffraction 63
3.3.5 Structural characterisation of $La_{1.5}Sr_{2.5}CoIrO_{8-y}H_y$ 65
3.3.5.1 Thermogravimetric analysis 66
3.3.5.2 Neutron powder diffraction 67
3.3.6 Structural characterisation of $La_2Sr_2CoIrO_{8-y}H_y$ 71
3.3.6.1 Thermogravimetric analysis 72
3.3.6.2 Neutron powder diffraction 72
3.3.7 Comparison of refined lattice parameters and bond lengths 76
3.3.8 X-ray absorption spectroscopy 78
3.3.9 Discussion 79
3.3.9.1 Anion site selectivity in $La_xSr_{4-x}CoIrO_{8-y}H_y$ oxyhydride phases 79
3.3.9.2 Anion compositions of $La_xSr_{4-x}CoIrO_{8-y}H_y$ oxyhydride phases 81
3.3.9.3 Presence of a phase gap and apparent anion disorder in $La_xSr_{4-x}CoIrO_{8-y}H_y$ phases 83
3.4 Magnetic characterisation 86
3.4.1 Magnetic characterisation of $Sr_4CoIrO_{6.5}H_{1.5}$ 86
3.4.2 Magnetic characterisation of $La_{0.5}Sr_{3.5}CoIrO_{5.5}H_{2.5}$ 89
3.4.3 Magnetic characterisation of $LaSr_3CoIrO_5H_3$ 91
3.4.4 Magnetic characterisation of $La_{1.5}Sr_{2.5}CoIrO_{8-y}H_y$ 93
3.4.5 Magnetic characterisation of $La_2Sr_2CoIrO_{8-y}H_y$ 94
3.4.6 Muon spin rotation spectroscopy 96
3.4.7 Discussion 98
3.4.7.1 Magnetic behaviour of $Sr_4CoIrO_{6.5}H_{1.5}$ 98
3.4.7.2 Magnetic behaviour of $La_xSr_{4-x}CoIrO_{8-y}H_y$ (x = 0.5, 1, 1.5, 2) phases 100
3.5 Conclusion 102
Chapter 4 – Topochemical reduction of $LaSr_3NiIrO_8$ using LiH and a Zr getter 104
4.1 Introduction 104
4.2 Experimental 104

4.2.1 Synthesis of $LaSr_3NiIrO_8$ 104
4.2.2 Exploration of the reactivity of $LaSr_3NiIrO_8$ 104
4.2.2.1 Reactivity with LiH 104
4.2.2.2 Reactivity with a Zr getter 105
4.2.3 Synthesis of $LaSr_3NiIrO_{5.4}H_{2.6}$ 105
4.2.4 Synthesis of $LaSr_3NiIrO_{6.4}$ 105
4.3 Structural characterisation 106
4.3.1 Structural characterisation of $LaSr_3NiIrO_8$ 106
4.3.2 Structural characterisation of $LaSr_3NiIrO_{5.4}H_{2.6}$ 107
4.3.2.1 Thermogravimetric analysis 108
4.3.2.2 Neutron powder diffraction 109
4.3.2.3 Discussion 111
4.3.3 Structural characterisation of $LaSr_3NiIrO_{6.4}$ 112
4.3.3.1 Synchrotron powder X-ray diffraction 112
4.3.3.2 Thermogravimetric analysis 113
4.3.3.3 Neutron powder diffraction 114
4.3.3.4 X-ray absorption spectroscopy 117
4.3.3.5 Discussion 118
4.4 Magnetic characterisation 121
4.4.1 Magnetic characterisation of $LaSr_3NiIrO_8$ 121
4.4.2 Magnetic characterisation of $LaSr_3NiIrO_{5.4}H_{2.6}$ 122
4.4.3 Magnetic characterisation of $LaSr_3NiIrO_{6.4}$ 126
4.4.4 Discussion 129
4.5 Conclusion 131
Chapter 5 – Topochemical reduction of Sr_4MnIrO_8 using CaH_2 and LiH 133
5.1 Introduction 133
5.2 Experimental 133
5.2.1 Synthesis of Sr_4MnIrO_8 133
5.2.2 Exploration of the reactivity of Sr_4MnIrO_8 133
5.2.3 Synthesis of $Sr_4MnIrO_{6.58}H_{1.42}$ 134
5.2.4 Synthesis of $Sr_4MnIrO_{5.32}H_{2.68}$ 135
5.3 Results 135
5.3.1 Structural characterisation of Sr_4MnIrO_8 135
5.3.2 Structural characterisation of $Sr_4MnIrO_{6.58}H_{1.42}$ 137
5.3.2.1 Thermogravimetric analysis 137
5.3.2.2 Neutron powder diffraction 138
5.3.3 Structural characterisation of $Sr_4MnIrO_{5.32}H_{2.68}$ 143

5.3.3.1 Thermogravimetric analysis 143
5.3.3.2 Neutron powder diffraction 144
5.3.4 X-ray absorption spectroscopy 149
5.3.4.1 X-ray absorption near edge structure 149
5.3.4.2 Extended X-ray absorption fine structure 150
5.3.5 Magnetic characterisation 153
5.3.5.1 Sr_4MnIrO_8 153
5.3.5.2 $Sr_4MnIrO_{6.58}H_{1.42}$ 155
5.3.5.3 $Sr_4MnIrO_{5.32}H_{2.68}$ 158
5.4 Discussion 159
5.4.1 Comparison of reactivity of CaH_2 and LiH 159
5.4.2 Distribution of hydride ions in $Sr_4MnIrO_{6.58}H_{1.42}$ and $Sr_4MnIrO_{5.32}H_{2.68}$ 161
5.4.3 Magnetic behaviour 164
5.5 Conclusion 166
Chapter 6 – Topochemical reduction of $Ba_3CoIr_2O_9$ using LiH 168
6.1 Introduction 168
6.2 Experimental 168
6.2.1 Synthesis of $Ba_3CoIr_2O_9$ 168
6.2.2 Exploration of the reactivity of $Ba_3CoIr_2O_9$ with LiH 168
6.2.3 Synthesis of $Ba_3CoIr_2O_{6.2}H_{2.8}$ 169
6.3 Structural characterisation 169
6.3.1 Structural characterisation of $Ba_3CoIr_2O_9$ 169
6.3.2 Structural characterisation of $Ba_3CoIr_2O_{6.2}H_{2.8}$ 173
6.3.2.1 Thermogravimetric analysis 173
6.3.2.2 Neutron and synchrotron X-ray powder diffraction 174
6.4 Magnetic characterisation 177
6.5 Discussion 179
6.6 Conclusion 184
Chapter 7 – Topochemical reduction of $La_xSr_{2-x}CoIrO_6$ (x = 0, 1) phases using LiH 185
7.1 Introduction 185
7.2 Experimental 185
7.2.1 Synthesis of $La_xSr_{2-x}CoIrO_6$ (x = 0, 1) phases 185
7.2.2 Exploration of the reactivity of $La_xSr_{2-x}CoIrO_6$ (x = 0, 1) phases with LiH 185
7.2.3 Synthesis of $Sr_2CoIrO_{4.4}H_{1.6}$ and $LaSrCoIrO_{4.4}H_{1.6}$ 186
7.3 Structural characterisation 186
7.3.1 Structural characterisation of $La_xSr_{2-x}CoIrO_6$ (x = 0, 1) phases 186

7.3.2 Structural characterisation of $Sr_2CoIrO_{4.4}H_{1.6}$ 189
7.3.2.1 Synchrotron X-ray diffraction 189
7.3.2.2 Thermogravimetric analysis 189
7.3.2.3 Neutron powder diffraction 191
7.3.3 Structural characterisation of $LaSrCoIrO_{4.4}H_{1.6}$ 195
7.3.3.1 Synchrotron X-ray diffraction 195
7.3.3.2 Thermogravimetric analysis 196
7.3.3.3 Neutron powder diffraction 198
7.4 Magnetic characterisation 201
7.4.1 Magnetic characterisation of $Sr_2CoIrO_{4.4}H_{1.6}$ 201
7.4.2 Magnetic characterisation of $LaSrCoIrO_{4.4}H_{1.6}$ 204
7.5 Discussion 207
7.6 Conclusion 211
Chapter 8 – Synthesis and magnetism of Sr_2CoIrO_5 212
8.1 Introduction 212
8.2 Exploration of the reactivity of Sr_2CoIrO_6 with a Zr getter 212
8.3 Synthesis of Sr_2CoIrO_5 213
8.4 Structural characterisation of Sr_2CoIrO_5 213
8.4.1 Synchrotron powder X-ray diffraction 213
8.4.2 Neutron powder diffraction 215
8.4.3 Thermogravimetric analysis 219
8.4.4 X-ray absorption spectroscopy 220
8.5 Magnetic characterisation of Sr_2CoIrO_5 221
8.5.1 Magnetic behaviour 221
8.5.2 Muon spin rotation spectroscopy 223
8.6 Discussion 225
8.6.1 Anion disorder in Sr_2CoIrO_5 225
8.6.2 Magnetic behaviour of Sr_2CoIrO_5 228
8.7 Conclusion 229
Chapter 9 – Synthesis and magnetism of Sr_2CoIrO_4 230
9.1 Introduction 230
9.2 Synthesis of Sr_2CoIrO_4 230
9.3 Structural characterisation of Sr_2CoIrO_4 230
9.3.1 Room temperature synchrotron powder X-ray diffraction 230
9.3.2 Room temperature neutron powder diffraction 232
9.3.3 Thermogravimetric analysis 236
9.3.4 X-ray absorption spectroscopy 237

9.4 Magnetic characterisation of Sr_2CoIrO_4 238
9.4.1 Magnetic behaviour 238
9.4.2 Muon spin rotation spectroscopy 240
9.4.3 Low temperature neutron powder diffraction 241
9.4.4 Variable temperature synchrotron powder X-ray diffraction 245
9.5 Discussion 247
9.5.1 Electronic structure of Sr_2CoIrO_4 247
9.5.2 Magnetic behaviour of Sr_2CoIrO_4 249
9.6 Synthesis and characterisation of Sr_2CoIrO_6 and Sr_2CoIrO_4 thin films 251
9.6.1 Synthesis of thin film samples 251
9.6.1.1 Synthesis of Sr_2CoIrO_6 thin film 251
9.6.1.2 Synthesis of Sr_2CoIrO_4 thin film 251
9.6.2 Structural characterisation of thin films 252
9.6.3 Physical characterisation of thin films 255
9.7 Conclusion 257

Chapter 10 – Synthesis and magnetism of $LaSrCoIrO_4$ 258
10.1 Introduction 258
10.2 Exploration of the reactivity of $LaSrCoIrO_6$ with a Zr getter 258
10.3 Synthesis of $LaSrCoIrO_4$ 259
10.4 Structural characterisation of $LaSrCoIrO_4$ 259
10.4.1 Synchrotron powder X-ray diffraction 259
10.4.2 Neutron powder diffraction 261
10.4.3 Thermogravimetric analysis 264
10.5 Magnetic characterisation of $LaSrCoIrO_4$ 264
10.5.1 Magnetic behaviour 264
10.5.2 Low temperature neutron powder diffraction 266
10.6 Conclusion 271

Chapter 11 – Effect of ball-milling on the reactivity of La_2CoRhO_6 with NaH and LiH 272
11.1 Introduction 272
11.2 Synthesis and characterisation of pristine and ball-milled La_2CoRhO_6 273
11.2.1 Synthesis of pristine and ball-milled La_2CoRhO_6 273
11.2.2 Microstructural analysis of pristine and ball-milled La_2CoRhO_6 273
11.2.3 Magnetic behaviour of pristine and ball-milled La_2CoRhO_6 276
11.3 Reactivity of La_2CoRhO_6 with NaH 280
11.4 Reactivity of La_2CoRhO_6 with LiH 282
11.4.1 Results 282

11.4.2 Discussion 284
11.5 Characterisation of $La_2CoRhO_4H_2$ 286
11.5.1 Neutron powder diffraction 286
11.5.2 Magnetic behaviour 291
11.6 Conclusion 296
Chapter 12 – Conclusions 297
Appendix 304
A1 – Supplementary data for Chapter 3 304
A2 – Supplementary data for Chapter 4 316
A3 – Supplementary data for Chapter 5 317
A4 – Supplementary data for Chapter 7 320
A5 – Supplementary data for Chapter 10 321
A5.1 Synthesis and characterisation of $LaSrCoIrO_5$ 321
A5.2 Possible magnetic structure of $LaSrCoIrO_4$ 326
Table of Figures 328
Bibliography 341

Chapter 1 – Introduction

1.1 Transition metal oxides

Transition metal oxides are a widely studied class of material, due to their wide abundance and their ability to exhibit a variety of useful chemical and physical properties, including magnetoresistivity,[1] ionic conductivity,[2] collective magnetism[3] and high temperature superconductivity.[4] These compounds can exhibit a diverse range of different structures, with the exact structure adopted depending on a delicate balance of factors, such as the enthalpic driving force to pack ions as efficiently as possible and the electronic preference of certain ions to adopt specific coordination environments. One of the most common structure types observed for transition metal oxides, and the focus of this thesis, is the perovskite structure and this will be discussed in detail below.

1.1.1 Perovskite structure

The general formula for the perovskite structure is ABX_3, and is formed of corner-sharing BX_6 octahedra, which leaves large 12-coordinate voids in the structure that are filled by the A-cation (Figure 1.1). The A-cation typically has a large ionic radius and is from the *s*-, *d*- or *f*-block, whilst the B-cation is smaller and is often a transition metal. Although the X-anion can be a variety of different *p*-block elements, only the oxide ion will be considered in this thesis.

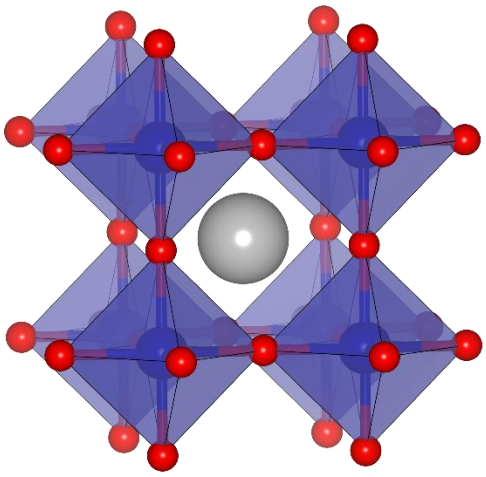

Figure 1.1: The cubic ABO_3 perovskite structure, where the grey sphere represents the A-cation, the blue spheres represent the B-cations and the red spheres represent the anions.

One reason that perovskites have been so widely studied is the fact that the framework can accommodate a vast array of different A- and B-site cations. This results from the high degree of flexibility that is exhibited by the perovskite structure, which arises from its ability to undergo cooperative tilting and twisting to accommodate size mismatches between the A- and B-site cations. This size mismatch can be evaluated using the Goldschmidt tolerance factor,[5]

$$t = \frac{r_A + r_O}{\sqrt{2}\,(r_B + r_O)} \quad . \tag{1}$$

When $t = 1$, the A−O and B−O bond lengths have the ideal ratio with respect to each other and, as a result, all B−O−B angles are 180°. For $t < 1$, the A-site cation is too small for the 12-coordinate cavity; the framework responds to this through coupled rotations of the BO_6 octahedra, leading to a lowering in symmetry of the structure. This tilting affects the overlap of the metal *d*- and O 2*p*-orbitals and can, therefore, have a large impact on the magnetic and electronic properties of the compound. For $t > 1$, the A-site cation is too large for the 12-coordinate cavity, causing the BO_6 octahedra to change their connectivity from corner-sharing to face-sharing, as will be discussed in Section 1.1.3.

The tilting arrangements of perovskites can be described using the Glazer tilt classification.[6] Using this notation, a three-letter symbol (eg. $a^0b^+c^+$) is used to describe the rotation of the BO_6 octahedron of the perovskite structure along each of its three 4-fold axes. The identity of the letter (*a*, *b* or *c*) is used to denote the relative magnitudes of the three tilts, whilst the superscripts denote whether the octahedra in adjacent layers rotate in phase (+), out of phase (−) or there is no rotation (0). Although symmetry analysis by Howard and Stokes[7] has shown that there are 15 unique Glazer tilts, there are three that are especially common. The first is $a^0a^0a^0$, which is simply the cubic perovskite with $Pm\bar{3}m$ symmetry (eg. $SrTiO_3$)[8]. The second is $a^-a^-a^-$, which gives rhombohedral $R\bar{3}c$ symmetry (eg. $LaNiO_3$)[9]. The final, and most common, tilting arrangement is $a^+b^-b^-$, which lowers the symmetry to orthorhombic *Pnma* (eg. $LaFeO_3$)[10].

1.1.2 Double perovskite structure

One approach for modifying the properties of perovskite-based oxides is to introduce multiple transition metals to the B-cation site. If two different cations occupy the B-site with a 1:1 ratio, the chemical formula of the perovskite can be represented as $AB_{0.5}B'_{0.5}O_3$ (or $A_2BB'O_6$). The B and B′ ions can then form either an ordered or a disordered arrangement. The main factors that drive ordering in these systems are the relative sizes and charges of the cations.[11–13] Typically, a disordered arrangement is observed if the charges of B and B′ differ by less than two (eg. La_2CrFeO_6)[14], whilst an ordered arrangement is observed if the charges differ by greater than two (eg. Sr_2NiWO_6)[15]. If the difference in charge is exactly two, it is possible for the structure to adopt ordered, disordered or partially ordered arrangements. In this case, ordering will be favoured if the ionic radii of the B and B′ cations differ by more than 0.2 Å. If cation ordering is present at the B-site, the structure is known as a double perovskite.

There are three simple ways of ordering the B-site cations in a double perovskite: rock-salt, columnar and layered ordering (Figure 1.2). In rock salt ordering, each B cation has six B′ cations as its nearest neighbours; this results in layering of B/B′ cations along the (111) plane and can be considered as zero-dimensional ordering. Meanwhile, columnar and layered ordering can be represented by B/B′ layers along the (110) and (001) planes, respectively, corresponding to 1D and 2D ordering. Of these three ordering motifs, rock salt ordering is the most common. There are a number of factors that drive this trend. Firstly, if one cation is more highly charged than the other, rock salt ordering maximises the separation between the more highly charged ions. Secondly, rock salt ordering provides a preferable bonding environment for the anions. In this type of ordering, each oxide ion is neighboured by one B-cation and one B′-cation, and the position of the oxide ion can shift towards the smaller B-site cation to optimise the bonding. In contrast, for columnar and layered ordering, there are oxide ions coordinated to solely one type of B-site cation, which will necessarily be under- or over-bonded. Therefore, for columnar or layered ordering to become favourable, other stabilising effects must be present, such as charge ordering (eg. $LaCaMn^{3+}Mn^{4+}O_6$)[16] or Jahn-Teller distortions (eg. La_2CuSnO_6)[17].

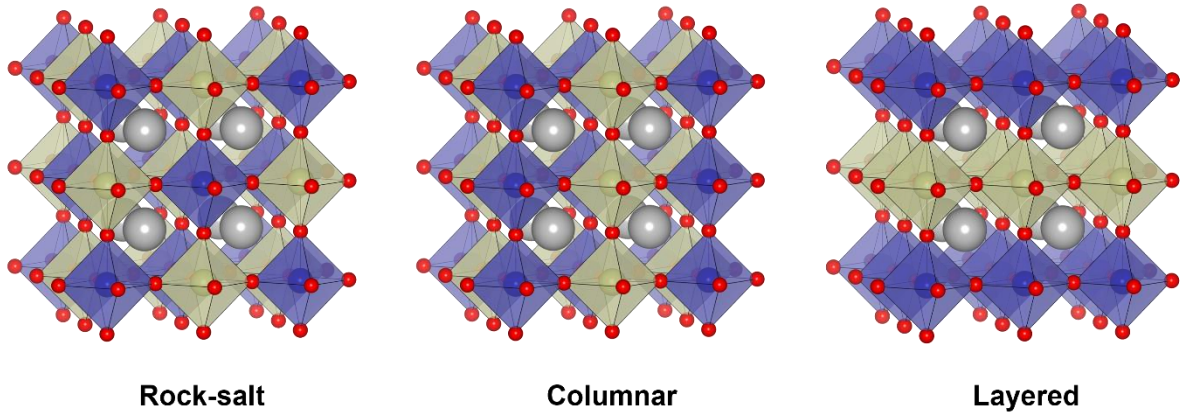

Figure 1.2: Possible ordering arrangements for B-site cations in the double perovskite structure.

1.1.3 Hexagonal perovskite structures

As discussed in Section 1.1.1, the type of perovskite structure adopted by a specific composition can be rationalised using the Goldschmidt tolerance factor. For $t > 1$, the A-site cation is too large for the 12-coordinate cavity and, as a result, the BO_6 octahedra change their connectivity such that they share faces, since this provides a larger volume in which the A-site cation can reside. This face-sharing arrangement of octahedra arises from hexagonal close-packing of the oxide ions and leads to the formation of columns of BO_6 octahedra within the structure.

A large number of hexagonal perovskite structures are known.[18] For compounds with a tolerance factor much greater than 1, such as $BaCoO_3$, the structure can contain solely hexagonal close-packing and, as a consequence, is made up of infinite columns of face-sharing BO_6 octahedra.[19] However, for many compounds, ordered intergrowths of hexagonal close-packing occur within an overall cubic close-packed structure. For example, $BaRuO_3$ can adopt a number of different hexagonal structures depending on the synthesis conditions. Using standard ceramic synthesis techniques under ambient pressure, the structure shown in Figure 1.3(a) is formed, which consists of trimers of face-sharing RuO_6 octahedra, which are themselves connected through corner-sharing.[20] Since this structure contains 9 layers within its unit cell and is based on rhombohedral stacking, it can be described as belonging to the 9R structure type. Meanwhile, synthesis at 1000°C under pressures of 3 GPa and 5 GPa results in the structures shown in Figure 1.3(b) and (c), respectively, which can be described as belonging to the 4H and 6H structure types.[21,22] It is also worth noting that $BaRuO_3$ can be synthesised as the cubic perovskite under a pressure of 18 GPa, and this can trivially be denoted as belonging to the 3C structure type.[23]

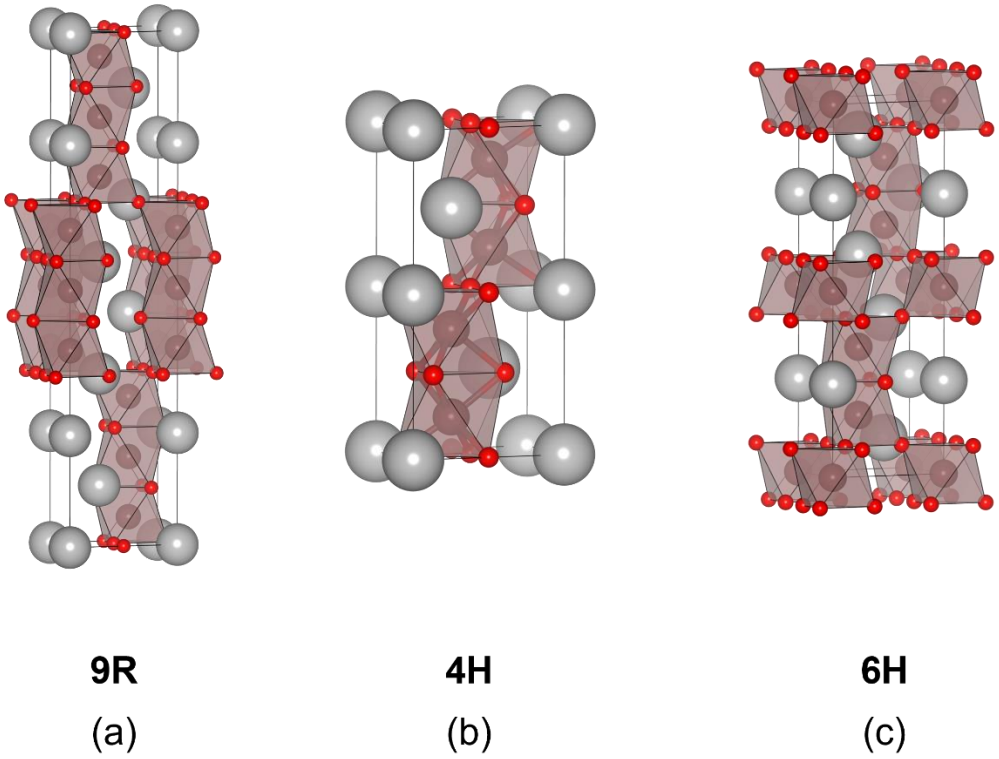

Figure 1.3: Different polymorphs of $BaRuO_3$ with hexagonal perovskite structures.

1.1.4 Ruddlesden-Popper structures

A common structure type related to perovskites are the Ruddlesden-Popper structures.[24–26] Compounds that adopt these structures have general formula $A_{n+1}B_nO_{3n+1}$, and are layered structures made up of ABO_3 perovskite sheets *n*-units thick that are separated by AO rock salt layers. The limit of $n = \infty$ corresponds to the conventional perovskite structure. The separation of the perovskite layers in the *c*-direction in Ruddlesden-Popper phases has a number of consequences for the properties of these materials. Firstly, any superexchange interactions in the *c*-direction are weak, so magnetic interactions are generally restricted to within the perovskite planes. Secondly, $n = 1$ Ruddlesden-Popper phases containing two types of B-site cation often exhibit paracrystalline order.[27] This is due to the fact that, although the B-site cations may be ordered within the perovskite layers, the registry of the positions of the B-site cations between the layers is weak and, as a result, there is very little B-site cation ordering between consecutive layers, as illustrated in Figure 1.4. Since diffraction methods only probe

the average crystal structure, this means that the B-site cations will always appear disordered from diffraction, despite the fact that ordering may be present withing the layers.

In addition, for compounds exhibiting this paracrystalline ordering, there is not a magnetic lattice present upon which long-range 3-dimenional ordering can propagate and, as a consequence, magnetic ordering peaks are typically not observed from neutron diffraction.

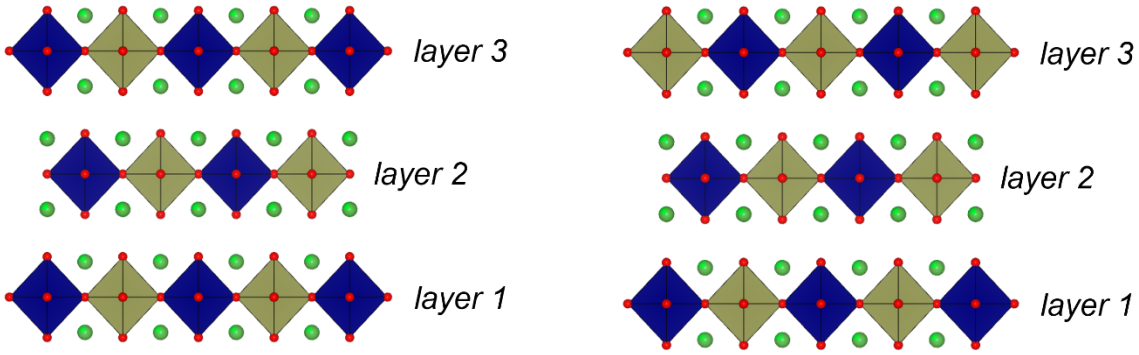

Figure 1.4: Schematic illustrating paracrystalline ordering in n = 1 Ruddlesden-Popper phases. Although the B-site cations may be ordered within the perovskite sheets, there is very little ordering between the sheets. As such, the B-site cations appear disordered from diffraction methods.

1.2 Magnetic properties of transition metal oxides

Magnetism in materials arises from the net angular momentum of electrons. This angular momentum can be divided into two parts: the electron orbiting around the nucleus (orbital angular momentum) and the electron spinning around its axis (spin angular momentum). Whilst in principle both of these factors will contribute to the total moment, there is typically strong quenching of the orbital angular momentum in compounds containing 3d transition metals, due to strong interactions between the metal and the ligands, so it is often appropriate to use a spin-only model.

It is possible to model the magnetic moment of a system at two limits: in weak applied magnetic fields and in strong applied magnetic fields. In weak magnetic fields at high temperature, the

effective moment, μ_{eff}, is measured, which corresponds to the absolute magnetic moment. In the spin-only case, this is given by

$$\mu_{\text{eff}} = 2\mu_{\text{B}}\sqrt{S(S+1)} \ . \tag{2}$$

In strong fields at low temperature, the saturated magnetic moment, μ_{sat}, is measured, which corresponds to the projection of the moment onto the *z*-axis. In the spin-only case, this is given by

$$\mu_{\text{sat}} = 2\mu_{\text{B}}S \ . \tag{3}$$

The magnetic properties of a material are typically characterised using the magnetic susceptibility, which quantifies the ability of a material to respond to an applied magnetic field, and is defined as

$$\chi = \frac{\mathrm{d}M}{\mathrm{d}H} \ , \tag{4}$$

where M is the magnetisation of the sample and H is the applied magnetic field.

In extended solids, there are a large number of electrons that can contribute to the magnetic behaviour, giving rise to a diverse range of different phenomena. The simplest cases, in which the atomic moments are isolated and acting independently from each other, are diamagnetism and paramagnetism. However, if the atomic moments are able to interact with each other, a number of different types of cooperative magnetism are possible, some of which will be discussed below.

1.2.1 Diamagnetism

Diamagnetism is a phenomenon exhibited by all materials and results from the movement of electrons in response to an applied field. This motion induces a field that is opposed to the

applied field and, as a consequence, diamagnetism acts to expel field from a material, giving a negative magnetic susceptibility. In general, diamagnetism is a relatively weak phenomenon and is only significant in materials that do not contain any unpaired electrons.

1.2.2 Paramagnetism

Paramagnetism is observed for compounds that contain atoms with unpaired electrons and describes the situation in which the atomic moments are randomly orientated. For systems that contain both non-interacting, localised electrons and temperature-independent moments, the magnetic susceptibility follows the Curie law,

$$\chi = \frac{C}{T} \ , \tag{5}$$

where C is the Curie constant. This temperature dependence arises from the competition between the tendency of thermal agitation to disorder the moments and the tendency of the moments to align with the applied field.

For materials in which the electrons are interacting (Section 1.2.4), the system only behaves as a paramagnet above a certain temperature (T_C or T_N) at which the thermal energy is sufficient to overcome the interactions. In these cases, the magnetic susceptibility can be described using the Cure-Weiss Law,

$$\chi = \frac{C}{T - \theta} \ , \tag{6}$$

where θ is the Weiss constant and, in general, approximately corresponds to the ordering temperature. For situations in which $|\theta|$ is very different to the ordering temperature, it indicates the presence of magnetic frustration.

To take into account effects such as core diamagnetism, Pauli paramagnetism or van Vleck paramagnetism,[28] a temperature independent term, *k*, can be added to the Curie-Weiss law to give

$$\chi = k + \frac{C}{T - \theta} \quad . \tag{7}$$

The magnetic susceptibility of a paramagnet can be related to the effective magnetic moment by the equation,

$$\chi_N = N \frac{\mu_{eff}^2 \mu_0}{3kT} \quad , \tag{8}$$

where *N* is the number of magnetic atoms for which the susceptibility is expressed. Following from this, the effective moment can be determined from *C* using the relationship, $\mu_{eff}^2 = 8C$.

1.2.3 Magnetic superexchange

For materials in which the magnetic atoms are in close enough proximity, it is possible for the moments to interact, giving rise to a variety of cooperative phenomena. In transition metal oxides, the magnetic information is often transmitted through the non-magnetic oxide ion ligands. This process is known as superexchange and arises from the overlap between the transition metal *d* orbitals and the oxide *p* orbitals. The magnetic ordering can be rationalised by considering partial electron transfer between the transition metals and the oxide ions. For the 180° d^3–O–d^3 case shown in Figure 1.5(a) or the 180° high-spin d^5–O–d^5 case shown in Figure 1.5(b), partial electron transfer results in the moments on the two metal centres being aligned antiparallel (antiferromagnetic exchange). Meanwhile, for the high spin d^5–O–d^3 case shown in Figure 1.5(c), partial electron transfer results in the moments on the two metal centres being aligned parallel (ferromagnetic exchange).

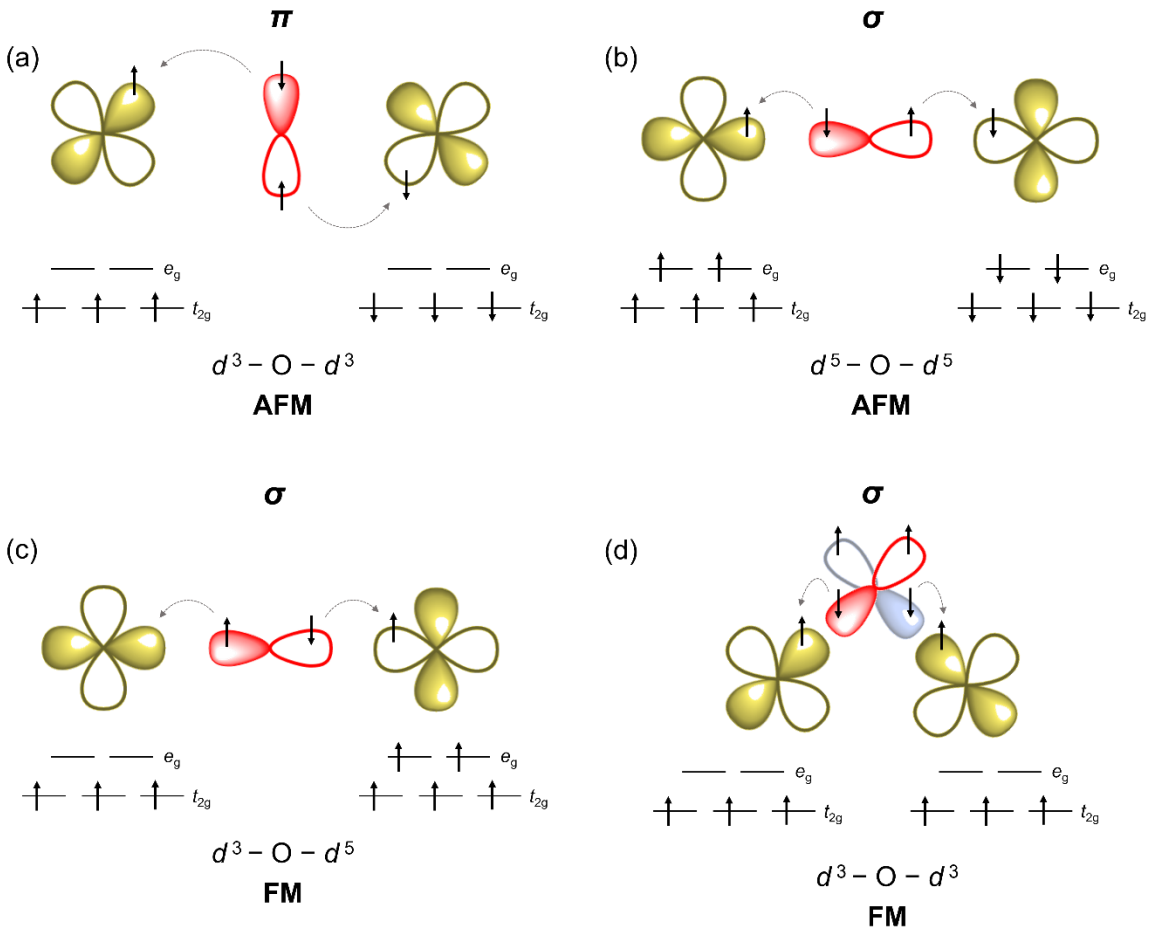

Figure 1.5: Superexchange interactions between octahedrally coordinated transition metals via oxide ligands.

When there is a 90° M−O−M angle, different *p* orbitals are overlapping with each metal, so the *p* electrons that are being partially transferred will be aligned parallel to each other. For the d^3–O–d^3 case, this leads to ferromagnetic coupling, as shown in Figure 1.5(d). Typically, superexchange arising from a 90° interaction is weaker than that arising from a 180° interaction.

These principles form the basis of a set of rules known as the Goodenough-Kanamori rules, which can be used to predict the type of superexchange expected between pairs of transition metal ions.[29,30]

Although the Goodenough-Kanamori rules are typically accurate for interactions between 3d transition metal cations, they often incorrectly predict the interactions between 3d and 4d or 5d

transition metals. For example, La_2CoRuO_6 and La_2NiRuO_6 contain Co^{II} ($t_{2g}^5e_g^2$)/Ni^{II} ($t_{2g}^6e_g^2$) and Ru^{IV} ($t_{2g}^4e_g^0$), so would be expected to adopt ferromagnetic structures from the Goodenough-Kanamori rules, but, in fact, adopt antiferromagnetic structures with ordering temperatures of around 25 K.[31,32] Similarly, Sr_2FeOsO_6 contains Fe^{III} ($t_{2g}^3e_g^2$) and Os^{V}(t_{2g}^3), so ferromagnetic ordering would be predicted, but the compound, in fact, orders antiferromagnetically at ~140 K.[33,34]

1.2.4 Types of magnetic order

Magnetic superexchange, along with other types of exchange interaction, can lead to a diverse range of complex magnetic ordering. A selection of these, that are commonly observed in transition metal oxides, will be considered below.

1.2.4.1 Ferromagnetism

In ferromagnetic materials, the spins are aligned parallel to each other below a temperature known as the Curie temperature, T_C. In these materials, the magnetisation preferentially aligns along a specific crystallographic direction and there is an energy barrier associated with reorientation of the magnetisation (anisotropy energy).

Despite the fact that individual coupling interactions work to align the spins parallel to each other, if a ferromagnet is cooled below T_C in the absence of a field, the initial magnetisation will be close to zero. This is due to the formation of magnetic domains within the structure, which arrange themselves such that the overall magnetisation is zero. This occurs because, although the formation of domain walls is energetically unfavourable, alignment of all the spins would require the material to send an opposing magnetic field through neighbouring space, which is also energetically unfavourable (magnetostatic energy). In general, in the absence of an applied field, the magnetostatic energy outweighs the energy required to form domain walls and, as a consequence, the material will have zero net magnetisation. However, if a ferromagnet

is cooled below T_C in the presence of a field, all the spins will align with the field, and the magnetisation of the material will be saturated. When the field is removed after saturation, ferromagnetic materials typically exhibit a remnant magnetisation, which occurs due to the anisotropy energy, which provides an energy barrier for reorientation of the moments. This results in the observation of a hysteresis loop in magnetisation-field isotherms.

1.2.4.2 Antiferromagnetism

In antiferromagnetic materials, the sum over all spin vectors is zero below a temperature known as the Néel temperature, T_N, which commonly arises from the alignment of spins anti-parallel to each other. As such, when an antiferromagnetic material is cooled below T_N, its susceptibility decreases below that of the paramagnetic state. In some antiferromagnets, the spins align themselves at a small angle to each other rather than being exactly anti-parallel. This is known as spin canting and results in the material having a net magnetic moment and behaving like a weak ferromagnet.

Ferrimagnetism is a special class of antiferromagnetism, in which inequivalent spins are aligned antiparallel to each other, which results in the presence of an overall net magnetic moment. As a consequence, the bulk properties of ferrimagnets are similar to those of ferromagnets.

1.2.4.3 Spin glasses

In some situations, it is not possible to simultaneously satisfy all the strong pairwise interactions in a system. For example, in a system containing a triangular arrangement of spins (Figure 1.6), if two of the spins are aligned antiferromagnetically, the third spin will necessarily be aligned ferromagnetically to one spin and antiferromagnetically to the other. As a consequence, both spin orientations are equally favourable. This situation is known as magnetic frustration and results in there being a large number of degenerate ground states, which do not

exhibit long-range magnetic order. If both chemical disorder and magnetic frustration are present in a system, then cooling the system below the glass transition temperature, T_g, will cause the spins to freeze into one of the degenerate ground states. This frozen arrangement of spins is known as a spin glass. When a spin glass is cooled through T_g under an applied field, a specific subset of the degenerate ground states is favoured and, as a result, magnetisation-field isotherms measured from spin glasses below T_g are vertically displaced. To confirm the presence of a spin glass state, AC susceptibility measurements can be performed. Application of a high frequency AC field will result in a higher T_g being observed, whilst application of a lower frequency field will result in a lower T_g being observed.

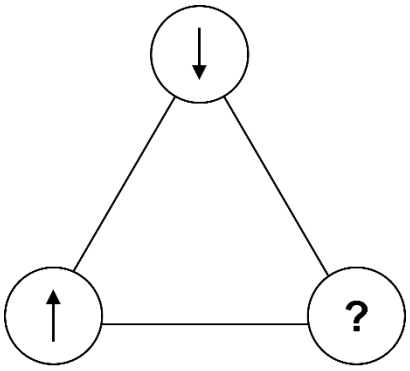

Figure 1.6: For a triangular arrangement of spins with antiferromagnetic coupling, the third spin must necessarily be aligned ferromagnetically to one spin and antiferromagnetically to the other, leading to magnetic frustration.

1.2.4.4 Superparamagnetism

For materials that contain ferromagnetic or ferrimagnetic superexchange interactions, superparamagnetic behaviour can be observed if the anisotropy energy is smaller than $k_B T$.[35] The weak anisotropy required to observe superparamagnetic behaviour is often achieved by decreasing the size of the particles below ~100 nm. In this regime, the weak anisotropy means that all the spins in the particle align themselves with the applied field and only a single domain is present. For these materials, no coercivity is observed and the magnetisation of the particles can be approximated as one large magnetic moment made up of the sum of the individual

moments of each constituent atom. As a result, the behaviour of superparamagnets is qualitatively similar to that of paramagnets, but with a much larger magnetic moment.

To observe superparamagnetic behaviour, the measurement time, τ_m, must be greater than the Neel relaxation time, τ_N. In this regime, the magnetisation flips several times during the measurement, so the net moment is zero and superparamagnetic behaviour is observed. If $\tau_m < \tau_N$, the magnetisation does not flip during the measurement, so the measured magnetisation is just the instantaneous magnetisation at the beginning of the measurement. The temperature at which $\tau_m = \tau_N$ is known as the blocking temperature, T_B. Above T_B, the material exhibits superparamagnetic behaviour, whereas, below T_B, the material behaves as a ferromagnet.

1.3 Electronic properties of transition metal oxides

1.3.1 Ligand field theory

For transition metals in octahedral coordination geometries, the energies of the *d*-orbitals are split into a t_{2g} level (d_{xy}, d_{xz} and d_{yz}) and an e_g level ($d_{x^2-y^2}$ and d_{z^2}). For transition metals with a *d*-electron count of greater than 3, the cations can adopt either a high-spin or a low-spin configuration. Which of these configurations a transition metal cation adopts depends on the relative magnitudes of the crystal field splitting energy (Δ) and the pairing energy (P). In general, when $\Delta < P$, a high-spin configuration is preferred, whereas, when $\Delta > P$, a low-spin configuration is preferred. The size of Δ depends on both the identity/charge of the transition metal cation and the type of ligand. For 3d transition metal cations with oxide ligands, Δ is typically relatively small, resulting in a high-spin configuration. However, for 5d transition metal cations, the spatially diffuse 5*d* orbitals have a strong degree of overlap with the ligand orbitals, leading to a larger value of Δ and, as a consequence, 5d transition metals with oxide ligands tend to adopt a low-spin configuration.

1.3.2 Band theory and the Hubbard model

In an extended array of atoms, the atomic orbitals interact with each other to form crystal orbitals. As the number of atoms increases, the crystal orbitals become more closely spaced in energy. When the number of atoms becomes sufficiently large, the energy levels of the crystal orbitals become so closely spaced that they can be considered as a continuous distribution of states that form an energy band, as shown in Figure 1.7.

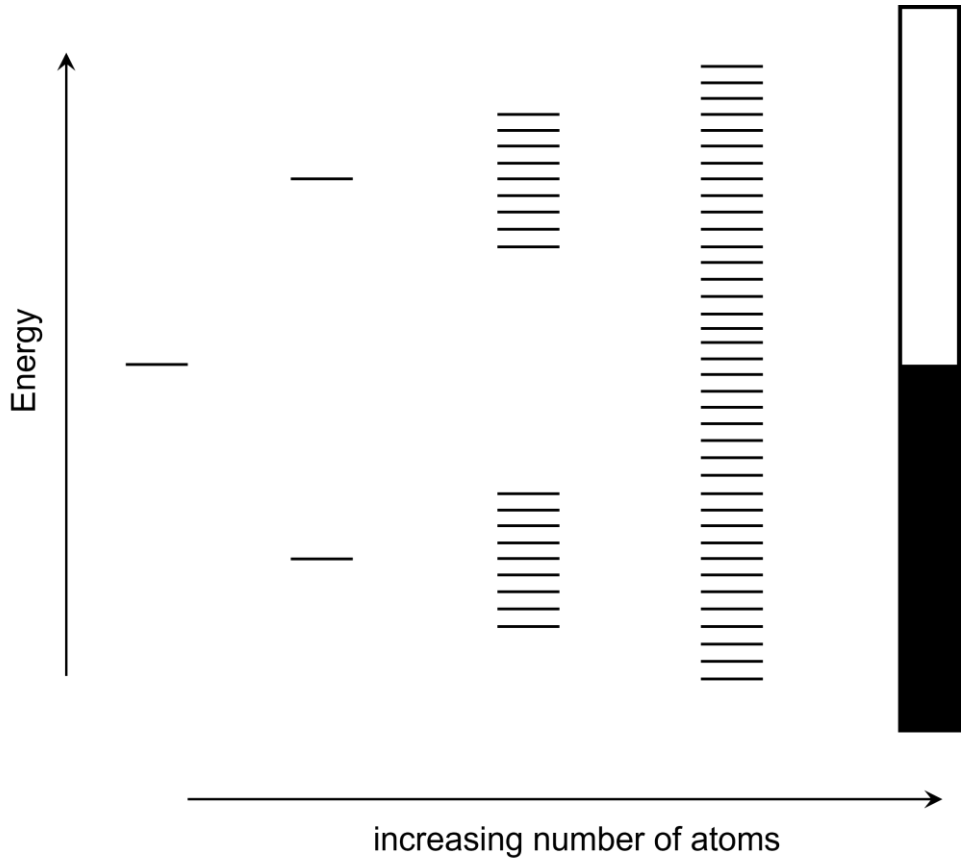

Figure 1.7: Schematic representing the crystal orbital energies as the number of interacting atomic orbitals increases. For an infinite periodic solid, the orbitals can be thought of as forming a continuous band, as shown on the right of the diagram.

If a material contains a partially filled band, it is classified as a metal. Meanwhile, if a material contains a fully occupied valence band and an empty conduction band separated by a band gap, E_g, it is classified as a semiconductor or an insulator.

There are some materials that might be predicted to be a metal, but are, in fact, insulators. For example, although NiO and CoO might be expected to have partially filled *d*-bands, they are actually antiferromagnetic insulators.[36,37] To account for this, it is necessary to incorporate on-site electronic repulsions into simple band theory, as described by the Hubbard model.[38] In this model, when an electron hops from an orbital on one atom to an orbital on a neighbouring atom, the electronic repulsion from the resulting double occupation means that there is an energy penalty associated with this hopping process. This energy penalty splits the band into two sub-bands, separated by a Mott-Hubbard gap with magnitude of the on-site electronic repulsion, *U*. Whether a system is metallic or insulating depends on the relative magnitudes of the bandwidth, *W*, and the on-site repulsion, *U*. When *W* is small, the on-site repulsion splits the band, leading to Mott insulating behaviour. However, when $W \geq U$, the sub-bands overlap, leading to metallic behaviour, as shown in Figure 1.8.

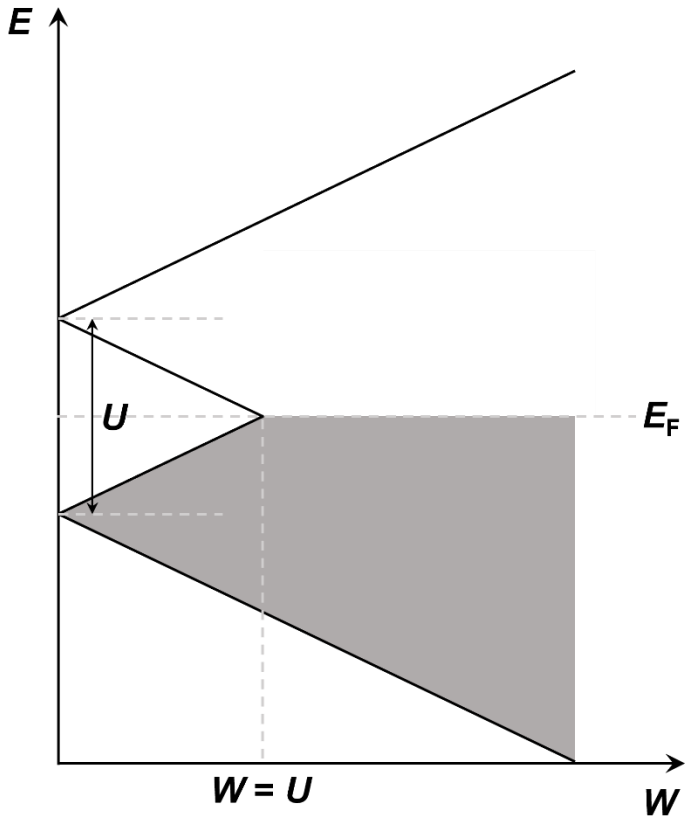

Figure 1.8: Schematic illustrating how competition between on-site repulsion, *U*, and bandwidth, *W*, determines whether a material is a metal or a Mott-Hubbard insulator.

1.3.3 Spin-orbit coupling

For an electron residing in an atomic orbital, the nucleus can be thought of as orbiting the electron with an angular momentum, *l*. The spin of the electron, *s*, can couple to this orbital angular momentum to give the total angular momentum, *j*.

The magnitude of this spin-orbit coupling is proportional to Z^4 and, as a result, spin-orbit coupling is small for relatively light elements, such as the 3d transition metals. Consequently, the Russell-Saunders coupling scheme can be used to describe the electronic structure. In this regime, the total angular momentum, *J*, can be obtained from the sum of the total spin, *S*, and the total angular momentum, *L*,

$$J = \sum_i l_i + \sum_i s_i \, . \tag{9}$$

For heavy elements, such as 5d transition metals, however, the strong-spin orbit coupling means that Russell-Saunders coupling can no longer be applied and, instead, *j-j* coupling must be considered. In this regime, each individual spin-orbit interaction, (*s* + *l*), must be considered separately and the total angular momentum, *J*, is obtained from the sum of these interactions. As such, the total angular momentum in the *j-j* coupling scheme is described by the equation,

$$J = \sum_i (s_i + l_i) \, . \tag{10}$$

Due to its large magnitude in 5d transition metals, spin-orbit coupling can have a significant effect on the band structure of Ir-containing oxides, and much attention has been focussed on the properties of materials containing Ir^{4+} and Ir^{5+}.[39] For example, in $NaIrO_3$, where Ir is present in the +5 oxidation state, the t_{2g} band is split into a fully-occupied $J_{eff} = 3/2$ quartet and unoccupied $J_{eff} = 1/2$ doublet and, as a result, the compound is an insulator (Figure 1.9(a)).[40,41]

Meanwhile, Sr_2IrO_4, which contains Ir in the +4 oxidation state, might be expected to have a half-occupied $J_{eff} = 1/2$ band and, therefore, be a metal. However, in fact, the $J_{eff} = 1/2$ band is

sufficiently narrow that it is split by relatively weak on-site repulsions (U), and, as a result, the compound is a Mott insulator (Figure 1.9(b)).[42,43]

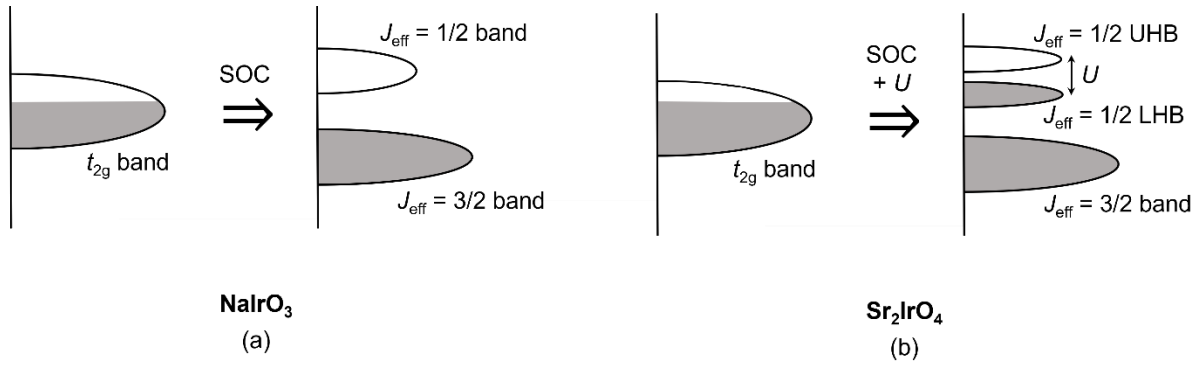

Figure 1.9: Schematic band diagrams for (a) $NaIrO_3$ ($5d^4$), in which the t_{2g} band is split into a J_{eff} = 3/2 band and a J_{eff} = 1/2 band by spin-orbit coupling, and (b) Sr_2IrO_4 ($5d^5$), in which the J_{eff} = 1/2 band is further split into two Hubbard bands by on-site repulsions, resulting in Mott insulating behaviour.

1.4 Topochemical reduction of transition metal oxides

Conventionally, transition metal oxides are synthesised via high temperature methods. Under these conditions, there is sufficient energy to overcome the activation energy barrier for all possible reaction products, so only the most thermodynamically stable product or mixture of products is formed. However, by performing reactions on transition metal oxides at relatively low temperature, it is possible to exploit the higher mobility of the anions relative to the cations to modify the anion sub-lattice whilst leaving the overall structural framework intact. This can lead to the formation of metastable structures, in which the transition metals have oxidation states or coordination environments that are not accessible using standard thermodynamic routes.

1.4.1 Topochemically reduced anion deficient phases

Binary metal hydrides are a common class of reagent to perform anion deintercalation from transition metal oxides. For example, NaH can act as a strong reducing agent at low temperatures (150−210 °C), allowing oxide ion deintercalation to be achieved via the reaction,

$$ABO_3 + NaH \rightarrow ABO_{3-x} + NaOH. \quad (11)$$

This is exemplified by the formation of the infinite-layer phase, $LaNiO_2$, from $LaNiO_3$ by reacting with NaH at temperatures between 190 and 210 °C (Figure 1.10).[44] Alternatively, CaH_2 can be used to perform anion deintercalation via the reaction,

$$ABO_3 + CaH_2 \rightarrow ABO_{3-x} + CaO + H_2. \quad (12)$$

For example, the infinite-layer phase, $SrFeO_2$, can be prepared by reacting $SrFeO_3$ with CaH_2 at 250 °C, allowing Fe^{2+} to be accessed in a highly unusual square-planar coordination environment.[45]

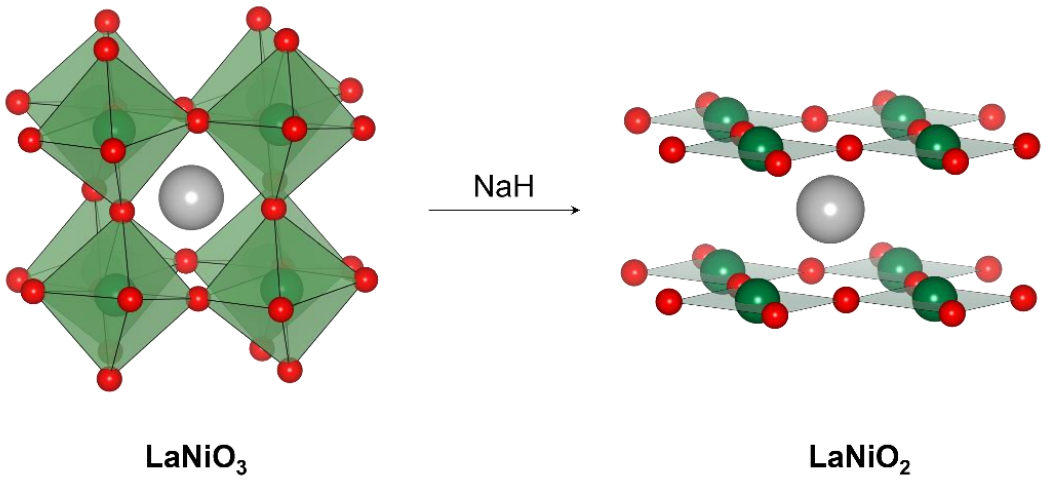

Figure 1.10: Reaction of $LaNiO_3$ with NaH to form the infinite-layer phase $LaNiO_2$.

An alternative approach that has been employed to perform anion deintercalation is the use of finely divided zirconium metal as an oxygen getter. The reaction mechanism when perovskite oxides are heated in the presence of a Zr getter is proposed to be:

$$ABO_3 \rightleftharpoons ABO_{3-x} + \tfrac{1}{2}\, x\, O_2 \quad (13)$$

$$Zr + \tfrac{1}{2}\, x\, O_2 \rightarrow ZrO_x. \quad (14)$$

The Zr getter maintains a very low partial pressure of oxygen in the reaction vessel, thereby favouring the formation of oxygen-deficient perovskite structures. This technique has been used to perform anion deintercalation from the n = 1 Ruddlesden-Popper phases, Sr_4CoIrO_8 and $LaSr_3CoIrO_8$, to form the infinite-chain phases, Sr_4CoIrO_6 and $LaSr_3CoIrO_6$, as shown in Figure 1.11.[46] These compounds contain iridium in the +2 oxidation state, which is much lower than the +4 or +5 oxidation states typically observed in extended oxide systems.

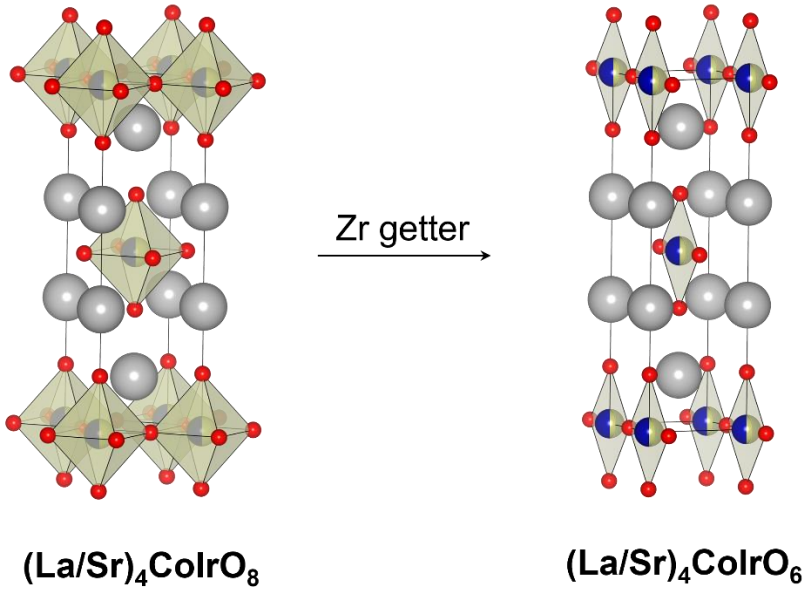

Figure 1.11: Reaction of $(La/Sr)_4CoIrO_8$ with a Zr getter to form $(La/Sr)_4CoIrO_6$.

1.4.2 Oxyhydride phases

In addition to anion deintercalation, binary metal hydrides (CaH_2 and LiH) have been widely used to perform anion exchange to yield oxyhydride materials. The first example of the preparation of a transition metal oxyhydride was the formation of $LaSrCoO_3H_{0.7}$ from the reaction of the n = 1 Ruddlesden-Popper phase, $LaSrCoO_4$, with CaH_2 at 450 °C.[47] The strong covalency associated with the Co−H bonds in this compound leads to strong magnetic coupling, resulting in a magnetic transition temperature of above 350 K.

Reaction of $SrVO_3$ with CaH_2 at 610 °C results in exchange of the apical oxide ions in the VO_6 octahedra with hydride ions to give a compound with composition, $SrVO_2H$, containing *trans*-

VO_4H_2 units.[48] Overall, the structure of this compound can be described as a layered structure consisting of planes of corner-sharing VO_4 square-planar units separated by ordered SrH layers, as shown in Figure 1.12(a). However, repeating the reaction with a titanium-doped analogue, $SrV_{0.95}Ti_{0.05}O_3$, does not yield an equivalent anion-ordered phase but instead gives a cubic, anion-disordered phase with composition $SrV_{0.95}Ti_{0.05}O_{1.5}H_{1.5}$ (Figure 1.12(b)).[49] To rationalise this, the interplay between the nature of the hydride ligand and the effect of the transition metal electronic configuration needs to be considered.

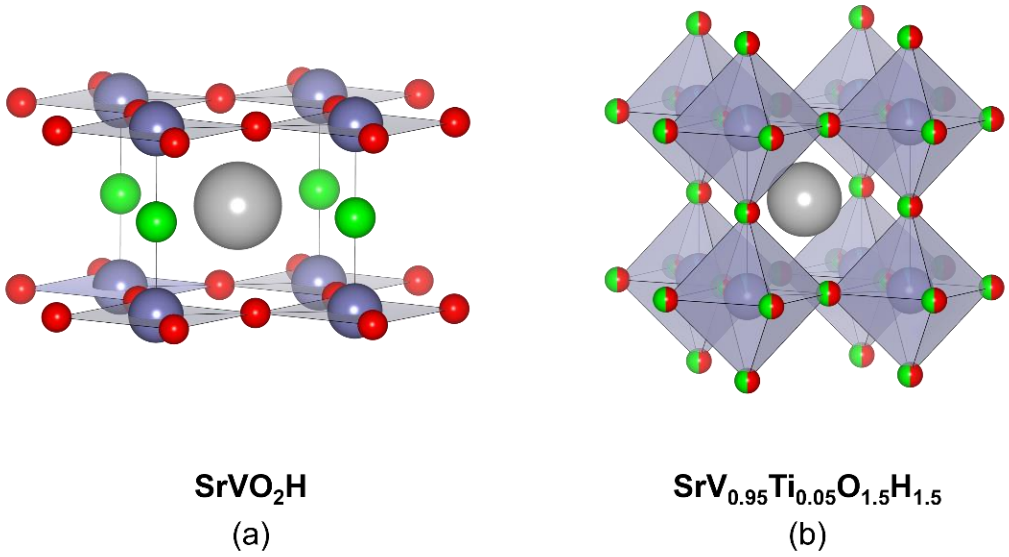

Figure 1.12: Crystal structure of (a) $SrVO_2H$ with an anion-ordered, tetragonal structure and (b) $SrV_{0.95}Ti_{0.05}O_{1.5}H_{1.5}$ with an anion-disordered, cubic structure.

In general, hydride ions prefer to adopt *cis*-arrangements with respect to each other around transition metal centres. This arises from the fact that hydride is a strong σ-donor, so exerts a strong *trans*-influence. However, when the transition metal centres have d^2 or high-spin d^7 configurations, maximum π-stabilisation is achieved when the hydride ions are located *trans* to each other, which overrides the preference for the hydride ions to be mutually *cis*. When the ligands are aligned in this way, the t_{2g} orbitals are split into a doubly degenerate (d_{xz}, d_{yz}) pair and a destabilised d_{xy} orbital, as shown in Figure 1.13, leading to a net electronic stabilisation. As such, this provides an electronic driving force for the hydride ions to adopt a *trans*-

arrangement when the transition metals have d^2 or high-spin d^7 configurations. Meanwhile, for other electronic configurations, such as those in $SrV_{0.95}Ti_{0.05}O_{1.5}H_{1.5}$ (d^1) and $SrCrO_2H$ (d^3),[50] there is no π-bonding preference for the hydride ions to adopt *cis*- or *trans*-arrangements, so the hydride ions preferentially adopt *cis*-arrangements.

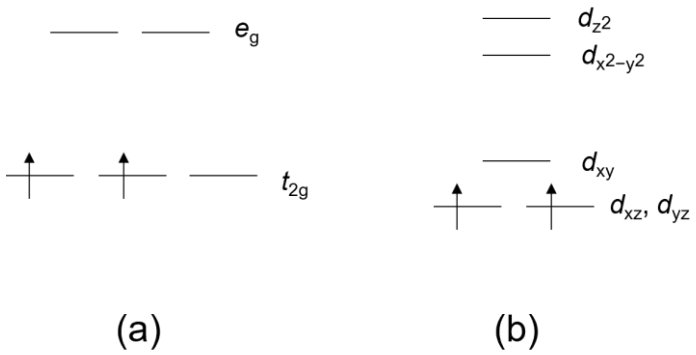

Figure 1.13: Crystal field splitting for (a) a regular octahedral environment and (b) V^{3+} centres in which the hydride σ-donors are *trans* to each other.

Recently, the compositional space of oxyhydrides has been expanded to include 4d transition metals with the synthesis of $LaSr_3NiRuO_4H_4$, $La_2Sr_2CoRhO_6H_2$ and $LaSr_3MnRhO_6H_2$.[51,52] These phases are all based on the n = 1 Ruddlesden-Popper structure, and are formed from the reaction of the all-oxide parent phases with CaH_2. The stability of these phases has been attributed to the formation of strong Ru−H and Rh−H σ-type bonds.

It is worth noting that, in addition to topochemical reduction, it is also possible to prepare oxyhydrides directly through either high-pressure, high-temperature synthesis (eg $LaSrMnO_{3.3}H_{0.7}$, Sr_2VO_3H, $SrCrO_2H$, $BaScO_2H$, Ba_2YHO_3)[50,53–56] or mechanochemical synthesis (eg $BaVO_2H$, $BaScO_2H$, $BaYO_2H$).[57,58] However, these methods are beyond the scope of this thesis.

1.5 Motivation of this work

Oxyhydrides represent an interesting class of materials due to the strongly contrasting features between oxide and hydride ions. The higher polarizability and lower electronegativity of

hydride ions compared to oxide ions can result in greater covalency and stronger magnetic interactions. Additionally, the absence of valence orbitals with π-symmetry in hydride ions means that they can block interactions between orbitals with π-symmetry, thereby dramatically altering the orbital connectivity within the compound and generating materials with interesting properties, such as reduced dimensionality in their electronic and magnetic structures. Meanwhile, in iridium, there is a competition between the spatially diffuse nature of the 5*d* orbitals, which would be expected to broaden the metal-based *d*-band (large *W*), and the strong spin-orbit coupling, which would be expected to split the bands. These competing tendencies to widen and narrow the bands could lead to materials with interesting electronic properties. Therefore, this thesis will explore the reactivity of Ir-containing phases with binary metal hydrides with the aim of preparing the first oxyhydride materials containing a 5d transition metal.

In addition, low oxidation states of iridium (eg Ir^{2+}, Ir^{3+}) in extended oxides have not been extensively studied. Therefore, the preparation of anion-deficient perovskite-based phases through topochemical methods have been performed to access iridium in these oxidation states, allowing their properties to be investigated.

In this thesis, mixed 3d/5d perovskite-based oxides were chosen to be investigated. This is because previous work has shown that the positive reduction potential of iridium ions with respect to the elemental metal ($Ir^{3+} + 3e^- \rightleftharpoons Ir$; $E° = +1.156$ V)[59] leads to the decomposition of the perovskite framework when materials containing only Ir at the B-site are treated with reducing agents. By incorporating 3d transition metals, which are more robust with respect to reduction, these ions hold the overall perovskite framework together, thereby allowing Ir to be reduced without decomposition of the overall framework.[60,61]

Chapter 2 – Experimental methods and techniques

2.1 Ceramic synthesis

All the thermodynamically stable transition metal oxide phases described in this thesis were prepared using conventional high-temperature ceramic synthesis techniques. Stoichiometric amounts of appropriate starting reagents, such as binary metal oxides and carbonates, were thoroughly mixed together using an agate mortar and pestle. The resulting powders were pressed into 13 mm diameter pellets to minimise diffusion lengths and improve grain contact of reagents. They were then typically heated at 1000 °C for 2 days to decompose any carbonates. Following this heating cycle, the pellets were thoroughly reground and repelletised, before being heated at the reaction temperature. In general, temperatures of over 1000 °C were required to overcome the large energetic barriers to diffusion within solids. The reaction progress was monitored using laboratory powder X-ray diffraction. The samples were heated for multiple 2 day cycles until a homogeneous single phase was achieved or until consecutive heating cycles showed no change in the PXRD pattern.

2.2 Topochemical reduction

The oxygen-deficient or oxyhydride phases prepared through topochemical reduction are typically air-sensitive and react slowly with oxygen in the air to reform the parent oxides. In addition, the reducing agents used to perform the reactions react readily with oxygen and water in the air to form oxides and hydroxides. Therefore, the reaction mixtures and products need to be handled under air-sensitive conditions.

To this end, topochemical reductions were set up, and the products were stored, in an Ar-filled glovebox, in which the oxygen and water partial pressures were maintained below 0.1 ppm. The internal atmosphere of the glovebox was constantly circulated over a copper catalyst to

maintain low oxygen and moisture contents. When the catalyst was saturated, it was regenerated by heating under 5% H_2/N_2 gas flow.

2.2.1 Binary metal hydride reactions

One approach to modify the anion sub-lattice of transition metal oxides is to react them with binary metal hydrides at relatively low temperature to form anion-deficient or oxyhydride phases.[62] The topochemical reductions can be described using the following reaction schemes:

$$ABO_3 + NaH \rightarrow ABO_{3-x} + NaOH \quad (15)$$

$$ABO_3 + CaH_2 \rightarrow ABO_{3-x}H_y + CaO + H_2 \quad (16)$$

$$ABO_3 + LiH \rightarrow ABO_{3-x}H_y + Li_2O + H_2. \quad (17)$$

Reaction of transition metal oxides with NaH results in the formation of anion-deficient phases, whilst reaction with CaH_2 or LiH can yield either anion-deficient phases or oxyhydride phases. Each of these reagents have different temperature ranges in which they are active: NaH is active in the range 150−220 °C,[44] LiH is active in the range 150−550 °C,[63] and CaH_2 is active in the range 200−885 °C.[59,64]

The reactions were performed by thoroughly mixing the parent oxide phase with the binary metal hydride in an Ar-filled glovebox, and sealing the mixture in an evacuated Pyrex® or silica ampoule. The sealed ampoule was heated to the desired reaction temperature at 1 °C min^{-1} and held at that temperature for a suitable period of time. The ampoule was opened inside the glovebox and the reaction was monitored by powder X-ray diffraction.

By performing the reaction inside a sealed glass ampoule, H_2 gas formed during the reaction can build up inside the reaction vessel. The generation of this hydrogen partial pressure can promote the formation of oxyhydride phases, as opposed to oxygen deficient phases.[65]

After reaction between transition metal oxides and binary metal hydrides, the product is contaminated with unreacted binary metal hydride (NaH, LiH, CaH_2) and the corresponding by-product (NaOH, Li_2O, CaO). These are removed by washing the reaction mixture with an appropriate solvent under an N_2 atmosphere using standard Schlenk techniques. Following the washing process, the sample is dried under vacuum and returned to the glovebox.

2.2.2 Zirconium getter reactions

An alternative approach to perform anion deintercalation in transition metal oxides is to heat the sample in the presence of finely divided zirconium metal.[66] This process can be described using the following reaction schemes:

$$ABO_3 \rightleftharpoons ABO_{3-x} + \tfrac{1}{2}\, x\, O_2 \quad (18)$$

$$Zr + \tfrac{1}{2}\, x\, O_2 \rightarrow ZrO_x. \quad (19)$$

In general, the Zr particles have a thin outer coating of ZrO_2. As such, to allow Zr to act as an effective getter, the oxide ion mobility between the surface and the bulk of the Zr particles must be high. Therefore, reactions with Zr getters typically require temperatures of 400 °C or above to allow the oxide ions in ZrO_x to be sufficiently mobile.

To perform the reactions, Zr metal was placed in a Pyrex® or silica ampoule with a dent several centimetres from its base. The parent oxide was then loaded into a small glass thimble, which was subsequently sealed in the dented ampoule under vacuum. This set-up is shown in Figure 2.1, and ensures that the two powders share an atmosphere but are not in physical contact. The sealed ampoule was heated to the desired reaction temperature at 1 °C min^{-1} and held at that temperature for a suitable period of time. The ampoule was opened inside the glovebox and the reaction was monitored by powder X-ray diffraction.

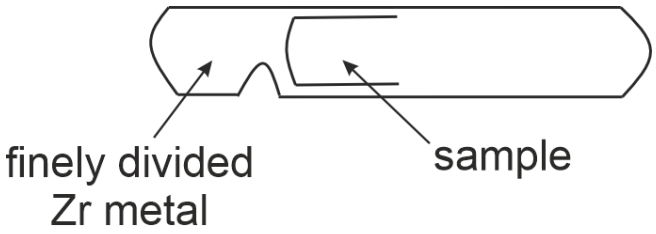

Figure 2.1: Schematic representation of Zr getter reaction set-up.

2.3 Powder diffraction

An ideal crystal is made up of an infinite array of atoms or molecules in an ordered arrangement such that the entire structure can be built up through translational displacements of a single unit cell. Since X-ray and neutron radiation have wavelengths that are comparable to the interatomic distances in a crystal, when they are incident on a crystal structure, there is elastic scattering of the radiation by the atoms. In most directions, there is destructive interference between the waves, resulting in regions of low intensity in the diffraction pattern. However, in specific directions, there is constructive interference and, as a result, maxima are observed at these positions.

If the atom types and positions are known, it is possible to calculate the structure factor for a crystal structure,

$$F_{hkl} = \sum_{1}^{N} f_n e^{2\pi i(hx_n + ky_n + lz_n)} \; e^{-B\sin^2\theta/\lambda}. \qquad (20)$$

In this expression, the sum is over all the atoms in the unit cell, f_n is the atomic form factor (which is replaced with the scattering length, b_n, in neutron diffraction), h, k and l are the Miller indices, x_n, y_n and z_n are the atomic fractional coordinates of atom n in the unit cell and B is the isotropic displacement parameter.[67] The detected intensity is then proportional to $|F_{hkl}|^2$. In this

way, radiation is scattered by a crystal in discrete directions determined by the periodicity of the structure, to give a diffraction pattern.

The simplest way of understanding the peak positions in diffraction patterns and determining information about the unit cell is through the Bragg equation.[68] This describes diffraction as the reflection of radiation by sets of lattice planes, separated by the distance, d_{hkl}, and characterised by the Miller indices. The Miller indices for a given plane are defined as the reciprocals of the fractional intercepts that the plane make with the crystallographic axes. From Figure 2.2, the path difference between the waves reflected off the two planes is given by $\Delta = PN + NQ$. For constructive interference to occur, this path difference must be an integer multiple, n, of the wavelength,

$$\Delta = n\lambda \quad . \tag{21}$$

For any other path difference, it is always possible to find a deeper plane with $\Delta = m\lambda$, where m is a half-integer, leading to destructive interference and, therefore, no signal. From Figure 2.2, we can obtain the trigonometric relation,

$$\Delta = 2d \sin \theta \quad . \tag{22}$$

Combining Equations 21 and 22 gives the Bragg equation,

$$n\lambda = 2d \sin \theta \quad . \tag{23}$$

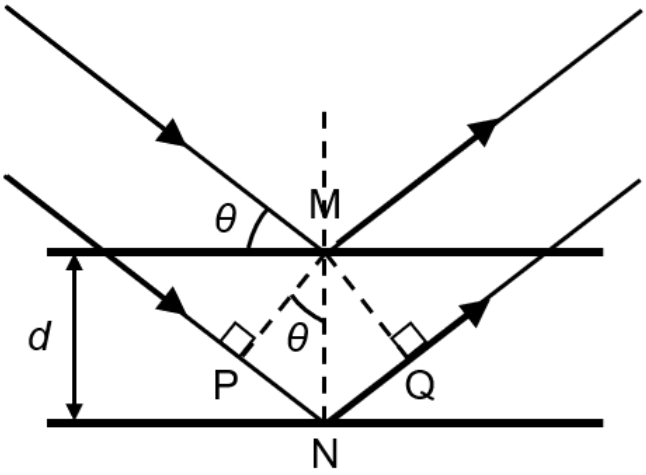

Figure 2.2: Geometry used for derivation of the Bragg equation.

For each of the seven crystal systems, it is possible to derive equations linking d_{hkl} with the cell parameters. For the orthorhombic crystal system, the expression is

$$\frac{1}{d_{hkl}^2} = \frac{h^2}{a^2} + \frac{k^2}{b^2} + \frac{l^2}{c^2} \quad . \tag{24}$$

2.3.1 Powder X-ray diffraction

In this thesis, powder X-ray diffraction was used to monitor reaction progress and to determine the crystal structure. X-ray radiation is scattered by the electrons bound to the atoms in the crystal structure and, as a result, the scattering power of an atom (f_n) increases with its atomic number (Z). As a consequence, X-ray diffraction is insensitive towards the identity and location of light elements in the presence of heavy elements.

2.3.1.1 Panalytical Empyrean diffractometer

A Panalytical Empyrean diffractometer, incorporating a PIXcel1D detector, was used to collect some of the X-ray diffraction data in this thesis. The diffractometer adopts Bragg-Brentano geometry and uses Cu Kα radiation. A Ge(111) monochromator is installed to ensure only Cu $K\alpha_1$ radiation is present. The measurements were performed using 0.04 radian soller slits. The

samples were prepared by loading the powder onto a lightly greased glass slide and mounting the slide into the flat stage sample holder of the diffractometer. For air sensitive measurements, a custom-made air-sensitive sample holder with Mylar windows was used, which was sealed by compressing a brass cap against an O-ring.

2.3.1.2 Bruker D8 Advance Eco diffractometer

A Bruker D8 Advance Eco diffractometer using Cu Kα radiation was also used to collect X-ray diffraction data in this thesis. The diffractometer is equipped with a Lynx-eye detector that filters Cu Kβ radiation. No monochromator is fitted to the diffractometer, so both Cu $K\alpha_1$ and Cu $K\alpha_2$ radiation irradiate the sample. 2.5° soller slits were used to limit axial divergence and a knife held at 2 mm over the sample was used to block X-rays scattered from air or slits. The samples were prepared by loading the powder onto a lightly greased glass slide and mounting the slide in the sample holder. For air sensitive measurements, a custom-made air-sensitive sample holder with Mylar windows was used, which was sealed by compressing the X-ray lid against an O-ring.

2.3.1.3 Synchrotron powder X-ray diffraction

In a synchrotron, electrons are accelerated to very high speeds through a series of particle accelerators before entering a storage ring. In the storage ring, the electron beam is bent by magnets, which causes it to emit X-ray radiation. The radiation has very high intensity and low beam divergence. This means that a very narrow wavelength range can be used to collect the data, which allows a very high resolution to be achieved, whilst maintaining an excellent signal-to-noise ratio.

All synchrotron powder X-ray diffraction data in this thesis were collected on the I11 beamline at the Diamond Light Source.[69–71] I11 is a high resolution powder diffraction beamline with an X-ray energy range of 5−25 keV. The wavelength of the incident X-ray radiation is selected

using a double-crystal-monochromator comprised of two liquid nitrogen cooled Si(111) crystals. Data are collected using a position sensitive detector made up of Mythen-2 modules. To collect data at temperatures of 30−1000 °C, a hot air blower is used to heat the sample, and to collect data at temperatures of 100−500 K, a Cryostream Plus is used to cool the sample.

Samples were loaded and sealed in borosilicate/quartz capillaries with diameter of 0.3 mm, which were then mounted into brass holders with magnetic bases. These sample holders were loaded onto a magnetic stage pre-aligned such that the capillary is located at the centre of the X-ray beam. The capillaries were spun during the measurement.

2.3.2 Neutron powder diffraction

Neutron powder diffraction is a useful technique for crystal structure determination, as it can provide information that is complementary to X-ray diffraction. The principal difference between X-ray diffraction and neutron diffraction is that neutrons are scattered from the nuclei of atoms. Each nucleus has a characteristic scattering length, which varies both across the periodic table and among the isotopes of a given element. The neutron scattering lengths of atoms do not follow a smooth trend as a function of atomic number and, as a consequence, neutron diffraction can be used to accurately determine the positions and occupancies of light atoms. In addition, unlike the atomic form factor, the neutron scattering length is independent of scattering angle, which means that diffraction peaks collected at high angle have high intensity and can be reliably used to extract structural information.

Since neutrons possess a magnetic dipole moment, if a compound exhibits magnetic ordering, the neutrons will scatter from the periodically arranged moments. This scattering allows the magnetic structure of the material to be determined.

For each measurement, the samples were loaded into vanadium cans, which were sealed under argon using indium wire. Vanadium was chosen for the sample cans since this has a small

scattering length of −0.382 fm,[72] which means that it only has a small scattering contribution to the diffraction data.

In this thesis, neutron powder diffraction data were collected using the POLARIS and GEM instruments at the ISIS neutron and muon source and the D20 and D2B instruments at the Institut Laue-Langevin (ILL).

2.3.2.1 ISIS neutron and muon source

The ISIS neutron and muon source uses spallation to generate neutrons. A proton accelerator produces intense pulses of protons that are fired at tungsten targets. When the protons hit the tungsten nuclei, this triggers emission of a pulse of neutrons. These neutrons have very high energies. Therefore, to slow down the neutrons so that they have an appropriate wavelength for diffraction, a moderator made from a material with low atomic number and low neutron absorption, such as hydrogen, is used. The neutrons scatter repeatedly off the hydrogen nuclei of the moderator until they reach thermal equilibrium with the moderator material and have an appropriate wavelength for diffraction measurements.

Diffraction measurements performed at the ISIS neutron and muon source use the time-of-flight technique. These measurements employ a pulse of neutrons with a range of energies, with detectors located at various fixed angles. The diffraction data are collected with respect to the time taken for the neutrons to travel from the moderator to the detector via the sample. The wavelength of the neutrons is related to time-of-flight by the equation,

$$\lambda = \frac{ht}{mL} , \tag{25}$$

where h is Planck's constant, m is the neutron mass and t is the time taken to travel distance L from the moderator to the detector.

The POLARIS and GEM diffractometers are general purpose, high intensity neutron diffractometers.[73,74] The POLARIS diffractometer has 5 detector banks that provide data over a combined *d*-spacing range of 0.2−40 Å. The GEM diffractometer has 6 detector banks that provide data over a combined *d*-spacing range of 0.1−26 Å.

2.3.2.2 Institut Laue-Langevin

The ILL uses a ^{235}U fission reactor to generate high-energy neutrons. These neutrons are slowed down by a D_2O moderator, both to sustain the fission process and so that the neutrons have an appropriate energy for diffraction experiments. At each instrument, monochromators are used to select neutrons with the desired wavelength.

The D20 instrument is a high intensity neutron diffractometer with variable resolution.[75] Ge(113) and Ge(115) monochromators with take-off angles of 45° and 90° were used to select neutrons with wavelengths of 2.41 and 1.54 Å, respectively. Data were collected using a position sensitive detector that covers 153.6°.

The D2B instrument is a high resolution powder neutron diffractometer.[76] A Ge(335) monochromator with take-off angle of 135° was used to select neutrons with a wavelength of 1.594 Å. Data were collected using a bank of 128 ^3He detectors spaced at 1.25° intervals, covering a total range of 156°. During the scans, the detectors were moved in small steps to allow the complete diffraction pattern to be obtained.

2.4 Rietveld refinement

Rietveld refinement[77] is a technique that involves fitting an entire diffraction pattern using a structural model by refining the parameters using a least squares procedure. In this method, the calculated intensities are obtained using[67]

$$y_{\mathrm{calc},i} = \sum_{p} \left(S_p \sum_{\mathbf{s}(p)} \left(\left| F_{\mathrm{calc},\mathbf{s},p} \right|^2 Corr_{\mathbf{s},p,i}\, \Phi_{\mathbf{s},p,i} \right) \right) + Bkg_i \quad . \tag{26}$$

In this expression, the outer sum is over all the crystalline phases, *p*, present and S_p is a scaling factor that accounts for the different weight fractions of each of each phase present. Meanwhile, the inner sum is over all the Bragg reflections, **s**, of the phase *p* that contribute to position *i* in the powder pattern. $|F_{\mathrm{calc},\mathbf{s},p}|^2\ Corr_{\mathbf{s},p,i}$ (where $Corr_{\mathbf{s},p,i}$ is a correction factor) gives the positions and intensities of the peaks. Meanwhile $\Phi_{\mathbf{s},p,i}$ denotes the peak profile, which is determined by the sample microstructure and instrumental factors. Finally, Bkg_i is the background signal, caused by factors such as sample environment and incoherent, inelastic or thermal diffuse scattering.

The fitting procedure then involves minimising the sum of the squares of the differences between the observed and calculated intensities:

$$\sum_{i} \left(w_i \left(y_{\mathrm{obs},i} - y_{\mathrm{calc},i} \right)^2 \right) \rightarrow \mathrm{Min} \quad , \tag{27}$$

where w_i is a weighting factor obtained by taking the reciprocal of $y_{\mathrm{obs},i}$.

In this thesis, all Rietveld refinements were performed using Topas Academic.[78] The peak shapes were modelled using the symmetric Thompson-Cox-Hastings pseudo-Voigt functional (TCHZ)[79] and the asymmetry of the peaks was described using a simple axial model. The background was modelled using a Chebyshev polynomial.

The quality of the fit between the observed and calculated patterns were determined using the agreement factor (R_{p}), the weighted agreement factor (R_{wp}) and the goodness of fit (gof):

$$R_{\mathrm{p}} = \frac{\sum_i \left| y_{\mathrm{obs},i} - y_{\mathrm{calc},i} \right|}{\sum_i y_{\mathrm{obs},i}} \quad , \tag{28}$$

$$R_{\mathrm{wp}} = \sqrt{\frac{\sum_i \left(w_i \left(y_{\mathrm{obs},i} - y_{\mathrm{calc},i} \right)^2 \right)}{\sum_i w_i y_{\mathrm{obs},i}^2}} \quad , \tag{29}$$

$$\mathrm{gof} = \frac{R_{\mathrm{wp}}}{R_{\mathrm{exp}}} , \tag{30}$$

$$\text{where} \quad R_{\mathrm{exp}} = \sqrt{\frac{N - P}{\sum_i w_i y_{\mathrm{obs},i}^2}} \quad , \tag{31}$$

where N is the number of data points and P is the number of parameters.

2.4.1 Sample contribution to diffraction peak broadening

The peak profile of a diffraction peak, $\Phi(X)$, can be described as a convolution of the instrumental resolution function, $IRF(X)$, and the sample microstructure, $MS(X)$,

$$\Phi(X) = (IRF \circ MS)\,(X) \quad . \tag{32}$$

The sample microstructure is, itself, a convolution of crystallite size and microstrain,

$$\Phi(X) = (Size \circ Strain) \quad . \tag{33}$$

The diffraction peak broadening contributions from crystallite size and microstrain depend on $1/\cos\theta_0$ and $\tan\theta_0$, respectively. A consequence of this is that size broadening is important at all angles, whereas microstrain broadening is more significant at high diffraction angles, as illustrated in Figure 2.3. This means that the contributions from size and microstrain

broadening can be separated and quantified if data with a sufficiently large 2θ range are measured.[67]

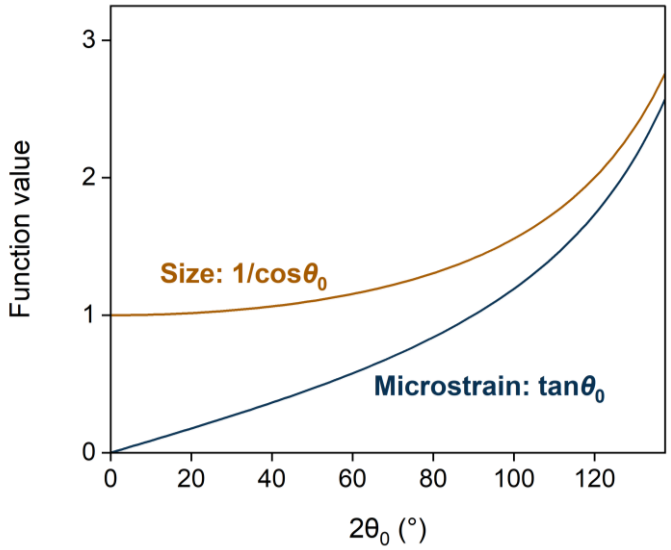

Figure 2.3: 2θ dependence of $1/\cos\theta_0$ and $\tan\theta_0$, highlighting that peak broadening due to crystallite size is significant at all angles, whereas broadening due to microstrain is more significant at high angles.

2.4.1.1 Crystallite domain size broadening

Broadening due to crystallite size can be described by a Gaussian peak shape, a Lorentzian peak shape or by an intermediate Gaussian-Lorentzian function, approximated by a pseudo-Voigt function in Topas. Assuming the size broadening is isotropic, the full width half maximum of a peak at 2θ, $fwhm_{2\theta}$ (in radians), can be related to the crystallite size by the Scherrer formula,

$$fwhm_{2\theta} = \frac{\lambda}{D_0 \cos\theta_0} , \tag{34}$$

where λ is the wavelength of the incident X-ray (in nm) and D_0 is a volume average of the crystallite size distribution (in nm).

2.4.1.2 Microstructural strain broadening

Similar to crystallite size broadening, broadening due to microstrain can be described by a Gaussian peak shape, a Lorentzian peak shape or by an intermediate Gaussian-Lorentzian

(pseudo-Voigt) function. The contribution of microstrain broadening to the full width half maximum of a peak at 2θ is given by,

$$fwhm_{2\theta} = 2\, fwhm_{\varepsilon} \tan\theta_0 \,. \quad (35)$$

In this expression $fwhm_{\varepsilon}$ represents the contribution of microstrain to $fwhm_{2\theta}$ and is given in radians.

2.4.2 Magnetic form factors of iridium

The Topas software includes a *magdata* file that contains the magnetic form factors for most transition metals and lanthanides, which are defined as 7-term exponential functions. However, it does not contain the form factors for iridium. Kobayashi *et al.*[80] have calculated magnetic form factors for all 5d transition metals, but these are defined as 9-term exponential functions. If the 9 terms are inputted into Topas, the last two terms are not read by the program and the magnetic moments determined are not valid. Therefore, to obtain magnetic form factors that can be used in Topas, the 9-term functions were reparametrised into 7-term functions using a least squares procedure similar to that described by Barbosa *et al.*[81].

2.5 Pawley refinement

The Pawley method allows the peaks of a diffraction pattern to be fitted without knowledge of the crystal structure.[82] As with Rietveld refinement, this method relies upon a least squares fitting procedure. However, rather than calculating the intensities from a structural model, the Pawley method treats the intensities as refinable parameters. This allows accurate lattice parameters to be determined and allows different space groups to be tested for phases with unknown crystal structures. In this thesis, all Pawley refinements were performed using Topas Academic.[78]

2.6 X-ray absorption spectroscopy

X-ray absorption spectroscopy (XAS) is a technique that involves exciting a core electron in an atom, which provides information about the oxidation state and local coordination environment of the atom.[83] Since each element has a characteristic excitation energy, XAS is an element-specific technique. The data from an XAS experiment can be divided into two parts: X-ray absorption near edge structure (XANES) and extended X-ray absorption fine structure (EXAFS). The XANES region of the spectrum provides information about the oxidation state, whilst the EXAFS region provides information about the local coordination environment.

In an XAS experiment, a core electron is excited either to an empty state in the solid or to the vacuum, which results in the observation of an edge in the XANES region of the spectrum. The edge shifts towards higher energy for cations with higher oxidation states, due to the stronger attraction between the nucleus and the 1*s* electron. In some cases, a pre-edge feature is observed in the XANES data, which results from a $1s \rightarrow n d$ transition. Although this transition is formally forbidden ($\Delta l \neq \pm 1$), the selection rules are relaxed if the absorbing atom is present in a non-centrosymmetric environment.

The electron that has been released by the absorbing atom can subsequently scatter off neighbouring atoms. The back-scattered electrons can undergo constructive or destructive interference with the outgoing electrons, resulting in a modulation of the absorption in the EXAFS region of the spectrum. The modulation can be expressed as

$$\chi(k) = S_0^2 \sum_i N_i \frac{f_i(k)}{kR_i^2} e^{-\frac{2R_i}{\lambda(k)}} e^{-2k^2\sigma_i^2} \sin(2R_i k + \delta_i(k)) \quad , \tag{36}$$

where S_0^2 is the amplitude reduction factor, N_i is the coordination number, $f_i(k)$ is the scattering amplitude, R_i is the half-length of the scattering path, $\lambda(k)$ is the photoelectron mean free path,

σ_i^2 is the Debye-Waller factor, k is the photoelectron wavenumber and $\delta_i(k)$ is the phase shift. By fitting this expression to the EXAFS data, it allows information about the coordination shells surrounding the absorbing atom to be extracted.

XAS measurements were performed on self-supported pellets, prepared by thoroughly mixing an appropriate mass of sample with ~70 mg of cellulose. Analysis of the data was performed using the DEMETER software package.[84] The data were normalised with a linear pre-edge and polynomial post-edge background subtracted from the raw $\ln(I_t/I_0)$ data using the Athena software. EXAFS fitting was performed using the Artemis software. The XAS data in this thesis were collected on the B18 beamline[85] at the Diamond Light Source or at the Warwick Manufacturing Group, University of Warwick, by Dr Ashok Menon.

2.7 Thermogravimetric analysis

In this thesis, thermogravimetric analysis (TGA) was used to estimate the oxygen content of topochemically reduced phases. To perform the measurements, 20−50 mg of sample was loaded into a small crucible and mounted in the instrument. The sample was then heated to 800 °C at a rate of 10 °C min^{-1} under a steady flow of either O_2 (oxidative TGA) or 5%/95% H_2/N_2 (reductive TGA). The sample was held at this temperature for 1 hour before being cooled back to room temperature at the same rate. During the measurement, the weight change as a function of time was recorded.

During an oxidative TGA measurement, the sample is oxidised back to the parent phase, resulting in a mass gain. Meanwhile, during a reductive TGA measurement, the sample decomposes into a mixture of binary metal oxides and elemental metal. In either case, by comparing the mass before and after the experiment, the oxygen content of the reduced phase can be deduced.

During oxidative TGA measurements, the H_2 (m/z = 2) and H_2O (m/z = 18) contents of the exhaust gas were monitored by mass spectrometry. By monitoring whether water/H_2 gas is released during oxidation of the sample, it is possible to confirm whether hydride is present in the phase and, therefore, whether the reduced phase is an oxyhydride or oxygen-deficient phase.

In this thesis, reductive TGA measurements were performed using a Mettler Toledo TGA/DSC 1 STARe system. Oxidative TGA measurements were performed using a PerkinElmer TGA 8000, with the exhaust gases monitored using a Hiden Analytical HPR-20 EGA mass spectrometer.

2.8 SQUID magnetometry

SQUID (Superconducting Quantum Interference Device) magnetometry is a widely used technique that is capable of measuring the magnetisation of a sample with extremely high accuracy. It consists of two Josephson junctions arranged on a superconducting ring, as illustrated in Figure 2.4.[86] When a small current is applied, the superconducting electrons can tunnel through the Josephson junctions, and the current in the ring is quantised. If the current exceeds the critical current, the superconducting state 'breaks' and a voltage is observed across the SQUID. When a magnetic field is applied inside the ring (from the sample), this induces a current inside the ring and a corresponding voltage appears across the junction. From the magnitude of this voltage, the magnetic moment of the sample can be deduced. The fact that the current in the ring is quantised allows the voltage, and, therefore, the magnetisation of the sample, to be determined with extremely high accuracy.

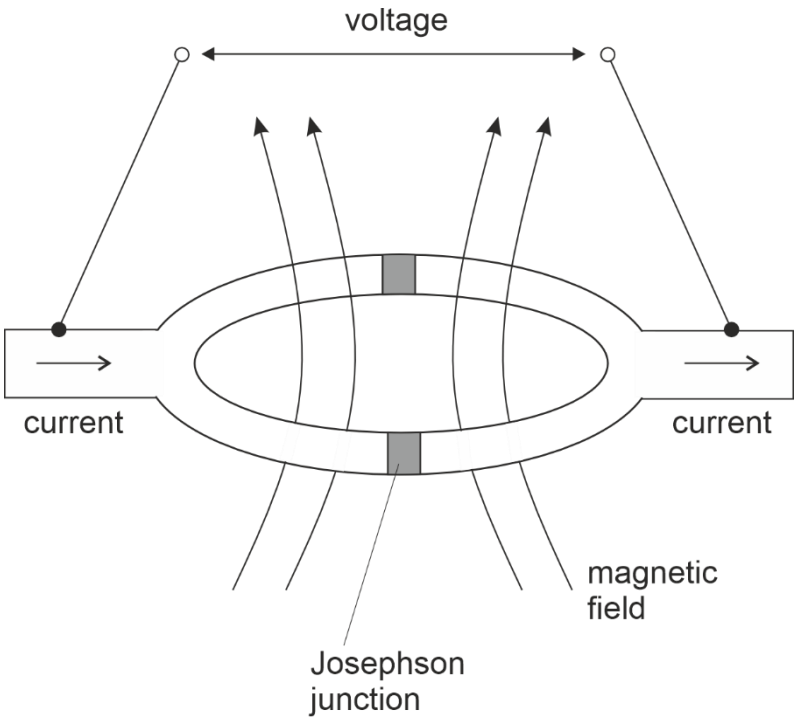

Figure 2.4: Schematic illustrating the superconducting ring in a DC SQUID magnetometer.

To perform the measurements, 15−30 mg of sample was accurately weighed and loaded into a gelatine capsule. This capsule was then fixed in place in a plastic straw and loaded into the instrument chamber. Zero-field-cooled (ZFC) and field-cooled (FC) measurements were collected using a magnetic field of 100 Oe over temperature ranges of 5−300 K or 5−350 K, with measurements taken every 5 K. Measurements as a function of applied field were conducted at constant temperature with fields between −5 and +5 T. In this thesis, all measurements were performed using a Quantum Design MPMS-3 magnetometer.

2.8.1 Ferrosubtraction technique

The parent oxide phases used in topochemical reactions often contain small quantities of binary transition metal oxides (eg Co_3O_4, NiO). Upon treatment with reducing agents, these are reduced to the elemental metals (eg Co, Ni). These ferromagnetic impurities can mask the magnetic properties of the reduced phases. To allow useful magnetic information to be obtained, a ferrosubtraction technique is used. In this technique, magnetisation is measured as a function of field at relatively high field (3−5 T) at temperatures between 5 and 300 K with

5 K increments. The sample is cooled to 5 K under an applied field of 100 Oe. Since the magnetisation of the ferromagnetic impurities are saturated at 3 T, this means that, by plotting magnetisation as a function of applied field at each temperature, the paramagnetic susceptibility of the reduced phase can be extracted from the gradient, and the intercept gives the saturated ferromagnetic moment of the sample. This is illustrated in Figure 2.5.

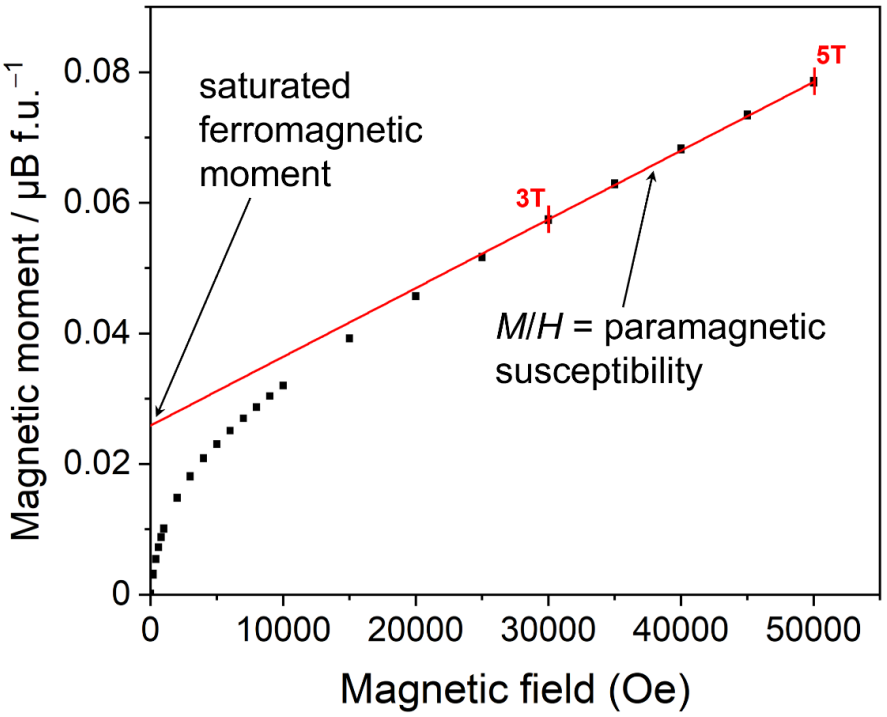

Figure 2.5: Schematic illustrating the principles of the ferrosubtraction technique.

2.9 Muon spin rotation spectroscopy

Muon spin rotation spectroscopy (μ^+SR) is a technique than involves implanting a muon into a material to act as a local probe of the surrounding magnetic environment.[87,88]

Muons are produced by directing protons, p, into a target made of light elements, such as carbon or beryllium. This yields pions, π, and neutrons, n, in the following process:

$$p + p \rightarrow p + n + \pi^+ \quad . \tag{37}$$

The pions then decay to form muons, μ, and muon neutrinos, ν_μ, in the following process:

$$\pi^+ \rightarrow \mu^+ + \nu_\mu \ . \tag{38}$$

The muons produced in this way are 100% spin polarised. The muons later decay, emitting a positron, e^+, and two neutrinos in the following process:

$$\mu^+ \rightarrow e^+ + \bar{\nu}_\mu + \nu_e \ . \tag{39}$$

The positrons formed from this process have a propensity to be emitted along the direction of the muon spin.

When a μ^+SR measurement is performed, a muon enters the material and localises at an interstitial site in the crystal structure. If long-range magnetic order is present, the muon spin precesses around the field in the sample. Since positron decay occurs preferentially in the spin direction, this precession can be observed by recording the time evolution of the positron emission, leading to the observation of oscillations in the signal. If static moments are present in the sample but there is no long-range magnetic order or the order is somewhat inhomogeneous, oscillations are not observed. However, the existence of the static moments can be deduced from the observation of very rapid loss of asymmetry in the positron emission, which results from dephasing of the muon spins as they precess around the fields in the sample. Meanwhile, if the sample is paramagnetic, the spins in the sample are fluctuating very fast relative to the timescale of the measurement. This means that the deviation of the muon spin from its initial polarisation essentially follows a random walk and, as a consequence, loss of asymmetry is very slow. As such, by observing the temperature at which the loss of asymmetry becomes much faster, it is possible to determine the approximate magnetic ordering temperature for the sample.

In this thesis, the μ^+SR data were collected by Dr Benjamin Huddart and Prof. Stephen Blundell on the GPS beamline at the Swiss Muon Source at the Paul Scherrer Institute in Switzerland.

This facility uses a cyclotron to produce a quasi-continuous source of muons. When using this type of muon source, there is typically only one muon in the sample at any given time, so muon-muon spin interactions do not need to be considered.

2.10 Iodometric titration

Iodometric titration provides a method to determine approximate transition metal oxidation states of a sample by performing oxidation/reduction using I_2/KI. In this thesis, iodometric titrations were used to establish the overall transition metal oxidation state in the $La_2CoRhO_{6-x}H_y$ oxyhydride phase by performing the following redox reactions:

$$Co^{a+} + (2-a)/2\ I_2 \rightarrow Co^{2+} + (2-a)\ I^- \quad (40)$$

$$Rh^{a+} + (3-a)/2\ I_2 \rightarrow Rh^{3+} + (3-a)\ I^- \quad (41)$$

To perform the titrations, approximately 30 mg of sample was dissolved in 10 mL of 2 M HCl solution. 10 mL of 0.001678 M KIO_3 solution was then added to the solution, followed by an excess of KI. This liberated a known quantity of I_2, which oxidised the Co^{a+} and Rh^{b+} species. The unreacted I_2 was titrated against $Na_2S_2O_4$ solution of known concentration (determined by standardisation with KIO_3) using starch as an indicator. The titration was performed under an Ar flow to avoid oxidation of the sample by air. By determining the amount of unreacted I_2, the overall transition metal oxidation state in $La_2CoRhO_{6-x}H_y$ could be deduced.

2.11 Thin-film synthesis and characterisation

2.11.1 Pulsed laser deposition

The thin-films presented in this thesis were prepared by puled laser deposition (PLD). In this technique, the target (a pellet with the desired thin-film composition) and a substrate are mounted in a vacuum chamber with a small oxygen flow and heated to a suitable temperature

(~700−800 °C). Pulses of a high energy laser are then directed at the target, leading to evaporation of the target material. These atoms are deposited onto the substrate, resulting in film growth. To achieve epitaxial growth of the film on the substrate, the substrate must be carefully chosen such that its lattice parameters are comparable to those of the desired film.

2.11.2 X-ray diffraction

X-ray diffraction data collected from thin film samples typically used a $2\theta/\omega$ scan, in which the incident angle, ω, is kept at half of 2θ; this is equivalent to a standard powder diffraction measurement.[89] When data are collected in this way, the Bragg plane is always kept parallel to the surface of the sample, so reflections are only observed for *hkl* planes that are parallel to the sample surface. Since substrate peaks often dominate the pattern for thin-film samples, the diffraction data tend to be plotted on a logarithmic intensity scale. To maximise the intensity and resolution of the desired peaks, the sample height and angle were adjusted using a rocking curve.

Reciprocal space mapping was used to collect data from the 103 perovskite peak of the thin-film samples.[90] In this technique, the sample is tilted in the ω axis such that *hkl* planes not parallel with the sample surface are brought into the Bragg plane (Figure 2.6). The 2θ and ω angles were initially set such that the area of reciprocal space being mapped was centred around the 103 peak. The data were then collected by varying the ω angle whilst measuring a fixed 2θ range using a 2-dimensional detector.

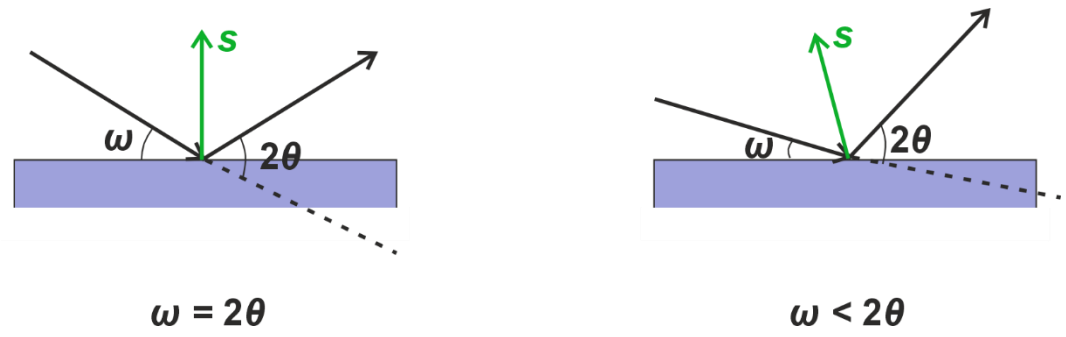

Figure 2.6: Schematic illustrating varying the ω angle, whilst keeping 2θ constant to bring *hkl* planes that are not parallel with the sample surface into the Bragg plane.

To estimate the thickness of thin-film samples, X-ray reflectivity measurements were performed. This technique uses X-rays incident on the sample at very low angles. This results in total internal reflection of the X-rays from both the surface of the film and the substrate. The X-rays reflected from the thin-film surface interfere with those reflected from the substrate, resulting in oscillations in the observed X-ray intensity. Increasing the thickness of films results in a higher oscillation frequency and, as a result, the thickness of the film can be estimated from the observed oscillations.

In this thesis, X-ray data collection from thin-film samples was performed using a Rigaku SmartLab diffractometer with Cu Kα_1 radiation.

2.11.3 SQUID magnetometry

Magnetisation data from the thin-film samples were collected using the same principles as described in Section 2.8. To perform the measurements, small samples (~ 5 mm × 5 mm) of the thin-film were fixed in place in a plastic straw such that the *c*-axis is aligned either parallel or perpendicular to the applied field. ZFC and FC measurements were then collected using a magnetic field of 100 Oe over a temperature range of 5−300 K, with measurements taken every 1 K. Measurements as a function of applied field were conducted at constant temperature with fields between −5 and +5 T. The measurements on thin-film samples were performed using a Quantum Design MPMS-XL magnetometer.

2.11.4 Transport measurements

Transport measurements were performed using the 4-point-probe technique. In this method, four probes are attached to the sample. A constant current is applied across the two outer probes and the potential difference between the two inner probes is measured, thereby allowing the resistance to be determined. The resistivity of the sample can then be obtained using the expression,

$$\rho = \frac{RA}{l} , \tag{42}$$

where A and l are the area and length, respectively, over which the resistance was measured.

In this thesis, the probes were attached to the sample using silver paint and the resistance measurements were performed using a Quantum Design PPMS instrument.

Chapter 3 – Topochemical reduction of $La_xSr_{4-x}CoIrO_8$ ($0 \leq x \leq 2$) phases using LiH

3.1 Introduction

Recently, a number of oxyhydrides have been prepared containing the 4*d* transition metals, Ru ($LaSr_3NiRuO_4H_4$, $LaSr_3CoRuO_4H_4$)[51,91] and Rh ($LaSr_3MnRhO_6H_2$, $La_2Sr_2CoRhO_6H_2$)[52]. Many of these oxyhydrides are based on the $n = 1$ Ruddlesden-Popper structure. To extend this work further to include the 5*d* transition metal, iridium, the reactivity of the structurally analogous $La_xSr_{4-x}CoIrO_8$ ($0 \leq x \leq 2$) phases with LiH has been explored.

3.2 Experimental

3.2.1 Synthesis of $La_xSr_{4-x}CoIrO_8$ ($0 \leq x \leq 2$) phases

Two-gram samples of polycrystalline $La_xSr_{4-x}CoIrO_8$ (x = 0, 0.5, 1, 1.5, 2) were prepared using conventional ceramic synthesis methods. Stoichiometric amounts of La_2O_3 (dried at 900 °C), $SrCO_3$, Co_3O_4, and IrO_2 (dried for 2 hours at 700 °C) were thoroughly ground together in an agate pestle and mortar, and pelletised. Samples of Sr_4CoIrO_8 were initially heated for 2 days at 950°C in air, followed by 2 further cycles of 2 days at 1000 °C. Samples of $La_{0.5}Sr_{3.5}CoIrO_8$ were initially heated for 2 days at 1000 °C in air, followed by 2 further cycles of 2 days at 1100 °C and 1200 °C, respectively. Samples of $LaSr_3CoIrO_8$ and $La_{1.5}Sr_{2.5}CoIrO_8$ were initially heated for 2 days at 1000 °C in air, followed by 2 further cycles of 2 days at 1300 °C. Samples of $La_2Sr_2CoIrO_8$ were initially heated for 2 days at 1000 °C in an approximately 0.5:99.5 O_2:Ar atmosphere (to favour formation of Ir^{IV} whilst also minimising reduction to Ir metal), followed by 2 further cycles of 2 days at 1300 °C in the same atmosphere. Intermediate grinding and pelletisation were performed between each heating cycle for all samples.

3.2.2 Exploration of the reactivity of $La_xSr_{4-x}CoIrO_8$ phases with LiH

Small-scale trial reactions of Sr_4CoIrO_8 and $LaSr_3CoIrO_8$ with LiH were performed to determine their reactivity as a function of temperature. The reaction mixtures were prepared by thoroughly grinding 200 mg of the all-oxide starting materials with 8 mole equivalents of LiH, sealing the mixtures in evacuated Pyrex® ampoules and then heating for 2 days at the trial temperature. After each heating cycle, the reaction mixtures were characterised using PXRD, before being reheated at an increased temperature. This process was repeated until decomposition was observed, signalled by the formation of La_2O_3, SrO and Ir metal.

The reactions between Sr_4CoIrO_8 and LiH showed that, at all temperatures below 250 °C, tetragonal symmetry was retained and that above 150 °C there was a continuous contraction in the *a*-lattice parameter and expansion in the *c*-lattice parameter. However, when heated at 250 °C or above, complete decomposition of the Ruddlesden-Popper structure into SrO, Co metal and Ir metal was observed.

The reactions between $LaSr_3CoIrO_8$ and LiH showed that, as with Sr_4CoIrO_8, tetragonal symmetry was retained until decomposition. At reaction temperatures up to 350 °C, there was a continuous contraction in the *a*-lattice parameter and expansion in the *c*-lattice parameter. Subsequently, between 380 °C and 420 °C, there appeared to be a discontinuous transition from a phase with lattice parameters of approximately $a = 3.76$ Å and $c = 13.07$ Å, possibly $LaSr_3CoIrO_6H_2$ (Section 3.3.9.3), to the final product with lattice parameters of $a = 3.66$ Å and $c = 13.27$ Å, characterised in Section 3.3.4. Above these temperatures, non-topochemical decomposition occurred. The reactivity of $La_{0.5}Sr_{3.5}CoIrO_8$, $La_{1.5}Sr_{2.5}CoIrO_8$ and $La_2Sr_2CoIrO_8$ was assumed to be similar to that of $LaSr_3CoIrO_8$.

When performing the reactions on a larger scale (> 1 g) to prepare samples for NPD measurements, it was observed that the success of the reaction was extremely sensitive to the

exact temperature and amount of LiH used, with the topochemical reactivity window of 380−420 °C being very close to the temperature of non-topochemical decomposition. The conditions used for the synthesis of samples for NPD measurements are described below.

3.2.3 Synthesis of $La_xSr_{4-x}CoIrO_{8-y}H_y$ ($0 \leq x \leq 2$) phases

3.2.3.1 Synthesis of $Sr_4CoIrO_{6.5}H_{1.5}$

2.25 g of Sr_4CoIrO_8 was thoroughly ground with 8 mole equivalents of LiH in an Ar-filled glovebox. The reaction mixture was then sealed in an evacuated Pyrex® ampoule and heated for 1 period of 6 days at 175 °C with a heating rate of 1 °C/min.

3.2.3.2 Synthesis of $La_{0.5}Sr_{3.5}CoIrO_{5.5}H_{2.5}$

1.7 g of $La_{0.5}Sr_{3.5}CoIrO_8$ was thoroughly ground with 9 mole equivalents of LiH in an Ar-filled glovebox. The reaction mixture was then sealed in an evacuated Pyrex® ampoule and heated for 2 periods of 5 days at 385 °C, followed by 1 period of 4 days at 400 °C, with heating rates of 1 °C/min. The sample was thoroughly reground between each heating cycle.

3.2.3.3 Synthesis of $LaSr_3CoIrO_5H_3$

2.25 g of $LaSr_3CoIrO_8$ was thoroughly ground with 9 mole equivalents of LiH in an Ar-filled glovebox. The reaction mixture was then sealed in an evacuated Pyrex® ampoule and heated for 1 period of 9 days at 420 °C, followed by 2 further periods of 2 days at 400 °C and 420 °C, respectively, with heating rates of 1 °C/min. The sample was thoroughly reground between each heating cycle.

3.2.3.4 Synthesis of $La_{1.5}Sr_{2.5}CoIrO_{8-y}H_y$

1.7 g of $La_{1.5}Sr_{2.5}CoIrO_8$ was thoroughly ground with 9 mole equivalents of LiH in an Ar-filled glovebox. The reaction mixture was then sealed in an evacuated Pyrex® ampoule and heated for 3 periods of 7 days, during which the sample was heated at 385 °C for the first 2 days,

before the temperature was raised to 400 °C for the remaining 5 days, with heating rates of 1 °C/min. The sample was thoroughly reground between each heating cycle.

3.2.3.5 Synthesis of $La_2Sr_2CoIrO_{8-y}H_y$

1.7 g of $La_2Sr_2CoIrO_8$ was thoroughly ground with 9 mole equivalents of LiH in an Ar-filled glovebox. The reaction mixture was then sealed in an evacuated Pyrex® ampoule and heated for 1 period of 7 days, during which the sample was heated at 385 °C for the first day, before the temperature was raised to 400 °C for the remaining 6 days, with heating rates of 1 °C/min. The sample was then reground and heated for 1 further period of 4 days at 410 °C.

3.2.4 Washing of $La_xSr_{4-x}CoIrO_{8-y}H_y$ ($0 \leq x \leq 2$) phases

The reaction of transition metal oxides with LiH to form oxyhydrides is driven by the formation of Li_2O as a by-product. To remove the Li_2O, as well as any excess LiH remaining after the reaction, the product mixture was washed with MeOH under an N_2 atmosphere. The resulting powder was then dried under vacuum and returned to the glovebox.

3.3 Structural characterisation

3.3.1 Structural characterisation of $La_xSr_{4-x}CoIrO_8$ ($0 \leq x \leq 2$) phases

Sr_4CoIrO_8 and $LaSr_3CoIrO_8$ have previously been reported as adopting n = 1 Ruddlesden-Popper structures with $I4/mmm$ symmetry.[46,92] SXRD data collected from the as-synthesised samples are consistent with the structures reported previously, as shown in Appendix A1. To describe the $La_xSr_{4-x}CoIrO_8$ (x = 0.5, 1.5, 2) phases, structural models were created based on $LaSr_3CoIrO_8$, and refined against SXRD data collected from each sample, all of which gave good fits to the data, as shown in Appendix A1. Although the cobalt and iridium ions were treated as disordered in all the models, it is possible that B-site paracrystalline order is present in the compounds, as discussed in Section 1.1.4. For $La_2Sr_2CoIrO_8$, a small impurity (< 2

weight percent) of Ir metal was formed, as well as a small amount of an additional unknown impurity with peaks at $2\theta \sim 16.4°$ and 16.9°. A generic structural model for the $La_xSr_{4-x}CoIrO_8$ phases is shown in Figure 3.1.

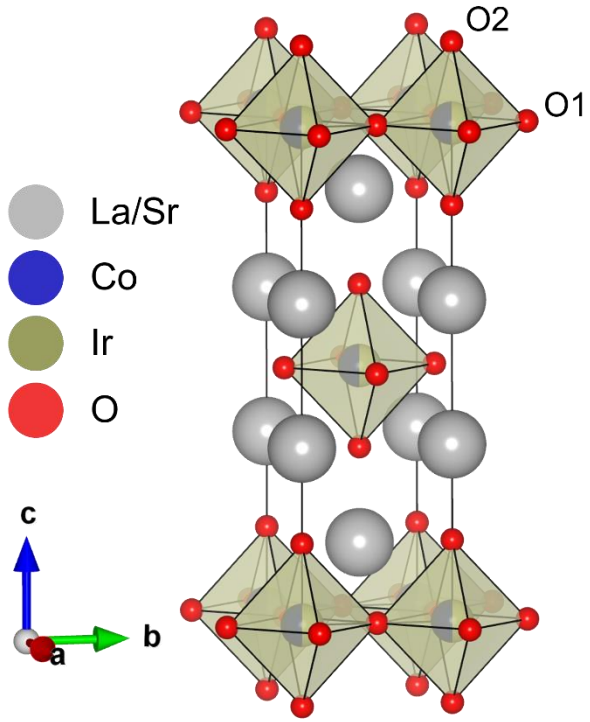

Figure 3.1: Structural model for $La_xSr_{4-x}CoIrO_8$ ($0 \leq x \leq 2$) phases with the $n = 1$ Ruddlesden-Popper structure.

3.3.2 Structural characterisation of $Sr_4CoIrO_{6.5}H_{1.5}$

SXRD data collected from the product of the reaction between Sr_4CoIrO_8 and LiH, henceforth referred to as $Sr_4CoIrO_{6.5}H_{1.5}$, indicated the presence of a single phase with *I*4/*mmm* symmetry. A substantial change in the lattice parameters was observed relative to the parent oxide material, with a contraction in the *xy*-plane from $a = 3.91778(6)$ Å to $a = 3.8088(2)$ Å and an expansion in the *z*-direction from $c = 12.4770(2)$ Å to $c = 13.1949(8)$ Å.

3.3.2.1 Thermogravimetric analysis

Thermogravimetric data were collected from $Sr_4CoIrO_{6.5}H_{1.5}$ whilst heating under flowing oxygen, indicating a mass gain of 2.3%, as shown in Figure 3.2. PXRD data collected from the

sample after the measurement are consistent with the structure of the parent oxide, Sr_4CoIrO_8. Assuming full oxidation back to Sr_4CoIrO_8, this corresponds to an initial composition of $Sr_4CoIrO_{6.94}H_y$. Due to the fact that the reduced phase may not have fully oxidised and that iridium can form volatile iridium oxides when heated under an oxidative atmosphere, this composition represents the maximum oxygen content possible for the compound. Analysis of the exhaust gas by mass spectrometry showed a clear release of water associated with the oxidation event, confirming that hydride is present in the phase.

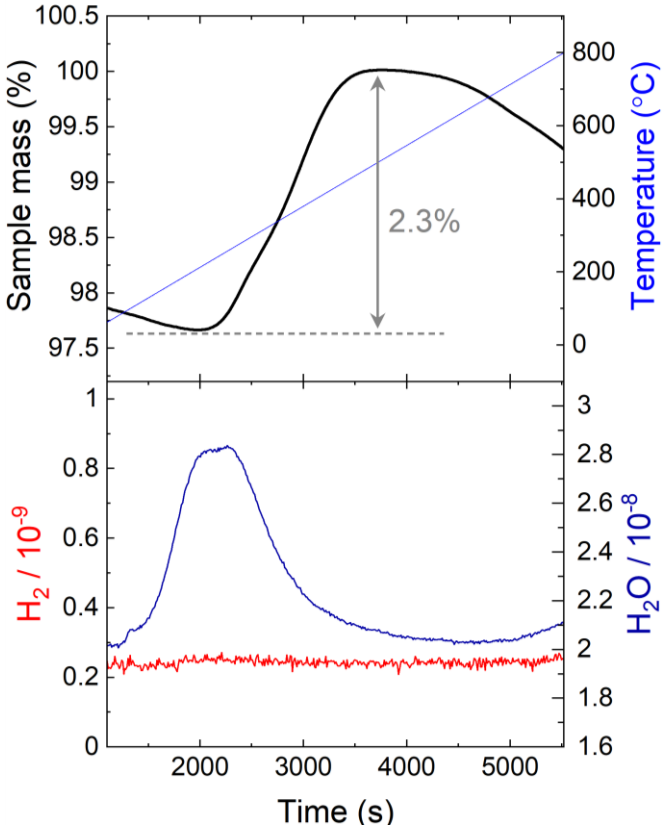

Figure 3.2: TGA trace (top panel) and H_2/H_2O contents of exhaust gas (bottom panel) when $Sr_4CoIrO_{6.5}H_{1.5}$ is heated under flowing oxygen.

3.3.2.2 Neutron powder diffraction

NPD data were collected from $Sr_4CoIrO_{6.5}H_{1.5}$ at ambient temperature using the POLARIS diffractometer at ISIS. A structural model based on Sr_4CoIrO_8 was constructed using the lattice

parameters obtained from the refinement against the SXRD data, which was then refined against the data from the 54°, 94° and 139° detector banks of the POLARIS diffractometer.

During the reaction between Sr_4CoIrO_8 and LiH, a number of different transformations are feasible. It is possible that oxide ions are deintercalated from the structure, resulting in a phase that contains only oxide ions and vacancies at the anion sites ($Sr_4CoIrO_{8-\delta}$). Alternatively, anion exchange could lead to structures that either contain only oxide ions and hydride ions at the anion sites ($Sr_4CoIrO_{8-x}H_x$) or contain a mixture of oxide ions, hydride ions and vacancies at the anion sites ($Sr_4CoIrO_{8-x}H_y$). Since the neutron scattering length of oxygen is 5.803 fm and the neutron scattering length of hydrogen is −3.7390 fm,[72] the same total scattering length can be obtained from a range of different site occupancies, and, as a result, the anion composition is ambiguous when determined solely by NPD data.

To address this problem, an initial model containing only oxide ions and vacancies in the equatorial positions was tested by allowing the oxide ion occupancy at the O1 (equatorial) site to freely refine. This yielded a good fit to the data and a value for the occupancy of 0.400(5), which corresponds to a composition of $Sr_4CoIrO_{5.60(2)}$. This composition is chemically unlikely because it would require some of the transition metals to have a coordination number of 3, which is not expected to be achievable for cobalt and iridium via topochemical reactions. This composition would also require an overall transition metal oxidation state of +3.2. Since cobalt appears to be present as Co^{II} (Section 3.3.8), this would require iridium to have an oxidation state of approximately +1, which is unlikely to be stable in the presence of Co^{II}. These observations strongly imply that hydride ions are present in the phase.

To take this into account, hydride ions were added at the O1 site and the occupancies of oxide and hydride allowed to refine, such that the total occupancy at this site summed to 1. This refinement yielded a hydride occupancy of 0.365(3) and an oxide occupancy of 0.635(3),

giving an overall composition of $Sr_4CoIrO_{6.54(2)}H_{1.46(2)}$. Since the average neutron scattering length at the equatorial site is ~2.2 fm, this composition represents the maximum oxide ion content that is possible for this phase. As the oxide ion content from TGA is larger than this ($Sr_4CoIrO_{6.94}H_y$), this suggests that $Sr_4CoIrO_{6.5}H_{1.5}$ is approximately the correct composition. Although it is possible that some vacancies are present in the structure, in addition to oxide and hydride ions, these are likely to be present at a relatively low concentration, so the composition is assumed to be $Sr_4CoIrO_{6.5}H_{1.5}$. This composition is supported by the observation that the *a*-lattice parameter for this phase is consistent with those of previously reported compounds with a similar anion composition (Figure A 11). The fits to the NPD data, assuming a composition of $Sr_4CoIrO_{6.5}H_{1.5}$, are shown in Figure 3.3-3.5, with the refinement parameters presented in Table 3.1. The structural model obtained from the NPD data was also refined against the SXRD data, which gave a good fit to the data, as shown in Appendix A1.

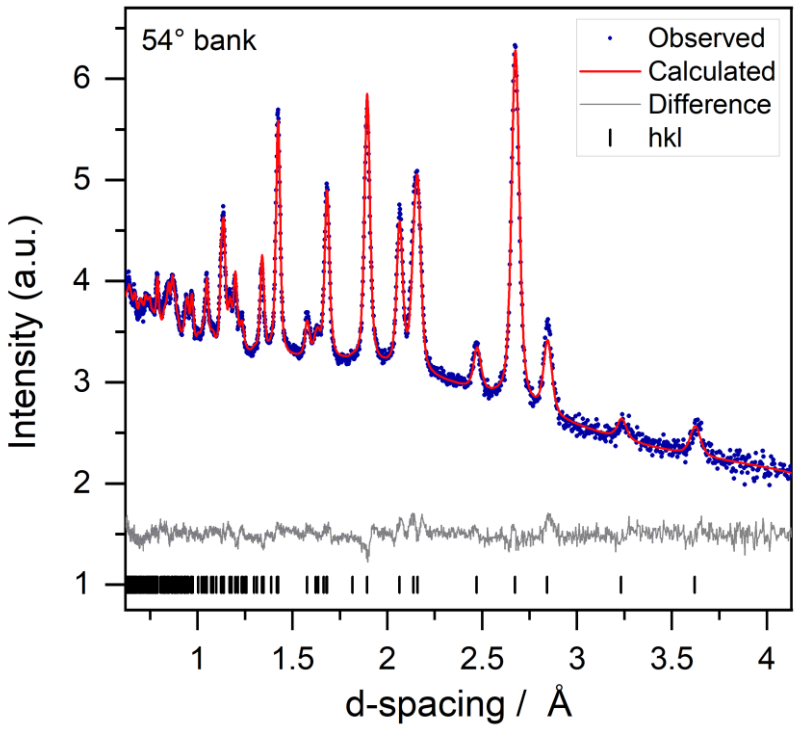

Figure 3.3: Observed, calculated and difference plots from the structural refinement of $Sr_4CoIrO_{6.5}H_{1.5}$ against NPD data collected at room temperature from the 54° bank of the POLARIS diffractometer.

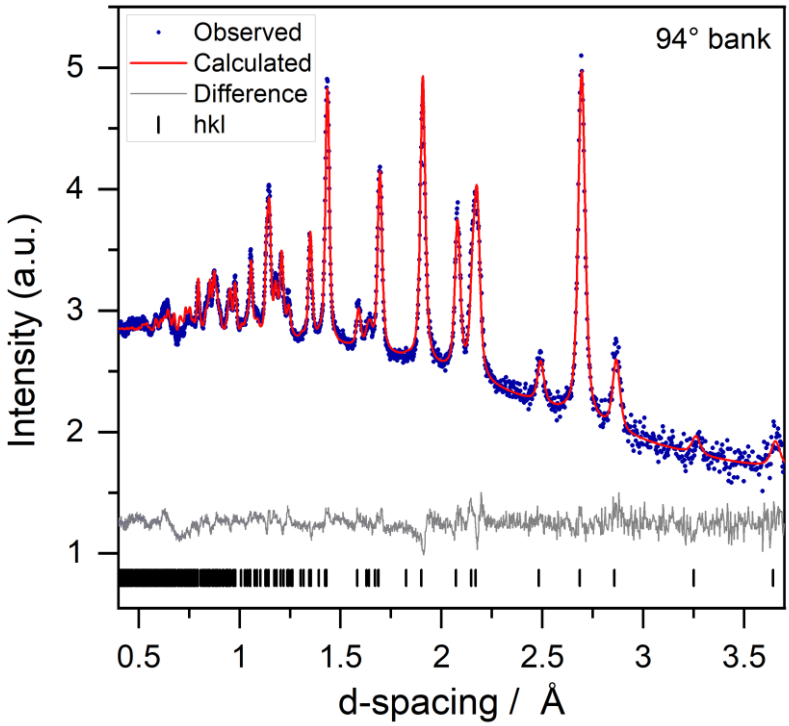

Figure 3.4: Observed, calculated and difference plots from the structural refinement of $Sr_4CoIrO_{6.5}H_{1.5}$ against NPD data collected at room temperature from the 94° bank of the POLARIS diffractometer.

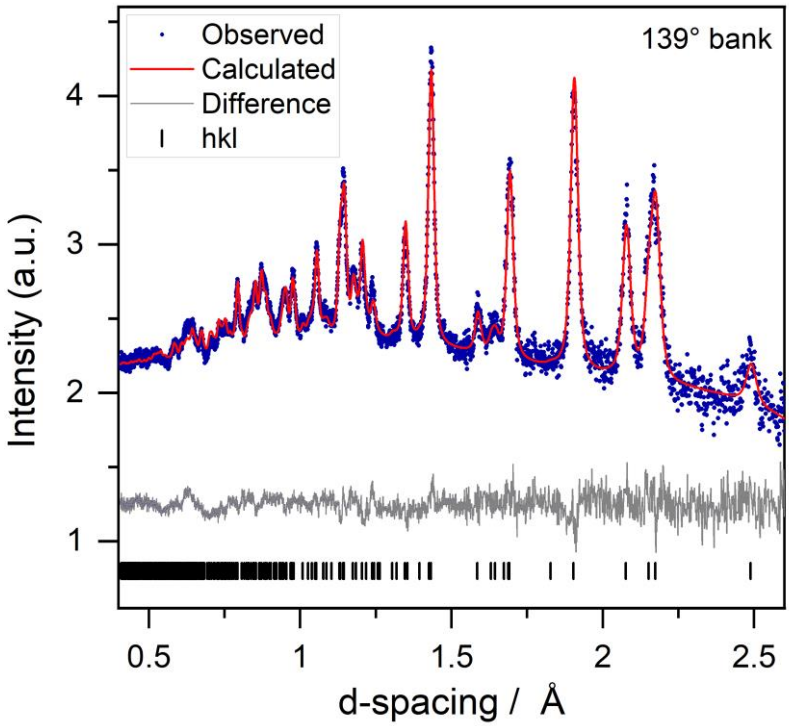

Figure 3.5: Observed, calculated and difference plots from the structural refinement of $Sr_4CoIrO_{6.5}H_{1.5}$ against NPD data collected at room temperature from the 139° bank of the POLARIS diffractometer.

Table 3.1: Parameters from the structural refinement of $Sr_4CoIrO_{6.5}H_{1.5}$ against NPD data collected at room temperature from the POLARIS diffractometer.

$Sr_4CoIrO_{6.54(2)}H_{1.46(2)}$, space group *I*4/*mmm* (No. 139)						
		x	***y***	***z***	**Occ.**	**B_{iso} (Å^2)**
Sr(1)	4*e*	0	0	0.3530(1)	1	1.18(4)
Co(1)/Ir(1)	2*a*	0	0	0	0.5/0.5	1.44(6)
O(1)/H(1)	4*c*	0	½	0	0.635(3)/0.365(3)	1.05(8)
O(2)	4*e*	0	0	0.1629(2)	1	1.60(6)
a = 3.8058(3) Å, c = 13.037(1) Å						
V = 188.84(4) Å^3						
R_{wp} = 2.11%, R_p = 1.63%, *gof* = 0.06						

3.3.3 Structural characterisation of $La_{0.5}Sr_{3.5}CoIrO_{5.5}H_{2.5}$

SXRD data collected from the product of the reaction between $La_{0.5}Sr_{3.5}CoIrO_8$ and LiH, henceforth referred to as $La_{0.5}Sr_{3.5}CoIrO_{5.5}H_{2.5}$, indicated the presence of a single phase with *I*4/*mmm* symmetry. The lattice parameters were found to be a = 3.6956(3) Å and c = 13.1509(9) Å, which corresponds to a significant contraction in the *xy*-plane relative to $Sr_4CoIrO_{6.5}H_{1.5}$.

3.3.3.1 Thermogravimetric analysis

Thermogravimetric data were collected from $La_{0.5}Sr_{3.5}CoIrO_{5.5}H_{2.5}$ whilst heating under flowing oxygen, indicating a mass gain of 3.6%, as shown in Figure 3.6. Assuming full oxidation back to $La_{0.5}Sr_{3.5}CoIrO_8$, this corresponds to an initial composition of $La_{0.5}Sr_{3.5}CoIrO_{6.32}H_y$, which represents the maximum oxygen content possible for the compound. Analysis of the exhaust gas by mass spectrometry showed a clear release of water associated with the oxidation event, confirming that hydride is present in the phase.

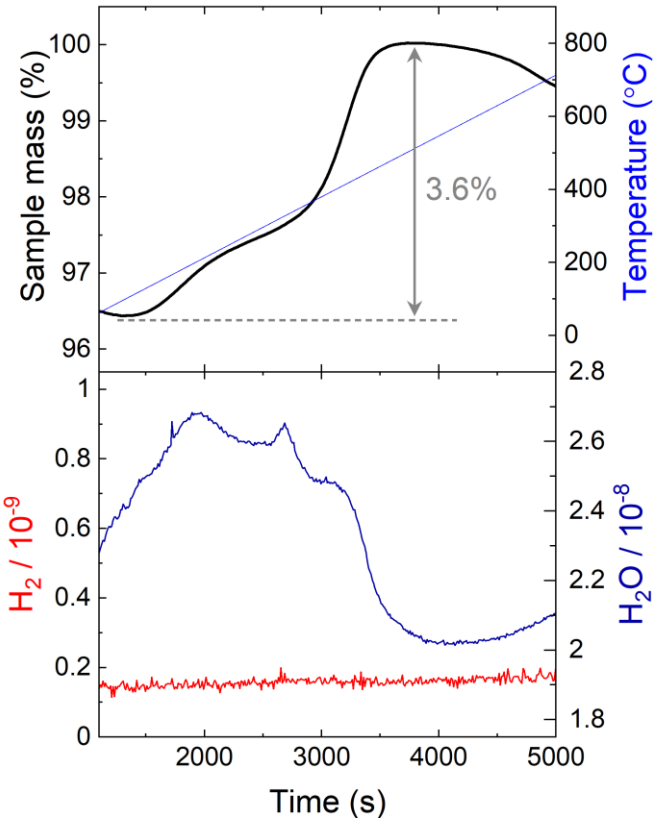

Figure 3.6: TGA trace (top panel) and H_2/H_2O contents of exhaust gas (bottom panel) when $La_{0.5}Sr_{3.5}CoIrO_{5.5}H_{2.5}$ is heated under flowing oxygen.

3.3.3.2 Neutron powder diffraction

NPD data were collected from $La_{0.5}Sr_{3.5}CoIrO_{5.5}H_{2.5}$ at ambient temperature using the POLARIS diffractometer at ISIS. A structural model similar to $Sr_4CoIrO_{6.5}H_{1.5}$ was constructed using the lattice parameters obtained from the refinement against the SXRD data, which was then refined against the data from the 54°, 94° and 139° detector banks of the POLARIS diffractometer.

Initially, a model containing only oxide ions and vacancies in the equatorial positions was tested by allowing the oxide ion occupancy to refine freely at the O1 site. This yielded a refined occupancy of 0 at this site, which would correspond to a composition of $La_{0.5}Sr_{3.5}CoIrO_4$. In this structure, the cobalt and iridium would have linear, dumbbell-type coordination and the

overall transition metal oxidation state would be −0.5, thereby confirming that the structure must contain hydride ions.

As such, hydride was added at the O1 site and the occupancies of oxide and hydride allowed to refine, such that the total occupancy at this site summed to 1. This refinement yielded an oxide occupancy of 0.369(3) and a hydride occupancy of 0.631(3), giving an overall composition of $La_{0.5}Sr_{3.5}CoIrO_{5.48(2)}H_{2.52(2)}$. Since this has a smaller oxygen content than the composition of $La_{0.5}Sr_{3.5}CoIrO_{6.32}H_y$ suggested from TGA measurements, $La_{0.5}Sr_{3.5}CoIrO_{5.5}H_{2.5}$ is assumed to be roughly the correct composition. The increased hydride content in the equatorial plane for $La_{0.5}Sr_{3.5}CoIrO_{5.5}H_{2.5}$ compared to $Sr_4CoIrO_{6.5}H_{1.5}$ is supported by the significant contraction of the *xy*-plane. The fits to the NPD data are shown in Figure 3.7-3.9, with the refinement parameters presented in Table 3.2. The structural model obtained from the NPD data was also refined against the SXRD data, which gave a good fit to the data, as shown in Appendix A1.

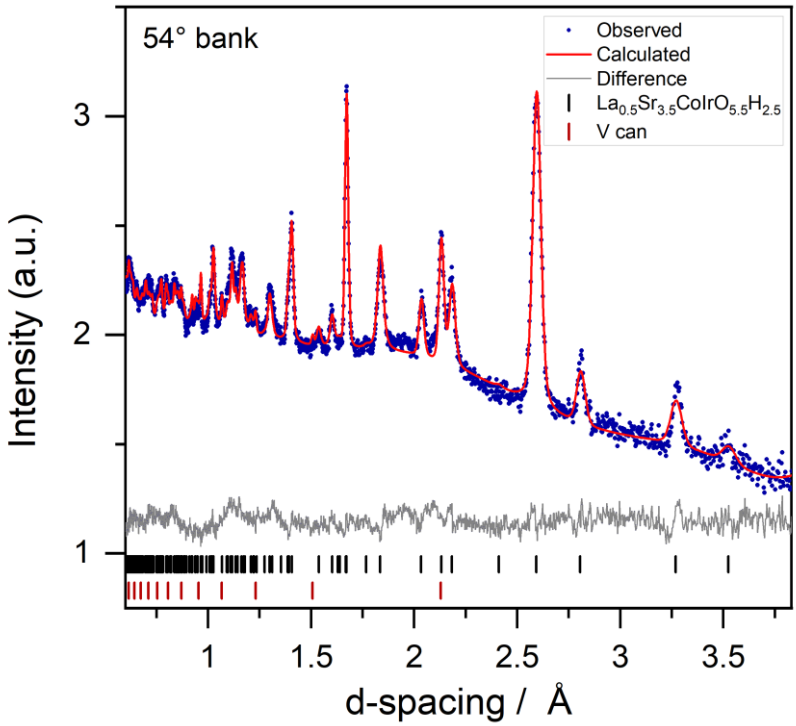

Figure 3.7: Observed, calculated and difference plots from the structural refinement of $La_{0.5}Sr_{3.5}CoIrO_{5.5}H_{2.5}$ against NPD data collected at room temperature from the 54° bank of the POLARIS diffractometer.

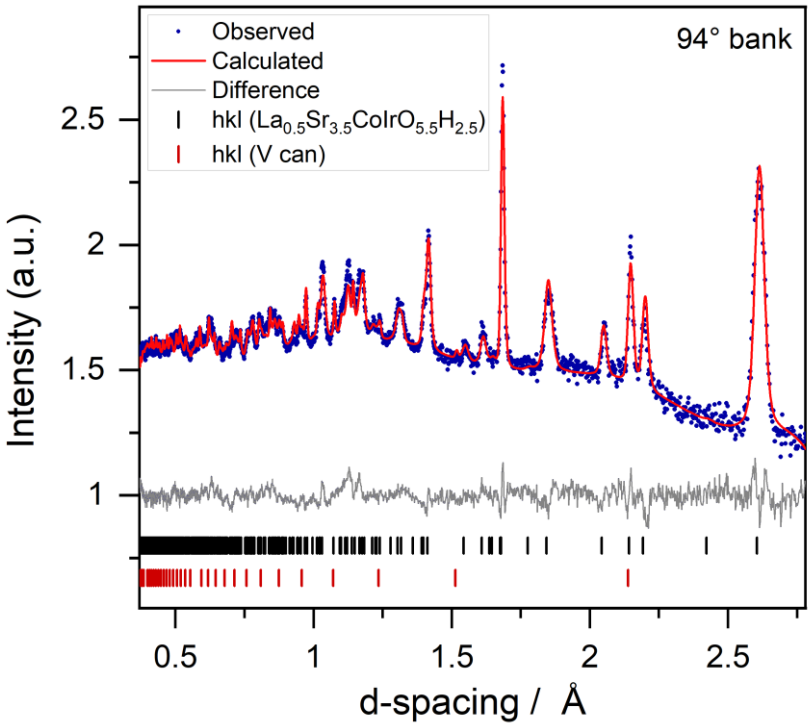

Figure 3.8: Observed, calculated and difference plots from the structural refinement of $La_{0.5}Sr_{3.5}CoIrO_{5.5}H_{2.5}$ against NPD data collected at room temperature from the 94° bank of the POLARIS diffractometer.

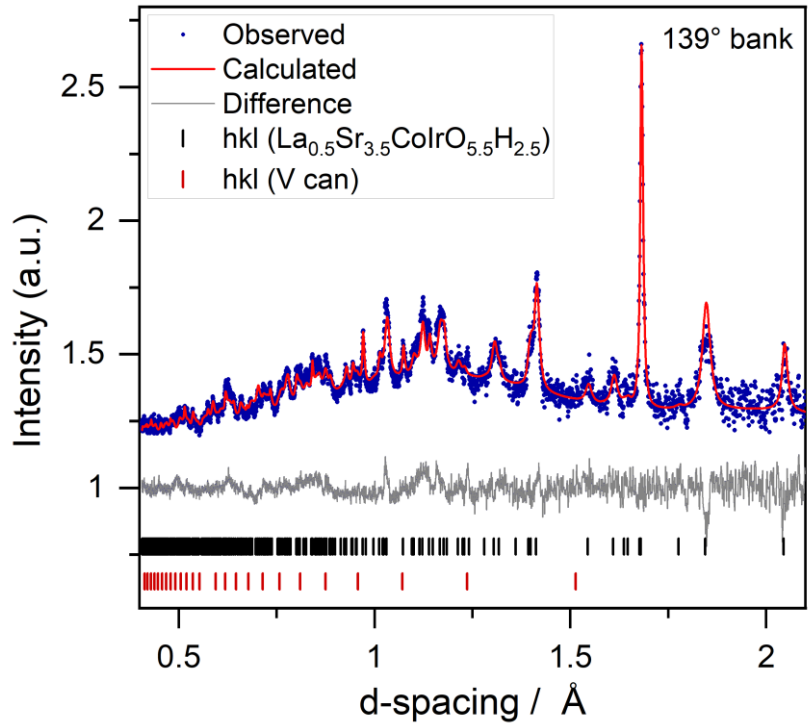

Figure 3.9: Observed, calculated and difference plots from the structural refinement of $La_{0.5}Sr_{3.5}CoIrO_{5.5}H_{2.5}$ against NPD data collected at room temperature from the 139° bank of the POLARIS diffractometer.

Table 3.2: Parameters from the structural refinement of $La_{0.5}Sr_{3.5}CoIrO_{5.5}H_{2.5}$ against NPD data collected at room temperature from the POLARIS diffractometer.

$La_{0.5}Sr_{3.5}CoIrO_{5.48(2)}H_{2.52(2)}$, space group *I*4/*mmm* (No. 139)						
		x	***y***	***z***	**Occ.**	**B_{iso} (Å^2)**
La(1)/Sr(1)	4*e*	0	0	0.3523(1)	0.125/0.875	0.14(4)
Co(1)/Ir(1)	2*a*	0	0	0	0.5/0.5	0.69(7)
O(1)/H(1)	4*c*	0	½	0	0.369(3)/0.631(3)	0.23(6)
O(2)	4*e*	0	0	0.1624(2)	1	0.23(6)
a = 3.6888(5) Å, c = 13.172(1) Å						
V = 179.23(5) Å^3						
R_{wp} = 1.84%, R_p = 1.41%, *gof* = 0.03						

3.3.4 Structural characterisation of $LaSr_3CoIrO_5H_3$

SXRD data collected from the product of the reaction between $LaSr_3CoIrO_8$ and LiH, henceforth referred to as $LaSr_3CoIrO_5H_3$, indicated the presence of a single phase with *I*4/*mmm* symmetry and lattice parameters of a = 3.6601(4) Å and c = 13.251(1) Å.

3.3.4.1 Thermogravimetric analysis

Thermogravimetric data were collected from $LaSr_3CoIrO_5H_3$ whilst heating under flowing oxygen, indicating a mass gain of 4.2%, as shown in Figure 3.10. Assuming full oxidation back to $LaSr_3CoIrO_8$, this corresponds to an initial composition of $LaSr_3CoIrO_{5.95}H_y$, which represents the maximum oxygen content possible for the compound. Analysis of the exhaust gas by mass spectrometry showed a clear release of both water and hydrogen gas associated with the oxidation event, confirming that hydride is present in the phase.

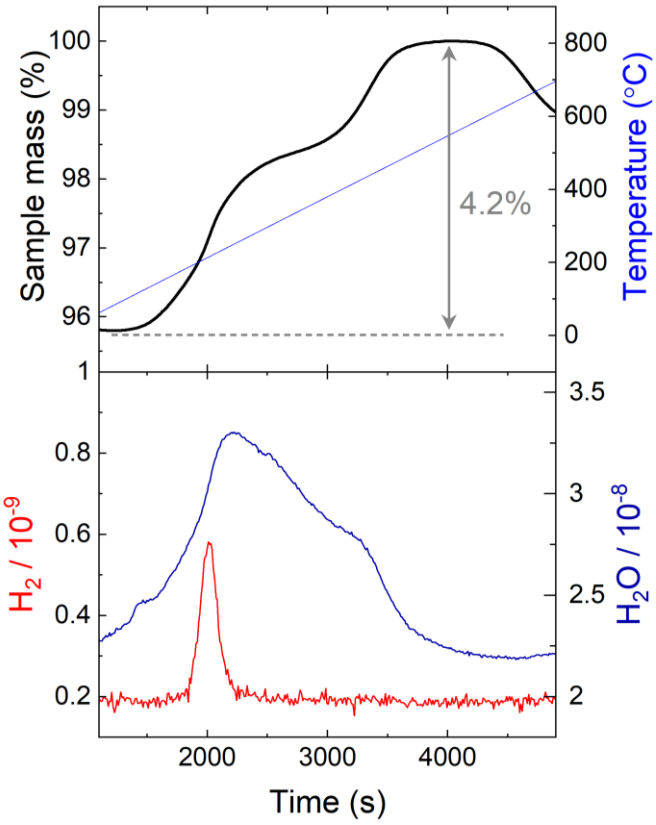

Figure 3.10: TGA trace (top panel) and H_2/H_2O contents of exhaust gas (bottom panel) when $LaSr_3CoIrO_5H_3$ is heated under flowing oxygen.

3.3.4.2 Neutron powder diffraction

NPD data were collected from $LaSr_3CoIrO_5H_3$ at ambient temperature using the POLARIS diffractometer at ISIS. A structural model based on $La_{0.5}Sr_{3.5}CoIrO_{5.5}H_{2.5}$ was constructed using the lattice parameters obtained from SXRD and this was refined against the data from the 54°, 94° and 139° banks of the POLARIS diffractometer. Similar to $La_{0.5}Sr_{3.5}CoIrO_{5.5}H_{2.5}$, the phase was assumed to be an oxyhydride with no anion vacancies. The refinement indicated that the equatorial site has an oxide occupancy of 0.253(4) and a hydride occupancy of 0.747(4), giving an overall composition of $LaSr_3CoIrO_{5.01(2)}H_{2.99(2)}$. The *a*-lattice parameter for this phase is comparable with that of $La_{0.5}Sr_{3.5}CoIrO_{5.5}H_{2.5}$, reflecting the similar hydride contents for these two compounds. The fits to the NPD data are shown in Figure 3.11-3.13, with the refinement parameters presented in Table 3.3. The structural model obtained from the

NPD data was also refined against the SXRD data, which gave a good fit to the data, as shown in Appendix A1.

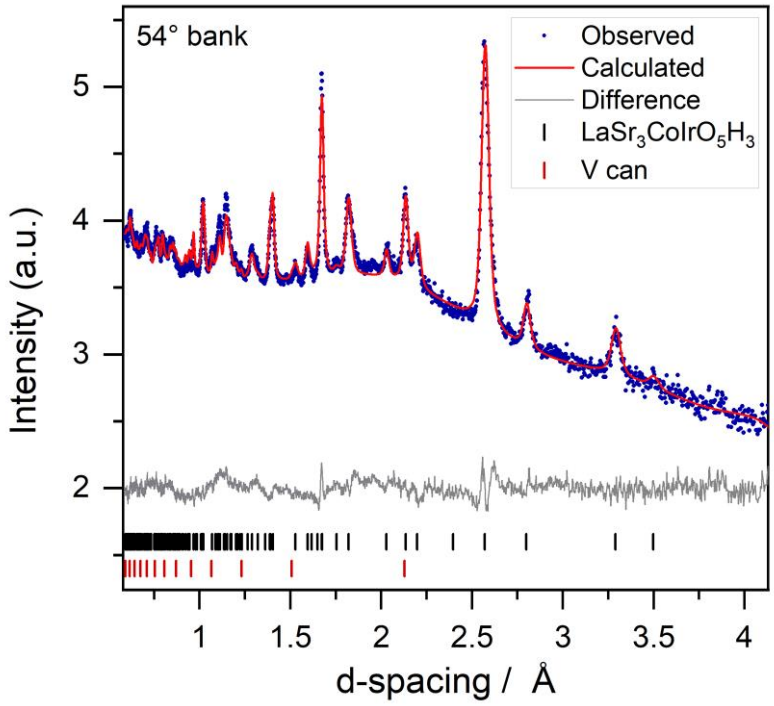

Figure 3.11: Observed, calculated and difference plots from the structural refinement of $LaSr_3CoIrO_5H_3$ against NPD data collected at room temperature from the 54° bank of the POLARIS diffractometer.

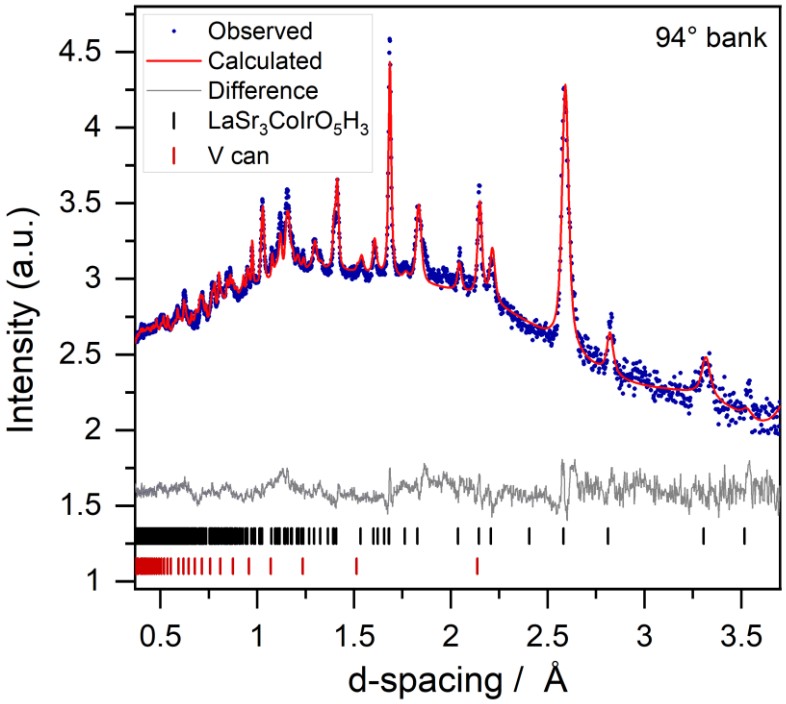

Figure 3.12: Observed, calculated and difference plots from the structural refinement of $LaSr_3CoIrO_5H_3$ against NPD data collected at room temperature from the 94° bank of the POLARIS diffractometer.

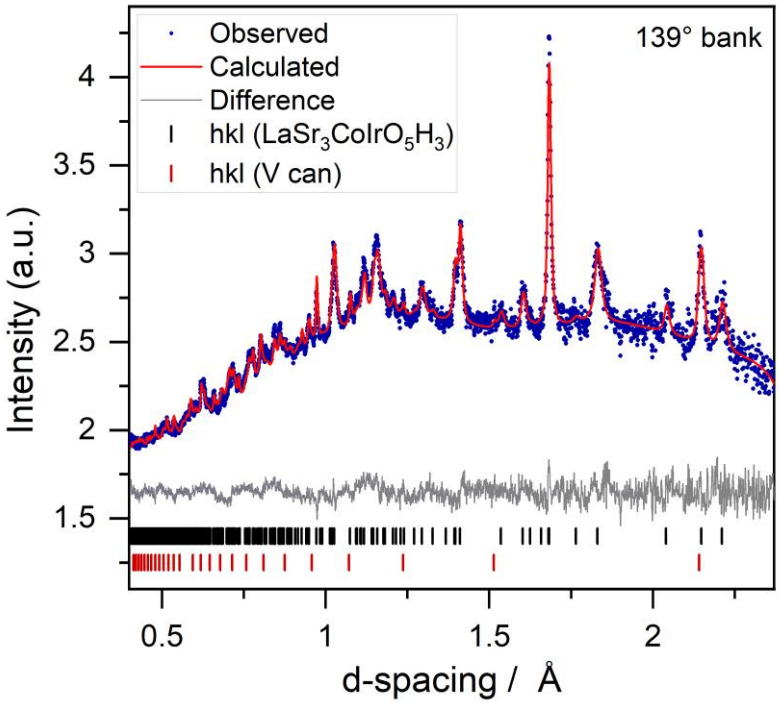

Figure 3.13: Observed, calculated and difference plots from the structural refinement of $LaSr_3CoIrO_5H_3$ against NPD data collected at room temperature from the 139° bank of the POLARIS diffractometer.

Table 3.3: Parameters from the structural refinement of $LaSr_3CoIrO_5H_3$ against NPD data collected at room temperature from the POLARIS diffractometer.

$LaSr_3CoIrO_{5.01(2)}H_{2.99(2)}$, space group *I*4/*mmm* (No. 139)						
		x	***y***	***z***	**Occ.**	**B_{iso} (Å^2)**
La(1)/Sr(1)	4*e*	0	0	0.3529(2)	0.25/0.75	0.08(4)
Co(1)/Ir(1)	2*a*	0	0	0	0.5/0.5	1.1(1)
O(1)/H(1)	4*c*	0	½	0	0.253(4)/0.747(4)	0.35(6)
O(2)	4*e*	0	0	0.1656(3)	1	0.35(6)
a = 3.6596(5) Å, c = 13.266(2) Å						
V = 177.67(6) Å^3						
R_{wp} = 1.67%, R_p = 1.29%, *gof* = 0.05						

3.3.5 Structural characterisation of $La_{1.5}Sr_{2.5}CoIrO_{8-y}H_y$

SXRD data was collected from the product of the reaction between $La_{1.5}Sr_{2.5}CoIrO_8$ and LiH, henceforth referred to as $La_{1.5}Sr_{2.5}CoIrO_{8-y}H_y$. Most of the reflections in the data could be indexed using a single phase with *I*4/*mmm* symmetry and lattice parameters of a = 3.6762(4) Å

and c = 13.221(2) Å. However, close inspection of the pattern showed the presence of additional features associated with some of the peaks. This is most prominent for the 110 reflection, as highlighted in Figure 3.14.

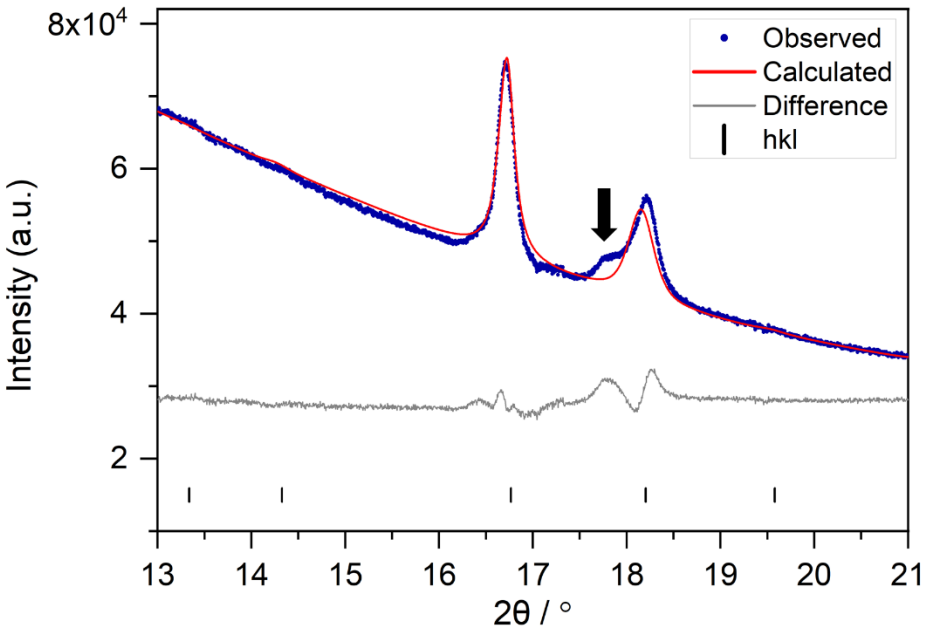

Figure 3.14: Observed, calculated and difference plots from the initial structural refinement of $La_{1.5}Sr_{2.5}CoIrO_{8-y}H_y$ against SXRD data. The additional feature close to the 110 reflection is highlighted.

These features are likely to arise from the presence of an additional phase for which the reduction has not gone to completion. The peaks could be indexed using a second *I*4/*mmm* phase with a larger *a*-lattice parameter (a = 3.7404(6) Å) and smaller *c*-lattice parameter (c = 13.037(4) Å), relative to the main phase.

3.3.5.1 Thermogravimetric analysis

Thermogravimetric data were collected from $La_{1.5}Sr_{2.5}CoIrO_{8-y}H_y$ whilst heating under flowing oxygen, indicating a mass gain of 4.4%, as shown in Figure 3.15. Assuming full oxidation back to $La_{1.5}Sr_{2.5}CoIrO_8$, this corresponds to an initial composition of $La_{1.5}Sr_{2.5}CoIrO_{5.84}H_y$. Analysis of the exhaust gas by mass spectrometry showed a clear release of both water and hydrogen gas associated with the oxidation event, confirming that hydride is present in the phase.

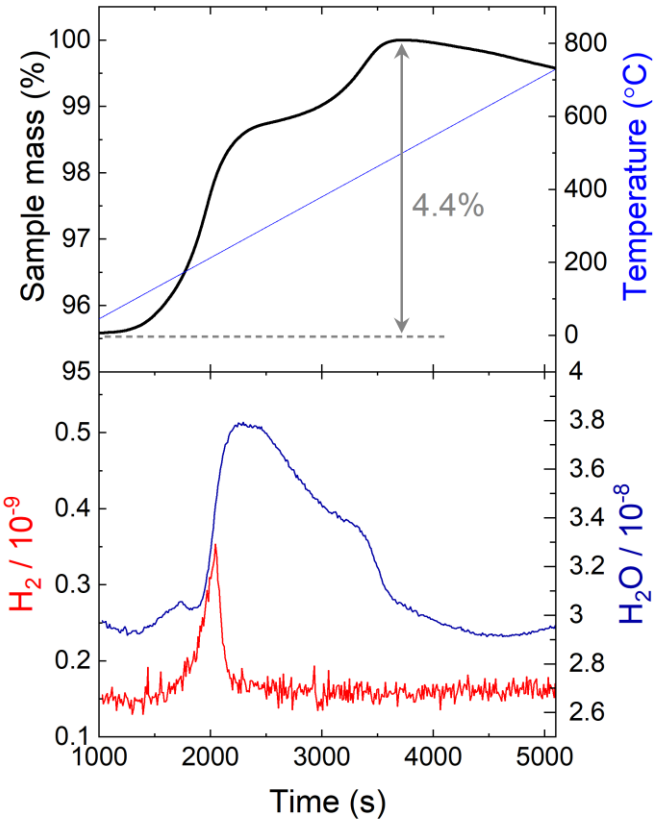

Figure 3.15: TGA trace (top panel) and H_2/H_2O contents of exhaust gas (bottom panel) when $La_{1.5}Sr_{2.5}CoIrO_{8-y}H_y$ is heated under flowing oxygen.

3.3.5.2 Neutron powder diffraction

NPD data were collected from $La_{1.5}Sr_{2.5}CoIrO_{8-y}H_y$ at ambient temperature using the POLARIS diffractometer at ISIS. As with the SXRD data, although an initial one-phase refinement against the data from the 54°, 94° and 139° detector banks of the POLARIS diffractometer could fit most of the peaks, many of the peaks had additional features that could not be fit using this model. The features are most prominent for the 200, 114 and 110 reflections, as highlighted in Figure 3.16.

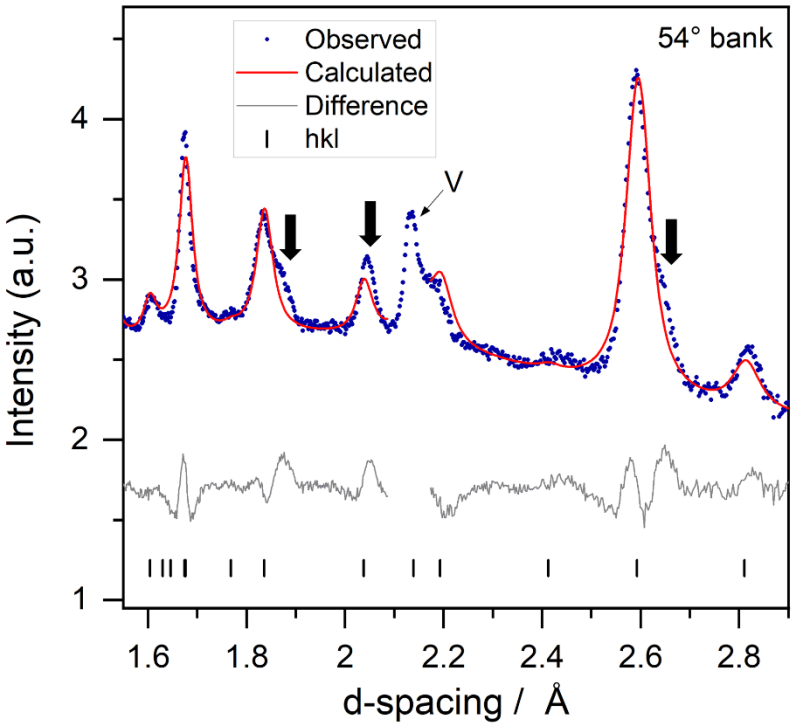

Figure 3.16: Observed, calculated and difference plots from the initial structural refinement of $La_{1.5}Sr_{2.5}CoIrO_{5.5}H_{2.5}$ against NPD data collected at room temperature from the 54° bank of the POLARIS diffractometer. The region around 2.14 Å contains a peak from the vanadium sample can so is excluded from the refinement. The additional features observed close to the 200, 114 and 110 reflections are highlighted.

To account for this, a second phase was added with the lattice parameters obtained from the refinement against SXRD data, which allowed an acceptable fit to the data to be achieved. The fits to the NPD data are shown in Figure 3.17-3.19, with the refinement parameters presented in Table 3.4.

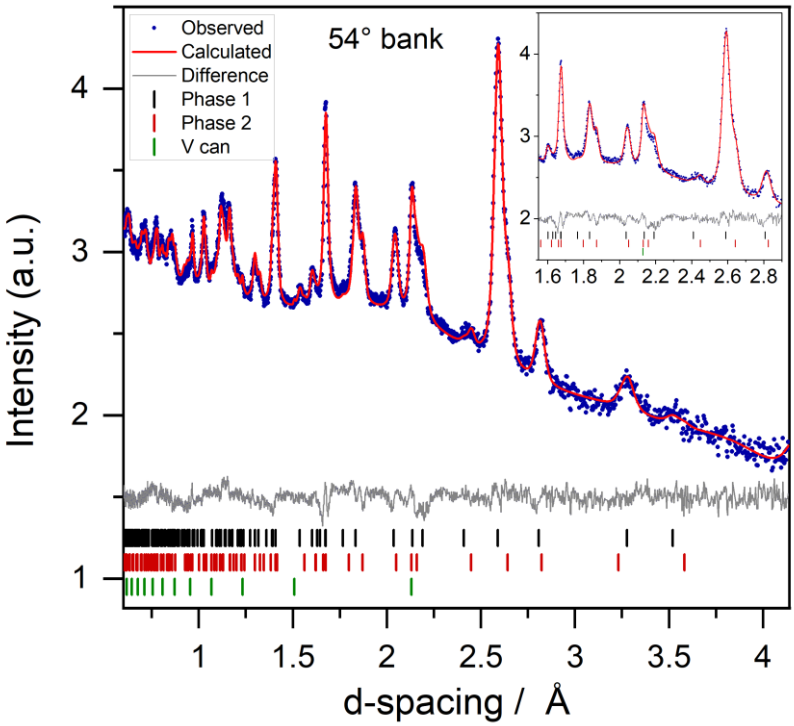

Figure 3.17: Observed, calculated and difference plots from the two-phase structural refinement of $La_{1.5}Sr_{2.5}CoIrO_{8-y}H_y$ against NPD data collected at room temperature from the 54° bank of the POLARIS diffractometer. Phase 1 has a refined composition of $La_{1.5}Sr_{2.5}CoIrO_{5.5}H_{2.5}$, whilst Phase 2 has a refined composition of $La_{1.5}Sr_{2.5}CoIrO_{6.8}H_{1.2.}$ The inset shows an expanded region from 1.5 to 2.9 Å to allow the fit to be compared to the initial one-phase refinement presented in Figure 3.16.

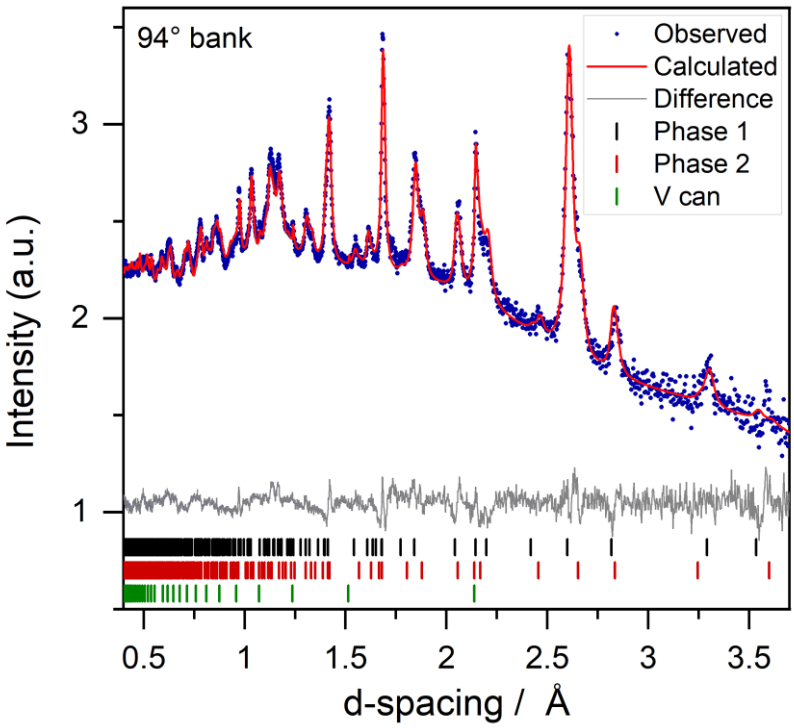

Figure 3.18: Observed, calculated and difference plots from the two-phase structural refinement of $La_{1.5}Sr_{2.5}CoIrO_{8-y}H_y$ against NPD data collected at room temperature from the 94° bank of the POLARIS diffractometer.

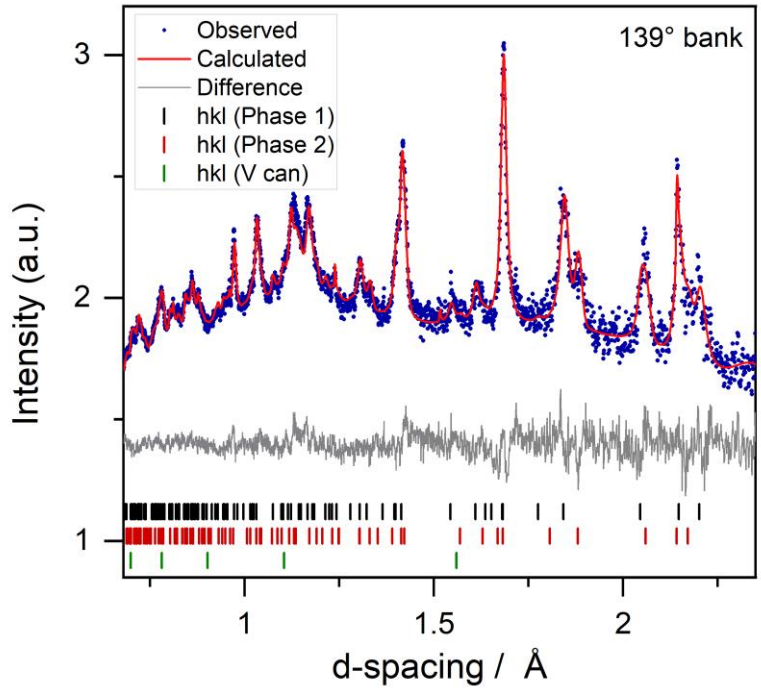

Figure 3.19: Observed, calculated and difference plots from the two-phase structural refinement of $La_{1.5}Sr_{2.5}CoIrO_{8-y}H_y$ against NPD data collected at room temperature from the 139° bank of the POLARIS diffractometer.

Table 3.4: Parameters from the two-phase structural refinement of $La_{1.5}Sr_{2.5}CoIrO_{8-y}H_y$ against NPD data collected at room temperature from the POLARIS diffractometer.

$La_{1.5}Sr_{2.5}CoIrO_{5.47(3)}H_{2.53(3)}$, space group *I*4/*mmm* (No. 139), 85.4(8) wt%						
		x	***y***	***z***	**Occ.**	**B_{iso} (Å^2)**
La(1)/Sr(1)	4*e*	0	0	0.3547(2)	0.625/0.375	0.07(6)
Co(1)/Ir(1)	2*a*	0	0	0	0.5/0.5	2.0(2)
O(1)/H(1)	4*c*	0	½	0	0.367(4)/0.633(4)	0.07(6)
O(2)	4*e*	0	0	0.1692(3)	1	0.07(6)
a = 3.6895(7) Å, c = 13.233(2) Å						
V = 180.13(7) Å^3						
$La_{1.5}Sr_{2.5}CoIrO_{6.79(5)}H_{1.21(5)}$, space group *I*4/*mmm* (No. 139), 14.6(7) wt%						
		x	***y***	***z***	**Occ.**	**B_{iso} (Å^2)**
La(1)/Sr(1)	4*e*	0	0	0.3547(2)	0.625/0.375	0.1(2)
Co(1)/Ir(1)	2*a*	0	0	0	0.5/0.5	3.1(5)
O(1)/H(1)	4*c*	0	½	0	0.70(1)/0.30(1)	0.3(2)
O(2)	4*e*	0	0	0.1692(3)	1	0.3(2)
a = 3.7661(8) Å, c = 13.029(5) Å						
V = 184.8(1) Å^3						
R_{wp} = 1.80%, R_p = 1.39%, *gof* = 0.04						

The refinement indicated that the main phase is present with a weight fraction of 85.4(7)%, and has an oxide occupancy of 0.367(4) and a hydride occupancy of 0.633(4) at the equatorial anion sites, yielding an overall composition of $La_{1.5}Sr_{2.5}CoIrO_{5.47(3)}H_{2.53(3)}$, which will henceforth be referred to as $La_{1.5}Sr_{2.5}CoIrO_{5.5}H_{2.5}$. The *a*-lattice parameter for this phase is 3.6895(7) Å, which is slightly larger than that for $LaSr_3CoIrO_5H_3$, consistent with the reduced hydride content.

Meanwhile, the secondary phase is present with a weight fraction of 14.6(7)%, and has an oxide occupancy of 0.70(1) and a hydride occupancy of 0.30(1) at the equatorial anion sites, yielding an overall composition of $La_{1.5}Sr_{2.5}CoIrO_{6.79(5)}H_{1.21(5)}$, which will henceforth be referred to as $La_{1.5}Sr_{2.5}CoIrO_{6.8}H_{1.2}$. The larger *a*-lattice parameter of 3.7671(8) Å and shorter *c*-lattice parameter of 13.022(5) Å, relative to $La_{1.5}Sr_{2.5}CoIrO_{5.5}H_{2.5}$, reflects the increased oxide ion content at the equatorial sites, and is consistent with what would be expected for compounds with this anion composition (Figure A 11). The average oxide ion content of $La_{1.5}Sr_{2.5}CoIrO_{5.69}H_y$ for the two phases is broadly consistent with the value of $La_{1.5}Sr_{2.5}CoIrO_{5.84}H_y$ obtained from the TGA data.

A two-phase refinement against the SXRD data was also performed using the structural models obtained from the NPD data, which gave a good fit to the data, as shown in Appendix A1.

3.3.6 Structural characterisation of $La_2Sr_2CoIrO_{8-y}H_y$

Similar to the data from $La_{1.5}Sr_{2.5}CoIrO_{8-y}H_y$, inspection of the SXRD data collected from $La_2Sr_2CoIrO_{8-y}H_y$ indicated the presence of two closely related Ruddlesden-Popper phases. Both phases could be indexed using *I*4/*mmm* cells, with the main phase having lattice parameters of a = 3.6996(9) Å and c = 13.374(6) Å and the secondary phase having lattice parameters of a = 3.745(1) Å and c = 13.068(3) Å. In addition, sharp peaks corresponding to Ir metal (inherited from the starting material) were observed.

3.3.6.1 Thermogravimetric analysis

Thermogravimetric data were collected from $La_2Sr_2CoIrO_{8-y}H_y$ whilst heating under flowing oxygen, indicating a mass gain of 4.0%, as shown in Figure 3.20. Assuming full oxidation back to $La_2Sr_2CoIrO_8$, this corresponds to an initial composition of $La_2Sr_2CoIrO_{5.91}H_y$. Analysis of the exhaust gas by mass spectrometry showed release of both water and hydrogen gas concurrent with the oxidation event, confirming that hydride is present in the phase.

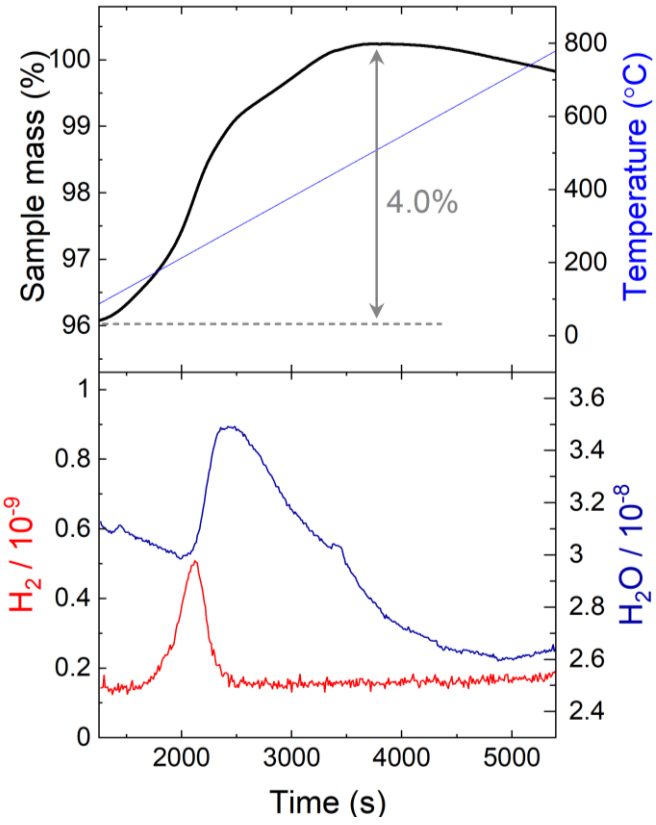

Figure 3.20: TGA trace (top panel) and H_2/H_2O contents of exhaust gas (bottom panel) when $La_2Sr_2CoIrO_{8-y}H_y$ is heated under flowing oxygen.

3.3.6.2 Neutron powder diffraction

NPD data were collected from $La_2Sr_2CoIrO_{8-y}H_y$ at ambient temperature using the POLARIS diffractometer at ISIS. Refinements were performed using two Ruddlesden-Popper based phases with the initial lattice parameters taken from the SXRD refinements and the initial

hydride contents taken to be the same as those for $La_{1.5}Sr_{2.5}CoIrO_{5.5}H_{2.5}$ and $La_{1.5}Sr_{2.5}CoIrO_{6.8}H_{1.2}$. Ir metal was also included as an impurity phase. The fits to the NPD data from the 54°, 94° and 139° detector banks of the POLARIS diffractometer are shown in Figure 3.21-3.23, with the refinement parameters presented in Table 3.5.

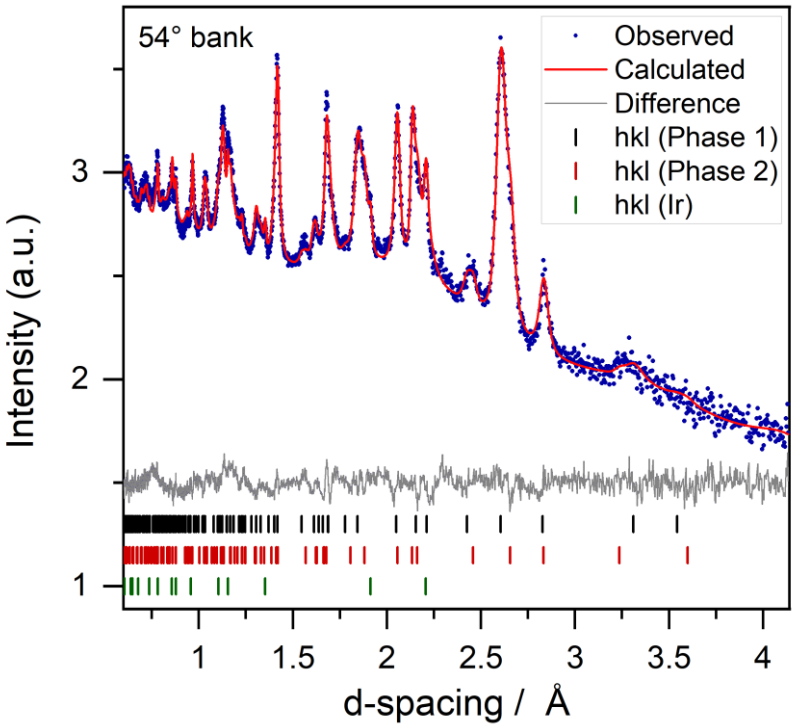

Figure 3.21: Observed, calculated and difference plots from the structural refinement of $La_2Sr_2CoIrO_{8-y}H_y$ against NPD data collected at room temperature from the 54° bank of the POLARIS diffractometer. Phase 1 has a refined composition of $La_2Sr_2CoIrO_6H_2$, whilst Phase 2 has a refined composition of $La_2Sr_2CoIrO_7H$.

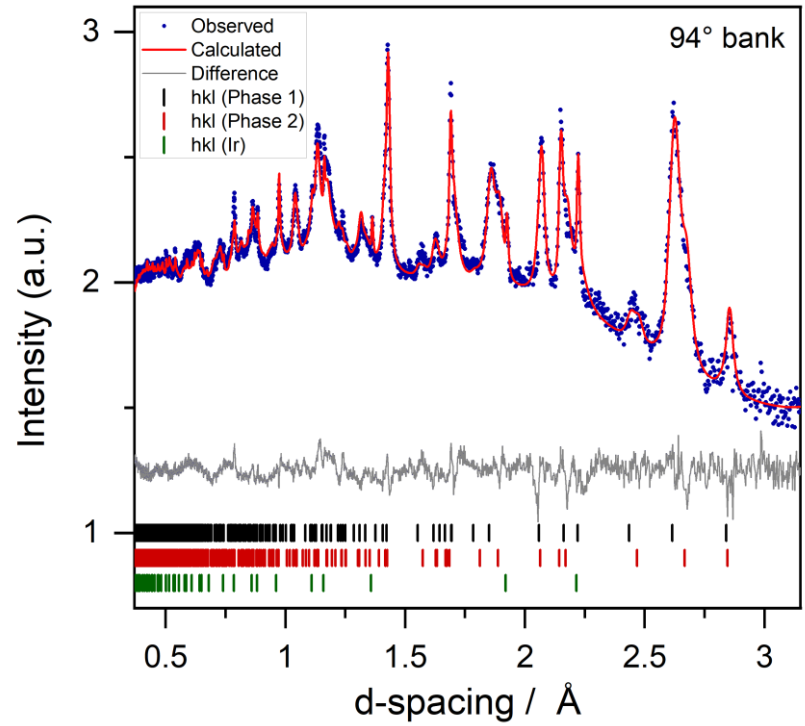

Figure 3.22: Observed, calculated and difference plots from the structural refinement of $La_2Sr_2CoIrO_{8-y}H_y$ against NPD data collected at room temperature from the 94° bank of the POLARIS diffractometer.

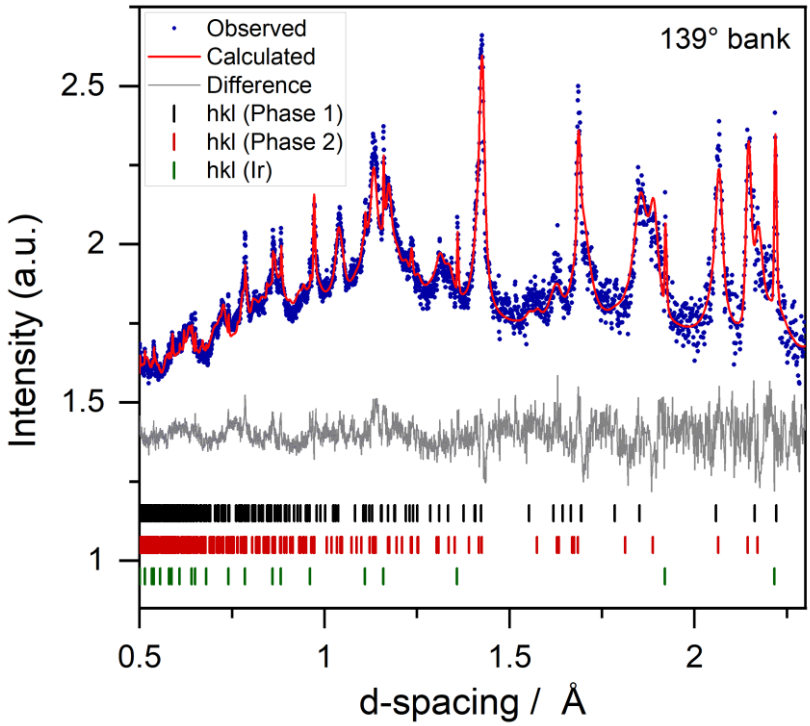

Figure 3.23: Observed, calculated and difference plots from the structural refinement of $La_2Sr_2CoIrO_{8-y}H_y$ against NPD data collected at room temperature from the 139° bank of the POLARIS diffractometer.

Table 3.5: Parameters from the structural refinement of $La_2Sr_2CoIrO_{8-y}H_y$ against NPD data collected at room temperature from the POLARIS diffractometer.

$La_2Sr_2CoIrO_{5.99(7)}H_{2.01(7)}$, space group *I*4/*mmm* (No. 139), 82.3(8) wt%						
		x	***y***	***z***	**Occ.**	**B_{iso} (Å^2)**
La(1)/Sr(1)	4*e*	0	0	0.3529(4)	0.5/0.5	0.36(8)
Co(1)/Ir(1)	2*a*	0	0	0	0.5/0.5	7.5(4)
O(1)/H(1)	4*c*	0	½	0	0.50(2)/0.50(2)	7(2)
O(2)	4*e*	0	0	0.1696(4)	1	0.11(9)
a = 3.7070(6) Å, c = 13.342(4) Å						
V = 183.35(8) Å^3						
$La_2Sr_2CoIrO_{6.97(5)}H_{1.03(5)}$, space group *I*4/*mmm* (No. 139), 15.9(8) wt%						
		x	***y***	***z***	**Occ.**	**B_{iso} (Å^2)**
La(1)/Sr(1)	4*e*	0	0	0.3606(4)	0.5/0.5	0.01(7)
Co(1)/Ir(1)	2*a*	0	0	0	0.5/0.5	0.01(7)
O(1)/H(1)	4*c*	0	½	0	0.74(1)/0.26(1)	0.01(7)
O(2)	4*e*	0	0	0.1719(6)	1	0.01(7)
a = 3.7789(8) Å, c = 13.040(2) Å						
V = 186.21(9) Å^3						
Ir, space group *Fm*−3*m* (No. 225), 1.8(1) wt%						
		x	***y***	***z***	**Occ.**	**B_{iso} (Å^2)**
Ir(1)	4*a*	0	0	0	1	0.05(8)
a = 3.8437(5) Å						
V = 56.79(2) Å^3						
R_{wp} = 1.79%, R_p = 1.39%, *gof* = 0.04						

Refinement of the $La_2Sr_2CoIrO_{8-y}H_y$ mixture against the NPD data showed that the main phase has an oxide occupancy of 0.50(2) and a hydride occupancy of 0.50(2) in the equatorial anion positions, yielding an overall composition of $La_2Sr_2CoIrO_{5.99(7)}H_{2.01(7)}$, which will henceforth be referred to as $La_2Sr_2CoIrO_6H_2$. The refined *a*-lattice parameter of a = 3.7070(6) Å shows an expansion of the *xy*-plane relative to $La_{1.5}Sr_{2.5}CoIrO_{5.5}H_{2.5}$, which is consistent with the increased oxide ion content in the equatorial plane. Meanwhile, the refinement showed that the equatorial anion positions in the secondary phase have an oxide occupancy of 0.74(1) and a

hydride occupancy of 0.26(1), corresponding to an overall composition of $La_2Sr_2CoIrO_{6.97(5)}H_{1.03(5)}$, which will henceforth be referred to as $La_2Sr_2CoIrO_7H$. The refined lattice parameters of $a = 3.7797(8)$ Å and $c = 13.037(2)$ Å are close to those of $La_{1.5}Sr_{2.5}CoIrO_{6.8}H_{1.2}$, which is congruous with the observation that these phases have a similar anion composition. The average oxide ion content of $La_2Sr_2CoIrO_{6.16}H_y$ for the two phases is slightly larger than the composition of $La_2Sr_2CoIrO_{5.91}H_y$ obtained from the TGA measurements. This discrepancy can be attributed to the presence of Ir metal in the sample, which is oxidised during the TGA measurement, resulting in a mass gain that is larger than expected.

Structural refinements were also performed against the SXRD data using the models obtained from the NPD data, which gave a good fit to the data, as shown in Appendix A1.

3.3.7 Comparison of refined lattice parameters and bond lengths

The lattice parameters and bond lengths obtained from the SXRD and NPD refinements for the all-oxide $La_xSr_{4-x}CoIrO_8$ and oxyhydride $La_xSr_{4-x}CoIrO_{8-y}H_y$ phases are summarised in Table 3.6.

Table 3.6: Selected lattice parameters, bond lengths and bond length ratios for $La_xSr_{4-x}CoIrO_8$ starting materials (SM) and $La_xSr_{4-x}CoIrO_{8-y}H_y$ reduced phases (RP) from SXRD and NPD refinements. For x = 1.5 and x = 2, only the parameters from the majority phases are shown.

x		a (Å)	c (Å)	Vol (Å^3)	M–(O/H)$_{eq.}$ (Å)	M–O$_{ax.}$ (Å)	M–O$_{ax.}$ / M–(O/H)$_{eq.}$
0	**SM**	3.91778(6)	12.4770(2)	191.510(7)	1.95889(3)	2.03375(4)	1.038
	RP	3.8058(3)	13.037(1)	188.84(4)	1.9029(2)	2.124(3)	1.116
0.5	**SM**	3.88836(3)	12.5844(1)	190.268(4)	1.94418(1)	2.05125(3)	1.055
	RP	3.6888(5)	13.172(1)	179.23(5)	1.8444(3)	2.139(3)	1.160
1	**SM**	3.87999(4)	12.5927(1)	189.574(4)	1.94000(1)	2.07023(3)	1.067
	RP	3.6596(5)	13.266(2)	177.67(6)	1.8298(3)	2.197(4)	1.201
1.5	**SM**	3.90328(7)	12.5893(2)	191.805(8)	1.95164(4)	2.05206(4)	1.051
	RP	3.6895(7)	13.233(2)	180.13(7)	1.8448(4)	2.239(4)	1.214
2	**SM**	3.89677(2)	12.5777(1)	190.990(3)	1.94839(1)	2.05017(1)	1.052
	RP	3.7070(6)	13.342(4)	183.35(8)	1.8535(4)	2.263(6)	1.221

The variation in a-lattice parameter as a function of A-site cation composition in the $La_xSr_{4-x}CoIrO_{8-y}H_y$ oxyhydride phases is shown in Figure 3.24. There is a sharp decrease from x = 0 to x = 1, consistent with the increase in equatorial hydride content from $Sr_4CoIrO_{6.5}H_{1.5}$ to $LaSr_3CoIrO_5H_3$. There is then a gradual increase in lattice parameter from x = 1 to x = 2, consistent with the decrease in hydride content from $LaSr_3CoIrO_5H_3$ to $La_2Sr_2CoIrO_6H_2$. The a-lattice parameters for $La_{0.5}Sr_{3.5}CoIrO_{5.5}H_{2.5}$ and $La_{1.5}Sr_{2.5}CoIrO_{5.5}H_{2.5}$ are very similar, reflecting the fact that they have the same anion composition.

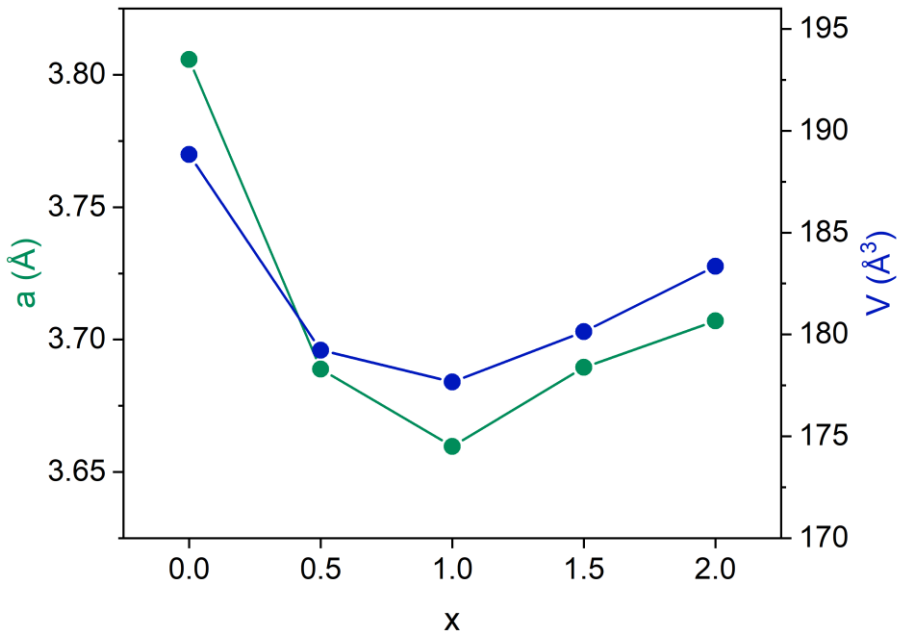

Figure 3.24: Variation in *a*-lattice parameter and volume as a function of A-site cation composition in $La_xSr_{4-x}CoIrO_{8-y}H_y$ phases.

3.3.8 X-ray absorption spectroscopy

XAS measurements were performed on $Sr_4CoIrO_{6.5}H_{1.5}$, $LaSr_3CoIrO_5H_3$ and $La_2Sr_2CoIrO_6H_2$, with Sr_2CoIrO_6 and $YBaCo_2O_5$ acting as standards. The measurements were performed with a laboratory instrument at energies between 7650 and 8200 eV to allow the Co K-edge (7709 eV) to be observed. The spectra were calibrated using Co foil and normalised up to 7950 eV. The data at the XANES edges are shown in Figure 3.25.

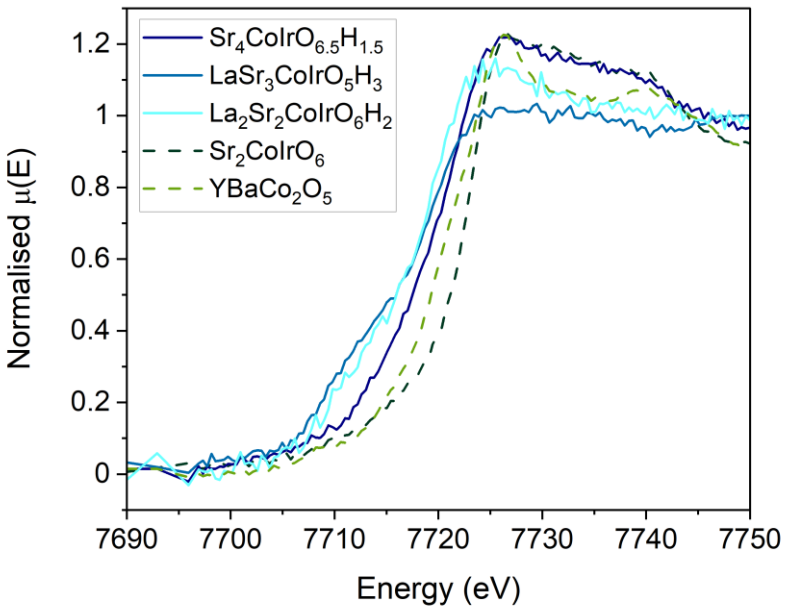

Figure 3.25: XANES Co K-edges for $Sr_4CoIrO_{6.5}H_{1.5}$, $LaSr_3CoIrO_5H_3$ and $La_2Sr_2CoIrO_6H_2$, with Sr_2CoIrO_6 (Co^{3+}) and $YBaCo_2O_5$ ($Co^{2.5+}$) acting as standards.

The position of the XANES edge for $Sr_4CoIrO_{6.5}H_{1.5}$ suggests that cobalt is present as Co^{II} in this compound. Meanwhile, the edges for $LaSr_3CoIrO_5H_3$ and $La_2Sr_2CoIrO_6H_2$ are very similar to each other and are located at lower energy than that of $Sr_4CoIrO_{6.5}H_{1.5}$. This indicates that cobalt is more reduced in these compounds and is consistent with the existence of Co^{I} in both phases. The absence of pre-edge features indicates that the cobalt adopts centrosymmetric coordination environments in all the compounds.

3.3.9 Discussion

3.3.9.1 Anion site selectivity in $La_xSr_{4-x}CoIrO_{8-y}H_y$ oxyhydride phases

Reaction of the Ruddlesden-Popper $La_xSr_{4-x}CoIrO_8$ phases with LiH allows the preparation of oxyhydride phases through oxide-to-hydride anion exchange at the equatorial sites. This is consistent with the reactivity that is typically observed when $n = 1$ Ruddlesden-Popper phases are reacted with binary metal hydrides.[47,48,51–53,93] The preference for locating hydride ions at the equatorial sites can be explained by considering the changes in the oxidation states of the

A- and B-site cations during the topochemical reductions. When perovskite-based transition metal oxides are reacted with binary metal hydrides, the B-site cations are reduced, whilst the oxidation states of the A-site cations remain constant. Therefore, it is most favourable to remove the oxide ions that have a larger bonding contribution from the B-site cations and a smaller contribution from the A-site cations.[94] To quantify this, the bond valence method can be used. This relates the valence of an ion to its bond lengths using empirically determined parameters. As such, by considering the anion bond valence sums at each anion site in the parent oxides, the relative bonding contributions of the A- and B-site cations at each anion site can be quantified. This is shown for $LaSr_3CoIrO_8$ in Table 3.7.

Table 3.7: Calculated anion bond valence sums with respect to the A- and B-site cations for $LaSr_3CoIrO_8$.

Anion	**Anion BVS**	
$O_{ax.}$	BVS(A)	1.191
	BVS(B)	0.487
	BVS(B) − BVS(A)	− 0.704
$O_{eq.}$	BVS(A)	0.993
	BVS(B)	1.385
	BVS(B) − BVS(A)	+ 0.392

The calculated value BVS(B) − BVS(A) can be interpreted as the degree to which the B-site cation contributes to the bonding of the oxide ion relative to the A-site cation. From Table 3.7, the equatorial site has a more positive value for BVS(B) − BVS(A), indicating that this has the greater bonding contribution from B-site cations. This is consistent with the qualitative picture of the coordination environments of the anions, in which the coordination of the equatorial oxide ion is A_4B_2, whilst that of the axial ion is A_5B. The consequence of this is that it is more favourable for oxide-to-hydride exchange to occur at the equatorial positions, compared to the axial positions.

3.3.9.2 Anion compositions of $La_xSr_{4-x}CoIrO_{8-y}H_y$ oxyhydride phases

The anion compositions of the oxyhydride Ruddlesden-Popper phases, $La_xSr_{4-x}CoIrO_{8-y}H_y$, vary across the solid solution series, as summarised in Table 3.8, and presented visually in Figure 3.26.

Table 3.8: Summary of the oxyhydride phases formed from the reaction of the solid solution series, $La_xSr_{4-x}CoIrO_8$, with LiH, and likely oxidation states for the transition metals in these compounds. For the $x = 1.5$ and $x = 2$ members of the series, only the composition of the principal phase is listed.

Starting material	Oxidation states	Oxyhydride phase	Oxidation states
Sr_4CoIrO_8	Co^{III}, Ir^{V}	$Sr_4CoIrO_{6.5}H_{1.5}$	Co^{II}, $Ir^{IV/V}$
$La_{0.5}Sr_{3.5}CoIrO_8$	$Co^{II/III}$, Ir^{V}	$La_{0.5}Sr_{3.5}CoIrO_{5.5}H_{2.5}$	Co^{II}, Ir^{III}
$LaSr_3CoIrO_8$	Co^{II}, Ir^{V}	$LaSr_3CoIrO_5H_3$	Co^{I}, Ir^{III}
$La_{1.5}Sr_{2.5}CoIrO_8$	Co^{II}, $Ir^{IV/V}$	$La_{1.5}Sr_{2.5}CoIrO_{5.5}H_{2.5}$	Co^{I}, Ir^{III}
$La_2Sr_2CoIrO_8$	Co^{II}, Ir^{IV}	$La_2Sr_2CoIrO_6H_2$	Co^{I}, Ir^{III}

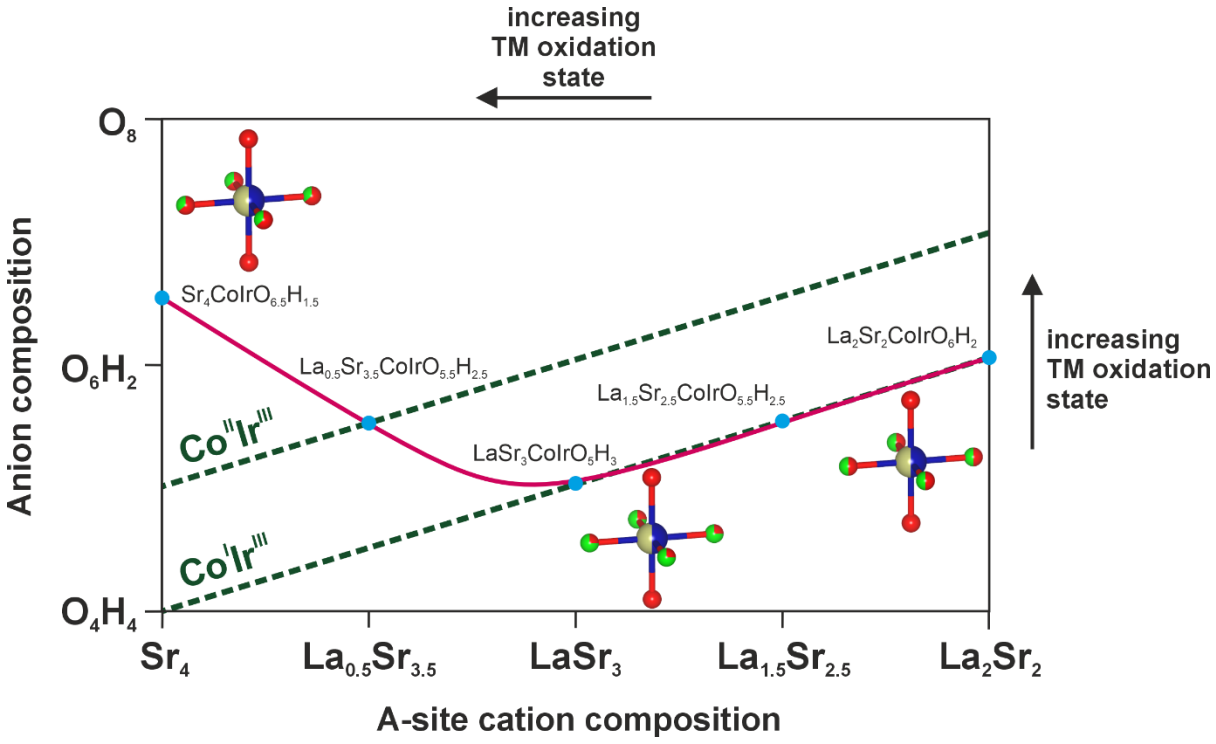

Figure 3.26: Composition space for the $La_xSr_{4-x}CoIrO_{8-y}H_y$ ($0 \leq x \leq 2$) series of oxyhydride phases as a function of anion composition and A-site cation composition. The blue, circular markers indicate the experimentally observed compositions. The pink, solid line connects the experimental compositions and is intended as a guide for the eye. The green, dashed lines represent the anion compositions corresponding to Co^{I}/Ir^{III} and Co^{II}/Ir^{III} transition metal oxidation state combinations. For a given A-site cation composition, transition metal oxidation state increases vertically, whilst, for a given anion composition, transition metal oxidation state increases towards the left of the diagram.

For the x = 1, 1.5 and 2 members of the series, the extent of reaction appears to be limited by the formation of the Co^{I}/Ir^{III} oxidation state combination. The presence of iridium in $La_xSr_{4-x}CoIrO_{8-y}H_y$ phases provides substantial covalent stabilisation to the oxyhydrides due to the formation of strong Ir−H σ-bonds, similar to the role of ruthenium in $LaSr_3NiRuO_4H_4$.[51] However, reduction of octahedrally coordinated iridium from Ir^{III} to Ir^{II} is unlikely to occur. This is because the strong crystal field splitting in iridium leads to the e_g orbitals being strongly antibonding. As a result, it is energetically unfavourable for these orbitals to be populated, thus preventing reduction below Ir^{III} (low-spin d^6). The formation of the Co^{I}/Ir^{III} oxidation state combination in $La_xSr_{4-x}CoIrO_{8-y}H_y$ (x = 1, 1.5, 2) phases is analogous to the transition metal oxidation states obtained in $La_2Sr_2CoRhO_6H_2$, whereby cobalt is present as Co^{I} (d^8) and rhodium is present as Rh^{III} (low-spin d^6).[52]

The covalent stabilisation arising from the formation of Ir−H σ-bonds is likely to be larger for compounds that have a higher hydride content and, as a result, the stability of oxyhydride phases with a Co^{I}/Ir^{III} combination should increase towards the left of Figure 3.26. This is consistent with the experimentally observed reactivity. For the x = 1.5 and 2 compounds, two-phase mixtures were observed, whereas for the x = 1 compound, it was possible to obtain a pure oxyhydride phase.

The secondary phases for the x = 1.5 and x = 2 compounds have compositions of $La_{1.5}Sr_{2.5}CoIrO_{6.8}H_{1.2}$ and $La_2Sr_2CoIrO_7H$, respectively. The oxidation states for the transition metals in both these phases are likely to be approximately Co^{II} and Ir^{III}. This suggests that there is a phase gap associated with the reduction from Co^{II} to Co^{I}, which is discussed further in Section 3.3.9.3.

For the x = 0.5 compound, the final oxyhydride phase obtained has composition $La_{0.5}Sr_{3.5}CoIrO_{5.5}H_{2.5}$, which corresponds to a $Co^{II}Ir^{III}$ oxidation state combination. This

suggests that, whilst it is possible to reduce the compound to this level, the reaction mixture cannot be heated to a sufficiently high temperature to overcome the phase gap without non-topochemical decomposition occurring.

Meanwhile, when the reaction is attempted for the $x = 0$ compound, the temperature at which the reaction can be heated without decomposition occurring is much lower than that required to achieve even the $Co^{II}Ir^{III}$ oxidation state combination. This is due to the fact that the transition metal oxidation states in the starting material ($Co^{III}Ir^{V}$) are higher than those for the rest of the series, so a greater degree of reduction is required to achieve the same oxidation states.

As such, the final composition obtained is a balance between the stability of the overall perovskite framework and the obtainment of the Co^{I}/Ir^{III} oxidation state combination. For $x = 0$ and 0.5, the final composition is limited by the temperature at which the temperature the reaction can be carried out without decomposition (as a greater degree of reduction is required to achieve the Co^{I}/Ir^{III} oxidation state combination), whilst for $x = 1$, 1.5 and 2, the final composition is limited by the formation of octahedrally-coordinated Ir^{III}, which cannot be reduced to Ir^{II}.

3.3.9.3 Presence of a phase gap and apparent anion disorder in $La_xSr_{4-x}CoIrO_{8-y}H_y$ phases

As noted in Section 3.3.9.2, a phase gap associated with the reduction of Co^{II} to Co^{I} is observed when $La_xSr_{4-x}CoIrO_8$ Ruddlesden-Popper phases are reacted with LiH. This can be rationalised by considering the contrasting coordination preferences of Co^{I} and Co^{II}.

In general, the strong *trans*-influence associated with hydride ions causes them to preferentially arrange *cis* to each other, as discussed in Section 1.4.2. However, if octahedrally coordinated transition metals with d^2, high-spin d^7 or low-spin d^5 configurations are present, then the hydride ions prefer to adopt a *trans*-configuration around the metal.

For oxyhydride phases containing a Co^{II}/Ir^{III} oxidation state combination (*i.e.* $La_xSr_{4-x}CoIrO_{5+x}H_{3-x}$), Co^{II} has a high-spin d^7 configuration, so the hydride ions preferentially occupy a *trans*-arrangement around this metal, whilst the low-spin Ir^{III} favours a *cis*-hydride arrangement. To simultaneously accommodate both these coordination requirements, it is necessary for the anions to adopt the ordering pattern shown in Figure 3.27 within the equatorial planes of the perovskite sheets.

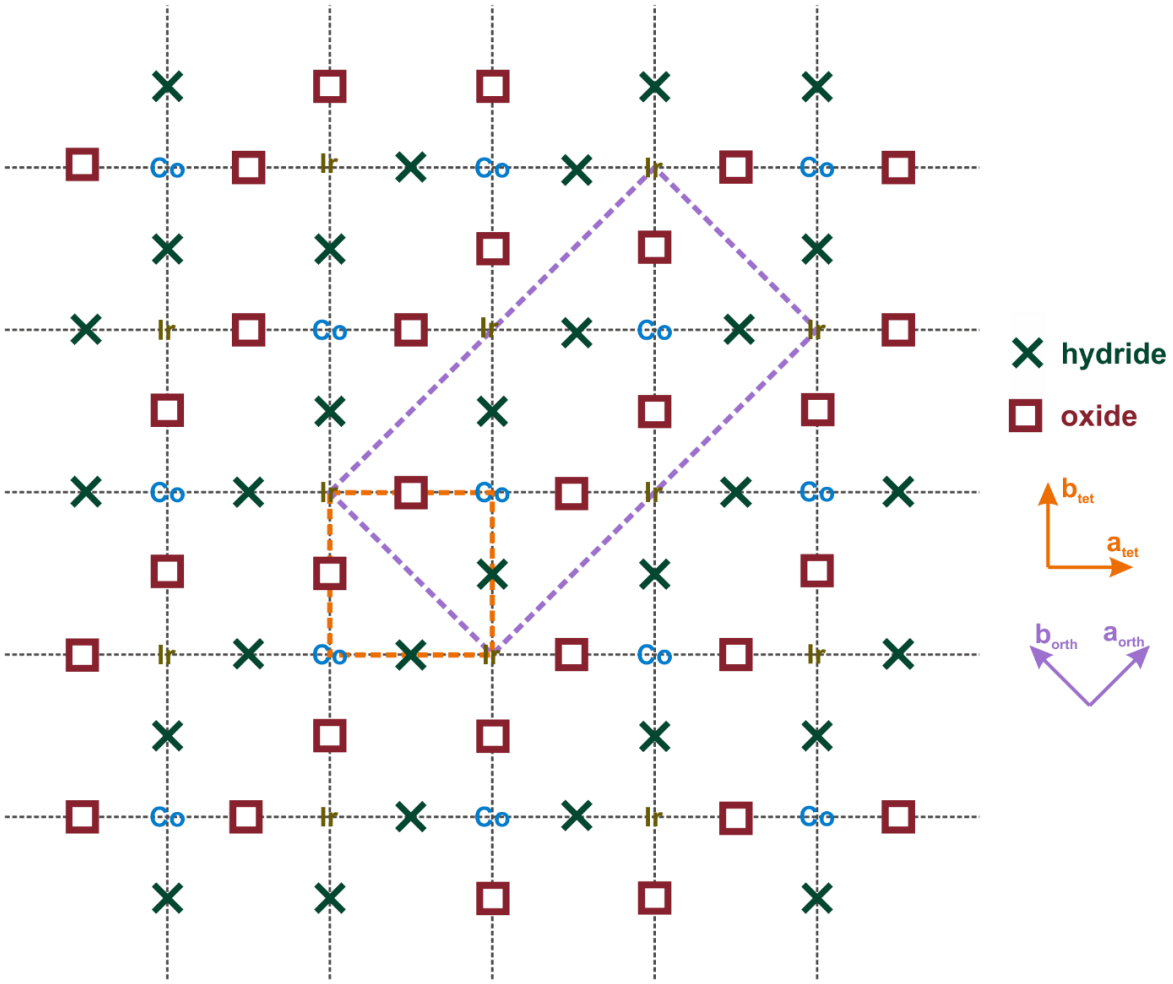

Figure 3.27: Schematic showing the anion ordering required to accommodate the *trans*-hydride coordination preference of Co^{II} and the *cis*-hydride coordination preference of Ir^{III} within the equatorial planes of the perovskite sheets in $La_xSr_{4-x}CoIrO_{5+x}H_{3-x}$, where $x = 1$. For $x < 1$, the oxide ions are partially replaced by hydride, whilst, for $x > 1$, the hydride ions are partially replaced by oxide. The green crosses represent hydride ions, whilst the red squares represent oxide ions. The dashed, orange line represents the simple, tetragonal unit cell of the all-oxide Ruddlesden-Popper phase. The dashed, purple line represents the $(2\sqrt{2} \times \sqrt{2} \times 1)$-expanded orthorhombic unit cell of the anion-ordered phase.

This anion ordering would lead to an orthorhombic unit cell, corresponding to a $(2\sqrt{2} \times \sqrt{2} \times 1)$ expansion relative to the original unit cell. However, close inspection of the NPD data for

$La_{0.5}Sr_{3.5}CoIrO_{5.5}H_{2.5}$ (which contains Co^{II}/Ir^{III} and would, therefore, be expected to exhibit this anion ordering) does not reveal the presence of any superstructure peaks. This can be attributed to the large degree of separation between the perovskite sheets. Although anion ordering may be present within the equatorial planes of the perovskite sheets, there is likely to be very little registry between the sheets and, as a result, the average structure observed by neutron diffraction is anion-disordered. This is in direct contrast to the reactivity observed when $(La/Sr)_4CoIrO_8$ is heated in the presence of a Zr getter to form $(La/Sr)_4CoIrO_6$.[46] In this case, oxide ions are removed to form infinite chains and the anion ordering 'direction' is transmitted between the perovskite sheets. This can be rationalised by considering the different anion ordering motifs within the perovskite sheets for these two cases. For the $(La/Sr)_4CoIrO_6$ case, all the equatorial oxide ions along one direction are removed, whilst the equatorial oxide ions along the orthogonal direction are retained. As such, there is a substantial contraction in one direction relative to the other, thereby allowing the anion ordering direction to be transmitted from one layer to the next through strain. However, for $La_xSr_{4-x}CoIrO_{5+x}H_{3-x}$, both the a_{orth}-direction and b_{orth}-directions contain the same ratio of oxide to hydride ions and, consequently, $a_{orth} \approx 2b_{orth}$. Since the lattice parameters for each perovskite sheet remain metrically tetragonal, the anion ordering motif is not transmitted between layers and, as a result, the average structure is anion-disordered. This is analogous to the fact that the B-site cations can be modelled as disordered, even if there is ordering within the perovskite sheets.

Meanwhile, for oxyhydride phases containing a Co^{I}/Ir^{III} oxidation state combination (*i.e.* $La_xSr_{4-x}CoIrO_{4+x}H_{4-x}$), both the Co^{I} ions and Ir^{III} ions favour a *cis*-hydride arrangement. As such, on reduction from Co^{II} to Co^{I}, there must be a rearrangement of the oxide/hydride ions within the equatorial planes of the perovskite sheets from the anion ordered arrangement shown in Figure 3.27 to a fully anion-disordered arrangement. There is an energy barrier associated with this process, which results in the experimentally observed phase gap.

3.4 Magnetic characterisation

3.4.1 Magnetic characterisation of $Sr_4CoIrO_{6.5}H_{1.5}$

Magnetisation data collected from $Sr_4CoIrO_{6.5}H_{1.5}$ as a function of temperature are shown in Figure 3.28, and magnetisation-field isotherms collected at 5 K and 300 K are shown in Figure 3.29. There is a substantial divergence of the ZFC and FC curves from 300 K, which, in combination with the presence of a saturated moment of ~0.05 μB fu^{-1} at 300 K (Figure 3.29), indicates the presence of an approximately 3 mole percent Co metal impurity. This results from the unavoidable presence of Co_3O_4 in the starting material, which is reduced to Co metal during the reaction with LiH. Therefore, to obtain useful magnetic information from the bulk phase, a 'ferrosubtraction' technique was employed, as described in Section 2.8.1. The results from this are shown in Figure 3.31. The saturated magnetic moment from 300 K to ~40 K is likely to result from the Co metal impurity. Below ~40K, the saturated moment increases more sharply, which is likely to result from an ordered moment in the bulk phase and is, therefore, consistent with the presence of a magnetic transition around this temperature. Fitting of the paramagnetic susceptibility to the Curie-Weiss Law yields an unphysical value for C of 6.63(1) cm^3 K mol^{-1}, whilst the value for θ of −312.0(5) K is negative and has a much larger magnitude than the observed transition temperature, suggesting a strongly frustrated antiferromagnetic system.

The vertical displacement of the 5 K magnetisation-field isotherm in Figure 3.29 suggests the formation of a spin glass state. This was confirmed by AC susceptibility measurements, shown in Figure 3.30, in which the susceptibility maximum shifts to higher temperature as the frequency of the applied field is increased.

The variation of the transition temperature, T_f, with frequency, ω, can be fitted using

$$\omega = \omega_0 \ (\frac{T_f}{T_{SG}} - 1)^{zv} \ , \tag{43}$$

as shown in the inset of Figure 3.30.[95–97] The values of T_f were taken from the maximum of each susceptibility curve, obtained by taking the point at which the first derivative of each curve is equal to zero. Fitting of the data to Equation 43 yields a value of $4(1) \times 10^5$ Hz for ω_0, corresponding to a relaxation time, τ_0, of $1.5(4) \times 10^{-5}$ s, and a value of 4.3(1) for the dynamical critical exponent, zv.

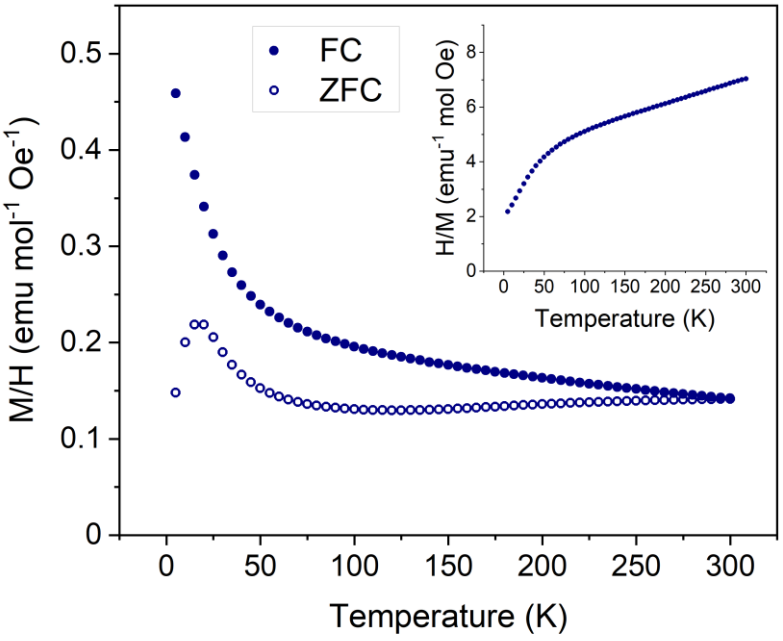

Figure 3.28: Magnetisation data collected from $Sr_4CoIrO_{6.5}H_{1.5}$ as a function of temperature, measured in a field of 100 Oe under both ZFC and FC conditions.

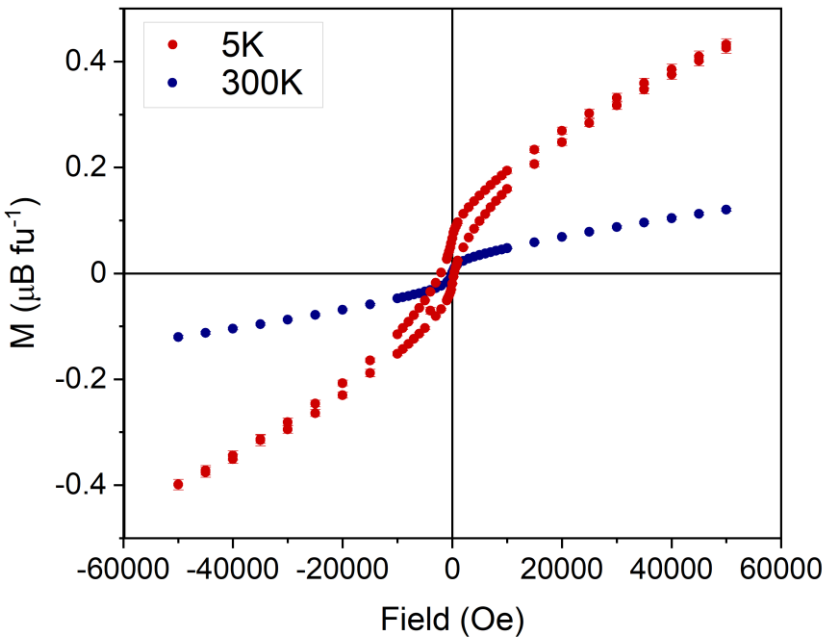

Figure 3.29: Magnetisation-field isotherms for $Sr_4CoIrO_{6.5}H_{1.5}$ measured at 5 K and 300 K.

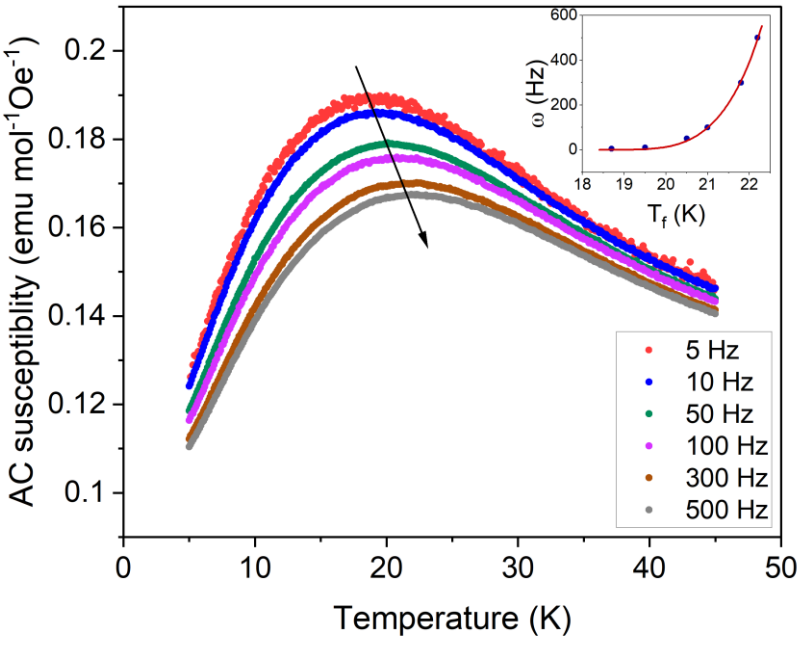

Figure 3.30: AC susceptibility as a function of temperature for $Sr_4CoIrO_{6.5}H_{1.5}$, measured at frequencies between 5 Hz and 500 Hz. The measurements were performed using an AC field with amplitude of 2.5 Oe, and an applied DC field of 2 Oe. The inset shows the variation of T_f with ω for $Sr_4CoIrO_{6.5}H_{1.5}$. The red line shows the fit to the data using the power law shown in Equation 43.

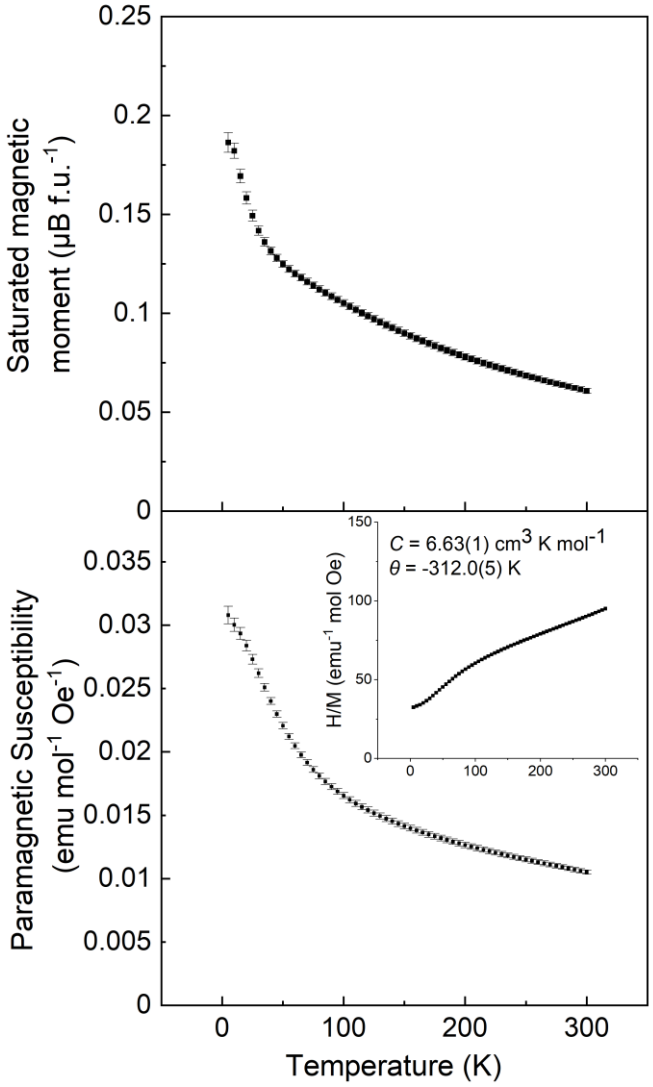

Figure 3.31: Saturated ferromagnetic moment (top panel) and paramagnetic susceptibility (bottom panel) obtained from $Sr_4CoIrO_{6.5}H_{1.5}$ using the 'ferrosubtraction' technique described in Section 2.8.1.

3.4.2 Magnetic characterisation of $La_{0.5}Sr_{3.5}CoIrO_{5.5}H_{2.5}$

Magnetisation data collected from $La_{0.5}Sr_{3.5}CoIrO_{5.5}H_{2.5}$ as a function of temperature are shown in Figure 3.32. The ZFC and FC curves show a slight divergence below about 150 K, which could suggest the presence of interactions between spins before the onset of long-range magnetic order. The divergence between the ZFC and FC curves increases at ~75 K, before a further divergence in the temperature range 15−30 K, indicating that magnetic transitions could

occur at these temperatures. The data could not be fit to the Curie-Weiss law in a physically reasonable way.

Magnetisation-field isotherms collected at 5 K and 300 K are shown in Figure 3.33. The presence of a small hysteresis loop in the 5 K data, in combination with the maximum value for the magnetisation of ~0.4 μB fu^{-1}, suggests that the compound adopts a canted antiferromagnetic state at this temperature.

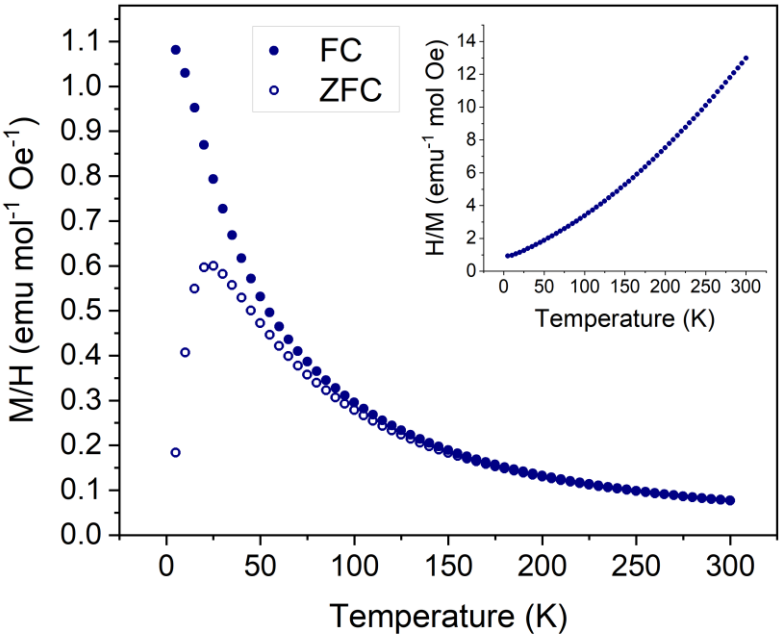

Figure 3.32: Magnetisation data collected from $La_{0.5}Sr_{3.5}CoIrO_{5.5}H_{2.5}$ as a function of temperature, measured in a field of 100 Oe under both ZFC and FC conditions.

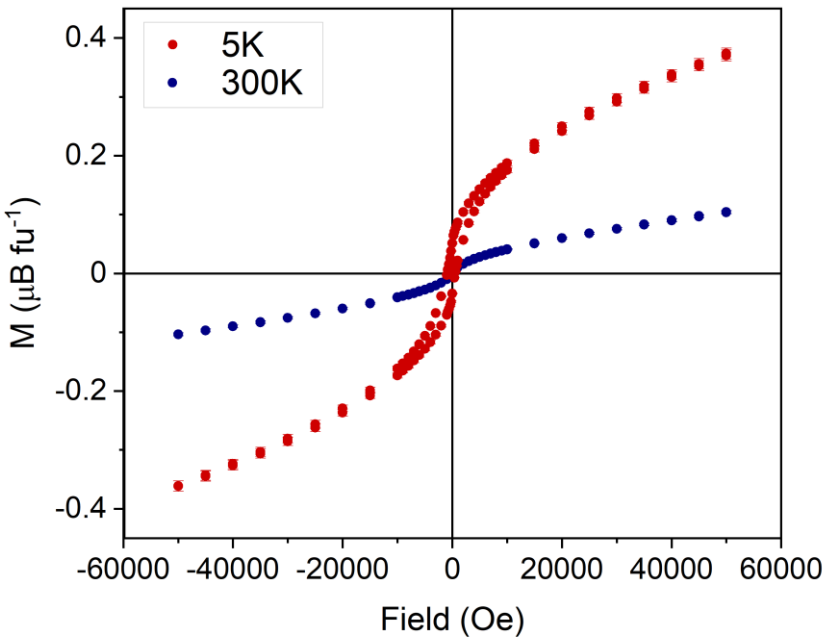

Figure 3.33: Magnetisation-field isotherms for $La_{0.5}Sr_{3.5}CoIrO_{5.5}H_{2.5}$ measured at 5 K and 300 K.

3.4.3 Magnetic characterisation of $LaSr_3CoIrO_5H_3$

Magnetisation data collected from $LaSr_3CoIrO_5H_3$ as a function of temperature are shown in Figure 3.34. The data are qualitatively very similar to $La_{0.5}Sr_{3.5}CoIrO_{5.5}H_{2.5}$. There is a slight divergence of the ZFC and FC curves below about 150 K, followed by an increased divergence at ~85 K and a dramatic divergence in the temperature range 20−35 K, indicating the possibility of magnetic transitions at these temperatures. As before, the data could not be fit to the Curie-Weiss law in a physically reasonable way.

Magnetisation-field isotherms collected at 5 K and 300 K are shown in Figure 3.35. Similar to $La_{0.5}Sr_{3.5}CoIrO_{5.5}H_{2.5}$, the presence of a small hysteresis loop in the 5 K data, in combination with the maximum value for the magnetisation of ~0.65 μB fu^{-1}, suggests that the compound adopts a canted antiferromagnetic state at this temperature.

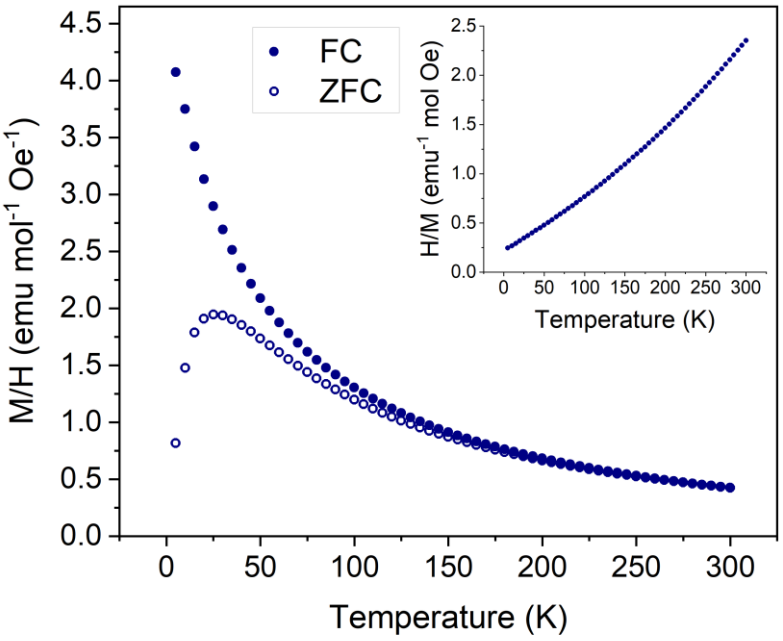

Figure 3.34: Magnetisation data collected from $LaSr_3CoIrO_5H_3$ as a function of temperature, measured in a field of 100 Oe under both ZFC and FC conditions.

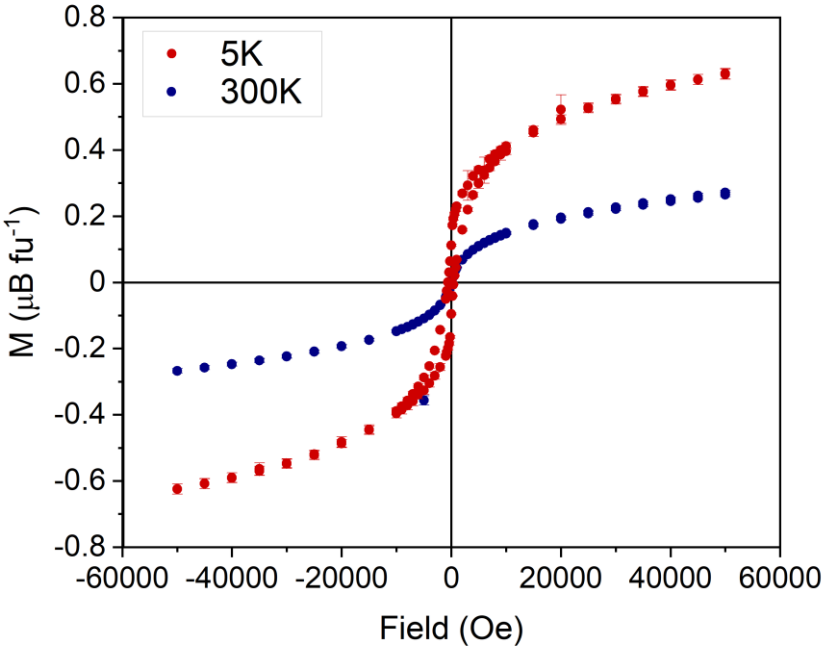

Figure 3.35: Magnetisation-field isotherms for $LaSr_3CoIrO_5H_3$ measured at 5 K and 300 K.

3.4.4 Magnetic characterisation of $La_{1.5}Sr_{2.5}CoIrO_{8-y}H_y$

Magnetisation data collected from $La_{1.5}Sr_{2.5}CoIrO_{8-y}H_y$ as a function of temperature are presented in Figure 3.36, and magnetisation-field isotherms collected at 5 K and 300 K are presented in Figure 3.37. The data appear qualitatively similar to those for $La_{0.5}Sr_{3.5}CoIrO_{5.5}H_{2.5}$ and $LaSr_3CoIrO_5H_3$. As with these compounds, $La_{1.5}Sr_{2.5}CoIrO_{8-y}H_y$ shows a transition to a canted antiferromagnetic state. The maximum moment at 5 K from Figure 3.37 is slightly lower, with a value of ~0.5 μ_B fu^{-1}. The susceptibility data could not be fit to the Curie-Weiss law in a physically reasonable way.

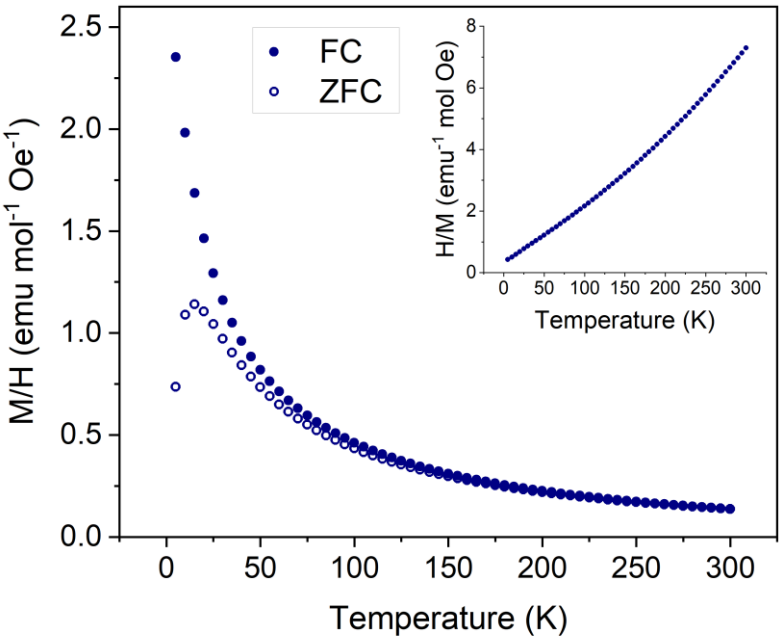

Figure 3.36: Magnetisation data collected from $La_{1.5}Sr_{2.5}CoIrO_{8-y}H_y$ as a function of temperature, measured in a field of 100 Oe under both ZFC and FC conditions.

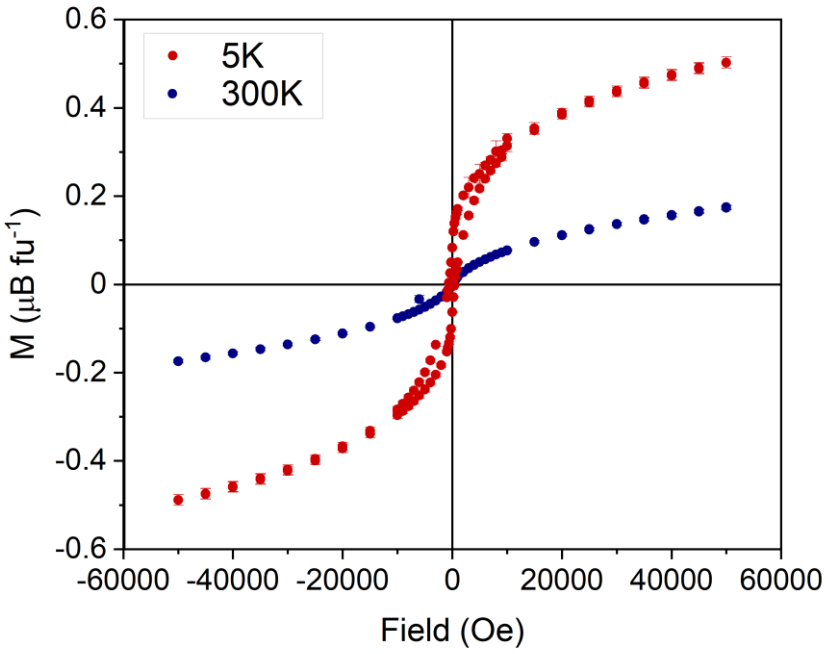

Figure 3.37: Magnetisation-field isotherms for $La_{1.5}Sr_{2.5}CoIrO_{8-y}H_y$ measured at 5 K and 300 K.

3.4.5 Magnetic characterisation of $La_2Sr_2CoIrO_{8-y}H_y$

Magnetisation data collected from $La_2Sr_2CoIrO_{8-y}H_y$ as a function of temperature are presented in Figure 3.38, and magnetisation-field isotherms collected at 5 K and 300 K are presented in Figure 3.39. The data for this sample appear qualitatively similar to that for $La_{1.5}Sr_{2.5}CoIrO_{8-y}H_y$, with divergences in the ZFC and FC curves at ~150 K and ~5−15 K. From Figure 3.39, the sample has a larger maximum moment at 5 K, with a magnitude of ~0.8 μ_B fu^{-1}. The susceptibility data could not be fit to the Curie-Weiss law in a physically reasonable way.

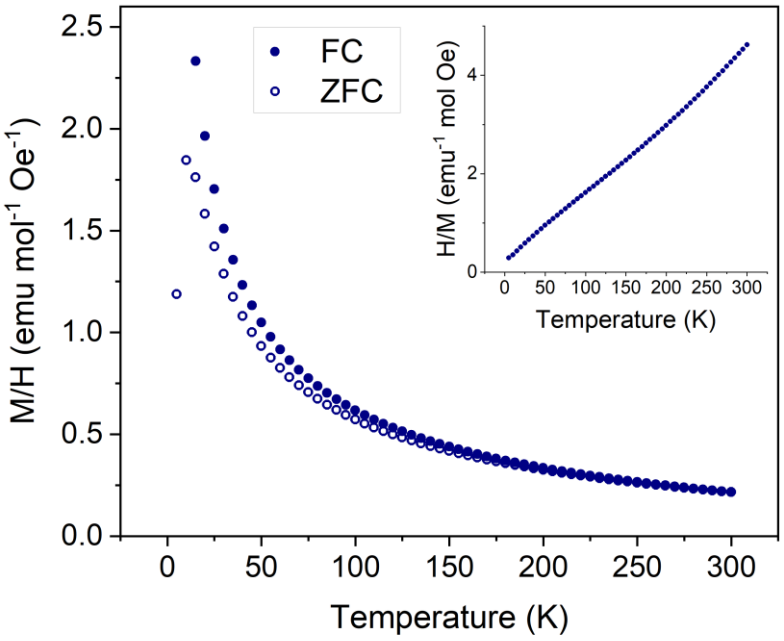

Figure 3.38: Magnetisation data collected from $La_2Sr_2CoIrO_{8-y}H_y$ as a function of temperature, measured in a field of 100 Oe under both ZFC and FC conditions

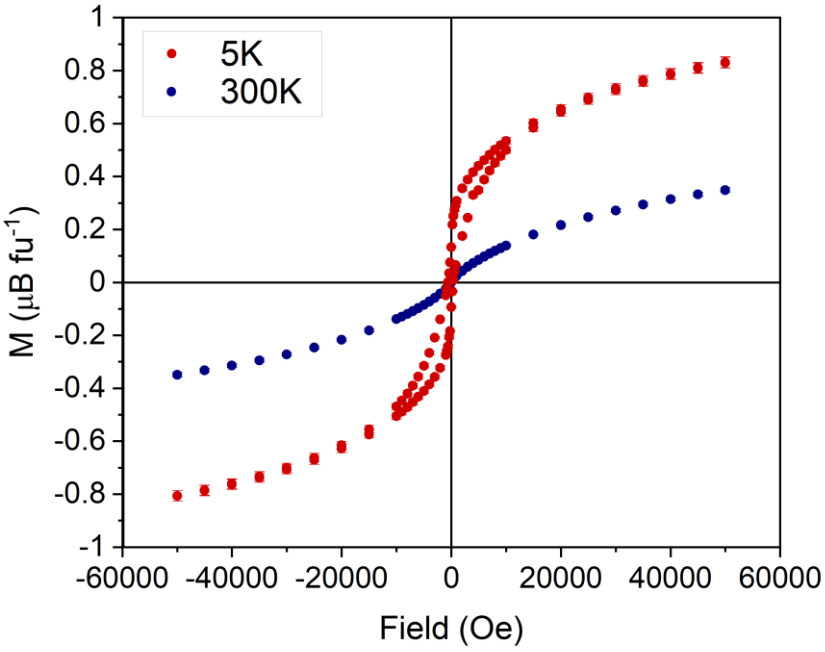

Figure 3.39: Magnetisation-field isotherms for $La_2Sr_2CoIrO_{8-y}H_y$ measured at 5 K and 300 K.

3.4.6 Muon spin rotation spectroscopy

μ^+-SR data were collected from $Sr_4CoIrO_{6.5}H_{1.5}$, $LaSr_3CoIrO_5H_3$ and $La_2Sr_2CoIrO_6H_2$ at a range of temperatures, as shown in Figure 3.40.

In a paramagnetic sample, the spins are fluctuating very fast relative to the timescale of the measurement. As such, the deviation of the muon spin from its initial polarisation essentially follows a random walk and, as a consequence, loss of asymmetry is very slow. This slow loss of asymmetry can be observed in the data collected from all samples at temperatures of 75 K and above, indicating that they are paramagnetic at these temperatures.

If the sample contains static moments (relative to the timescale of the measurement), the muon spin precesses around the field in the sample. Due to this precession, there is much faster dephasing of the muon spins, leading to a rapid loss of asymmetry. If long-range magnetic order is present in the sample, the precession of the muon spins can be observed as oscillations superimposed upon the curve.

Relatively fast loss of asymmetry is observed below 75 K for all the samples, indicating that static moments are present at these temperatures and implying that the magnetic transition temperature for all the samples is 50−75 K. For $Sr_4CoIrO_{6.5}H_{1.5}$, the observation that the apparent transition temperature of 50−75 K from μ^+-SR is higher than that of ~18 K from the data in Section 3.4.1 can be attributed to the fact that the timescale of the μ^+-SR measurement (< 7 μs) is much shorter than that of the magnetisation measurements (> 1 ms). This means that, although T_g appears to be in the range 18−22 K from AC susceptibility measurements, the slow nature of the spin fluctuations above T_g means that the spins appear static up to 50−75 K in the μ^+-SR measurements. The absence of oscillations in the data is consistent with the result expected for a spin-glass, due to the fact that there is no long-range magnetic order present.

For $LaSr_3CoIrO_5H_3$ and $La_2Sr_2CoIrO_6H_2$, the absence of oscillations suggests that the magnetic order in the compounds is somewhat inhomogeneous, which could result from the presence of B-site cation disorder or a non-uniform distribution of anions across the sample. Furthermore, the observation that the muon spin relaxation between 75 and 200 K is intermediate between that expected for a magnetically ordered compound and that for a paramagnetic compound for the two samples suggests that there could be strong spin correlations above the transition temperature in these compounds.

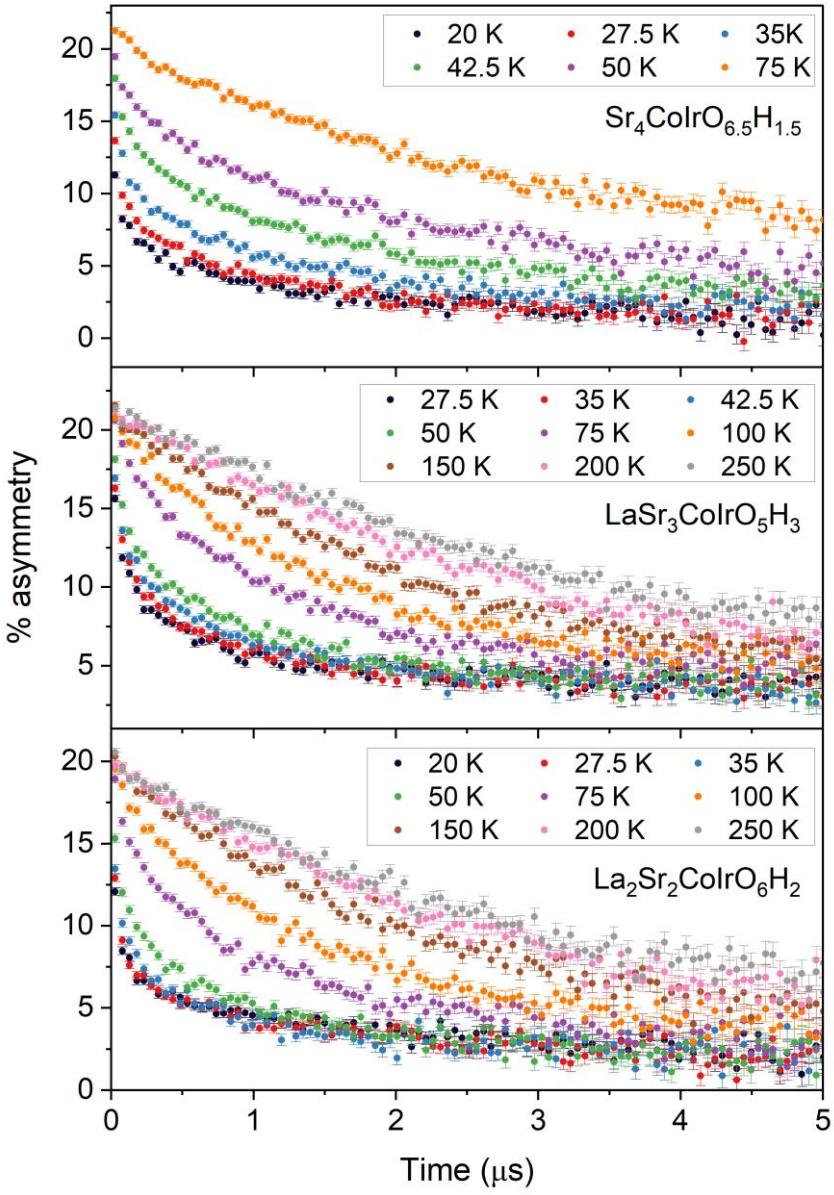

Figure 3.40: μ^+-SR data collected from $Sr_4CoIrO_{6.5}H_{1.5}$, $LaSr_3CoIrO_5H_3$ and $La_2Sr_2CoIrO_6H_2$ as a function of temperature.

3.4.7 Discussion

3.4.7.1 Magnetic behaviour of $Sr_4CoIrO_{6.5}H_{1.5}$

The magnetic behaviour of $Sr_4CoIrO_{6.5}H_{1.5}$ is markedly different from the rest of the series. Whilst most members of the series appear to adopt magnetically ordered states at low temperature, $Sr_4CoIrO_{6.5}H_{1.5}$ exhibits a transition to a spin glass state. This can be attributed to the observation that the transition metals in $Sr_4CoIrO_{6.5}H_{1.5}$ adopt a $Co^{II}/Ir^{IV/V}$ oxidation state combination, rather than the Co^{I}/Ir^{III} or Co^{II}/Ir^{III} combinations adopted by the other oxyhydride phases.

The Co^{II} ions have a high-spin d^7 configuration, as shown in Figure 3.41, whilst Ir^{IV} adopts a J_{eff} = ½ state and Ir^{V} adopts a diamagnetic J_{eff} = 0 state, which are simplistically shown as a low-spin d^5 and d^4 configurations, respectively. In $Sr_4CoIrO_{6.5}H_{1.5}$, the transition metal cations have a disordered arrangement, inherited from the parent phase, as confirmed by the observation of spin glass behaviour in Sr_4CoIrO_8 (Figure A 12).

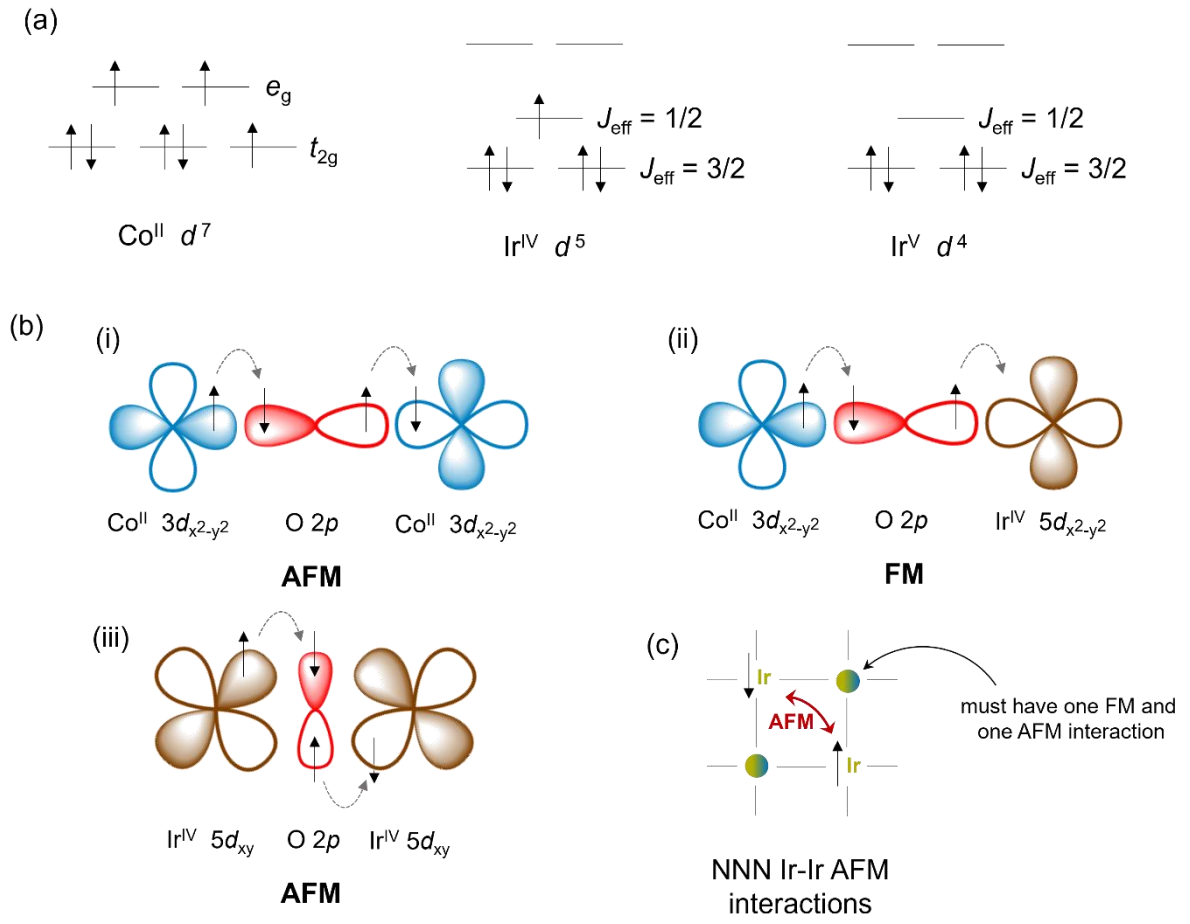

Figure 3.41: (a) simplistic crystal field splitting diagrams for Co^{II}, Ir^{IV} and Ir^{V} in $Sr_4CoIrO_{6.5}H_{1.5}$, (b) schematics illustrating superexchange interactions between orbitals in $Sr_4CoIrO_{6.5}H_{1.5}$, whereby (i) and (ii) can be mediated by either oxide 2*p* or hydride 1*s* orbitals and (c) schematic illustrating next-nearest-neighbour Ir−Ir antiferromagnetic interactions, mediated by overlap between spatially diffuse $5d_{xy}$ orbitals.

As discussed in Chapter 1, the system must contain both chemical disorder and magnetic frustration for a spin glass state to propagate. The requirement for chemical disorder can clearly be fulfilled by the disordered arrangement of transition metal cations. To identify the cause of the magnetic frustration, $Sr_4CoIrO_{6.5}H_{1.5}$ can be compared to $La_{0.5}Sr_{3.5}CoIrO_{5.5}H_{2.5}$. $La_{0.5}Sr_{3.5}CoIrO_{5.5}H_{2.5}$ contains Co^{II} and diamagnetic Ir^{III}, whilst $Sr_4CoIrO_{6.5}H_{1.5}$ contains Co^{II}, Ir^{IV} and diamagnetic Ir^{V}. As such, it is likely that the frustration in $Sr_4CoIrO_{6.5}H_{1.5}$ arises from the presence of Ir^{IV}. By applying the Goodenough-Kanamori rules, nearest-neighbour Co^{II}−(O/H)−Co^{II} or Ir^{IV}−O−Ir^{IV} interactions are expected to be antiferromagnetic, whilst nearest-neighbour Co^{II}−(O/H)−Ir^{IV} interactions are expected to be ferromagnetic. However, these interactions by themselves do not lead to magnetic frustration.

The frustration can be explained by taking into account direct exchange between Ir^{IV} ions. Since the octahedra in $Sr_4CoIrO_{6.5}H_{1.5}$ are elongated along the *z*-direction, the unpaired electron is likely to have significant $5d_{xy}$ character. As such, if two Ir^{IV} are located diagonally from each other, overlap of the spatially diffuse $5d_{xy}$ orbitals can occur, leading to direct antiferromagnetic exchange. Since the nearest neighbours to these two Ir^{IV} ions must then have at least one ferromagnetic and one antiferromagnetic interaction each, the Ir^{IV}–Ir^{IV} next-nearest-neighbour interaction is incompatible with the nearest-neighbour interactions, regardless of whether they are ferromagnetic or antiferromagnetic, thereby resulting in magnetic frustration.

3.4.7.2 Magnetic behaviour of $La_xSr_{4-x}CoIrO_{8-y}H_y$ (x = 0.5, 1, 1.5, 2) phases

As presented in Section 3.3, the oxyhydride phases, $La_xSr_{4-x}CoIrO_{8-y}H_y$ (x = 0.5, 1, 1.5, 2), all exhibit qualitatively similar magnetic behaviour. They show transitions to likely canted antiferromagnetic states with transition temperatures between 50 and 100 K, as determined from muon spin-rotation spectroscopy. This can be rationalised by a superexchange pathway between the Co^{I} ions through the diamagnetic Ir^{III} ions, as shown in Figure 3.42.

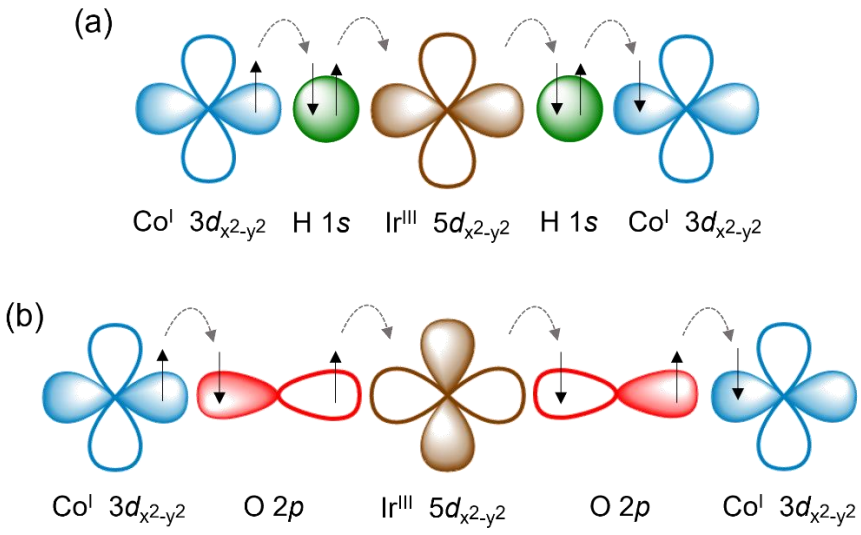

Figure 3.42: Orbital diagrams illustrating the σ-superexchange pathway between Co^{I} ions via (a) hydride ions and (b) oxide ions.

Each Co^{I} ion contains an unpaired electron in its $3d_{x^2-y^2}$ orbital, which can couple antiferromagnetically to the unpaired electron in the $3d_{x^2-y^2}$ orbital of a next-nearest-neighbouring Co^{I} ion, via the empty $5d_{x^2-y^2}$ orbital of the diamagnetic Ir^{III} ion. This type of coupling is analogous to that observed in $LaSrNiIrO_6$, in which antiferromagnetic coupling is observed between Ni^{II} d^8 ions, via diamagnetic (J_{eff} = 0) Ir^{V} ions, through the same orbital exchange pathway as in Figure 3.42.[98]

It is worth noting that, due to the fact that next-nearest-neighbour exchange is the strongest coupling interaction in the $La_xSr_{4-x}CoIrO_{8-y}H_y$ systems, each perovskite sheet essentially contains two independent antiferromagnetic magnetic lattices, which cross over at the diamagnetic Ir^{III} ions, and the coupling between these lattices is likely to be very weak. This is illustrated schematically in Figure 3.43.

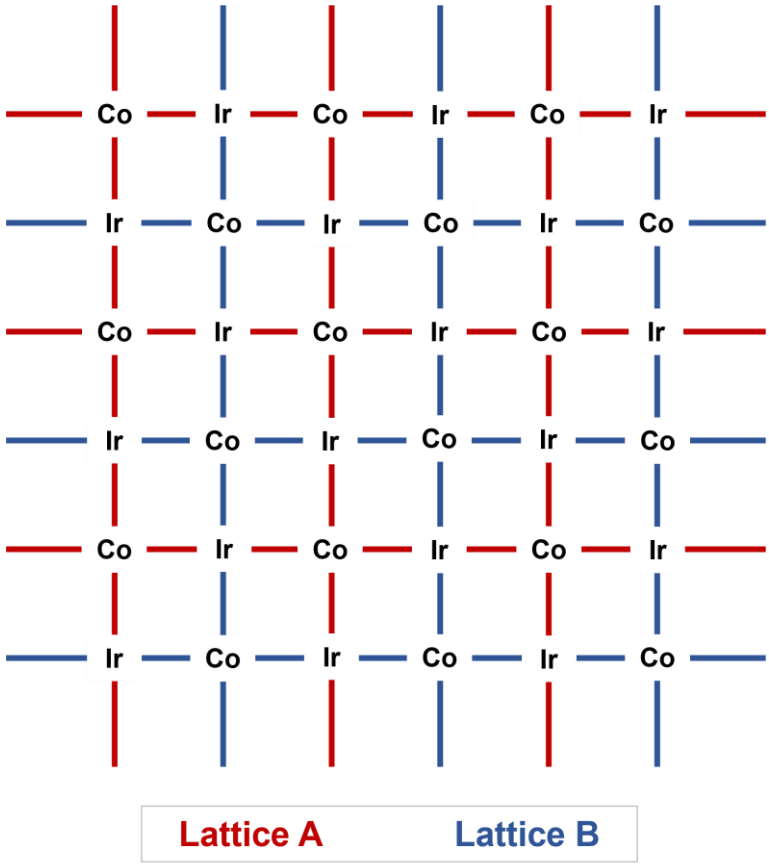

Figure 3.43: Schematic illustrating the two independent magnetic lattices present within the perovskite sheets of $La_xSr_{4-x}CoIrO_{8-y}H_y$ phases.

Despite that antiferromagnetic ordering is present within the perovskite layers, the observation of magnetic Bragg peaks from NPD is unlikely.[27] This is because, although the B-site cations may be ordered within the layers, there is very little registry between the layers, as discussed in Section 1.1.4, and, as a result, there is not a magnetic lattice present upon which long-range three-dimensional order can propagate.

3.5 Conclusion

Reaction of the n = 1 Ruddlesden-Popper phases, $La_xSr_{4-x}CoIrO_8$ ($0 \leq x \leq 2$), with LiH has allowed a series of oxyhydride, $La_xSr_{4-x}CoIrO_{8-y}H_y$, phases to be prepared, in which oxide-to-hydride exchange has occurred at the equatorial anion sites. For x = 1, 1.5 and 2, the final hydride content is controlled by realisation of the $Co^{I}Ir^{III}$ transition metal oxidation state combination. The iridium provides strong covalent stabilisation to the oxyhydride phases through the formation of Ir−H σ-bonds, but cannot be reduced further than Ir^{III} due to the strongly antibonding nature of the e_g orbitals. The role of covalency in the stabilisation of these oxyhydride phases is reinforced by the observation that their stability appears to increase with increasing hydride content, evidenced by the fact that only $LaSr_3CoIrO_5H_3$ could be prepared as a single phase. Meanwhile, for x = 0 and 0.5, the degree of reduction required to achieve the $Co^{I}Ir^{III}$ oxidation state combination cannot be achieved without non-topochemical decomposition occurring, so the observed hydride content is instead limited by the temperature at which the reaction can be carried out.

$Sr_4CoIrO_{6.5}H_{1.5}$ shows significantly different magnetic behaviour to the rest of the series, which can be attributed to direct antiferromagnetic exchange between next-nearest-neighbouring Ir^{IV}, leading to magnetic frustration within the system. Meanwhile, the remaining members of the $La_xSr_{4-x}CoIrO_{8-y}H_y$ series exhibit transitions to antiferromagnetic states, which are mediated

by the presence of $Co(3d_{x^2-y^2})^1-O(2p)/H(1s)-Ir(5d_{x^2-y^2})^0-O(2p)/H(1s)-Co(3d_{x^2-y^2})^1$ σ-superexchange pathways.

Chapter 4 – Topochemical reduction of $LaSr_3NiIrO_8$ using LiH and a Zr getter

4.1 Introduction

The synthesis of a series of $La_xSr_{4-x}CoIrO_{8-y}H_y$ phases was discussed in Chapter 3. To explore the effect of changing the 3d transition metal cation, the reactivity of $LaSr_3NiIrO_8$ with LiH has been investigated. To compare the product from this reaction with an analogous topochemically-reduced oxygen-deficient phase, the reactivity of $LaSr_3NiIrO_8$ with a Zr-getter has also been investigated.

4.2 Experimental

4.2.1 Synthesis of $LaSr_3NiIrO_8$

Two-gram polycrystalline samples of $LaSr_3NiIrO_8$ were prepared using conventional ceramic synthesis methods. Suitable stoichiometric ratios of La_2O_3 (dried at 900 °C), $SrCO_3$, NiO, and IrO_2 (dried for 2 hours at 700 °C) were thoroughly ground together in an agate pestle and mortar, pelletised and heated in air at 1000 °C for 2 days. The samples were then reground, pelletised and heated for a further 2 days at a temperature of 1300 °C.

4.2.2 Exploration of the reactivity of $LaSr_3NiIrO_8$

4.2.2.1 Reactivity with LiH

The reactivity of $LaSr_3NiIrO_8$ with LiH was explored as function of temperature. The reaction mixture was prepared by thoroughly grinding 200 mg of $LaSr_3NiIrO_8$ with 8 mole equivalents of LiH in an Ar-filled glovebox. The mixture was then sealed in an evacuated Pyrex® ampoule, heated at the desired temperature for 2 days and subsequently analysed by PXRD. The reaction temperature was increased for each heating cycle until non-topochemical decomposition was

observed, signalled by the formation of SrO and Ir metal. It was observed that tetragonal symmetry was retained until decomposition and that, at reaction temperatures of 300−400 °C, there was a contraction of the *xy*-plane and expansion in the *z*-direction. Heating the reaction mixture above 400 °C led to non-topochemical decomposition.

4.2.2.2 Reactivity with a Zr getter

The reactivity of $LaSr_3NiIrO_8$ with a Zr getter was explored as function of temperature. Approximately 300 mg of $LaSr_3NiIrO_8$ was sealed in an evacuated silica ampoule with 4 mole equivalents of finely-divided Zr metal. It was observed that heating at temperatures of 500−525 °C led to the formation of a new phase that could be indexed using an orthorhombic unit cell with lattice parameters of a = 3.59 Å, b = 3.90 Å and c = 12.83 Å. Heating the sample above 525 °C resulted in non-topochemical decomposition.

4.2.3 Synthesis of $LaSr_3NiIrO_{5.4}H_{2.6}$

A sample of $LaSr_3NiIrO_{5.4}H_{2.6}$ was prepared by thoroughly grinding 1.7 g of $LaSr_3NiIrO_8$ with 9 mole equivalents of LiH in an Ar-filled glovebox. The reaction mixture was then sealed in an evacuated Pyrex® ampoule and heated for 2 periods of 5 days at 380 °C and 390 °C, respectively, followed by 1 period of 2 days at 400 °C, with heating rates of 1 °C/min. To remove the Li_2O by-product and any excess LiH, the reaction mixture was washed with MeOH under an N_2 atmosphere. The product was then dried under vacuum and returned to the glovebox.

4.2.4 Synthesis of $LaSr_3NiIrO_{6.4}$

A sample of $LaSr_3NiIrO_{6.4}$ was prepared by placing 1.2 g of $LaSr_3NiIrO_8$ in a glass thimble and sealing this in an evacuated silica ampoule with 1 g of finely-divided Zr metal. The sample was then heated for 10 periods of 5 days at 510 °C, with thorough grinding between each heating cycle in an Ar-filled glovebox.

4.3 Structural characterisation

4.3.1 Structural characterisation of $LaSr_3NiIrO_8$

A cation-disordered structural model with *I*4/*mmm* symmetry (shown in Figure 4.1) was created for $LaSr_3NiIrO_8$ based on the n = 1 Ruddlesden-Popper structure of $LaSr_3CoIrO_8$, discussed in Chapter 3.[46] This model was refined against SXRD data collected from $LaSr_3NiIrO_8$ and gave a good fit to the data, as shown in Figure 4.2, with the refinement parameters detailed in Table 4.1. Although there is no evidence for B-site cation order from the diffraction data, it is likely that this compound exhibits paracrystalline ordering (Section 1.1.4), due to the large difference in oxidation states between the B-site cations (Ni^{II} and Ir^{V}). The observation that the magnetisation data collected from this phase (Section 4.4.1) do not show signatures of spin glass behaviour is consistent with the existence of B-site paracrystalline order.

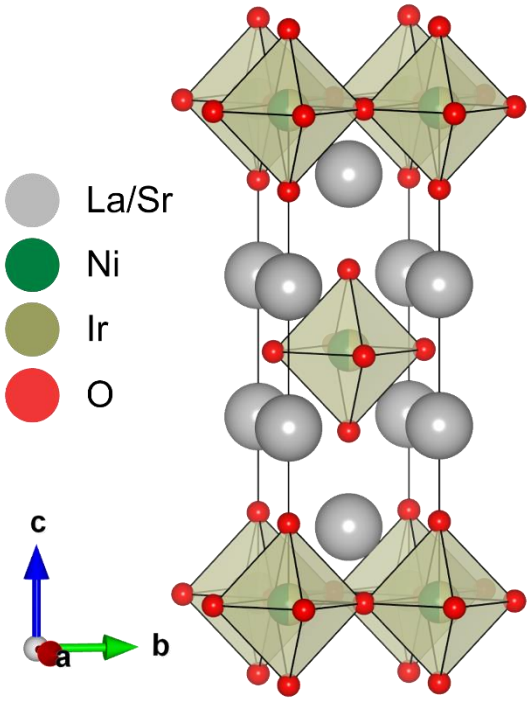

Figure 4.1: Structural model of $LaSr_3NiIrO_8$ with the n = 1 Ruddlesden-Popper structure.

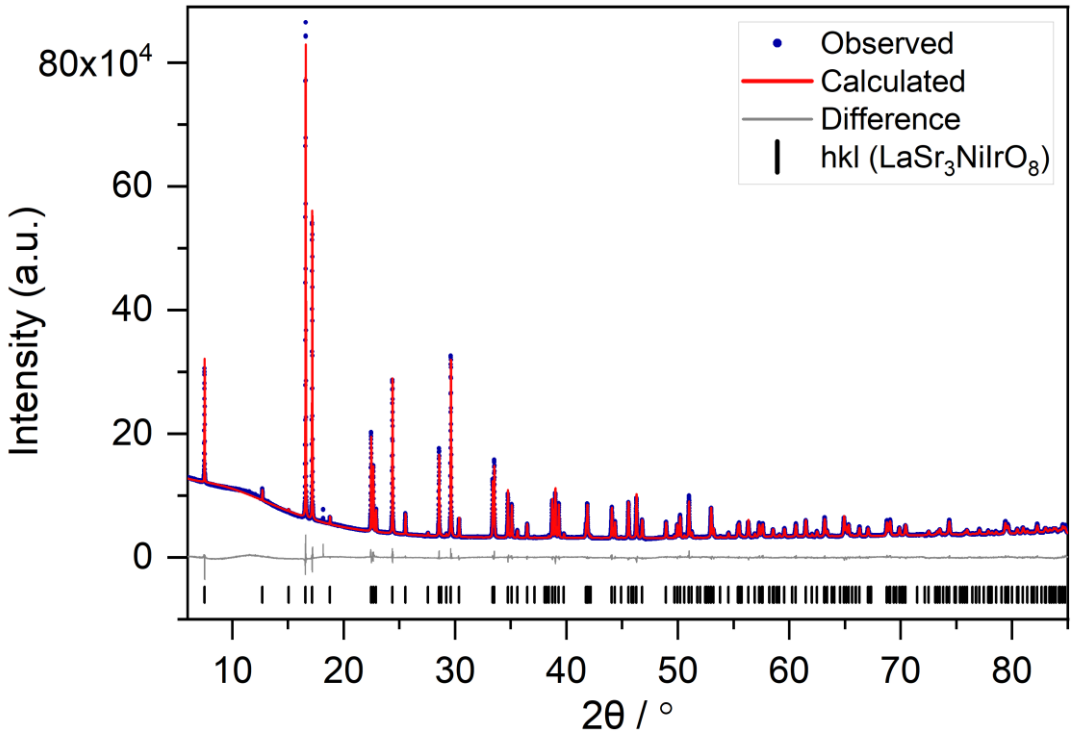

Figure 4.2: Observed, calculated and difference plots from the structural refinement of $LaSr_3NiIrO_8$ against SXRD data collected at room temperature using a wavelength of 0.825 Å.

Table 4.1: Parameters from the structural refinement of $LaSr_3NiIrO_8$ against SXRD data collected at room temperature. The fractional coordinates of the oxide sites were fixed to be the same as those of $LaSr_3CoIrO_8$.

$LaSr_3NiIrO_8$, space group *I*4/*mmm* (No. 139)						
		x	***y***	***z***	**Occ.**	**B_{iso} (Å^2)**
La(1)/Sr(1)	4*e*	0	0	0.35715(2)	0.25/0.75	0.805(9)
Ni(1)/Ir(1)	2*a*	0	0	0	0.5/0.5	0.408(8)
O(1)	4*c*	0	½	0	1	1.08(3)
O(2)	4*e*	0	0	0.163	1	1.08(3)
a = 3.90648(1) Å, c = 12.59753(4) Å						
V = 192.246(1) Å^3						
R_{wp} = 2.27%, R_p = 1.70%, *gof* = 5.03						

4.3.2 Structural characterisation of $LaSr_3NiIrO_{5.4}H_{2.6}$

The product from the reaction between $LaSr_3NiIrO_8$ and LiH, which will be shown to be $LaSr_3NiIrO_{5.4}H_{2.6}$, was analysed by SXRD, indicating the presence of a single phase with reflection conditions consistent with the *I*4/*mmm* space group. A substantial change in the

lattice parameters was observed relative to the parent material, with a contraction in the *xy*-plane from a = 3.90648(1) Å to a = 3.6842(2) Å and an expansion in the *z*-direction from c = 12.59753(4) Å to c = 13.1185(6) Å.

4.3.2.1 Thermogravimetric analysis

Thermogravimetric data were collected from $LaSr_3NiIrO_{8-x}H_y$ whilst heating under flowing oxygen, indicating a mass gain of 4.4%, as shown in Figure 4.3. Assuming full oxidation back to $LaSr_3NiIrO_8$, this corresponds to an initial composition of $LaSr_3NiIrO_{6.15}H_y$. Analysis of the exhaust gas by mass spectrometry showed release of water and hydrogen gas associated with oxidation of the reduced phase, indicating that hydride is present in the phase.

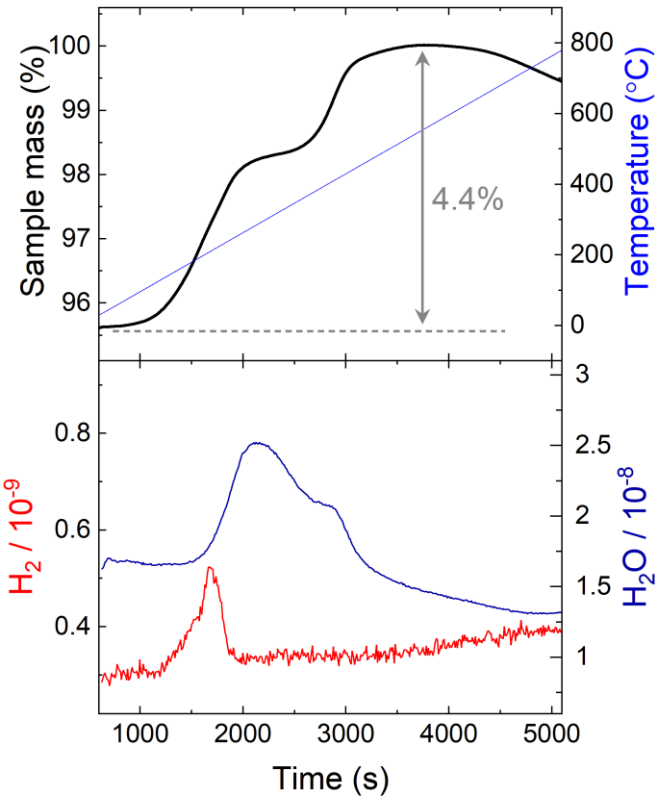

Figure 4.3: TGA trace (top panel) and contents of exhaust gas (bottom panel) when $LaSr_3NiIrO_{5.4}H_{2.6}$ is heated under flowing oxygen.

4.3.2.2 Neutron powder diffraction

NPD data were collected from $LaSr_3NiIrO_{5.4}H_{2.6}$ at 200 K using the D20 diffractometer at the ILL. For the refinements, a structural model based on the parent oxide, with the lattice parameters obtained from SXRD of the reduced phase was created. A small nickel metal impurity was also observed, so this was added to the refinement. From the NPD data, it was determined that the average neutron scattering length at the equatorial anion site of the main phase is −0.39 fm, thereby confirming that hydride must be present at this site. To obtain the overall anion composition, the oxide and hydride occupancies at the equatorial site were refined, such that the total occupancy of the site summed to one. This yielded an oxide occupancy of 0.351(3) and a hydride occupancy of 0.649(3), which corresponds to a composition of $LaSr_3NiIrO_{5.40(5)}H_{2.60(5)}$. Although the oxygen content is somewhat lower than the value determined from TGA, the discrepancy could arise from incomplete oxidation of the reduced phase during the TGA measurement. The lattice parameters of the phase (a = 3.6787(4) Å, c = 13.074(1) Å) are consistent with a composition of $LaSr_3NiIrO_{5.4}H_{2.6}$ (Figure A 11). It is possible that vacancies are present at the equatorial sites, in addition to oxide and hydride, but it is likely that these are only present at relatively low concentrations, so the sites were assumed to be fully occupied. The fit to the data is shown in Figure 4.4, with the refinement parameters presented in Table 4.2 and the refined structure shown in Figure 4.5. A structural refinement was also performed against the SXRD data using the model obtained from NPD, which gave a good visual fit, as shown in Appendix A2.

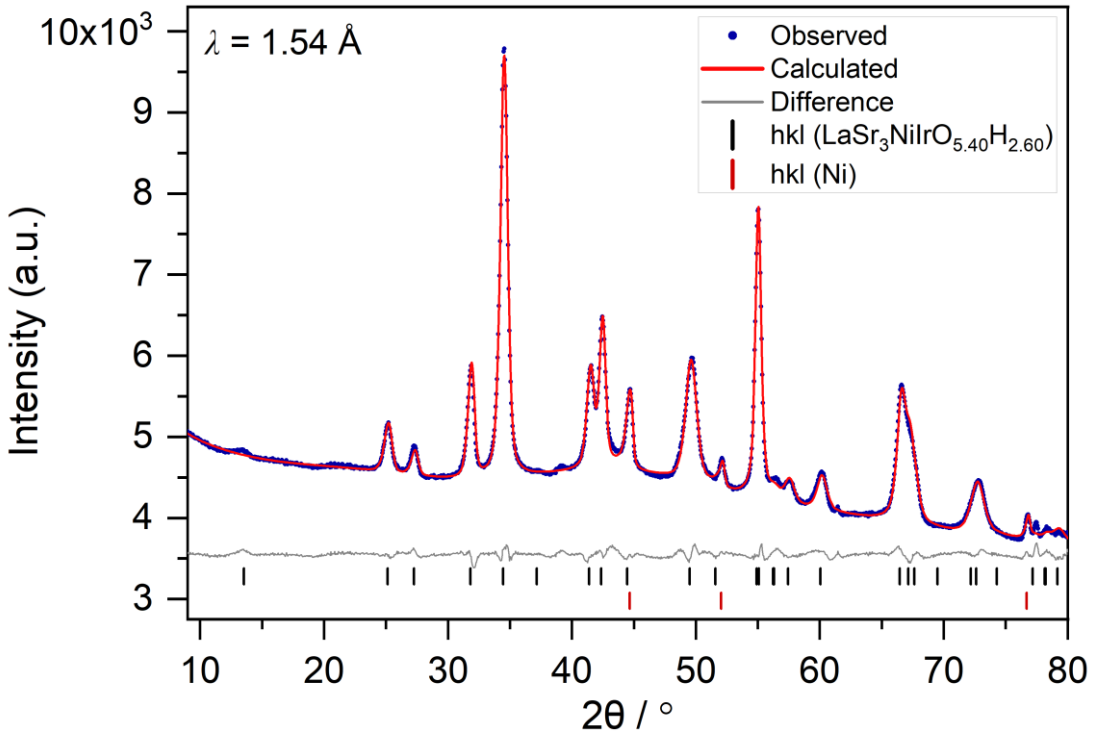

Figure 4.4: Observed, calculated and difference plots from the structural refinement of $LaSr_3NiIrO_{5.4}H_{2.6}$ against NPD data collected at 200 K from the D20 diffractometer using a wavelength of 1.54 Å.

Table 4.2: Parameters from the structural refinement of $LaSr_3NiIrO_{5.4}H_{2.6}$ against NPD data collected at 200 K from the D20 diffractometer using a wavelength of 1.54 Å.

$LaSr_3NiIrO_{5.40(5)}H_{2.60(5)}$, space group *I*4/*mmm* (No. 139), 97.1(2) wt%						
		x	***y***	***z***	**Occ.**	**B_{iso} (Å^2)**
La(1)/Sr(1)	4*e*	0	0	0.3550(1)	0.25/0.75	0.05(7)
Ni(1)/Ir(1)	2*a*	0	0	0	0.5/0.5	3.42(9)
O(1)/H(1)	4*c*	0	½	0	0.351(3)/0.649(3)	0.73(6)
O(2)	4*e*	0	0	0.1677(3)	1	0.73(6)
a = 3.6787(4) Å, c = 13.074(1) Å						
V = 176.93(4) Å^3						
Ni, space group *Fm*$\bar{3}$*m* (No. 225), 2.9(2) wt%						
		x	***y***	***z***	**Occ.**	**B_{iso} (Å^2)**
Ni(1)	4*a*	0	0	0	1	3.5(5)
a = 3.5108(5) Å						
V = 43.27(2) Å^3						
R_{wp} = 0.69%, R_p = 0.53%, *gof* = 3.35						

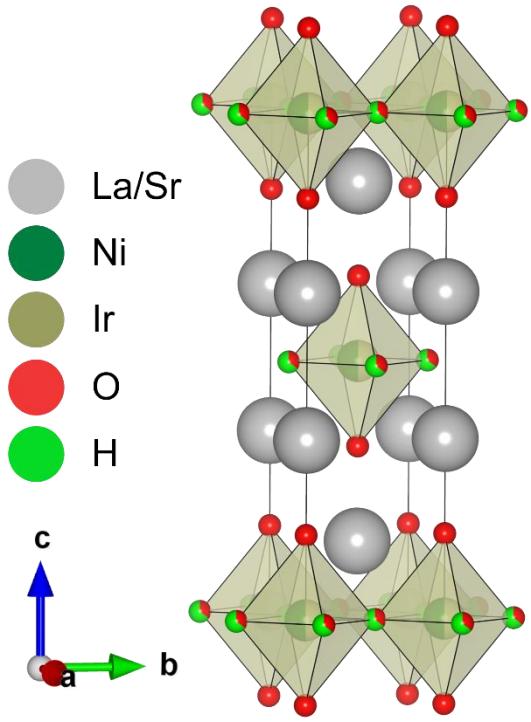

Figure 4.5: Refined structure of $LaSr_3NiIrO_{5.4}H_{2.6}$, showing hydride ions substituted into the equatorial positions.

4.3.2.3 Discussion

The reactivity of $LaSr_3NiIrO_8$ with LiH is similar to that of the $La_xSr_{4-x}CoIrO_8$ series discussed in Chapter 3. The hydride ions in $LaSr_3NiIrO_{5.4}H_{2.6}$ are located exclusively at the equatorial positions, as expected from the enthalpic arguments described in Section 3.3.9.1. Moreover, the compound has *I*4/*mmm* symmetry with the oxide and hydride ions disordered across the equatorial anion positions. This is consistent with the electronic configurations of Ni^{I} (d^9 configuration), Ni^{II} (d^8 configuration) and Ir^{III} (low-spin d^6 configuration). These do not provide an electronic driving force for the hydride ions to adopt *trans*-arrangements relative to each other (Section 1.4.2) and, consequently, the strong *trans*-influence associated with the hydride ions leads to a *cis*-arrangement being preferred. This results in an overall structure in which the oxide and hydride ions are disordered across the equatorial sites.

In $LaSr_3NiIrO_{5.4}H_{2.6}$, iridium is likely to adopt the +3 oxidation state, due to the fact that further reduction to Ir^{II} in an octahedral coordination environment would be highly unfavourable, as it

would require an electron to occupy a strongly antibonding e_g orbital. This would mean that nickel is present as a mixture of 60% Ni^{I} and 40% Ni^{II}. It is likely that reduction from $Ni^{II}Ir^{V}$ in the starting material to $Ni^{II}Ir^{III}$ occurs rapidly, but that reduction from $Ni^{II}Ir^{III}$ to $Ni^{I}Ir^{III}$ occurs very slowly. The comparative difficulty in forming $LaSr_3NiIrO_5H_3$ relative to $LaSr_3CoIrO_5H_3$ is likely to arise from the fact that reduction from Ni^{II} to Ni^{I} requires an electron to be added to an antibonding e_g orbital, whereas reduction from Co^{II} to Co^{I} involves an electron being added to a non-bonding t_{2g} orbital. Although previously reported oxyhydride phases, such as $LaSr_3NiRuO_4H_4$,[51] contain nickel solely in the +1 oxidation state, it is likely that full reduction to $LaSr_3Ni^{I}Ir^{III}O_5H_3$ cannot be achieved, as this would require higher reaction temperatures or longer reaction times and the $LaSr_3NiIrO_8$ framework is insufficiently stable to withstand these conditions without the onset of non-topochemical decomposition.

4.3.3 Structural characterisation of $LaSr_3NiIrO_{6.4}$

4.3.3.1 Synchrotron powder X-ray diffraction

SXRD data were collected from the phase obtained when $LaSr_3NiIrO_8$ is heated in the presence of a Zr getter, henceforth referred to as $LaSr_3NiIrO_{6.4}$. A structural model of an infinite-chain phase, similar to $LaSr_3CoIrO_6$,[46] with *Immm* symmetry and composition of $LaSr_3NiIrO_6$ was constructed and refined against the data. Additional peaks that could be attributed to SrO were also observed, so this was added to the refinement as a secondary phase. The fit to the data is shown in Figure 4.6, and the refinement parameters are detailed in Table 4.3. The refinement yielded lattice parameters of a = 3.89666(8) Å, b = 3.5873(1) Å and c = 12.8352(3) Å, which corresponds to a substantial contraction in the y-direction and expansion in the z-direction, relative to the parent material, consistent with the formation of an infinite-chain phase.

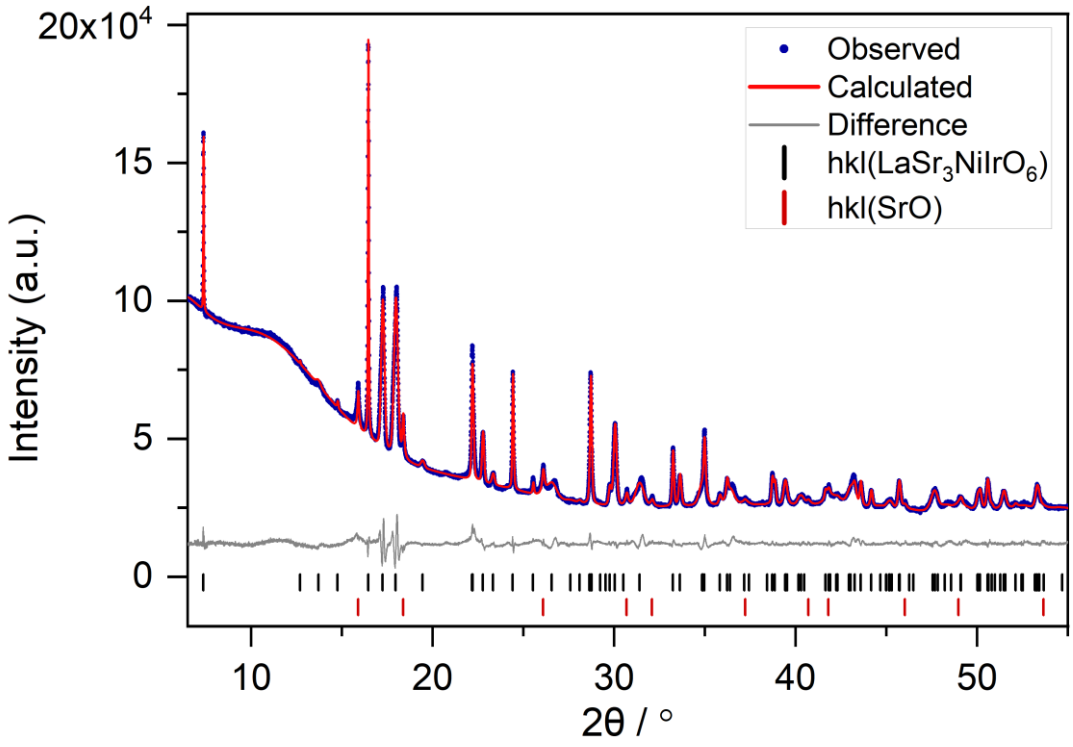

Figure 4.6: Observed, calculated and difference plots from the structural refinement of $LaSr_3NiIrO_{6.4}$ against SXRD data collected at room temperature using a wavelength of 0.825 Å.

Table 4.3: Parameters from the structural refinement of $LaSr_3NiIrO_{6.4}$ against SXRD data, using an infinite-chain model in the *Immm* space group with composition $LaSr_3NiIrO_6$. The fractional coordinates of the O2 site were fixed to be the same as the all-oxide parent phase.

$LaSr_3NiIrO_6$, space group *Immm* (No. 71)						
		x	***y***	***z***	**Occ.**	**B_{iso} (Å^2)**
La(1)/Sr(1)	4*i*	0	0	0.35548(6)	0.25/0.75	0.74(4)
Ni(1)/Ir(1)	2*a*	0	0	0	0.5/0.5	0.25(3)
O(1)	2*b*	½	0	0	1	0.2(1)
O(2)	4*i*	0	0	0.163	1	0.2(1)
a = 3.89666(8) Å, b = 3.5873(1) Å, c = 12.8352(3) Å						
V = 179.417(7) Å^3						
R_{wp} = 2.24%, R_p = 1.49%, *gof* = 4.61						

4.3.3.2 Thermogravimetric analysis

Thermogravimetric data collected from $LaSr_3NiIrO_{6.4}$ whilst heating under flowing oxygen indicated a mass gain of 3.8%, as shown in Figure 4.7. Assuming full oxidation back to $LaSr_3NiIrO_8$, this corresponds to an initial composition of $LaSr_3NiIrO_{6.14}$. The oxidation

appears to occur in two stages. By comparing the mass of the sample at ~400 °C to the final mass, a composition of approximately $LaSr_3NiIrO_{6.83}$ is obtained for the intermediate phase, which is likely to correspond to an actual composition of $LaSr_3NiIrO_7$, whereby nickel is present as Ni^{II} and iridium is present as Ir^{III}.

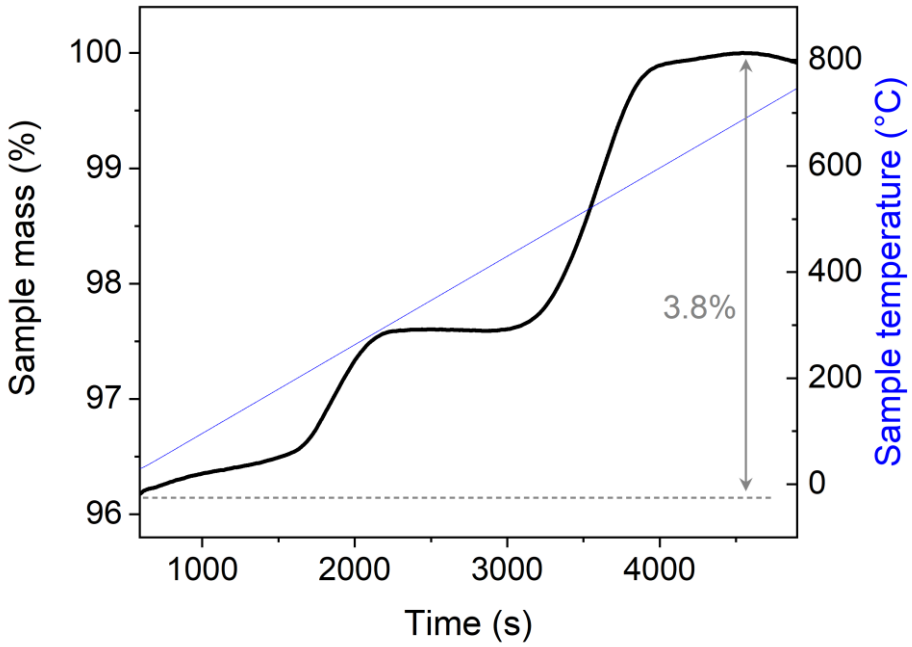

Figure 4.7: TGA trace when $LaSr_3NiIrO_{6.4}$ is heated under flowing oxygen.

4.3.3.3 Neutron powder diffraction

NPD data were collected from $LaSr_3NiIrO_{6.4}$ at ambient temperature with a wavelength of 1.594 Å using the D2B diffractometer at the ILL. For the initial refinements, the infinite-chain model constructed in Section 4.3.3.1 was used, which provided a good fit to the data. To evaluate whether complete anion deintercalation to $LaSr_3NiIrO_6$ had been achieved, oxide ions were added at the 2*d* site, (0, 0.5, 0), and the occupancy at this site was allowed to refine, which provided an improved fit to the data. The occupancy refined to a value of 0.201(8), corresponding to an overall composition of $LaSr_3NiIrO_{6.4}$. The fact that there are some oxide ions remaining along the *b*-axis is consistent with the observation that the *b*-lattice parameter

of $LaSr_3NiIrO_{6.4}$ (b = 3.5891 Å) is slightly larger than that of $LaSr_3CoIrO_6$ (b = 3.5763 Å). In addition, the presence of some oxide ions in the O2 site is supported by the observation of strong anisotropic peak broadening along the 0k0 direction in both the X-ray and neutron data, which is accounted for during the refinements using the Stephens model.[99] The fit to the data is shown in Figure 4.8, with the refinement parameters presented in Table 4.4 and the refined structure shown in Figure 4.9.

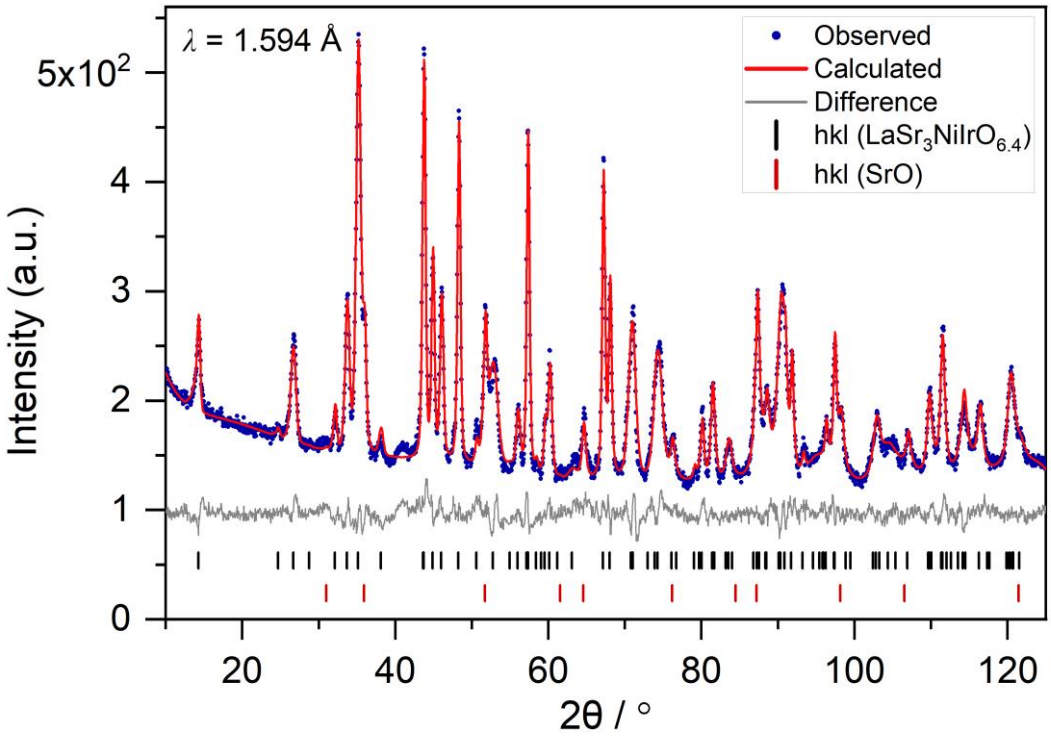

Figure 4.8: Observed, calculated and difference plots from the structural refinement of $LaSr_3NiIrO_{6.4}$ against NPD data collected at room temperature from the D2B diffractometer using a wavelength of 1.594 Å.

Table 4.4: Parameters from the structural refinement of $LaSr_3NiIrO_{6.4}$ against NPD data collected at room temperature from the D2B diffractometer using a wavelength of 1.594 Å.

$LaSr_3NiIrO_{6.40(2)}$, space group *Immm* (No. 71), 88.8(3) wt%						
		x	***y***	***z***	**Occ.**	**B_{iso} (Å^2)**
La(1)/Sr(1)	4*i*	0	0	0.3544(1)	0.25/0.75	0.23(5)
Ni(1)/Ir(1)	2*a*	0	0	0	0.5/0.5	0.31(6)
O(1)	2*b*	½	0	0	1	0.38(5)
O(2)	2*d*	0	½	0	0.201(8)	0.38(5)
O(3)	4*i*	0	0	0.1652(2)	1	0.38(5)
a = 3.9007(2) Å, b = 3.5891(3) Å, c = 12.8471(7) Å						
V = 179.86(2) Å^3						
SrO, space group *Fm$\bar{3}$m* (No. 225), 11.2(3) wt%						
		x	***y***	***z***	**Occ.**	**B_{iso} (Å^2)**
Sr(1)	4*a*	0	0	0	1	0.5(1)
O(1)	4*b*	½	½	½	1	0.5(1)
a = 5.1687(5) Å						
V = 138.08(4) Å^3						
R_{wp} = 3.62%, R_p = 2.84%, *gof* = 1.72						

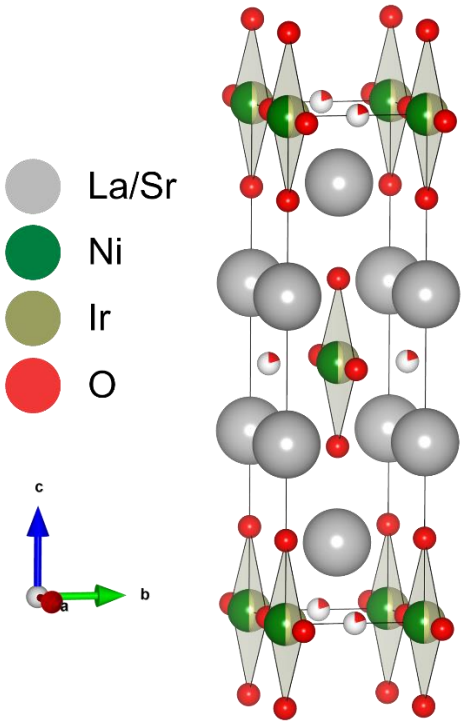

Figure 4.9: Refined structure of $LaSr_3NiIrO_{6.4}$.

4.3.3.4 X-ray absorption spectroscopy

XAS measurements were performed on NiO, $LaSr_3NiIrO_{5.4}H_{2.6}$ and $LaSr_3NiIrO_{6.4}$. The measurements were performed with a laboratory instrument at energies between 8250 and 8800 eV to allow the Ni K-edge (8333 eV) to be observed. The spectra were calibrated using Ni foil and normalised up to 8800 eV. The data at the XANES edges are shown in Figure 4.10.

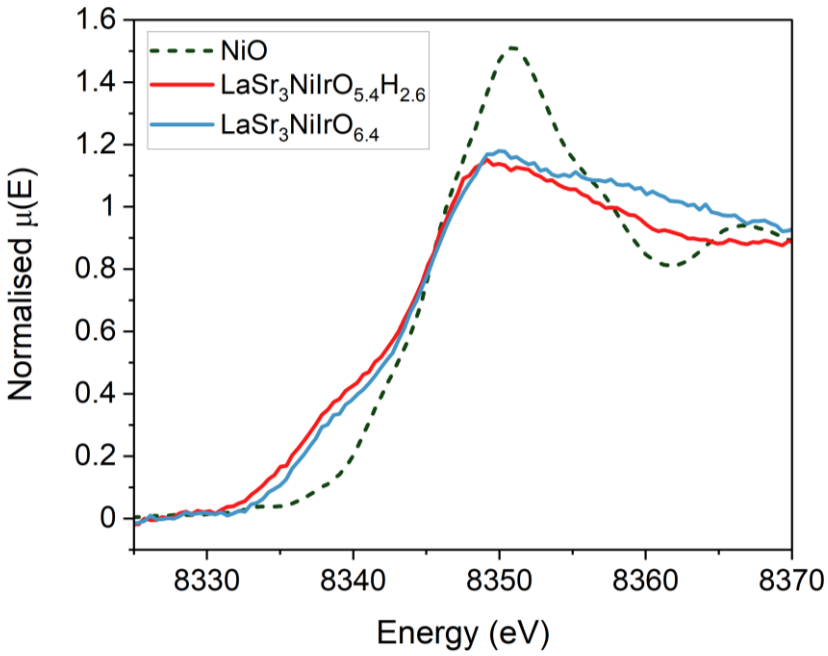

Figure 4.10: XANES Ni K-edges for NiO, $LaSr_3NiIrO_{5.4}H_{2.6}$ and $LaSr_3NiIrO_{6.4}$.

The position of the XANES edge for $LaSr_3NiIrO_{5.4}H_{2.6}$ is at lower energy than that of NiO, consistent with the notion that the compound contains 60% Ni^{I} and 40% Ni^{II}. Meanwhile, the XANES edge for $LaSr_3NiIrO_{6.4}$ is similar to that of $LaSr_3NiIrO_{5.4}H_{2.6}$ but at slightly higher energy, suggesting that there is a higher proportion of Ni^{II} in $LaSr_3NiIrO_{6.4}$ than in $LaSr_3NiIrO_{5.4}H_{2.6}$. Upon initial inspection, this appears counterintuitive as $LaSr_3NiIrO_{6.4}$ has a smaller total transition metal oxidation state (+3.8) than $LaSr_3NiIrO_{5.4}H_{2.6}$ (+4.4). However, in the structure of $LaSr_3NiIrO_{5.4}H_{2.6}$, iridium is octahedrally coordinated, so is likely to be present as Ir^{III} (Section 4.3.2.3). This would correspond to nickel being present with an average oxidation state of +1.4. Meanwhile, $LaSr_3NiIrO_{6.4}$ contains square-planar iridium, thereby

allowing it to adopt lower oxidation states, such as Ir^{II} (*vide infra*). Assuming iridium has an average oxidation state of +2 in this compound, this would correspond to nickel being present with an average oxidation state of +1.8.

As such, when the likely oxidation states of iridium in $LaSr_3NiIrO_{5.4}H_{2.6}$ and $LaSr_3NiIrO_{6.4}$ are taken into account, the XANES data are consistent with the expected nickel oxidation states in these compounds. To confirm that iridium is present as Ir^{III} in $LaSr_3NiIrO_{5.4}H_{2.6}$ and Ir^{II} in $LaSr_3NiIrO_{6.4}$, XANES data could be collected at the Ir L-edge.

4.3.3.5 Discussion

Reaction of $LaSr_3NiIrO_8$ with a Zr getter yields a compound with composition $LaSr_3NiIrO_{6.4}$, which adopts an infinite-chain-type structure but with ~20% of the equatorial sites along the *b*-axis occupied by oxide ions. The anion vacancy ordering observed in this compound arises so that the lattice strain associated with the substantially different Ni−O−Ir and Ni−□−Ir distances is minimised.

Previous work has shown that heating $LaSr_3CoIrO_8$ in the presence of a Zr getter yields $LaSr_3CoIrO_6$, in which the transition metals are present as Co^{I} and Ir^{II}.[46] Meanwhile, heating $La_2Sr_2NiRhO_8$ in the presence of a Zr getter yields $La_2Sr_2NiRhO_{6.5}$, with the stability of this anion composition attributed to the disproportionation of Rh^{II} into Rh^{I} and Rh^{III}.[100] The anion composition of $LaSr_3NiIrO_{6.4}$ is close to that of $La_2Sr_2NiRhO_{6.5}$ and suggests that, whilst initial reduction (likely to $Ni^{II}Ir^{II}$) occurs rapidly, further reduction to $LaSr_3NiIrO_6$ occurs very slowly.

In $LaSr_3NiIrO_{6.4}$, 60% of the transition metals adopt square-planar coordination (D_{4h}) and the remaining 40% adopt square-pyramidal coordination (C_{4v}). The total transition metal oxidation state in this compound is +3.8 and, as such, the possible transition metal oxidation states are Ni^{I}, Ni^{II}, Ir^{I}, Ir^{II} and Ir^{III}. The electronic configuration for each of these oxidation states in square-planar and square-pyramidal coordination is shown in Figure 4.11.

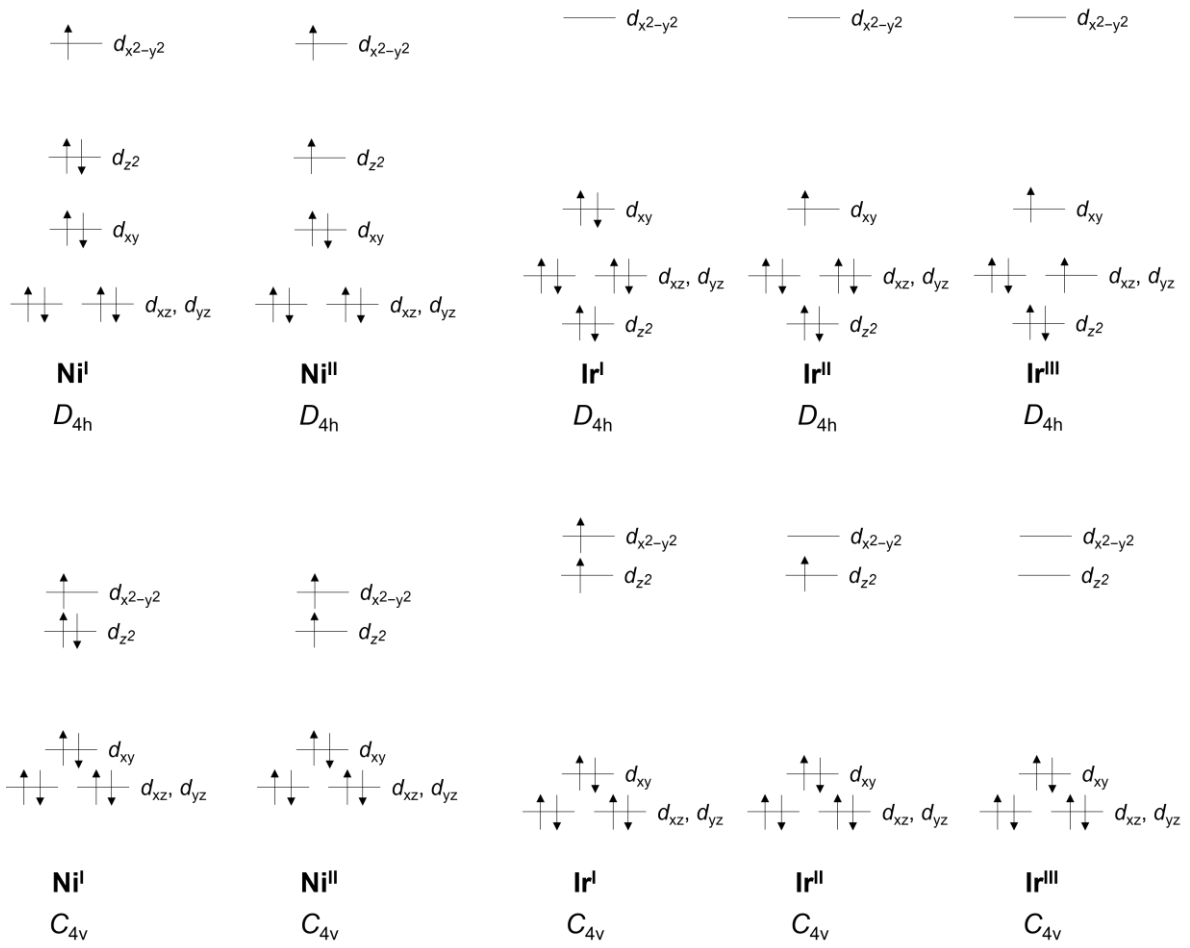

Figure 4.11: Electronic configurations of Ni^{I}, Ni^{II}, Ir^{I}, Ir^{II} and Ir^{III} in square-planar (D_{4h}) and square-pyramidal (C_{4v}) coordination environments.

Considering the XAS data in Section 4.3.3.4, and by analogy with Sr_4CoIrO_6 and $LaSr_3CoIrO_6$,[46] nickel is likely to be present as 80% Ni^{II} and 20% Ni^{I}, whilst the iridium is likely to be nominally present as Ir^{II}. To allow iridium to be reduced below Ir^{III}, strong stabilisation of the $5d_{z^2}$ orbital is required. Although adoption of a square-pyramidal geometry lowers the energy of this orbital, the stabilisation is likely to be insufficient to allow the orbital to be occupied. As such, any Ir^{I} or Ir^{II} present must adopt a square-planar coordination environment. To accommodate this, it is likely that the Ir^{II} disproportionates into Ir^{I} (located at D_{4h} sites) and Ir^{III} (located at C_{4v} sites), as shown in Figure 4.12. This is analogous to the disproportionation of Rh^{II} into Rh^{I} and Rh^{III} in $La_2Sr_2NiRhO_{6.5}$.[100] The fact that disproportionation has not been observed previously for Ir^{II}-containing compounds can be

attributed to the fact that it requires the presence of both iridium in the +2 oxidation state and cation sites with different coordination environments. In all previously reported compounds containing Ir^{II}, the iridium is present solely in square-planar coordination environments,[46,101] so there is no driving force for disproportionation into Ir^{I} and Ir^{III}. As such, $LaSr_3NiIrO_{6.4}$ is the first example of a compound containing Ir^{II} that has two different iridium coordination environments that can drive disproportionation into Ir^{I} and Ir^{III}.

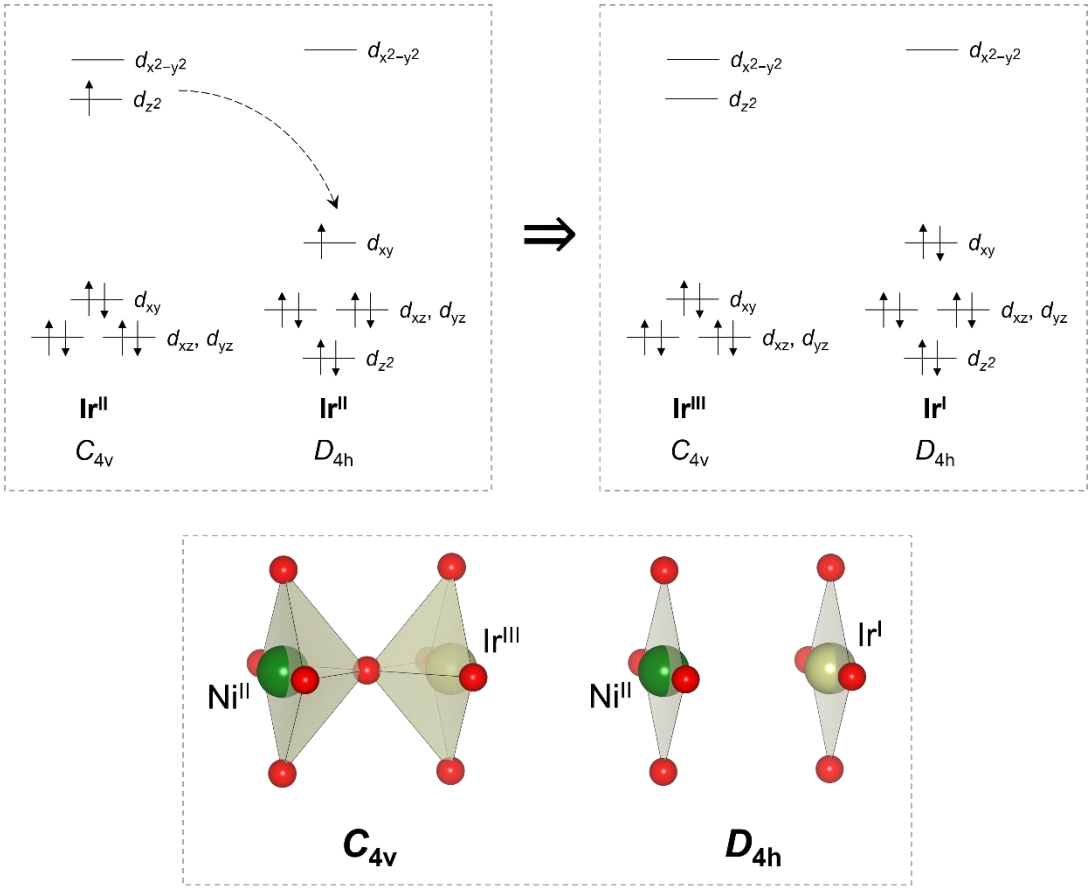

Figure 4.12: Top: Illustration of electronic driving force for disproportionation of Ir^{II} into Ir^{I} (D_{4h}) and Ir^{III} (C_{4v}). Bottom: Illustration of coordination environments of Ni^{II}, Ir^{I} and Ir^{III} in disproportionated $LaSr_3NiIrO_{6.4}$.

The comparative difficulty in forming $LaSr_3NiIrO_6$, as opposed to $LaSr_3CoIrO_6$, is likely to result from the fact that reduction from Co^{II} to Co^{I} requires filling of a $3d_{xy}$ orbital, whilst reduction from Ni^{II} to Ni^{I} requires filling of a higher energy $3d_{z^2}$ orbital. As a result, the reaction temperatures that would be required to reduce beyond $LaSr_3NiIrO_{6.4}$ would lead to the onset of non-topochemical decomposition.

4.4 Magnetic characterisation

4.4.1 Magnetic characterisation of $LaSr_3NiIrO_8$

Magnetisation data collected from $LaSr_3NiIrO_8$ as a function of temperature are presented in Figure 4.13, and magnetisation-field isotherms collected at 5 K and 300 K are presented in Figure 4.14. Fitting of the Curie-Weiss law to the data gives a value for C of 1.12(3) cm^3 K mol^{-1} and a value for θ of −131(4) K. The value for C is close to the value of 1 cm^3 K mol^{-1} that would be expected for two unpaired electrons using the spin-only approximation, consistent with a combination of Ni^{II} (d^8 configuration) and Ir^{V} ($J_{eff} = 0$). Meanwhile, the large, negative value of θ indicates the presence of antiferromagnetic interactions. There is a small divergence of the ZFC and FC curves starting at ~150 K, before a more substantial divergence occurs at ~10 K, suggesting the presence of a magnetic transition, possibly to an antiferromagnetic state.

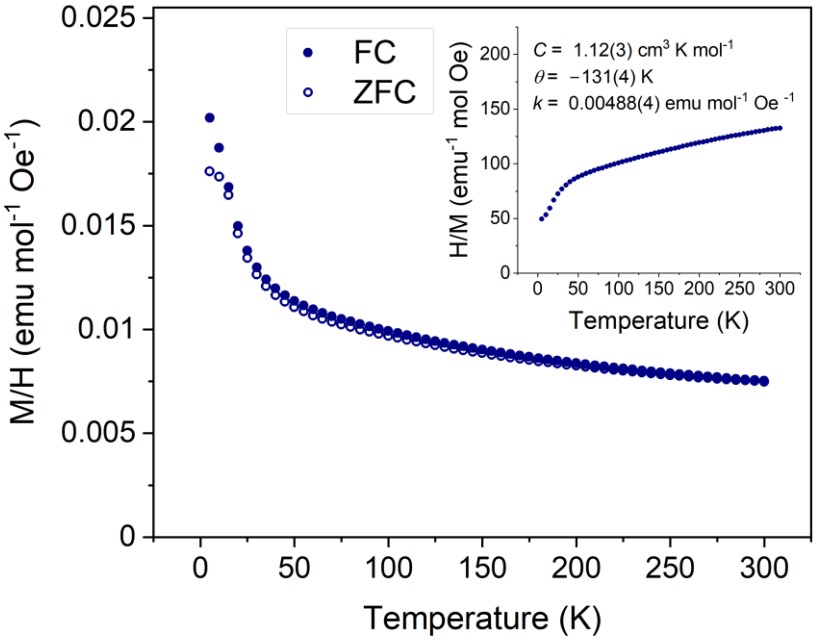

Figure 4.13: Magnetisation data collected from $LaSr_3NiIrO_8$ as a function of temperature, measured in a field of 100 Oe under both ZFC and FC conditions.

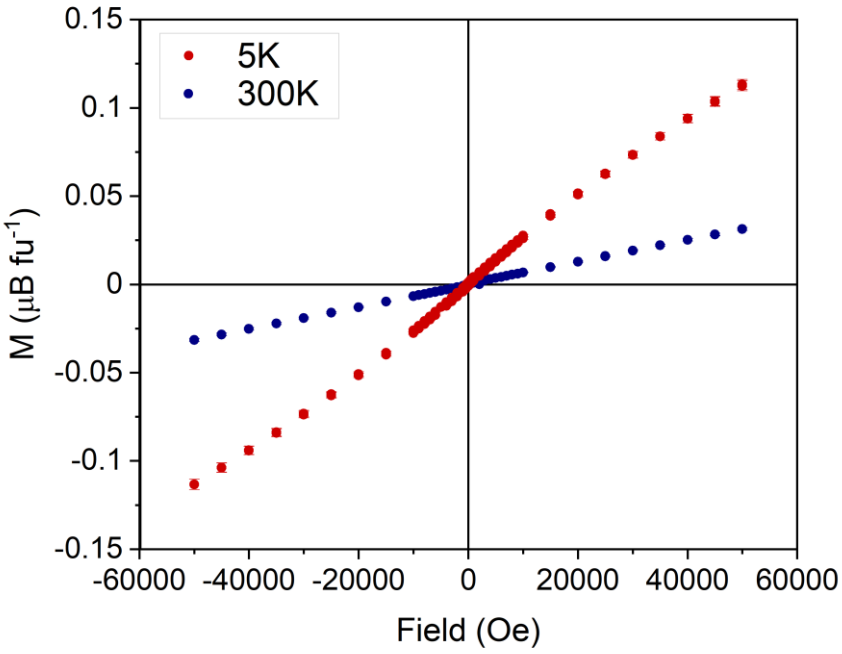

Figure 4.14: Magnetisation-field isotherms for $LaSr_3NiIrO_8$ measured at 5 K and 300 K.

4.4.2 Magnetic characterisation of $LaSr_3NiIrO_{5.4}H_{2.6}$

Magnetisation data collected from $LaSr_3NiIrO_{5.4}H_{2.6}$ as a function of temperature are presented in Figure 4.15, and magnetisation-field isotherms collected at 5 K and 300 K are presented in Figure 4.16. The substantial divergence of the ZFC and FC curves from 300 K, in combination with the saturated magnetic moment of ~0.07 μ_B fu^{-1} at room temperature, indicates the presence of a Ni metal impurity. Therefore, to extract useful magnetic information about the bulk phase, a 'ferrosubtraction' technique was employed, as described in Section 2.8.1. The results from this are shown in Figure 4.17. Fitting of the paramagnetic susceptibility to the Curie-Weiss law gives a value for C of 0.989(6) cm^3 K mol^{-1} and a value for θ of −36.0(5) K. The negative value for θ suggests the presence of antiferromagnetic interactions. Although the value for C is slightly larger than the value of 0.625 cm^3 K mol^{-1} expected for a mixture of 40% Ni^{II} and 60% Ni^{I} with Ir^{III}, the observation that the value of C for $LaSr_3NiIrO_{5.4}H_{2.6}$ is

smaller than that for the parent oxide is consistent with the reduction of nickel from Ni^{II} to Ni^{I}. The increase in the saturated ferromagnetic moment at ~40 K indicates that a magnetic transition is likely to occur around this temperature. This is supported by the observation of a local maximum in the ZFC curve in Figure 4.15, suggesting the presence of a magnetically ordered state at low temperature. However, no magnetic features are observed in NPD data collected at 5 K, as shown in Figure 4.18.

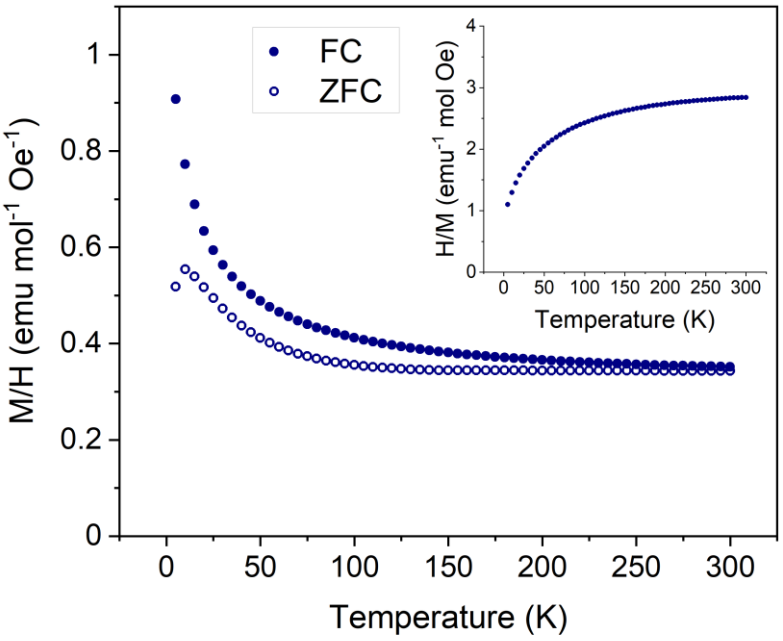

Figure 4.15: Magnetisation data collected from $LaSr_3NiIrO_{5.4}H_{2.6}$ as a function of temperature, measured in a field of 100 Oe under both ZFC and FC conditions.

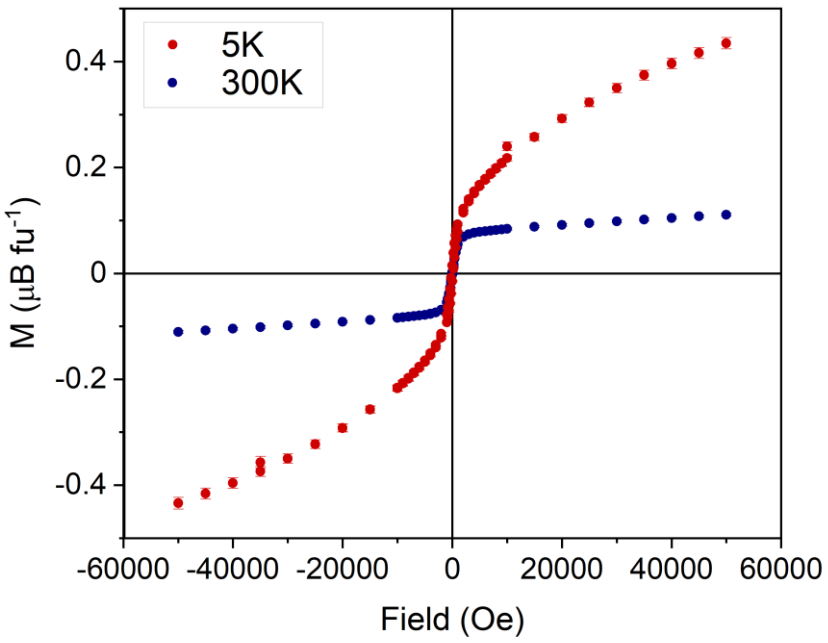

Figure 4.16: Magnetisation-field isotherms for $LaSr_3NiIrO_{5.4}H_{2.6}$ measured at 5 K and 300 K.

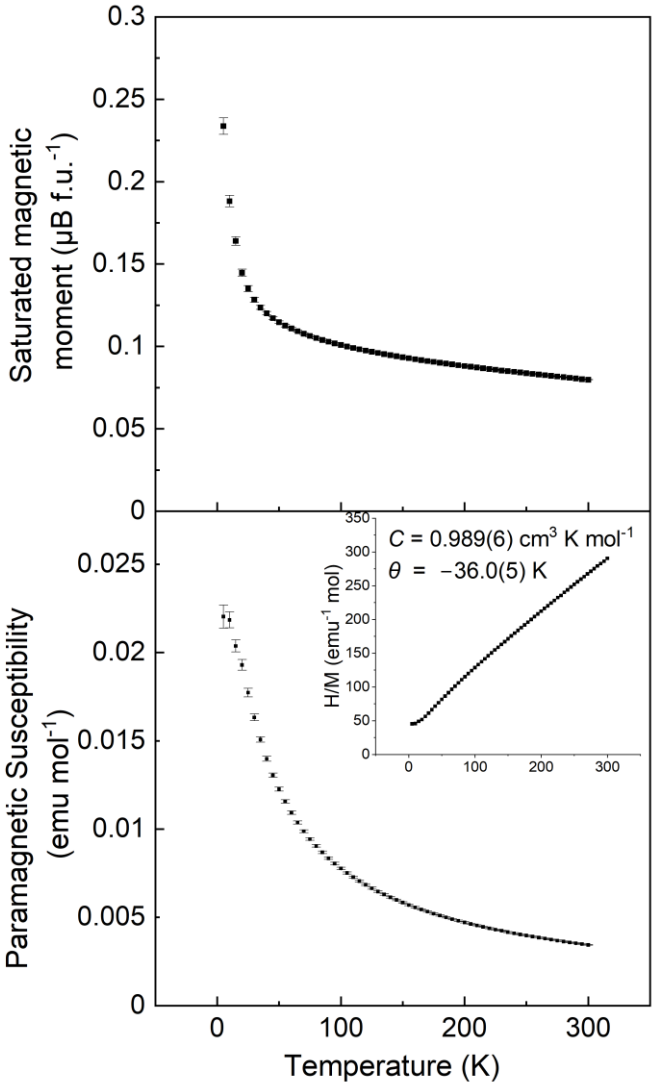

Figure 4.17: Saturated ferromagnetic moment (top panel) and paramagnetic susceptibility (bottom panel) obtained from $LaSr_3NiIrO_{5.4}H_{2.6}$ using the 'ferrosubtraction' technique described in Section 2.8.1.

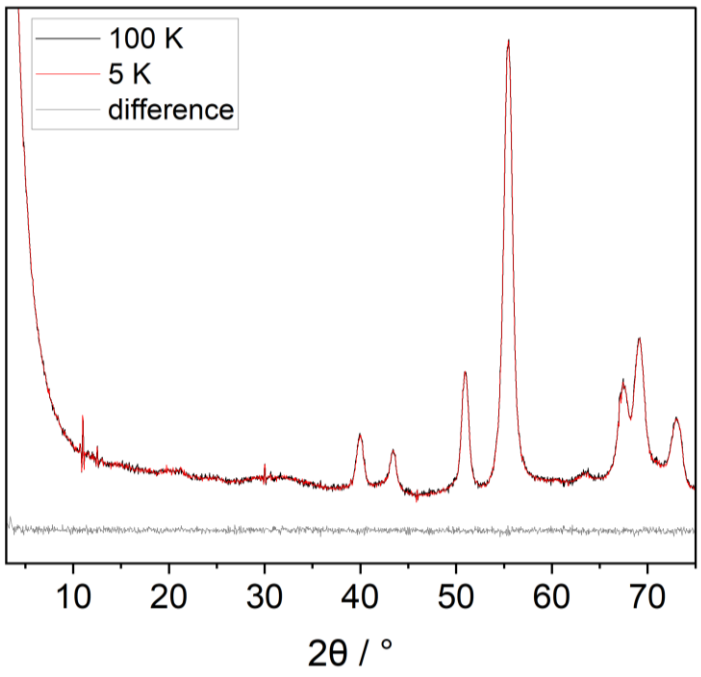

Figure 4.18: NPD data collected from $LaSr_3NiIrO_{5.4}H_{2.6}$ using the D20 diffractometer with a wavelength of 2.41 Å at 5 K and 100 K, and the difference between the patterns at these two temperatures.

4.4.3 Magnetic characterisation of $LaSr_3NiIrO_{6.4}$

Magnetisation data collected from $LaSr_3NiIrO_{6.4}$ as a function of temperature are presented in Figure 4.19, and magnetisation-field isotherms collected at 5 K and 300 K are presented in Figure 4.20. As with $LaSr_3NiIrO_{5.4}H_{2.6}$, there is a divergence in the ZFC and FC curves from 300 K, indicating the presence of a Ni metal impurity. Therefore, a 'ferrosubtraction' technique was employed, with the results from this shown in Figure 4.21. Fitting of the paramagnetic susceptibility to the Curie-Weiss law yields a value for C of 0.392(9) cm^3 K mol^{-1} and a value for θ of +1(2) K. The value for C is considerably smaller than the value of 1 cm^3 K mol^{-1} that would be expected for the transition metal combination in $LaSr_3Ni^{II}Ir^{I/III}O_{6.4}$. Although there is no obvious transition in Figure 4.19 and no magnetic features are observed in NPD data collected at 5 K (Figure 4.22), there is a sharp increase in the saturated magnetic moment below ~30 K (Figure 4.21). This suggests that, although the compound does not adopt a magnetically ordered state, there is likely to be a change in the magnetic interactions below 30 K.

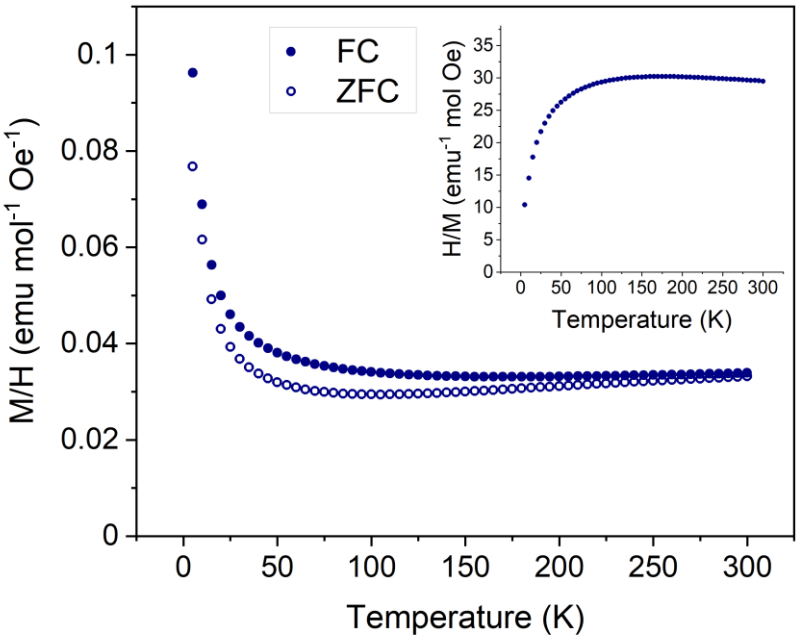

Figure 4.19: Magnetisation data collected from $LaSr_3NiIrO_{6.4}$ as a function of temperature, measured in a field of 100 Oe under both ZFC and FC conditions.

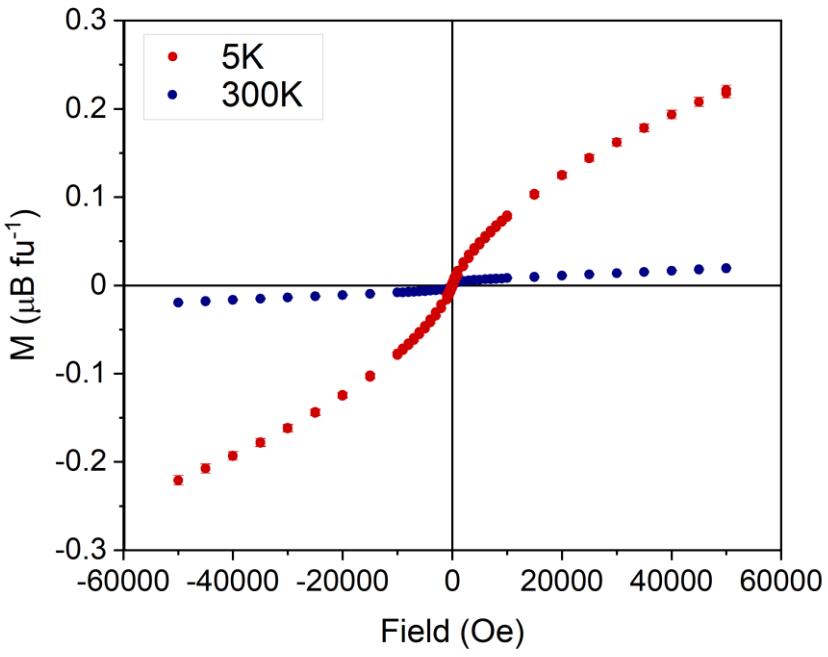

Figure 4.20: Magnetisation-field isotherms for $LaSr_3NiIrO_{6.4}$ measured at 5 K and 300 K.

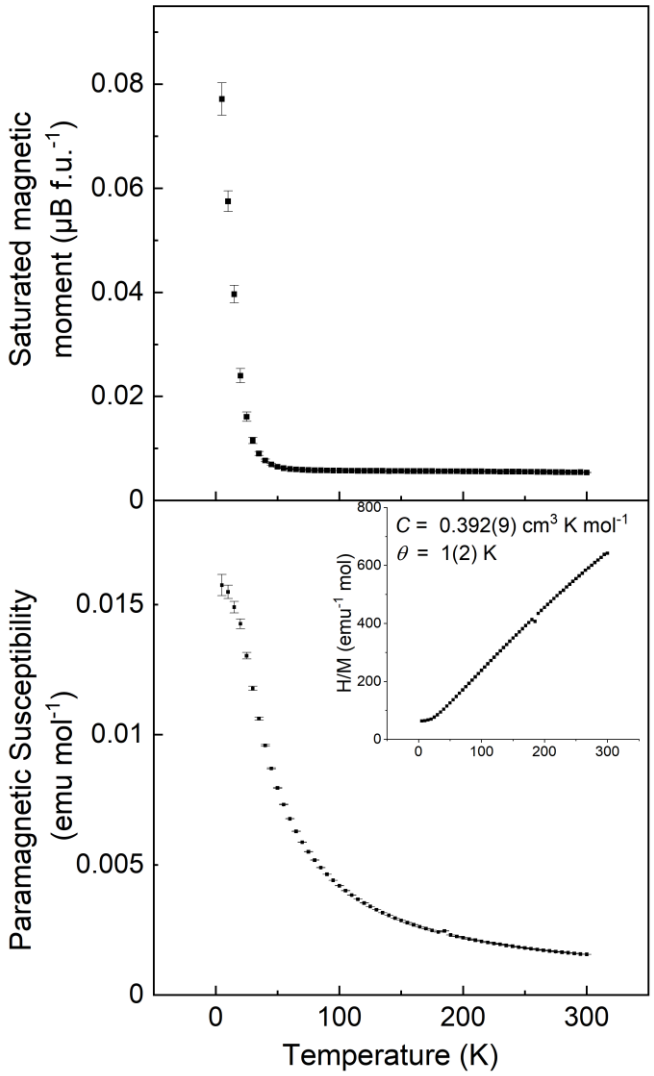

Figure 4.21: Saturated ferromagnetic moment (top panel) and paramagnetic susceptibility (bottom panel) obtained from $LaSr_3NiIrO_{6.4}$ using the 'ferrosubtraction' technique described in Section 2.8.1.

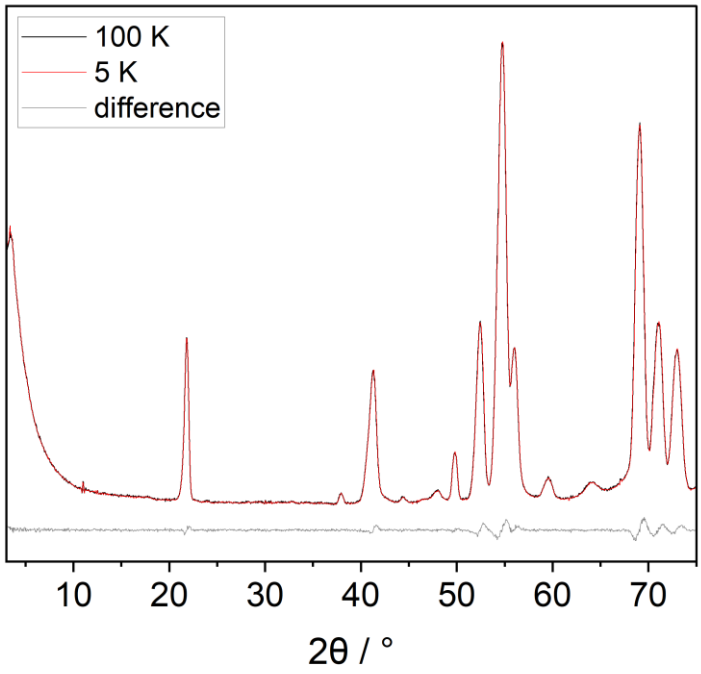

Figure 4.22: NPD data collected from $LaSr_3NiIrO_{6.4}$ using the D20 diffractometer with a wavelength of 2.41 Å at 5 K and 100 K, and the difference between the patterns at these two temperatures.

4.4.4 Discussion

The magnetisation data collected from $LaSr_3NiIrO_8$ indicate a possible transition to an antiferromagnetic state at low temperature. This is likely to occur through a $Ni(3d_{x^2-y^2})^1-O(2p)-Ir(5d_{x^2-y^2})^0-O(2p)-Ni(3d_{x^2-y^2})^1$ σ-superexchange pathway (Figure 4.23), analogous to that observed in $LaSrNiIrO_6$.[98]

The magnetisation data collected from $LaSr_3NiIrO_{5.4}H_{2.6}$ are qualitatively very similar to that from $LaSr_3NiIrO_8$. This is consistent with the fact that both Ir^{III} and Ir^{V} are diamagnetic and contain an empty $d_{x^2-y^2}$ orbital that can mediate antiferromagnetic σ-superexchange between next-nearest-neighbouring Ni^{I} or Ni^{II} ions (Figure 4.23). However, no long-range magnetic order is observed from low temperature neutron diffraction, which can be attributed to the paracrystalline nature of the B-site cation ordering, so there is not a magnetic lattice present upon which three-dimensional order can propagate.

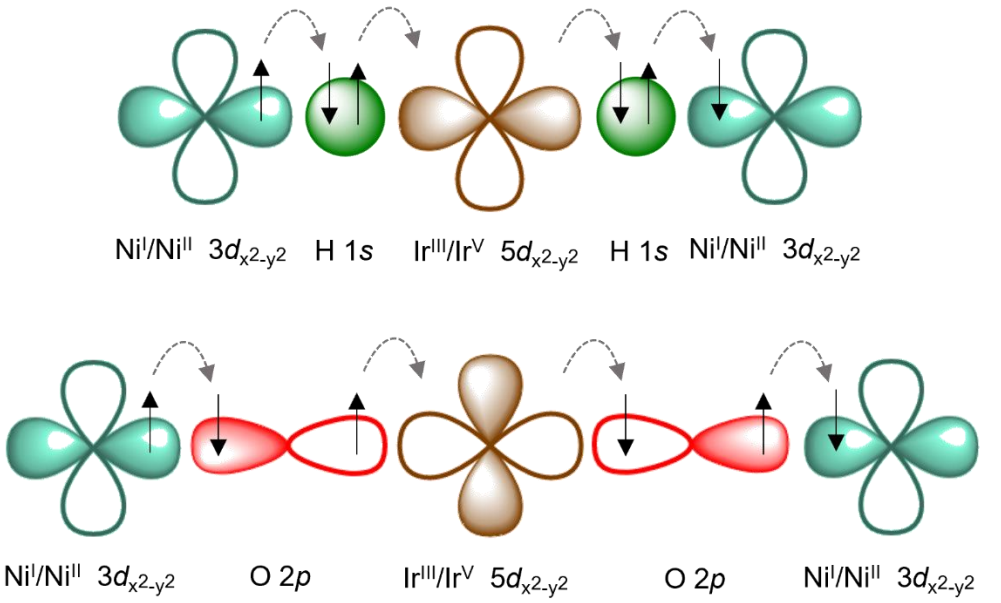

Figure 4.23: Orbital diagrams illustrating the antiferromagnetic σ-superexchange pathway between Ni^{I} or Ni^{II} ions via diamagnetic Ir^{III} or Ir^{V} ions.

In $LaSr_3NiIrO_{6.4}$, there are a number of different coupling interactions that are possible, which can be grouped into three categories: intrachain coupling, interchain coupling within the perovskite sheets and interchain coupling between the perovskite sheets. Ni^{II} has an unpaired electron in its $d_{x^2-y^2}$ orbital whilst the $d_{x^2-y^2}$ orbitals of diamagnetic Ir^{I} (D_{4h}) and Ir^{III} (C_{4v}) are unoccupied; this might be expected to give strong intrachain magnetic couplings through extended σ-superexchange interactions, similar to those shown in Figure 4.23. Meanwhile, interchain coupling interactions are mediated by electrons in the d_{z^2}, d_{xz} and d_{yz} orbitals. The d_{xz} and d_{yz} orbitals are fully occupied in all the transition metals, so are unlikely to participate in magnetic coupling. Whilst the d_{z^2} orbital in Ni^{II} is half-occupied, the neighbouring iridium ions are diamagnetic and, as such, the interchain interactions are likely to be very weak. As a result, although magnetic ordering is likely to be present within the chains, the weak registry between the chains means that long-range 3-dimensional order is unlikely to be present. This can account for the magnetic data presented in Section 4.3.4.3. The increase in saturated magnetic moment observed at ~30 K in Figure 4.21 results from magnetic ordering within the

chains, whilst the absence of any obvious feature in Figure 4.19 results from the lack of magnetic ordering between the chains.

4.5 Conclusion

Reaction of the $n = 1$ Ruddlesden-Popper phase, $LaSr_3NiIrO_8$, with LiH yields the oxyhydride phase, $LaSr_3NiIrO_{5.4}H_{2.6}$, whilst reaction with a Zr getter yields the oxygen-deficient phase $LaSr_3NiIrO_{6.4}$. This reactivity has clear parallels to that observed for $LaSr_3CoIrO_8$. The extent of reduction of iridium in $LaSr_3NiIrO_{5.4}H_{2.6}$ is limited by the obtainment of a fully-occupied t_{2g} level in octahedrally-coordinated Ir^{III} (low-spin d^6 configuration), which means that any further reduction would require occupation of antibonding e_g orbitals. Meanwhile, in $LaSr_3NiIrO_{6.4}$, iridium is likely to be present as Ir^{II}, which disproportionates into Ir^{III} (occupying C_{4v} sites) and Ir^{I} (occupying D_{4h} sites). The reduction of iridium to oxidation states lower than +3 is possible in this compound because the adoption of a square-planar geometry lowers the energy of the $5d_{z^2}$ orbital, thereby making it energetically accessible.

In both $LaSr_3NiIrO_{5.4}H_{2.6}$ and $LaSr_3NiIrO_{6.4}$, it is not possible to obtain the 'fully reduced' phase. This is likely to be because the reaction times or temperatures required for this to occur would lead to the onset of non-topochemical decomposition. This is analogous to the behaviour observed for the reaction of $La_{0.5}Sr_{3.5}CoIrO_8$ with LiH.

$LaSr_3NiIrO_8$ and $LaSr_3NiIrO_{5.4}H_{2.6}$ exhibit very similar magnetic behaviour, which is attributed to the fact that both compounds contain Ni^{I} or Ni^{II} in combination with diamagnetic iridium (Ir^{V} or Ir^{III}). They both appear to undergo a transition to an antiferromagnetic state at low temperature, which is likely to be mediated by a $Ni(3d_{x^2-y^2})^1-O(2p)/H(1s)-Ir(5d_{x^2-y^2})^0-O(2p)/H(1s)-Ni(3d_{x^2-y^2})^1$ σ-superexchange pathway. However, long range 3-dimensional magnetic ordering is not observed from NPD due to the likely presence of B-site paracrystalline order in the compound.

Meanwhile, magnetisation data from $LaSr_3NiIrO_{6.4}$ do not show any obvious magnetic transition. This can be attributed to the observation that, although there are likely to be strong intrachain magnetic couplings, the interchain magnetic couplings are likely to be weak and, as a result, long-range 3-dimensional magnetic order is not established.

Chapter 5 – Topochemical reduction of Sr_4MnIrO_8 using CaH_2 and LiH

5.1 Introduction

In addition to LiH, CaH_2 is a commonly used reducing agent in the topochemical synthesis of oxyhydrides and oxygen-deficient phases, as discussed in Chapter 2. In this chapter, the reactivity of both LiH and CaH_2 with the n = 1 Ruddlesden-Popper phase, Sr_4MnIrO_8, is explored.

5.2 Experimental

5.2.1 Synthesis of Sr_4MnIrO_8

Two-gram polycrystalline samples of Sr_4MnIrO_8 were prepared using conventional ceramic synthesis methods. Stoichiometric amounts of $SrCO_3$, MnO_2, and IrO_2 (dried for 2 hours at 700 °C) were thoroughly ground together in an agate pestle and mortar, pelletised and heated in air at 1000 °C for 2 days. The samples were then reheated for several 2 day cycles at temperatures of 1300-1385 °C with intermediate grinding and pelletisation until no further change was observed by PXRD.

5.2.2 Exploration of the reactivity of Sr_4MnIrO_8

The reactivity of Sr_4MnIrO_8 with CaH_2 and LiH was explored as a function of temperature. The reaction mixtures were prepared by thoroughly grinding 200 mg of Sr_4MnIrO_8 with 4 mole equivalents of CaH_2 or 8 mole equivalents of LiH in an Ar-filled glovebox. The mixtures were then sealed in evacuated Pyrex® ampoules, heated at 250 °C for 1 period of 2 days and subsequently analysed by PXRD. This process was repeated, increasing the temperature for each heating cycle, until non-topochemical decomposition was observed, signalled by the formation of SrO and Ir metal. It was observed that tetragonal symmetry was retained until

decomposition, and that there was a continuous contraction of the *xy*-plane and expansion in the *z*-direction as the reaction temperature was increased. The results from these reactions indicated that non-topochemical decomposition occurs above 360 °C with CaH_2 and above 400 °C with LiH.

5.2.3 Synthesis of $Sr_4MnIrO_{6.58}H_{1.42}$

A sample of $Sr_4MnIrO_{6.58}H_{1.42}$ was prepared by thoroughly grinding 1.7 g of Sr_4MnIrO_8 with 2 mole equivalents of CaH_2 in an Ar-filled glovebox. The reaction mixture was then sealed in an evacuated Pyrex® ampoule and heated for 1 period of 7 days at 360 °C with a heating rate of 1 °C/min.

In previous work, a 0.1 M solution of NH_4Cl in MeOH has been used to remove the CaO by-product that results from the reaction of transition metal oxides with CaH_2.[45,47] However, treatment of the products from the reaction between $LaSr_3CoIrO_8$ and CaH_2 with NH_4Cl solutions led to decomposition of the reaction product into finely divided Ir metal (Appendix A3). Therefore, glycerol was used to remove the CaO from $Sr_4MnIrO_{6.58}H_{1.42}$, since this is able to dissolve CaO through the formation of calcium glyceroxides,[102] which can easily be washed away with MeOH, whilst the lower acidity of glycerol ($pK_a \sim 14.4$)[103] relative to NH_4Cl ($pK_a \sim 9.24$) avoids decomposition to Ir metal. However, the low acidity of glycerol also means that it is not able to remove any CaH_2 remaining in the reaction mixture and, as a consequence, the amount of CaH_2 used in the reaction must be carefully chosen such that there is none remaining at the end of the reaction period.

Thus, the CaO by-product was removed by stirring the $Sr_4MnIrO_{6.58}H_{1.42}$ reaction mixture in glycerol overnight under a static N_2 atmosphere. The glycerol solution was then filtered and the product was washed with 3 × 25 ml MeOH under an N_2 atmosphere to remove the calcium

glyceroxides and any excess glycerol. The washed product was dried under vacuum and returned to the glovebox.

5.2.4 Synthesis of $Sr_4MnIrO_{5.32}H_{2.68}$

A sample of $Sr_4MnIrO_{5.32}H_{2.68}$ was prepared by thoroughly grinding 1.7 g of Sr_4MnIrO_8 with 9 mole equivalents of LiH in an Ar-filled glovebox. The reaction mixture was then sealed in an evacuated Pyrex® ampoule and heated for 1 period of 4 days at 400 °C with a heating rate of 1 °C/min. To remove the Li_2O by-product and any excess LiH, the reaction mixture was washed with MeOH under an N_2 atmosphere. The product was then dried under vacuum and returned to the glovebox.

5.3 Results

5.3.1 Structural characterisation of Sr_4MnIrO_8

A cation-disordered structural model with *I*4/*mmm* symmetry (shown in Figure 5.1) was created for Sr_4MnIrO_8 based on the previously reported n = 1 Ruddlesden-Popper phase, Sr_4CoIrO_8, which is also cation-disordered.[46,92] This model was refined against SXRD data collected from Sr_4MnIrO_8 and gave a good fit to the data, as shown in Figure 5.2, with the refinement parameters detailed in Table 5.1.

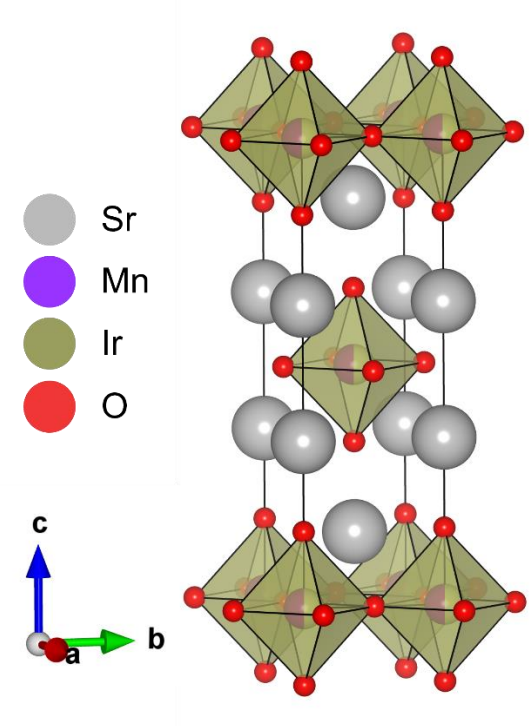

Figure 5.1: Structural model of Sr_4MnIrO_8 with the n = 1 Ruddlesden-Popper structure.

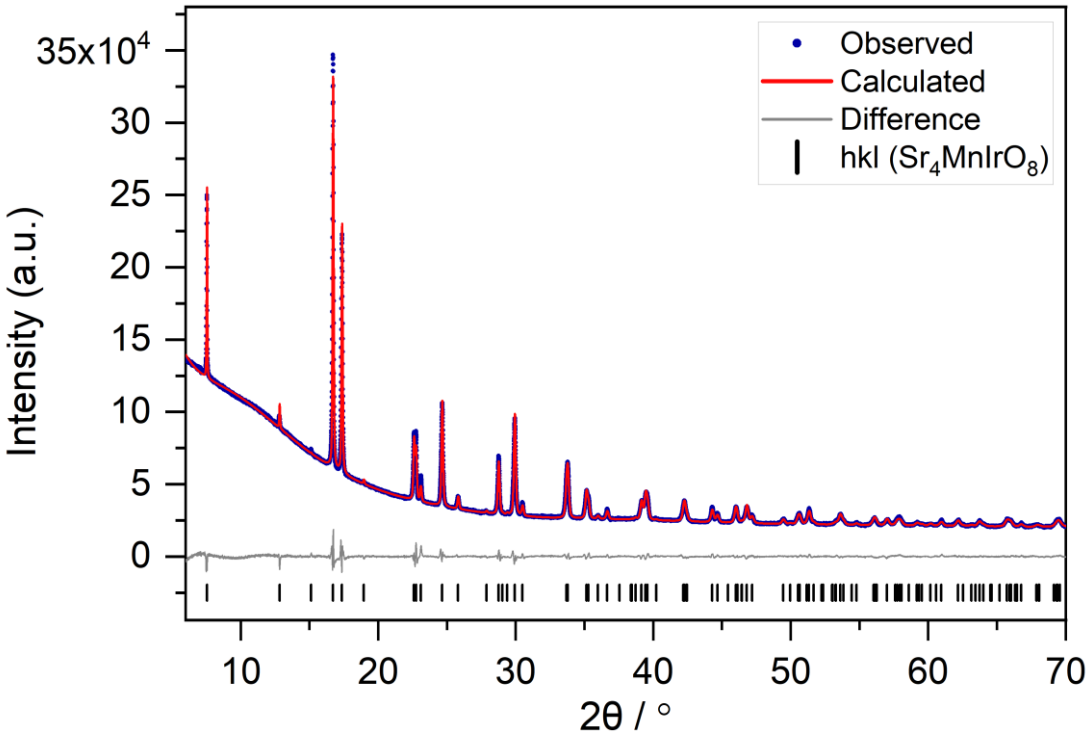

Figure 5.2: Observed, calculated and difference plots from the structural refinement of Sr_4MnIrO_8 against SXRD data collected at room temperature using a wavelength of 0.825 Å.

Table 5.1: Parameters from the structural refinement of Sr_4MnIrO_8 against SXRD data collected at room temperature. The fractional coordinates of the oxide sites were fixed to be the same as those of Sr_4CoIrO_8.

Sr_4MnIrO_8, space group *I*4/*mmm* (No. 139)						
		x	***y***	***z***	**Occ.**	**B_{iso} (Å^2)**
Sr(1)	4*e*	0	0	0.35532(4)	1	0.86(1)
Mn(1)/Ir(1)	2*a*	0	0	0	0.5/0.5	2.06(2)
O(1)	4*c*	0	½	0	1	1.40(4)
O(2)	4*e*	0	0	0.1604	1	1.40(4)
a = 3.86076(3) Å, c = 12.5364(2) Å						
V = 186.861(4) Å^3						
R_{wp} = 1.88%, R_p = 1.20%, *gof* = 3.87						

5.3.2 Structural characterisation of $Sr_4MnIrO_{6.58}H_{1.42}$

The product from the reaction between Sr_4MnIrO_8 and CaH_2, henceforth referred to as $Sr_4MnIrO_{6.58}H_{1.42}$, was analysed by SXRD, which indicated the presence of a single phase with *I*4/*mmm* symmetry. A substantial change in the lattice parameters was observed relative to the parent material, with a contraction in the *xy*-plane from a = 3.86076(3) Å to a = 3.7890(1) Å and an expansion in the *z*-direction from c = 12.5364(2) Å to c = 12.8060(4) Å.

5.3.2.1 Thermogravimetric analysis

Thermogravimetric data collected from $Sr_4MnIrO_{6.58}H_{1.42}$ whilst heating under flowing oxygen indicate a mass gain of 2.2%, as shown in Figure 5.3. Assuming full oxidation back to Sr_4MnIrO_8, this corresponds to an initial composition of $Sr_4MnIrO_{6.99}H_y$. Analysis of the exhaust gas by mass spectrometry showed a broad water peak concurrent with oxidation of the reduced phase, indicating that hydride is present in the phase.

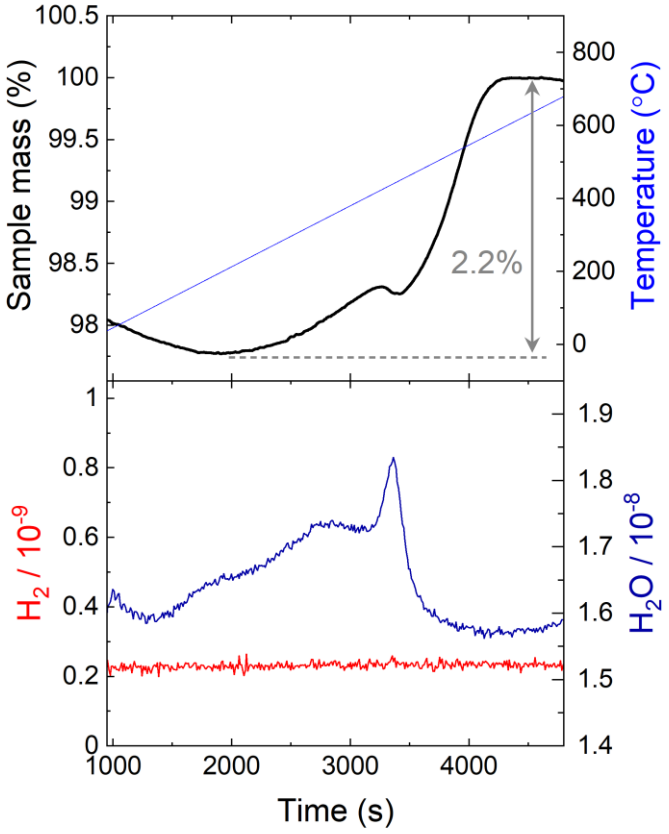

Figure 5.3: TGA trace (top panel) and H_2/H_2O contents of exhaust gas (bottom panel) when $Sr_4MnIrO_{6.58}H_{1.42}$ is heated under flowing oxygen.

5.3.2.2 Neutron powder diffraction

NPD data were collected from $Sr_4MnIrO_{6.58}H_{1.42}$ at ambient temperature using the GEM diffractometer at ISIS. A structural model based on the Sr_4MnIrO_8 parent phase was constructed using the lattice parameters obtained from the SXRD data, which was then refined against the data from the 35°, 64°, 91° and 154° detector banks of the GEM diffractometer.

Initially, the occupancy at the O2 (axial) site was allowed to refine. The oxide occupancy at this site refined to 1, indicating that this site must be fully occupied by oxide, so this site was fixed to be fully occupied in further refinements.

As discussed in Chapter 3, NPD data provides the average scattering power at each site. However, since there are three possible species that can occupy each anion site (oxide, hydride or vacancy), the exact composition at these sites is ambiguous from a single measurement. Therefore, to determine the anion content, either an assumption must be made or information from an alternative method must be included.

Initially, it was assumed that only anion deintercalation occurs at the O1 (equatorial) site. To evaluate this situation, the oxide ion occupancy at the O1 site was allowed to refine freely, corresponding to only oxide ions or vacancies being present in these positions (with no hydride). This yielded an occupancy of 0.393(8), which corresponds to a composition of $Sr_4MnIrO_{5.57(3)}$. This composition is chemically unlikely because it would require some of the transition metals to have a coordination number of 3, which would be highly unfavourable for both manganese and iridium. In addition, a composition of $Sr_4MnIrO_{5.57(3)}$ would have a combined transition metal oxidation state of +3.14. Since the XAS data (Section 5.3.5.1) suggest that manganese is present as a mixture of Mn^{III} and Mn^{IV} in this compound, it would require iridium to have an oxidation state between 0 and +1. This strongly implies that the compound must contain hydride ions.

To take this into account, hydride ions were added at the O1 site and the occupancies of oxide and hydride allowed to refine, such that the total occupancy at the site summed to 1. The refinement yielded a hydride occupancy of 0.356(5) and an oxide occupancy of 0.644(5), giving an overall composition of $Sr_4MnIrO_{6.58(2)}H_{1.42(2)}$. This composition is broadly similar to the composition of $Sr_4MnIrO_{6.99}H_y$ obtained from oxidative TGA. Considering the average scattering length of ~2.4 fm at the O1 site, $Sr_4MnIrO_{6.58}H_{1.42}$ is the maximum oxide ion content that is possible for this compound. Since the TGA measurement indicates a higher oxide ion content than this, it is likely that $Sr_4MnIrO_{6.58}H_{1.42}$ is roughly the correct composition, with the discrepancy with the TGA data arising from incomplete oxidation of the reduced phase to

Sr_4MnIrO_8 during the measurement. This composition would also be consistent with the XAS data (Section 5.3.5.1), allowing the iridium to be present as a mixture of Ir^{III} and Ir^{IV}. It is possible that there are a small number of vacancies present at the equatorial anion sites. However, it is challenging to definitively confirm the presence/absence of these anion vacancies, so the composition is assumed to be $Sr_4MnIrO_{6.58}H_{1.42}$.

The fits to the NPD data, assuming full oxide/hydride occupation at the equatorial sites, are shown in Figure 5.4-5.7, with the refinement parameters presented in Table 5.2. The refined structure, with hydride ions substituted at the equatorial positions, is shown in Figure 5.8. A structural refinement was also performed against the SXRD data using the model obtained from the NPD data, which gave a good visual fit, as shown in Appendix A3.

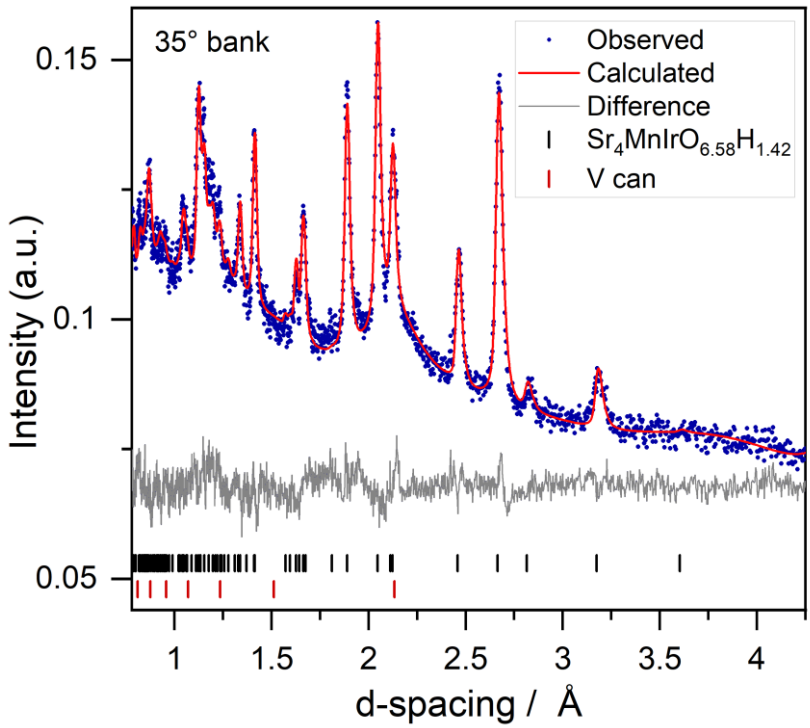

Figure 5.4: Observed, calculated and difference plots from the structural refinement of $Sr_4MnIrO_{6.58}H_{1.42}$ against NPD data collected at room temperature from the 35° bank of the GEM diffractometer.

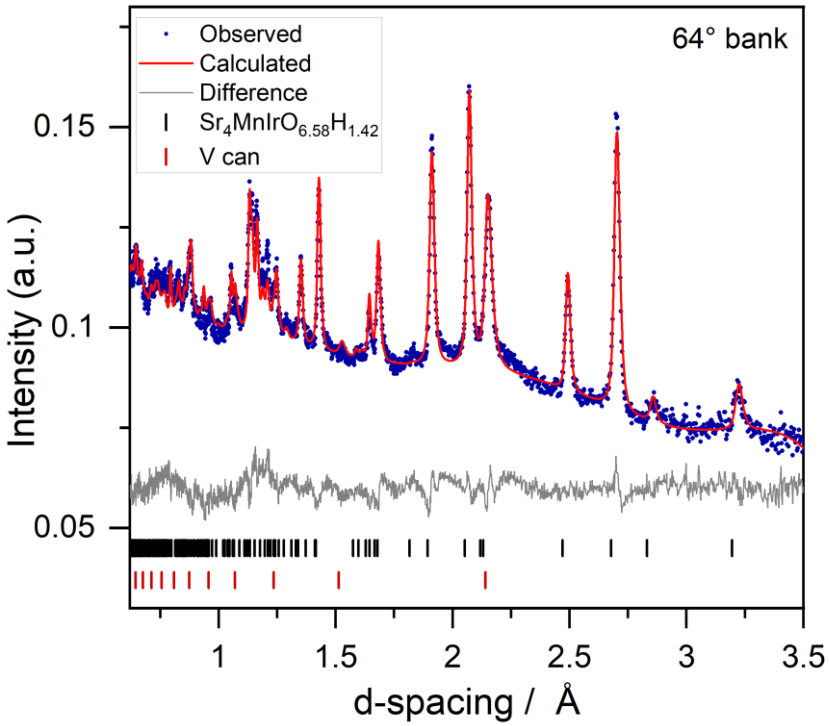

Figure 5.5: Observed, calculated and difference plots from the structural refinement of $Sr_4MnIrO_{6.58}H_{1.42}$ against NPD data collected at room temperature from the 64° bank of the GEM diffractometer.

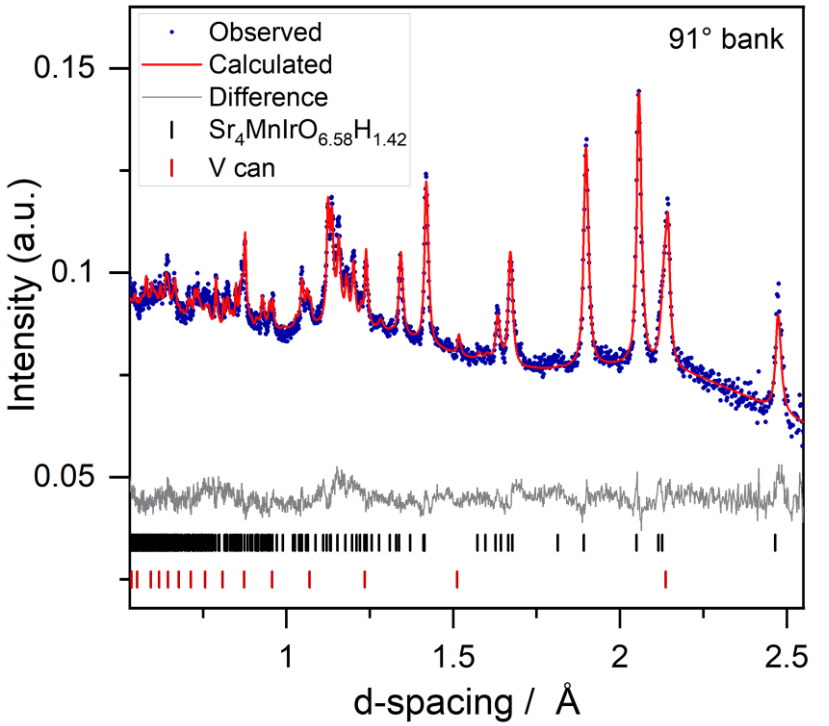

Figure 5.6: Observed, calculated and difference plots from the structural refinement of $Sr_4MnIrO_{6.58}H_{1.42}$ against NPD data collected at room temperature from the 91° bank of the GEM diffractometer.

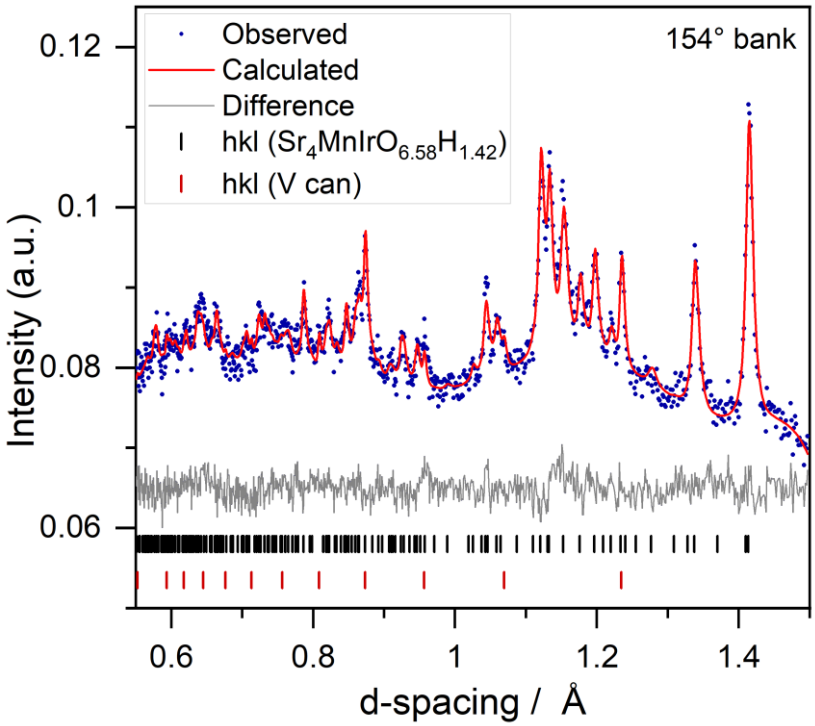

Figure 5.7: Observed, calculated and difference plots from the structural refinement of $Sr_4MnIrO_{6.58}H_{1.42}$ against NPD data collected at room temperature from the 154° bank of the GEM diffractometer.

Table 5.2: Parameters from the structural refinement of $Sr_4MnIrO_{6.58}H_{1.42}$ against NPD data collected at room temperature from the GEM diffractometer.

$Sr_4MnIrO_{6.58(2)}H_{1.42(2)}$, space group *I*4/*mmm* (No. 139)						
		x	***y***	***z***	**Occ.**	**B_{iso} (Å^2)**
Sr(1)	4*e*	0	0	0.3527(3)	1	0.71(8)
Mn(1)/Ir(1)	2*a*	0	0	0	0.5/0.5	9.2(6)
O(1)/H(1)	4*c*	0	½	0	0.644(5)/0.356(5)	0.5(1)
O(2)	4*e*	0	0	0.1571(4)	1	0.8(1)
a = 3.7935(5) Å, c = 12.796(2) Å						
V = 184.14(5) Å^3						
R_{wp} = 2.58%, R_p = 2.02%, *gof* = 0.002						

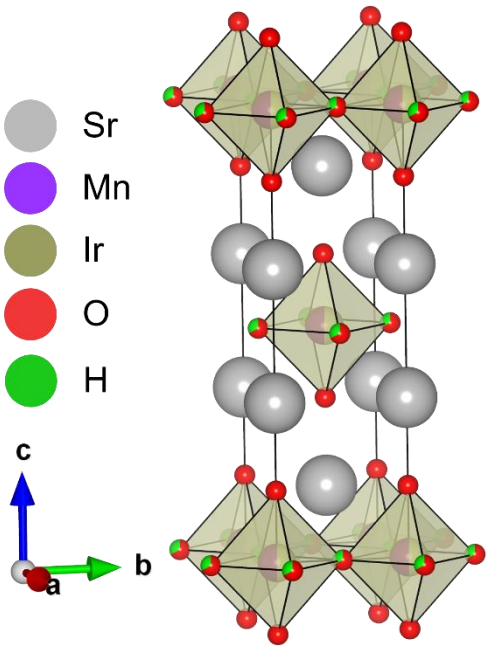

Figure 5.8: Refined structure of $Sr_4MnIrO_{6.58}H_{1.42}$ with hydride ions substituted into the equatorial positions.

5.3.3 Structural characterisation of $Sr_4MnIrO_{5.32}H_{2.68}$

The product from the reaction between Sr_4MnIrO_8 and LiH, henceforth referred to as $Sr_4MnIrO_{5.32}H_{2.68}$, was analysed by SXRD, which indicated the presence of a single phase with *I*4/*mmm* symmetry. The lattice parameters for this phase were observed to be a = 3.8070(2) Å and c = 12.9772(7) Å, which corresponds to a slight expansion in the *xy*-plane and a significant expansion in the *z*-direction relative to $Sr_4MnIrO_{6.58}H_{1.42}$.

5.3.3.1 Thermogravimetric analysis

Thermogravimetric data collected from $Sr_4MnIrO_{5.32}H_{2.68}$ whilst heating under flowing oxygen indicate a mass gain of 5.5%, as shown in Figure 5.9. Assuming full oxidation back to Sr_4MnIrO_8, this corresponds to an initial composition of $Sr_4MnIrO_{5.50}H_y$. Analysis of the exhaust gas by mass spectrometry showed release of water concurrent with the oxidation process, indicating that hydride is present in the phase.

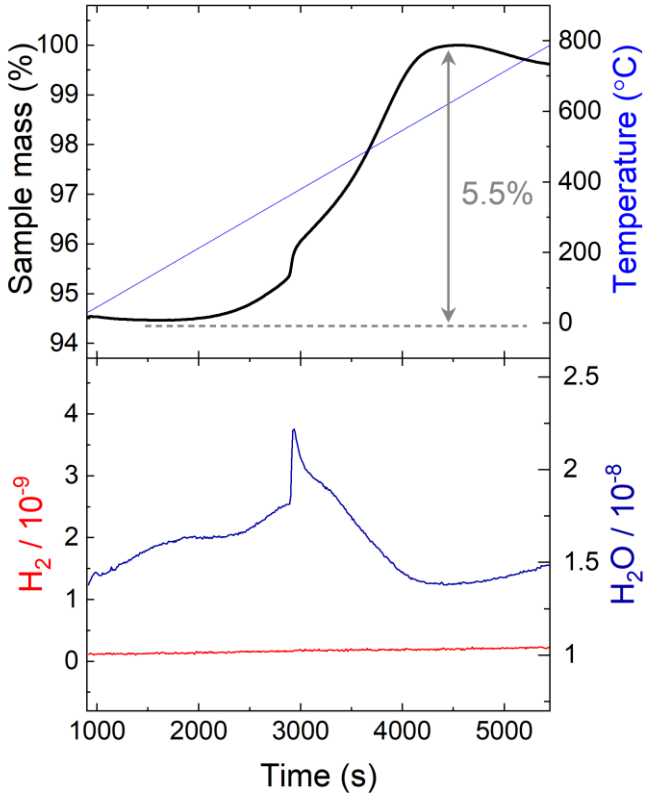

Figure 5.9: TGA trace (top panel) and H_2/H_2O contents of exhaust gas (bottom panel) when $Sr_4MnIrO_{5.32}H_{2.68}$ is heated under flowing oxygen.

5.3.3.2 Neutron powder diffraction

NPD data were collected from $Sr_4MnIrO_{5.32}H_{2.68}$ at ambient temperature using the GEM diffractometer at ISIS. A structural model based on $Sr_4MnIrO_{6.58}H_{1.42}$ using the lattice parameters from SXRD was constructed and refined against the data from the 35°, 64°, 91° and 154° banks of the GEM diffractometer.

Initially, a model containing only oxide ions and vacancies at the anion sites was tested. The refinement yielded an oxide ion occupancy of 0.101(3) at the O1 site and 0.799(6) at the O2 site, which corresponds to an overall composition of $Sr_4MnIrO_{3.60(2)}$. This composition is

unrealistic, as it would require the transition metals to have negative oxidation states and, as such, indicates that hydride ions are present in the structure.

To test a model containing only oxide and hydride (with no vacancies) at the anion sites, the occupancies of oxide and hydride at both anion positions were allowed to refine, constrained such that the overall occupancy at each site was equal to 1. From this refinement, the equatorial site was found to have an oxide occupancy of 0.454(2) and a hydride occupancy of 0.546(2), whilst the axial site was found to have an oxide occupancy of 0.877(3) and a hydride occupancy of 0.123(3). This gives an overall composition of $Sr_4MnIrO_{5.32(2)}H_{2.68(2)}$. As before, this represents the maximum oxide ion content possible considering the total neutron scattering lengths at the anion sites. Since the composition obtained from oxidative TGA is $Sr_4MnIrO_{5.50}H_y$, it is likely that $Sr_4MnIrO_{5.32}H_{2.68}$ is roughly the correct composition, with the discrepancy from the TGA data arising from incomplete oxidation of the reduced phase to Sr_4MnIrO_8 during the measurement. The composition is also consistent with the XAS data (Section 5.3.5.1), which indicates manganese oxidation states of +2 and +3, allowing iridium to adopt an oxidation state of +3. Although it is possible that there are some vacancies at the anion sites, they are likely to be present in a relatively low concentration, so the composition is assumed to be $Sr_4MnIrO_{5.32}H_{2.68}$.

Comparison of the lattice parameters for this phase with those of $LaSr_3CoIrO_5H_3$ (a = 3.66 Å, c = 13.27 Å) and $LaSr_3MnRhO_6H_2$ (a = 3.73 Å, c = 13.14 Å)[52] provides some support for the presence of hydride ions at the axial positions. The c-lattice parameter for $Sr_4MnIrO_{5.32}H_{2.68}$ (c = 12.97 Å) is significantly shorter than that of $LaSr_3CoIrO_5H_3$ (c = 13.27 Å) or $LaSr_3MnRhO_6H_2$ (c = 13.14 Å), as would be expected if the axial oxide ions had been partially replaced by smaller hydride ions.

The fits to the NPD data are shown in Figure 5.10-5.13, with the refinement parameters presented in Table 5.3. The refined structure, with hydride ions substituted at the equatorial positions, is shown in Figure 5.14. A structural refinement was also performed against the SXRD data using the model obtained from NPD, which gave a good visual fit, as shown in Appendix A3.

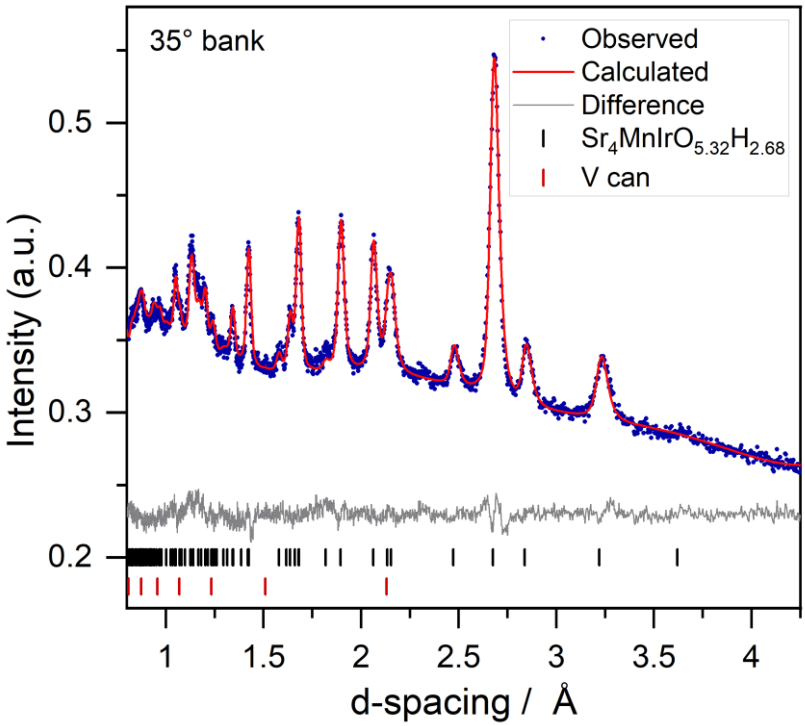

Figure 5.10: Observed, calculated and difference plots from the structural refinement of $Sr_4MnIrO_{5.32}H_{2.68}$ against NPD data collected at room temperature from the 35° bank of the GEM diffractometer.

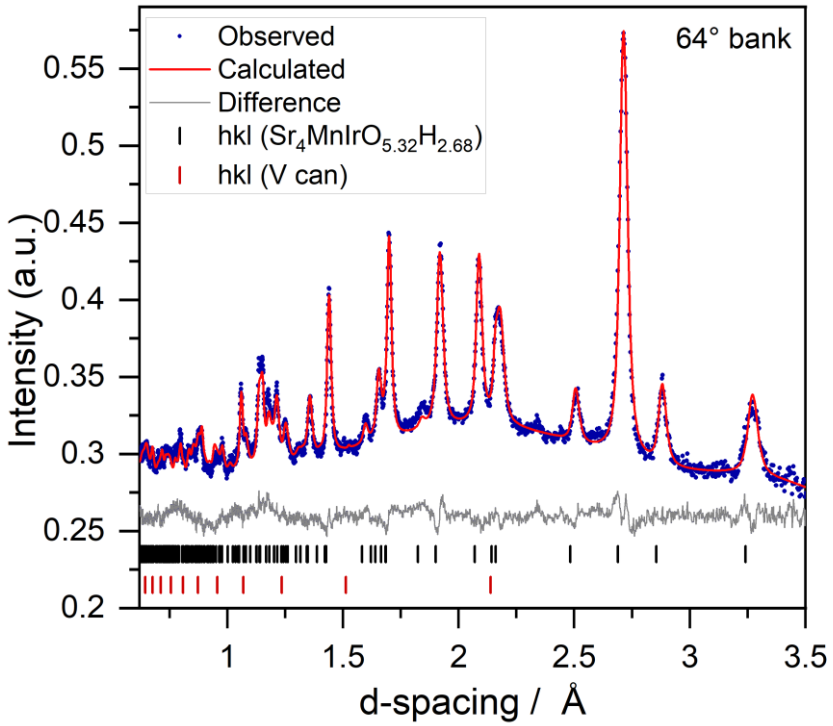

Figure 5.11: Observed, calculated and difference plots from the structural refinement of $Sr_4MnIrO_{5.32}H_{2.68}$ against NPD data collected at room temperature from the 64° bank of the GEM diffractometer.

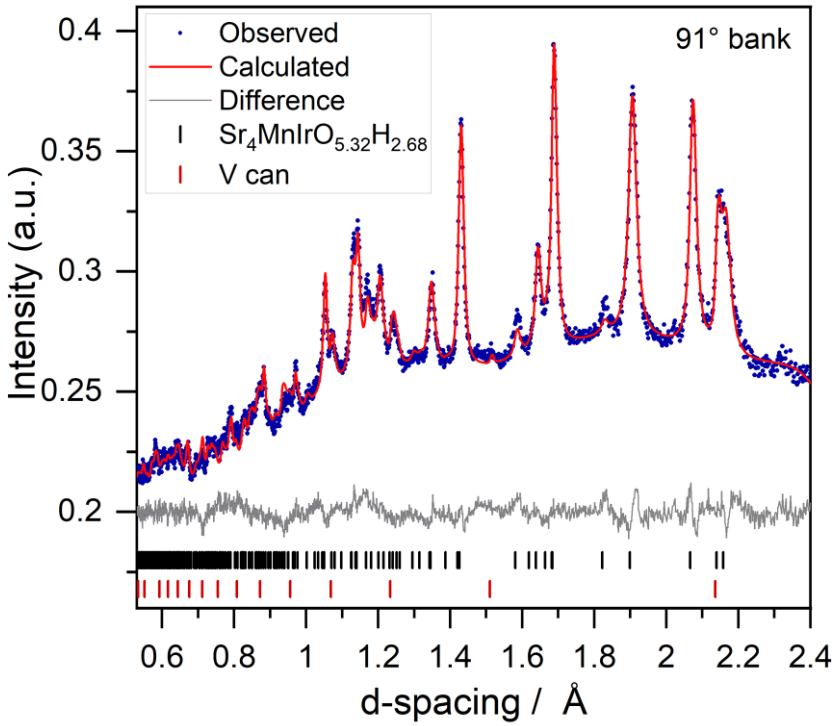

Figure 5.12: Observed, calculated and difference plots from the structural refinement of $Sr_4MnIrO_{5.32}H_{2.68}$ against NPD data collected at room temperature from the 91° bank of the GEM diffractometer.

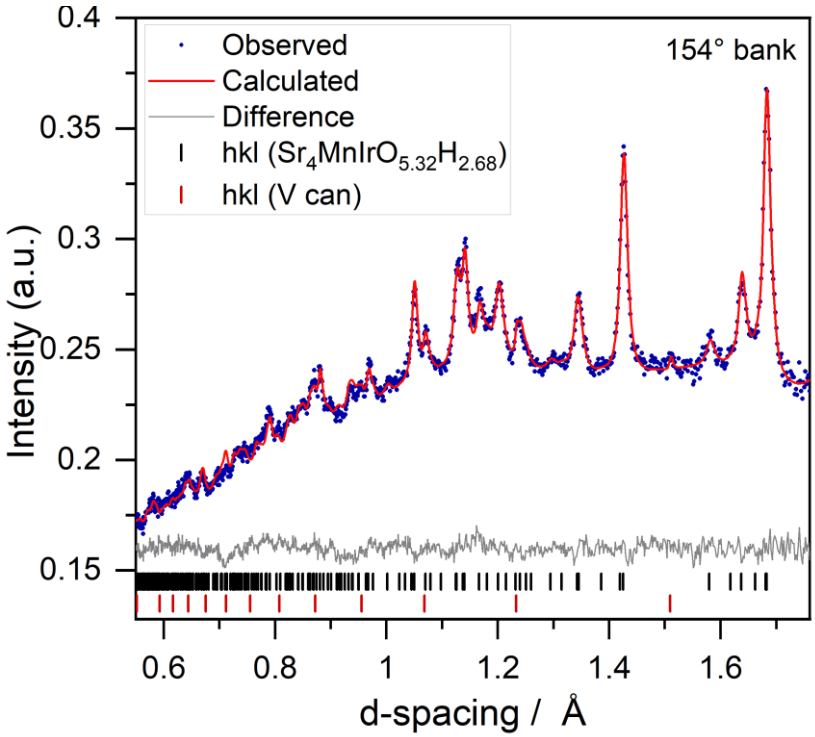

Figure 5.13: Observed, calculated and difference plots from the structural refinement of $Sr_4MnIrO_{5.32}H_{2.68}$ against NPD data collected at room temperature from the 154° bank of the GEM diffractometer.

Table 5.3: Parameters from the structural refinement of $Sr_4MnIrO_{5.32}H_{2.68}$ against NPD data collected at room temperature from the GEM diffractometer.

$Sr_4MnIrO_{5.32(2)}H_{2.68(2)}$, space group *I*4/*mmm* (No. 139)						
		x	***y***	***z***	**Occ.**	**B_{iso} (Å^2)**
Sr(1)	4*e*	0	0	0.3524(1)	1	0.96(6)
Mn(1)/Ir(1)	2*a*	0	0	0	0.5/0.5	4.2(2)
O(1)/H(1)	4*c*	0	½	0	0.454(2)/0.546(2)	0.14(5)
O(2)/H(2)	4*e*	0	0	0.1640(2)	0.877(3)/0.122(3)	0.14(5)
a = 3.8039(4) Å, c = 12.970(1) Å						
V = 187.66(4) Å^3						
R_{wp} = 1.39%, R_p = 1.09%, *gof* = 0.004						

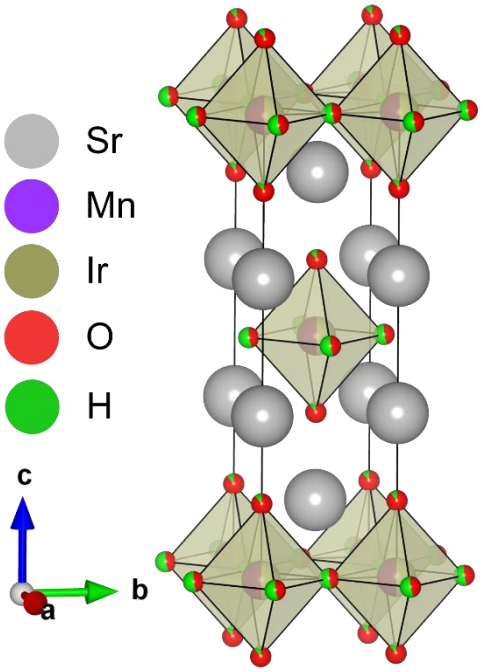

Figure 5.14: Refined structure of $Sr_4MnIrO_{5.32}H_{2.68}$ with hydride ions substituted into both the axial and the equatorial positions.

5.3.4 X-ray absorption spectroscopy

XAS measurements were performed on Sr_4MnIrO_8, $Sr_4MnIrO_{6.58}H_{1.42}$ and $Sr_4MnIrO_{5.32}H_{2.68}$ using the B18 beamline at Diamond Light Source, with MnO, Mn_2O_3 and Li_2MnO_3 used as standards. The measurements were performed at energies between 6340 and 7390 eV to allow the Mn K-edge (6539 eV) to be observed. Normalisation of the data was performed up to 7100 eV, and the spectra were calibrated using Mn foil measured concurrently with each sample.

5.3.4.1 X-ray absorption near edge structure

The data at the XANES edges are shown in Figure 5.15. For Sr_4MnIrO_8, these show that manganese is present in the +4 oxidation state, which necessarily means that iridium must also be present in the +4 oxidation state.

For $Sr_4MnIrO_{6.58}H_{1.42}$, the position of the edge has shifted to lower energy, indicating that the manganese has been reduced relative to the parent Sr_4MnIrO_8 phase. The edge is located between that of Mn_2O_3 and Li_2MnO_3, suggesting that manganese is present as a mixture of Mn^{III} and Mn^{IV}. Considering the composition determined from the NPD data, this would mean that the iridium is also present as a mixture of Ir^{III} and Ir^{IV}.

Meanwhile, for $Sr_4MnIrO_{5.32}H_{2.68}$, the XANES data show that manganese is further reduced relative to $Sr_4MnIrO_{6.58}H_{1.42}$, and the position of the edge is located between that of MnO and Mn_2O_3. This would indicate that manganese is present as a mixture of Mn^{II} and Mn^{III}, which would be consistent with iridium adopting a +3 oxidation state, as has been observed for the oxyhydride phases in Chapters 3 and 4.

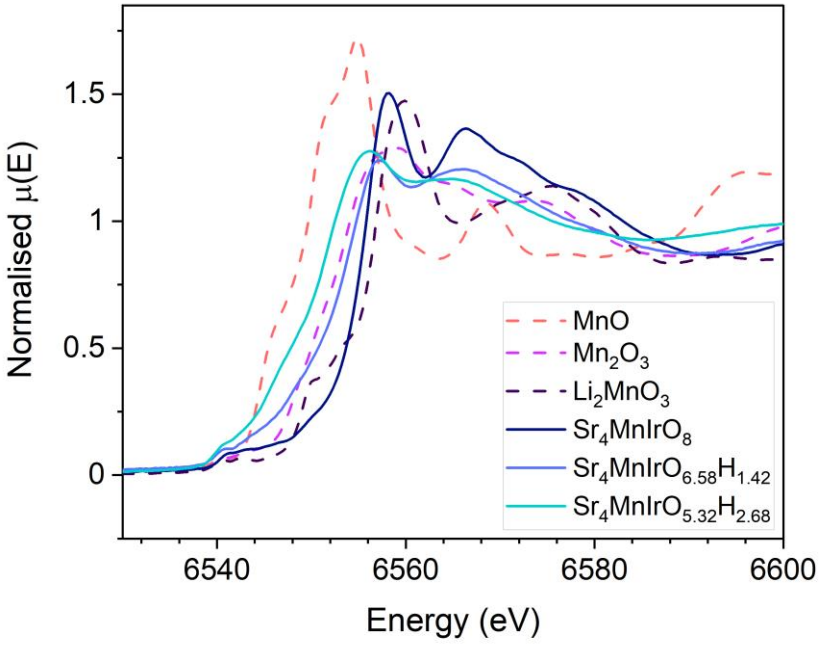

Figure 5.15: XANES Mn K-edges for Sr_4MnIrO_8, $Sr_4MnIrO_{6.58}H_{1.42}$ and $Sr_4MnIrO_{5.32}H_{2.68}$. A wide energy range is presented in Appendix A3 to show the normalisation of the spectra.

5.3.4.2 Extended X-ray absorption fine structure

The EXAFS regions of the XAS spectra were fitted for Sr_4MnIrO_8, $Sr_4MnIrO_{6.58}H_{1.42}$ and $Sr_4MnIrO_{5.32}H_{2.68}$, as shown in Figure 5.16, with the detailed refinement parameters presented

in Table 5.4. The $\chi(k)$ curves were extracted from the EXAFS signals in the k-range 3-11 Å^{-1} using a sine window, and fits were then performed on the magnitude of the Fourier-transform of k^3-weighted $\chi(k)$ in the R-range 1.0−4.3 Å.

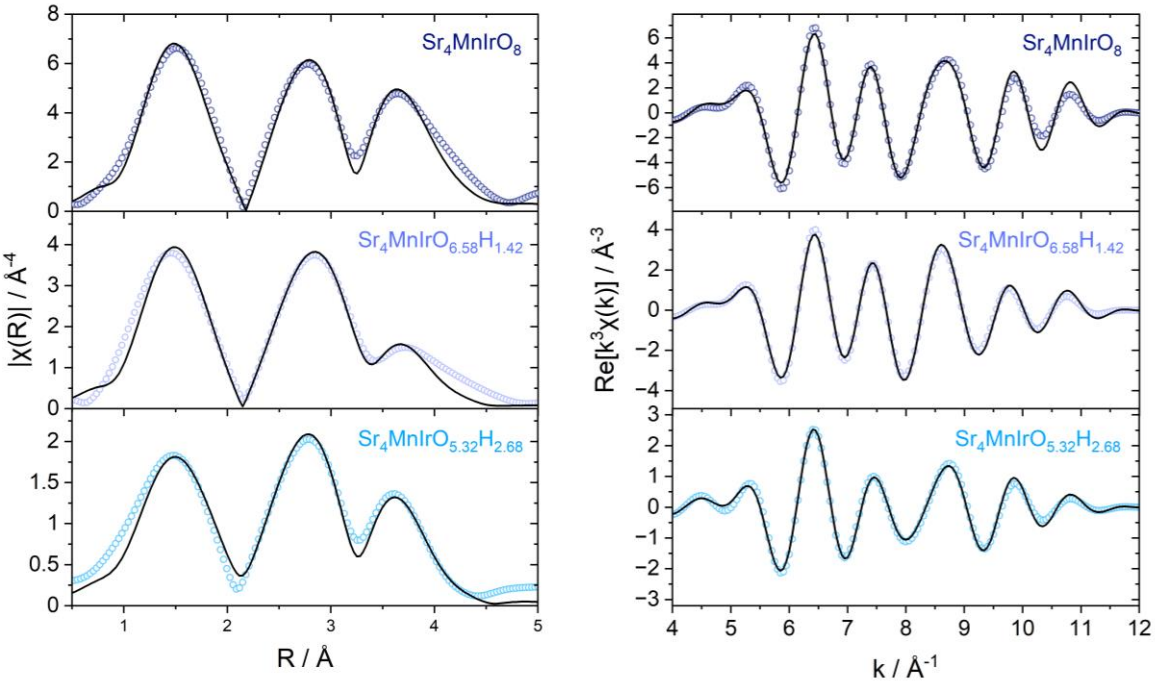

Figure 5.16: Fits of the magnitude of the Fourier-transform of k^3-weighted $\chi(k)$, extracted from EXAFS data collected at the Mn K-edge, performed in the R-range 1.0−4.3 Å (left) and corresponding fits of the real part of Fourier back-filtered $\chi(k)$ in the R-range 1.0−4.3 Å (right). The experimental data are shown as circles, with the fits represented by the solid lines.

Table 5.4: Parameters from the refinements of the EXAFS regions of the XAS spectra for Sr_4MnIrO_8, $Sr_4MnIrO_{6.58}H_{1.42}$ and $Sr_4MnIrO_{5.32}H_{2.68}$ collected at the Mn K-edge.

Compound	Path	*N*	*R* (Å)	σ^2 (Å^2)	*R*-factor
Sr_4MnIrO_8	Mn−O	6	1.92(1)	0.0064(7)	0.02
	Mn−Sr	8	3.28(1)	0.0072(7)	
	Mn−Ir	4	3.66(2)	−0.0014(8)	
$Sr_4MnIrO_{6.58}H_{1.42}$	Mn−O	4.58	1.912(8)	0.0062(6)	0.01
	Mn−Sr	8	3.29(1)	0.0090(5)	
	Mn−Ir	4	3.66(2)	0.004(1)	
$Sr_4MnIrO_{5.32}H_{2.68}$	Mn−O	3.57	1.93(1)	0.0111(8)	0.02
	Mn−Sr	8	3.26(2)	0.0138(6)	
	Mn−Ir	4	3.66(2)	0.0060(9)	

During the refinements, the first-shell coordination numbers were fixed to the average values expected from the NPD results. Since hydride ions have a very weak scattering power, they are essentially invisible in EXAFS data[104] and, as such, only the first-shell oxide ions need to be considered. By performing the refinement in this way, it was possible to achieve good fits to the data, indicating that the local structure as probed by EXAFS is consistent with the average structure as probed by neutron diffraction.

The Mn−O bond lengths extracted from the EXAFS data are comparable to those extracted from the SXRD and NPD refinements, presented in Table 5.5. It should be noted that a Jahn-Teller distortion might be expected for compounds containing Mn^{III}, due to uneven filling of the e_g orbitals, but attempts to include this in the EXAFS refinements of $Sr_4MnIrO_{6.58}H_{1.42}$ and $Sr_4MnIrO_{5.32}H_{2.68}$ did not lead to any improvement in the fits.

Table 5.5: Selected (Mn/Ir)−(O/H) bond lengths obtained from refinements against SXRD/NPD data. The ratios between the axial and equatorial bonds within the Mn/Ir-octahedra are also presented. All bond lengths are given in Å.

	Sr_4MnIrO_8	**$Sr_4MnIrO_{6.58}H_{1.42}$**	**$Sr_4MnIrO_{5.32}H_{2.68}$**
$M-(O/H)_{ax.}$	2.04343(3)	2.029(6)	2.127(3)
$M-(O/H)_{eq.}$	1.93038(1)	1.8950(3)	1.9020(3)
$(M-(O/H)_{ax.}) / (M-(O/H)_{eq.})$	1.059	1.071	1.118

It is worth noting that the Debye-Waller factor for the Mn−Ir shell in Sr_4MnIrO_8 has an unphysical, negative value. The Debye-Waller factor for this shell is expected to be small due to the heavy nature of iridium. The observation that it is negative is likely to be related to the fact that the Ir scattering envelope occurs at relatively large *k*-values (8−16 $Å^{-1}$), but only data up to $k = 11$ $Å^{-1}$ were used to perform the fitting. Data at larger *k*-values could not be used due to the presence of an iron impurity. As such, although it was necessary to include the Mn−Ir shell in the refinement to allow the other two shells to be fitted correctly, the values extracted from the refinement of this shell are not reliable.

5.3.5 Magnetic characterisation

5.3.5.1 Sr_4MnIrO_8

Magnetisation data collected from Sr_4MnIrO_8 as a function of temperature are shown in Figure 5.17. The ZFC and FC curves start to diverge at around 150 K, with a broad maximum observed in both curves between 75 and 95 K, before diverging sharply at 15 K. This could result from the formation of short-range 2-dimensional ordering within the perovskite layers at around 90 K, before 3-dimensional freezing of the spins occurs at 15 K. Fitting of the Curie-Weiss law to the data at temperatures above 250 K gives a value for C of 2.71(2) cm^3 K mol^{-1}, which is slightly larger than the value of 2.25 cm^3 K mol^{-1} predicted for Mn^{IV}/Ir^{IV} using the spin-only approximation, and a value for θ of +10(5) K.

The magnetisation-field isotherm at 300 K, shown in Figure 5.18, is consistent with paramagnetic behaviour, whilst the isotherm at 5 K shows a hysteresis and is vertically displaced from the origin, suggesting the formation of a spin glass state. This spin glass character was confirmed by AC susceptibility measurements, shown in Figure 5.19, in which the susceptibility maximum shifts to higher temperature as the frequency of the applied field is increased. Fitting of the data to Equation 43 yields a value of $3(1) \times 10^6$ Hz for ω_0, corresponding to a relaxation time, τ_0, of $1.8(7) \times 10^{-6}$ s, and a value of 4.3(2) for the dynamical critical exponent, zv. The observation of spin glass behaviour provides evidence for B-site cation disorder, as would be expected for a Mn^{IV}/Ir^{IV} oxidation state combination (Section 5.3.5.1), since chemical disorder is required for a spin glass state to propagate.

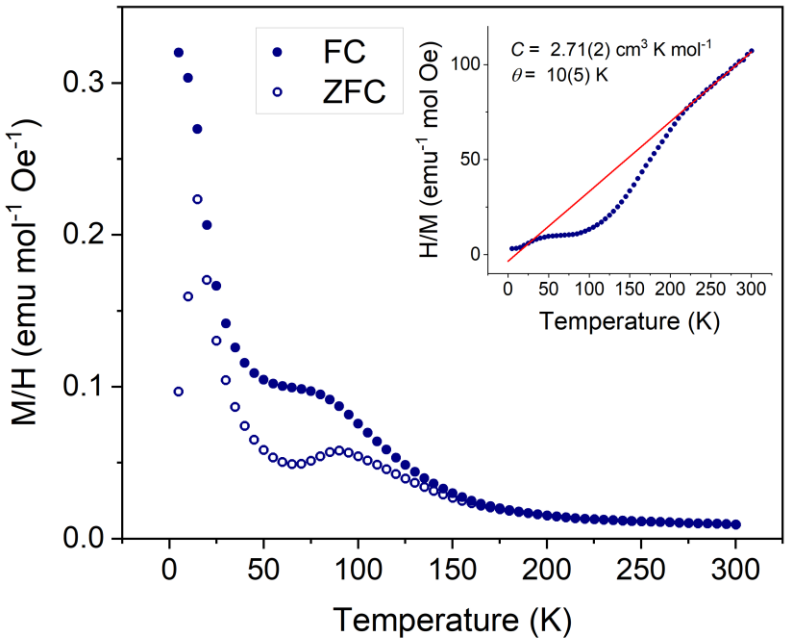

Figure 5.17: Magnetisation data collected from Sr_4MnIrO_8 as a function of temperature, measured in a field of 100 Oe under both ZFC and FC conditions.

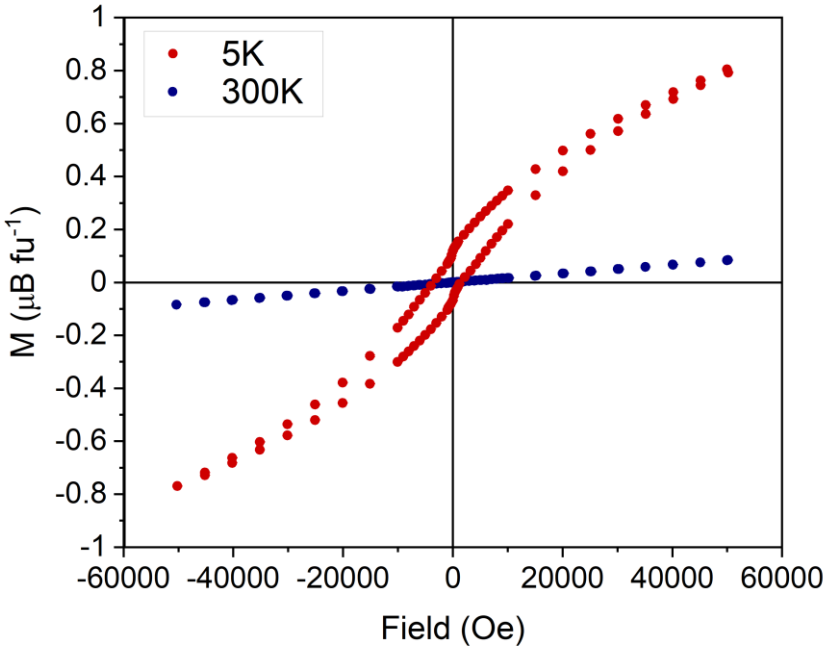

Figure 5.18: Magnetisation-field isotherms for Sr_4MnIrO_8 measured at 5 K and 300 K.

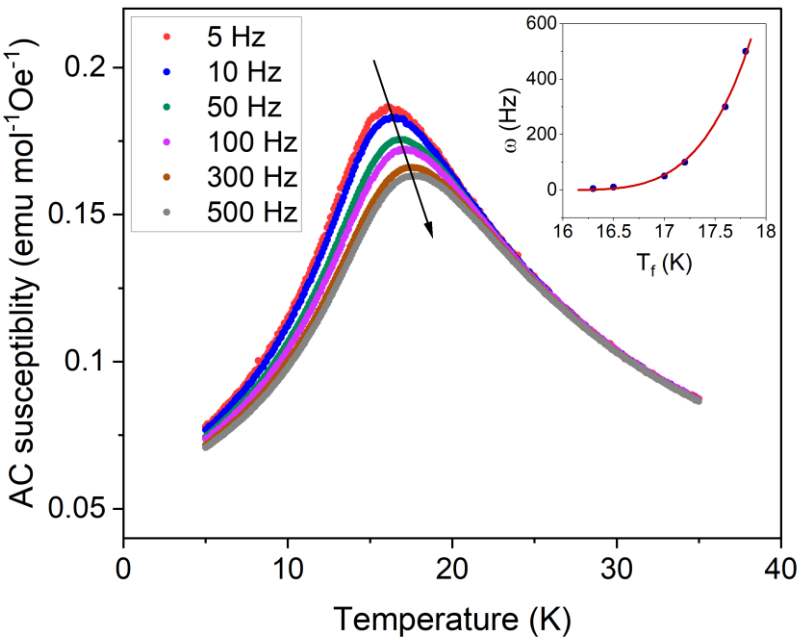

Figure 5.19: AC susceptibility as a function of temperature for Sr_4MnIrO_8, measured at frequencies between 5 Hz and 500 Hz. The measurements were performed using an AC field with amplitude of 2.5 Oe, and an applied DC field of 2 Oe. The inset shows the variation of T_f with ω for Sr_4MnIrO_8. The red line shows the fit to the data using the power law shown in Equation 43.

5.3.5.2 $Sr_4MnIrO_{6.58}H_{1.42}$

Magnetisation data collected from $Sr_4MnIrO_{6.58}H_{1.42}$ as a function of temperature are shown in Figure 5.20. Similar to the behaviour observed for Sr_4MnIrO_8, there is a sharp divergence between the ZFC and FC curves at 15 K, indicating freezing of the spins below this temperature. However, unlike in Sr_4MnIrO_8, a broad feature at around 90 K is not observed, which could suggest weaker intralayer interactions in this compound. Fitting of the data to the Curie-Weiss law above 250 K gives a value for C of 1.41(2) cm^3 K mol^{-1}, which is significantly smaller than would be expected using the spin-only approximation for a compound containing a mixture of $Mn^{III/IV}$ and $Ir^{III/IV}$, and a value for θ of −28(2) K.

As with Sr_4MnIrO_8, the magnetisation-field isotherm at 300 K, shown in Figure 5.21, is consistent with paramagnetic behaviour, whilst the isotherm at 5 K shows a hysteresis and is vertically displaced from the origin, indicating that this compound also adopts a spin glass state below 15 K. However, both the magnitude of the displacement and the size of the hysteresis

loop are reduced compared to Sr_4MnIrO_8, indicating that the interactions between the magnetic moments are weaker in the reduced phase. This is supported by the AC susceptibility data, shown in Figure 5.22, whereby the shift in the susceptibility maximum shows a weaker dependence on the frequency of the applied field. This can be quantified by fitting the data to Equation 43, as shown in the inset of Figure 5.22, which reveals a shorter relaxation time ($\tau_0 = 6 \times 10^{-10}$ s) and larger dynamical critical exponent (zv = 6.8) for the reduced phase, compared to Sr_4MnIrO_8.

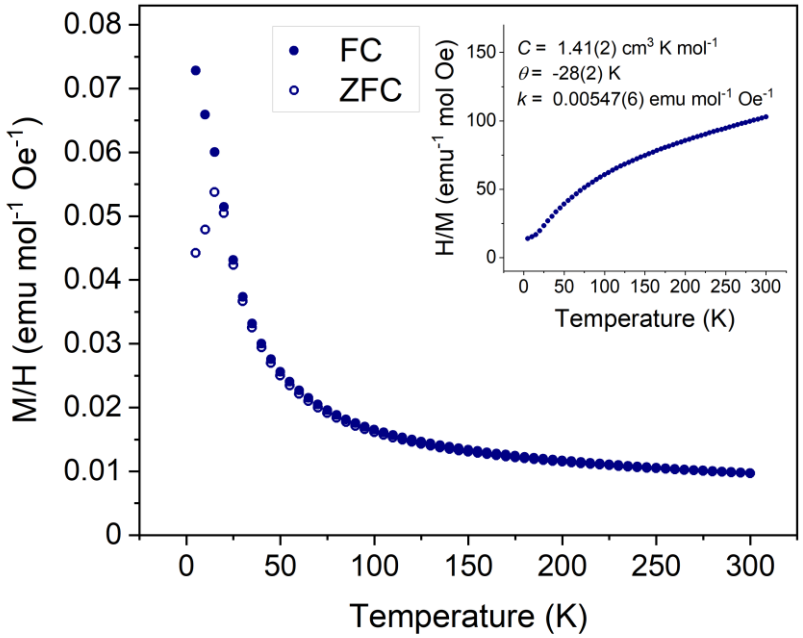

Figure 5.20: Magnetisation data collected from $Sr_4MnIrO_{6.58}H_{1.42}$ as a function of temperature, measured in a field of 100 Oe under both ZFC and FC conditions.

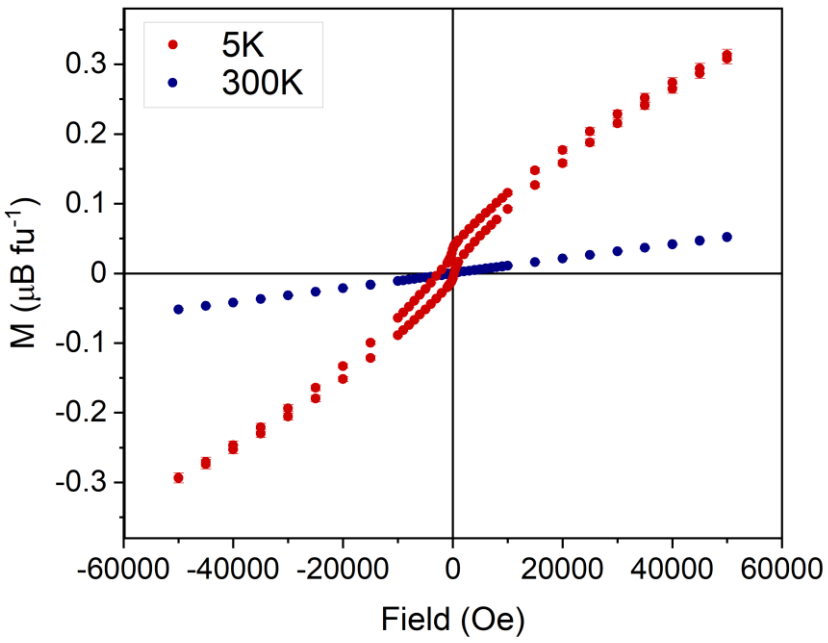

Figure 5.21: Magnetisation-field isotherms for $Sr_4MnIrO_{6.58}H_{1.42}$ measured at 5 K and 300 K.

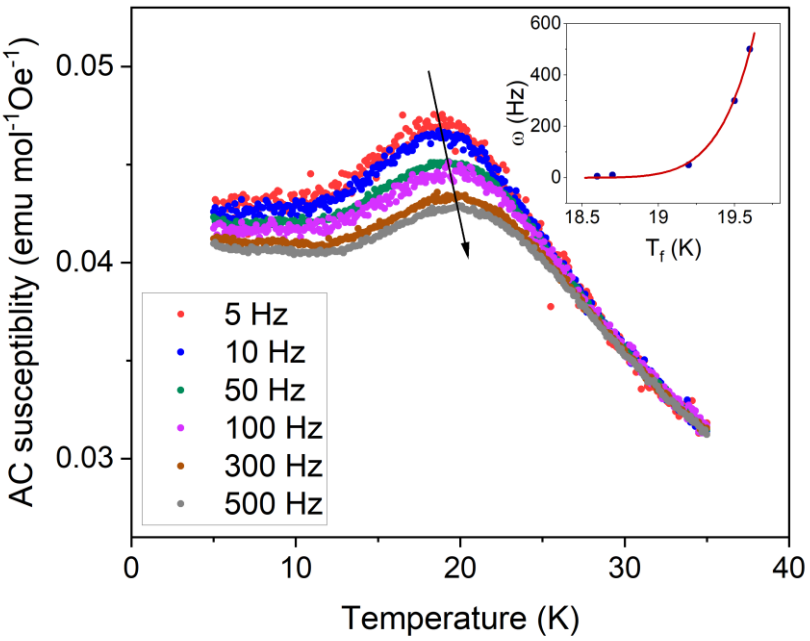

Figure 5.22: AC susceptibility as a function of temperature for $Sr_4MnIrO_{6.58}H_{1.42}$, measured at frequencies between 5 Hz and 500 Hz. The measurements were performed using an AC field with amplitude of 2.5 Oe, and an applied DC field of 2 Oe. The inset shows the variation of T_f with ω for $Sr_4MnIrO_{6.58}H_{1.42}$. The red line shows the fit to the data using the power law shown in Equation 43.

5.3.5.3 $Sr_4MnIrO_{5.32}H_{2.68}$

Magnetisation data collected from $Sr_4MnIrO_{5.32}H_{2.68}$ as a function of temperature are shown in Figure 5.23 and magnetisation-field isotherms collected at 5 K and 300 K are shown in Figure 5.24. In contrast to Sr_4MnIrO_8 and $Sr_4MnIrO_{6.58}H_{1.42}$, these data show no obvious magnetic transition between 5 K and 300 K. Fitting of the Curie-Weiss law to the inverse susceptibility data above 200 K gives a value for C of 2.42(4) cm^3 K mol^{-1}, which is smaller than the spin-only value of 3.91 cm^3 K mol^{-1} expected for $Mn^{+2.32}/Ir^{III}$, and a value for θ of −26(1) K.

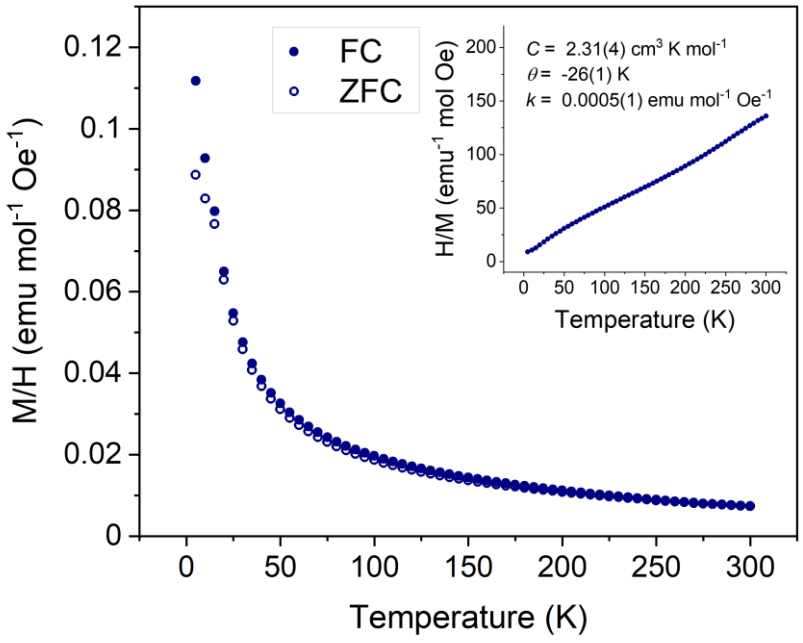

Figure 5.23: Magnetisation data collected from $Sr_4MnIrO_{5.32}H_{2.68}$ as a function of temperature, measured in a field of 100 Oe under both ZFC and FC conditions.

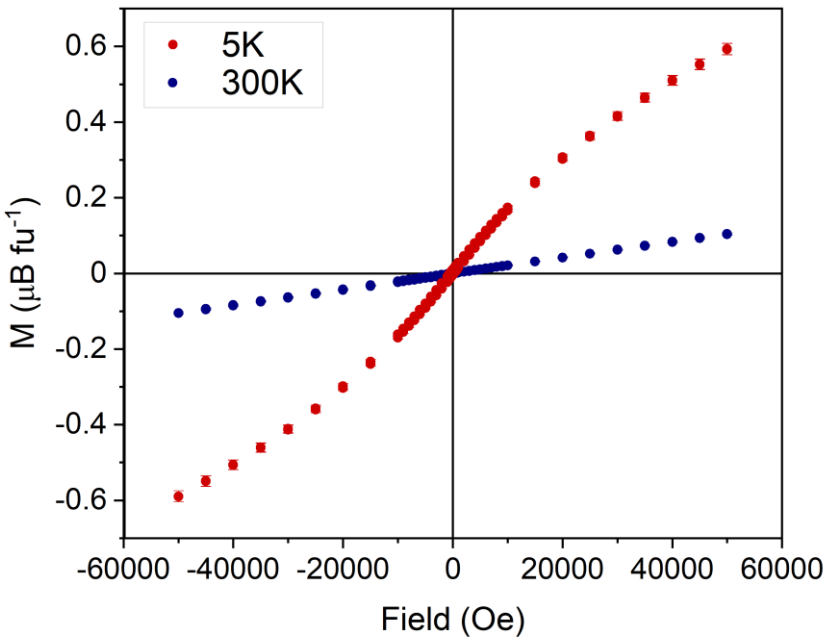

Figure 5.24: Magnetisation-field isotherms for $Sr_4MnIrO_{5.32}H_{2.68}$ measured at 5 K and 300 K.

5.4 Discussion

5.4.1 Comparison of reactivity of CaH_2 and LiH

The reaction of Sr_4MnIrO_8 with CaH_2 or LiH to form oxyhydrides is markedly different from the reactivity observed for Sr_2MnO_4 and $LaSrMnO_4$.[105,106] When these Mn-only oxides are reacted with CaH_2, they do not form oxyhydrides, but instead form the oxygen-deficient compounds, $Sr_2MnO_{3.63}$ and $LaSrMnO_{3.5}$, respectively. In contrast, oxyhydride phases are formed when the reactions are performed with Sr_4MnIrO_8. This is likely to be due to stabilisation from the formation of strong Ir–H σ-type bonds. In this way, the role of iridium in $Sr_4MnIrO_{6.58}H_{1.42}$ and $Sr_4MnIrO_{5.32}H_{2.68}$ is similar to that of rhodium in $LaSr_3MnRhO_6H_2$.[52]

From the results in Section 5.3, it is observed that LiH allows a greater extent of reduction compared to CaH_2, in contrast to the reactivity reported for Sr_2MnO_4, in which CaH_2 and LiH were observed to have essentially equivalent reactivity.[105] This difference can be explained by considering the effect of the presence of iridium on the stability of Sr_4MnIrO_8 when treated

with reducing agents. In contrast to manganese ions, which are relatively robust with respect to reduction, all iridium cation oxidation states have a positive reduction potential with respect to the formation of Ir metal. This lowers the energy barrier for non-topochemical decomposition of Sr_4MnIrO_8, compared to Sr_2MnO_4, and, as a consequence, lowers the decomposition temperature. As a result, the temperature required for Sr_4MnIrO_8 to react to form an oxyhydride is very close to the temperature at which non-topochemical decomposition occurs (360-420 °C). Therefore, very subtle differences in the reactivity of CaH_2 and LiH have a more significant effect when reacted with Sr_4MnIrO_8 compared to Sr_2MnO_4.

From a kinetic perspective, CaH_2 has a higher lattice energy per hydride (1205 kJ mol^{-1}) than LiH (916 kJ mol^{-1}),[59] which means that CaH_2 requires a higher temperature before it is active for topochemical reactions (~300 °C compared to ~150 °C for LiH). Meanwhile, from a thermodynamic perspective, since CaO has a larger lattice energy (3414 kJ mol^{-1}) than Li_2O (2799 kJ mol^{-1}), the difference in lattice energies for the CaH_2 reaction ($U_{CaH2} - U_{CaO}$ = −1004 kJ mol^{-1}) is slightly larger than that for the LiH reaction ($2U_{LiH} - U_{Li2O}$ = −967 kJ mol^{-1}). Subtle differences in the thermodynamics, such as these, are likely to account for the difference in reactivity between CaH_2 and LiH.

It appears that it is not possible to reduce Sr_4MnIrO_8 further than approximately $Sr_4MnIrO_{5.32}H_{2.68}$ using CaH_2 or LiH under ambient pressure. Reduction of iridium to an oxidation state below +3 while retaining an octahedral coordination environment is unlikely, as this would require filling of a high energy e_g orbital. Interestingly, the oxidation state of manganese in $Sr_4MnIrO_{5.32}H_{2.68}$ (+2.32) is very close to that of +2.3 observed in $LaSrMnO_{3.3}H_{0.7}$, synthesised at 1000 °C under a pressure of 5 GPa.[53] Whilst Mn^{II} is known in oxygen-deficient compounds ($LaSrMnO_{3.5}$)[106] and oxyhydrides ($LaSr_3MnRhO_6H_2$)[52], it is likely that the Sr_4MnIrO_8 framework is insufficiently stable to allow reduction all the way to

$Sr_4MnIrO_5H_3$, in which all the manganese is present as Mn^{II}. As such, $Sr_4MnIrO_{5.32}H_{2.68}$ is observed to be the most reduced compound that can be prepared for this system.

5.4.2 Distribution of hydride ions in $Sr_4MnIrO_{6.58}H_{1.42}$ and $Sr_4MnIrO_{5.32}H_{2.68}$

Typically, oxyhydride Ruddlesden-Popper phases exhibit strong oxide/hydride site selectivity, whereby hydride ions are preferentially located at the equatorial positions, due to the enthalpic considerations discussed in Chapter 3. The only exceptions to this appear to be $Sr_2TiO_{3.91}H_{0.14}$, $Sr_3Ti_2O_{6.32}H_{0.12}$, Ba_2ScHO_3, Ba_2YHO_3 and Sr_2LiOH_3-type compounds.[56,107–111]

For Sr_4MnIrO_8, the initial oxide-to-hydride exchange occurs at the equatorial positions, as expected, evidenced by the fact that the hydride ions in $Sr_4MnIrO_{6.58}H_{1.42}$ are exclusively located at these sites (i.e. $Sr_4MnIr[O_4]_{ax.}[O_{2.58}H_{1.42}]_{eq.}$). This is consistent with the reactivity described in Chapters 3 and 4, as well as that observed in many other Ruddlesden-Popper phases.[47,48,51–53,93]

However, upon further reduction, oxide-to-hydride exchange also occurs at the axial positions, such that, in $Sr_4MnIrO_{5.32}H_{2.68}$, the axial sites are ~12% occupied by hydride ions, whilst the equatorial sites are ~55% occupied by hydride ions (i.e. $Sr_4MnIr[O_{3.51}H_{0.49}]_{ax.}[O_{1.81}H_{2.19}]_{eq.}$). This suggests that beyond a certain point, likely to be $Sr_4MnIrO_6H_2$, it becomes approximately equally favourable for anion exchange to occur at either the axial or the equatorial sites, with a slight preference for axial exchange.

For $Sr_2TiO_{3.91}H_{0.14}$ and $Sr_3Ti_2O_{6.32}H_{0.12}$, exchange at the axial position is attributed to the observation that this allows a metallic state to be achieved in the perovskite sheets.[107] Meanwhile, Ba_2ScHO_3, Ba_2YHO_3 and the Sr_2LiOH_3-type compounds are synthesised under high-pressure and high temperature conditions and, therefore, thermodynamic, rather than kinetic, considerations determine the site selectivity.[56,108] As such, neither of these explanations are applicable to the site selectivity observed in Sr_4MnIrO_8. It is also worth noting that, for

$Sr_2TiO_{3.91}H_{0.14}$, $Sr_3Ti_2O_{6.32}H_{0.12}$, Ba_2ScHO_3 and Ba_2YHO_3, the axial positions are always the preferred sites for the hydride ions, whereas for Sr_4MnIrO_8, the site selectivity appears to change during the reaction.

The behaviour of the $Sr_4MnIrO_{8-x}H_x$ phases can be partially explained by considering the preference of hydride ions to occupy *cis*-/*trans*-arrangements relative to each other. As discussed in Section 1.4.2, hydride ions prefer to adopt a *trans*-configuration around octahedrally coordinated transition metals with d^2, high-spin d^7 or low-spin d^5 configurations. However, for other *d*-configurations, the strong *trans*-influence of the hydride ligand is the dominant factor and leads to a *cis*-arrangement being preferred.

To explain the site selectivity in Sr_4MnIrO_8, the reaction can be considered as a sequence of hypothetical steps, as shown in Figure 5.25. When the first oxide ion is exchanged, the hydride ion occupies the equatorial site, as expected. When the second oxide ion is exchanged, it is possible for the new hydride ion to both occupy an equatorial site and adopt a *cis*-arrangement relative to the other hydride, so exchange again occurs at the equatorial position. This would result in a hypothetical composition of $Sr_4MnIrO_6H_2$, whereby the transition metals would be present as Mn^{III} and Ir^{III} (interpolated from the XANES data in Section 5.3.4). These ions would have high-spin d^4 and low-spin d^6 configurations, respectively, so there is no electronic driving force for the next hydride ion to occupy a position *trans* to another hydride. However, if this hydride ion substituted at an equatorial site, it would necessarily be *trans* to another hydride ion. Therefore, the choice of site for this hydride ion is a balance between the enthalpic driving force to exchange at an equatorial position and the preference of hydride ions to adopt *cis*-arrangements, which would favour exchange at an axial position.

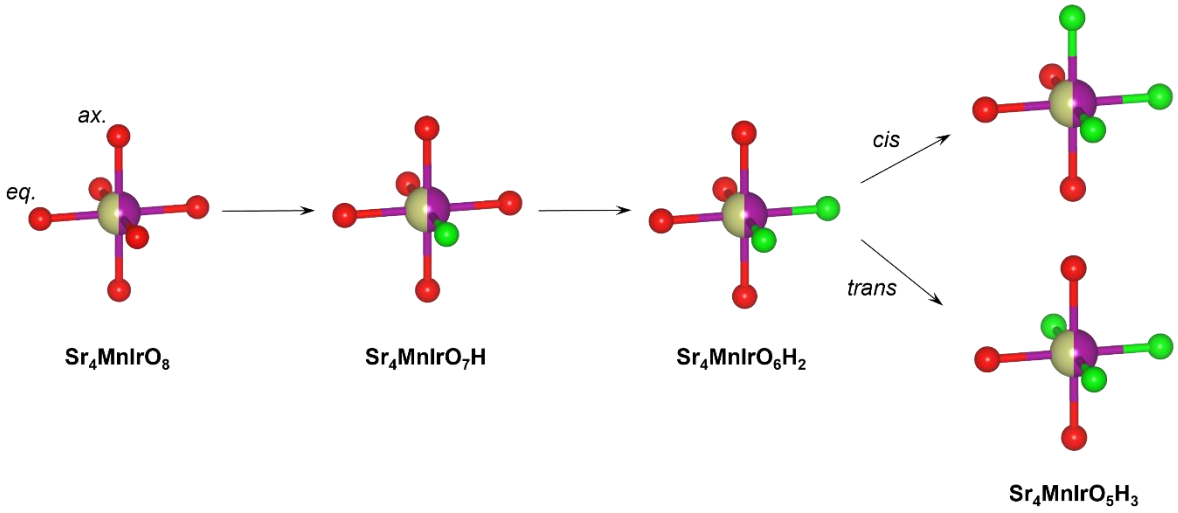

Figure 5.25: Hypothetical stages during the reaction of Sr_4MnIrO_8 with binary metal hydrides, highlighting the choice between axial and equatorial exchange when $Sr_4MnIrO_6H_2$ is converted to $Sr_4MnIrO_5H_3$. Axial exchange results in a *fac*-configuration, whilst equatorial exchange results in a *mer*-configuration.

However, the above argument applies for all n = 1 Ruddlesden-Popper oxyhydride phases for which the hydride to oxide ratio exceeds 1:3. For the small number of known compounds for which this is the case ($La_{0.5}Sr_{3.5}CoIrO_{5.5}H_{2.5}$, $LaSr_3CoIrO_5H_3$, $La_{1.5}Sr_{2.5}CoIrO_{5.5}H_{2.5}$, $LaSr_3NiIrO_{5.4}H_{2.6}$, $LaSr_3NiRuO_4H_4$, $LaSr_3CoRuO_4H_4$),[51,91] all of them exhibit oxide-to-hydride exchange exclusively at the equatorial position. One factor that could contribute to the difference in reactivity between these compounds and Sr_4MnIrO_8 is the identity of the A-site cation. Whilst all the previously reported compounds contain a mixture of La^{3+} and Sr^{2+} at the A-site, Sr_4MnIrO_8 contains only Sr^{2+}. The lower average charge of the cations in the rock-salt layer of Sr_4MnIrO_8 means that exchange at the axial site is less unfavourable.

A further effect that could contribute to the difference in reactivity between Sr_4MnIrO_8 and other Ruddlesden-Popper phases arises from the electronic configuration of the 3*d* transition metal cation. In the reaction of Sr_4MnIrO_8, the transitional $Sr_4MnIrO_6H_2$ contains Mn^{III}, which is Jahn-Teller active. This electronic driving force to elongate the axial bonds destabilises the oxide ions at these positions, thereby favouring oxide-to-hydride exchange at these sites. Meanwhile, for the other Ruddlesden-Popper oxyhydrides with a hydride to oxide ratio greater

than 1:3, the transitional $A_4BB'O_6H_2$ phases contain Co^{I}, Co^{II} or Ni^{II} ions in combination with Ir^{III} or Ru^{III} ions, which are not Jahn-Teller active.

An additional factor to consider is that iridium ions preferentially occupy highly symmetric coordination environments, as this enhances the stabilisation from spin-orbit coupling, as observed in Sr_2FeIrO_6.[112] Since the C_{3v} point group associated with the *fac*-configuration has a higher symmetry than the C_{2v} point group associated with the *mer*-configuration, this could provide an additional driving force for exchange at the axial position.

As such, the lower cation charge in the rock-salt layer in combination with the Jahn-Teller effect associated with Mn^{III}, the preference of iridium to adopt highly symmetric coordination environments and the preference of hydride ions to adopt a *cis*-arrangement relative to each other causes axial exchange to be approximately equally as favourable as equatorial exchange for the third hydride ion, yielding the site selectivity observed in Sr_4MnIrO_8.

5.4.3 Magnetic behaviour

From Figure 5.18 and Figure 5.19, it is observed that Sr_4MnIrO_8 exhibits a transition to a spin-glass state below ~15 K. As discussed in Section 1.2.4.3, both chemical disorder and magnetic frustration are required for a spin-glass state to be obtained. In this system, the chemical disorder arises from the disordered arrangement of manganese and iridium within the perovskite layers. The origin of the magnetic frustration can be explained by considering the electronic configurations of the transition metal ions. As determined in Section 5.3.4, the transition metals in this compound are present as Mn^{IV} and Ir^{IV}. A simplified picture of the crystal field splitting is shown in Figure 5.26(a). Mn^{IV} has a d^3 configuration, whilst Ir^{IV} adopts a J_{eff} = ½ state, which is simplistically shown as a low-spin d^5 configuration.

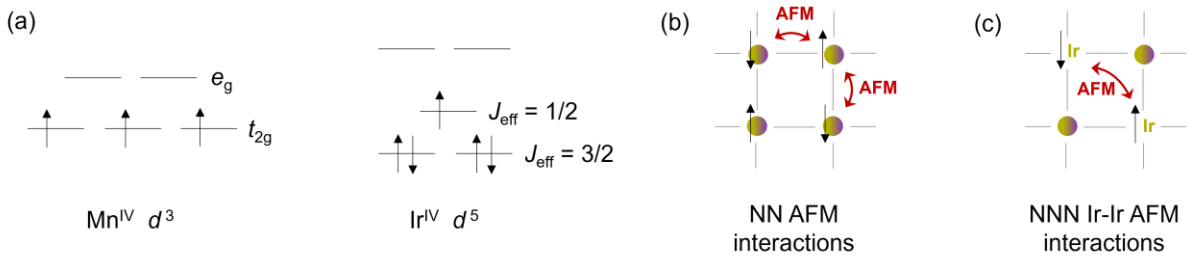

Figure 5.26: (a) simplistic crystal field splitting diagrams for Mn^{IV} and Ir^{IV} in Sr_4MnIrO_8, (b) schematic illustrating nearest-neighbour antiferromagnetic interactions in Sr_4MnIrO_8 and (c) schematic illustrating next-nearest-neighbour Ir-Ir antiferromagnetic interactions, mediated by overlap between spatially diffuse $5d_{xy}$ orbitals.

From a simple superexchange perspective, all nearest-neighbour interactions within the perovskite sheets should be antiferromagnetic, as shown in Figure 5.26(b). Meanwhile, since the octahedra are elongated along *z*, the unpaired electron in Ir^{IV} is likely to have substantial d_{xy} character, which means that, for any Ir ions located diagonally from each other, as shown in Figure 5.26(c), there can be direct antiferromagnetic exchange, mediated by the overlap of the spatially diffuse $5d_{xy}$ orbitals. Since these two interactions are incompatible, this will lead to frustration if they are of a comparable magnitude, in a situation analogous to $Sr_4CoIrO_{6.5}H_{1.5}$.

In $Sr_4MnIrO_{6.58}H_{1.42}$, the manganese is present as $Mn^{III/IV}$ and the iridium is present as $Ir^{III/IV}$ (Section 5.3.4). The complete filling of the t_{2g} level in some of the iridium ions disrupts the antiferromagnetic Ir-Ir interactions, thereby reducing the frustration, as reflected by the diminished frequency dependence of the AC susceptibility in Figure 5.22.

For $Sr_4MnIrO_{5.32}H_{2.68}$, all the iridium is present as Ir^{III}, thus entirely removing the magnetic frustration. However, Figure 5.24 shows that there is no obvious magnetic transition in this compound between 5 K and 300 K. This is in direct contrast to the oxyhydride phases discussed in Chapters 3 and 4, which exhibit magnetic transitions at low temperature despite the fact that they also contain diamagnetic Ir^{III}, which could potentially disrupt the magnetic ordering. This can be attributed to the fact that, unlike cobalt and nickel in the previous compounds, manganese is present as both Mn^{II} and Mn^{III}, which are likely to be randomly distributed within the compound. Nearest-neighbour manganese ions can participate in a variety of AFM or FM

exchange mechanisms, as summarised in Table 5.6. However, since next-nearest-superexchange via diamagnetic Ir^{III} requires the manganese to contain a half-occupied $3d_{x^2-y^2}$ orbital, the only possible next-nearest-neighbour superexchange is Mn^{II}–O–Ir–O–Mn^{II}. For any random system, there is a percolation threshold, below which long-range connectivity cannot occur.[113] In $Sr_4MnIrO_{5.32}H_{2.68}$, the loss of coupling between manganese and iridium, in combination with the lack of next-nearest-neighbour superexchange, means that the concentration of magnetic interactions is likely to be lower than the percolation threshold and, as such, magnetic order cannot propagate through the perovskite sheets, so the magnetic transition is suppressed to very low temperature.

Table 5.6: Predicted magnetic interactions for Mn^{II} and Mn^{III} ions in $Sr_4MnIrO_{5.32}H_{2.68}$.

Superexchange pathway	Expected interaction
Mn^{III}–O–Mn^{III}	AFM
Mn^{II}–O–Mn^{II}	AFM
Mn^{II}–O–Mn^{III}	FM
Mn^{II}–O–Ir–O–Mn^{II}	AFM

5.5 Conclusion

The reactivity of the $n = 1$ Ruddlesden-Popper phase, Sr_4MnIrO_8, with CaH_2 and LiH has been explored. Reaction with CaH_2 allows the oxyhydride phase, $Sr_4MnIrO_{6.58}H_{1.42}$, to be synthesised, in which oxide-to-hydride exchange occurs at the equatorial position. Meanwhile, reaction with LiH allows the compound to be reduced further, yielding a phase with composition, $Sr_4MnIrO_{5.32}H_{2.68}$. In this reaction, oxide-to-hydride exchange occurs at both the equatorial and the axial sites, which is unprecedented for this family of compounds. This unusual behaviour has been attributed to the delicate balance between the Jahn-Teller effect in Mn^{III}, the tendency for hydride ions to adopt *cis*-arrangements with respect to each other, the

preference for iridium to adopt highly symmetric coordination environments and the enthalpic driving force to substitute at the equatorial positions.

Sr_4MnIrO_8 was observed to adopt a spin-glass state at low temperature, with the frustration arising from competition between nearest-neighbour antiferromagnetic interactions and Ir−Ir next-nearest-neighbour antiferromagnetic interactions. The partial reduction of Ir^{IV} to Ir^{III} in $Sr_4MnIrO_{6.58}H_{1.42}$ reduces the frustration, whilst full reduction to Ir^{III} in $Sr_4MnIrO_{5.32}H_{2.68}$ leads to the complete loss of magnetic ordering, due to the concentration of magnetic interactions falling below the percolation threshold.

Chapter 6 – Topochemical reduction of $Ba_3CoIr_2O_9$ using LiH

6.1 Introduction

$Ba_3CoIr_2O_9$ adopts a 6H-hexagonal perovskite structure, in which IrO_6 octahedra adopt a face-sharing arrangement to form Ir_2O_9 dimers that are separated by layers of CoO_6 octahedra.[114–116] In this arrangement, there are relatively short separations between the iridium ions, thereby potentially enabling Ir−Ir bonding. To determine whether it is possible to tune the electronic properties of this compound through oxide-to-hydride exchange, the reactivity of $Ba_3CoIr_2O_9$ with LiH has been explored.

6.2 Experimental

6.2.1 Synthesis of $Ba_3CoIr_2O_9$

Two-gram samples of polycrystalline $Ba_3CoIr_2O_9$ were prepared using conventional ceramic synthesis methods. Suitable stoichiometric ratios of $BaCO_3$, Co_3O_4 and IrO_2 (dried for 2 hours at 700 °C) were thoroughly ground together in an agate pestle and mortar, pelletised and heated in air at 1000 °C for 2 days. The samples were then reheated in air for two further cycles of 2 days at 1100 °C, with intermediate grinding and pelletisation performed between each heating cycle.

6.2.2 Exploration of the reactivity of $Ba_3CoIr_2O_9$ with LiH

To explore the reactivity of $Ba_3CoIr_2O_9$ with LiH, 200 mg of the all-oxide starting material was mixed with 8 mole equivalents of LiH, sealed in an evacuated Pyrex® ampoule and heated for 2 days at 150 °C. It was observed that a reaction occurred at this temperature, signalled by the formation of Li_2O and a substantial broadening of the diffraction peaks. The reaction

temperature was then increased in 25 °C steps, with the reaction mixture analysed by PXRD after each heating cycle. It was observed that non-topochemical decomposition occurred at temperatures above 200 °C.

6.2.3 Synthesis of $Ba_3CoIr_2O_{6.2}H_{2.8}$

A sample of $Ba_3CoIr_2O_{6.2}H_{2.8}$ was prepared by thoroughly grinding 1.7 g of $Ba_3CoIr_2O_9$ with 8 mole equivalents of LiH in an Ar-filled glovebox, and sealing the mixture in an evacuated Pyrex® ampoule. The reaction mixture was then heated for 1 period of 6 days at 150 °C, followed by 2 periods of 6 days at 160 °C. Heating rates of 1 °C/min were used and the samples were thoroughly reground between each heating cycle. The Li_2O by-product and any excess LiH were removed from the final product by washing with MeOH under an N_2 atmosphere. The product was then dried under vacuum and returned to the glovebox.

6.3 Structural characterisation

6.3.1 Structural characterisation of $Ba_3CoIr_2O_9$

SXRD data were collected from $Ba_3CoIr_2O_9$ at room temperature. Previous reports have indicated that this compound adopts a 6H-perovskite structure at 300 K, described in the $P6_3/mmc$ space group.[114–116] However, attempts to refine this model against the data from the synthesised sample could not describe the observed intensities well, as shown in Figure 6.1, and yielded a goodness of fit of 6.20. In an attempt to achieve an improved fit, a distorted unit cell described in the *Cmcm* space group was constructed, corresponding to a $(1 \times \sqrt{3} \times 1)$-expansion of the original hexagonal unit cell. This removes the 6-fold symmetry, thereby allowing off-centre displacement of the barium and iridium atoms and allowing the *a*- and *b*-lattice parameters of the unit cell to be different from each other. This improved the fit to the data (Figure 6.1), as reflected by the smaller value for the goodness of fit (*gof* = 2.55).

It has been reported that $Ba_3CoIr_2O_9$ undergoes a structural transition to a structure of *C*2/*c* symmetry at 107 K, and that this transition is associated with the onset of magnetic order.[115] A further refinement was performed using a model based on this *C*2/*c* structure, which provided the best fit to the data, with a goodness of fit of 2.05. The fit is shown in Figure 6.1, with the refinement parameters detailed in Table 6.1 and the refined structure shown in Figure 6.2. It is unclear why this sample of $Ba_3CoIr_2O_9$ appears to adopt the distorted, low temperature structure at room temperature, in contrast to the previous reports. However, a number of other 6H-type phases have been reported to adopt structures with *C*2/*c* symmetry at room temperature, such as $Ba_3BiIr_2O_9$ and $Ba_3LaIr_2O_9$.[117,118] These phases undergo a transition from the ideal $P6_3/mmc$ structure at high temperature to the distorted *C*2/*c* structure upon cooling to room temperature, with the distortion corresponding to rotations of the BO_6 octahedra about the *b*-axis (relative to the monoclinic cell) to alleviate under-bonding of the Ba^{2+} ions.

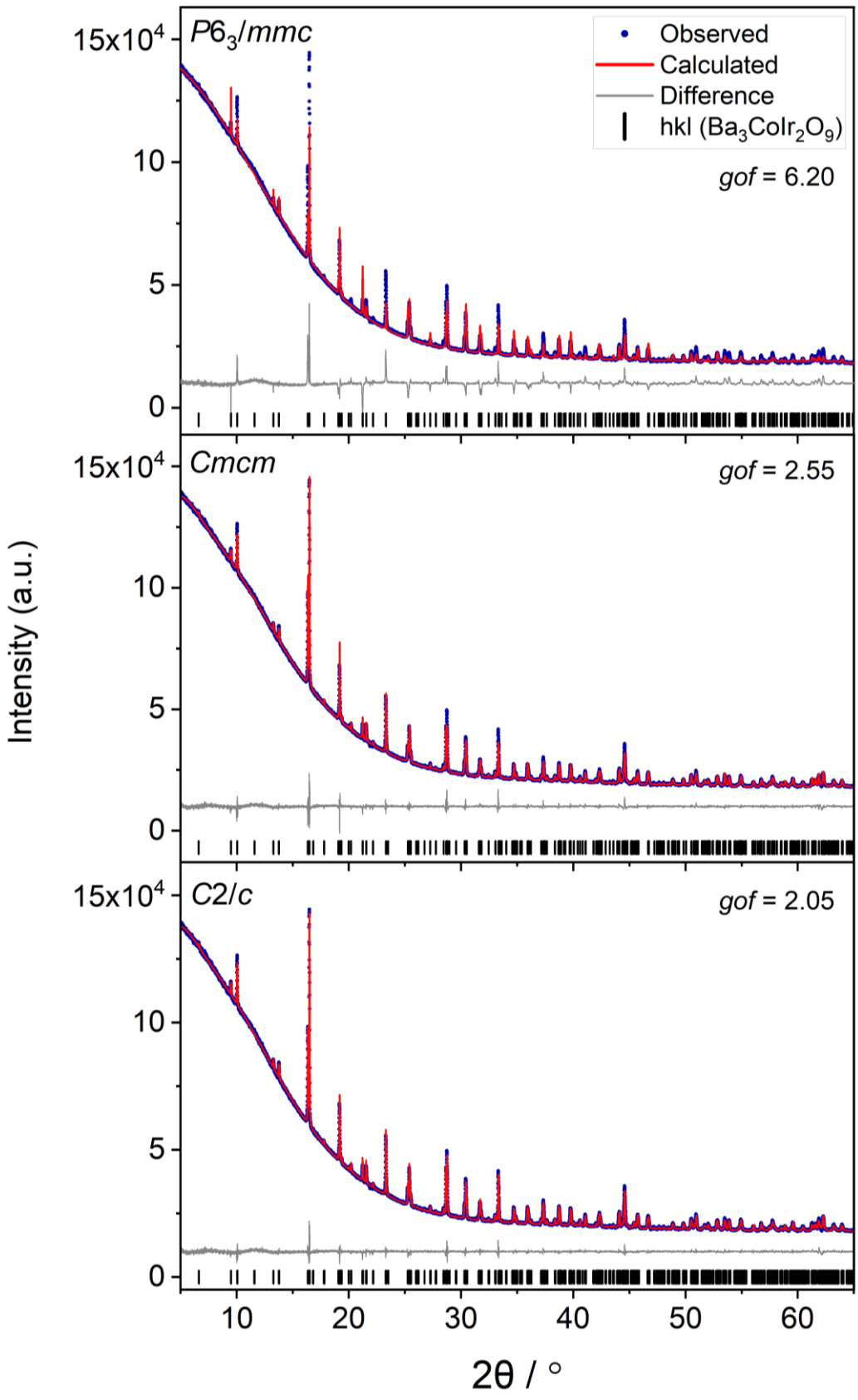

Figure 6.1: Observed, calculated and difference plots from the structural refinement of $Ba_3CoIr_2O_9$ against SXRD data (λ = 0.825 Å) collected at room temperature using the undistorted *P*6$_3$/*mmc* model and distorted models in the *Cmcm* and *C*2/*c* space groups.

Table 6.1: Parameters from the structural refinement of $Ba_3CoIr_2O_9$ against SXRD data collected at room temperature using a distorted model in the *C*2/*c* space group. The fractional coordinates of the oxide sites were fixed at the previously reported values.[115]

$Ba_3CoIr_2O_9$, space group *C*2/*c* (No. 15)						
		x	***y***	***z***	**Occ.**	**B_{iso} (Å^2)**
Ba(1)	8*f*	0.0011(3)	0.3334(8)	0.08865(6)	1	0.95(2)
Ba(2)	4*e*	0	0.0044(7)	¼	1	1.01(5)
Co(1)	4*a*	0	0	0	1	0.21(8)
Ir(1)	8*f*	0.0010(3)	0.3346(5)	0.84608(4)	1	0.87(1)
O(1)	4*e*	0	0.5030	¼	1	0.58(8)
O(2)	8*f*	0.2662	0.24714	0.2381	1	0.58(8)
O(3)	8*f*	0.0296	0.8401	0.0805	1	0.58(8)
O(4)	8*f*	0.2567	0.1003	0.0814	1	0.58(8)
O(5)	8*f*	0.7709	0.0744	0.0784	1	0.58(8)
a = 5.75575(8) Å, b = 9.9784(2) Å, c = 14.2806(2) Å						
β = 90.1305(7)°						
V = 820.18(2) Å^3						
R_{wp} = 1.03%, R_p = 0.62%, *gof* = 2.05						

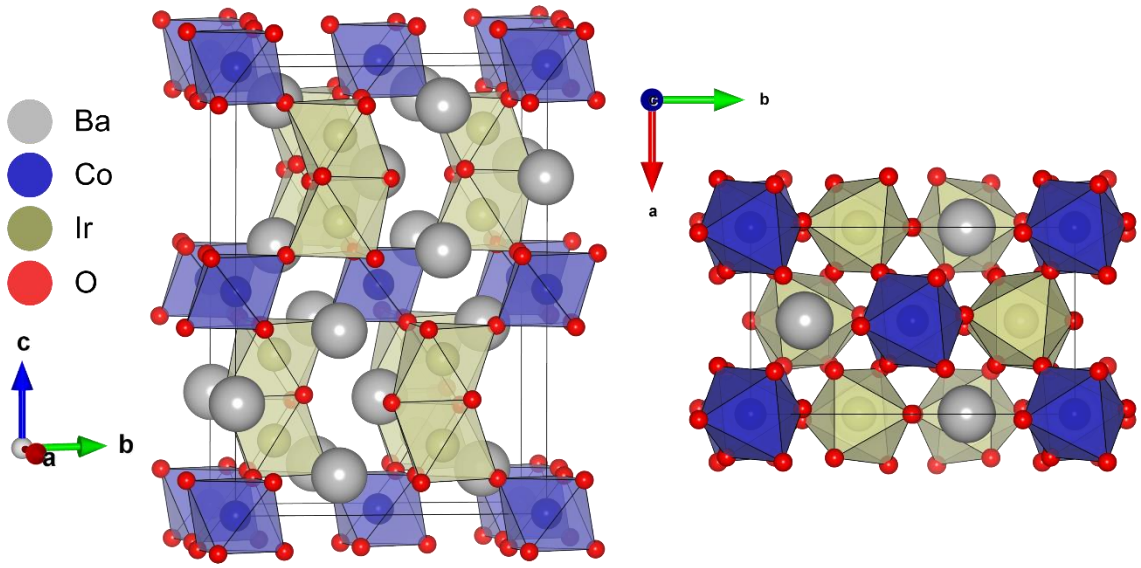

Figure 6.2: Structural model of $Ba_3CoIr_2O_9$ with an ortho-hexagonally distorted 6H-perovskite structure in the *C*2/*c* space group.

6.3.2 Structural characterisation of $Ba_3CoIr_2O_{6.2}H_{2.8}$

6.3.2.1 Thermogravimetric analysis

Thermogravimetric data were collected from the product of the reaction between $Ba_3CoIr_2O_9$ and LiH, henceforth referred to as $Ba_3CoIr_2O_{6.2}H_{2.8}$, whilst heating under flowing oxygen. The sample showed a mass gain of 4.9%, as shown in Figure 6.3. Assuming full oxidation back to $Ba_3CoIr_2O_9$, this corresponds to an initial composition of $Ba_3CoIr_2O_{5.96}H_y$. Analysis of the exhaust gas by mass spectrometry showed a clear release of water and hydrogen gas, confirming that hydride is present in the phase. During the oxidation process, it appears that water is released in four distinct steps, suggesting that oxidation of $Ba_3CoIr_2O_{6.2}H_{2.8}$ occurs in a stepwise fashion.

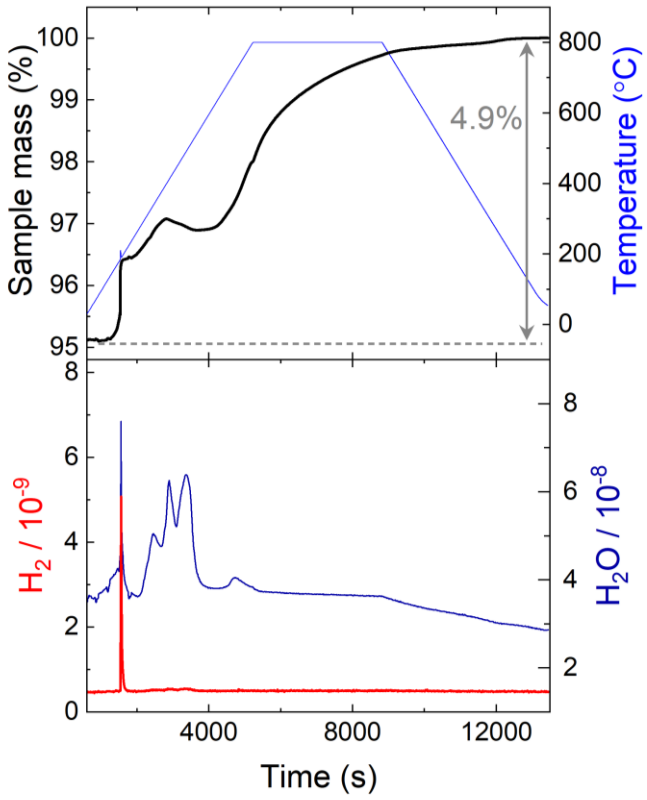

Figure 6.3: TGA trace (top panel) and H_2/H_2O contents of exhaust gas (bottom panel) when $Ba_3CoIr_2O_{6.2}H_{2.8}$ is heated under flowing oxygen.

6.3.2.2 Neutron and synchrotron X-ray powder diffraction

SXRD data were collected from $Ba_3CoIr_2O_{6.2}H_{2.8}$ at room temperature and NPD data were collected at 200 K using the D20 diffractometer at the ILL. The neutron diffraction pattern exhibits a high background, which can be attributed to strong incoherent and inelastic scattering from the hydride ions in the structure. This, in combination with the broad nature of the diffraction peaks, the large absorption cross-section of iridium and the small 2θ range of the data, means that it is difficult to extract reliable information from the refinements, and that several assumptions must be made during the refinement process.

Firstly, it was assumed that the reduced phase retains the *C*2/*c* symmetry of the starting material, which is not inconsistent with the reflections observed in the diffraction data. In the *C*2/*c* model, there are five distinct anion sites. To determine the anion composition, oxide and hydride were added at each of these sites and the occupancies allowed to refine, such that the overall anion composition at each site summed to one (i.e. no anion vacancies are present). Although it is possible for vacancies to be present on sites containing both oxide and hydride, it is difficult to conclusively establish their concentration, so the sites were assumed to be fully occupied. To refine the atomic positions, it was assumed that the atoms remain close to their corresponding positions in the parent oxide and, to this end, the atomic positions were restrained such that they do not deviate substantially from these values. A combined refinement was performed against the SXRD and NPD data. The results of the refinement yielded a composition of $Ba_3CoIr_2O_{6.2}H_{2.8}$, which is broadly consistent with the approximate composition of $Ba_3CoIr_2O_{5.96}H_y$ obtained from TGA. The fits to the SXRD and NPD data are shown in Figure 6.4 and Figure 6.5, respectively, with the refinement parameters detailed in Table 6.2 and the refined structure shown in Figure 6.6.

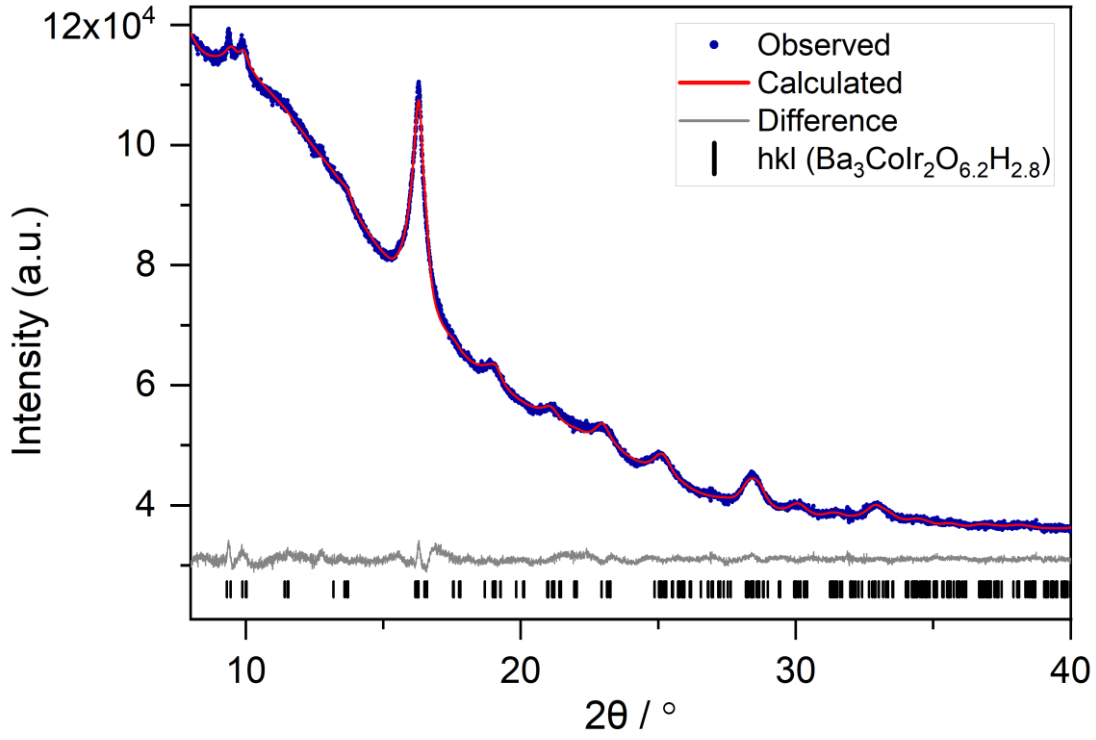

Figure 6.4: Observed, calculated and difference plots from the structural refinement of $Ba_3CoIr_2O_{6.2}H_{2.8}$ against SXRD data collected at room temperature using a wavelength of 0.825 Å.

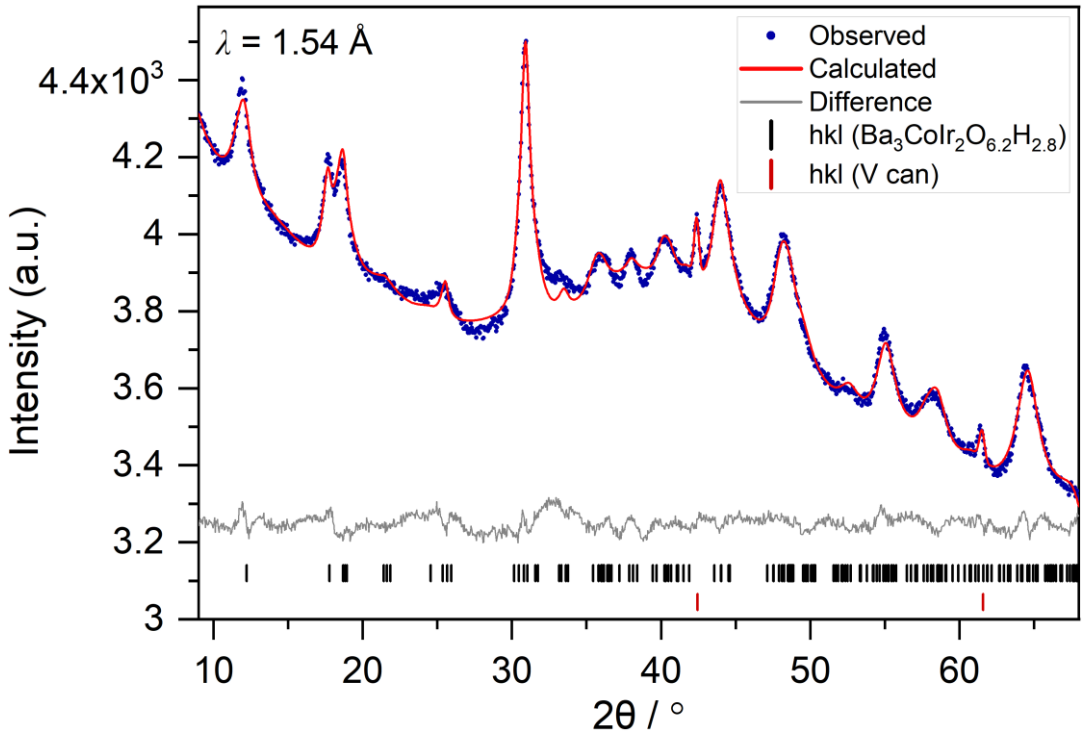

Figure 6.5: Observed, calculated and difference plots from the structural refinement of $Ba_3CoIr_2O_{6.2}H_{2.8}$ against NPD data collected at 200 K from the D20 diffractometer using a wavelength of 1.54 Å.

Table 6.2: Parameters from the combined structural refinement of $Ba_3CoIr_2O_{6.2}H_{2.8}$ against SXRD and NPD data. The values for B_{iso} and the lattice parameters are taken from the neutron refinement.

$Ba_3CoIr_2O_{6.2(1)}H_{2.8(1)}$, space group *C*2/*c* (No. 15)						
		x	***y***	***z***	**Occ.**	**B_{iso} (Å^2)**
Ba(1)	8*f*	0.991(4)	0.325(1)	0.0987(7)	1	0.1(3)
Ba(2)	4*e*	0	0.996(2)	¼	1	0.1(3)
Co(1)	4*a*	0	0	0	1	0.1(3)
Ir(1)	8*f*	0.011(3)	0.3444(9)	0.8458(5)	1	0.1(3)
O(1)/H(1)	4*e*	0	0.513(4)	¼	0.89(4)/0.11(4)	0.1(3)
O(2)/H(2)	8*f*	0.246(8)	0.247(3)	0.248(4)	0.83(2)/0.17(1)	0.1(3)
O(3)/H(3)	8*f*	0.040(8)	0.850(4)	0.091(2)	0.86(2)/0.14(4)	0.1(3)
O(4)/H(4)	8*f*	0.27(2)	0.090(5)	0.071(3)	0.03(3)/0.97(3)	0.1(3)
O(5)/H(5)	8*f*	0.761(9)	0.065(3)	0.088(2)	0.95(2)/0.05(2)	0.1(3)
a = 5.759(4) Å, b = 9.973(5) Å, c = 14.49(1) Å						
β = 88.6(1)°						
V = 828(1) Å^3						
R_{wp} = 0.72%, R_p = 0.63%, *gof* = 2.06						

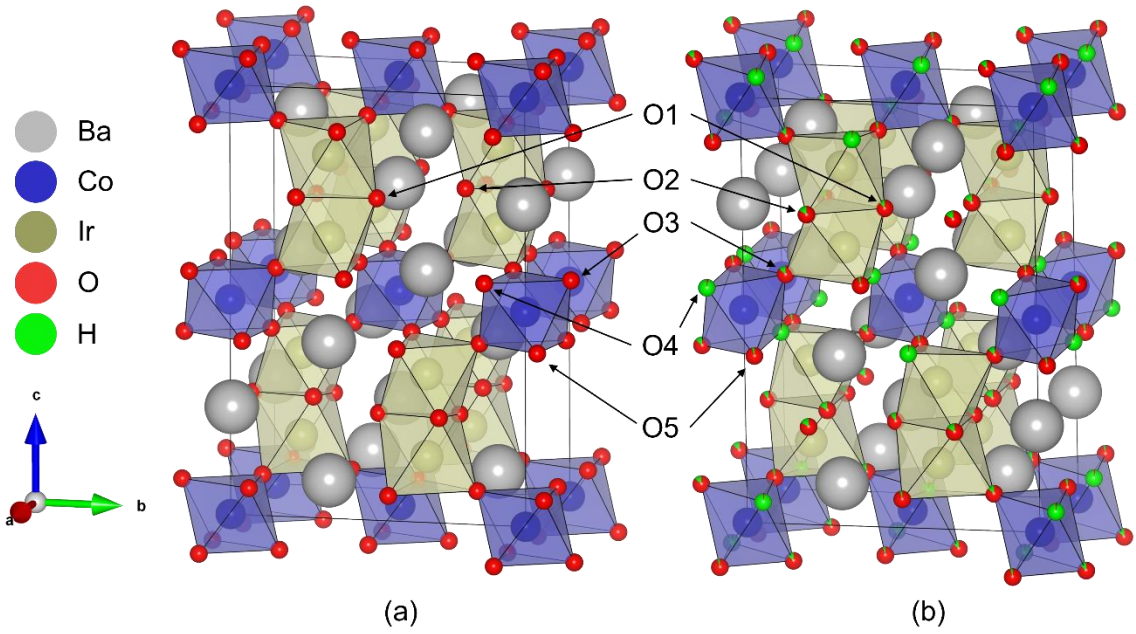

Figure 6.6: Refined structures of (a) the $Ba_3CoIr_2O_9$ parent oxide and (b) the $Ba_3CoIr_2O_{6.2}H_{2.8}$ reduced phase in the *C*2/*c* space group.

6.4 Magnetic characterisation

Magnetisation data collected from $Ba_3CoIr_2O_{6.2}H_{2.8}$ as a function of temperature are shown in Figure 6.7, and magnetisation-field isotherms collected at 5 K and 300 K are shown in Figure 6.8. The ZFC and FC curves diverge sharply below ~10 K, which, in combination with the observation of a hysteresis loop in Figure 6.8, suggests a magnetic transition at this temperature. The magnetisation data could not be fit to the Curie-Weiss law in a physically reasonable way. Neutron diffraction data collected at 5 K do not show the presence of any magnetic features, as shown in Figure 6.9.

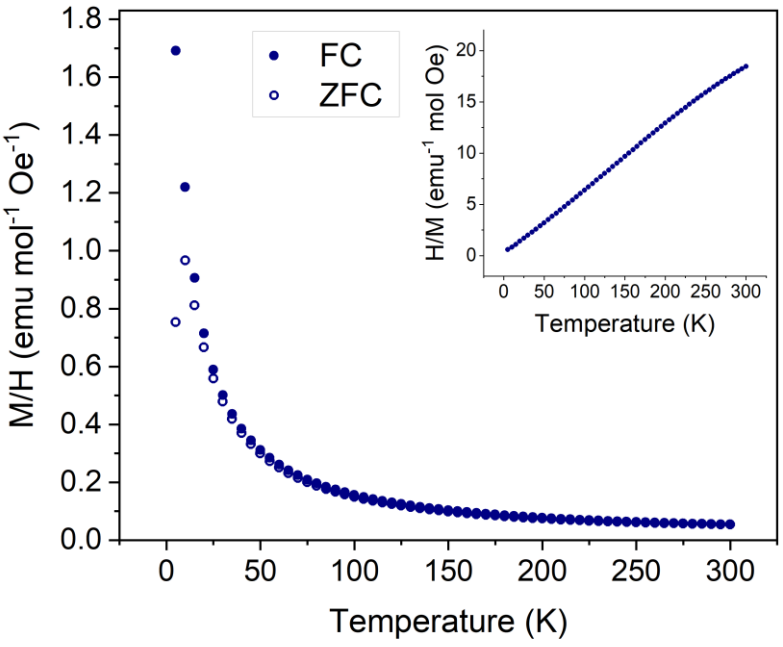

Figure 6.7: Magnetisation data collected from $Ba_3CoIr_2O_{6.2}H_{2.8}$ as a function of temperature, measured in a field of 100 Oe under both ZFC and FC conditions.

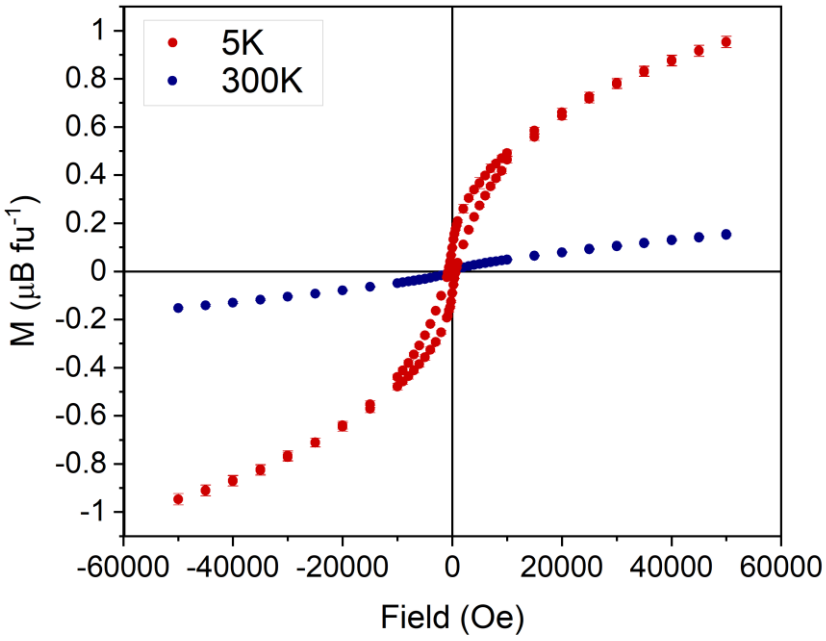

Figure 6.8: Magnetisation-field isotherms for $Ba_3CoIr_2O_{6.2}H_{2.8}$ measured at 5 K and 300 K.

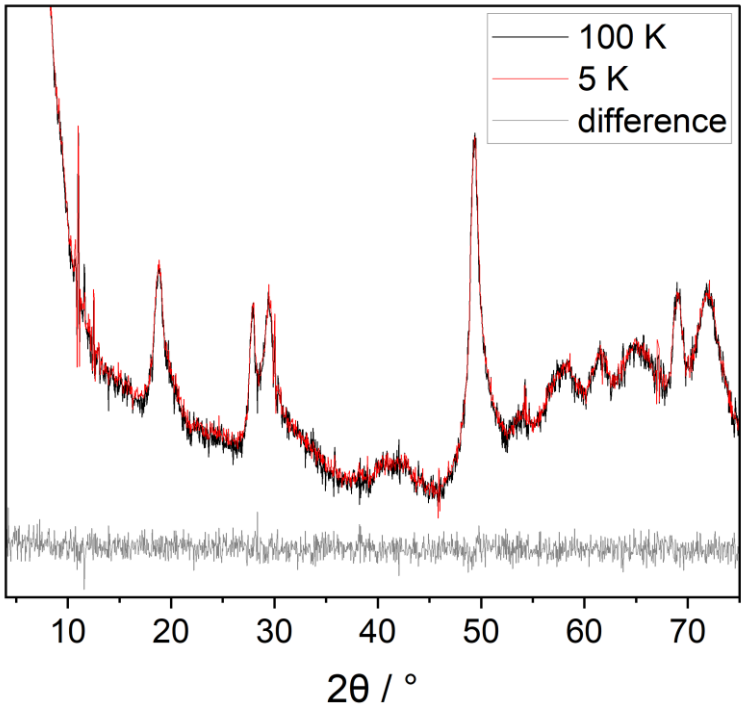

Figure 6.9: NPD data collected from $Ba_3CoIr_2O_{6.2}H_{2.8}$ using the D20 diffractometer with a wavelength of 2.41 Å at 5 K and 100 K, and the difference between the patterns at these two temperatures.

6.5 Discussion

The total transition metal oxidation state in $Ba_3CoIr_2O_{6.2}H_{2.8}$ is +9.2, which is likely to correspond to cobalt being present as Co^{II} and iridium being present as a mixture of 40% Ir^{III} and 60% Ir^{IV}. For the $La_xSr_{4-x}CoIrO_{8-y}H_y$ ($0 \leq x \leq 2$) series of oxyhydride phases discussed in Chapter 3, it was established that Co^{I} and Ir^{III} represent the reduction limits for cobalt and iridium in octahedral coordination environments. The observation that the Co^{I}/Ir^{III} oxidation state combination is not obtained in $Ba_3CoIr_2O_{6.2}H_{2.8}$ suggests that the 6*H*-perovskite framework is too fragile to accommodate this extent of reduction. The fragile nature of this compound in comparison with the compounds discussed in Chapter 3 can be attributed to the higher iridium content and the absence of a stabilising rock salt layer.

In $Ba_3CoIr_2O_{6.2}H_{2.8}$, the O4 site (Figure 6.6) is fully occupied by hydride, whilst the remaining anion sites have oxide occupancies of > 0.8. This site selectivity is in direct contrast to previously reported hexagonal perovskite oxyhydride[119–122] and oxygen-deficient phases,[123–125] in which the hydride ions or vacancies are preferentially located at the face-sharing sites. The site selectivity in these compounds is generally attributed either to the difference in Ba−O bond lengths at each anion site[124] or to the weaker bonding associated with the smaller M−O−M bond angles at the face-sharing sites.[119] It is worth noting that, although the hydride ions are exclusively located at the face-sharing sites in $BaVO_{2.7}H_{0.3}$, some hydride ions are located at the corner-sharing sites in $BaVO_{2.2}H_{0.8}$, which is attributed to the strong driving force for hydride ions to adopt a *trans*-arrangement around V^{3+} ions.[119] Furthermore, although the hydride ions preferentially occupy the face-sharing sites in $BaCrO_2H$, there is also a non-negligible hydride occupancy at the corner-sharing sites, suggesting that the driving force for hydride to occupy the face-sharing sites in this compound is relatively weak.[121] It is also worth noting that there are some oxygen-deficient compounds, such as 5H-type $BaMO_{2.8}$ phases (M

= V, Cr, Fe), in which the oxygen vacancies are located at the corner-sharing sites, but this is driven by the formation of layers of MO_4 tetrahedra, so the same argument cannot necessarily be applied to $Ba_3CoIr_2O_{6.2}H_{2.8}$.[126–128]

The contribution of the A-site cation to the site selectivity observed in $Ba_3CoIr_2O_{6.2}H_{2.8}$ can be rationalised by considering the bond valence sums of the oxide ions in $Ba_3CoIr_2O_9$ with respect to the A- and B-site cations, using the same arguments as described in Section 3.3.9.1.[129] The calculated bond valence sums are presented in Table 6.3.

Table 6.3: Calculated anion bond valence sums with respect to the A- and B-site cations for $Ba_3CoIr_2O_9$.

Anion	**Anion BVS**	
O1	BVS(A)	0.827
	BVS(B)	1.143
	BVS(B) – BVS(A)	+ 0.316
O2	BVS(A)	0.786
	BVS(B)	1.385
	BVS(B) – BVS(A)	+ 0.598
O3	BVS(A)	0.769
	BVS(B)	1.178
	BVS(B) – BVS(A)	+ 0.410
O4	BVS(A)	0.772
	BVS(B)	1.493
	BVS(B) – BVS(A)	+ 0.721
O5	BVS(A)	0.748
	BVS(B)	1.190
	BVS(B) – BVS(A)	+ 0.442

The O4 site has the most positive value for BVS(B) – BVS(A), indicating that this site has the smallest relative bonding contribution from the electropositive A-site cation and, therefore, suggesting that oxide-to-hydride exchange is likely to be most favourable at this site. This is consistent with the observation that the O4 site is almost fully occupied by hydride ions. It is

worth noting that, in the undistorted $P6_3/mmc$ structure, the O1 site is equivalent to the O2 site and the O4 site is equivalent to the O3 and O5 sites, so the fact that the BVS calculations correctly predict that the O4 site is the most favourable for exchange could suggest that the distortions in the parent oxide play a significant role in determining the anion distribution in the final oxyhydride phase. Nevertheless, if the average value of BVS(B) − BVS(A) is calculated for O1/O2 and O3/O4/O5, corresponding to the two anion sites in the $P6_3/mmc$ structure, a value of +0.504 is obtained for the face-sharing sites and a value of +0.524 is obtained for the corner-sharing sites, which is consistent with the general result that exchange at the corner-sharing sites is more favourable.

Another feature of $Ba_3CoIr_2O_{6.2}H_{2.8}$ that could contribute to the observed site selectivity is the fact that two different transition metals are present, which are ordered across the two B-cation sites. It is possible that, in $Ba_3CoIr_2O_{6.2}H_{2.8}$, the lower charge of hydride relative to oxide means that the hydride ions preferentially coordinate to the cobalt ions, due to their lower charge with respect to the iridium ions, resulting in the observed selectivity for the corner-sharing sites. By contrast, the previously reported hexagonal perovskite oxyhydride[119–122] and oxygen-deficient[123–125] phases only contain a single transition metal cation, so do not have this driving force for the hydride ions to be located at the corner-sharing sites.

An additional factor to consider is the temperature at which the reaction was performed. The previously reported hexagonal perovskite oxyhydrides were either synthesised directly at high temperature[119,121,122] or topochemically at temperatures of 450 °C or above.[120] Under these conditions, all the anions are likely to be mobile and in equilibrium with each other. As such, the relative mobility of the anions at each site does not affect the product obtained and the most 'thermodynamically' stable arrangement of anions is adopted in the product. By contrast, the synthesis of $Ba_3CoIr_2O_{6.2}H_{2.8}$ was performed at very low temperatures (≤ 160 °C). It has previously been observed that the oxide ion mobility at the corner-sharing sites in hexagonal

perovskites is higher than at the face-sharing sites.[130–132] As such, at the low reaction temperature, the mobility of the anions at the corner-sharing sites is likely to be substantially higher than at the face-sharing sites and, as a result, exchange occurs at the corner-sharing sites. The anion ordering observed, in which the hydride ions occupy *trans*-configurations with respect to each other, arises as this local anion arrangement optimises π-bonding between the oxide ions and the Co^{II} ions, as described in Section 1.4.2. The formation of the *trans*-CoO_4H_2 unit is likely to represent a local minimum in the reaction pathway, with a comparatively high energy barrier for exchange at the other anion sites. This is similar to the behaviour observed for $SrVO_2H$, which occupies a relatively deep well on the potential energy surface, due to the π-stabilisation associated with formation of *trans*-VO_4H_2 units.[48,49] This means that the activation energy required for further oxide-to-hydride exchange is greater than that for non-topochemical decomposition, so it is not possible to isolate a more reduced species than $SrVO_2H$. Destabilising the *trans*-VO_4H_2 units through hole doping with titanium lowers the activation energy barrier for further reduction, allowing more reduced $SrV_{1-x}Ti_xO_{1.5}H_{1.5}$ phases to be isolated. The observation that there is some oxide-to-hydride exchange beyond $Ba_3CoIr_2O_7H_2$ when $Ba_3CoIr_2O_9$ is reacted with LiH suggests that $Ba_3CoIr_2O_7H_2$ lies in a slightly shallower energy well than $SrVO_2H$, so a small amount of exchange can occur at the other sites without the onset of non-topochemical decomposition.

The magnetisation data collected from $Ba_3CoIr_2O_{6.2}H_{2.8}$ suggest the presence of a magnetic transition at ~10 K. However, no magnetic Bragg peaks are observed in the NPD data at 5 K, indicating that long range magnetic order is not present. A possible rationalisation for this is that, below 10 K, there are ferromagnetic interactions between the Co^{II} ions, mediated through superexchange with Ir^{IV} ions in the Ir_2O_9 dimers (Figure 6.10), similar to the coupling observed in the parent oxide. This would explain the sharp divergence of the FC and ZFC curves in Figure 6.7 and the large magnetisation observed at 5 K in Figure 6.8. However, the

establishment of long-range magnetic order is disrupted by the presence of diamagnetic Ir^{III} in the dimers.

It is worth noting that it is possible that long-range magnetic order is, in fact, present, but that the large background arising from the incoherent scattering from hydride, in combination with the weak signal expected for magnetic scattering from iridium, means that the magnetic peaks are hidden.

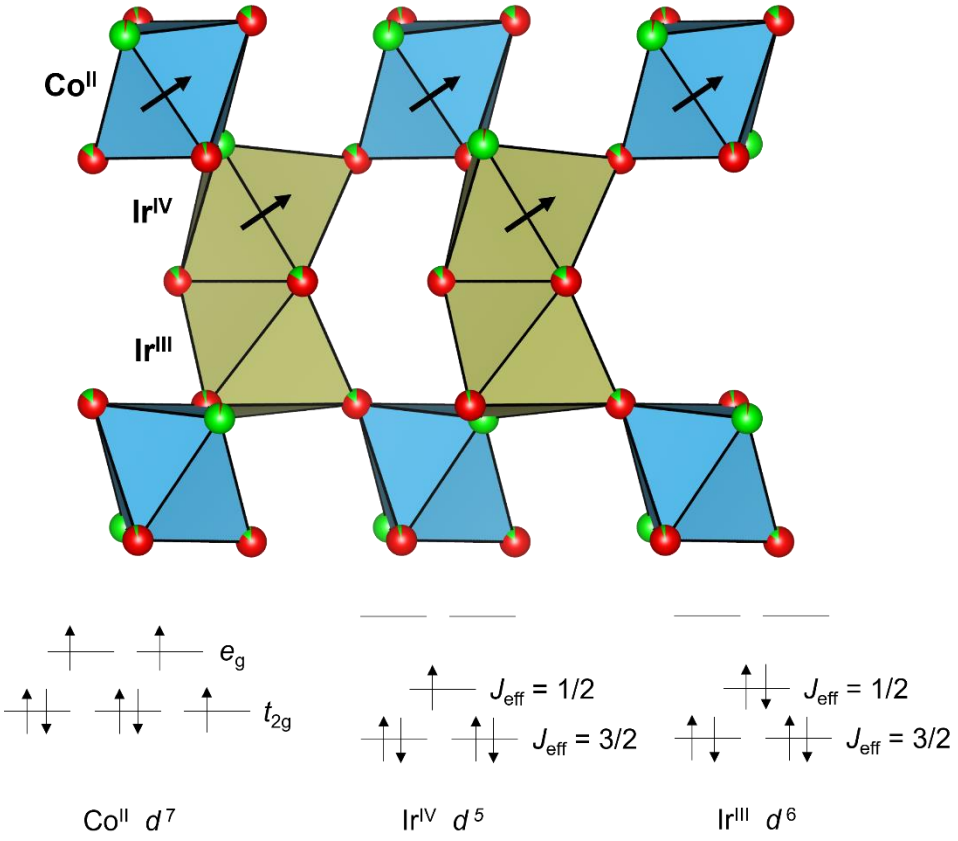

Figure 6.10: Top: Schematic illustrating ferromagnetic interactions between the Co^{II} ions in the Co layers, mediated by Ir^{IV} ions in the Ir_2O_9 dimers, with long-range magnetic ordering disrupted by the presence of diamagnetic Ir^{III}. Bottom: Proposed electronic configurations for the cobalt and iridium ions in $Ba_3CoIr_2O_{6.2}H_{2.8}$.

6.6 Conclusion

The reaction between the 6H-hexagonal perovskite, $Ba_3CoIr_2O_9$, and LiH yields the oxyhydride phase, $Ba_3CoIr_2O_{6.2}H_{2.8}$, in which hydride ions fully occupy the O4 site, corresponding to a *trans*-arrangement of hydride around the Co^{II} ions. The magnetisation data show that a magnetic transition is likely to occur at ~10 K, but no long-range magnetic ordering is observed from NPD. This could result from the presence of diamagnetic Ir^{III} disrupting magnetic interactions in the structure, so only short-range ferromagnetic order is observed, which arises from coupling between the Co^{II} and Ir^{IV} ions.

Chapter 7 – Topochemical reduction of $La_xSr_{2-x}CoIrO_6$ (x = 0, 1) phases using LiH

7.1 Introduction

The previous chapters have demonstrated that LiH is an effective reagent for the formation of oxyhydrides from Ir-containing, perovskite-derived oxide phases. To extend this work further, the reactivity of double perovskite $La_xSr_{2-x}CoIrO_6$ (x = 0, 1) phases with LiH has been explored.

7.2 Experimental

7.2.1 Synthesis of $La_xSr_{2-x}CoIrO_6$ (x = 0, 1) phases

Four-gram polycrystalline samples of $La_xSr_{2-x}CoIrO_6$ (x = 0, 1) were prepared using conventional ceramic synthesis methods. Suitable stoichiometric ratios of La_2O_3 (dried at 900 °C), $SrCO_3$, Co_3O_4, and IrO_2 (dried for 2 hours at 700 °C) were thoroughly ground together in an agate pestle and mortar, pelletised and heated in air at 1000 °C for 2 days. The samples were then reground, pelletised and heated in air at 1050 °C for a further 2 days. At the end of this heating cycle, the samples were cooled to 800 °C at 5 °C/min, followed by quench-cooling into dry ice.

7.2.2 Exploration of the reactivity of $La_xSr_{2-x}CoIrO_6$ (x = 0, 1) phases with LiH

Small-scale trial reactions of Sr_2CoIrO_6 and $LaSrCoIrO_6$ with LiH were performed to determine their reactivity as a function of temperature. The reaction mixtures were prepared by thoroughly grinding 200 mg of the all-oxide starting material with 8 mole equivalents of LiH, sealing the mixtures in evacuated Pyrex® ampoules and then heating for 2 days at the trial temperature. After each heating cycle, the reaction mixture was characterised by PXRD, before

being reheated at an increased temperature. This process was repeated until decomposition was observed, signalled by the formation of La_2O_3, SrO and Ir metal.

PXRD data show that the products of reactions between the $La_xSr_{2-x}CoIrO_6$ phases and LiH remain metrically cubic until decomposition. For Sr_2CoIrO_6, a reaction took place at temperatures ≥ 125 °C, signalled by the appearance of Li_2O, along with substantial broadening of the perovskite diffraction peaks. At reaction temperatures above 200 °C, non-topochemical decomposition occurred. Meanwhile, for $LaSrCoIrO_6$, a reaction took place at temperatures of ≥ 200 °C, with non-topochemical decomposition occurring above 320 °C.

7.2.3 Synthesis of $Sr_2CoIrO_{4.4}H_{1.6}$ and $LaSrCoIrO_{4.4}H_{1.6}$

Samples of $Sr_2CoIrO_{4.4}H_{1.6}$ and $LaSrCoIrO_{4.4}H_{1.6}$ were prepared by thoroughly grinding 1.7 g of the corresponding $La_xSr_{2-x}CoIrO_6$ phase with 10 mole equivalents of LiH in an Ar-filled glovebox. The reaction mixtures were then sealed in evacuated Pyrex® ampoules. The $x = 0$ reaction mixture was heated for 6 periods of 7 days at temperatures of 150−200 °C, whilst the $x = 1$ reaction mixture was heated for 4 periods of 7 days at temperatures of 270−320 °C. Heating rates of 1 °C/min were used. The samples were thoroughly reground between each heating cycle. The Li_2O by-product and any excess LiH were removed by washing the reaction mixtures with MeOH under an N_2 atmosphere. The products were then dried under vacuum and returned to the glovebox.

7.3 Structural characterisation

7.3.1 Structural characterisation of $La_xSr_{2-x}CoIrO_6$ ($x = 0, 1$) phases

Sr_2CoIrO_6 and $LaSrCoIrO_6$ have previously been reported as adopting B-site cation-ordered double perovskite structures.[133–135] Sr_2CoIrO_6 was reported to adopt a structure in the $I2/m$ space group, corresponding to a $a^-a^-c^0$ tilting arrangement, whilst $LaSrCoIrO_6$ was reported to

adopt a structure in the $P2_1/n$ space group, corresponding to a $a^-a^-c^+$ tilting arrangement. Models of double perovskite structures in these space groups were refined against SXRD data collected from samples of Sr_2CoIrO_6 and $LaSrCoIrO_6$, which gave good fits to the data. Plots of the fits against the SXRD data are shown in Figure 7.1 and Figure 7.2, with the refined structural parameters detailed in Table 7.1 and Table 7.2.

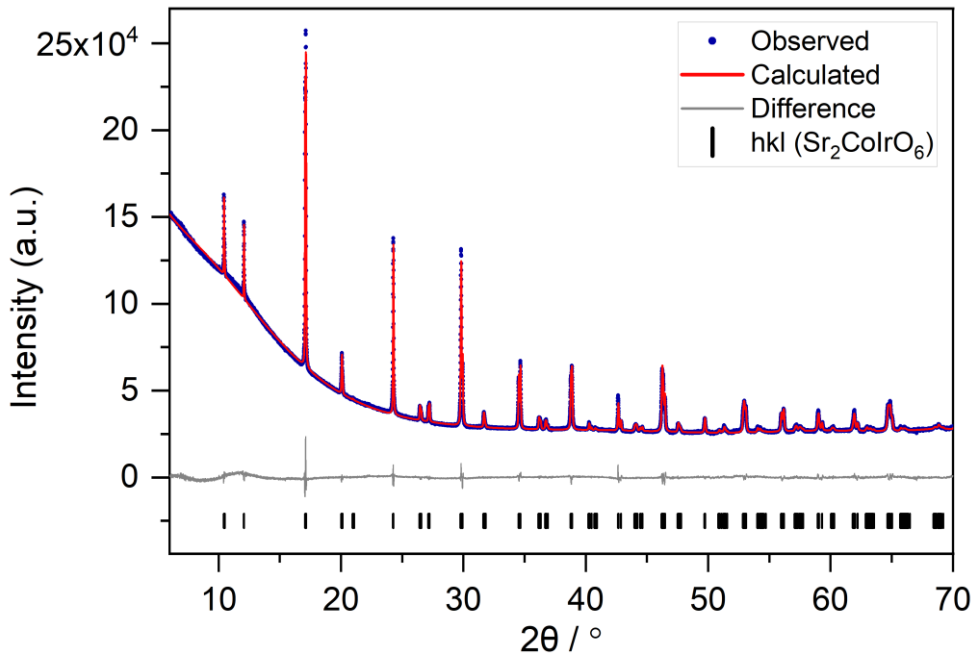

Figure 7.1: Observed, calculated and difference plots from the structural refinement of Sr_2CoIrO_6 against SXRD data collected at room temperature using a wavelength of 0.825 Å.

Table 7.1: Parameters from the structural refinement of Sr_2CoIrO_6 against SXRD data collected at room temperature. The fractional coordinates of the oxide sites were fixed at the values reported by Mikhailova *et al.*[134].

Sr_2CoIrO_6, space group *I*2/*m* (No. 12)						
		x	***y***	***z***	**Occ.**	**B_{iso} (Å^2)**
Sr(1)	4*i*	0.5006(8)	0	0.7490(7)	1	1.07(1)
Co(1)/Ir(1)	2*d*	0	0	½	0.934(2)/0.066(2)	0.58(3)
Ir(2)/Co(2)	2*a*	0	0	0	0.934(2)/0.066(2)	0.751(9)
O(1)	4*i*	0.9801	0	0.2514	1	1.77(6)
O(2)	8*j*	0.2417	0.2634	0.0273	1	1.77(6)
a = 5.5360(1) Å, b = 5.55219(9) Å, c = 7.8485(1) Å						
β = 90.3222(9)°						
V = 241.233(7) Å^3						
R_{wp} = 1.61%, R_p = 0.46%, *gof* = 3.43						

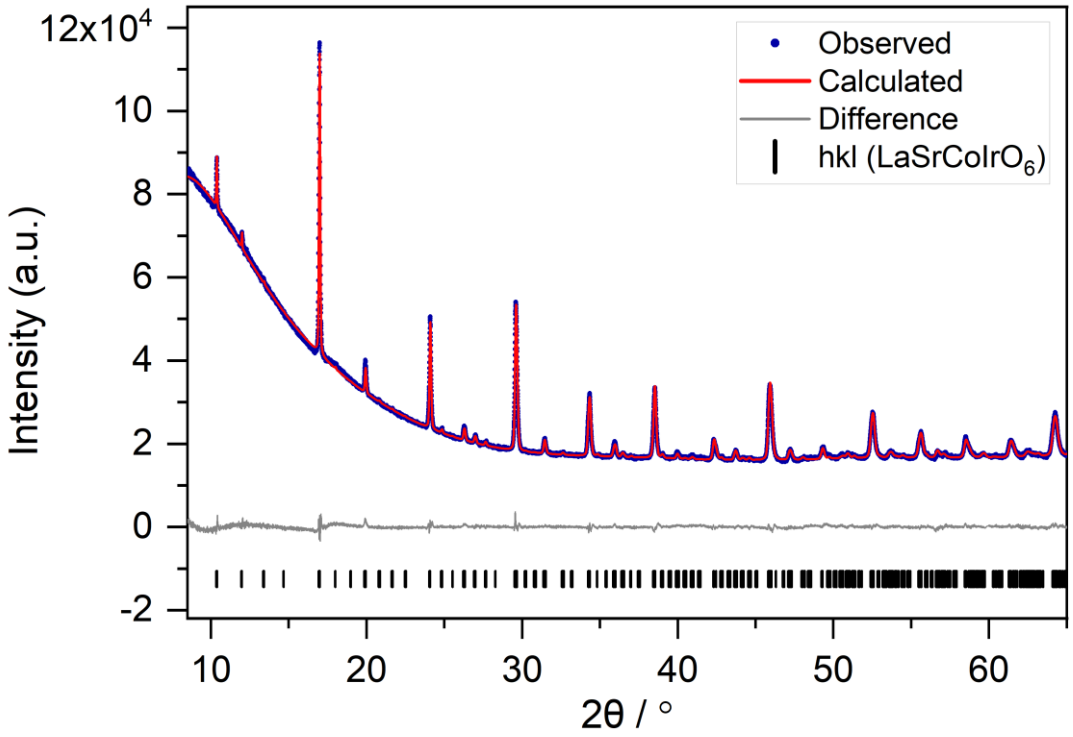

Figure 7.2: Observed, calculated and difference plots from the structural refinement of $LaSrCoIrO_6$ against SXRD data collected at room temperature using a wavelength of 0.825 Å.

Table 7.2: Parameters from the structural refinement of $LaSrCoIrO_6$ against SXRD data collected at room temperature. The fractional coordinates of the oxide sites were fixed at the values reported by Narayanan *et al.*[135].

$LaSrCoIrO_6$, space group $P2_1/n$ (No. 14)						
		x	***y***	***z***	**Occ.**	**B_{iso} (Å^2)**
Sr(1)/La(1)	4*e*	0.4996(8)	0.5243(3)	0.7383(6)	0.5/0.5	0.95(3)
Co(1)/Ir(1)	2*c*	½	0	½	0.8985(8)/0.1015(8)	0.46(6)
Ir(2)/Co(2)	2*d*	½	0	0	0.8985(8)/0.1015(8)	0.63(2)
O(1)	4*e*	0.206	0.206	0.045	1	0.03(8)
O(2)	4*e*	0.738	0.225	0.015	1	0.03(8)
O(3)	*4e*	0.579	0.003	0.245	1	0.03(8)
a = 5.5809(3) Å, b = 5.5931(2) Å, c = 7.9108(4) Å						
β = 90.230(3)°						
V = 246.93(2) Å^3						
R_{wp} = 1.28%, R_p = 0.61%, *gof* = 2.10						

7.3.2 Structural characterisation of $Sr_2CoIrO_{4.4}H_{1.6}$

7.3.2.1 Synchrotron X-ray diffraction

SXRD data were collected from the product of the reaction between Sr_2CoIrO_6 and LiH, henceforth referred to as $Sr_2CoIrO_{4.4}H_{1.6}$. A Pawley refinement was performed against the data using the $Fm\bar{3}m$ space group, yielding a lattice parameter of a = 7.775(2) Å, which is significantly shorter than that of the Sr_2CoIrO_6 starting material ($a \approx 7.84$ Å). The peak shapes were observed to be asymmetrically broadened, which is likely to result from inhomogeneous anion compositions across the sample. The fit to the data is shown in Figure 7.3.

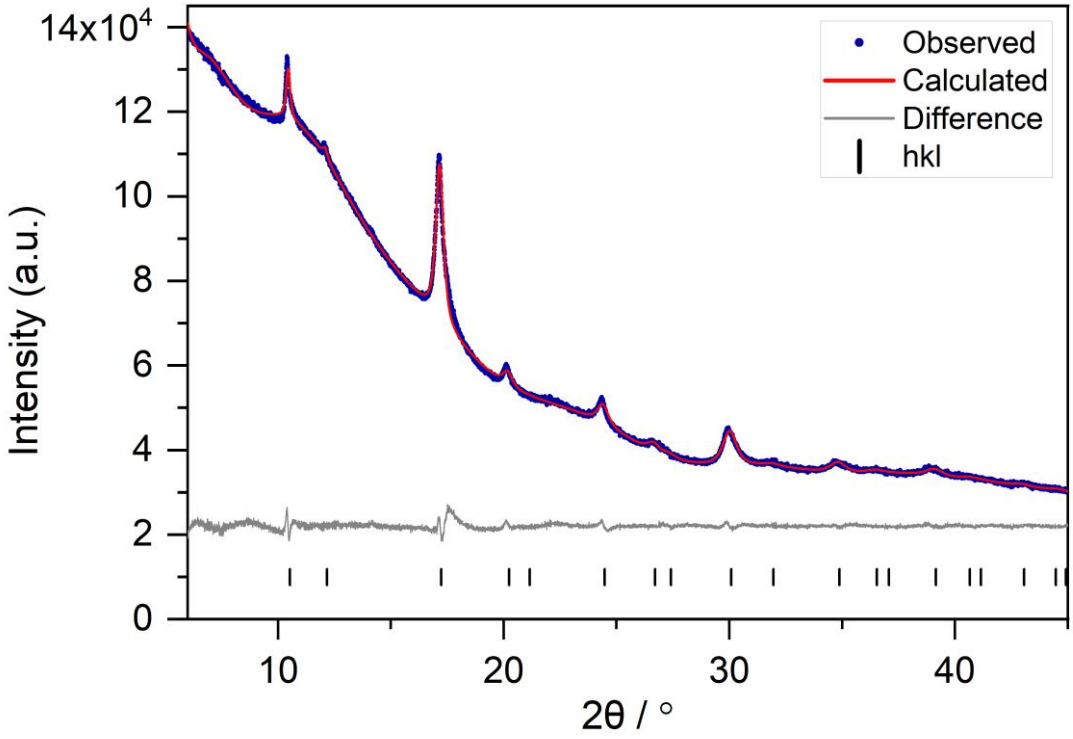

Figure 7.3: Observed, calculated and difference plots from the Pawley refinement against SXRD data from $Sr_2CoIrO_{4.4}H_{1.6}$ using the $Fm\bar{3}m$ space group using a wavelength of 0.825 Å.

7.3.2.2 Thermogravimetric analysis

Thermogravimetric data were collected from $Sr_2CoIrO_{4.4}H_{1.6}$ whilst heating under a flow of 5%/95% H_2/N_2 gas (Figure 7.4). A decrease in mass was observed, which is attributed to decomposition of the perovskite phase into SrO, CoO and Ir metal, as supported by PXRD data

collected after the measurement (Appendix A4). During the measurement, the sample showed a mass loss of 5.4%, which would correspond to an initial composition of $Sr_2CoIrO_{4.40}H_y$.

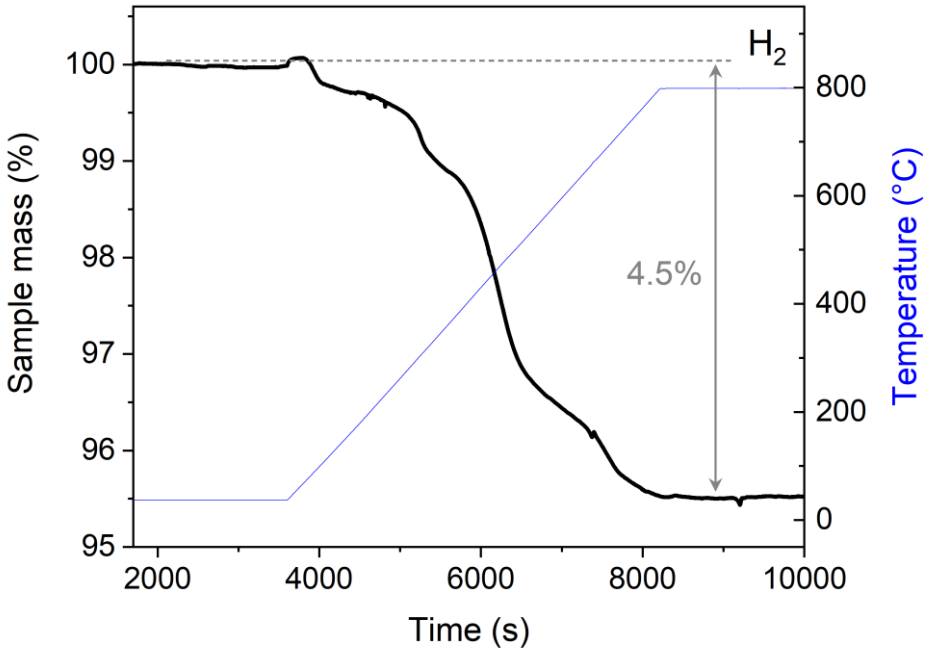

Figure 7.4: TGA trace when $Sr_2CoIrO_{4.4}H_{1.6}$ is heated under a flow of 5%/95% H_2/N_2.

To confirm the presence of hydride in the phase, the sample was heated under flowing oxygen and the exhaust gases were monitored. As shown in Figure 7.5, there was a clear release of water and hydrogen gas concurrent with oxidation of the sample, indicating that hydride is present in the phase. The sharp decrease in sample mass is attributed to loss of sample from the crucible during oxidation.

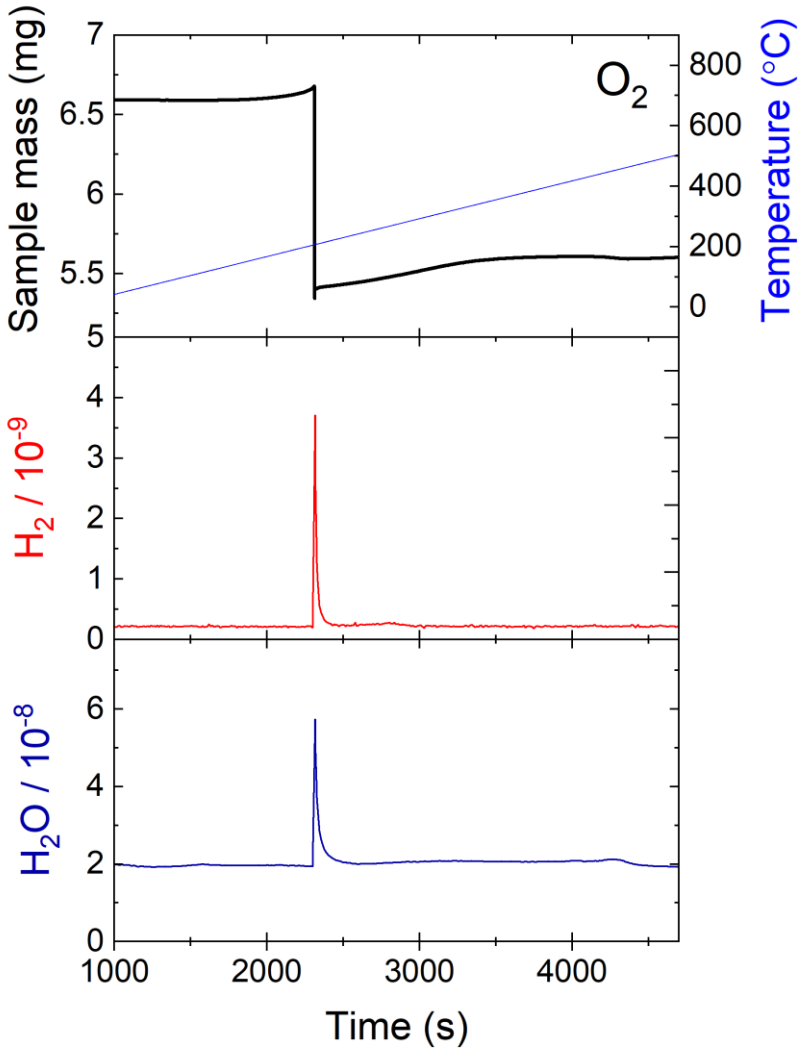

Figure 7.5: Sample mass change and H_2/H_2O content of the exhaust gas when $Sr_2CoIrO_{4.4}H_{1.6}$ is heated under flowing oxygen.

7.3.2.3 Neutron powder diffraction

NPD data were collected from $Sr_2CoIrO_{4.4}H_{1.6}$ at ambient temperature using the POLARIS diffractometer at ISIS. Due to the strong incoherent and inelastic scattering from hydride, in combination with the large absorption cross-section of iridium and poor crystallinity of the sample, detailed crystallographic analysis of the sample is challenging. Despite that higher angle detector banks are typically used for crystal structure determination due to their higher resolution, these banks showed poor signal-to-noise ratios for this sample and so provide

limited structural information (Figure 7.6). As such, refinements were only performed using data from the 27° and 54° detector banks.

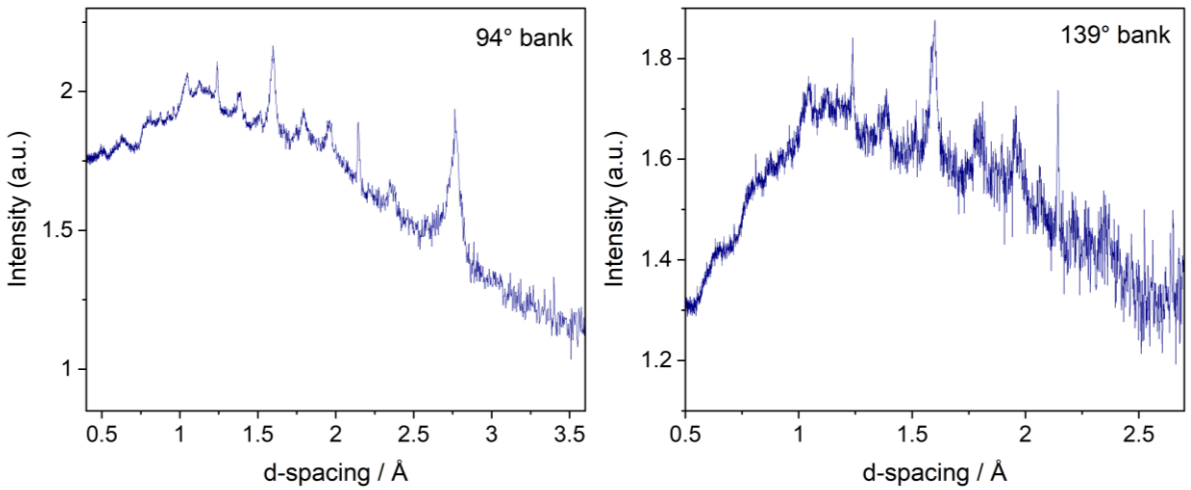

Figure 7.6: NPD data collected from $Sr_2CoIrO_{4.4}H_{1.6}$ using the 94° and 139° detector banks of the POLARIS diffractometer.

To describe the structure of $Sr_2CoIrO_{4.4}H_{2.6}$, a model based on the double perovskite structure in the $Fm\bar{3}m$ space group was constructed and refined against the NPD data. The oxide occupancy was fixed to 0.733, as this corresponds to the composition of $Sr_2CoIrO_{4.40}H_y$ obtained from reductive TGA. Hydride was then added at the anion site and the occupancy allowed to refine. This yielded a value for the occupancy of 0.27(7), indicating that the anion sites are fully occupied by oxide and hydride with no vacancies.

It was initially assumed that the anions sit at the 24*e* special position with fractional coordinates (*x*, 0, 0). However, when the model was refined against the data, the *x*-coordinate of this site refined to an unphysical value and the isotropic thermal factors refined to very large values (Figure 7.9(a)). When anisotropic thermal factors were used at the anion sites, they refined to a disc-type shape (Figure 7.9(b)), indicating that the anions are displaced away from the 24*e* site. In an attempt to describe the structure in a more physically reasonable way, the *y*- and *z*-coordinates of the anion site were constrained to be equal and allowed to refine, yielding a

value of 0.059(1). In the resulting structure, the oxide ions are split across four sites, which models a distortion of the Co−O−Ir bond angle away from 180°. Since the oxide and hydride anions are disordered, these distortions cannot propagate through the structure in an ordered way and, as such, the oxide ions are displaced away from the ideal 24*e* site in a disordered manner and $Fm\bar{3}m$ symmetry is retained. Overall, this can be thought of as a disordered arrangement of octahedral tilting distortions. The fits to the data are shown in Figure 7.7 and Figure 7.8, with the refinement parameters detailed in Table 7.3. The disordered coordination environment around cobalt in $Sr_2CoIrO_{4.4}H_{1.6}$ is shown in Figure 7.9(c), along with possible octahedral tilting arrangements in Figure 7.9(d).

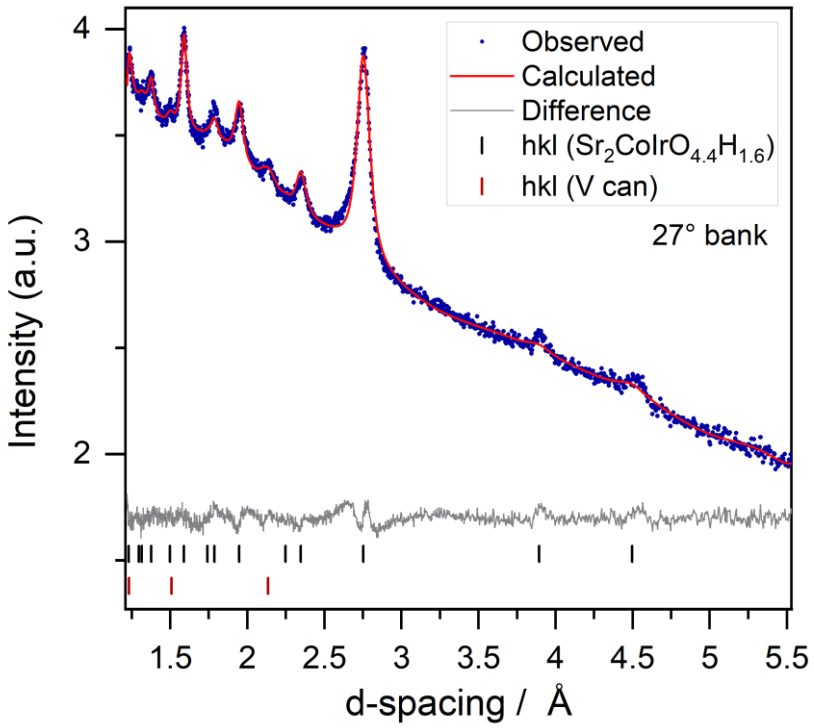

Figure 7.7: Observed, calculated and difference plots from the structural refinement of $Sr_2CoIrO_{4.4}H_{1.6}$ against NPD data collected at room temperature from the 27° bank of the POLARIS diffractometer.

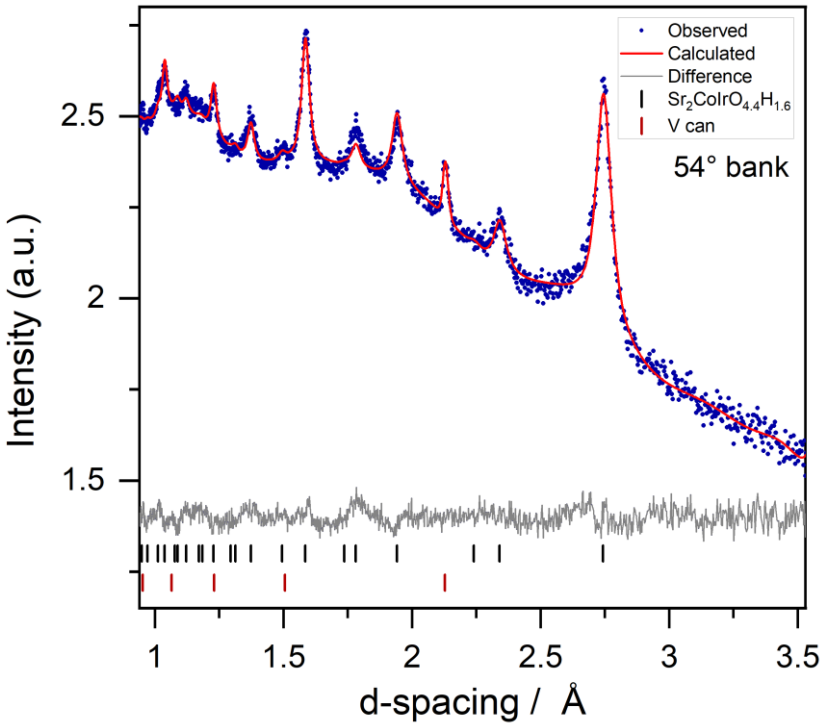

Figure 7.8: Observed, calculated and difference plots from the structural refinement of $Sr_2CoIrO_{4.4}H_{1.6}$ against NPD data collected at room temperature from the 54° bank of the POLARIS diffractometer.

Table 7.3: Parameters from the structural refinement of $Sr_2CoIrO_{4.4}H_{1.6}$ against NPD data collected at room temperature from the POLARIS diffractometer. The transition metal occupancies were fixed at the values in the parent oxide.

$Sr_2CoIrO_{4.40}H_{1.6(4)}$, space group $Fm\bar{3}m$ (No. 225)						
		x	***y***	***z***	**Occ.**	**B_{iso} (Å^2)**
Sr(1)	8*c*	¼	¼	¼	1	2.4(3)
Co(1)/Ir(1)	4*a*	0	0	0	0.934/0.066	0.1(3)
Ir(2)/Co(2)	4*b*	½	½	½	0.934/0.066	0.1(3)
O(1)	96*k*	0.206(2)	0.059(1)	0.059(1)	0.183	6(2)
H(1)	96*k*	0.206(2)	0.059(1)	0.059(1)	0.07(2)	6(2)
a = 7.790(3) Å						
V = 472.7(5) Å^3						
R_{wp} = 0.95%, R_p = 0.76%, *gof* = 0.03						

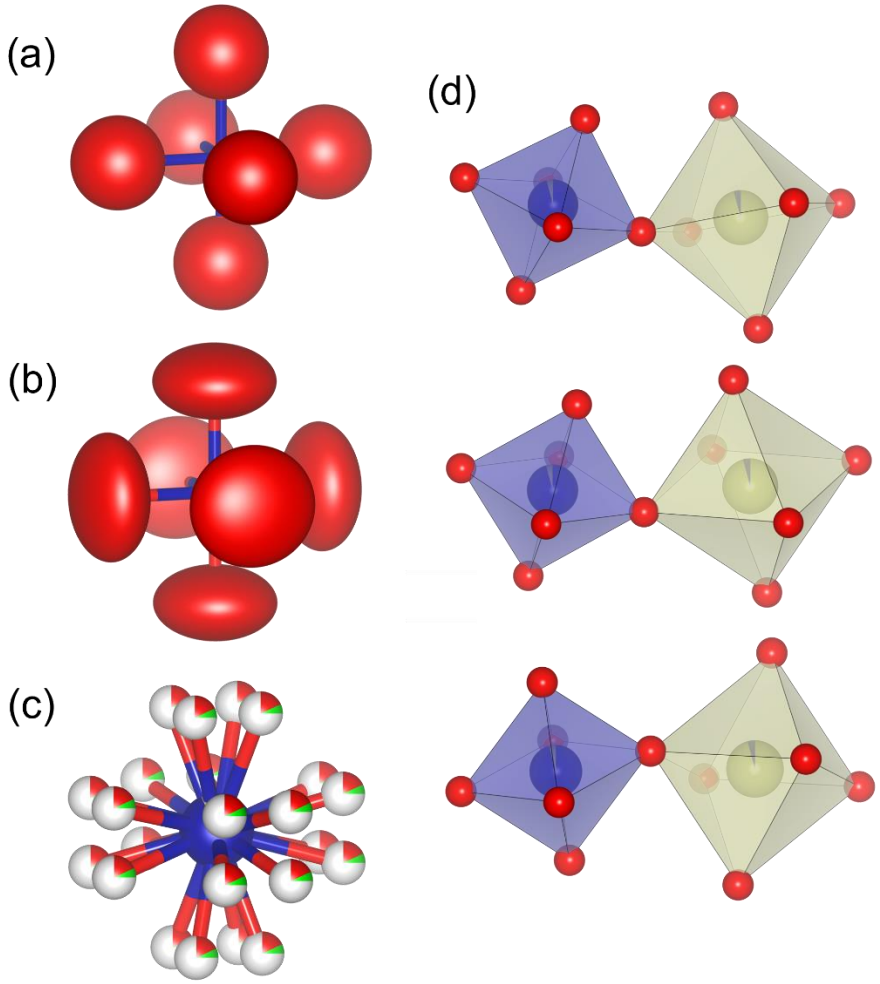

Figure 7.9: Local Co−O coordination in $Sr_2CoIrO_{4.4}H_{1.6}$ using (a) isotropic thermal factors, (b) anisotropic thermal factors and (c) split anion sites. Possible octahedral tilting distortions are shown in (d).

7.3.3 Structural characterisation of $LaSrCoIrO_{4.4}H_{1.6}$

7.3.3.1 Synchrotron X-ray diffraction

SXRD data were collected from the product of the reaction between $LaSrCoIrO_6$ and LiH, henceforth referred to as $LaSrCoIrO_{4.4}H_{1.6}$. A Pawley refinement was performed against the data using the $Fm\bar{3}m$ space group, yielding a lattice parameter of a = 7.7935(7) Å, which is significantly shorter than that of the $LaSrCoIrO_6$ starting material ($a \approx 7.90$ Å). The fit to the data is shown in Figure 7.10.

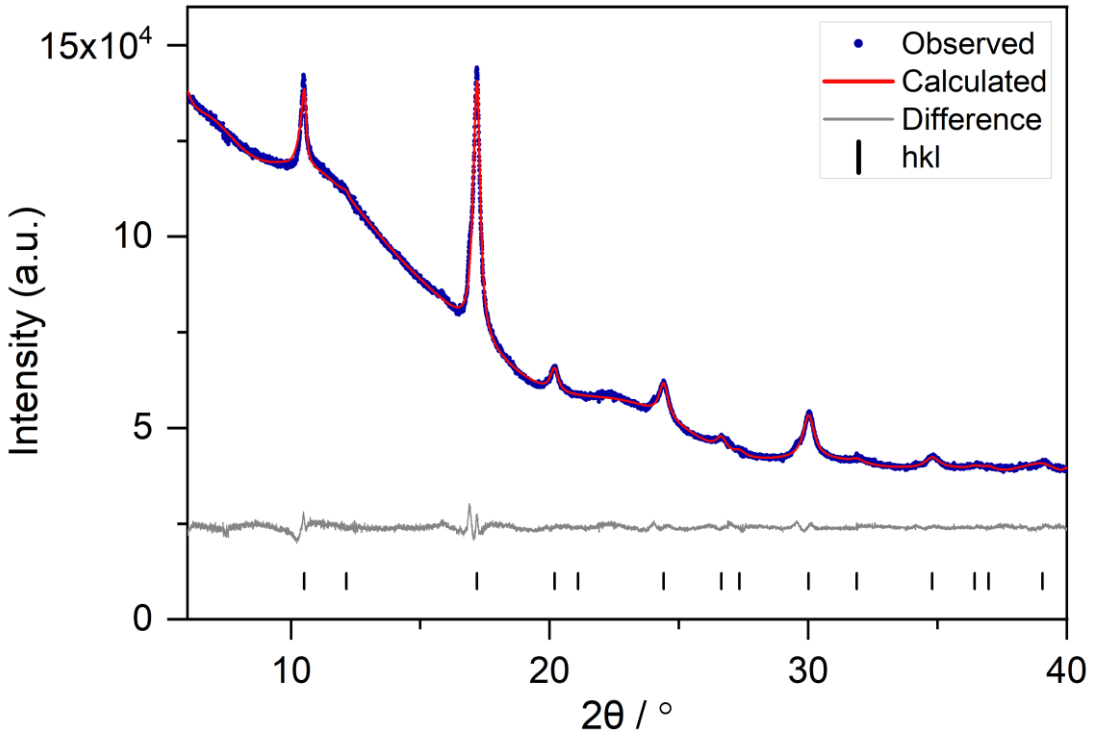

Figure 7.10: Observed, calculated and difference plots from the Pawley refinement against SXRD data from $LaSrCoIrO_{4.4}H_{1.6}$ using the $Fm\bar{3}m$ space group.

7.3.3.2 Thermogravimetric analysis

Thermogravimetric data were collected from $LaSrCoIrO_{4.4}H_{1.6}$ whilst heating under a flow of 5%/95% H_2/N_2 gas (Figure 7.11). A decrease in mass was observed, which is attributed to decomposition of the perovskite phase into La_2O_3, SrO, CoO and Ir metal, as supported by PXRD data collected after the measurement (Appendix A4). During the measurement, the sample showed a mass loss of 2.5%, which would correspond to an initial composition of $LaSrCoIrO_{4.36}H_y$.

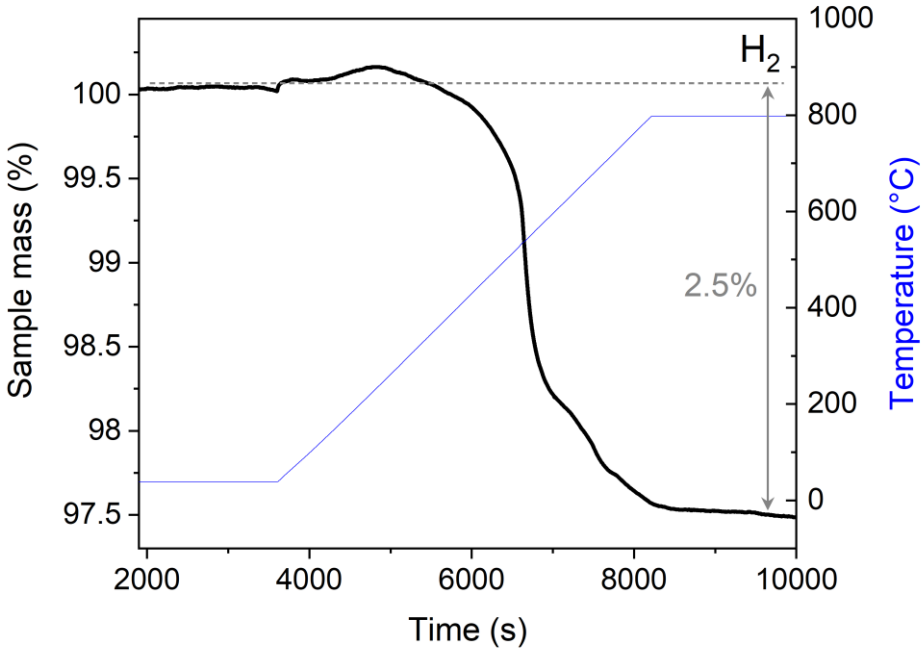

Figure 7.11: TGA trace when $LaSrCoIrO_{4.4}H_{1.6}$ is heated under a flow of 5%/95% H_2/N_2.

To confirm the presence of hydride in the phase, the sample was heated under flowing oxygen and the exhaust gases were monitored. As shown in Figure 7.12, there was a clear release of water and hydrogen gas concurrent with oxidation of the sample, indicating that hydride is present in the phase. The sample mass gain observed during the measurement would indicate an initial composition of $LaSrCoIrO_{3.32}H_y$. The discrepancy between this and the results from reductive TGA is likely to result from the presence of elemental cobalt and iridium in the sample. Since these impurities are oxidised during oxidative TGA measurements but remain unchanged during reductive TGA measurements, their presence has a greater effect on the results obtained from oxidative TGA than from reductive TGA and, as such, the composition obtained from reductive TGA is likely to be more reliable.

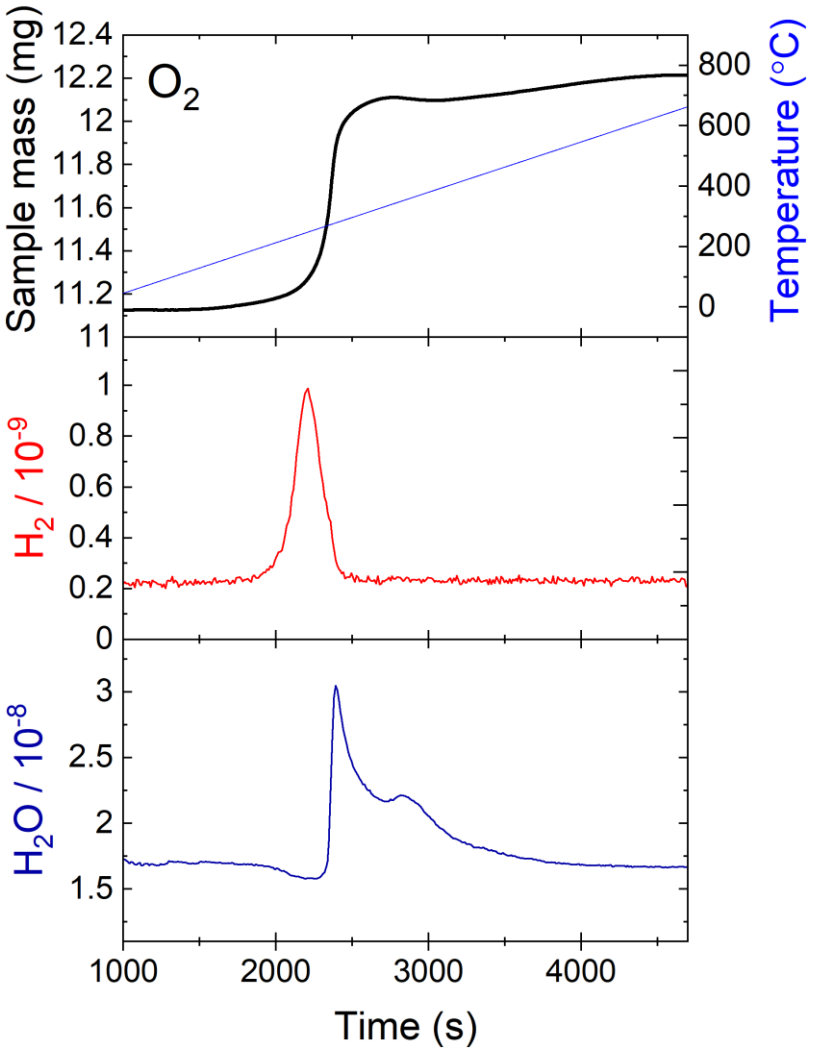

Figure 7.12: Sample mass change and H_2/H_2O content of the exhaust gas when $LaSrCoIrO_{4.4}H_{1.6}$ is heated under flowing oxygen.

7.3.3.3 Neutron powder diffraction

NPD data were collected from $LaSrCoIrO_{4.4}H_{1.6}$ at ambient temperature using the POLARIS diffractometer at ISIS. As before, strong incoherent and inelastic scattering was observed from the hydride in the phase. To describe the structure, a model based on the double perovskite structure in the $Fm\bar{3}m$ space group was constructed and refined against the data from the 27° and 54° detector banks of the diffractometer.

Similar to $Sr_2CoIrO_{4.4}H_{1.6}$, oxide and hydride ions were placed at (0.25, 0, 0) and the fractional coordinates allowed to refine, constrained such that the *y*- and *z*-coordinates were equal. The oxide occupancy at the site was fixed such that the overall oxygen content is consistent with the value obtained from reductive TGA. The *y*- and *z*-coordinates refined to a value of 0.0490(9), indicating that the oxide ions are locally distorted away from the 24*e* site. Meanwhile, the hydride occupancy refined to a value of 0.07(1). This corresponds to an overall composition of $LaSrCoIrO_{4.36}H_{1.6(2)}$, indicating that the anion sites are likely to be fully occupied by oxide and hydride. The fits to the NPD data are shown in Figure 7.13 and Figure 7.14, with the refinement parameters detailed in Table 7.4.

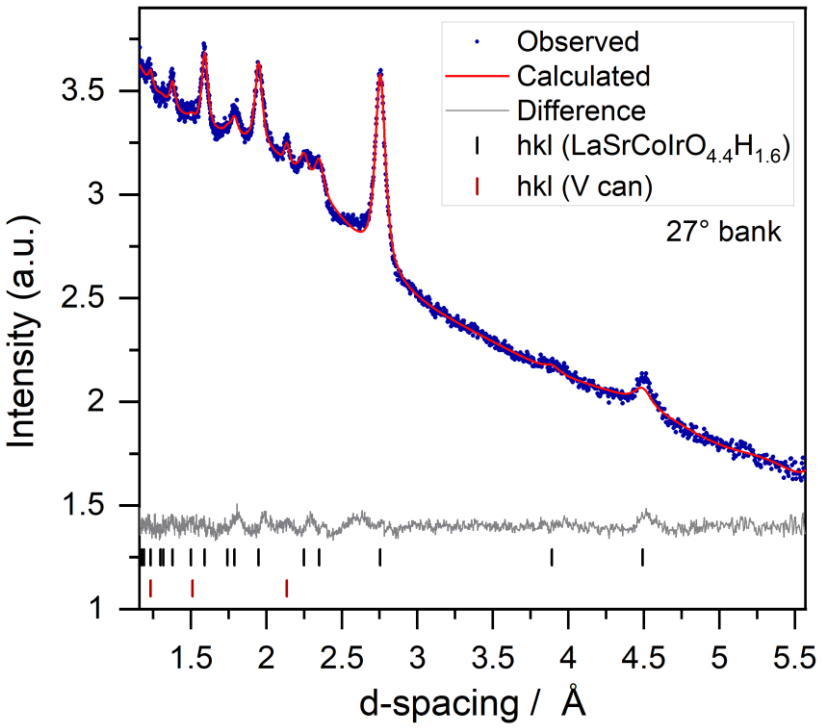

Figure 7.13: Observed, calculated and difference plots from the structural refinement of $LaSrCoIrO_{4.4}H_{1.6}$ against NPD data collected at room temperature from the 27° bank of the POLARIS diffractometer.

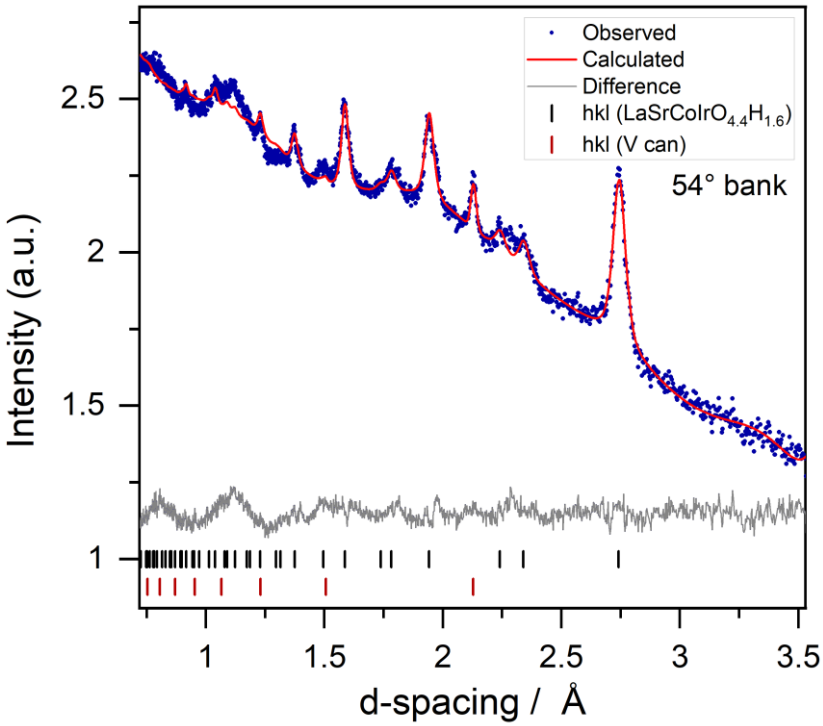

Figure 7.14: Observed, calculated and difference plots from the structural refinement of $LaSrCoIrO_{4.4}H_{1.6}$ against NPD data collected at room temperature from the 54° bank of the POLARIS diffractometer.

Table 7.4: Parameters from the structural refinement of $LaSrCoIrO_{4.4}H_{1.6}$ against NPD data collected at room temperature from the POLARIS diffractometer. The transition metal occupancies were fixed at the values in the parent oxide.

$LaSrCoIrO_{4.36}H_{1.6(2)}$, space group $Fm\bar{3}m$ (No. 225)						
		x	***y***	***z***	**Occ.**	**B_{iso} (Å^2)**
La(1)/Sr(1)	8*c*	¼	¼	¼	0.5/0.5	6.1(4)
Co(1)/Ir(1)	4*a*	0	0	0	0.8985/0.1015	2.7(4)
Ir(2)/Co(2)	4*b*	½	½	½	0.8985/0.1015	2.7(4)
O(1)	96*k*	0.225(1)	0.0490(9)	0.0490(9)	0.18167	2.3(8)
H(1)	96*k*	0.225(1)	0.0490(9)	0.0490(9)	0.07(1)	2.3(8)
a = 7.810(3) Å						
V = 476.4(6) Å^3						
R_{wp} = 1.05%, R_p = 0.86%, *gof* = 0.03						

7.4 Magnetic characterisation

7.4.1 Magnetic characterisation of $Sr_2CoIrO_{4.4}H_{1.6}$

Magnetisation data collected from $Sr_2CoIrO_{4.4}H_{1.6}$ as a function of temperature are shown in Figure 7.15, and magnetisation-field isotherms collected at 5 K and 300 K are shown in Figure 7.16. Although the ZFC and FC curves display behaviour that appears paramagnetic above ~15 K, the magnetisation-field isotherms show that the sample does not exhibit simple paramagnetic behaviour at any temperature between 5 K and 300 K. The maximum magnetisation at 300 K has a relatively large value of ~0.4 μ_B fu^{-1}, which increases to ~1.0 μ_B fu^{-1} on cooling to 5 K. Although this magnetisation is relatively large, it is not high enough to represent bulk ferromagnetism in the compound. The magnetisation-field isotherm at 5 K shows the presence of coercivity, which has disappeared by 15 K, as shown in Figure 7.17. AC susceptibility data collected from $Sr_2CoIrO_{4.4}H_{1.6}$ are shown in Figure 7.18. A peak is observed in χ'' in the temperature range 10−15 K, and the maxima of both χ' and χ'' show a strong frequency dependence. Overall, the data indicate that simple models involving independent local atomic moments are inappropriate for this compound.

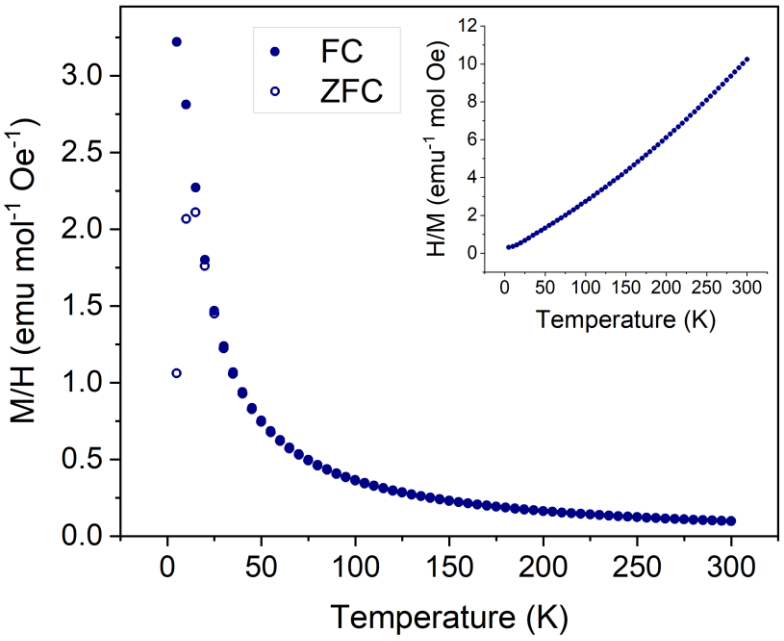

Figure 7.15: Magnetisation data collected from $Sr_2CoIrO_{4.4}H_{1.6}$ as a function of temperature, measured in a field of 100 Oe under both ZFC and FC conditions.

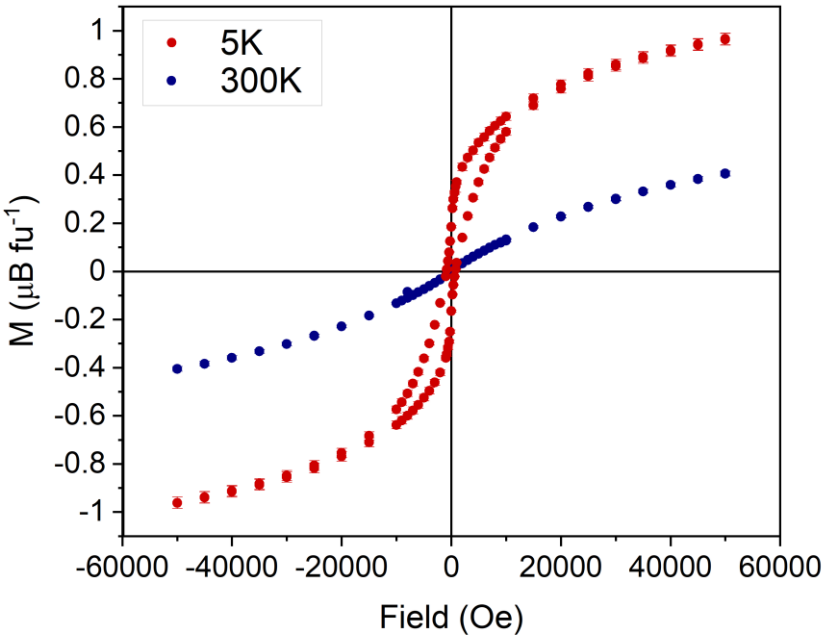

Figure 7.16: Magnetisation-field isotherms for $Sr_2CoIrO_{4.4}H_{1.6}$ measured at 5 K and 300 K.

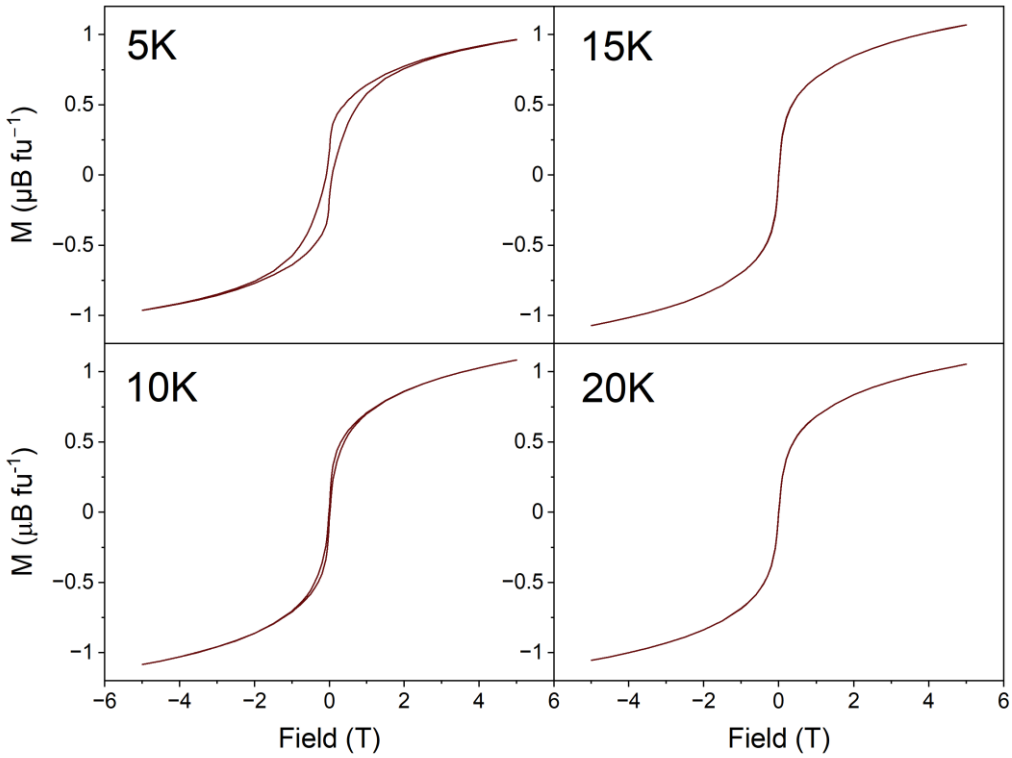

Figure 7.17: Magnetisation-field isotherms collected from $Sr_2CoIrO_{4.4}H_{1.6}$ at temperatures between 5 and 20 K, highlighting the change in coercivity as a function of temperature for the sample.

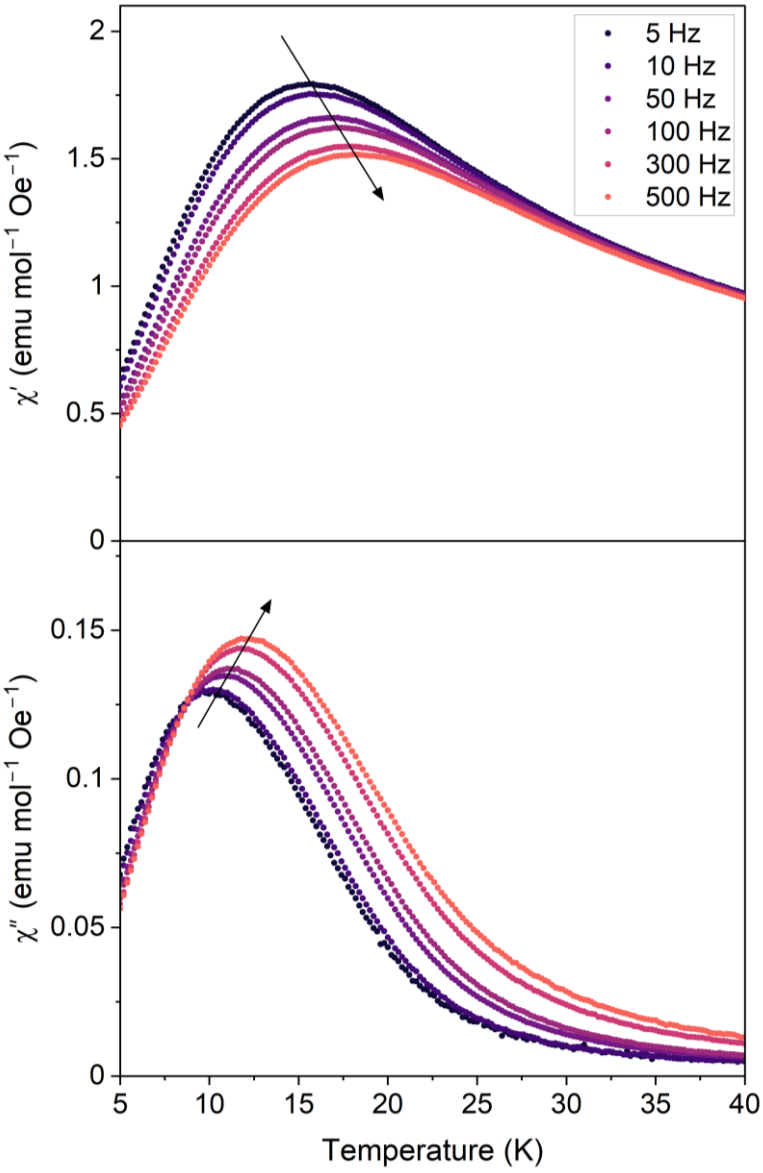

Figure 7.18: AC susceptibility data, χ' (top) and χ'' (bottom), collected as a function of temperature from $Sr_2CoIrO_{4.4}H_{1.6}$ at frequencies between 5 Hz and 500 Hz. The measurements were performed using an AC field with amplitude of 2.5 Oe, and an applied DC field of 2 Oe.

7.4.2 Magnetic characterisation of $LaSrCoIrO_{4.4}H_{1.6}$

Magnetisation data collected from $LaSrCoIrO_{4.4}H_{1.6}$ as a function of temperature are shown in Figure 7.19, and magnetisation-field isotherms collected at 5 K and 300 K are shown in Figure 7.20. Similar to $Sr_2CoIrO_{4.4}H_{1.6}$, the ZFC and FC curves show behaviour that appears qualitatively similar to paramagnetic behaviour at high temperature. However, the data could not be fit to the Curie-Weiss law in a physically reasonable way. In addition, the magnetisation-

field isotherms show that the maximum magnetisation of the sample has a relatively large value of 0.7 μB fu^{-1} at 300 K, which increases to 1.2 μB fu^{-1} on cooling to 5 K. Although this magnetisation is relatively large, the value is not large enough to represent bulk ferromagnetism. The magnetisation-field isotherm at 5 K shows the presence of coercivity, which has disappeared by 20 K, as shown in Figure 7.21. AC susceptibility data collected from $LaSrCoIrO_{4.4}H_{1.6}$ are shown in Figure 7.22. A peak is observed in χ'' in the temperature range 15−20 K, and there is a shift in the positions of the maxima of both χ' and χ'' as the frequency of the applied field is varied.

Overall, these results indicate that the sample does not exhibit simple paramagnetic behaviour at any temperature between 5 K and 300 K, and that the magnetism of this compound cannot be described as a collection of independent local atomic moments.

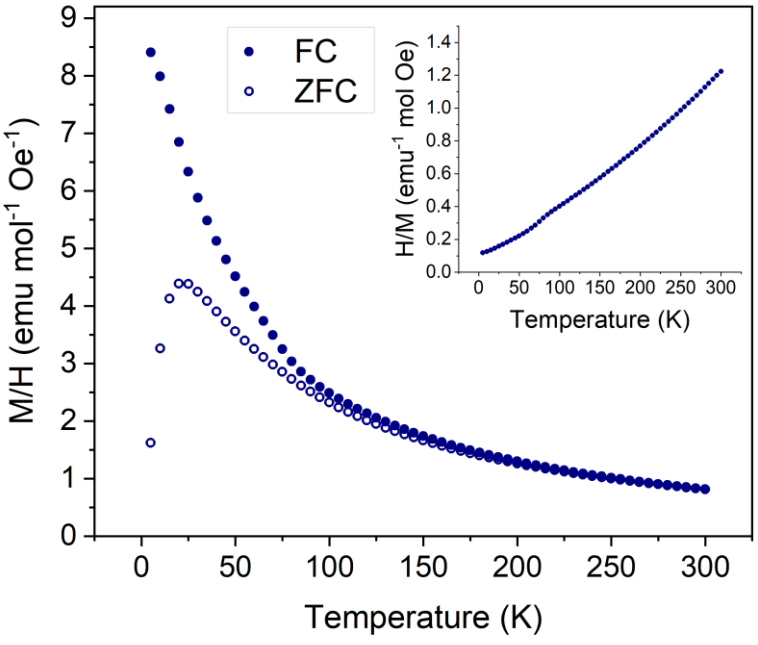

Figure 7.19: Magnetisation data collected from $LaSrCoIrO_{4.4}H_{1.6}$ as a function of temperature, measured in a field of 100 Oe under both ZFC and FC conditions.

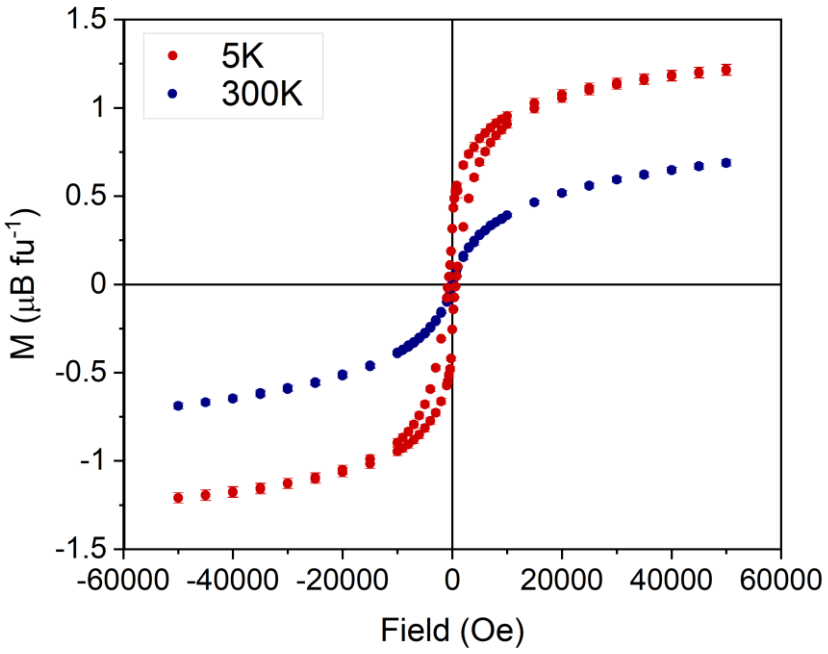

Figure 7.20: Magnetisation-field isotherms for $LaSrCoIrO_{4.4}H_{1.6}$ measured at 5 K and 300 K.

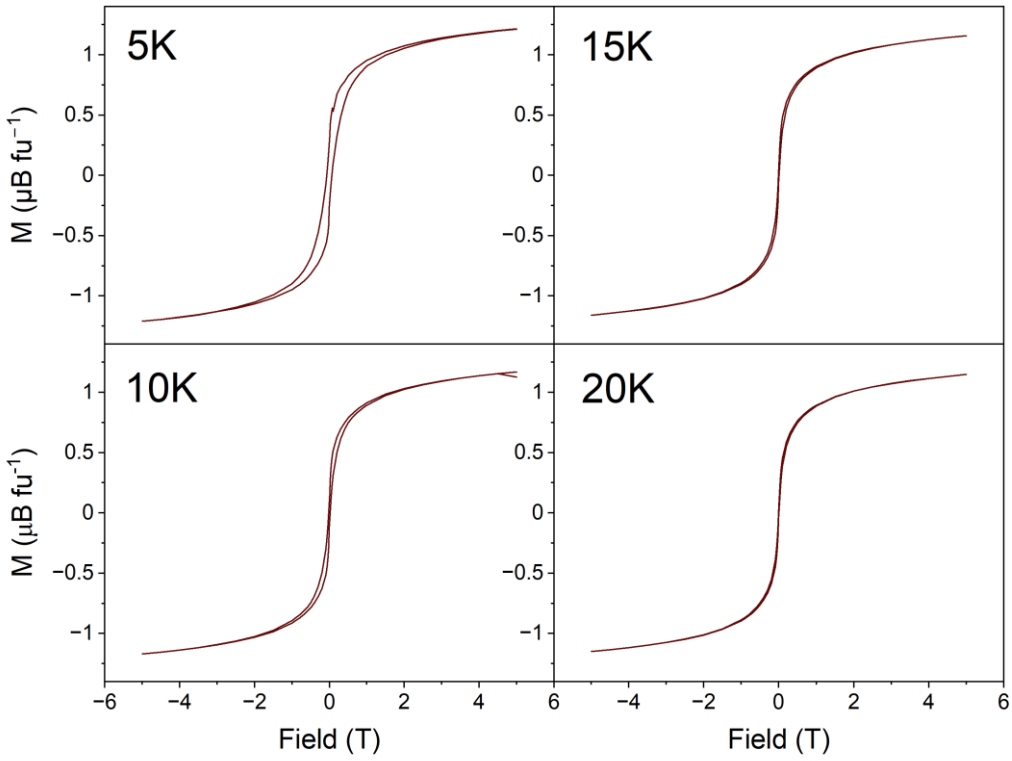

Figure 7.21: Magnetisation-field isotherms collected from $LaSrCoIrO_{4.4}H_{1.6}$ at temperatures between 5 and 20 K, highlighting the change in coercivity as a function of temperature for the sample.

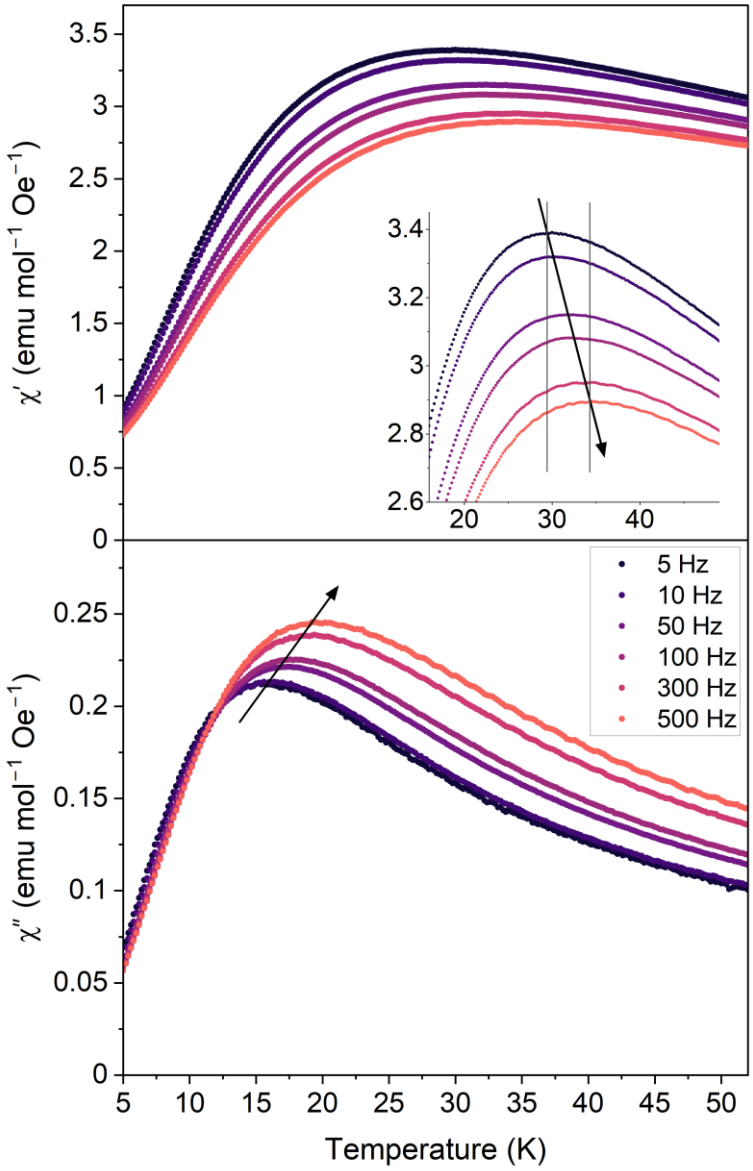

Figure 7.22: AC susceptibility data, χ' (top) and χ'' (bottom), collected as a function of temperature from $LaSrCoIrO_{4.4}H_{1.6}$ at frequencies between 5 Hz and 500 Hz. The measurements were performed using an AC field with amplitude of 2.5 Oe, and an applied DC field of 2 Oe. The inset shows an expanded region of χ' as a function of temperature to highlight the shift in susceptibility maximum as a function of frequency.

7.5 Discussion

Reaction of Sr_2CoIrO_6 and $LaSrCoIrO_6$ with LiH yield phases with compositions of $Sr_2CoIrO_{4.4}H_{1.6}$ and $LaSrCoIrO_{4.4}H_{1.6}$, respectively. These phases are unlikely to be line phases and the exact combination of oxide, hydride and vacancy obtained is likely to vary depending on the reaction conditions used (reaction temperature, H_2 partial pressure etc.). The

asymmetrically broadened peaks observed in the diffraction data are likely to arise from the presence of a range of anion compositions across the sample.

Considering the challenges associated with fitting the NPD data from these phases (Section 7.3.2.3), there is a high degree of uncertainty in their anion compositions. However, the observation that both phases appear to have roughly the same anion composition suggests that the extent of reduction is not controlled by the transition metal oxidation states, but is instead limited by the amount of oxygen that can be removed before decomposition of the perovskite framework occurs. It appears that, for these Co,Ir-perovskite type oxyhydride phases, the oxygen content cannot be lowered below approximately $La_xSr_{2-x}CoIrO_{4.4}H_y$ without decomposition occurring. This type of reactivity is analogous to that observed for Sr_4CoIrO_8 in Chapter 3, in which the extent of reduction is limited by the temperature at which the reaction can be performed without non-topochemical decomposition occurring, rather than the obtainment of the Co^{I}/Ir^{III} oxidation state combination.

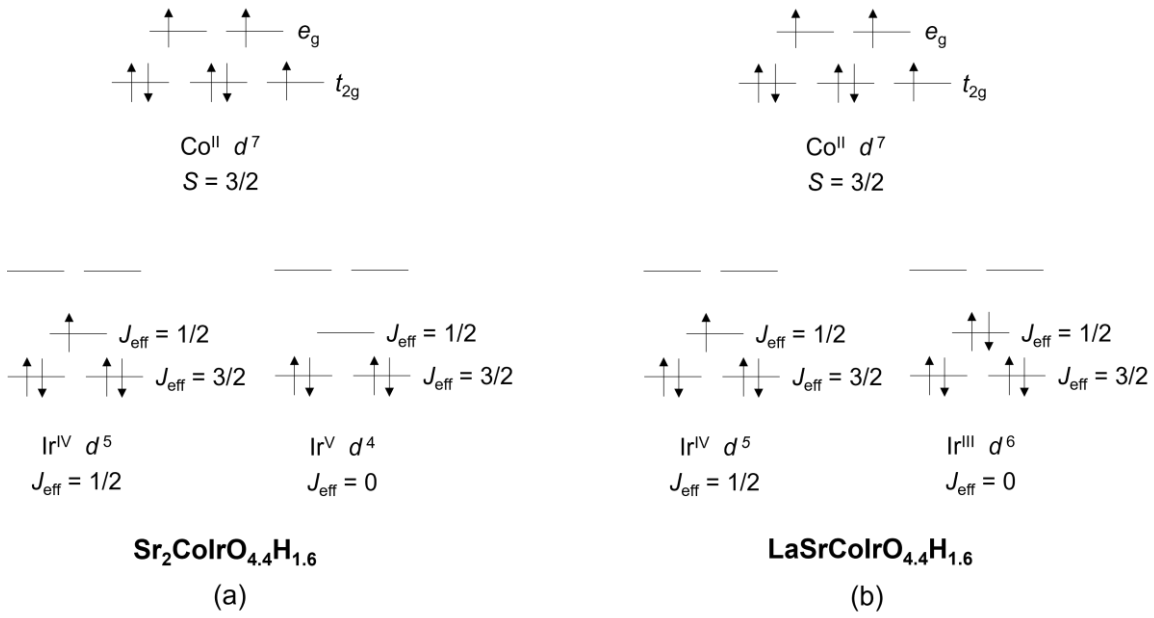

Figure 7.23: Proposed electronic configurations of cobalt and iridium in $Sr_2CoIrO_{4.4}H_{1.6}$ and $LaSrCoIrO_{4.4}H_{1.6}$.

In $Sr_2CoIrO_{4.4}H_{1.6}$, the total transition metal oxidation state is +6.4, which is likely to correspond to cobalt being present as Co^{II} and iridium being present as a mixture of Ir^{IV} and

Ir^{V} (Figure 7.23a). Meanwhile, in $LaSrCoIrO_{4.4}H_{1.6}$, the total transition metal oxidation state is +5.4, which is likely to correspond to cobalt and iridium being present as Co^{II} and a mixture of Ir^{III} and Ir^{IV} (Figure 7.23b). As such, the qualitatively similar magnetic behaviour of both $Sr_2CoIrO_{4.4}H_{1.6}$ and $LaSrCoIrO_{4.4}H_{1.6}$ can be attributed to the fact that they both contain Co^{II} in combination with a mixture of Ir^{IV} (J_{eff} = ½) and either Ir^{III} or Ir^{V}, both of which are diamagnetic.

A possible rationalisation of the magnetisation data presented in Section 7.4 is that the sample has regions that predominantly contain Ir^{IV} surrounded by regions that predominantly contain Ir^{III}/Ir^{V}. This separation of Ir^{IV} and Ir^{III}/Ir^{V} could be driven by inhomogeneity in the hydride composition across the sample, whereby hydride rich regions contain a higher concentration of iridium in the lower oxidation state. Ir^{IV} contains empty e_g-type orbitals and an unpaired electron in a t_{2g}-type orbital and, as a result, the Co^{II}–Ir^{IV} interaction might be expected to be ferromagnetic. Meanwhile, Ir^{III} and Ir^{V} are diamagnetic so the dominant superexchange interaction is likely to be antiferromagnetic via a next-nearest-neighbour $Co(3d_{x^2-y^2})^1$–$O(2p)$/$H(1s)$–$Ir(5d_{x^2-y^2})^0$–$O(2p)$/$H(1s)$–$Co(3d_{x^2-y^2})^1$ pathway. Due to the extended nature of this superexchange pathway, the transition temperature for these antiferromagnetic interactions is likely to be comparatively low. As such, the Ir^{IV}-rich regions would form ferromagnetic clusters within an antiferromagnetic/paramagnetic Ir^{III}/Ir^{V}-containing matrix, which would explain the large magnetisations observed in the magnetisation-field isotherms and the large values of C obtained when fitting of the magnetisation data to the Curie-Weiss law was attempted. Since the ferromagnetic regions are expected to be small, they are likely to behave in a similar manner to superparamagnets. The observation of coercivity below ~15 K indicates that this is the blocking temperature, T_B, for the material, below which superparamagnetic behaviour is not observed for the ferromagnetic clusters. This is similar to the model proposed for the alloys, $Y_{60}Fe_{30}Al_{10}$ and $Nd_{60}Fe_{30}Al_{10}$,

which are hypothesised to contain Fe-rich clusters that behave as superparamagnets.[136,137] Similar magnetic behaviour has also been observed for small magnetic particles contained within non-magnetic glasses, such as Fe_2O_3 particles contained within a $CaO\text{-}SiO_2$ matrix or $BaFe_{12}O_{19}/SrFe_{12}O_{19}$ particles contained within borate matrices.[138–141] The observation of maxima in the plots of χ'' against temperature (Figure 7.18 and Figure 7.22) for both $Sr_2CoIrO_{4.4}H_{1.6}$ and $LaSrCoIrO_{4.4}H_{1.6}$, along with the strong frequency dependence of both χ' and χ'', is consistent with the behaviour of superparamagnets, whereby there is a transition from superparamagnetic behaviour above T_B to single-domain ferromagnetic behaviour below T_B.[142] The strong frequency dependence of the AC susceptibility arises from the fact that the observed value of T_B depends entirely on the measurement time used, with T_B marking the crossover point at which the measurement time becomes shorter than the Neel relaxation time.

It might be expected that $La_{1.5}Sr_{0.5}CoIrO_6$ would exhibit similar magnetic behaviour to $Sr_2CoIrO_{4.4}H_{1.6}$, as they both contain Co^{II} and a mixture of Ir^{IV} and Ir^{V}. However, the magnetisation data collected from $La_{1.5}Sr_{0.5}CoIrO_6$ is significantly different to $Sr_2CoIrO_{4.4}H_{1.6}$, and the compound was found to adopt a simple antiferromagnetic state at low temperature.[135] A possible explanation for this is that $Sr_2CoIrO_{4.4}H_{1.6}$ contains hydride that is distributed inhomogeneously across the sample, whereas the composition of $La_{1.5}Sr_{0.5}CoIrO_6$ is homogeneous across the sample. This means that Ir^{IV} and Ir^{V} will be evenly distributed throughout the sample in $La_{1.5}Sr_{0.5}CoIrO_6$ and, as a result, ferromagnetic clusters do not form.

In both $Sr_2CoIrO_{4.4}H_{1.6}$ and $LaSrCoIrO_{4.4}H_{1.6}$, the oxide and hydride ions are disordered across the anion sublattice. Although cobalt is present as Co^{II} with a high-spin d^7 configuration so might be expected to favour a *trans*-hydride arrangement (Section 1.4.2), the preference for *cis*-arrangements around Ir^{V} (in the case of $Sr_2CoIrO_{4.4}H_{1.6}$) and Ir^{III} (in the case of $LaSrCoIrO_{4.4}H_{1.6}$) means that the overall structure is anion-disordered.

7.6 Conclusion

Reactions between $La_xSr_{2-x}CoIrO_6$ (x = 0, 1) phases and LiH yield oxyhydrides with compositions of $Sr_2CoIrO_{4.4}H_{1.6}$ and $LaSrCoIrO_{4.4}H_{1.6}$. These phases remain metrically cubic and adopt disordered arrangements of oxide and hydride across the anion sites. Both compounds exhibit unusual magnetism with extremely large values of C and large magnetisations in the magnetisation-field isotherms up to 300 K. It is proposed that this could result from the formation of ferromagnetic clusters within the materials (which behave as superparamagnets), driven by the inhomogeneous hydride distributions across the samples.

Chapter 8 – Synthesis and magnetism of Sr_2CoIrO_5

8.1 Introduction

Following from the preparation of the $La_xSr_{2-x}CoIrO_{6-y}H_y$ series of oxyhydride phases, described in Chapter 7, the reactivity of Sr_2CoIrO_6 in the presence of a Zr getter is explored. Using this method, it is possible to prepare an infinite-layer phase with composition Sr_2CoIrO_4, which forms via an Sr_2CoIrO_5 intermediate. In this chapter, the synthesis and magnetic behaviour of the intermediate Sr_2CoIrO_5 phase is discussed.

8.2 Exploration of the reactivity of Sr_2CoIrO_6 with a Zr getter

The synthesis and characterisation of Sr_2CoIrO_6 is described in Chapter 7. Trial reactions were performed by sealing ~300 mg of Sr_2CoIrO_6 in an evacuated Pyrex® ampoule with 4 mole equivalents of finely-divided Zr metal. It was observed that a reaction occurred when this apparatus was heated at 400°C, signalled by the appearance of two new sets of peaks in the PXRD data, the first of which could be indexed using a tetragonal cell with lattice parameters of a = 5.46 Å and c = 8.05 Å (Sr_2CoIrO_5) and the second of which could be indexed using another tetragonal cell with lattice parameters of a = 5.64 Å and c = 6.94 Å (Sr_2CoIrO_4). Below this temperature, the reaction proceeded on an impractically slow timescale, whilst heating above this temperature led to non-topochemical decomposition to SrO, Co metal and Ir metal. By heating the sample for several cycles at 400°C with intermediate grinding between cycles, it was possible to obtain the second tetragonal phase (Sr_2CoIrO_4) as a pure phase. In the intermediate heating cycles, the sample contained a mixture of the two tetragonal phases along with Sr_2CoIrO_6 starting material. The synthesis of the Sr_2CoIrO_5 intermediate for NPD measurements is described below, and the synthesis of Sr_2CoIrO_4 is described in Chapter 9.

8.3 Synthesis of Sr_2CoIrO_5

A sample of Sr_2CoIrO_5 was prepared by placing 1.2 g of Sr_2CoIrO_6 in a glass thimble and sealing this in an evacuated Pyrex® ampoule with 1 g of finely-divided Zr metal, such that the Sr_2CoIrO_6 sample was held approximately 5 cm from the Zr getter. The ampoule was then heated such that the temperature at the Zr getter was 400°C. The sample was initially heated for 2 cycles of 4 days at 400°C. At this point, the PXRD data indicated that the sample contained a mixture of Sr_2CoIrO_4, Sr_2CoIrO_5 and Sr_2CoIrO_6. In an attempt to equilibrate the reaction mixture, the Zr getter was removed and the sample was annealed in an empty, flame-dried Pyrex® tube at 380°C for 10 days. Following this heating cycle, the PXRD data showed that the reaction mixture contained predominantly Sr_2CoIrO_5 with a small amount of Sr_2CoIrO_6. The reaction mixture was, therefore, heated for a final cycle of 7 days with a Zr getter at 400°C to yield the pure Sr_2CoIrO_5 phase. The sample was thoroughly reground between each heating cycle in an Ar-filled glovebox.

8.4 Structural characterisation of Sr_2CoIrO_5

8.4.1 Synchrotron powder X-ray diffraction

SXRD data collected from 'Sr_2CoIrO_5' could be indexed using the *I*4/*mmm* space group. Therefore, a B-site cation ordered structural model with this symmetry based on the double perovskite structure was constructed (Figure 8.1). Due to the similarity of the diffraction pattern with that from $LaSrCoRuO_5$,[143] the composition was assumed to be Sr_2CoIrO_5 and the occupancy at the O1 ('equatorial') site was set to 0.75. A small impurity of the infinite-layer Sr_2CoIrO_4 phase (Chapter 9) was also observed, so this was added as a secondary phase. These models were then refined against the SXRD data, yielding lattice parameters of a = 5.4533(2) Å and c = 8.0444(3) Å for Sr_2CoIrO_5, which corresponds to a contraction in the

xy-plane and expansion in the *z*-direction relative to the parent Sr_2CoIrO_6 phase (a = 5.54 Å, b = 5.56 Å, c = 7.84 Å). The fit to the SXRD data is shown in Figure 8.2, with the refinement parameters detailed in Table 8.1

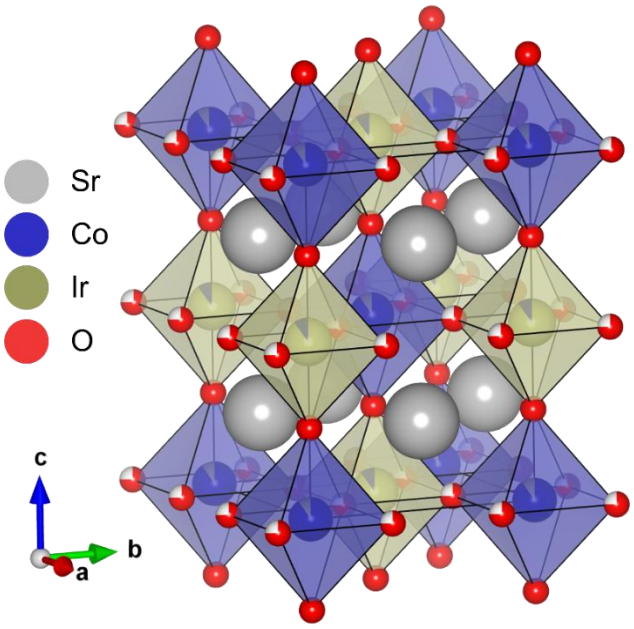

Figure 8.1: Structural model of Sr_2CoIrO_5 based on the double perovskite structure with *I*4/*mmm* symmetry. The occupancy of the oxide ions at the O1 site was fixed to 0.75.

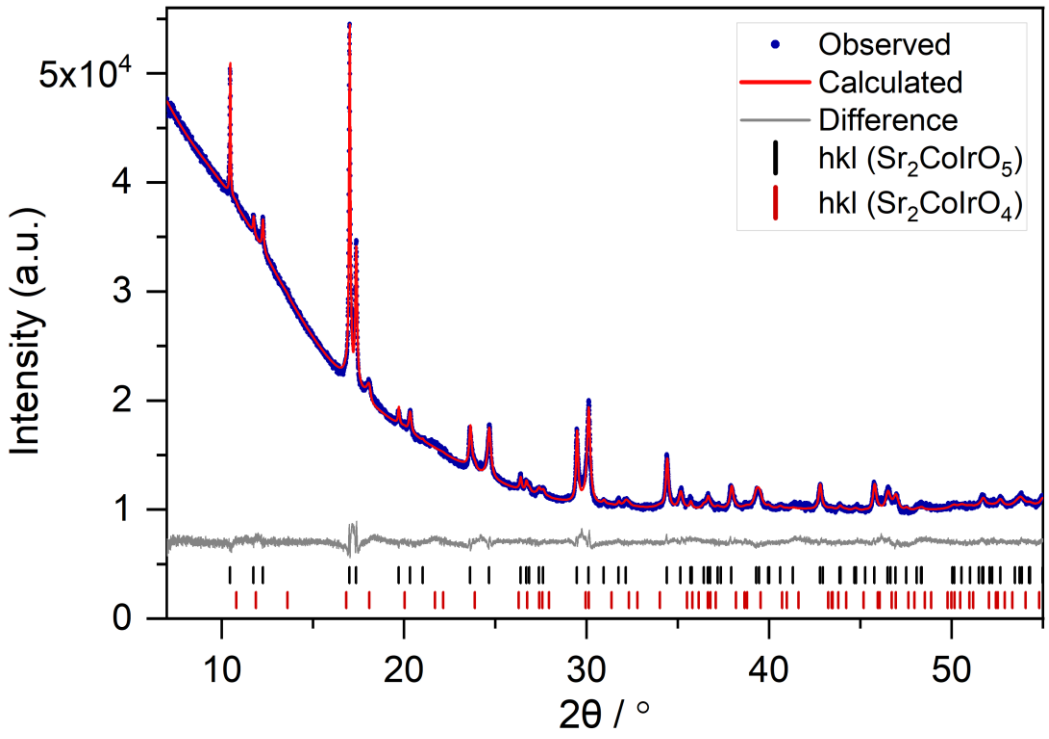

Figure 8.2: Observed, calculated and difference plots from the structural refinement of Sr_2CoIrO_5 against SXRD data (λ = 0.825 Å) collected at room temperature, with Sr_2CoIrO_4 included as a secondary phase.

Table 8.1: Parameters from the structural refinement of Sr_2CoIrO_5 against SXRD data collected at room temperature. The occupancies at the transition metal sites were fixed at the values observed in the Sr_2CoIrO_6 parent phase. The fractional coordinates of the $SrCoIrO_4$ phase were fixed at the values determined from NPD in Chapter 9.

Sr_2CoIrO_5, space group *I*4/*mmm* (No. 139), 85.7(6) wt%						
		x	***y***	***z***	**Occ.**	**B_{iso} (Å^2)**
Sr(1)	4*d*	0	½	¼	1	2.04(5)
Co(1)/Ir(1)	2*a*	0	0	0	0.934/0.066	0.73(9)
Ir(2)/Co(2)	2*b*	½	½	0	0.934/0.066	1.69(4)
O(1)	8*h*	¼	¼	0	0.75	2.7(2)
O(2)	4*e*	0	0	¼	1	2.7(2)
a = 5.4533(2) Å, c = 8.0444(3) Å						
V = 239.22(2) Å^3						
Sr_2CoIrO_4, space group *I*4/*mmm* (No. 139), 13.1(6) wt%						
		x	***y***	***z***	**Occ.**	**B_{iso} (Å^2)**
Sr(1)	4*d*	0	½	¼	1	2.3(2)
Co(1)	2*a*	0	0	0	1	2.3(2)
Ir(2)	2*b*	½	½	0	1	2.3(3)
O(1)	8*h*	0.2509	0.2509	0	1	2.3(2)
a = 5.628(1) Å, c = 6.952(2) Å						
V = 220.2(1) Å^3						
R_{wp} = 1.38%, R_p = 0.98%, *gof* = 1.80						

8.4.2 Neutron powder diffraction

NPD data were collected from Sr_2CoIrO_5 at ambient temperature using the POLARIS diffractometer at ISIS. The *I*4/*mmm* structural model from Section 8.4.1 was refined against the data from the 54°, 94° and 139° detector banks of the POLARIS diffractometer. When the O1 site occupancy was allowed to vary, it refined to a value of 0.743(6), which is broadly consistent with the composition of Sr_2CoIrO_5 and indicates that the anion vacancies are disordered across the O1 sites. Close inspection of the diffraction patterns did not provide any evidence for symmetry-lowering distortions. Small peaks arising from the infinite-layer phase, Sr_2CoIrO_4, and the parent phase, Sr_2CoIrO_6, were also observed in the patterns, so these were

added as additional phases, with Sr_2CoIrO_6 modelled as a simple undistorted cubic double perovskite to minimise the number of refined parameters for this phase. The fits to the NPD data are shown in Figure 8.3-8.5, with the refined parameters presented in Table 8.2 and selected bond lengths in Table 8.3.

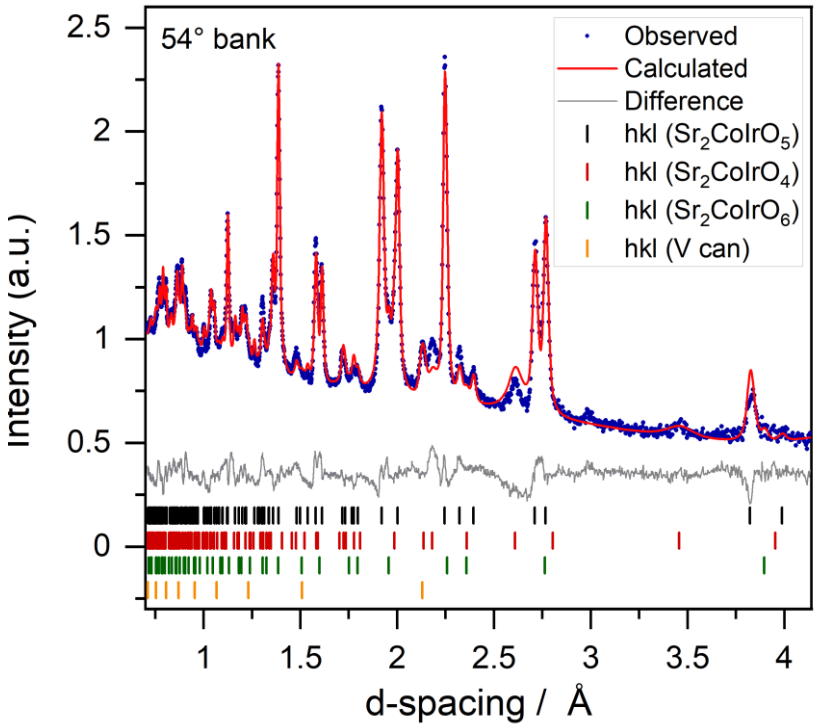

Figure 8.3: Observed, calculated and difference plots from the structural refinement of Sr_2CoIrO_5 against NPD data collected at room temperature from the 54° bank of the POLARIS diffractometer.

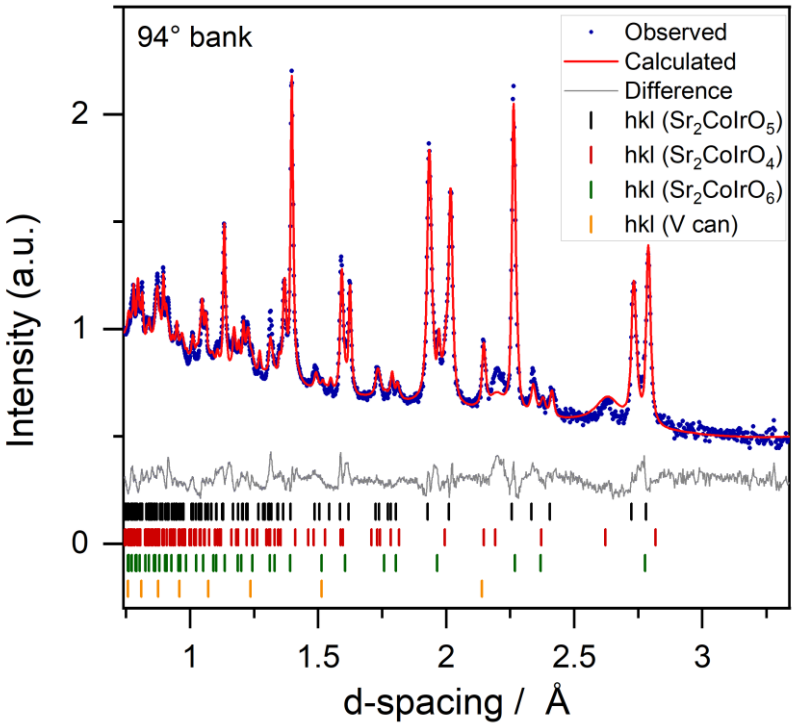

Figure 8.4: Observed, calculated and difference plots from the structural refinement of Sr_2CoIrO_5 against NPD data collected at room temperature from the 94° bank of the POLARIS diffractometer.

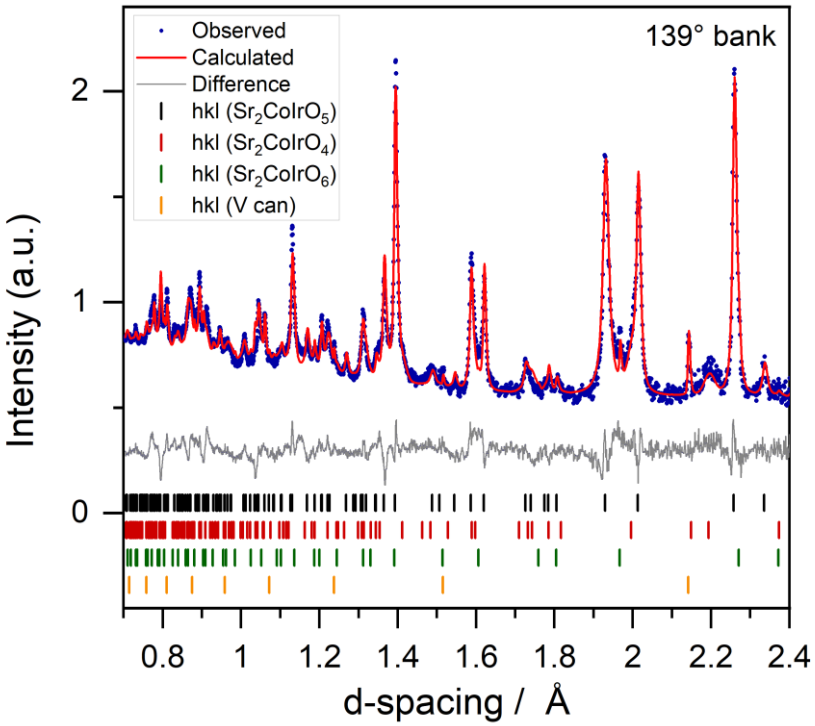

Figure 8.5: Observed, calculated and difference plots from the structural refinement of Sr_2CoIrO_5 against NPD data collected at room temperature from the 139° bank of the POLARIS diffractometer.

Table 8.2: Parameters from the structural refinement of Sr_2CoIrO_5 against NPD data collected at room temperature from the POLARIS diffractometer. The occupancies at the transition metal sites were fixed at the values observed in the Sr_2CoIrO_6 parent phase. The fractional coordinates of the Sr_2CoIrO_4 phase were fixed at the values determined from NPD in Chapter 9.

Sr_2CoIrO_5, space group *I*4/*mmm* (No. 139), 83.3(8) wt%						
		x	***y***	***z***	**Occ.**	**B_{iso} (Å^2)**
Sr(1)	4*d*	0	½	¼	1	0.18(6)
Co(1)/Ir(1)	2*a*	0	0	0	0.934/0.066	0.9(2)
Ir(2)/Co(2)	2*b*	½	½	0	0.934/0.066	0.11(8)
O(1)	8*h*	0.2600(8)	0.2600(8)	0	0.743(6)	2.6(1)
O(2)	4*e*	0	0	0.254(1)	1	0.94(8)
a = 5.4590(4) Å, c = 8.0541(6) Å						
V = 240.02(4) Å^3						
Sr_2CoIrO_4, space group *I*4/*mmm* (No. 139), 14.6(8) wt%						
		x	***y***	***z***	**Occ.**	**B_{iso} (Å^2)**
Sr(1)	4*d*	0	½	¼	1	1.3(2)
Co(1)/Ir(1)	2*a*	0	0	0	0.934/0.066	1.3(2)
Ir(2)/Co(2)	2*b*	½	½	0	0.934/0.066	1.3(2)
O(1)	8*h*	0.2509	0.2509	0	1	1.3(2)
a = 5.649(1) Å, c = 6.972(5) Å						
V = 222.5(2) Å^3						
Sr_2CoIrO_6, space group *Fm*$\bar{3}$*m* (No. 225), 2.1(8) wt%						
		x	***y***	***z***	**Occ.**	**B_{iso} (Å^2)**
Sr(1)	8*c*	¼	¼	¼	1	0.1(2)
Co(1)/Ir(1)	4*a*	0	0	0	0.934/0.066	0.1(2)
Ir(2)/Co(2)	4*b*	½	0	0	0.934/0.066	0.1(2)
O(1)	24*e*	¼	0	0	1	0.1(2)
a = 7.8703(9) Å						
V = 487.5(2) Å^3						
R_{wp} = 4.41%, R_p = 3.44%, *gof* = 0.04						

Table 8.3: Selected bond lengths in Sr_2CoIrO_5 at room temperature, extracted from the structural parameters in Table 8.2, and corresponding bond valence sums for cobalt and iridium.

Bond	Bond length (Å)	BVS
Co−O1	2.006(5)	+2.01
Co−O2	2.067(8)	
Ir−O1	1.854(5)	+4.70
Ir−O2	1.960(8)	

8.4.3 Thermogravimetric analysis

Thermogravimetric data were collected from Sr_2CoIrO_5 whilst heating under flowing oxygen, indicating a mass gain of 3.9%, as shown in Figure 8.6. Assuming full oxidation back to Sr_2CoIrO_6, this corresponds to an initial composition of $Sr_2CoIrO_{4.74}$. This is broadly consistent with the expected composition of Sr_2CoIrO_5, with the discrepancy arising from the presence of Sr_2CoIrO_4 in the sample.

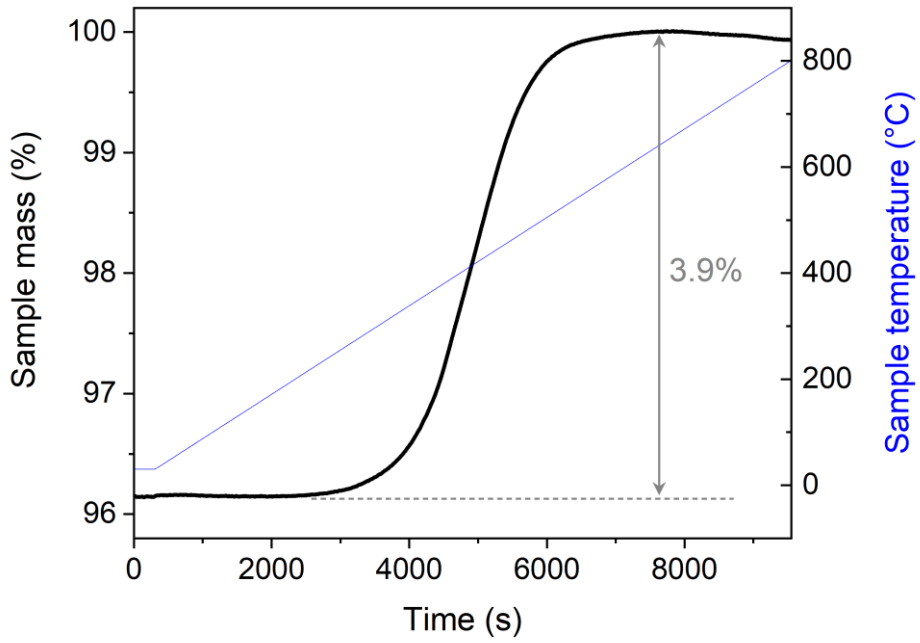

Figure 8.6: TGA trace when Sr_2CoIrO_5 is heated under flowing oxygen.

8.4.4 X-ray absorption spectroscopy

XAS measurements were performed on Sr_2CoIrO_5, with Sr_2CoIrO_6 and $YBaCo_2O_5$ acting as standards. The measurements were performed with a laboratory instrument at energies between 7650 and 8200 eV to allow the Co K-edge (7709 eV) to be observed. The spectra were calibrated using Co foil and normalised up to 7950 eV. The data at the XANES edges are shown in Figure 8.7.

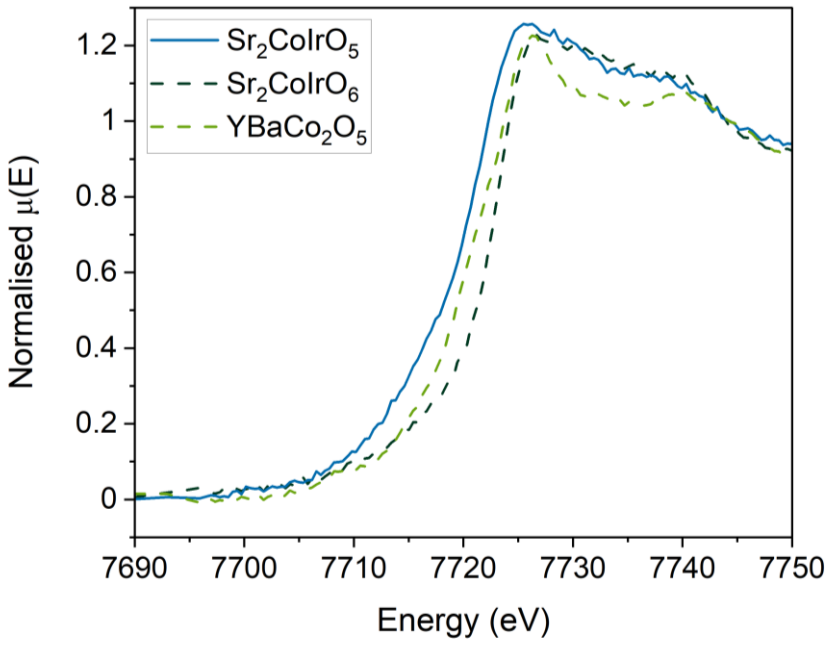

Figure 8.7: XANES Co K-edge for Sr_2CoIrO_5, with Sr_2CoIrO_6 (Co^{3+}) and $YBaCo_2O_5$ ($Co^{2.5+}$) included as standards.

The position of the XANES edge for Sr_2CoIrO_5 is at lower energy than $YBaCo_2O_5$, suggesting that cobalt is present as Co^{II} in this compound. This is consistent with the bond valence sum of +2.01 for cobalt in Sr_2CoIrO_5, calculated using the Co−O bond lengths in Table 8.3. A cobalt oxidation state of +2 would imply that iridium is present as Ir^{IV} in this compound.

8.5 Magnetic characterisation of Sr_2CoIrO_5

8.5.1 Magnetic behaviour

Magnetisation data collected from Sr_2CoIrO_5 as a function of temperature are presented in Figure 8.8, and magnetisation-field isotherms collected at 5 K and 300 K are presented in Figure 8.9. Fitting of the Curie-Weiss law to the data at temperatures above 200 K gives a value for C of 4.63(2) cm^3 K mol^{-1} and a value for θ of +74(1) K. The value for C is larger than the value of 2.25 cm^3 K mol^{-1} predicted for Co^{II}/Ir^{IV} using the spin-only approximation, suggesting that the magnetism of this compound does not follow simple Curie-Weiss behaviour.

The observation of a local maximum in the ZFC curve at 35 K indicates that a magnetic transition occurs at this temperature. The slight divergence of the curves below 35 K, in combination with the vertical displacement of the hysteresis loop at 5 K suggests that the compound adopts a spin glass state at low temperature. This spin glass behaviour was confirmed by AC susceptibility measurements, shown in Figure 8.10, in which the susceptibility maximum shifts to higher temperature as the frequency of the applied field is increased. Fitting of the data to Equation 43 yields a value of $6(3) \times 10^6$ Hz for ω_0, corresponding to a relaxation time, τ_0, of $1.0(5) \times 10^{-6}$ s, and a value of 3.6(2) for the dynamical critical exponent, zv.

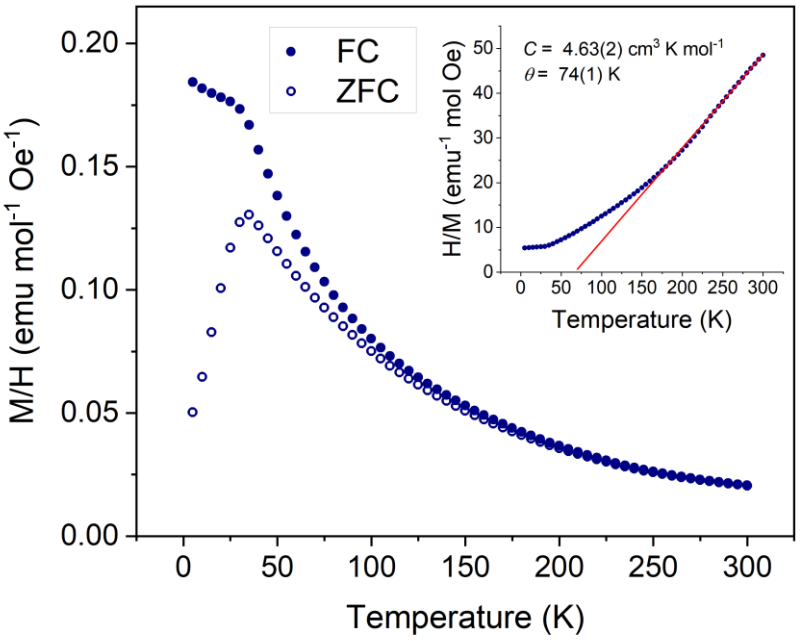

Figure 8.8: Magnetisation data collected from Sr_2CoIrO_5 as a function of temperature, measured in a field of 100 Oe under both ZFC and FC conditions.

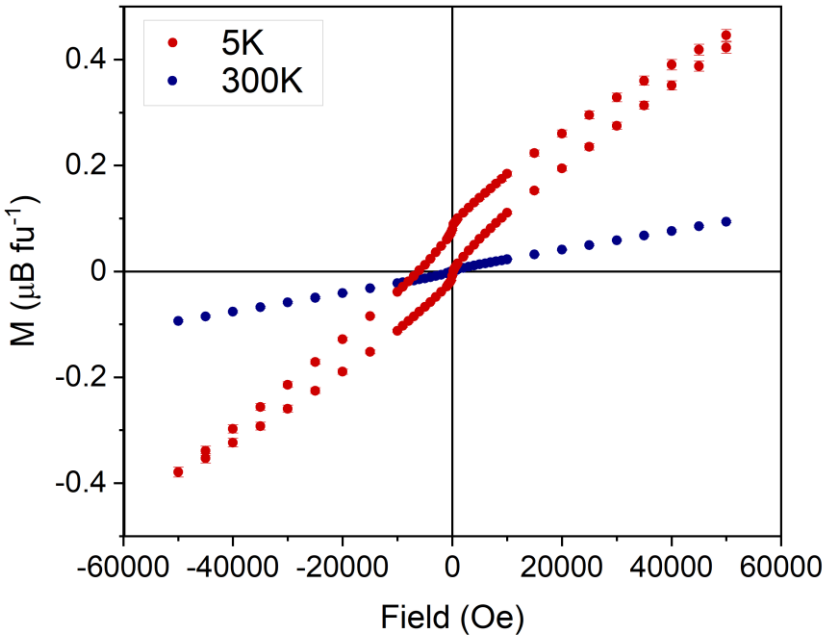

Figure 8.9: Magnetisation-field isotherms for Sr_2CoIrO_5 measured at 5 K and 300 K.

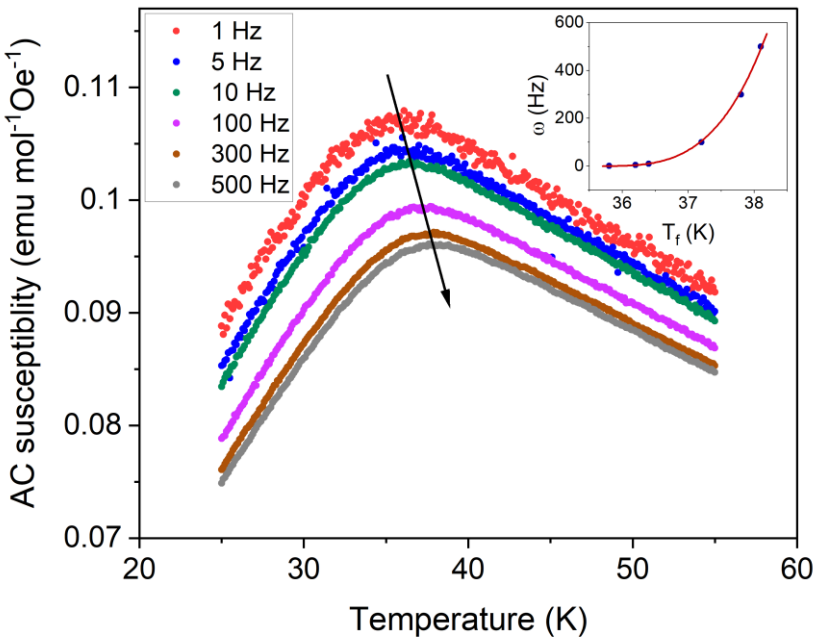

Figure 8.10: AC susceptibility as a function of temperature for Sr_2CoIrO_5, measured at frequencies between 1 Hz and 500 Hz. The measurements were performed using an AC field with amplitude of 2.5 Oe, and an applied DC field of 2 Oe. The inset shows the variation of T_f with ω for Sr_2CoIrO_5. The red line shows the fit to the data using the power law shown in Equation 43.

8.5.2 Muon spin rotation spectroscopy

μ^+-SR data collected from Sr_2CoIrO_5 as a function of temperature are shown in Figure 8.11.

In a paramagnetic sample, the spins are fluctuating very fast relative to the timescale of the measurement. As such, the deviation of the muon spin from its initial polarisation essentially follows a random walk and, as a consequence, loss of asymmetry is very slow. This slow loss of asymmetry can be observed in the data collected from Sr_2CoIrO_5 at 150 K, indicating that the sample is paramagnetic at this temperature.

If the sample contains static moments (relative to the timescale of the measurement), the muon spin precesses around the field in the sample. Due to this precession, there is much faster dephasing of the muon spins, leading to a rapid loss of asymmetry. If long-range magnetic

order is present in the sample, the precession of the muon spins can be observed as oscillations superimposed upon the curve.

At temperatures below 75 K, there is very fast loss of asymmetry observed in the data collected from Sr_2CoIrO_5, indicating that static moments are present in the sample at these temperatures. The observation that the apparent transition temperature of 50−75 K from μ^+-SR is higher than that of ~36 K from the data in Section 8.5.1 can be attributed to the fact that the timescale of the μ^+-SR measurement (< 7 μs) is much shorter than that of the magnetisation measurements (> 1 ms). This means that, although T_g appears to be in the range 36−38 K from AC susceptibility measurements, the slow nature of the spin fluctuations above T_g means that the spins appear static up to 50−75 K in the μ^+-SR measurements. The absence of oscillations in the data is consistent with the result expected for a spin-glass, due to the fact that there is no long-range magnetic order present.

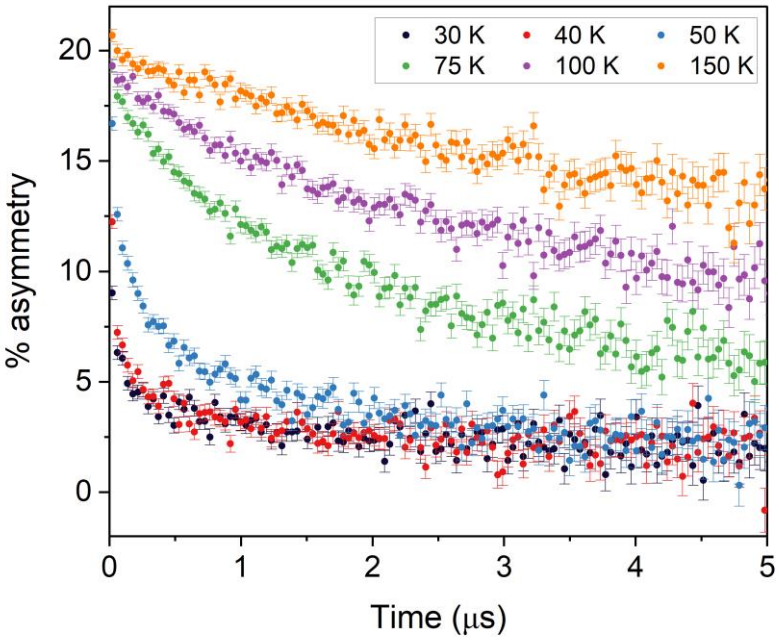

Figure 8.11: μ^+-SR data collected from Sr_2CoIrO_5 as a function of temperature.

8.6 Discussion

8.6.1 Anion disorder in Sr_2CoIrO_5

Many different types of anion ordering have been observed for oxygen-deficient perovskites with general formula $A_2B_2O_5$, with some examples shown in Figure 8.12. In some cases, the anion ordering is driven by the requirement to satisfy the preferred coordination environments of the transition metals. For example, the d^8 electronic configuration of Ni^{II} drives $La_2Ni_2O_5$ to adopt the anion-ordered structure shown in Figure 8.12(b), due to the energetic favourability for Ni^{II} to adopt a square-planar coordination environment.[144] Similarly, the d^4 electronic configuration of Mn^{III} drives $Sr_2Mn_2O_5$ to adopt the MnO_5 'herringbone' structure shown in Figure 8.12(c) to accommodate the strong Jahn-Teller effect associated with this electronic configuration.[145–147] Meanwhile, $LaSrCoRuO_5$ adopts the structure shown in Figure 8.12(d), which is associated with charge ordering of Co^+ and Co^{3+} across the square-planar and octahedral sites, respectively.[143]

If there is no electronic driving force for the transition metals to adopt a specific coordination environment, the brownmillerite structure (shown in Figure 8.12(a)) is often adopted, as this represents the most efficient packing arrangement of ions; this structure is adopted by compounds such as $Sr_2Co_2O_5$ and $Sr_2Fe_2O_5$.[148,149] However, it is rare for compounds to exhibit both B-site rock-salt cation order and brownmillerite anion ordering, as there is no relationship between these two ordering motifs and results in the two B-site cations occupying both octahedral and tetrahedral coordination sites.

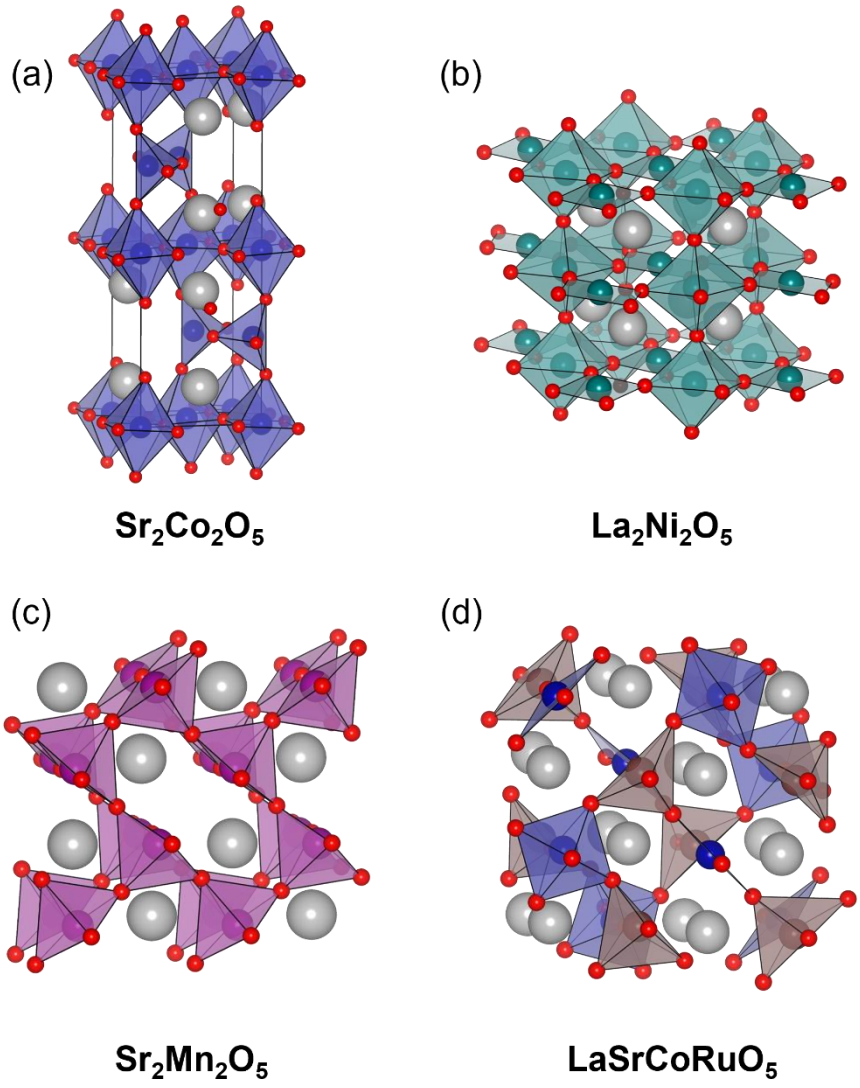

Figure 8.12: Crystal structures of some perovskite-based $A_2B_2O_5$ compounds with different anion vacancy ordered arrangements.

The d^7 electronic configuration of Co^{II} and the d^5 electronic configuration of Ir^{IV} in Sr_2CoIrO_5 do not provide any strong driving force for the transition metals to adopt specific coordination environments and, as such, the $La_2Ni_2O_5$- and $Sr_2Mn_2O_5$-type ordering arrangements are not adopted. Furthermore, the compound does not adopt the brownmillerite structure, in contrast to the all-cobalt analogue ($Sr_2Co_2O_5$), as it would require some of the Ir^{IV} ions to have tetrahedral coordination. Ir^{IV} ions in this environment would contain an electron in a relatively high energy t_2-type orbital, which is energetically unfavourable. As such, an anion disordered arrangement, in which the transition metals are present in square-pyramidal coordination

environments, is adopted. This is analogous to the situation for Ca_2MnIrO_5, whereby the structure consists of a disordered arrangement of MnO_5 and IrO_5 square-based pyramids.[150]

NPD data show that the anion vacancies in Sr_2CoIrO_5 are disordered across the O1 sites. Although this initially implies that there is complete freedom in the positions of the vacancies, the likely requirement for the transition-metals to be 5-coordinate would constrain the possible sites that the vacancies can occupy. As illustrated in Figure 8.13, when a vacancy is introduced at an anion site, the remaining anion sites on both the neighbouring transition metals must be occupied by oxide ions and, as such, Sr_2CoIrO_5 is, in fact, composed of corner-sharing $(Co/Ir)_2O_{10}$ units (Figure 8.13(c)). The positions of the anion vacancies are, therefore, unlikely to be completely random, but constrained by the possible packing arrangements of these $(Co/Ir)_2O_{10}$ units.

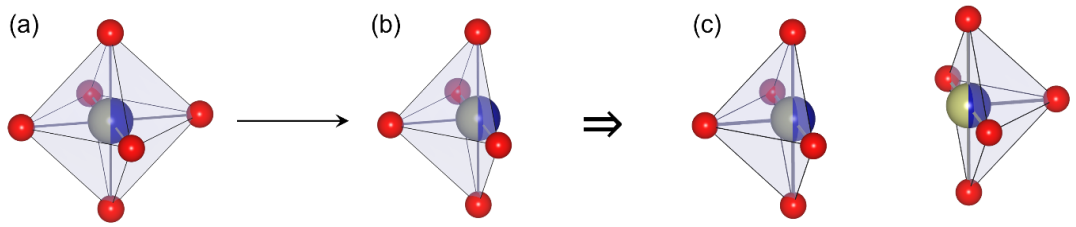

Figure 8.13: Removal of an oxide ion from a $(Co/Ir)O_6$ octahedron, (a), to give $(Co/Ir)O_5$ in a square-based pyramidal coordination, (b), which imposes a specific coordination on the neighbouring $(Co/Ir)O_5$ species, resulting in the $(Co/Ir)_2O_{10}$ unit in (c). As such, the anion vacancy positions in Sr_2CoIrO_5 are likely to be constrained by the packing arrangements of $(Co/Ir)_2O_{10}$ units.

Unlike Ca_2MnIrO_5, which adopts an $a^+b^-b^-$ tilted structure in the *Pnma* space group, Sr_2CoIrO_5 adopts an *I*4/*mmm* structure with no tilting distortions. This can be attributed to the smaller sizes of the B-site cations (Co^{II} and Ir^{IV} compared to Mn^{III} and Ir^{III}) and the larger size of the A-site cation (Sr^{2+} compared to Ca^{2+}), which means that the Goldschmidt tolerance factor of Sr_2CoIrO_5 is larger than that of Ca_2MnIrO_5.

8.6.2 Magnetic behaviour of Sr_2CoIrO_5

As determined in Section 8.4.4, the cobalt in Sr_2CoIrO_5 is likely to be present as Co^{II}, which would imply an iridium oxidation state of Ir^{IV}. In the Sr_2CoIrO_5 structure, both cobalt and iridium adopt square-based pyramidal geometries, which would yield the crystal field splitting arrangements shown in Figure 8.14(a), assuming that Co^{II} is high-spin and Ir^{IV} is low-spin.

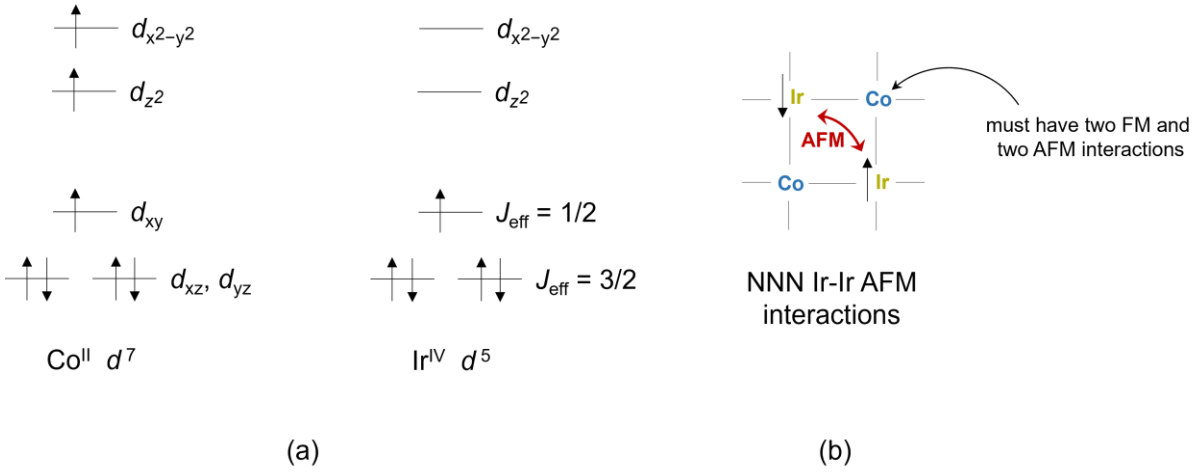

Figure 8.14: Proposed electronic configurations for the transition metals in Sr_2CoIrO_5 (a) and illustration of a possible source of magnetic frustration in Sr_2CoIrO_5 (b).

The magnetic data in Section 8.5 show that Sr_2CoIrO_5 forms a spin glass state below ~35 K. For a spin glass state to propagate, both chemical disorder and magnetic frustration must be present. The requirement for chemical disorder is satisfied by the anion vacancy disorder at the O1 site. The magnetic frustration can be attributed to the presence of Ir^{IV} in the compound, using a similar argument as for $Sr_4CoIrO_{6.5}H_{1.5}$ and Sr_4MnIrO_8. From the Goodenough-Kanamori rules, the nearest-neighbour superexchange interactions between Co^{II} and Ir^{IV} in Sr_2CoIrO_5 are expected to be ferromagnetic. However, Ir^{IV} contains an unpaired electron in a spatially diffuse $5d_{xy}$-type orbital, which means that relatively strong direct antiferromagnetic exchange can occur between iridium ions located diagonally from each other. If all the Ir^{IV}–Ir^{IV} antiferromagnetic interactions are satisfied, this would mean that only 50% of the ferromagnetic Co^{II}–Ir^{IV} interactions can be satisfied, as illustrated in Figure 8.14(b). As such,

if these two coupling interactions have a similar magnitude, this would lead to magnetic frustration.

8.7 Conclusion

Reaction of the double perovskite, Sr_2CoIrO_6, with a Zr getter yields the infinite-layer phase, Sr_2CoIrO_4, which forms via an Sr_2CoIrO_5 intermediate. In this chapter, the synthesis and magnetic properties of Sr_2CoIrO_5 were discussed. Sr_2CoIrO_5 adopts a structure with *I*4/*mmm* symmetry in which 25% of the equatorial oxide ion sites are vacant, with the vacancies adopting an anion-disordered arrangement. Below 35 K, this compound exhibits spin glass behaviour, with the magnetic frustration attributed to incompatible Co−Ir ferromagnetic superexchange and Ir−Ir antiferromagnetic direct exchange interactions.

Chapter 9 – Synthesis and magnetism of Sr_2CoIrO_4

9.1 Introduction

As described in Chapter 8, heating Sr_2CoIrO_6 in the presence of a Zr getter allows the oxygen-deficient phases, Sr_2CoIrO_5 and Sr_2CoIrO_4, to be prepared. This chapter discusses the synthesis and magnetic behaviour of the infinite-layer phase, Sr_2CoIrO_4. To investigate the effects of epitaxial strain, the reactions were performed on both powder and a thin-film sample of Sr_2CoIrO_6 grown on a single-crystal $SrTiO_3$ substrate orientated along the (001) direction.

9.2 Synthesis of Sr_2CoIrO_4

To prepare a sample of Sr_2CoIrO_4, a reaction was set up as described in Section 8.3. The sample was initially heated with a Zr getter for 5 cycles of 4 days at 400 °C. At this point, PXRD data showed that the reaction was almost complete, but a small amount of Sr_2CoIrO_5 was still present. Previous synthesis attempts indicated that continued heating at 400 °C would lead to the onset of non-topochemical decomposition. Therefore, the sample was heated for 2 further cycles of 6 hours at 380 °C and 390 °C, respectively, to yield Sr_2CoIrO_4 as a pure phase. Thorough grinding was performed between each heating cycle in an Ar-filled glovebox.

9.3 Structural characterisation of Sr_2CoIrO_4

9.3.1 Room temperature synchrotron powder X-ray diffraction

A structural model of a B-site cation-ordered infinite-layer phase with *I*4/*mmm* symmetry and composition Sr_2CoIrO_4 was constructed and refined against SXRD data collected from the sample, with the fit shown in Figure 9.1 and refinement parameters detailed in Table 9.1. This yielded lattice parameters of a = 5.6461(2) Å and c = 6.9453(3) Å, corresponding to an expansion of the *xy*-plane and contraction in the *z*-direction relative to the Sr_2CoIrO_6 parent

phase (a = 5.54 Å, b = 5.56 Å, c = 7.84 Å). A small, broad peak is observed at 2θ ~ 17.2°, which is attributed to a cubic perovskite-type phase, likely related to unreacted Sr_2CoIrO_6 or Sr_2CoIrO_5.

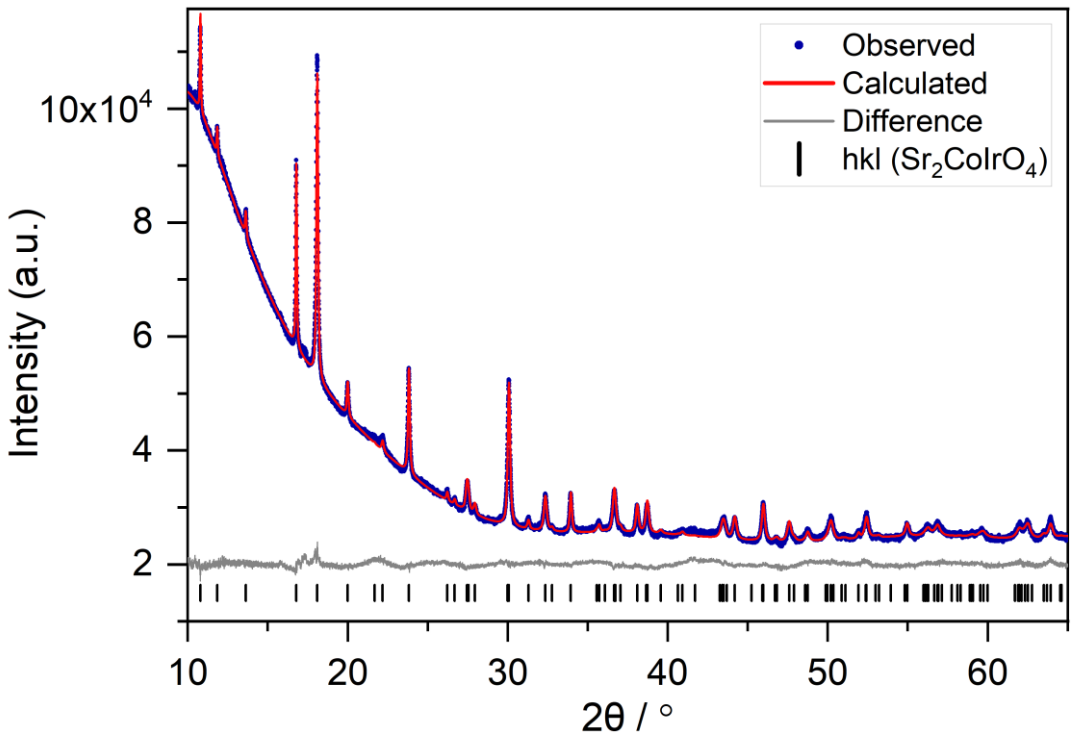

Figure 9.1: Observed, calculated and difference plots from the structural refinement of Sr_2CoIrO_4 against SXRD data collected at room temperature using a wavelength of 0.825 Å.

Table 9.1: Parameters from the structural refinement of Sr_2CoIrO_4 against SXRD data collected at room temperature. The occupancies at the transition metal sites were fixed at the values observed in the Sr_2CoIrO_6 parent phase.

Sr_2CoIrO_4, space group *I*4/*mmm* (No. 139)						
		x	***y***	***z***	**Occ.**	**B_{iso} (Å^2)**
Sr(1)	4*d*	0	½	¼	1	1.28(6)
Co(1)/Ir(1)	2*a*	0	0	0	0.934/0.066	1.42(7)
Ir(2)/Co(2)	2*b*	½	½	0	0.934/0.066	1.75(3)
O(1)	8*h*	¼	¼	0	1	0.53(7)
a = 5.6463(2) Å, c = 6.9457(3) Å						
V = 221.44(2) Å^3						
R_{wp} = 1.18%, R_p = 0.90%, *gof* = 2.25						

9.3.2 Room temperature neutron powder diffraction

The ideal, undistorted infinite-layer structure is described by *I*4/*mmm* symmetry. However, the MO_4 square-planar units can in principle undergo rotations and deformations that lower the symmetry. To evaluate whether Sr_2CoIrO_4 adopts any of these symmetry-lowering distortions, structural models were constructed in the *I*4/*m*, *I*112/*m* and *P*12$_1$1 space groups. In the *I*4/*m* space group, the MO_4 square-planar units retain their 4-fold symmetry but are allowed to rotate around the *z*-axis. Meanwhile, the *I*112/*m* and *P*12$_1$1 space groups allow deformations of the MO_4 square-planes such that they no longer have 4-fold symmetry. These two monoclinic models differ in the phase of rotations of the MO_4 units between layers; the *I*112/*m* model describes an $a^0a^0c^-$ rotation, whilst the *P*12$_1$1 model describes an $a^0a^0c^+$ rotation.[101] Models in these four space groups, with exaggerated distortions, are shown in Figure 9.2. These models were then refined against NPD data from the 54°, 94° and 139° banks of the POLARIS diffractometer. The fitting statistics from these refinements, along with selected bond lengths and angles, are shown in Table 9.2. Refinements performed using the distorted models did not provide any visual improvement to the fits. Comparison of the fitting statistics for the refinements using the *I*4/*mmm*, *I*4/*m* and *I*112/*m* models (Table 9.2) show that the lower-symmetry models do not provide any significant improvement to the fits. Whilst the *P*12$_1$1 model appears to give improved fitting statistics, the increased number of oxygen sites, each of which have refinable coordinates, means that the errors associated with the bond angles and bond lengths are larger and, as a result, the refined model is essentially indistinguishable from the undistorted model. Therefore, it was concluded that Sr_2CoIrO_4 adopts an undistorted infinite-layer structure that can be described in the *I*4/*mmm* space group. The final fits to the NPD data using the *I*4/*mmm* structural model are shown in Figure 9.3-9.5, with the refinement parameters detailed in Table 9.2 and selected bond lengths presented in Table 9.4. The refined structure is shown in Figure 9.6.

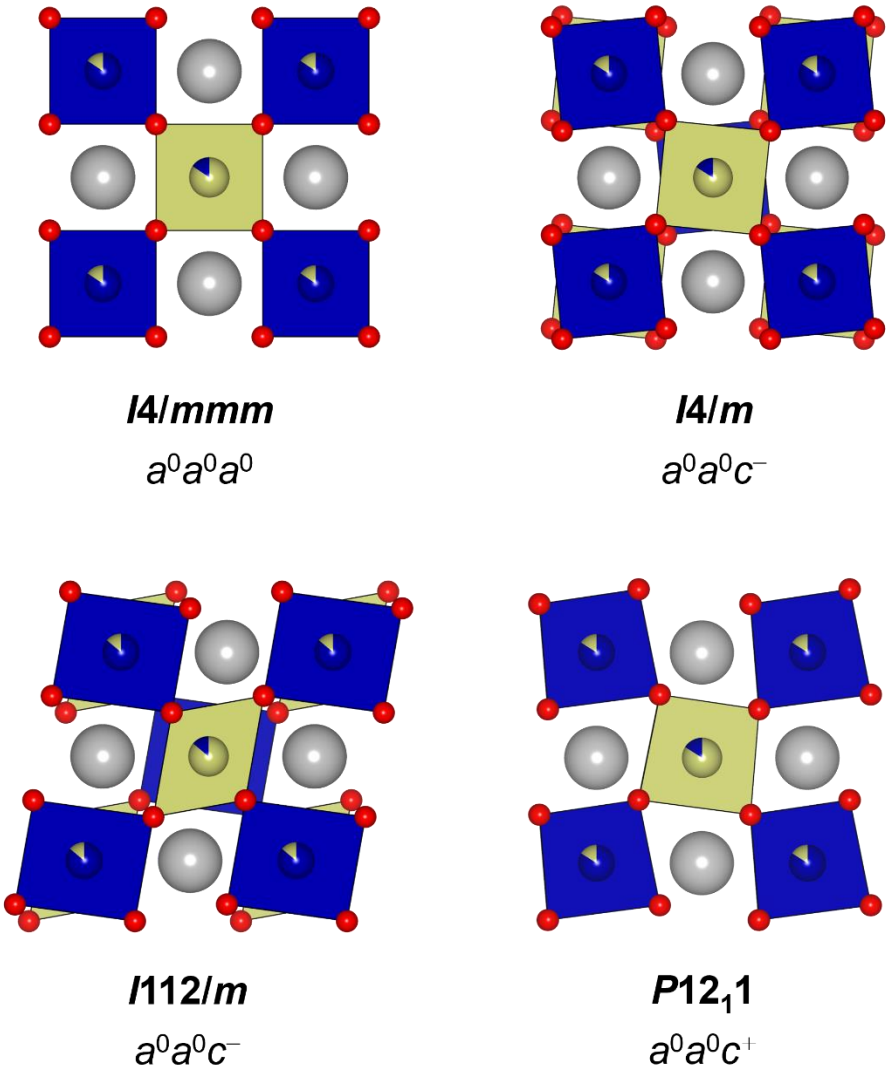

Figure 9.2: Comparison of the undistorted *I*4/*mmm* infinite-layer structure with the distorted *I*4/*m*, *I*112/*m* and $P12_11$ structures. The magnitudes of the distortions have been exaggerated for clarity.

Table 9.2: Fitting statistics and selected bond lengths/angles from the refinements against NPD data collected from Sr_2CoIrO_4 using an undistorted *I*4/*mmm* structural model and distorted *I*4/*m*, *I*112/*m* and $P12_11$ structural models.

	I*4/*mmm	***I*4/*m***	***I*112/*m***	***P*12$_1$1**
R_{wp} (%)	4.389	4.387	4.386	4.326
R_p (%)	3.404	3.403	3.377	3.369
Co−O−Ir angles (°)	180	180(3)	179(1),178(1)	180(7), 180(3)
O−Co−O distances (Å)	3.986(4)	3.99(8)	4.05(4), 3.95(5)	4.0(2), 4.0(2)
O−Ir−O distances (Å)	3.996(4)	3.99(8)	4.03(4), 3.94(5)	4.0(2), 4.0(2)

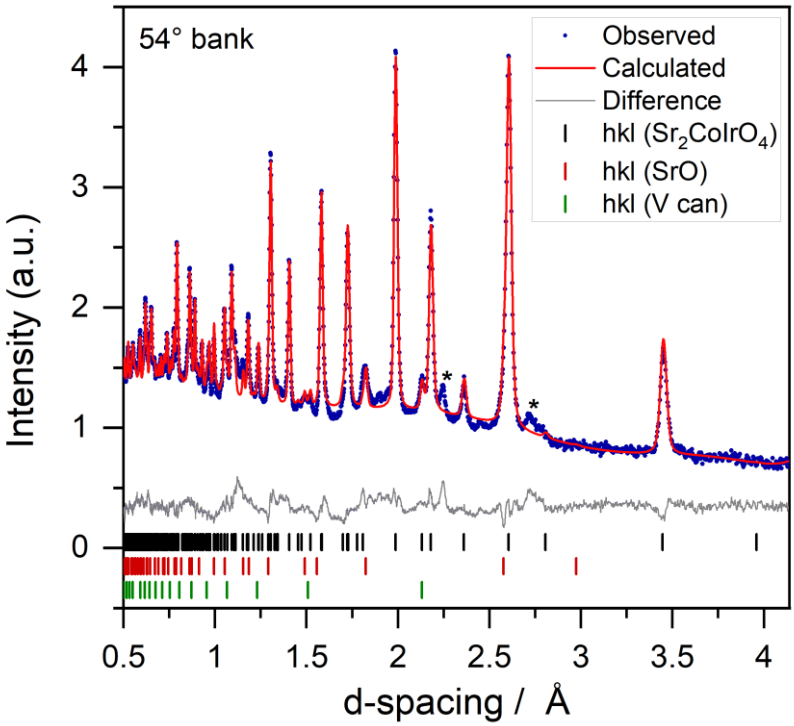

Figure 9.3: Observed, calculated and difference plots from the structural refinement of Sr_2CoIrO_4 against NPD data collected at room temperature from the 54° bank of the POLARIS diffractometer using the undistorted *I*4/*mmm* structural model. The peaks denoted by asterisks are attributed to the cubic perovskite-type impurity identified in Section 9.3.1.

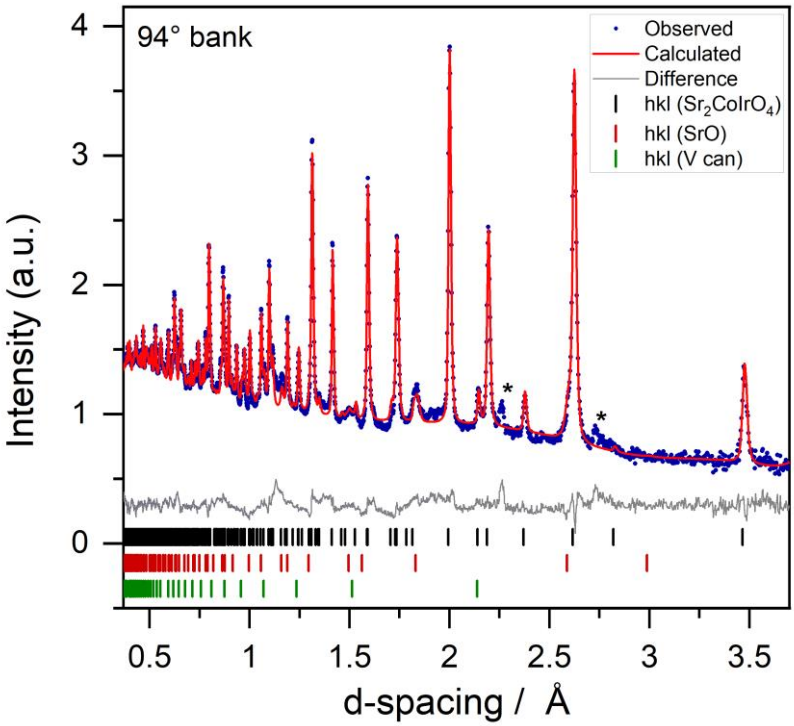

Figure 9.4: Observed, calculated and difference plots from the structural refinement of Sr_2CoIrO_4 against NPD data collected at room temperature from the 94° bank of the POLARIS diffractometer using the undistorted *I*4/*mmm* structural model. The peaks denoted by asterisks are attributed to the cubic perovskite-type impurity identified in Section 9.3.1.

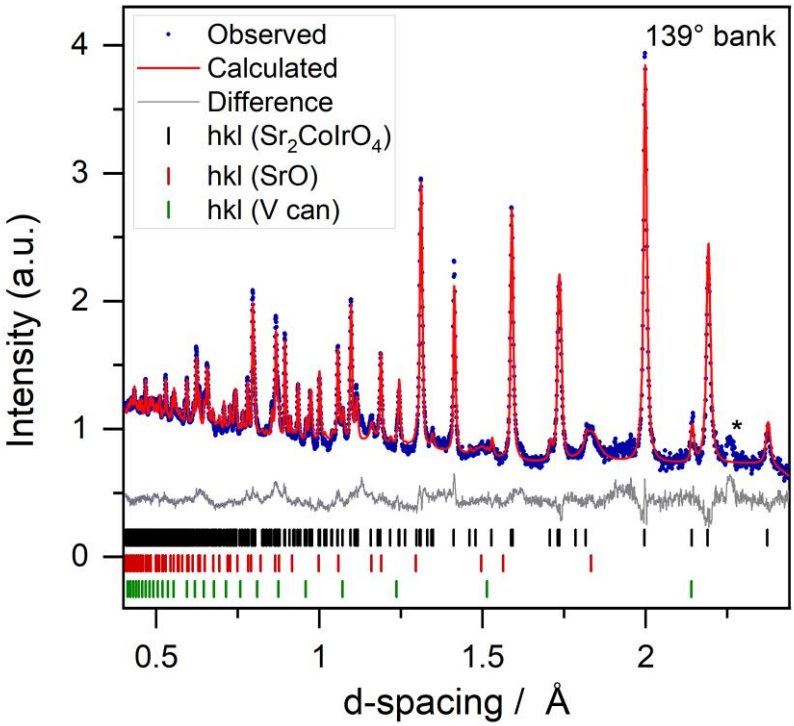

Figure 9.5: Observed, calculated and difference plots from the structural refinement of Sr_2CoIrO_4 against NPD data collected at room temperature from the 54° bank of the POLARIS diffractometer using the undistorted *I*4/*mmm* structural model. The peaks denoted by asterisks are attributed to the cubic perovskite-type impurity identified in Section 9.3.1.

Table 9.3: Parameters from the structural refinement of Sr_2CoIrO_4 against NPD data collected at room temperature from the POLARIS diffractometer using the undistorted *I*4/*mmm* structural model. The occupancies at the transition metal sites were fixed at the values observed in the Sr_2CoIrO_6 parent phase.

Sr_2CoIrO_4, space group *I*4/*mmm* (No. 139)						
		x	***y***	***z***	**Occ.**	**B_{iso} (Å^2)**
Sr(1)	4*d*	0	½	¼	1	0.08(2)
Co(1)/Ir(1)	2*a*	0	0	0	0.934/0.066	0.1(1)
Ir(2)/Co(2)	2*b*	½	½	0	0.934/0.066	0.09(3)
O(1)	8*h*	0.2509(3)	0.2509(3)	0	1	0.17(2)
a = 5.6456(2) Å, c = 6.9430(3) Å						
V = 221.29(2) Å^3						
R_{wp} = 3.90%, R_p = 3.09%, *gof* = 0.05						

Table 9.4: Selected bond lengths in Sr_2CoIrO_4 at room temperature, extracted from the structural parameters in Table 9.3, and corresponding bond valence sums for cobalt and iridium.

Bond	Bond length (Å)	BVS
Co−O	2.003(2)	+1.73
Ir−O	1.989(2)	+2.90

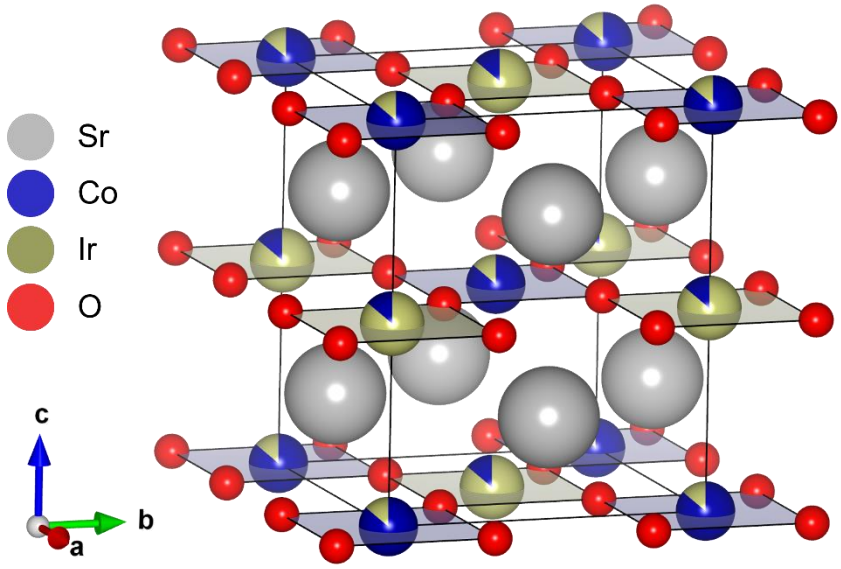

Figure 9.6: Refined structure of Sr_2CoIrO_4 with *I*4/*mmm* symmetry.

9.3.3 Thermogravimetric analysis

Thermogravimetric data were collected from Sr_2CoIrO_4 whilst heating under flowing oxygen, indicating a mass gain of 6.6%, as shown in Figure 9.7. Assuming full oxidation back to Sr_2CoIrO_6, this corresponds to an initial composition of $Sr_2CoIrO_{3.87}$. This is broadly consistent with the expected composition of Sr_2CoIrO_4, with the discrepancy likely to arise from the presence of small amounts of Co and Ir metal in the sample, which are oxidised during the measurement.

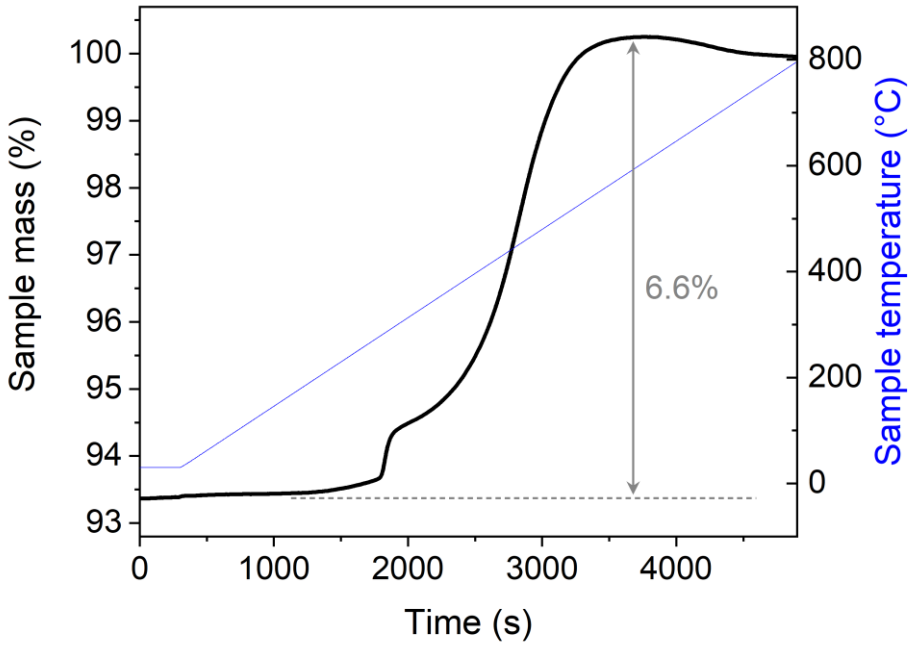

Figure 9.7: TGA trace when Sr_2CoIrO_4 is heated under flowing oxygen.

9.3.4 X-ray absorption spectroscopy

XAS measurements were performed on Sr_2CoIrO_4, with Sr_2CoIrO_6 and $YBaCo_2O_5$ acting as standards. The measurements were performed with a laboratory instrument at energies between 7650 and 8200 eV to allow the Co K-edge (7709 eV) to be observed. The spectra were calibrated using Co foil and normalised up to 7950 eV. The data at the XANES edges are shown in Figure 9.8.

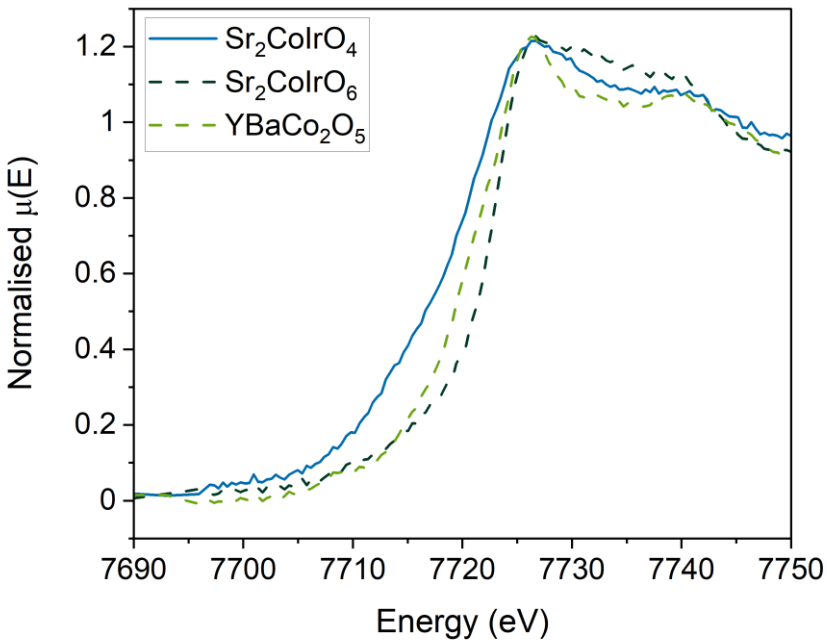

Figure 9.8: XANES Co K-edge for Sr_2CoIrO_4, with Sr_2CoIrO_6 (Co^{3+}) and $YBaCo_2O_5$ ($Co^{2.5+}$) included as standards.

The position of the XANES edge for Sr_2CoIrO_4 is at lower energy than $YBaCo_2O_5$, suggesting that cobalt is present as Co^{II} in this compound. This is broadly consistent with the bond valence sum of +1.73 for cobalt in Sr_2CoIrO_4 (Table 9.4) and would imply that iridium has an oxidation state of Ir^{II}.

9.4 Magnetic characterisation of Sr_2CoIrO_4

9.4.1 Magnetic behaviour

Magnetisation data collected from Sr_2CoIrO_4 as a function of temperature are presented in Figure 9.9, and magnetisation-field isotherms collected at 5 K and 300 K are presented in Figure 9.10. The local maximum in the ZFC curve at 35 K, in combination with the opening of the hysteresis loop at 5 K, indicates that the compound adopts a canted antiferromagnetic ground state at low temperature. Inspection of the inverse magnetisation curve in the inset of Figure 9.9 shows a substantial deviation from linearity below 175 K, suggesting a higher

transition temperature than that of ~35 K implied from the magnetisation curve. Fitting of the data to the Curie-Weiss law above 250 K gives a value for θ of +170(3) K and a value for C of 5.11(4) cm^3 K mol^{-1}, which cannot be rationalised on the basis of the spin-only approximation, indicating that the magnetic behaviour of this compound does not follow simple Curie-Weiss behaviour.

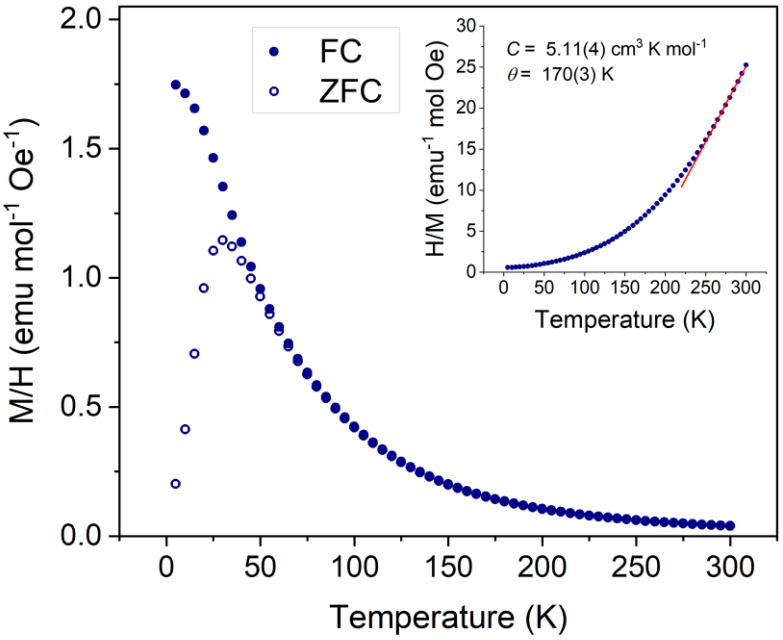

Figure 9.9: Magnetisation data collected from Sr_2CoIrO_4 as a function of temperature, measured in a field of 100 Oe under both ZFC and FC conditions.

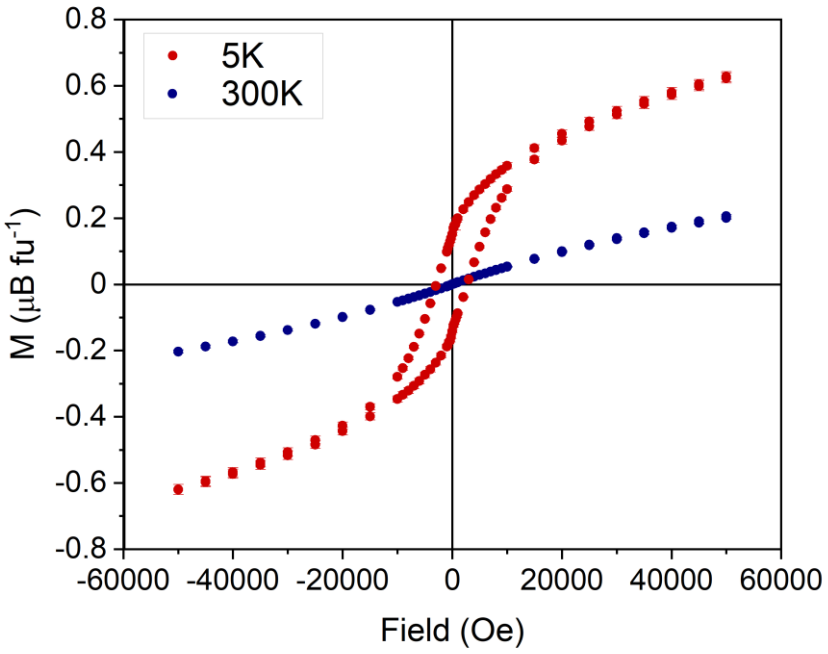

Figure 9.10: Magnetisation-field isotherms for Sr_2CoIrO_4 measured at 5 K and 300 K.

9.4.2 Muon spin rotation spectroscopy

μ^+-SR data collected from Sr_2CoIrO_4 as a function of temperature are shown in Figure 9.11.

Similar to the disucssion in Chapter 8, the slow loss of asymmetry observed in the data above 140 K suggests that the sample exhibits paramagnetic behaviour at these temperatures. Meanwhile, the much faster loss of asymmetry below 140 K suggests that static moments are present in the sample at these temperatures. This would imply that the magnetic transition temperature for Sr_2CoIrO_4 is 135−140 K. Since compounds with long-range magnetic order typically exhibit oscillations in the signal due to the precession of the muon spin, the absence of these oscillations suggests that the magnetic order is somewhat inhomogeneous, which could arise from the presence of anti-site disorder at the B-sites.

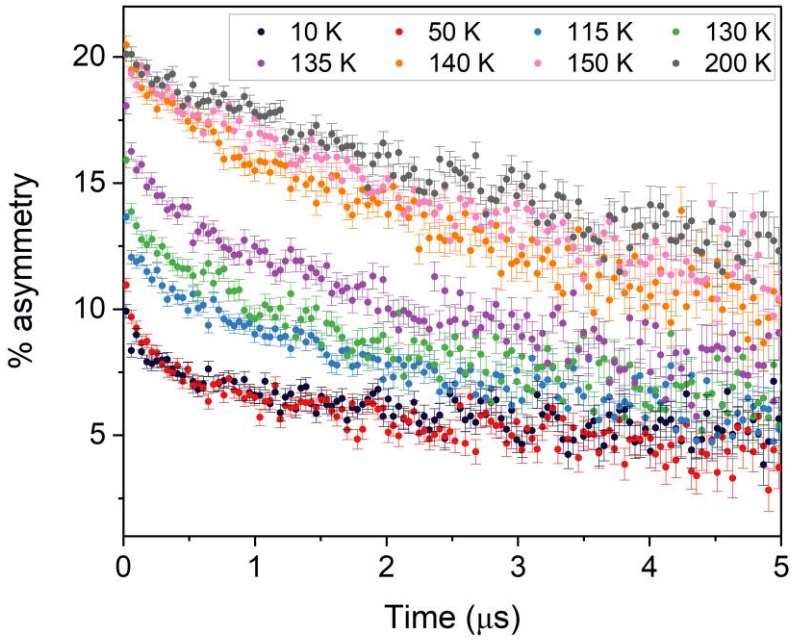

Figure 9.11: μ^+-SR data collected from Sr_2CoIrO_4 as a function of temperature.

9.4.3 Low temperature neutron powder diffraction

NPD data were collected from Sr_2CoIrO_4 at temperatures between 2 and 50 K using the POLARIS diffractometer. The NPD data at 2 K can be well described by the *I*4/*mmm* structural model, indicating that there is no structural distortion down to this temperature. Comparison of the background-subtracted patterns from the 27° detector bank of the diffractometer at 2 K and room temperature showed the presence of additional peaks at 2 K, as shown in Figure 9.12.

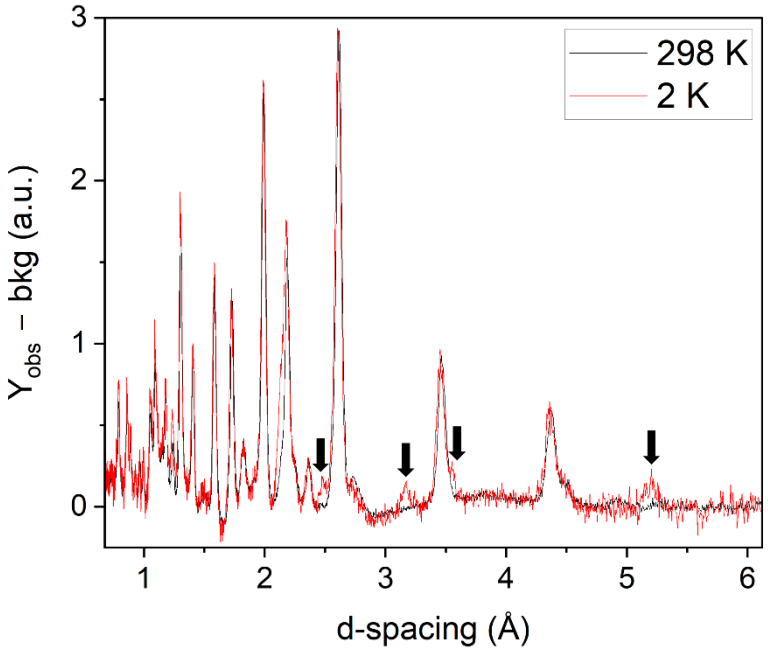

Figure 9.12: Comparison of background-subtracted NPD data collected from Sr_2CoIrO_4 at 2 K and 298 K using the 27° bank of the POLARIS diffractometer. Additional peaks present at 2 K are highlighted by arrows.

The additional diffraction peaks could be indexed by a ($\sqrt{2} \times \sqrt{2} \times 1$)-expansion of the crystallographic unit cell, suggesting that the magnetic propagation vector is k = (½,½,0). Using the ISODISTORT software suite,[151,152] it was determined that there are three irreducible representations (mX^{2+}, mX^{3+}, mX^{4+}) of the *I*4/*mmm* space group associated with this propagation vector when only magnetic distortions on the Co and Ir atoms are considered. The magnetic structures that arise from these distortions are shown in Figure 9.13. The best fit to the 2 K NPD data is achieved for a distortion that transforms as the mX^{2+} irreducible representation, described in magnetic space group 64.480 (in BNS notation), in which the Co and Ir moments are aligned along the *z*-direction (relative to the nuclear unit cell). The fit to the 2 K NPD data from the 27° detector bank of the POLARIS diffractometer is shown in Figure 9.14, with the refinement parameters detailed in Table 9.5. The magnetic Bragg peaks are present in the NPD data up to 50 K, with the refined moments remaining constant within

error, consistent with the transition temperature of 135−140 K determined from μ^+-SR spectroscopy.

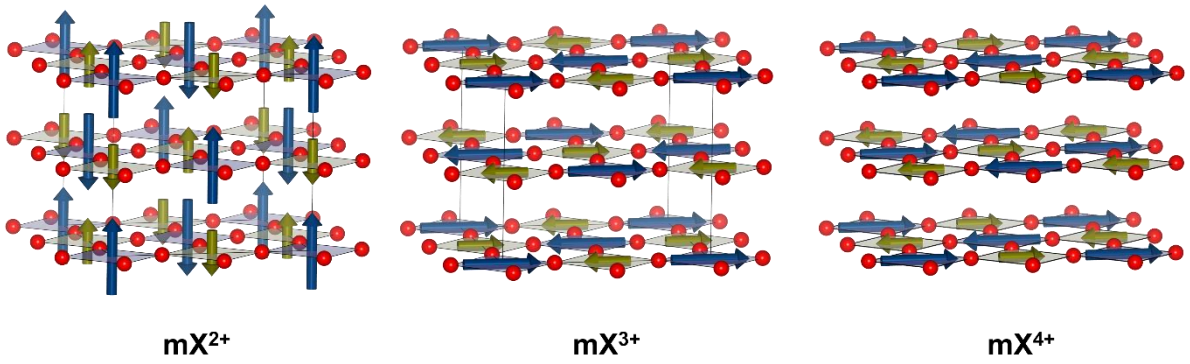

Figure 9.13: Magnetic structures that arise from distortions described by the mX^{2+}, mX^{3+} and mX^{4+} irreducible representations of the *I*4/*mmm* space group.

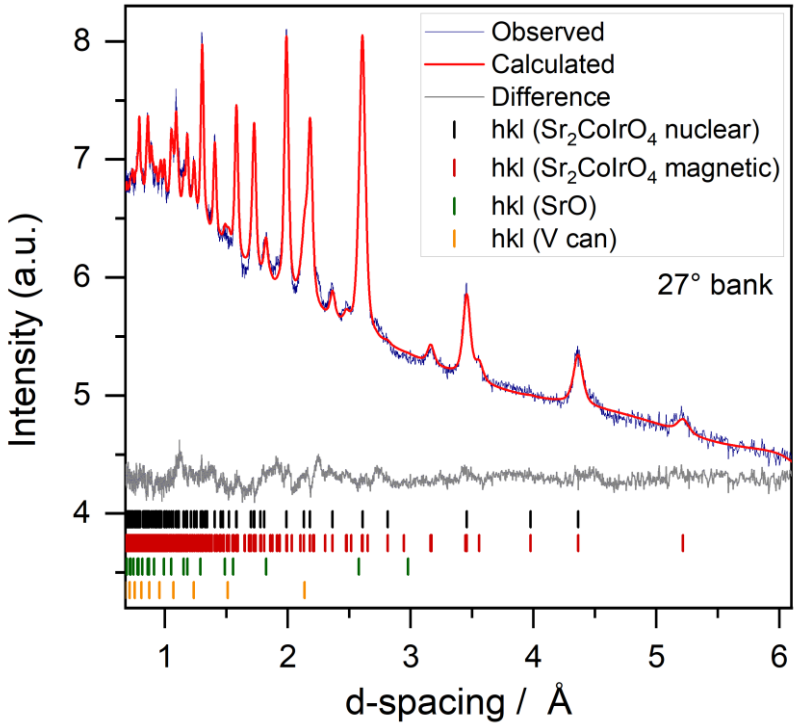

Figure 9.14: Observed, calculated and difference plots from the magnetic refinement of Sr_2CoIrO_4 against NPD data collected at 2 K from the 27° bank of the POLARIS diffractometer.

Table 9.5: Parameters from the magnetic refinement of Sr_2CoIrO_4 against NPD data collected at 2 K from the POLARIS diffractometer, including the refined magnetic moments at the Co and Ir sites. The occupancies and fractional coordinates were fixed to the values from the nuclear refinement. Subsequent to the refinement, the phase describing the magnetic structure was transformed by the matrix [(0, 1, 0), (0, 0, 1), (1, 0, 0)], so that the direction of the *z*-axis is consistent with that of the nuclear unit cell.

Sr_2CoIrO_4 nuclear, space group *I*4/*mmm* (No. 139)						
		x	***y***	***z***	**Occ.**	**B_{iso} (Å^2)**
Sr(1)	4*d*	0	½	¼	1	0.68(8)
Co(1)/Ir(1)	2*a*	0	0	0	0.934/0.066	3.1(1)
Ir(2)/Co(2)	2*b*	½	½	0	0.934/0.066	3.1(1)
O(1)	8*h*	0.2509	0.2509	0	1	1.14(8)
a = 5.631(1) Å, c = 6.919(2) Å						
V = 219.5(1) Å^3						
Sr_2CoIrO_4 magnetic, magnetic space group 64.480						
		x	***y***	***z***	**Occ.**	**B_{iso} (Å^2)**
Co(1)	4*a*	0	0	0	1	3.1(1)
	***M* (μB)**	0	0	3.0(1)		
Ir(2)	4*b*	0	½	0	1	3.1(1)
	***M* (μB)**	0	0	−0.17(17)		
a = 7.965(1) Å, c = 6.919(2) Å						
V = 438.9(2) Å^3						
R_{wp} = 1.13%, R_p = 0.87%, *gof* = 0.07						

During the refinement, the magnetic moments at the cobalt and iridium centres were allowed to refine along the *z*-direction (relative to the nuclear unit cell). This yielded a moment of 3.0(1) μ_B at the cobalt site, whilst the moment at the iridium site refined to 0.17(17) μ_B, as shown in Figure 9.15(a). The magnitude of the moment at the cobalt site is consistent with the value of 3 μ_B that would be expected for high-spin d^7 Co^{II} with three unpaired electrons.

Despite that low-spin d^7 Ir^{II} would be expected to have one unpaired electron, the magnitude of the moment at the iridium site refines to a negligibly small value. Since the magnitude of the moment is small and that fixing the moment to zero leads to no visual change in the quality of the fit, it was assumed that there is very little magnetic ordering at the iridium sites. It is

worth noting that the magnetic scattering from the two B-site cations in double perovskites are strongly correlated, with the refinements being most sensitive to the difference in the moments.[34,153,154] However, manually fixing the moment at the iridium sites to ~1 μ_B and allowing the Co moment to refine led to a deterioration in the quality of the fit, suggesting that the moment at the iridium site is likely to be close to zero.

Overall, the moments on the cobalt ions in Sr_2CoIrO_4 can be described as adopting a 'type I' antiferromagnetic ground state,[155] in which there is antiferromagnetic order between successive (001) ferromagnetic planes, as shown in Figure 9.15(b).

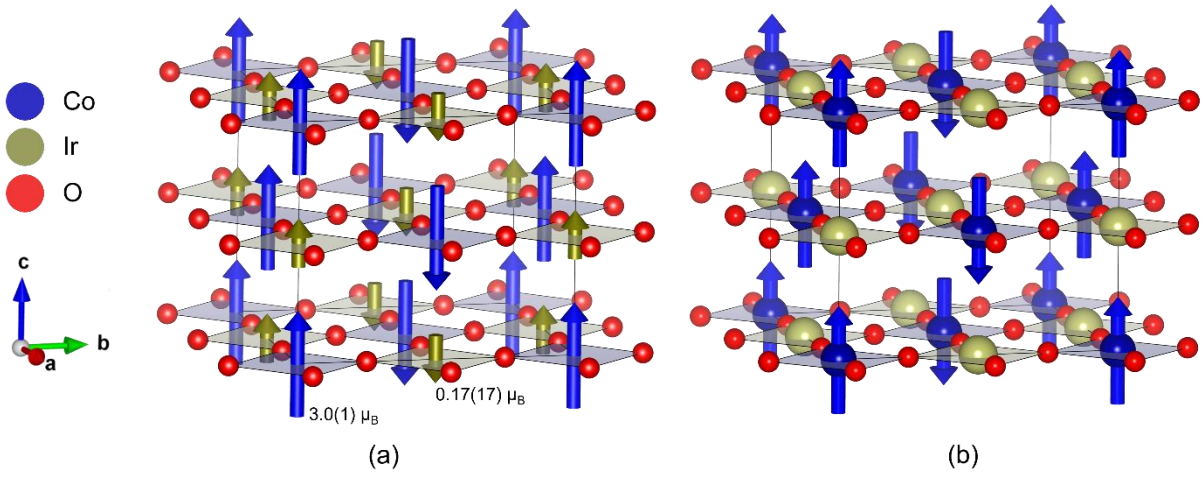

Figure 9.15: Refined magnetic model for Sr_2CoIrO_4 at 2 K (a), and representation of Sr_2CoIrO_4 with a 'type I' antiferromagnetic structure (b), with the arrows representing the moments at the cobalt and iridium sites. The strontium ions have been omitted for clarity.

9.4.4 Variable temperature synchrotron powder X-ray diffraction

Since the magnetic structure of Sr_2CoIrO_4 is orthorhombic but the crystal structure is tetragonal, the compound might be expected to undergo a structural transition to a distorted orthorhombic structure at the magnetic transition temperature. To confirm if this is the case, SXRD data were collected from Sr_2CoIrO_4 between 100 and 300 K. Close inspection of the patterns show no evidence for a structural transition between these temperatures; this is

illustrated in Figure 9.16 by comparing the fits to the 200 reflection in SXRD data collected at 100 K and 300 K.

Refinements were performed at each temperature for which data were collected using the undistorted *I*4/*mmm* structural model from Section 9.4.3. The change in lattice parameters as function of temperature is shown in Figure 9.17. On cooling from 300 K, the lattice parameters decrease linearly until ~150 K. There is then a reduction in the gradient as the sample is cooled below this temperature. Although this flattening is observed for all materials at low temperature as there is no longer enough thermal energy to populate excited vibrational states, 150 K is a relatively high temperature for this to occur. As such, the flattening is likely to be related to a stiffening of the crystal structure arising from the onset of magnetic order at around 150 K.

The apparent absence of magnetostriction in this compound can be rationalised by the fact that there are no oxide ions present between the planes to mediate superexchange interactions. This means that the interlayer coupling interactions are likely to be weak and, therefore, cannot drive a structural transition.

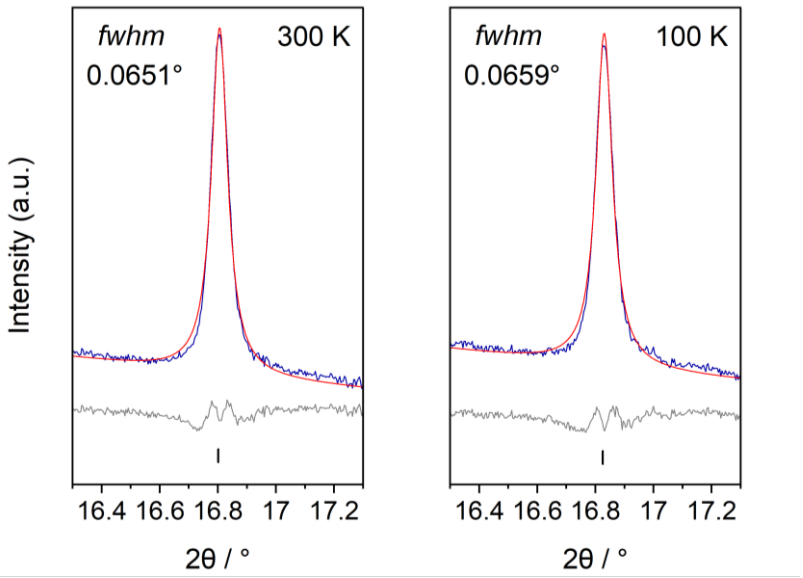

Figure 9.16: Comparison of 200 reflections in SXRD data collected from Sr_2CoIrO_4 at 300 K and 100 K.

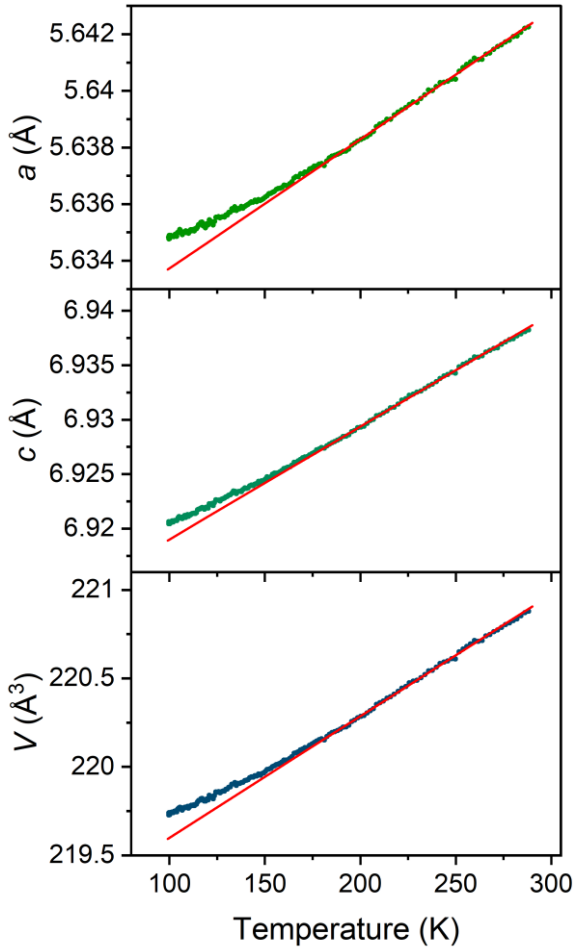

Figure 9.17: Change in *a*-lattice parameter, *c*-lattice parameter and volume as a function of temperature obtained from refinements against SXRD data collected from Sr_2CoIrO_4 between 100 and 290 K.

9.5 Discussion

9.5.1 Electronic structure of Sr_2CoIrO_4

From the XANES data in Section 9.3.4, the cobalt in Sr_2CoIrO_4 is present as Co^{II}, which would imply an iridium oxidation state of Ir^{II}. These transition metal oxidation states are analogous to those in Sr_2FeIrO_4, in which iron is present as Fe^{II} and iridium is present as Ir^{II}.[101] However, analysis of the lattice parameters for these two phases show that, whilst the *a*-lattice parameters are similar, the *c*-lattice parameter of Sr_2CoIrO_4 (6.943 Å) is significantly more contracted than that of Sr_2FeIrO_4 (7.060 Å). The *c*-lattice parameter of infinite-layer phases is typically dictated by the identity of the A-site cation. However, both Sr_2FeIrO_4 and Sr_2CoIrO_4 contain only

strontium at the A-site. Therefore, the difference in *c*-lattice parameters is likely to arise from the electronic configurations of the two compounds (Figure 9.18). In Sr_2FeIrO_4, the $3d_{z^2}$ orbital is the lowest energy valence orbital in Fe^{II}, which is attributed to extensive s/d_{z^2} mixing.[156] As such, this orbital is doubly occupied, whilst the remaining 3*d* orbitals are singly occupied. Since Co^{II} has one more *d*-electron than Fe^{II}, this means that, assuming the same crystal field splitting, the extra electron in Sr_2CoIrO_4 would be located in a d_{xz}/d_{yz} orbital. However, weaker s/d_{z^2} hybridisation in Co^{II}, compared to Fe^{II}, would lead to the energy of the d_{z^2} orbital being raised above that of the d_{xz}/d_{yz} orbitals, and possibly above that of the d_{xy} orbital. This effect has been observed previously for square-planar cobalt in infinite-layer phases, such as in $LaSrCoRuO_4$.[157] As a result, it is the d_{xz}/d_{yz} orbitals of Co^{II} in Sr_2CoIrO_4 that are fully occupied, whilst the d_{z^2} orbital is half-occupied. Since the Co^{II} d_{z^2} orbital is only half-occupied, the electronic repulsion between the Co^{II} d_{z^2} and Ir^{II} d_{z^2} is reduced, accounting for the contraction in the *c*-lattice parameter. A similar phenomenon is observed when the lattice parameters of $LaSrCoRuO_4$ are compared to those of $LaSrNiRuO_4$: $LaSrCoRuO_4$ has a shorter *c*-lattice parameter than $LaSrNiRuO_4$, which is attributed to the full occupation of the $3d_{z^2}$ orbital in Ni^{II}, compared to only single occupation of the $3d_{z^2}$ orbital in Co^{II}.[157,158]

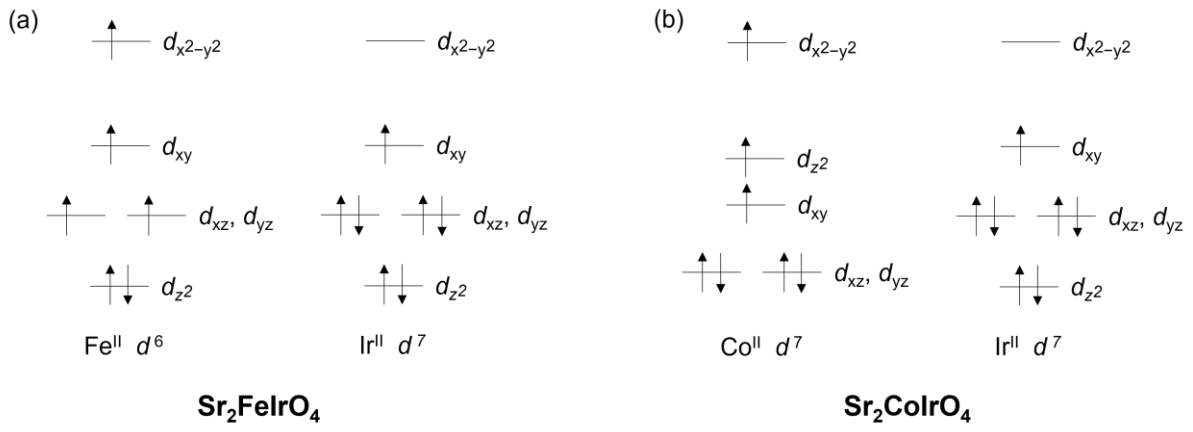

Figure 9.18: Simple crystal field splitting diagram for Sr_2FeIrO_4 as determined by Page *et al.*[101] (left) and proposed crystal field splitting diagram for Sr_2CoIrO_4 (right).

9.5.2 Magnetic behaviour of Sr_2CoIrO_4

The magnetic structure of Sr_2CoIrO_4 is shown in Figure 9.15, with possible coupling interactions within and between the planes illustrated in Figure 9.19.

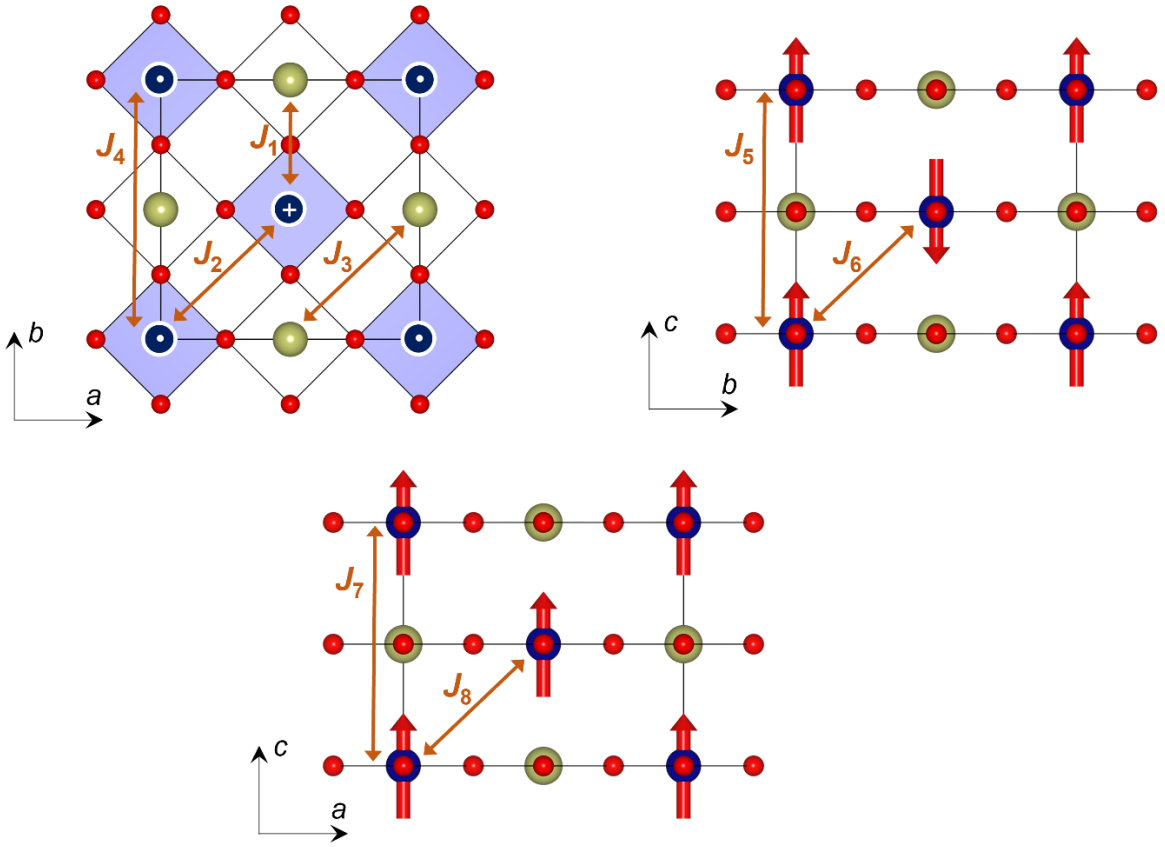

Figure 9.19: Possible intralayer (J_1, J_2, J_3, J_4) and interlayer (J_5, J_6, J_7, J_8) coupling interactions in Sr_2CoIrO_4. The ● represents a moment coming out of the page, whilst the + represents a moment going into the page.

The overall intralayer arrangement of moments at the cobalt sites in Sr_2CoIrO_4 is the same as that at the iron sites in Sr_2FeIrO_4.[101] The dominant coupling interactions in Sr_2FeIrO_4 are antiferromagnetic Fe−Ir interactions (equivalent to J_1 in Figure 9.19) and antiferromagnetic Ir−Ir interactions (equivalent to J_3 in Figure 9.19). If the same interactions determined the magnetic structure of Sr_2CoIrO_4, magnetic ordering should be present at the iridium sites and a structural transition should occur accompanying the magnetic transition. The fact that these are not observed suggests that the coupling interactions that determine the magnetic ordering in Sr_2CoIrO_4 are subtly different to those in Sr_2FeIrO_4. This is likely to arise from the different

occupations of the 3*d* orbitals in Co^{II} and Fe^{II}, which arises from the different relative energies of the orbitals. In Co^{II}, the d_{xz} and d_{yz} orbitals are fully occupied, whilst the remaining orbitals are half-occupied, whereas in Fe^{II}, the d_{z^2} orbital is fully occupied, whilst the remaining orbitals are half-occupied (Figure 9.18). The differing occupancies of π-type and σ-type orbitals in Co^{II} and Fe^{II} is likely to have a significant effect on their magnetic coupling interactions with Ir^{II}. Another factor to consider is that the lower energy of Co^{II} 3*d* orbitals, relative to those of Fe^{II}, means that there is likely to be a greater energy mismatch between the Co^{II} and Ir^{II} valence orbitals, compared to the Fe^{II} and Ir^{II} valence orbitals, which would lead to the Co−Ir coupling being weaker than the Fe−Ir coupling.

From the Goodenough-Kanamori rules, it might be expected that the interactions in Sr_2CoIrO_4 are ferromagnetic, as has been observed for Ru-containing analogues, such as $LaSrCoRuO_4$.[65] The fact that the compound adopts an antiferromagnetic structure suggests that simple nearest-neighbour superexchange does not dominate the coupling interactions in this compound. The 'failure' of the Goodenough-Kanamori rules for this compound is not surprising, due to the large energy mismatch between the 3*d* and 5*d* orbitals of cobalt and iridium and the strong spin-orbit coupling that is likely to be present in iridium. To fully understand the coupling interactions in Sr_2CoIrO_4, DFT calculations will need to be performed.

An unusual feature of the magnetic behaviour of this compound is that, although the onset of magnetic ordering occurs at 135−140 K, as determined by μ^+-SR spectroscopy, there is no feature at this temperature in the magnetic susceptibility. A similar phenomenon has been observed previously for Sr_2VO_3H, which undergoes antiferromagnetic ordering at 170 K despite there being no observable change in the magnetisation at this temperature.[48] This was attributed to the presence of strong dynamic magnetic correlations above the transition temperature in this compound.

9.6 Synthesis and characterisation of Sr_2CoIrO_6 and Sr_2CoIrO_4 thin films

The synthesis and characterisation of the thin film samples in this Section were performed under the supervision of Prof. Hiroshi Kageyama at Kyoto University, Japan on a placement as part of the OxICFM CDT program.

9.6.1 Synthesis of thin film samples

9.6.1.1 Synthesis of Sr_2CoIrO_6 thin film

A target for pulsed laser deposition (PLD) was prepared by sintering a pellet of Sr_2CoIrO_6, synthesised as described in Section 7.2.1, for 24 hours in air at 1050°C. The thin film was then fabricated by PLD onto a (001)-orientated $SrTiO_3$ (STO) substrate at 750°C over the course of 1 hour using a KrF laser (λ = 248 nm) with a 2 Hz repetition rate at an oxygen pressure of 0.01 Pa. After the growth, the oxygen pressure was maintained whilst the films were cooled to room temperature. Following this, the film was annealed for 1 hour at 700°C in air. Attempts to grow the film on a (111)-oriented STO substrate were unsuccessful.

To protect the surface of the film during the reaction with the Zr getter, a CaO cap was grown on the Sr_2CoIrO_6 film by PLD at room temperature over the course of 10 minutes with a 5 Hz repetition rate and a pressure of $< 1 \times 10^{-3}$ Pa.

9.6.1.2 Synthesis of Sr_2CoIrO_4 thin film

An Sr_2CoIrO_4 thin film sample was prepared by sealing the Sr_2CoIrO_6 film in an evacuated Pyrex® tube with ~150 mg of finely-divided Zr metal, and heating the sample at 390°C for 24 hours. The resulting film was then washed with 0.1 M NH_4Cl in MeOH, followed by clean MeOH, to remove the CaO cap. Attempts to perform the reaction for Sr_2CoIrO_6 grown on a (001)-oriented $La_{0.18}Sr_{0.82}Al_{0.59}Ta_{0.41}O_3$ (LSAT) substrate were unsuccessful.

9.6.2 Structural characterisation of thin films

XRD patterns collected from the Sr_2CoIrO_6 thin film deposited onto a (001)-oriented STO substrate without annealing did not show any sharp Bragg peaks (other than those from the substrate), indicating that a crystalline Sr_2CoIrO_6 film was not present. However, a broad feature (highlighted by the asterisk in Figure 9.20) was observed in the vicinity of the STO 002 peak, suggesting that Sr_2CoIrO_6 could be present as an amorphous film. Annealing the film at 500°C in air led to no change in the XRD pattern, whilst annealing at 700°C in air resulted in the appearance of two relatively sharp peaks at slightly lower angles than the STO 001 and 002 peaks, respectively, as shown in Figure 9.20. The positions of these peaks are consistent with the formation of a metrically cubic phase with *c*-lattice parameter of 3.94 Å, thereby suggesting that Sr_2CoIrO_6 had been successfully grown on the STO substrate. X-ray reflectometry measurements on the film indicated a thickness of ~37 nm.

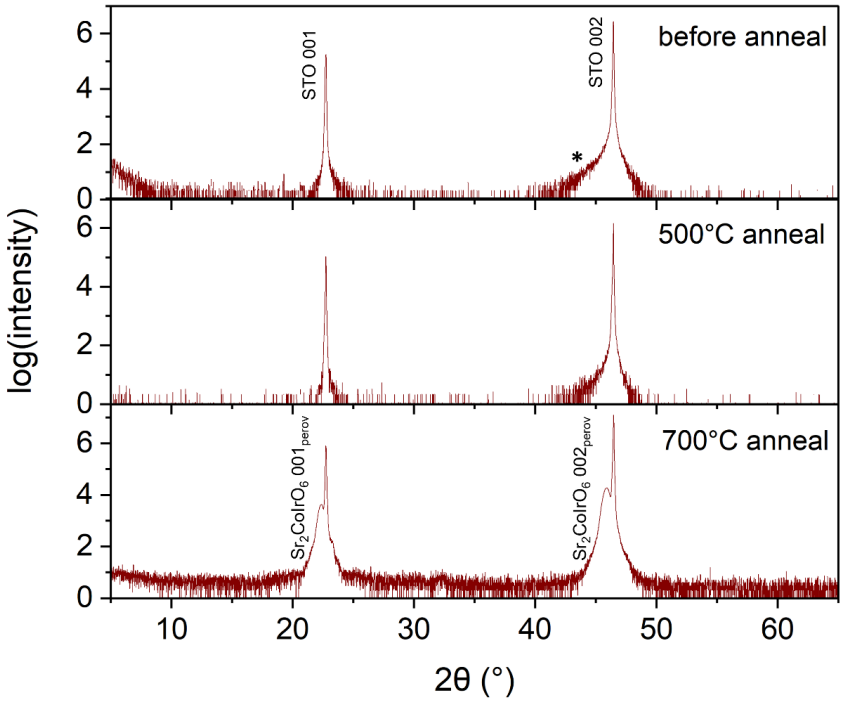

Figure 9.20: X-ray diffraction pattern (λ = 1.5406 Å) collected from Sr_2CoIrO_6 deposited onto (001)-oriented STO without annealing (top), after annealing in air at 500°C (middle) and after annealing in air at 700°C (bottom). The asterisk highlights the apparent presence of an amorphous Sr_2CoIrO_6 film after deposition. The miller indices labelling the Sr_2CoIrO_6 peaks correspond to the equivalent simple perovskite containing a single B-site cation.

Reciprocal space mapping (RSM) measurements on the Sr_2CoIrO_6 film centred around the 103 peak (Figure 9.21) showed that, whilst the *a*-lattice parameter of Sr_2CoIrO_6 is the same as STO ($a \approx 3.90$), the *c*-lattice parameter is significantly larger ($c \approx 3.94$ Å). This indicates that there is a high degree of epitaxial strain in the film.

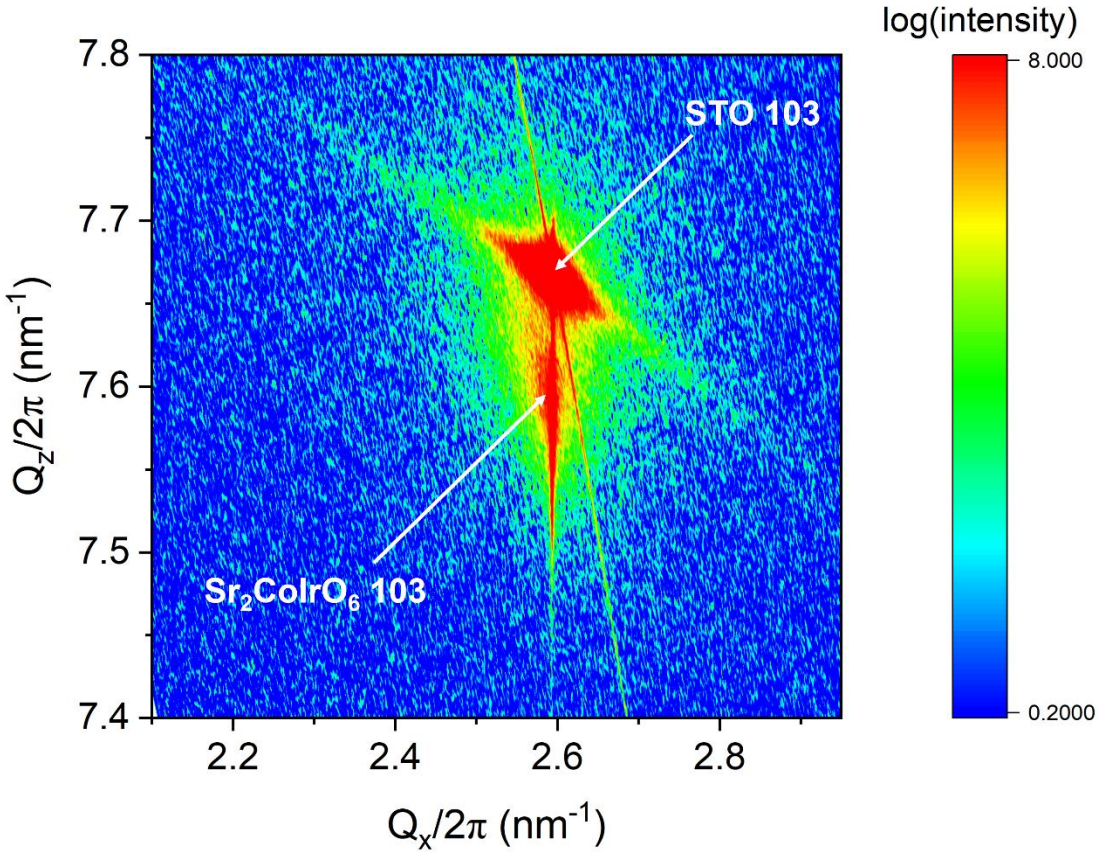

Figure 9.21: RSM plot for the Sr_2CoIrO_6 film centred around the 103 peak, collected using an X-ray wavelength of 1.5406 Å.

Reaction of the Sr_2CoIrO_6 film with a Zr getter yielded an XRD pattern in which the 00*l* peaks are shifted to higher angle (Figure 9.22), indicating a substantial contraction in the *c*-direction. The peaks could be indexed with a *c*-lattice parameter of 3.52 Å. This is comparable to the value of $c_{perov} = 3.47$ Å obtained from bulk Sr_2CoIrO_4 and, as such, indicates the formation of an infinite-layer Sr_2CoIrO_4 thin film. It is worth noting that there was no evidence for the formation of Sr_2CoIrO_5 during the reaction.

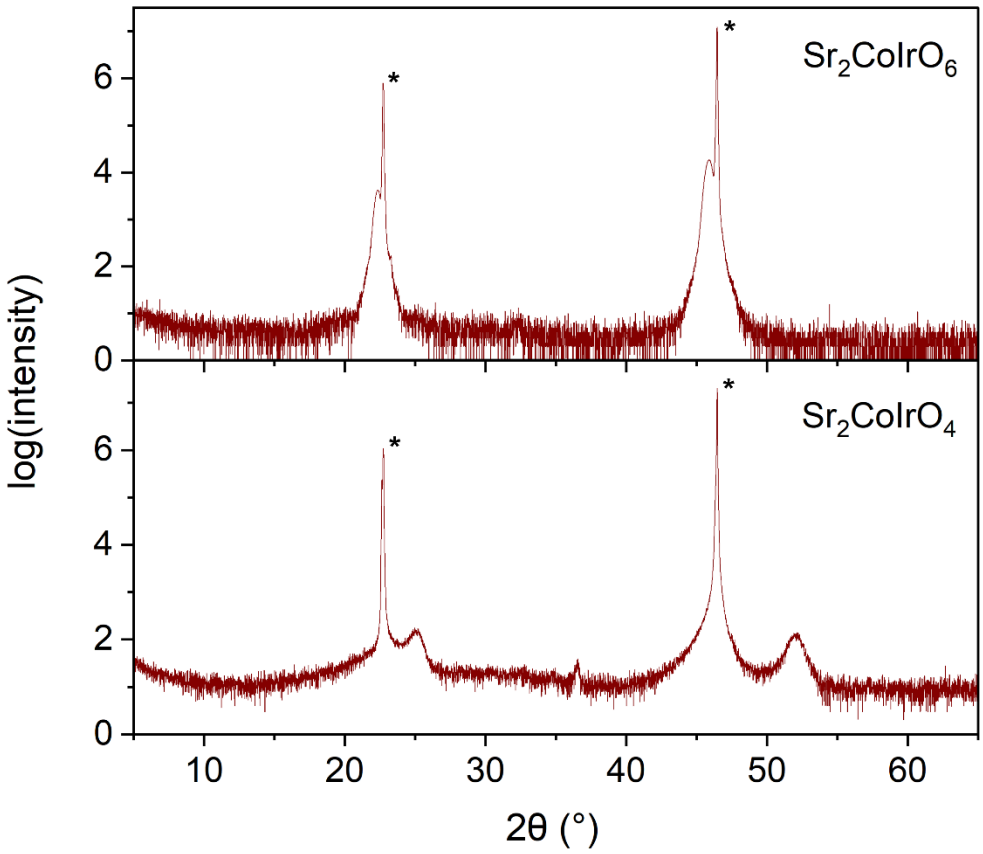

Figure 9.22: X-ray diffraction pattern (λ = 1.5406 Å) from as-deposited Sr_2CoIrO_6 film (top) and after reaction with a Zr getter (bottom). The shift in 00*l* peaks to higher angle is consistent with the formation of Sr_2CoIrO_4. The peaks denoted by asterisks correspond to the STO 001 and 002 reflections.

RSM measurements on the Sr_2CoIrO_4 film centred around the 103 reflection are shown in Figure 9.23. They show that, unlike in Sr_2CoIrO_6, the *a*-lattice parameter of Sr_2CoIrO_4 is substantially larger than that of STO, with a value of ~4.00 Å, comparable to the value of a_{perov} = 3.99 Å obtained from the bulk sample. This suggests that the epitaxial strain present in Sr_2CoIrO_6 is relaxed during the reaction with the Zr getter.

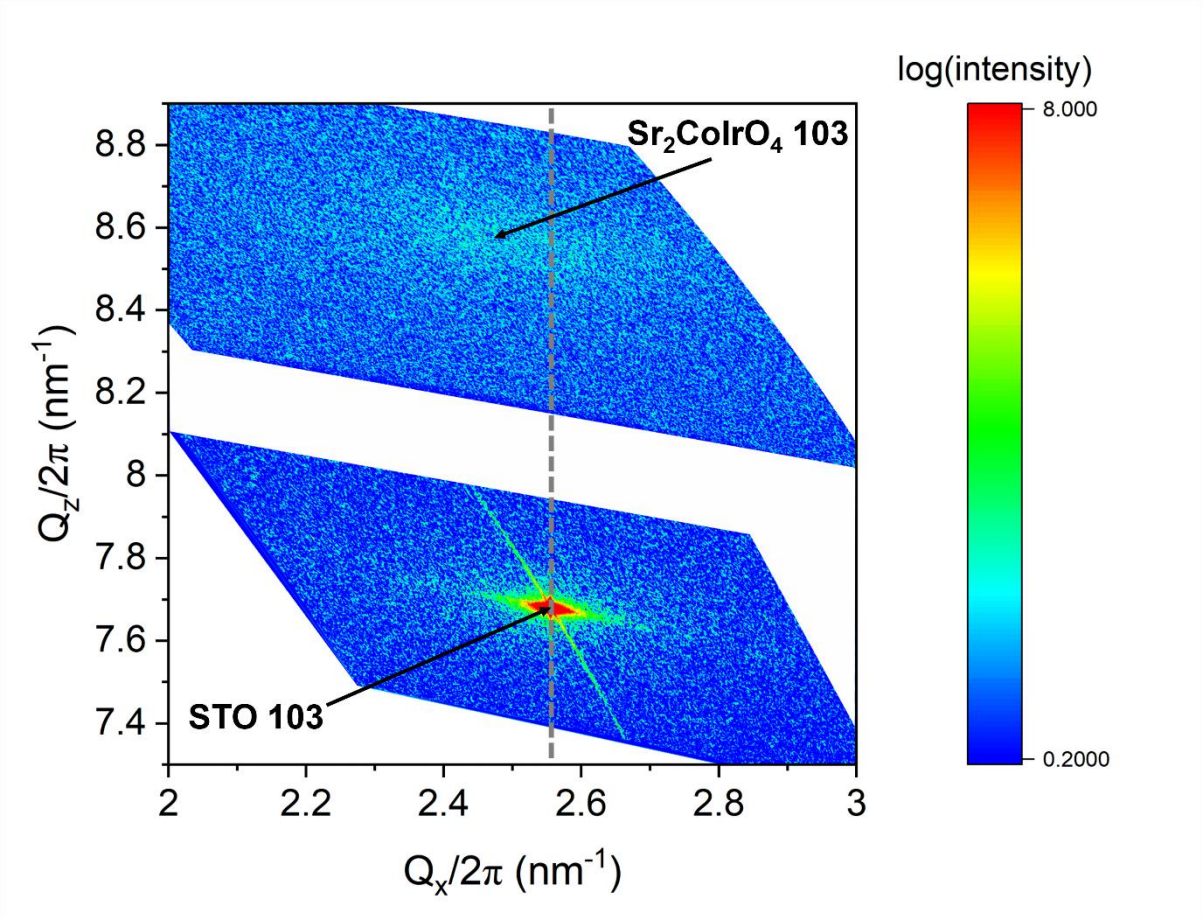

Figure 9.23: RSM plot for the Sr_2CoIrO_4 film centred around the 103 peak, collected using an X-ray wavelength of 1.5406 Å.

9.6.3 Physical characterisation of thin films

Electrical transport measurements were performed on the Sr_2CoIrO_6 and Sr_2CoIrO_4 films as a function of temperature, with the results shown in Figure 9.24. For both samples, the resistivity decreased with increasing temperature, indicating insulating behaviour. This is consistent with the properties of previously reported Sr_2CoIrO_6 thin film samples,[159] which were shown to be insulators with likely transitions to an antiferromagnetic state at around 43 K. The magnitude of the resistivity for Sr_2CoIrO_4 is significantly higher than that of Sr_2CoIrO_6, with the voltage below 100 K exceeding the maximum that could be measured by the instrument. The Sr_2CoIrO_4 film showed no change in resistivity when the measurement was repeated in a field of 7 T, indicating that the compound does not exhibit magnetoresistance.

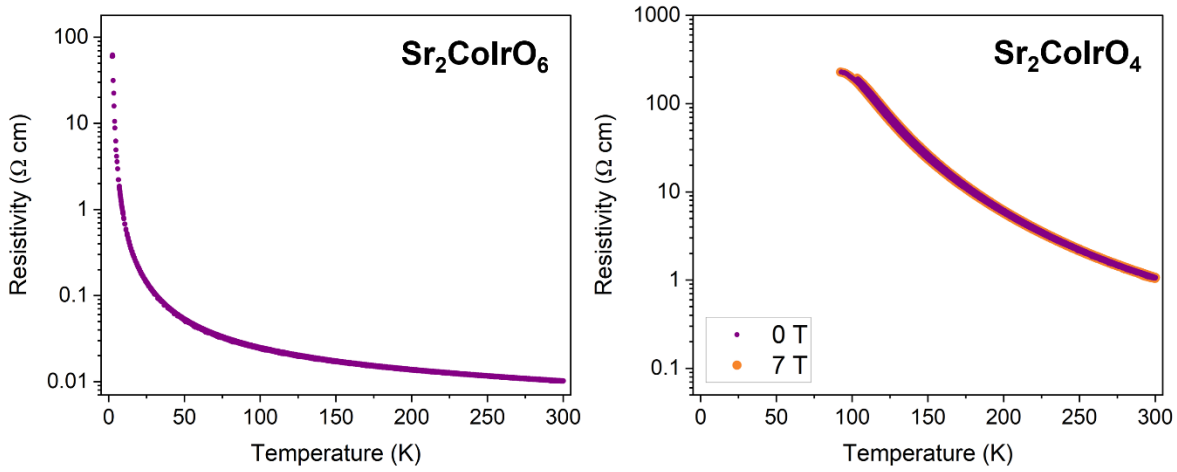

Figure 9.24: Resistivity of Sr_2CoIrO_6 and Sr_2CoIrO_4 thin films measured as a function of temperature. The resistivity of Sr_2CoIrO_4 was measured in fields of 0 T and 7 T.

The in-plane and out-of-plane magnetisation of Sr_2CoIrO_4 was measured as a function of temperature, as shown in Figure 9.25. Unless the sample is ferromagnetic, the magnetisation of thin film samples is typically dominated by the diamagnetic substrate. As such, it is often difficult to extract information about the magnetic behaviour of these samples. From the data shown in Figure 9.25, the small magnitude of the magnetisation and small bifurcations are compatible with paramagnetic behaviour and do not rule out the presence of an antiferromagnetic transition, as exhibited by bulk Sr_2CoIrO_4.

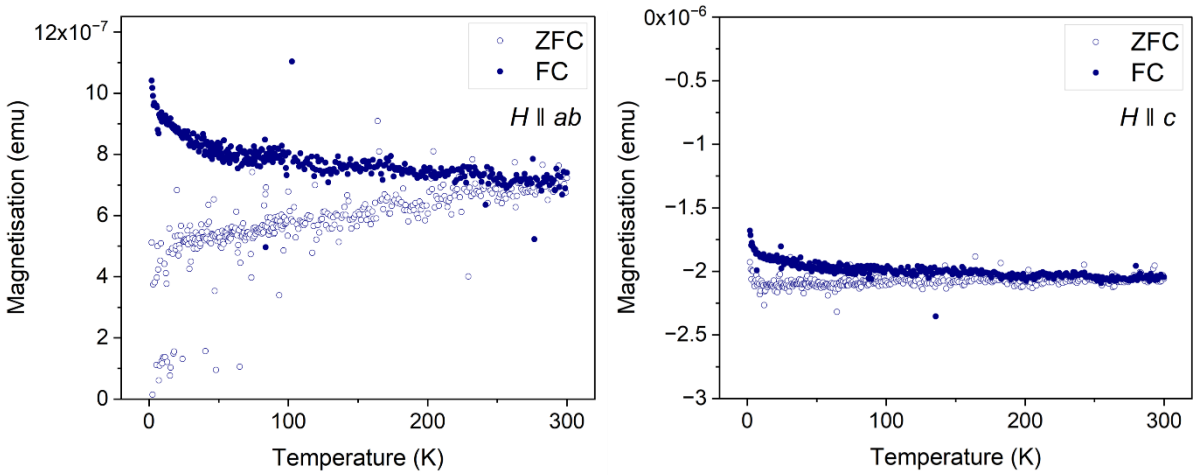

Figure 9.25: Magnetisation data collected from Sr_2CoIrO_4 as a function of temperature in a field of 100 Oe orientated parallel to the *ab*-plane (left) and parallel to the *c*-axis (right).

9.7 Conclusion

This chapter described the synthesis and magnetic properties of the infinite-layer phase, Sr_2CoIrO_4. The compound exhibits an undistorted *I*4/*mmm* structure down to 2 K. Below 135−140 K, there is a magnetic transition to an antiferromagnetic state in which the magnetic moments are exclusively located on the cobalt ions and adopt a 'type I' antiferromagnetic arrangement. This magnetic behaviour is markedly different from that of Sr_2FeIrO_4, which is likely to stem from the significantly different electronic configurations of Co^{II} and Fe^{II} ions.

The synthesis of a sample of Sr_2CoIrO_4 thin film was also performed. Whilst the parent Sr_2CoIrO_6 film exhibited significant epitaxial strain, the Sr_2CoIrO_4 film was substantially more relaxed. Both Sr_2CoIrO_6 and Sr_2CoIrO_4 films showed insulating behaviour.

Chapter 10 – Synthesis and magnetism of $LaSrCoIrO_4$

10.1 Introduction

The syntheses of Sr_2CoIrO_5 and Sr_2CoIrO_4 were discussed in Chapters 8 and 9. To investigate the effect of changing the transition metal electron count on the properties of these compounds, synthesis of the analogous $LaSrCoIrO_4$ and $LaSrCoIrO_5$ phases was also attempted.

10.2 Exploration of the reactivity of $LaSrCoIrO_6$ with a Zr getter

The synthesis and characterisation of $LaSrCoIrO_6$ is described in Chapter 7. Trial reactions were performed by sealing ~300 mg of $LaSrCoIrO_6$ in an evacuated Pyrex® ampoule with 4 mole equivalents of finely-divided Zr metal. It was observed that a reaction occurred when this apparatus was heated at temperatures of 400−425 °C, signalled by the appearance of two new sets of peaks in the PXRD data, the first of which could be indexed using a tetragonal cell with lattice parameters of a = 5.40 Å and c = 8.18 Å ($LaSrCoIrO_5$) and the second of which could be indexed using another tetragonal cell with lattice parameters of a = 5.70 Å and c = 6.80 Å ($LaSrCoIrO_4$). No reaction was observed when the sample was heated below these temperatures, whilst heating above these temperatures led to non-topochemical decomposition, signalled by the formation of SrO, Co metal and Ir metal. In contrast to the reaction with Sr_2CoIrO_6, it was not possible to obtain pure $LaSrCoIrO_4$ or $LaSrCoIrO_5$. All samples of $LaSrCoIrO_5$ contained a substantial amount of unreacted $LaSrCoIrO_6$, whilst all samples of $LaSrCoIrO_4$ contained a substantial $LaSrCoIrO_5$ impurity. In an attempt to obtain pure phases, trial reactions were performed using NaH in sealed ampoules, as well as CaH_2 and LiH under flowing argon. Additionally, the reaction with a Zr getter was repeated using a ball-milled sample of the starting material to establish whether it was possible to activate the topochemical reaction in this way. However, these approaches were unsuccessful in synthesising pure

$LaSrCoIrO_4$ or $LaSrCoIrO_5$. Therefore, although the reactions could not be performed to completion, the Zr getter method was used to prepare ~1 g samples of $LaSrCoIrO_4$ and $LaSrCoIrO_5$ from $LaSrCoIrO_6$. The considerable $LaSrCoIrO_6$ impurity present in the sample of $LaSrCoIrO_5$ means that detailed structural characterisation is not possible, as discussed in Appendix A5. The synthesis and characterisation of the infinite-layer phase, $LaSrCoIrO_4$, is described below.

10.3 Synthesis of $LaSrCoIrO_4$

A sample of $LaSrCoIrO_4$ was prepared by placing 1.2 g of $LaSrCoIrO_6$ in a glass thimble and sealing this in an evacuated Pyrex® ampoule with 1 g of finely-divided Zr metal, such that the $LaSrCoIrO_6$ sample was held approximately 5 cm from the Zr getter. The ampoule was then heated such that the temperature at the Zr getter was 400 °C. The sample was heated with the Zr getter for 15 cycles of 4 days at temperatures of 400−425 °C, with the reaction being deemed complete when no further change was observed in the PXRD data after successive heating cycles. Thorough grinding was performed between each heating cycle in an Ar-filled glovebox.

10.4 Structural characterisation of $LaSrCoIrO_4$

10.4.1 Synchrotron powder X-ray diffraction

A structural model of a B-site cation ordered infinite-layer phase with *I*4/*mmm* symmetry and composition of $LaSrCoIrO_4$ was constructed and refined against SXRD data collected from the sample. $LaSrCoIrO_5$ was added as a secondary phase, assuming an anion-disordered structure analogous to Sr_2CoIrO_5. The fit to the data is shown in Figure 10.1 and the refinement parameters are detailed in Table 10.1. This yielded lattice parameters of a = 5.6926(3) Å and c = 6.8015(4) Å for $LaSrCoIrO_4$, corresponding to an expansion of the *xy*-plane and contraction in the *z*-direction relative to the $LaSrCoIrO_6$ parent phase (a = 5.58 Å, b = 5.59 Å, c = 7.91 Å).

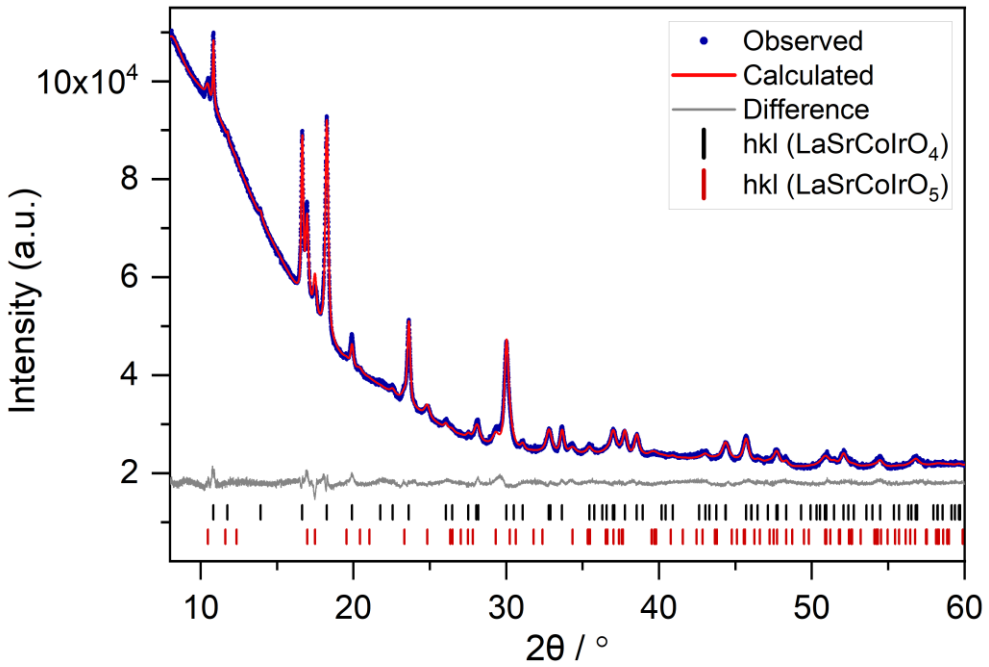

Figure 10.1: Observed, calculated and difference plots from the structural refinement of $LaSrCoIrO_4$ against SXRD data (λ = 0.825 Å) collected at room temperature, with $LaSrCoIrO_5$ included as a secondary phase.

Table 10.1: Parameters from the structural refinement of $LaSrCoIrO_4$ against SXRD data collected at room temperature. The occupancies at the transition metal sites were fixed at the values obtained from refinements of the parent oxide.

$LaSrCoIrO_4$, space group *I*4/*mmm* (No. 139), 67.9(3) wt%						
		x	***y***	***z***	**Occ.**	**B_{iso} (Å^2)**
Sr(1)/La(1)	4*d*	0	½	¼	0.5/0.5	3.34(5)
Co(1)/Ir(1)	2*a*	0	0	0	0.8985/0.1015	1.86(4)
Ir(2)/Co(2)	2*b*	½	½	0	0.8985/0.1015	1.86(4)
O(1)	8*h*	¼	¼	0	1	4.2(2)
a = 5.6927(4) Å, c = 6.8008(5) Å						
V = 220.39(3) Å^3						
$LaSrCoIrO_5$, space group *I*4/*mmm* (No. 139), 32.1(3) wt%						
		x	***y***	***z***	**Occ.**	**B_{iso} (Å^2)**
Sr(1)/La(1)	4*d*	0	½	¼	0.5/0.5	2.3(2)
Co(1)/Ir(1)	2*a*	0	0	0	0.8985/0.1015	6.0(3)
Ir(2)/Co(2)	2*b*	½	½	0	0.8985/0.1015	6.0(3)
O(1)	8*h*	¼	¼	0	0.75	20(2)
O(2)	4*e*	0	0	¼	1	20(2)
a = 5.4180(7) Å, c = 8.146(1) Å						
V = 239.12(8) Å^3						
R_{wp} = 1.10%, R_p = 0.81%, *gof* = 2.15						

10.4.2 Neutron powder diffraction

NPD data were collected from $LaSrCoIrO_4$ at 200 K with a wavelength of 1.54 Å using the D20 diffractometer at the ILL. To evaluate if there are any distortions to the infinite-layer structure of $LaSrCoIrO_4$, structural models were constructed in the *I*4/*mmm*, *I*4/*m*, *I*112/*m* and $P12_11$ space groups, as described in Chapter 9. It was observed that, whilst the *I*4/*mmm* model provides an adequate fit to the data, lowering the symmetry to *I*4/*m* improves the visual fit and gives a smaller R_{wp} value (Table 10.2). Lowering the symmetry further to *I*112/*m* does not provide any improvement to the fit. Although the $P12_11$ model appears to give improved fitting statistics, there is no visual improvement to the fit and the large errors associated with the bond angles and bond lengths (resulting from the large number of refined parameters) means that the structure is essentially indistinguishable from the *I*4/*m* structure. As such, the *I*4/*m* model is likely to provide the best description of the structure, so this model was used for all subsequent refinements. The fit to the data using the *I*4/*m* model is shown in Figure 10.2, with the refinement parameters detailed in Table 10.3. From the refinement, it is observed that the square-planar units in $LaSrCoIrO_4$ undergo a small tilting distortion, such that the Co−O−Ir bond angle is 174.8(3)°, as shown in Figure 10.3. The observation that $LaSrCoIrO_4$ adopts the *I*4/*m* structure is in direct contrast to Sr_2CoIrO_4 which adopts the undistorted *I*4/*mmm* structure. This difference can be attributed to the smaller ionic radius of La^{3+} relative to Sr^{2+} leading to a decrease in the tolerance factor from Sr_2CoIrO_4 to $LaSrCoIrO_4$.

The refined lattice parameters of $LaSrCoIrO_4$ are a = 5.6807(7) Å and c = 6.7754(9) Å. Whilst the a-lattice parameter is slightly larger than that of Sr_2CoIrO_4 (a = 5.646 Å) and Sr_2FeIrO_4 (a = 5.646 Å), the c lattice parameter is significantly more contracted than that of Sr_2CoIrO_4 (c = 6.943 Å) and Sr_2FeIrO_4 (c = 7.060).[101] This has been observed previously with $LaSrCoRuO_4$ (c = 6.88 Å)[157] and Sr_2CoRuO_4 (c = 7.01 Å),[160] and can be attributed to the fact that 50% of the Sr^{2+} ions have been replaced with smaller La^{3+} ions.

Table 10.2: Fitting statistics and selected bond lengths/angles from the refinements against NPD data collected from $LaSrCoIrO_4$ using an undistorted *I*4/*mmm* structural model and distorted *I*4/*m*, *I*112/*m* and *P*12$_1$1 structural models.

	I*4/*mmm	***I*4/*m***	***I*112/*m***	***P*12$_1$1**
R_{wp} (%)	2.80	2.78	2.78	2.71
R_p (%)	2.04	2.02	2.02	1.94
Co−O−Ir angles (°)	180	174.3(9)	173(3),175(3)	169(8), 172(5)
O−Co−O distances (Å)	4.05(2)	4.06(3)	4.0(1), 4.1(1)	4.0(3), 4.1(3)
O−Ir−O distances (Å)	3.98(2)	3.98(3)	3.9(1), 4.0(1)	4.0(3), 4.1(3)

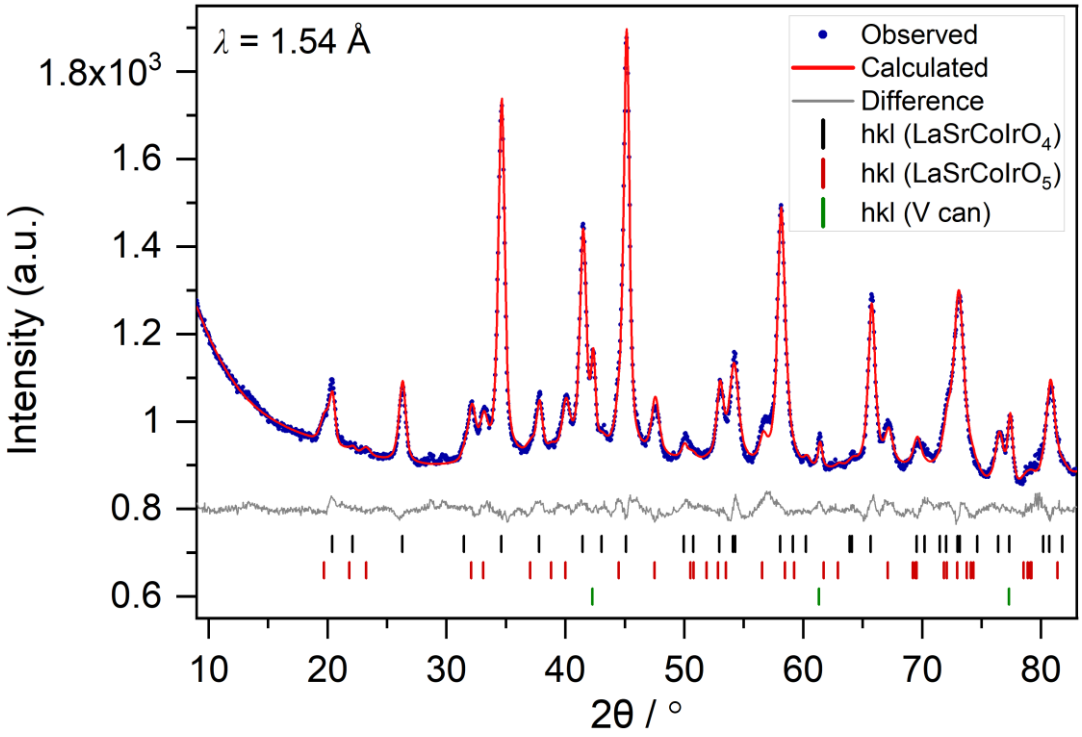

Figure 10.2: Observed, calculated and difference plots from the structural refinement of $LaSrCoIrO_4$ against NPD data collected using the D20 diffractometer at 200 K with a wavelength of 1.54 Å, with $LaSrCoIrO_5$ included as a secondary phase.

Table 10.3: Parameters from the structural refinement of $LaSrCoIrO_4$ against NPD data collected at 200 K from the D20 diffractometer using a structural model in the *I*4/*m* space group. The occupancies at the transition metal sites were fixed at the values observed in the parent phase.

$LaSrCoIrO_4$, space group *I*4/*m* (No. 87), 73(2) wt%						
		x	***y***	***z***	**Occ.**	**B_{iso} (Å^2)**
Sr(1)/La(1)	4*d*	0	½	¼	0.5/0.5	0.05(8)
Co(1)/Ir(1)	2*a*	0	0	0	0.8985/0.1015	1.19(8)
Ir(2)/Co(2)	2*b*	½	½	0	0.8985/0.1015	1.19(8)
O(1)	8*h*	0.2352(7)	0.2578(8)	0	1	0.20(6)
a = 5.6807(7) Å, c = 6.7754(9) Å						
V = 218.64(6) Å^3						
$LaSrCoIrO_5$, space group *I*4/*mmm* (No. 139), 27(2) wt%						
		x	***y***	***z***	**Occ.**	**B_{iso} (Å^2)**
Sr(1)/La(1)	4*d*	0	½	¼	0.5/0.5	0.1(4)
Co(1)/Ir(1)	2*a*	0	0	0	0.8985/0.1015	7(2)
Ir(2)/Co(2)	2*b*	½	½	0	0.8985/0.1015	2.0(6)
O(1)	8*h*	0.265(3)	0.265(3)	0	0.75	9.5(5)
O(2)	4*e*	0	0	0.240(3)	1	9.5(5)
a = 5.409(1) Å, c = 8.136(3) Å						
V = 238.0(2) Å^3						
R_{wp} = 1.07%, R_p = 0.84%, *gof* = 2.55						

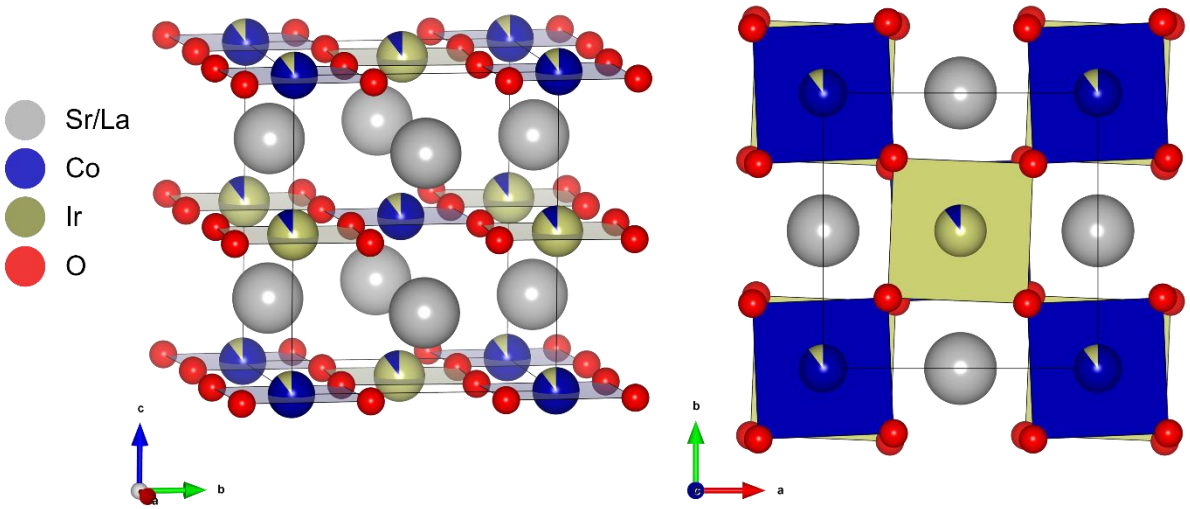

Figure 10.3: Refined crystal structure of $LaSrCoIrO_4$.

10.4.3 Thermogravimetric analysis

Thermogravimetric data were collected from $LaSrCoIrO_4$ whilst heating under flowing oxygen, indicating a mass gain of 5.1%, as shown in Figure 10.4. Assuming full oxidation back to $LaSrCoIrO_6$, this corresponds to an initial composition of $LaSrCoIrO_{4.16}$. This is broadly consistent with the expected composition of $LaSrCoIrO_4$, with the discrepancy arising from the presence of $LaSrCoIrO_5$ in the sample.

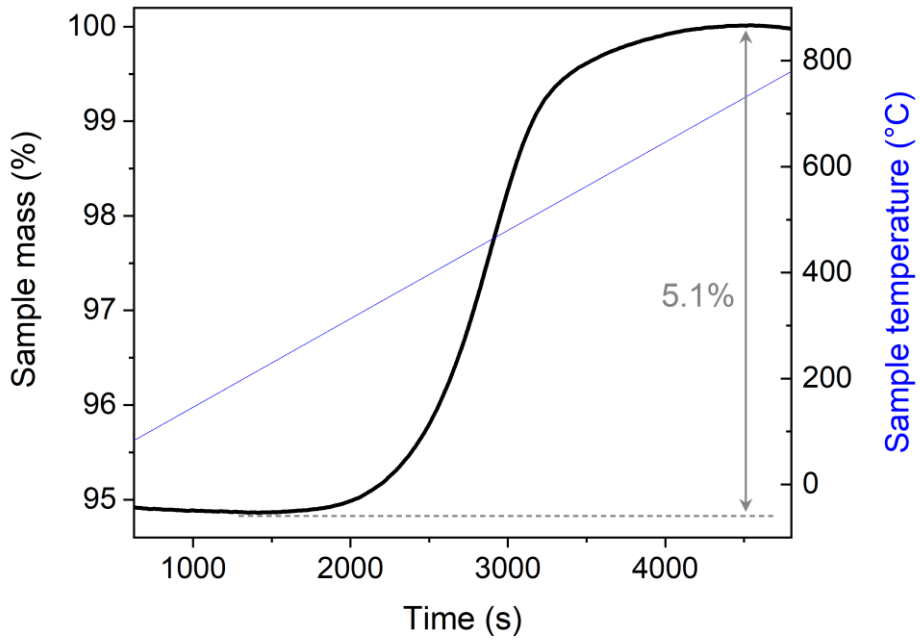

Figure 10.4: TGA trace when $LaSrCoIrO_4$ is heated under flowing oxygen.

10.5 Magnetic characterisation of $LaSrCoIrO_4$

10.5.1 Magnetic behaviour

Magnetisation data collected from $LaSrCoIrO_4$ as a function of temperature are presented in Figure 10.5, and magnetisation-field isotherms collected at 5 K and 300 K are presented in Figure 10.6. Fitting the data to the Curie-Weiss law yields a value for C of 8.02(7) cm^3 K mol^{-1} and a value for θ of 45(2) K. There is a divergence in the ZFC and FC curves at 85 K, which

is likely to originate from the $LaSrCoIrO_5$ impurity (Appendix A5). There is also a change in gradient of the ZFC curve at ~50 K, which is likely to represent a magnetic transition in the bulk $LaSrCoIrO_4$ phase to a canted antiferromagnetic state. The observation that θ has a value of 45(2) K supports the proposition that there is a transition at ~50 K.

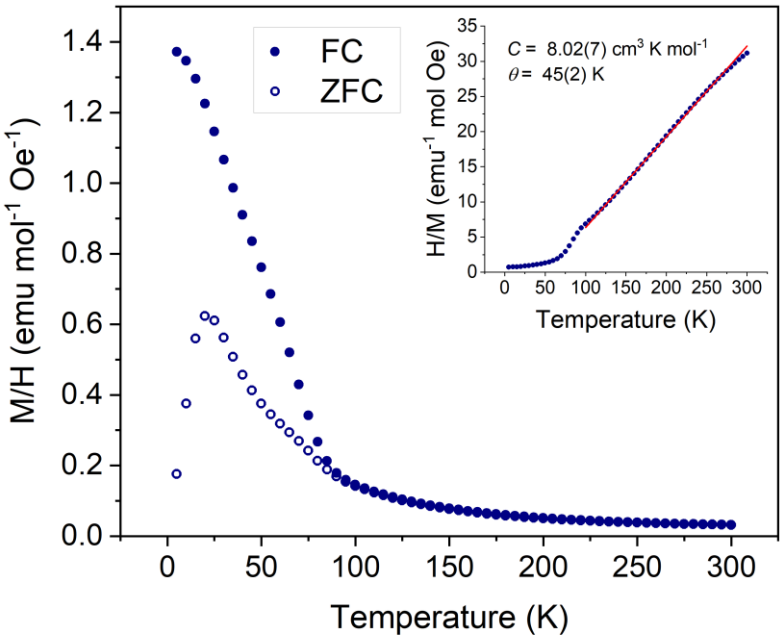

Figure 10.5: Magnetisation data collected from $LaSrCoIrO_4$ as a function of temperature, measured in a field of 100 Oe under both ZFC and FC conditions.

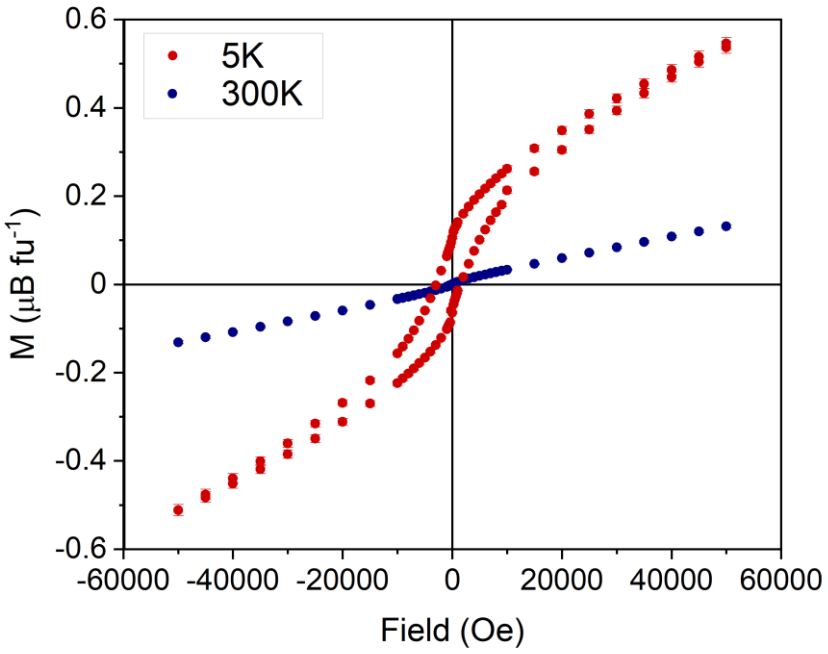

Figure 10.6: Magnetisation-field isotherms for $LaSrCoIrO_4$ measured at 5 K and 300 K.

10.5.2 Low temperature neutron powder diffraction

NPD data were collected from $LaSrCoIrO_4$ at 10 K with a wavelength of 2.41 Å using the D20 diffractometer at the ILL. A comparison of this data with data collected at ~100 K is shown in Figure 10.7. Two additional Bragg peaks are observed at 10 K, which are attributed to magnetic scattering from the $LaSrCoIrO_4$ phase. The weak nature of the peaks could suggest that, although the magnetic ordering occurs on a sufficient length scale that features are observable from neutron diffraction, the ordering is relatively short-range. In an attempt to quantify the length scale of the magnetic ordering, a crude particle size analysis was performed by extracting values for the *fwhm* of the nuclear reflections at 2θ ~ 32.2° and 41.9° and the magnetic reflections at 2θ ~ 11.5° and 24.5°, and using the Scherrer equation (Equation 34) to calculate approximate values of D_0 for the crystallite and magnetic domains.[161] It is worth noting that in the NPD data, the peak broadening has a substantial instrumental contribution. During the analysis, these instrumental contributions were not considered and, as such, the

values of D_0 obtained should only be used as an approximate gauge of the relative sizes of the crystallite and magnetic domains and not as true representations of the domain sizes. The results from this analysis are shown in Table 10.4 and indicate that the domain size associated with the magnetic ordering is significantly smaller than the crystallite domain size.

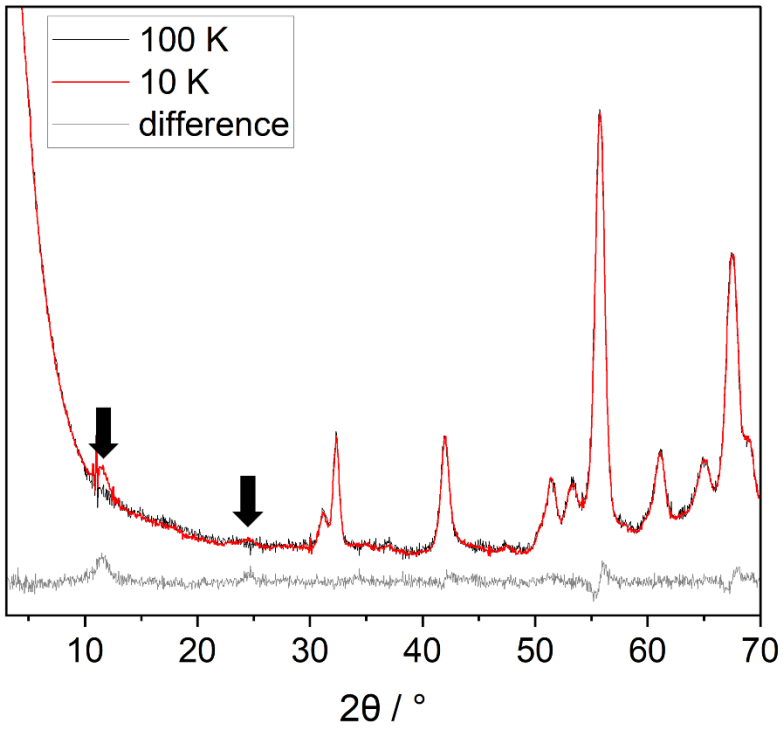

Figure 10.7: Comparison between NPD data collected from $LaSrCoIrO_4$ at 10 K and 100 K using the D20 diffractometer with a wavelength of 2.41 Å, and the difference between the patterns at these two temperatures. The arrows highlight possible magnetic peaks.

Table 10.4: Results from crude particle size analysis using the peak widths of the magnetic reflections at $2\theta \sim 11.5°$ and 24.5° and the nuclear reflections at $2\theta \sim 32.2°$ and 41.9° in the NPD data collected from $LaSrCoIrO_4$ at 10 K.

	2θ (°)	*fwhm* (rad)	D_0 (Å)
Magnetic	11.48	0.0235	105
	24.50	0.0175	151
Nuclear	32.21	0.00774	368
	41.89	0.00895	362

The magnetic Bragg peak observed at $2\theta \sim 24.5°$ can be indexed by the 100 reflection of a cell with the same dimensions as the nuclear unit cell and is consistent with a magnetic propagation

vector of k = (1,1,1). Using the ISODISTORT software suite,[151,152] it was determined that there are two irreducible representations (mM^{1+} and $mM^{3+}M^{4+}$) of the $I4/m$ space group associated with this propagation vector when only magnetic distortions on the Co and Ir atoms are considered. The distortions associated with both of these irreducible representations result in C-type antiferromagnetic ordering, with the magnetic moments aligned along the *z*-axis for mM^{1+} and aligned in the *xy*-plane for $mM^{3+}M^{4+}$. It is possible to achieve an adequate fit to the data for both types of magnetic ordering and the intensity of the peak is too low to ascertain which model provides the most accurate description of the magnetic structure.

The model in which the moments are aligned along the *z*-axis can be described in magnetic space group 83.50. Due to the strong correlation between the magnetic scattering from the two B-site cations, it is not possible to definitively establish the moments at the two transition metal sites. Fixing the moment at the Ir sites to zero and allowing the moment at the Co sites to refine yields a moment of 0.7(2) μ_B at the Co sites, which is significantly smaller than the value of 2 μ_B expected for Co^{I}. Increasing the value of the moment at the Ir sites leads to a decrease in the value of the moment at the Co sites with the total value of the moments at the two sites remaining approximately constant at ~0.7−1.1 μ_B. A representative fit to the data, with the moment at the Co sites constrained to be double that at the Ir sites, is shown in Figure 10.8(a), along with the corresponding magnetic structure.

The model in which the moments are aligned in the *xy*-plane can be described in magnetic space group 14.83. Similar to previously, the strong correlation between the magnetic scattering from the two B-site cations means that it is not possible to definitively establish the moments at the Co and Ir sites. A representative fit to the data using this model is shown in Figure 10.8(b), along with the corresponding magnetic structure.

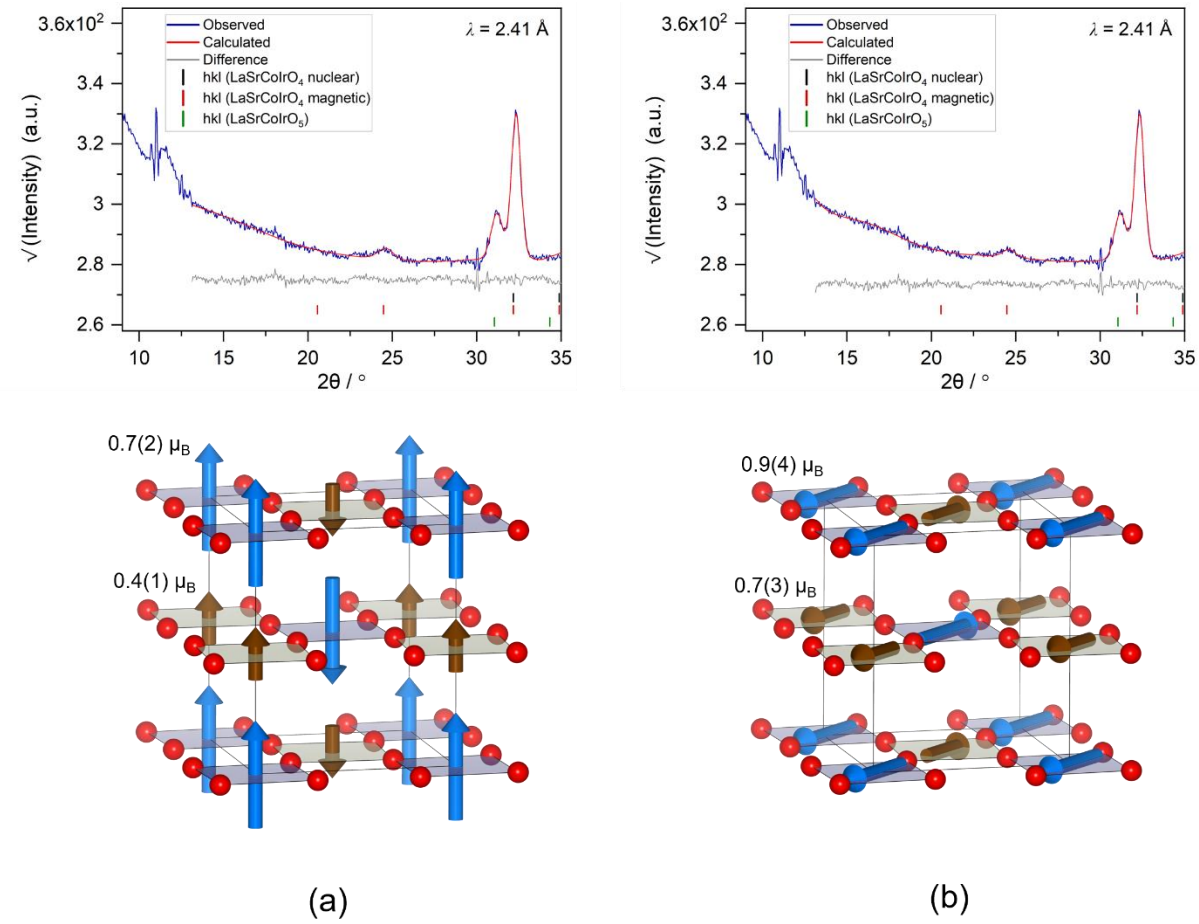

Figure 10.8: (a) Fit to the NPD data collected from $LaSrCoIrO_4$ at 10 K when a magnetic distortion that transforms as the mM^{1+} irreducible representation is applied, corresponding to C-type antiferromagnetic order with the moments aligned along the *z*-axis. In this refinement, the value of the Co moment was constrained to be double that of the Ir moment. (b) Fit to the NPD data when a magnetic distortion that transforms as the $mM^{3+}M^{4+}$ irreducible representation is applied, corresponding to C-type antiferromagnetic order with the moments aligned in the *xy*-plane.

In addition to the magnetic peak at $2\theta \sim 24.5°$, there is also a magnetic peak at $2\theta \sim 11.5°$. This can be indexed by the 110 reflection of a (3 × 3 × 1)-expanded unit cell, as discussed in Appendix A5, or by the 004 reflection of a (1 × 1 × 7)-expanded unit cell. However, neither of these unit cell expansions seem likely for a phase based on the double-perovskite structure. One possible origin for the peak is the presence of an incommensurate modulation in the magnetic structure due to spin canting. For example, if the spins are canted in such a way that they form a spiral arrangement along the *z*-direction, this could lead to a magnetic structure with an incommensurate propagation vector, accounting for the reflection at $2\theta \sim 11.5°$.

However, it is difficult to derive a magnetic structure given that only a single peak is present in the NPD data.

It is worth noting that it is possible that the magnetic peaks could arise from the $LaSrCoIrO_5$ secondary phase. However, the peaks cannot be indexed using a simple unit cell expansion of $LaSrCoIrO_5$, and NPD data collected from an impure sample of $LaSrCoIrO_5$ show no evidence of magnetic peaks at $2\theta \sim 11.5°$ or 24.5° (Appendix A5).

In conclusion, the magnetic structure of $LaSrCoIrO_4$ is likely to be based on C-type antiferromagnetic ordering, similar to the models shown in Figure 10.8, with a possible incommensurate modulation, which could arise from canting of the spins. The magnetic structure is strikingly different from that of Sr_2CoIrO_4 (Chapter 9) and Sr_2FeIrO_4.[101] The observation that $LaSrCoIrO_4$ adopts a different magnetic structure to Sr_2CoIrO_4 suggests that the unpaired electron in the $3d_{xy}$ orbital of Co^{II} plays an important role in determining the magnetic structure of Sr_2CoIrO_4.

The adoption of C-type magnetic ordering in $LaSrCoIrO_4$ implies that the nearest-neighbour Co−Ir coupling interactions are antiferromagnetic within the layers and ferromagnetic between the layers. The ferromagnetic interlayer coupling can be rationalised on the basis that Co^{I} has a half-filled d_{z^2} orbital and Ir^{II} has a fully occupied d_{z^2} orbital (Figure 10.9). The observation that this interaction appears to be stronger in $LaSrCoIrO_4$ than in Sr_2CoIrO_4 or Sr_2FeIrO_4 is consistent with the fact that the $LaSrCoIrO_4$ interlayer distance is significantly shorter (Section 10.4.2), leading to greater overlap of the cobalt and iridium d_{z^2} orbitals. However, it is difficult to rationalise the presence of antiferromagnetic coupling within the layers, reinforcing the notion that simple superexchange considerations based on the Goodenough-Kanamori rules are often not applicable to the interactions between 3d and 5d transition metals, as discussed in Chapter 9. A surprising feature of the magnetic structure of $LaSrCoIrO_4$ is that the moments at

the Ir sites are arranged ferromagnetically with respect to each other within the layers. This is in direct contrast to the situation observed for Sr_2FeIrO_4, in which the strongest coupling interaction is antiferromagnetic exchange between the Ir^{II} ions. This implies that direct exchange between Ir^{II} ions is, in effect, switched off in $LaSrCoIrO_4$, comparable to the situation observed for Sr_2CoIrO_4, in which there is no ordering at the Ir sites. To fully understand the coupling interactions in this compound, DFT calculations will need to be performed.

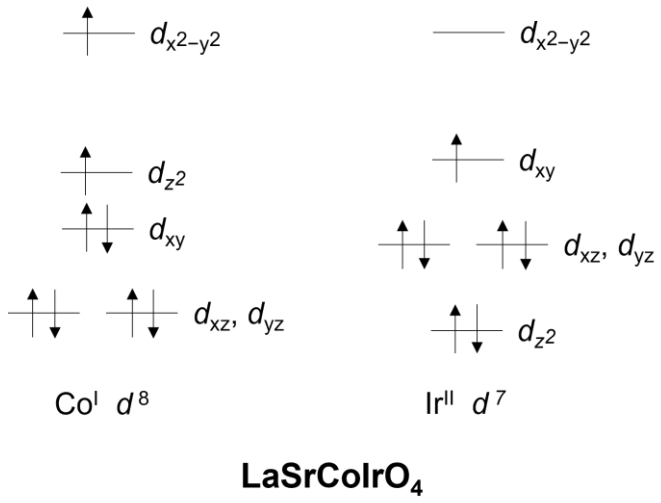

Figure 10.9: Proposed electronic structure of $LaSrCoIrO_4$, assuming the same transition metal oxidation states as those observed in $LaSr_3CoIrO_6$.[46]

10.6 Conclusion

Heating the double perovskite, $LaSrCoIrO_6$, in the presence of a Zr getter yields the infinite layer phase, $LaSrCoIrO_4$, which occurs via a tetragonal $LaSrCoIrO_5$ intermediate. $LaSrCoIrO_4$ adopts a structure in the $I4/m$ space group with a small $a^0a^0c^-$ tilting distortion. At low temperature, the compound exhibits magnetic ordering that is likely to be based on a C-type antiferromagnetic structure, with a possible incommensurate modulation arising from spin canting.

Chapter 11 – Effect of ball-milling on the reactivity of La_2CoRhO_6 with NaH and LiH

11.1 Introduction

La_2CoRhO_6 adopts a B-site cation disordered perovskite structure.[162–164] Heating this compound in the presence of a Zr getter leads to the formation of $La_2CoRhO_{4.5}$, which is a partially anion-vacancy ordered phase consisting of a disordered arrangement of corner-sharing MO_4 square-plane and MO_5 square-based pyramidal units.[165] In this phase, cobalt is present as Co^{I} and, whilst rhodium is nominally present as Rh^{II}, it is, in fact, disproportionated into Rh^{I} and Rh^{III}, which occupy square-planar and square-based pyramidal coordination sites, respectively. The lattice parameters for this phase are a = 5.649 Å and c = 7.337 Å (in a ($\sqrt{2} \times \sqrt{2} \times 2$)-expanded unit cell relative to the simple cubic perovskite).

Recent unpublished exploratory work has suggested that reaction of La_2CoRhO_6 with NaH yields a phase with lattice parameters of a = 4.011 Å and c = 3.592 Å (corresponding to a = 5.672 Å and c = 7.184 Å in the expanded unit cell).[166] The c-lattice parameter for this phase is significantly more contracted compared to $La_2CoRhO_{4.5}$ and would be consistent with the formation of an infinite-layer phase with composition La_2CoRhO_4, in which cobalt and rhodium are both present in the +1 oxidation state. However, it is not possible to obtain La_2CoRhO_4 as a pure phase; substantial quantities (> 20%) of the La_2CoRhO_6 parent material remain in the reaction mixture after many heating cycles, and an increased reaction temperature leads to the onset of non-topochemical decomposition.

To investigate whether decreasing the crystallite size or increasing the lattice strain of the La_2CoRhO_6 starting material improves its reactivity, ball-milling was performed on the synthesised La_2CoRhO_6 samples. The ball-milled samples were then reacted with NaH and LiH to determine the effect of microstructure on the reactivity of this compound.

11.2 Synthesis and characterisation of pristine and ball-milled La_2CoRhO_6

11.2.1 Synthesis of pristine and ball-milled La_2CoRhO_6

Three-gram polycrystalline samples of La_2CoRhO_6 were prepared using conventional ceramic synthesis methods. Suitable stoichiometric ratios of La_2O_3 (dried at 900 °C), Co_3O_4 and Rh_2O_3 (dried for 2 hours at 850 °C) were thoroughly ground together in an agate pestle and mortar, pelletised and heated in air at 1000 °C for 2 days. The samples were then reheated for two further cycles of 2 days at temperatures of 1200 °C and 1250 °C, respectively, with intermediate grinding and pelletisation performed between each heating cycle. The structure obtained is consistent with the previously reported B-site cation disordered perovskite in the *Pnma* space group (*vide infra*).[162–164]

To prepare ball-milled samples, 2 g of La_2CoRhO_6 was placed in a 14 mL jar with a 7 g ball and milled for 15 minutes at 30 Hz.

11.2.2 Microstructural analysis of pristine and ball-milled La_2CoRhO_6

To allow the effect of ball-milling on crystallite domain size and lattice strain to be quantified, microstructural analysis (Section 2.4.1) was performed on both pristine and ball-milled La_2CoRhO_6 within the Rietveld method using SXRD data collected from each sample. For the pristine sample, both the broadening from crystallite size and the broadening from microstrain were modelled using intermediate Gaussian-Lorentzian peak shapes. This yielded a value for D_{vol} of 210(10) nm and a value for the strain, $fwhm_{\varepsilon}$, of 0.00289(2) rad. The fit to the data is shown in Figure 11.1, with the refinement parameters detailed in Table 11.1.

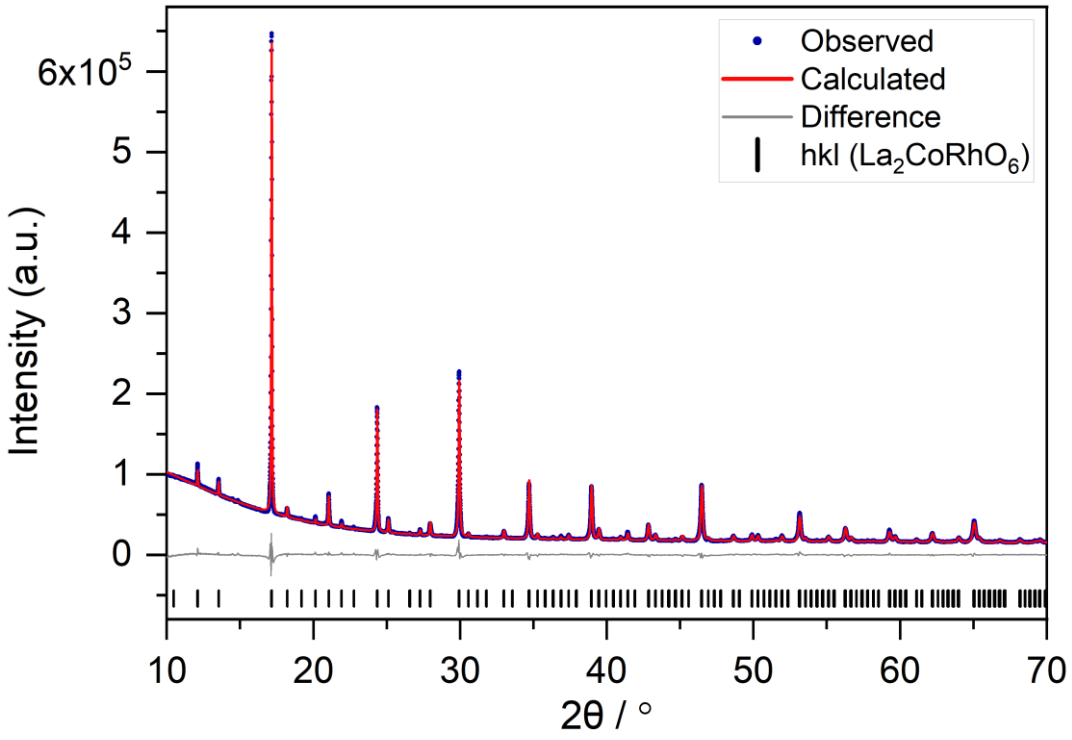

Figure 11.1: Observed, calculated and difference plots from the structural refinement of pristine La_2CoRhO_6 against SXRD data (λ = 0.825 Å), with the isotropic crystallite size broadening and the isotropic microstrain broadening modelled using intermediate Gaussian-Lorentzian line shapes.

Table 11.1: Parameters from the structural refinement of pristine La_2CoRhO_6 against SXRD data. The fractional coordinates of the oxide sites were fixed at the reported values.[165]

La_2CoRhO_6, space group *Pnma* (No. 62)						
		x	***y***	***z***	**Occ.**	**B_{iso} (Å^2)**
La(1)	4*c*	0.46514(8)	¼	0.4943(3)	1	0.855(9)
Co(1)/Rh(1)	4*b*	0	0	½	0.5/0.5	0.49(1)
O(1)	4*c*	0.004	¼	0.4336	1	1.22(5)
O(2)	8*d*	0.2232	0.0353	0.7661	1	1.22(5)
a = 5.52291(8) Å, b = 7.8109(2) Å, c = 5.5293(1) Å						
V = 238.53(1) Å^3						
R_{wp} = 2.68%, R_p = 1.83%, *gof* = 4.41						

The SXRD data collected from the ball-milled sample showed substantially broader peaks compared to the pristine sample, indicating smaller crystallite domains and/or greater lattice strain. Furthermore, the *fwhm* of the diffraction peaks from the ball-milled sample showed a different 2θ dependence compared to the pristine sample, as illustrated in Figure 11.2, which

suggests different relative peak broadening contributions from crystallite domain size and microstrain.

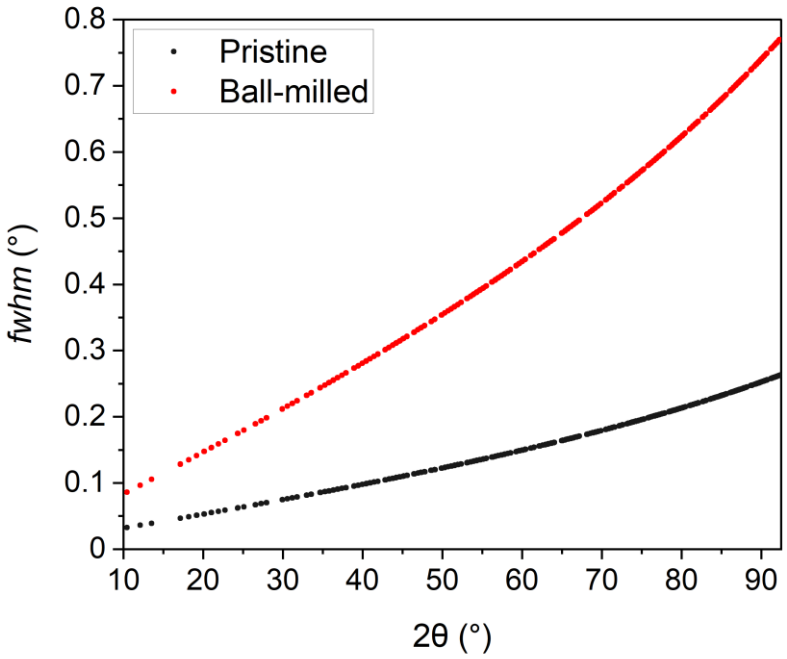

Figure 11.2: Plot of peak *fwhm* as a function of 2θ in SXRD data collected from pristine and ball-milled La_2CoRhO_6.

As before, Rietveld analysis was performed to quantify the microstructural properties of the sample. Both the broadening from crystallite size and the broadening from microstrain were modelled using intermediate Gaussian-Lorentzian peak shapes, yielding a value for D_{vol} of 94(5) nm and a value for the strain, $fwhm_{\varepsilon}$, of 0.0061(4) rad. These results indicate that the broadening of the peaks in the SXRD data arises from both the presence of smaller crystallite domains and greater lattice strain, compared to the pristine sample. The fit to the SXRD data is shown in Figure 11.3, and the refinement parameters are detailed in Table 11.2.

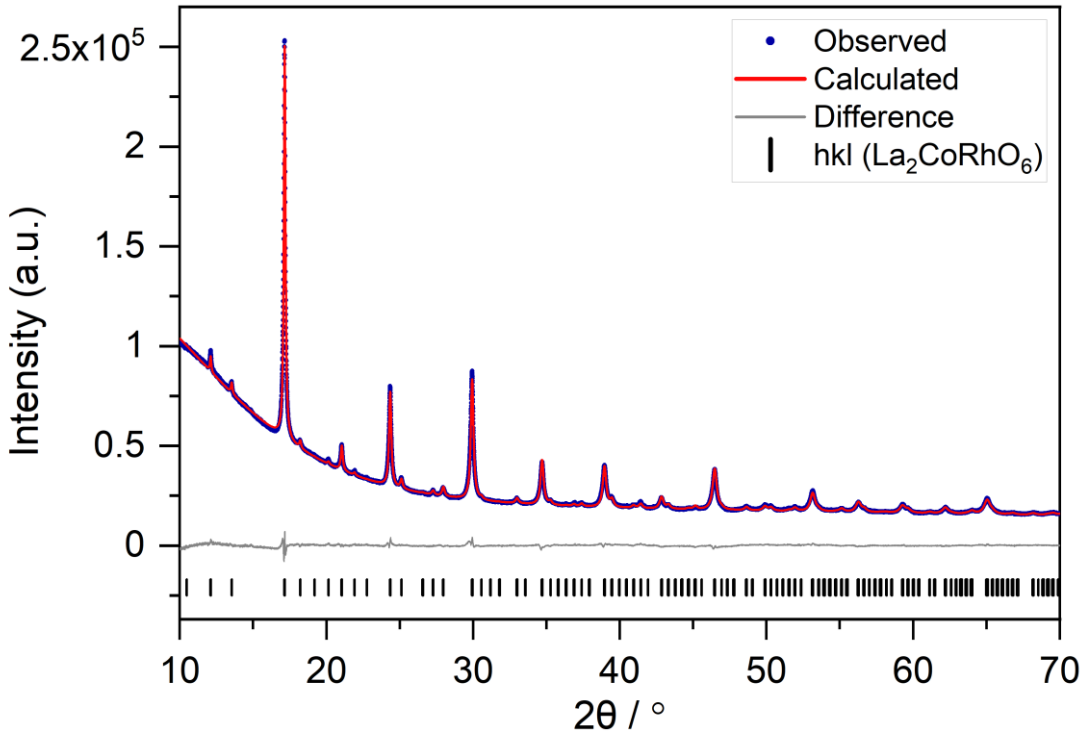

Figure 11.3: Observed, calculated and difference plots from the structural refinement of ball-milled La_2CoRhO_6 against SXRD data (λ = 0.825 Å), with the isotropic crystallite size broadening and the isotropic microstrain broadening modelled using intermediate Gaussian-Lorentzian line shapes.

Table 11.2: Parameters from the structural refinement of ball-milled La_2CoRhO_6 against SXRD data. The fractional coordinates of the oxide sites were fixed at the reported values.[165]

La_2CoRhO_6, space group *Pnma* (No. 62)						
		x	***y***	***z***	**Occ.**	**B_{iso} (Å^2)**
La(1)	4*c*	0.4669(1)	¼	0.499(2)	1	0.99(1)
Co(1)/Rh(1)	4*b*	0	0	½	0.5/0.5	0.82(1)
O(1)	4*c*	0.004	¼	0.4336	1	1.34(5)
O(2)	8*d*	0.2232	0.0353	0.7661	1	1.34(5)
a = 5.5225(3) Å, b = 7.8097(6) Å, c = 5.5300(5) Å						
V = 238.50(3) Å^3						
R_{wp} = 1.43%, R_p = 1.11%, *gof* = 2.33						

11.2.3 Magnetic behaviour of pristine and ball-milled La_2CoRhO_6

Magnetisation data collected from pristine La_2CoRhO_6 as a function of temperature are shown in Figure 11.4, and magnetisation-field isotherms collected at 5 K and 300 K are shown in Figure 11.5. There is a sharp increase in the FC curve below ~90 K and a substantial divergence

from the ZFC curve, indicating the presence of a magnetic transition around this temperature. Considering the magnitude of the magnetisation in Figure 11.5, the phase is likely to adopt a canted antiferromagnetic ground state at low temperature. Fitting of the susceptibility data to the Curie-Weiss law yields a value for C of 0.819(4) cm^3 K mol^{-1} and a value for θ of 6.8(3) K.

There is some debate over the nature of the oxidation states in La_2CoRhO_6. Li *et al.*[162] proposed that the compound contains a mixture of Co^{II} (high-spin d^7), Co^{III} (low-spin d^6), Co^{III} (high-spin d^6), Rh^{III} (low-spin d^6) and Rh^{IV} (low-spin d^5), with the relative quantities of each being strongly dependent on temperature. Whilst the results from Streltsov *et al.*[164] were in agreement with this for most of the $La_2Co_{2-x}Rh_xO_6$ series, they suggested that full charge ordering into Co^{II} and Rh^{IV} occurs for La_2CoRhO_6. Conversely, Knížek *et al.*[163] and Asai *et al.*[167] proposed that the transition metals in La_2CoRhO_6 are present only as Co^{III} and Rh^{III}, with cobalt being present in both high-spin and low-spin states.

The value for C is close to that expected for a system containing 2 unpaired electrons. As such, it is unlikely that the system contains solely Co^{II} and Rh^{IV}. However, from this data, it is not possible to conclude whether only Co^{III} and Rh^{III} are present, with the magnetic behaviour arising from the coexistence of high-spin and low-spin cobalt, or whether some Co^{II} and Rh^{IV} are also present.

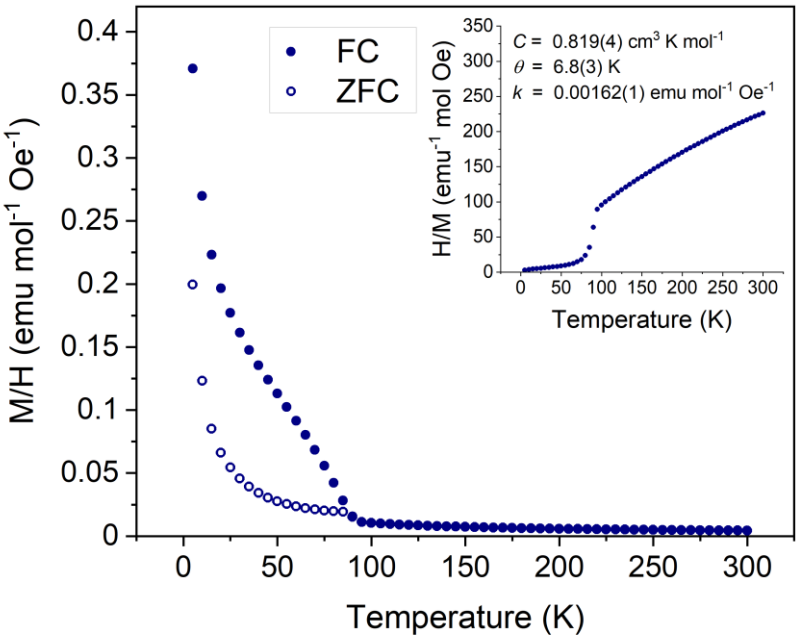

Figure 11.4: Magnetisation data collected from pristine La_2CoRhO_6 as a function of temperature, measured in a field of 100 Oe under both ZFC and FC conditions.

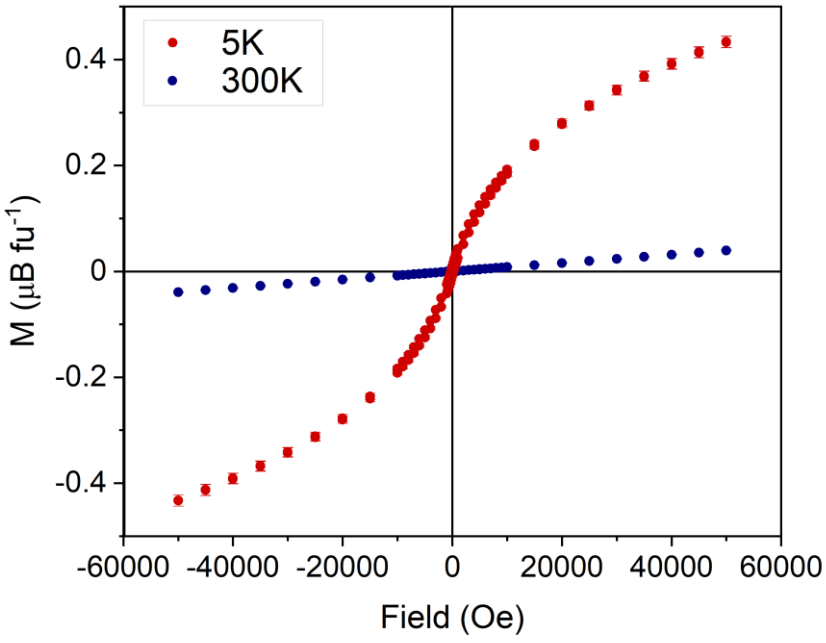

Figure 11.5: Magnetisation-field isotherms for pristine La_2CoRhO_6 measured at 5 K and 300 K.

Magnetisation data collected from ball-milled La_2CoRhO_6 as a function of temperature are shown in Figure 11.6, and magnetisation-field isotherms collected at 5 K and 300 K are shown

in Figure 11.7. The magnetic behaviour of this sample is qualitatively different from that of the pristine sample. Although the magnetisation-field isotherms appear similar, there is no longer an obvious magnetic transition in the magnetisation collected as a function of temperature. This is likely to result from the smaller particle sizes in the ball-milled sample, which means that surface effects (eg. uncompensated surface spins) are much more significant. Similar surface effects have been observed previously for ball-milled, thin-layer and nanoparticle antiferromagnetic materials.[168–171]

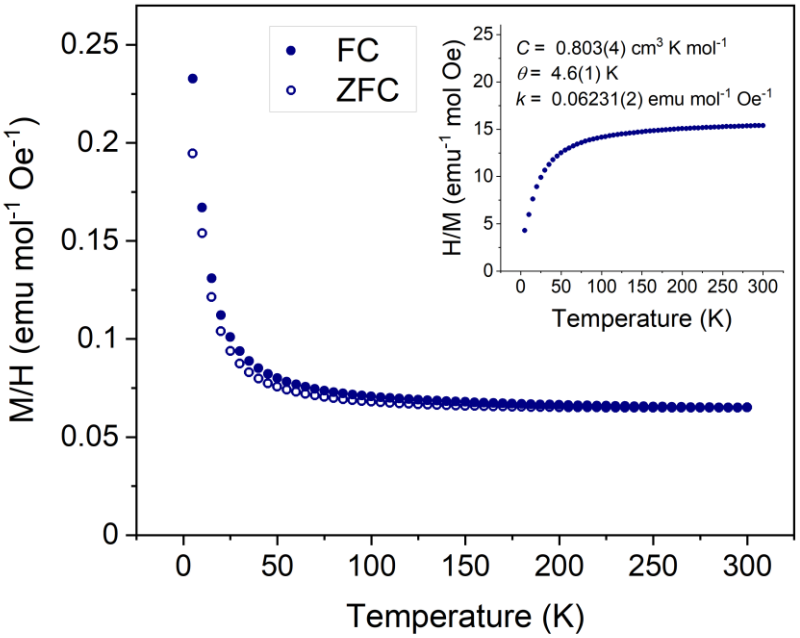

Figure 11.6: Magnetisation data collected from ball-milled La_2CoRhO_6 as a function of temperature, measured in a field of 100 Oe under both ZFC and FC conditions.

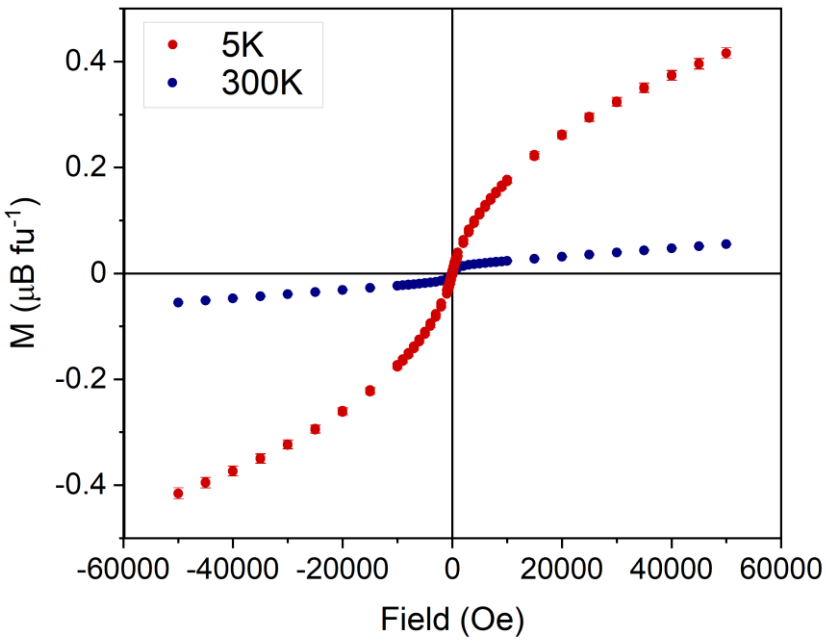

Figure 11.7: Magnetisation-field isotherms for ball-milled La_2CoRhO_6 measured at 5 K and 300 K.

11.3 Reactivity of La_2CoRhO_6 with NaH

In Section 11.2.2, it was determined that ball-milling La_2CoRhO_6 results in smaller crystallite domains and greater lattice strain compared to the pristine sample. It can be imagined that these microstructural changes could decrease the activation energy for topochemical reduction to a greater extent than non-topochemical decomposition, thereby allowing previously inaccessible phases to be synthesised.

To investigate this, 250 mg samples of pristine and ball-milled La_2CoRhO_6 were mixed with 4 mole equivalents of NaH in an Ar-filled glovebox, sealed in evacuated Pyrex® ampoules and heated at 170 °C for 2 days. After this heating cycle, the reaction mixture was analysed by PXRD. The reaction temperature was increased in 10 °C steps, with several heating cycles performed at each temperature. Analysis by PXRD was performed after each heating cycle. The results from these heating cycles are shown in Figure 11.8 for the pristine sample and Figure 11.9 for the ball-milled sample.

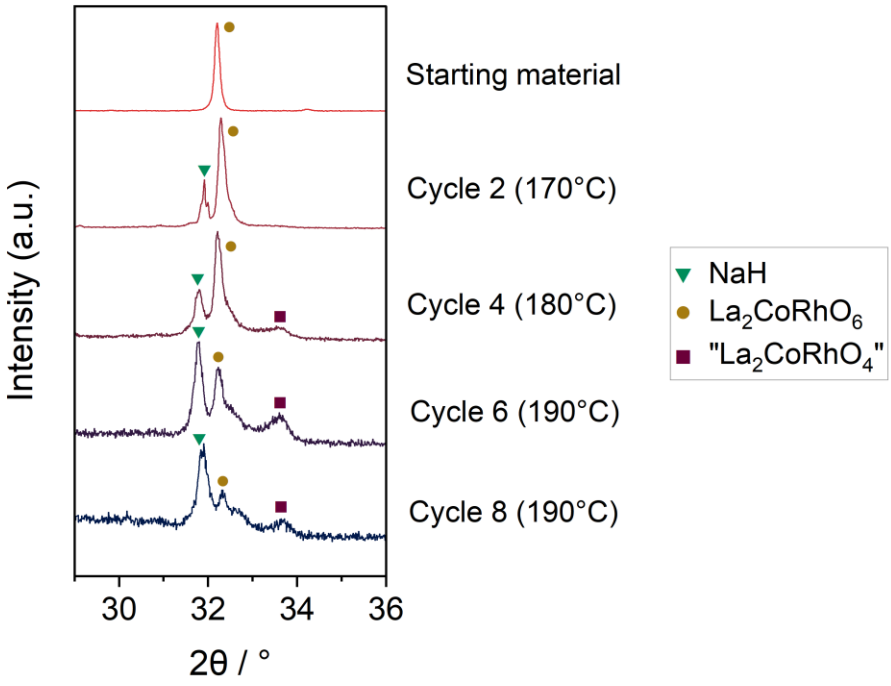

Figure 11.8: Evolution of PXRD patterns (λ = 1.5406 Å) for the reaction between pristine La_2CoRhO_6 and NaH at several intervals when the reaction mixture is heated at temperatures of 170−190 °C.

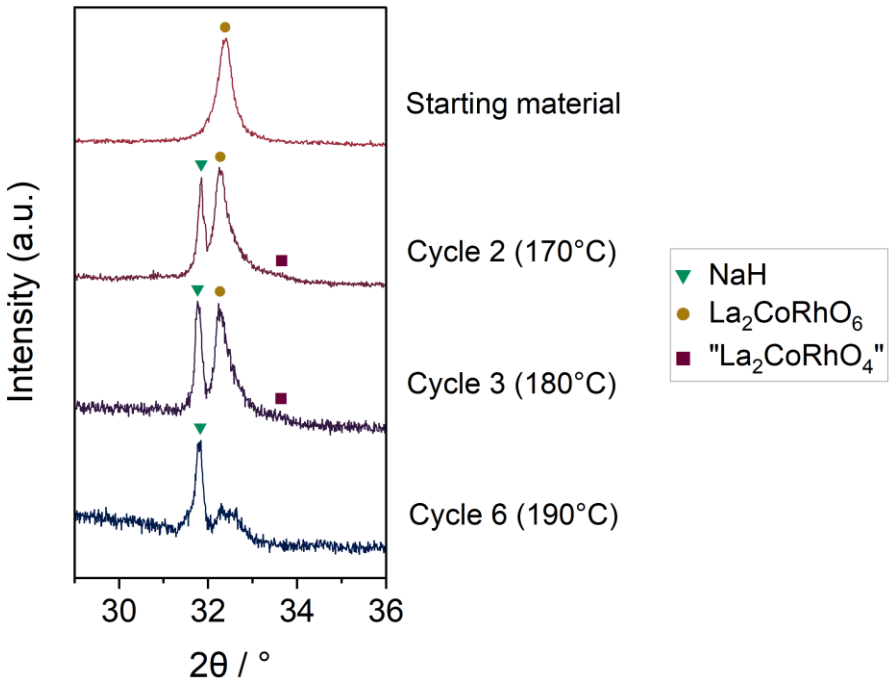

Figure 11.9: Evolution of PXRD patterns (λ = 1.5406 Å) for the reaction between ball-milled La_2CoRhO_6 and NaH at several intervals when the reaction mixture is heated at temperatures of 170−190 °C.

Reaction of pristine La_2CoRhO_6 with NaH results in the emergence of a peak at $2\theta \sim 33.5°$ in the PXRD data when the mixture is heated at 180 °C. This can be indexed using a tetragonal cell with lattice parameters a = 4.01 Å and c = 3.59 Å, consistent with the formation of La_2CoRhO_4. When the reaction mixture is heated at 190 °C, this peak increases in intensity. However, a substantial amount of the parent oxide phase is still present and further heating at this temperature leads to the onset of non-topochemical decomposition.

Meanwhile, when ball-milled La_2CoRhO_6 is reacted with NaH, heating at 180 °C yields a feature at $2\theta \sim 33.5°$ in the PXRD data, consistent with the reactivity observed for the pristine sample. However, this feature has a much lower intensity than that observed for the pristine sample. Further heating at 180 °C does not result in any change to the pattern and raising the temperature to 190 °C leads to the onset of non-topochemical decomposition. This indicates that ball-milling does not lead to any improvement in the reactivity of La_2CoRhO_6 with NaH. It is worth noting that the lower intensity of the tetragonal 101 peak for the ball-milled sample partly results from the fact that the peaks for this sample are substantially broader, which lowers the intensity of the peaks and can make it difficult to distinguish small peaks from the background.

11.4 Reactivity of La_2CoRhO_6 with LiH

11.4.1 Results

Trial reactions were prepared by mixing 200 mg of pristine and ball-milled La_2CoRhO_6 with 8 mole equivalents of LiH in an Ar-filled glovebox, sealing the reaction mixtures in evacuated Pyrex® ampoules and heating at the desired temperature for 2 days. The reaction mixtures were subsequently analysed by PXRD and reheated at an increased temperature. At all temperatures up to decomposition, the samples remained metrically cubic but, at temperatures of 130 °C and above, a reaction was observed to occur for both the pristine and ball-milled samples, signalled

by a broadening of the diffraction peaks and the formation of Li_2O. Heating the reaction mixtures above 235 °C led to the onset of non-topochemical decomposition.

To investigate more closely the effect of ball-milling on the reactivity of La_2CoRhO_6 with LiH, the reactions were repeated using 1.5 g samples of La_2CoRhO_6. The reaction mixtures were heated for 1 period of 7 days at a temperature of 210 °C. Both samples showed a broadening of the diffraction peaks and the formation of Li_2O, indicating that a reaction had occurred. The samples were then washed with MeOH under an N_2 atmosphere and dried under vacuum.

Thermogravimetric data were collected under flowing oxygen from the product of the reaction between pristine La_2CoRhO_6 and LiH, as shown in Figure 11.10. The sample showed a mass gain of 2.55%, corresponding to an initial composition of $La_2CoRhO_{5.14}H_y$. Analysis of the exhaust gas showed a release of water and hydrogen gas concurrent with the oxidation, indicating that hydride is present in the phase.

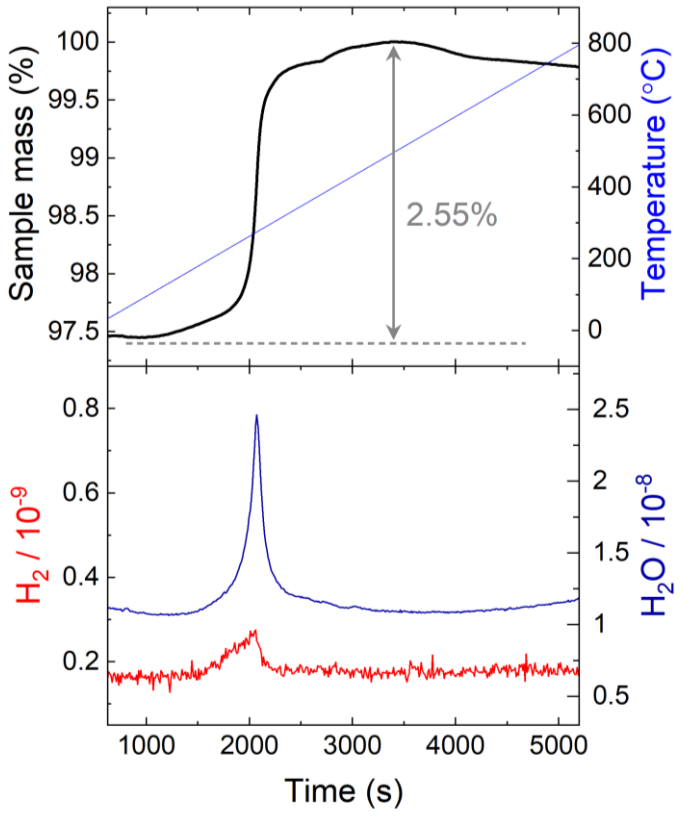

Figure 11.10: TGA trace (top panel) and H_2/H_2O contents of exhaust gas (bottom panel) when the product from the reaction between pristine La_2CoRhO_6 and LiH is heated under flowing oxygen.

Meanwhile, thermogravimetric data collected under flowing oxygen from the product of the reaction between ball-milled La_2CoRhO_6 and LiH (Figure 11.11) showed a mass gain of 6.23%, corresponding to an initial composition of $La_2CoRhO_{3.92}H_y$. Similar to before, analysis of the exhaust gas showed a release of water concurrent with the oxidation, indicating that hydride is present in the phase. Iodometric titration indicated an overall transition metal oxidation state of approximately +3.7, which would be roughly consistent with a composition of $La_2CoRhO_4H_2$.

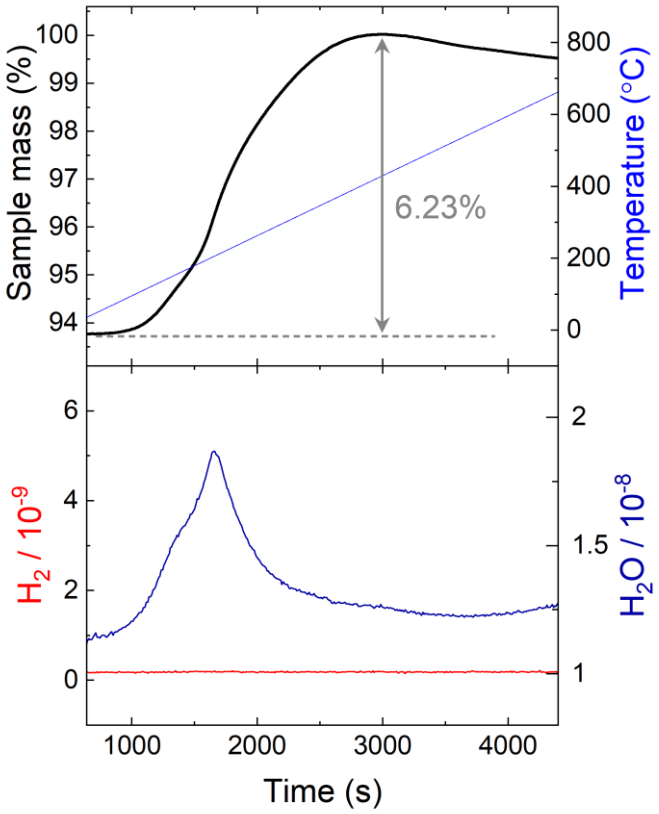

Figure 11.11: TGA trace (top panel) and H_2/H_2O contents of exhaust gas (bottom panel) when the product from the reaction between ball-milled La_2CoRhO_6 and LiH is heated under flowing oxygen.

11.4.2 Discussion

From the results in Section 11.4.1, it is likely that, by reacting La_2CoRhO_6 with LiH, a continuous range of $La_2CoRhO_{6-x}H_y$ compounds can be prepared with varying oxide/hydride contents. Ball-milling of the all-oxide La_2CoRhO_6 phase prior to reaction with LiH allows a

greater extent of reduction to be achieved. This is in direct contrast to the reaction with NaH, in which ball-milling showed no improvement to the reactivity. This can be rationalised by considering possible effects of lattice strain and crystallite size on the reaction energy profiles for the reactions of La_2CoRhO_6 with LiH and NaH. As shown in Figure 11.12, smaller crystallite domains lower the energy barrier for reaction by directly lowering the activation energy through enhanced flexibility of the particles.[172] This will lower the energy barrier for both the topochemical reaction and non-topochemical decomposition in both the NaH and LiH reactions and, as such, is unlikely to be the origin of the difference in reactivity. Meanwhile, greater lattice strain lowers the energy barrier for reaction by raising the energies of the phases. It is likely to be this effect that accounts for the difference in the effect of ball-milling on the reactivity of La_2CoRhO_6 with LiH, compared to with NaH, as discussed below.

Despite the substantial change in lattice parameters associated with the formation of infinite-layer phases, a consequence of the anion vacancy ordering in these compounds is that the structures retain relatively high crystallinity. However, for perovskite oxyhydride phases with an anion disordered structure, the fact that oxide and hydride ions, with their strongly contrasting sizes, occupy the same crystallographic sites results in these phases having intrinsically high lattice strain and low crystallinity (as demonstrated by $Sr_2CoIrO_{4.4}H_{1.6}$ and $LaSrCoIrO_{4.4}H_{1.4}$ in Chapter 7). For the reaction with NaH (Figure 11.12(a)), the lattice strain induced by ball-milling increases the energy of both La_2CoRhO_6 and La_2CoRhO_4 and, consequently, reduces the energy barrier for both the topochemical reaction and non-topochemical decomposition. As a result, the reactivity of ball-milled La_2CoRhO_6 with NaH is comparable to that of pristine La_2CoRhO_6.

However, for the LiH reaction (Figure 11.12(b)), the disordered arrangement of oxide and hydride means that the products after the reactions of both pristine and ball-milled La_2CoRhO_6 with LiH are likely to be highly strained. This means that, although ball-milling raises the

energy of the La_2CoRhO_6 starting material, the energy of the oxyhydride product is likely to be similar for both the pristine and the ball-milled sample. As a consequence, ball-milling decreases the energy barrier for the topochemical reaction to a greater extent than non-topochemical decomposition, thereby allowing a greater extent of reduction to be achieved.

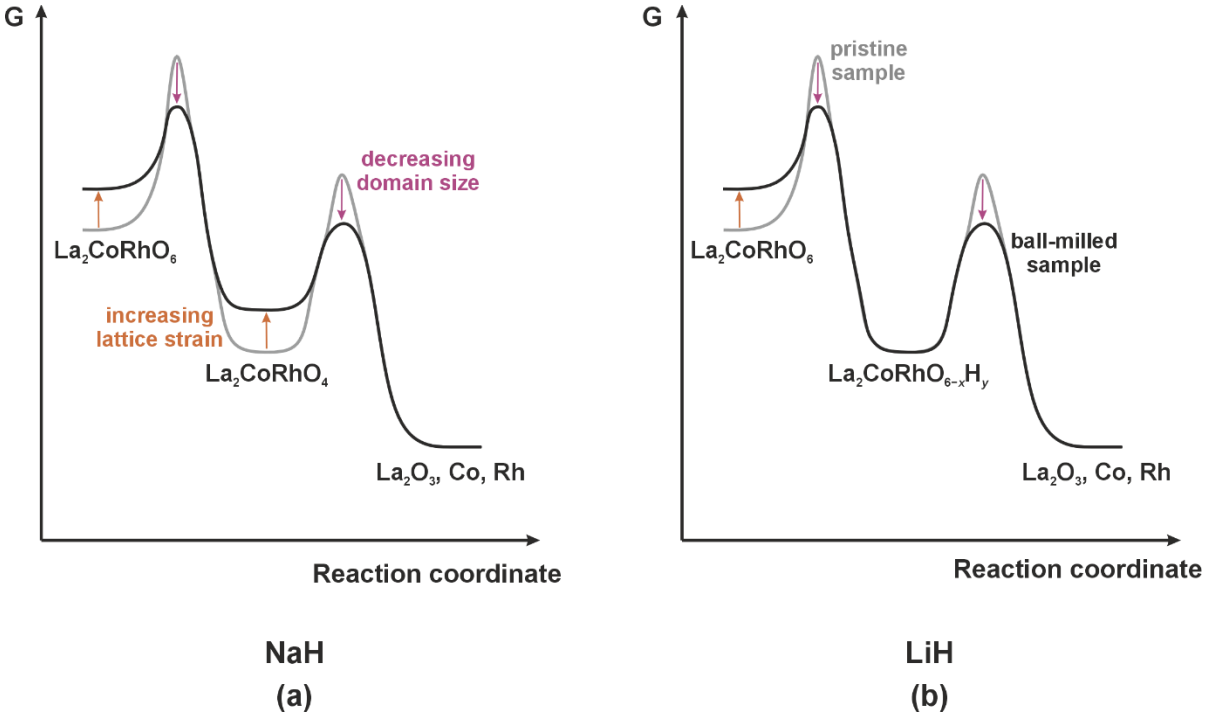

Figure 11.12: Schematics of the reaction energy profiles for the reactions of pristine and ball-milled La_2CoRhO_6 with NaH (left) and LiH (right). For the NaH reaction, the activation energies for the topochemical reaction and for non-topochemical decomposition are decreased by roughly the same extent for both the ball-milled sample and the pristine sample, whereas for the LiH reaction, the activation energy for the topochemical reaction is decreased by a greater extent than that for non-topochemical decomposition.

11.5 Characterisation of $La_2CoRhO_4H_2$

In this section, the product of the reaction between ball-milled La_2CoRhO_6 and LiH, henceforth referred to as $La_2CoRhO_4H_2$, is characterised.

11.5.1 Neutron powder diffraction

NPD data were collected from $La_2CoRhO_4H_2$ at ambient temperature using the POLARIS diffractometer at ISIS. A structural model based on the perovskite structure in the $Pm\bar{3}m$ space group was constructed and refined against the data from the 54°, 94° and 139° detector banks

of the diffractometer. Oxide and hydride were included at the anion site and the occupancies allowed to refine such that the total occupancy at the anion site summed to one. This yielded an oxide occupancy of 0.672(8) and a hydride occupancy of 0.328(8), which corresponds to an overall composition of $La_2CoRhO_{4.03(5)}H_{1.97(5)}$. It is possible that the anion sites are, in fact, not fully occupied and that some anion vacancies are present. However, given that the refined composition is broadly consistent with the data from thermogravimetric analysis and iodometric titration (Section 11.4.1), it is likely that any anion vacancies present are at relatively low concentrations.

To evaluate whether anion ordering or octahedral tilting distortions are present, structural models in lower symmetry space groups were tested. However, these did not provide any visual improvement to the fits and the anion occupancies refined to be the same across all the anion sites. This suggests that the structure can be accurately described using the undistorted $Pm\bar{3}m$ model with complete anion disorder. The disordered anion arrangement is likely to arise from the fact that neither Co^{I} or Rh^{III} provide an electronic driving force for the hydride ions to arrange *trans* relative to each other (Section 1.4.2), so the strong *trans*-influence associated with hydride results in the hydride ions adopting *cis*-arrangements with respect to each other. This anion disorder is likely to impede octahedral tilting distortions from propagating through the structure in an ordered way, accounting for the observation of an undistorted average structure. Locally, however, it is possible that the anions are displaced away from the ideal 3*d* site, as suggested by the presence of a relatively large isotropic thermal factor at this site.

The fits to the NPD data are shown in Figure 11.13-11.15, with the refined parameters detailed in Table 11.3 and the refined structure shown in Figure 11.16.

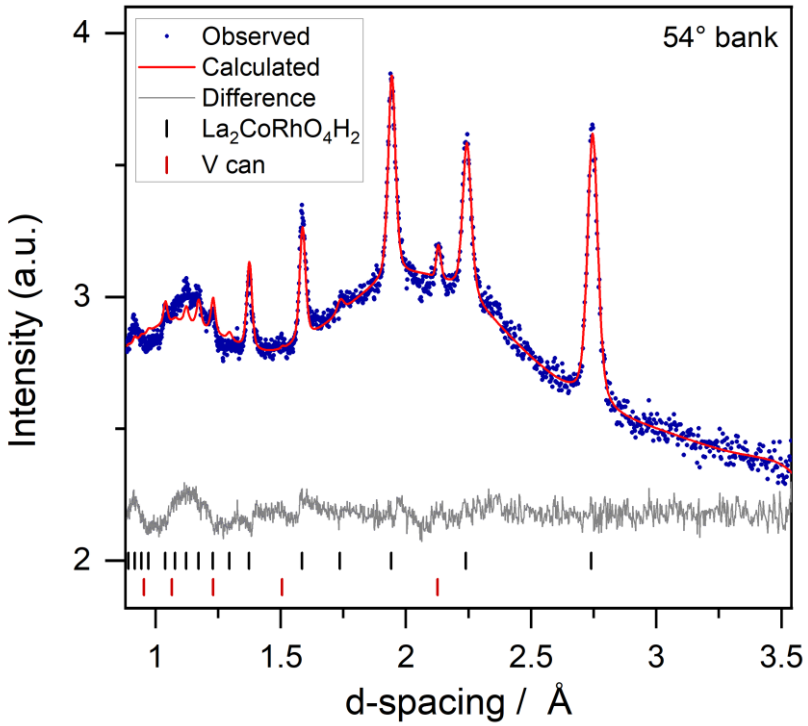

Figure 11.13: Observed, calculated and difference plots from the structural refinement of $La_2CoRhO_4H_2$ against NPD data collected at room temperature from the 54° bank of the POLARIS diffractometer.

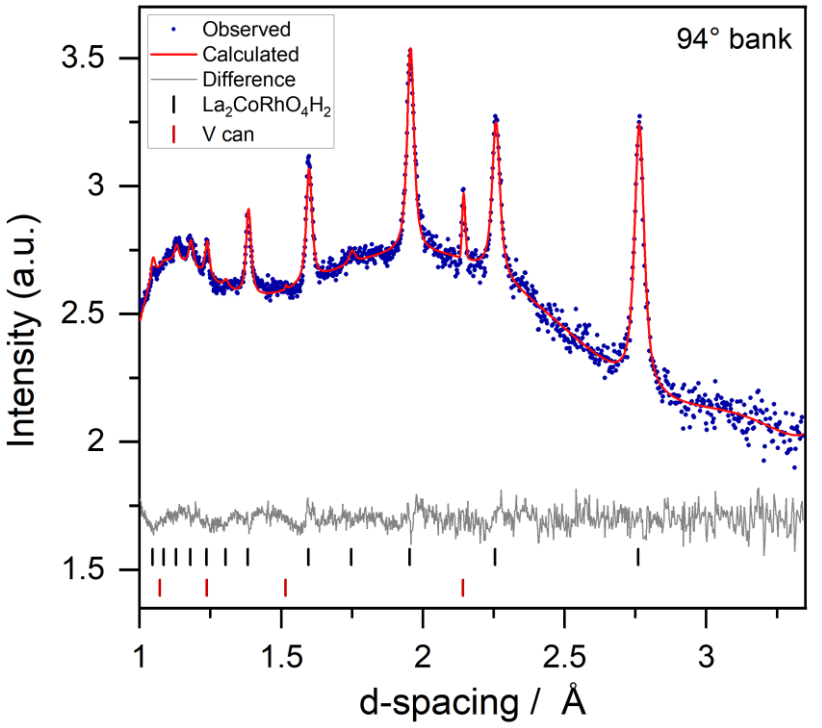

Figure 11.14: Observed, calculated and difference plots from the structural refinement of $La_2CoRhO_4H_2$ against NPD data collected at room temperature from the 94° bank of the POLARIS diffractometer.

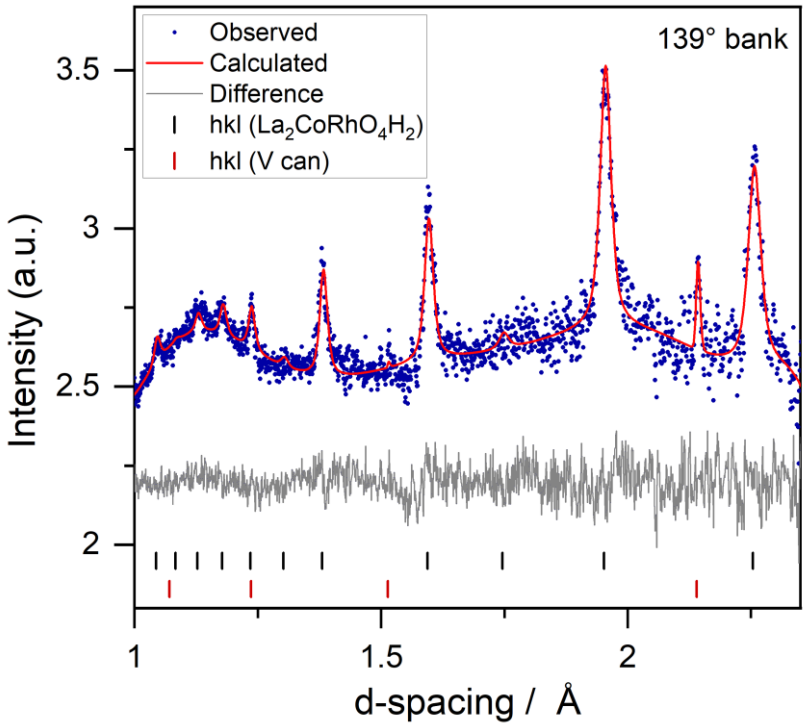

Figure 11.15: Observed, calculated and difference plots from the structural refinement of $La_2CoRhO_4H_2$ against NPD data collected at room temperature from the 139° bank of the POLARIS diffractometer.

Table 11.3: Parameters from the structural refinement of $La_2CoRhO_4H_2$ against NPD data collected at room temperature from the POLARIS diffractometer.

$La_2CoRhO_{4.03(5)}H_{1.97(5)}$, space group $Pm\bar{3}m$ (No. 221)						
		x	***y***	***z***	**Occ.**	**B_{iso} (Å^2)**
La(1)	1*b*	½	½	½	1	5.4(3)
Co(1)/Rh(1)	1*a*	0	0	0	0.5/0.5	7.6(4)
O(1)/H(1)	3*d*	½	0	0	0.672(8)/0.328(8)	8.9(3)
a = 3.9050(9) Å						
V = 59.55(4) Å^3						
R_{wp} = 1.51%, R_p = 1.16%, *gof* = 0.04						

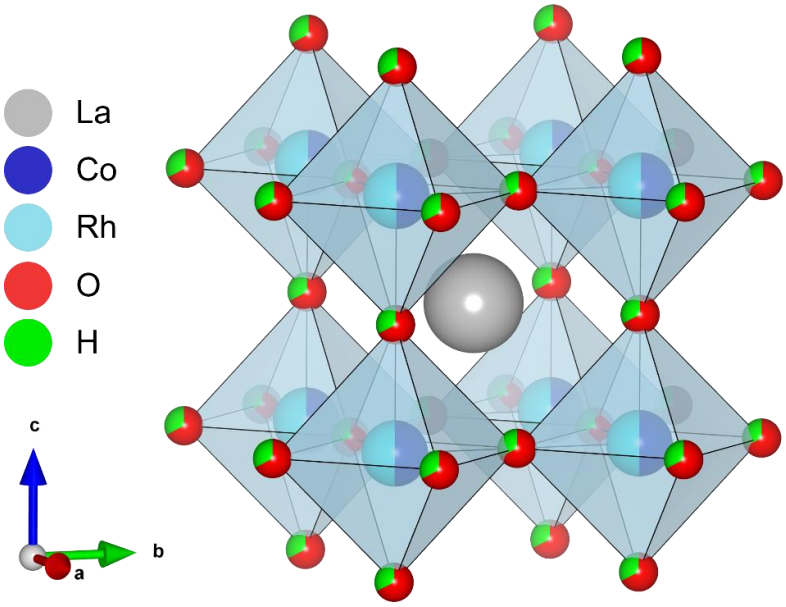

Figure 11.16: Refined structure of $La_2CoRhO_4H_2$.

The maximum extent of reduction when La_2CoRhO_6 is reacted with LiH appears to be $La_2CoRhO_4H_2$. In this compound the overall transition metal oxidation state is +4, which is likely to correspond to cobalt being present as Co^{I} and rhodium being present as Rh^{III}. Further reduction of Co^{I} would lead to the formation of cobalt metal, whilst the reduction of octahedrally-coordinated rhodium from Rh^{III} to Rh^{II} is likely to be unfavourable, due to the requirement for a strongly antibonding e_g orbital to be occupied. As such, $La_2CoRhO_4H_2$ is the most reduced phase that can be prepared under these conditions. This is analogous to the obtainment of the Co^{I}/Ir^{III} oxidation state combination limiting the degree of oxide-to-hydride exchange in the $La_xSr_{4-x}CoIrO_{8-y}H_y$ ($0 \leq x \leq 2$) oxyhydride phases, discussed in Chapter 3. In addition, the formation of $La_2CoRhO_4H_2$ is consistent with the reactivity observed for the equivalent n = 1 Ruddlesden-Popper phase, whereby reaction of $La_2Sr_2CoRhO_8$ with CaH_2 yields $La_2Sr_2CoRhO_6H_2$, in which cobalt is present as Co^{I} and rhodium is present as Rh^{III}.[52]

11.5.2 Magnetic behaviour

Magnetisation data collected from $La_2CoRhO_4H_2$ as a function of temperature are shown in Figure 11.17, and magnetisation-field isotherms collected at 5 K and 350 K are shown in Figure 11.18. Although the ZFC and FC curves display behaviour that appears paramagnetic above ~10 K, attempts to fit the data to the Curie-Weiss law yielded an unphysically large value for *C* and the magnetisation-field isotherm at 350 K is not consistent with a simple paramagnet. A possible rationalisation for the large magnetisations observed in the magnetisation-field isotherm at 350 K is that a substantial Co metal impurity is present in the sample. In an attempt to account for this, magnetisation data were collected from $La_2CoRhO_4H_2$ using the 'ferrosubtraction' technique described in Section 2.8.1, which are shown in Figure 11.19. However, the paramagnetic susceptibility determined using this method also does not follow the behaviour of a simple paramagnet, which could result from the magnetisation of the ferromagnetic impurity not being fully saturated at 3 T.

Below 10 K there is a sharp increase in the FC curve and a local maximum in the ZFC curve. In addition, the magnetisation-field isotherm at 5 K shows a much larger saturated magnetisation of ~1.2 μ_B fu^{-1}, along with a slight hysteresis. This indicates that a magnetic transition occurs at ~10 K. To further understand the nature of this transition, AC susceptibility measurements were performed, which are shown in Figure 11.20. Both χ' and χ'' show a strong frequency dependence and a peak is observed in χ'' at ~10 K, which suggests that the compound adopts a spin glass state at low temperature.

For a spin glass state to propagate, both chemical disorder and magnetic frustration must be present. The requirement for chemical disorder is satisfied both by the B-site cation disorder and by the anion disorder in the compound. The magnetic frustration can be rationalised by considering the Co−Co nearest-neighbour and Co−Rh−Co next-nearest-neighbour interactions,

both of which are expected to be antiferromagnetic. Figure 11.21(a) shows the superexchange interactions expected for an ordered arrangement of Co^{I} and Rh^{III}. Replacing the Rh^{III} ion with a Co^{I} ion (Figure 11.21(b)) changes the dominant coupling interaction from Co−Rh−Co next-nearest-neighbour exchange to Co−Co nearest-neighbour exchange. If the surrounding Co^{I} spins are left intact, it is not possible for all the Co−Co nearest-neighbour interactions to be satisfied, leading to magnetic frustration and the observation of a spin-glass state at low temperature.

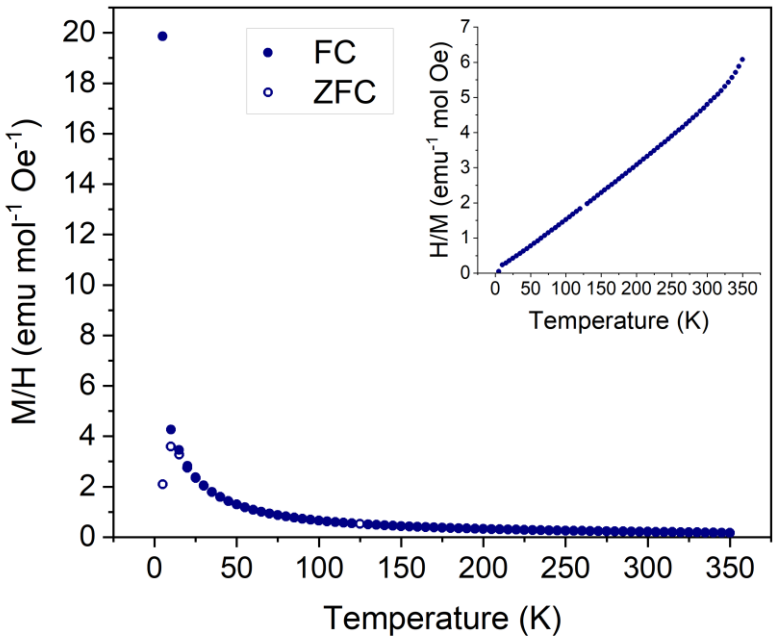

Figure 11.17: Magnetisation data collected from $La_2CoRhO_4H_2$ as a function of temperature, measured in a field of 100 Oe under both ZFC and FC conditions.

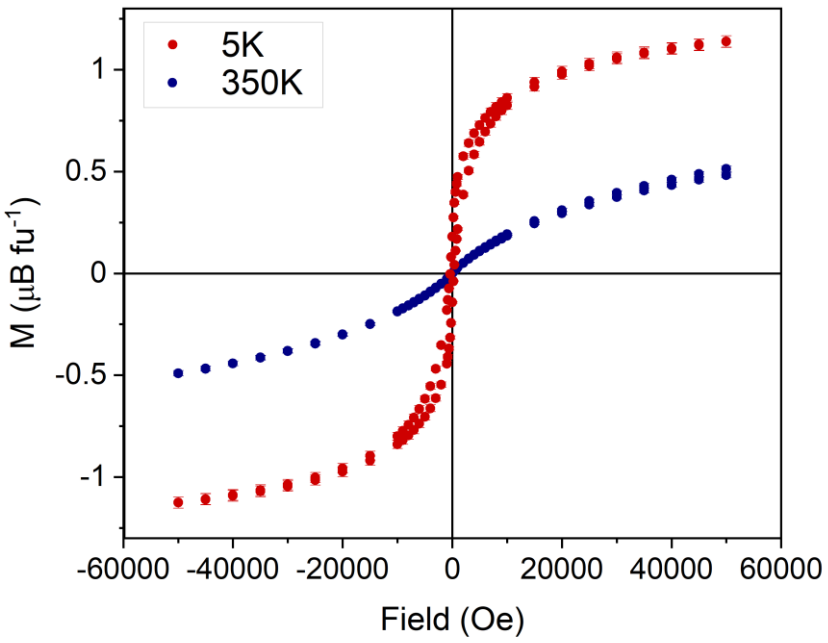

Figure 11.18: Magnetisation-field isotherms for $La_2CoRhO_4H_2$ measured at 5 K and 350 K.

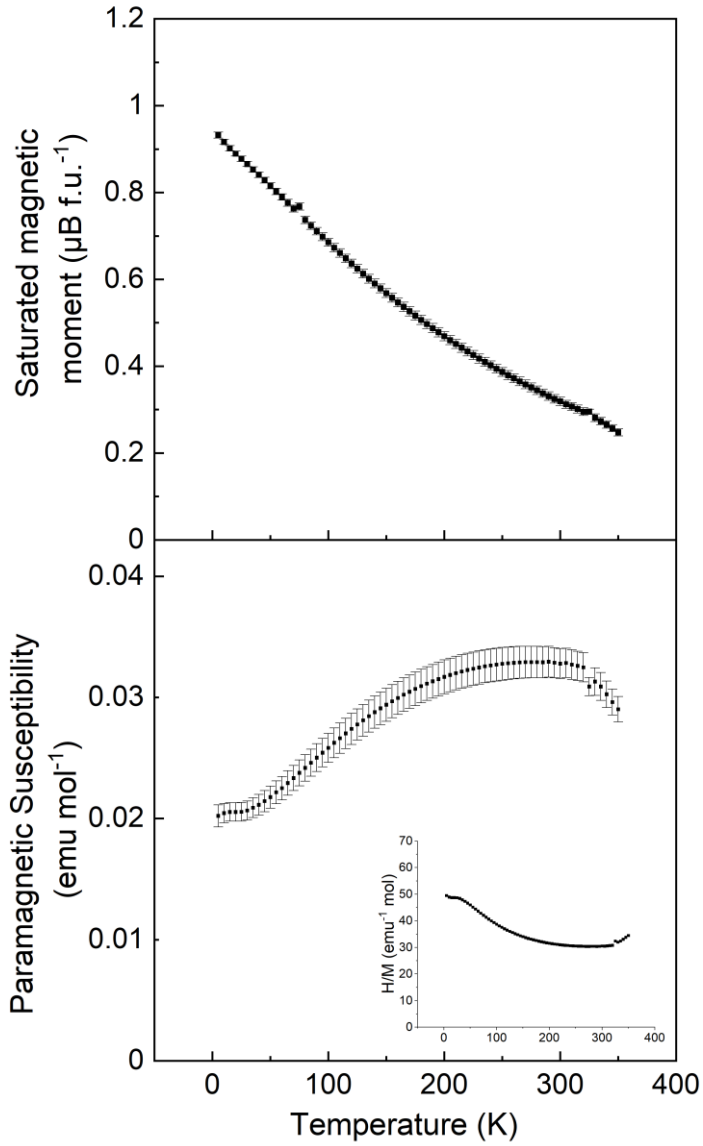

Figure 11.19: Saturated ferromagnetic moment (top panel) and paramagnetic susceptibility (bottom panel) obtained from $La_2CoRhO_4H_2$ using the 'ferrosubtraction' technique described in Section 2.8.1.

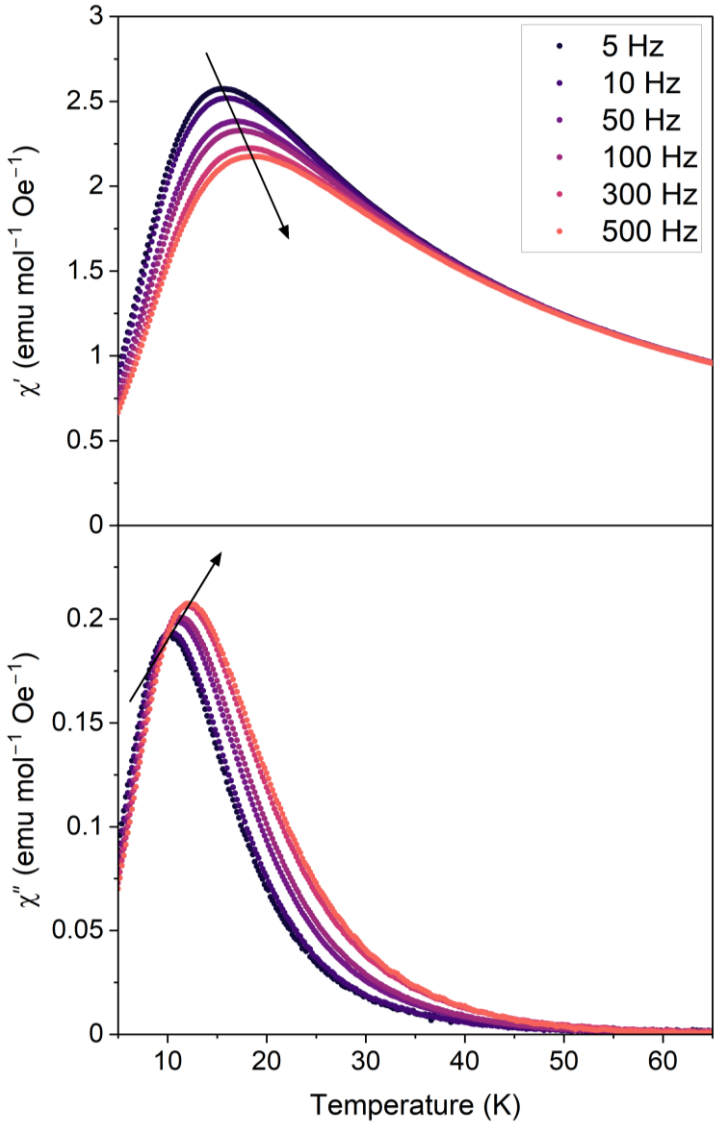

Figure 11.20: AC susceptibility data, χ' (top) and χ'' (bottom), collected as a function of temperature from $La_2CoRhO_4H_2$ at frequencies between 5 Hz and 500 Hz. The measurements were performed using an AC field with amplitude of 2.5 Oe, and an applied DC field of 2 Oe.

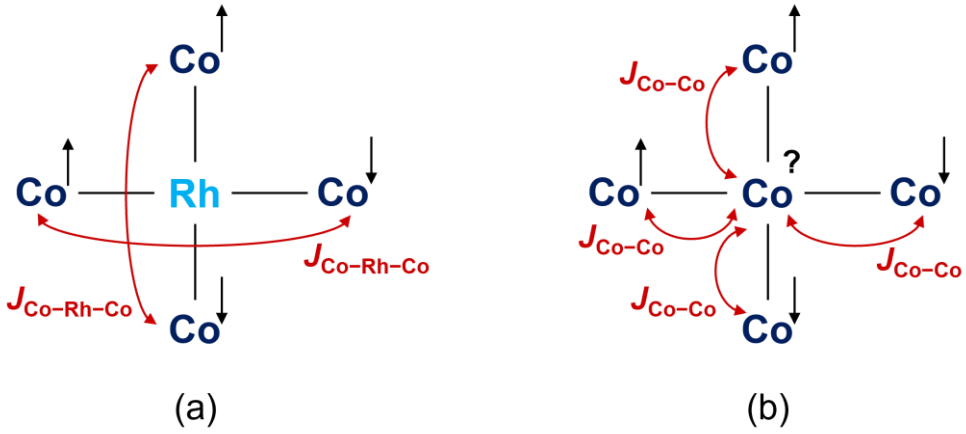

Figure 11.21: (a) the coupling regime for an ordered arrangement of Co^{I} and Rh^{III} ions and (b) a possible source of magnetic frustration arising from B-site cation disorder.

11.6 Conclusion

Ball-milling of B-site cation-disordered perovskite, La_2CoRhO_6, leads to both a decrease in crystallite size and an increase in lattice strain, as determined from Rietveld analysis. Although ball-milling La_2CoRhO_6 does not lead to any improvement in the reactivity for its reaction with NaH, ball-milling allows a greater extent of reduction to be achieved for the reaction with LiH. This can be attributed to the degree of strain in the reaction product. The infinite-layer phase formed by reaction of La_2CoRhO_6 with NaH has relatively low intrinsic lattice strain and, as such, ball-milling destabilises both La_2CoRhO_6 and La_2CoRhO_4, thereby decreasing the activation energy for both the topochemical reaction and non-topochemical decomposition. However, the oxyhydride phase formed by reaction of La_2CoRhO_6 with LiH has relatively high intrinsic lattice strain as a result of the disordered arrangement of oxide and hydride. As such, ball-milling destabilises La_2CoRhO_6 to a greater extent than the oxyhydride phase, thereby lowering the activation energy for the topochemical reaction to a greater extent than non-topochemical decomposition and allowing a greater extent of reduction to be achieved at the same reaction temperature. This indicates that ball-milling can be an effective method for the microstructural activation of topochemical reactions if the product of the reaction has substantially higher lattice strain than the parent phase.

The most reduced phase that can be achieved for this system appears to be $La_2CoRhO_4H_2$, limited by the obtainment of the Co^{I}/Rh^{III} oxidation state combination, analogous to the formation of the Co^{I}/Ir^{III} oxidation state combination in the $La_xSr_{4-x}CoIrO_{8-y}H_y$ phases discussed in Chapter 3. The magnetisation data collected from this compound suggest the adoption of a spin glass state, with the magnetic frustration rationalised on the basis of the presence of strong nearest-neighbour Co−Co and next-nearest-neighbour Co−Rh−Co interactions.

Chapter 12 – Conclusions

In this thesis, the reactivity of perovskite-based Ir-containing oxides has been explored when treated with reducing agents. Reaction with binary metal hydrides has allowed the first oxyhydride phases containing a 5d transition metal to be prepared, with LiH typically found to be the most effective reagent for the formation of Ir-containing oxyhydride phases. A number of oxygen-deficient phases have also been prepared using a Zr getter method to allow comparisons to be made to the oxyhydride phases.

Determination of the anion content of topochemically reduced Ir-containing phases was found to be challenging. Firstly, oxidative thermogravimetric analysis frequently provided inaccurate values for the oxygen content of the iridates, with a tendency to overestimate the oxygen content of the compounds. Secondly, the collection of high-quality NPD data was often not possible, due to the large absorption cross-section of iridium, the strong incoherent scattering from hydride and the modest crystallinity that is typical of topochemically reduced phases. However, by making some assumptions, such as assuming that the anion sites of oxyhydride phases are fully occupied, it was possible to determine the compositions of the topochemically reduced phases.

Chapters 3, 4 and 5 described the synthesis of oxyhydride phases based on the $n = 1$ Ruddlesden-Popper structure with mixed 3d/5d transition metal cations at the B-site. It was observed that, for these compounds, iridium could not be reduced below Ir^{III} (low-spin d^6). As such, this was perceived to be the reduction limit for octahedrally-coordinated iridium, which was attributed to the energetic unfavorability of occupying a high energy e_g orbital.

For most members of the $La_xSr_{4-x}CoIrO_{8-y}H_y$ ($0 \leq x \leq 2$) series of oxyhydride phases, the transition metals are present as a Co^I/Ir^{III} combination, which represents the reduction limit for these compounds. However, the $x = 0$ and 0.5 members have higher transition metal oxidation

states, indicating that the extent of reduction is instead limited by the stability of the overall Ruddlesden-Popper framework. This was also observed for $LaSr_3NiIrO_{5.4}H_{2.6}$ and $Sr_4MnIrO_{5.32}H_{2.68}$, in which iridium is present as Ir^{III} but it is not possible to fully reduce nickel to Ni^{I} or manganese to Mn^{II} without the onset of non-topochemical decomposition.

The observation that it is possible to form oxyhydride phases by treating Sr_4MnIrO_8 with binary metal hydrides is in direct contrast to the behaviour of Sr_2MnO_4 and $LaSrMnO_4$, which form oxygen-deficient phases.[105,106] This suggests that the presence of iridium in the compound favours the formation of oxyhydride phases, which is likely to be due to the covalent stabilisation associated with the formation of strong Ir−H σ-type bonds. This parallels the chemistry observed for molecular hydride systems of late 5d transition metals, and is analogous to the formation of strong M−H covalent bonds in Rh-and Ru-containing oxyhydrides.[51,52,173–176]

The presence of the combination of a d^8 3d transition metal cation and diamagnetic Ir^{III} in many of the Ruddlesden-Popper oxyhydride phases means that they exhibit qualitatively similar magnetic behaviour, whereby extended antiferromagnetic coupling occurs between next-nearest-neighbouring 3d transition metal cations through diamagnetic Ir^{III} via $M(3d_{x^2-y^2})^1$−$O(2p)$/$H(1s)$−$Ir(5d_{x^2-y^2})^0$−$O(2p)$/$H(1s)$−$M(3d_{x^2-y^2})^1$ superexchange pathways. However, long-range magnetic order is not observed from neutron diffraction, due to the presence of B-site paracrystalline order.

Meanwhile, phases that contain iridium in the +4 oxidation state tend to exhibit spin glass behaviour, with a possible source of frustration arising from the presence of direct antiferromagnetic exchange between the $5d_{xy}$ orbitals of iridium ions located diagonally from each other, which is incompatible with the nearest-neighbour coupling interactions.

In Chapters 6 and 7, the syntheses of the oxyhydride phases, $Ba_3CoIr_2O_{6.2}H_{2.8}$, $Sr_2CoIrO_{4.4}H_{1.6}$ and $LaSrCoIrO_{4.4}H_{1.6}$, were presented. In these phases, the transition metals do not achieve the Co^{I}/Ir^{III} oxidation states that represent the overall reduction limit, and the extent of anion exchange is instead limited by the stability of the perovskite frameworks. $Ba_3CoIr_2O_{6.2}H_{2.8}$ adopts a structure in which the hydride ions are predominantly located at the corner-sharing sites and the hydride ions adopt a *trans*-configuration with respect to each other around Co^{II} to allow optimal Co−O π-bonding. In this compound, there is likely to be ferromagnetic coupling between Co^{II} and Ir^{IV} but the establishment of long-range magnetic order is disrupted by the presence of diamagnetic Ir^{III}. Meanwhile, the magnetic behaviour exhibited by $Sr_2CoIrO_{4.4}H_{1.6}$ and $LaSrCoIrO_{4.4}H_{1.6}$ was attributed to the formation of ferromagnetic clusters within the material, driven by inhomogeneities in the distribution of anions across the samples.

The results from Chapters 3, 6 and 7 provide insights into the sequence of reductions when Co,Ir-containing phases are treated with reducing agents. Initially, the Co^{III} (if present) is reduced to Co^{II}. The Ir^{IV} or Ir^{V} is then reduced to Ir^{III}. Finally, if the overall framework is sufficiently stable, Co^{II} is reduced to Co^{I}.

From the results presented in this thesis, a general feature of the reactivity of Ir-containing compounds is that it is often not possible to fully reduce the transition metals to their lowest possible oxidation states. This is exemplified by the reduction of $LaSr_3NiIrO_8$, whereby the products obtained are $LaSr_3NiIrO_{5.4}H_{2.6}$ and $LaSr_3NiIrO_{6.4}$, and it is not possible to prepare the fully reduced $LaSr_3NiIrO_5H_3$ and $LaSr_3NiIrO_6$ phases. This is in direct contrast to the reactivity of Rh- and Ru-containing compounds, whereby phases with integer transition metal oxidation states, such as $LaSr_3NiRuO_4H_4$ and $LaSr_3MnRhO_6H_2$, are readily obtained.[51,52] This attributable to the weak nature of the Ir−O bonds and the strong metallic bonding in Ir metal, which means that iridium is more readily reduced to the elemental metal than rhodium or ruthenium. This means that the activation energy for decomposition is slightly lower for Ir-

containing compounds than for Ru- or Rh-containing compounds and, as a result, slightly lower reaction temperatures need to be used, which prevents the reactions from going to completion. The differences in reaction temperature for the synthesis of Ir-containing oxyhydride phases, compared to Ru- and Rh-containing oxyhydride phases are shown in Table 12.1.

Table 12.1: Reaction temperatures for the preparation of Ir-containing and Ru-/Rh-containing oxyhydride phases, illustrating the fact that lower reaction temperatures are required for Ir-containing phases to prevent the onset of non-topochemical decomposition and, as a result, it is often not possible to achieve full reduction to integer transition metal oxidation states. Data from Refs [51,52].

Ir-containing phases		**Ru-/Rh-containing phases**	
Compound	**Reaction temperature**	**Compound**	**Reaction temperature**
$LaSr_3CoIrO_5H_3$	400−420 °C	$La_2Sr_2CoRhO_6H_2$	450 °C
$Sr_4MnIrO_{5.32}H_{2.68}$	400 °C	$LaSr_3MnRhO_6H_2$	450 °C
$LaSr_3NiIrO_{5.4}H_{2.6}$	380−400 °C	$LaSr_3NiRuO_4H_4$	450 °C

The propensity for the topochemical reduction of Ir-containing compounds to form non-stoichiometric phases could contribute to the fact that many of the prepared phases do not exhibit long-range magnetic order. The non-integer transition metal oxidation states in these compounds are likely to disrupt their ability to establish an ordered structure, thereby accounting for the absence of magnetic Bragg peaks in the low temperature NPD data.

Another interesting feature of the reactivity of Ir-containing compounds relative to their Ru- and Rh-containing analogues is the absence of any oxygen-deficient intermediates during the formation of the oxyhydride phases. When $LaSr_3NiRuO_8$ is reacted with CaH_2 to form $LaSr_3NiRuO_4H_4$, orthorhombic $LaSr_3NiRuO_7$ and $LaSr_3NiRuO_6$ intermediates are observed.[51] Similarly, orthorhombic or tetragonal intermediate phases are observed during the conversion of $La_2Sr_2CoRhO_8$ and $LaSr_3MnRhO_8$ to $La_2Sr_2CoRhO_6H_2$ and $LaSr_3MnRhO_6H_2$.[52] However, for Ir-containing Ruddlesden-Popper phases, there is generally a continuous change in lattice parameters (sometimes followed by a discontinuous change) to form the final oxyhydride

phases, without the observation of any discrete, isolable intermediates. This indicates that the reactions do not occur via a two-step route with an isolable oxygen-deficient step, but instead that the oxyhydride phases are formed continuously. This implies that the energy barrier for hydride insertion in these phases is much lower than the barrier for oxide deintercalation and, as such, the reactions occur through a mechanism in which anion exchange occurs immediately after oxide deintercalation without the accumulation of oxygen-deficient species.[65] This is in direct contrast to the Ru- and Rh-phases described above, in which the reactions initially occur through reductive anion deintercalation processes to form isolable oxygen-deficient phases, which are subsequently converted to oxyhydrides via redox-neutral anion exchange processes.

Chapters 8, 9 and 10 described the syntheses of $La_xSr_{2-x}CoIrO_4$ (x = 0, 1) infinite-layer phases from double perovskite $La_xSr_{2-x}CoIrO_6$ phases, which occur via $La_xSr_{2-x}CoIrO_5$ intermediates. In the infinite-layer phases, it is possible to reduce iridium to Ir^{II}. This behaviour is different from the oxyhydride phases described above and results from the fact that iridium has a square-planar coordination geometry, thereby making the $5d_{z^2}$ orbital energetically accessible.

The infinite-layer phases, Sr_2FeIrO_4,[101] Sr_2CoIrO_4 and $LaSrCoIrO_4$, all adopt markedly different magnetic structures, as shown in Figure 12.1. Whilst the arrangement of moments at the Co sites in Sr_2CoIrO_4 is the same as at the Fe sites in Sr_2FeIrO_4, there is no ordering at the Ir sites and no structural distortion is observed at the magnetic transition temperature. This implies that the coupling interactions in Sr_2CoIrO_4 are subtly different from those in Sr_2FeIrO_4. Meanwhile, $LaSrCoIrO_4$ adopts a magnetic structure based on C-type antiferromagnetic ordering, suggesting that the nearest-neighbour Co−Ir interactions are antiferromagnetic within the layers and ferromagnetic between the layers. An additional magnetic Bragg peak is also observed in the NPD data that cannot be indexed on the basis of C-type ordering, which could arise from the presence of an incommensurate modulation due to spin canting. The strikingly different magnetic ordering exhibited by the three compounds is somewhat surprising and is

likely to arise from the different electronic configurations of the 3d transition metals in these compounds (Figure 12.1). In Sr_2FeIrO_4, the Fe^{II} $3d_{z^2}$ orbital is fully occupied, whilst the remaining 3*d* orbitals are half-filled. Meanwhile, in Sr_2CoIrO_4, it is the $3d_{xz}$ and $3d_{yz}$ orbitals of Co^{II} that are fully occupied, with the remaining orbitals being half-filled. In $LaSrCoIrO_4$, the additional electron (relative to Sr_2CoIrO_4) occupies the $3d_{xy}$ orbital of Co^{I}, which means that all the π-type 3*d* orbitals are fully occupied, with the σ-type orbitals remaining half-filled. The observation that Sr_2CoIrO_4 and $LaSrCoIrO_4$ adopt different magnetic structures suggests that the unpaired electron in the Co^{II} $3d_{xy}$ orbital of Sr_2CoIrO_4 plays an important role in determining the magnetic structure of this compound. Meanwhile, in both Sr_2CoIrO_4 and $LaSrCoIrO_4$, the strong Ir−Ir antiferromagnetic exchange that is observed in Sr_2FeIrO_4 appears to be switched off. Since all the compounds contain Ir^{II}, which is expected to contain an unpaired electron in a spatially diffuse $5d_{xy}$ orbital, this result is somewhat surprising. To fully understand the coupling interactions in these compounds, DFT calculations will need to be performed.

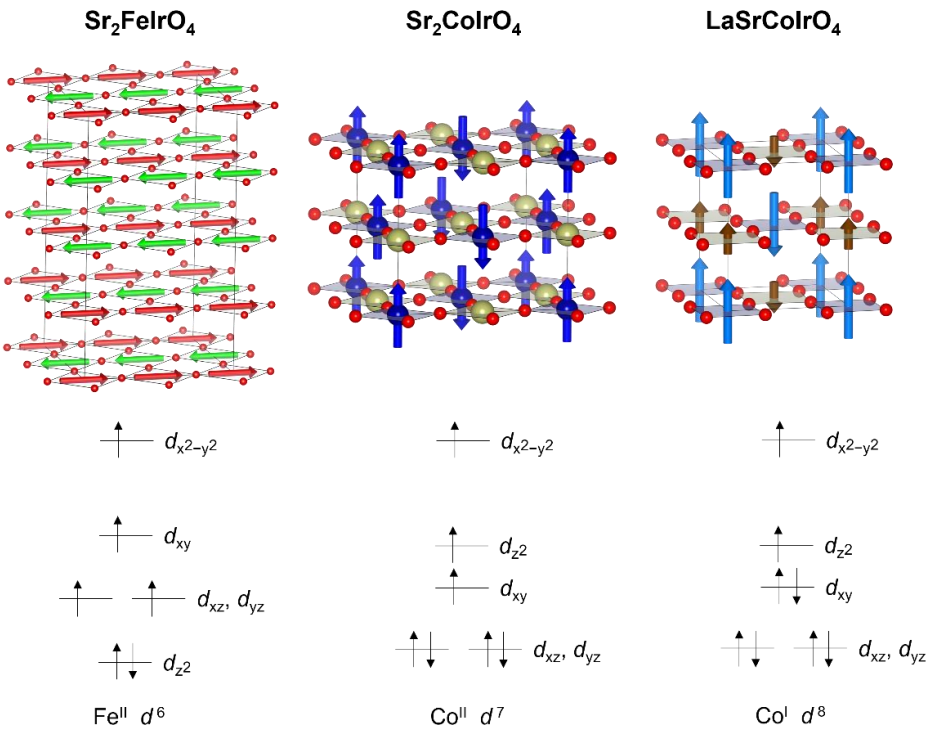

Figure 12.1: Magnetic structures and 3d transition metal electronic configurations in Sr_2FeIrO_4,[101] Sr_2CoIrO_4 and $LaSrCoIrO_4$.

Chapter 11 investigated the possibility of ball-milling as a method to activate transition metal oxides for topochemical reduction. To evaluate this, ball-milled and pristine La_2CoRhO_6 were reacted with NaH and LiH. Whilst the reaction with NaH showed no improvement in reactivity when the parent oxide was ball milled, the reaction with LiH showed a greater extent of reduction for the ball-milled sample. It was proposed that ball-milling is only an effective method for activation of topochemical reactions when the product of the reaction is intrinsically highly strained. Further work is required to ascertain whether this principle can be applied to other systems.

In conclusion, LiH has been shown to be an effective reducing agent for the topochemical reduction of Ir-containing oxides to form oxyhydride phases. The extent of reduction during these reactions is limited either by the stability of the perovskite framework or the obtainment of iridium in the +3 oxidation state. Meanwhile, heating Ir-containing oxides in the presence of a Zr getter yields infinite-chain or infinite-layer phases, allowing iridium to be obtained in the +2 oxidation state. In general, the stability of topochemically reduced Ir-containing phases with respect to non-topochemical decomposition is relatively low, which can be attributed to the weakness of the Ir–O bonds and the strong thermodynamic driving force for formation of Ir metal. These factors are common to many of the late 5d transition metals and, as such, whilst this thesis has shown that it is possible to prepare oxyhydride and oxygen-deficient phases containing these elements, it is likely that the number of topochemically reduced phases containing 5d metals that can be isolated will be lower than the number of phases containing 3d metals.

Appendix

A1 – Supplementary data for Chapter 3

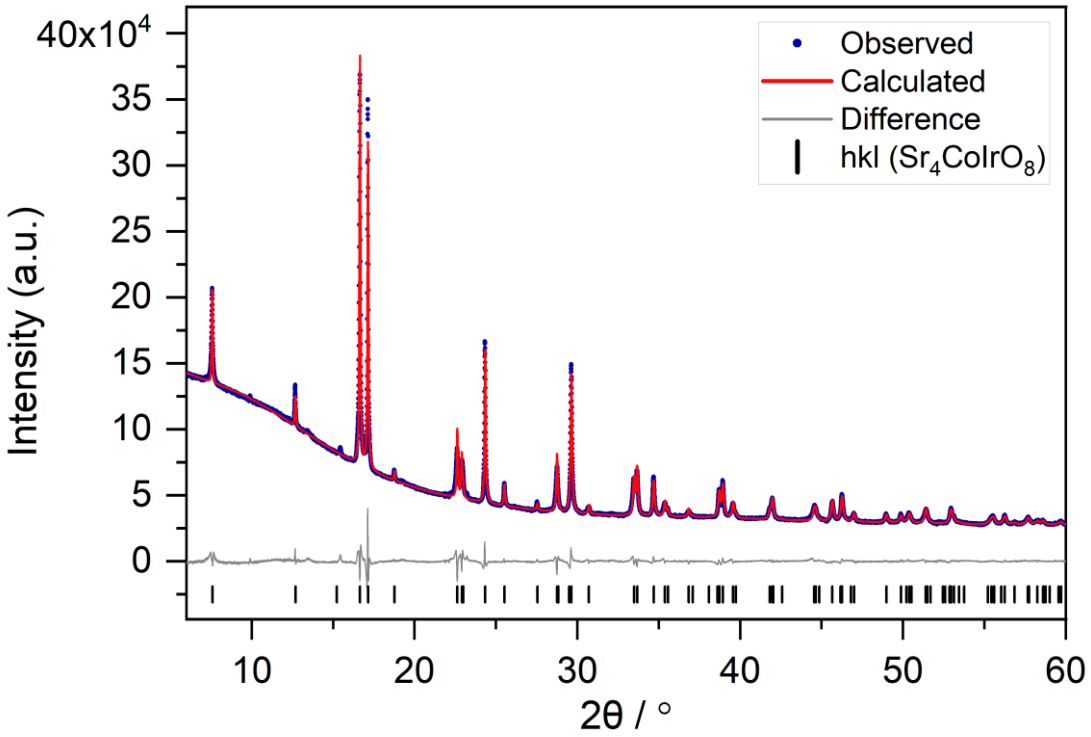

Figure A 1: Observed, calculated and difference plots from the structural refinement of Sr_4CoIrO_8 against SXRD data collected at room temperature using a wavelength of 0.825 Å.

Table A 1: Structural parameters from the refinement of Sr_4CoIrO_8 against SXRD data collected at room temperature. The fractional coordinates of the oxide sites were fixed to be the same as the reported values.[46,92]

Sr_4CoIrO_8, space group *I*4/*mmm* (No. 139)						
		x	***y***	***z***	**Occ.**	**B_{iso} (Å^2)**
Sr(1)	4*e*	0	0	0.35550(7)	1	0.46(3)
Co(1)/Ir(1)	2*a*	0	0	0	0.5/0.5	0.27(3)
O(1)	4*c*	0	½	0	1	1.19(7)
O(2)	4*e*	0	0	0.1604	1	1.19(7)
a = 3.91778(6) Å, c = 12.4770(2) Å						
V = 191.510(7) Å^3						
R_{wp} = 2.26%, R_p = 1.38%, *gof* = 5.31						

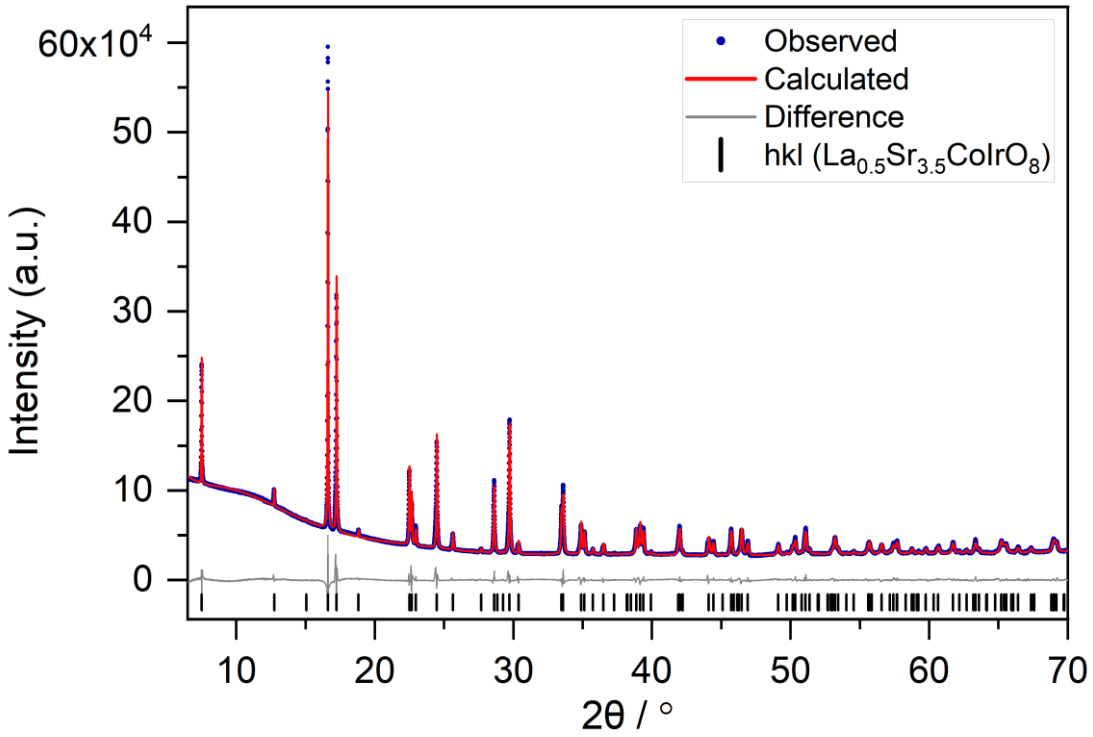

Figure A 2: Observed, calculated and difference plots from the structural refinement of $La_{0.5}Sr_{3.5}CoIrO_8$ against SXRD data collected at room temperature using a wavelength of 0.825 Å.

Table A 2: Structural parameters from the refinement of $La_{0.5}Sr_{3.5}CoIrO_8$ against SXRD data collected at room temperature. The fractional coordinates of the oxide sites were fixed to be the same as those of $LaSr_3CoIrO_8$.

$La_{0.5}Sr_{3.5}CoIrO_8$, space group *I*4/*mmm* (No. 139)						
		x	***y***	***z***	**Occ.**	**B_{iso} (Å^2)**
La(1)/Sr(1)	4*e*	0	0	0.35622(4)	0.125/0.875	0.77(2)
Co(1)/Ir(1)	2*a*	0	0	0	0.5/0.5	0.46(2)
O(1)	4*c*	0	½	0	1	1.07(5)
O(2)	4*e*	0	0	0.1647	1	1.07(5)
a = 3.88836(3) Å, c = 12.5844(1) Å						
V = 190.268(4) Å^3						
R_{wp} = 2.93%, R_p = 1.76%, *gof* = 6.22						

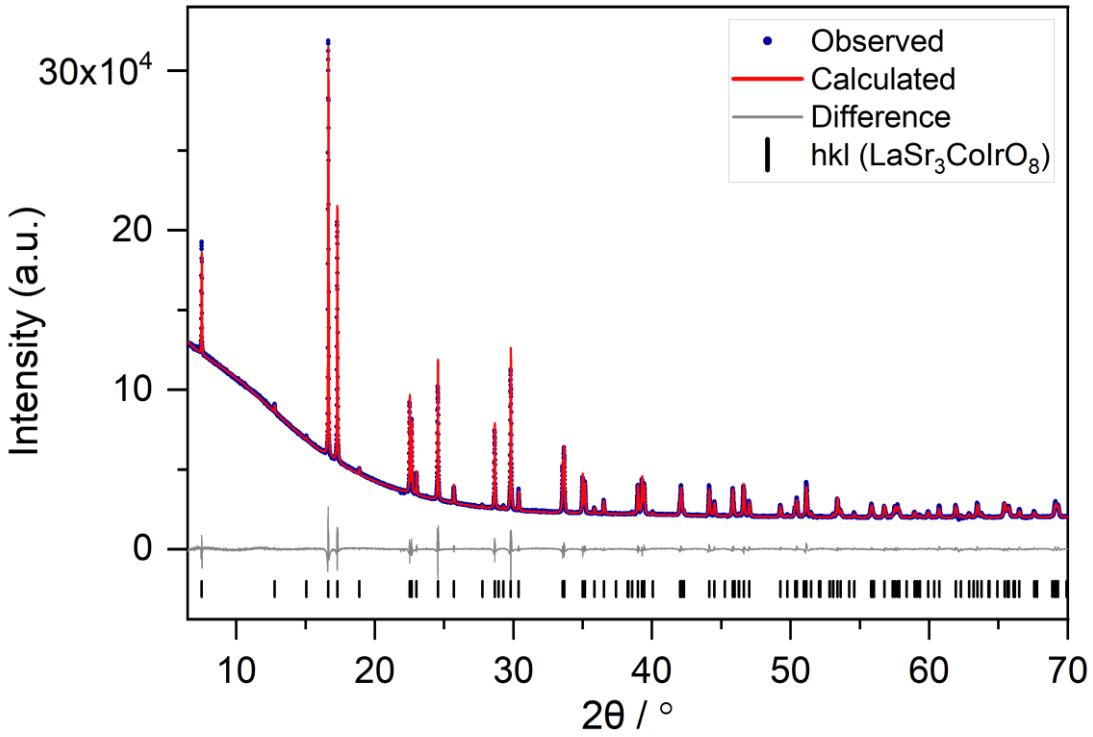

Figure A 3: Observed, calculated and difference plots from the structural refinement of $LaSr_3CoIrO_8$ against SXRD data collected at room temperature using a wavelength of 0.825 Å.

Table A 3: Structural parameters from the refinement of $LaSr_3CoIrO_8$ against SXRD data collected at room temperature. The fractional coordinates of the oxide sites were fixed to be the same as the reported values.[46]

$LaSr_3CoIrO_8$, space group *I*4/*mmm* (No. 139)						
		x	***y***	***z***	**Occ.**	**B_{iso} (Å^2)**
La(1)/Sr(1)	4*e*	0	0	0.35697(4)	0.25/0.75	0.72(2)
Co(1)/Ir(1)	2*a*	0	0	0	0.5/0.5	0.58(2)
O(1)	4*c*	0	½	0	1	1.28(6)
O(2)	4*e*	0	0	0.1647	1	1.28(6)
a = 3.87999(4) Å, c = 12.5927(1) Å						
V = 189.574(4) Å^3						
R_{wp} = 2.20%, R_p = 1.16%, *gof* = 4.28						

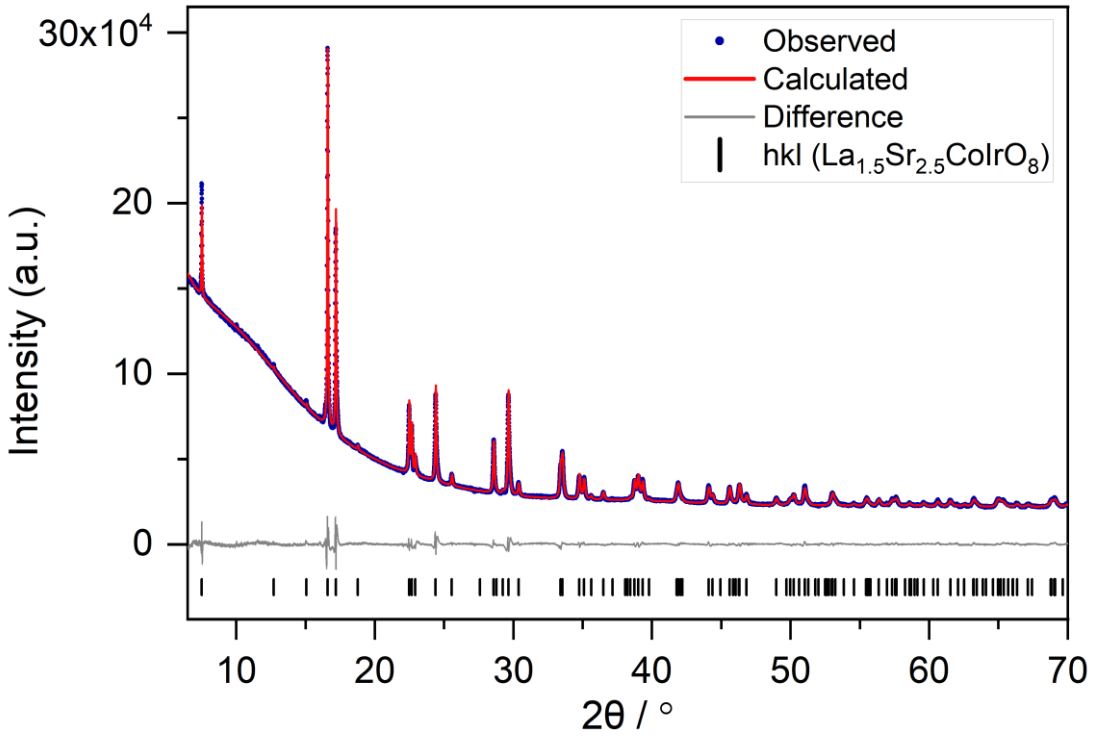

Figure A 4: Observed, calculated and difference plots from the structural refinement of $La_{1.5}Sr_{2.5}CoIrO_8$ against SXRD data collected at room temperature using a wavelength of 0.825 Å.

Table A 4: Structural parameters from the refinement of $La_{1.5}Sr_{2.5}CoIrO_8$ against SXRD data collected at room temperature. The fractional coordinates of the oxide sites were fixed to be the same as those of $LaSr_3CoIrO_8$.

$La_{1.5}Sr_{2.5}CoIrO_8$, space group *I*4/*mmm* (No. 139)						
		x	***y***	***z***	**Occ.**	**B_{iso} (Å^2)**
La(1)/Sr(1)	4*e*	0	0	0.35744(5)	0.375/0.625	1.51(2)
Co(1)/Ir(1)	2*a*	0	0	0	0.5/0.5	1.16(2)
O(1)	4*c*	0	½	0	1	2.03(7)
O(2)	4*e*	0	0	0.1647	1	2.03(7)
a = 3.90328(7) Å, c = 12.5893(2) Å						
V = 191.805(8) Å^3						
R_{wp} = 1.85%, R_p = 1.11%, *gof* = 3.01						

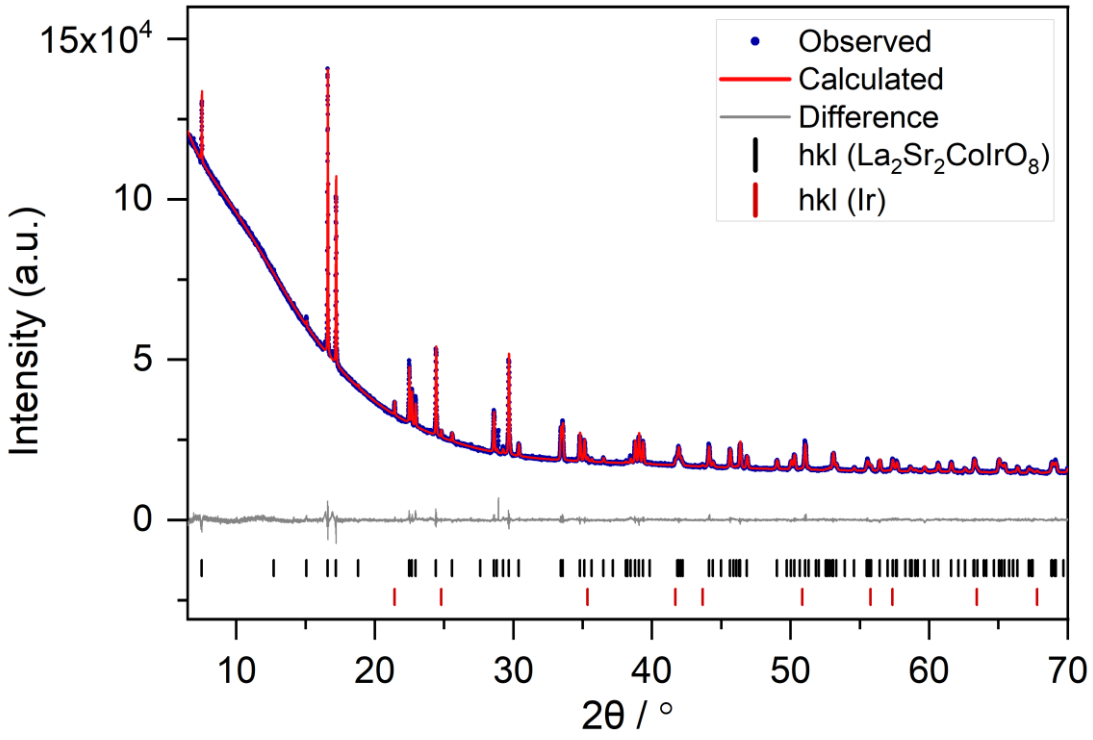

Figure A 5: Observed, calculated and difference plots from the structural refinement of $La_2Sr_2CoIrO_8$ against SXRD data collected at room temperature using a wavelength of 0.825 Å.

Table A 5: Structural parameters from the refinement of $La_2Sr_2CoIrO_8$ against SXRD data collected at room temperature. The fractional coordinates of the oxide sites were fixed to be the same as those of $LaSr_3CoIrO_8$.

$La_2Sr_2CoIrO_8$, space group *I*4/*mmm* (No. 139), 98.70(5) wt%						
		x	***y***	***z***	**Occ.**	**B_{iso} (Å^2)**
La(1)/Sr(1)	4*e*	0	0	0.35939(4)	0.5/0.5	0.49(1)
Co(1)/Ir(1)	2*a*	0	0	0	0.5/0.5	1.21(1)
O(1)	4*c*	0	½	0	1	0.84(5)
O(2)	4*e*	0	0	0.1647	1	0.84(5)
a = 3.89677(2) Å, c = 12.5777(1) Å						
V = 190.990(3) Å^3, Z = 2						
Ir, space group *Fm*$\bar{3}$*m* (No. 225), 1.30(5) wt%						
		x	***y***	***z***	**Occ.**	**B_{iso} (Å^2)**
Ir(1)	4*a*	0	0	0	1	0.17(7)
a = 3.8386(1) Å						
V = 56.562(7) Å^3, Z = 4						
R_{wp} = 1.12%, R_p = 0.73%, *gof* = 1.98						

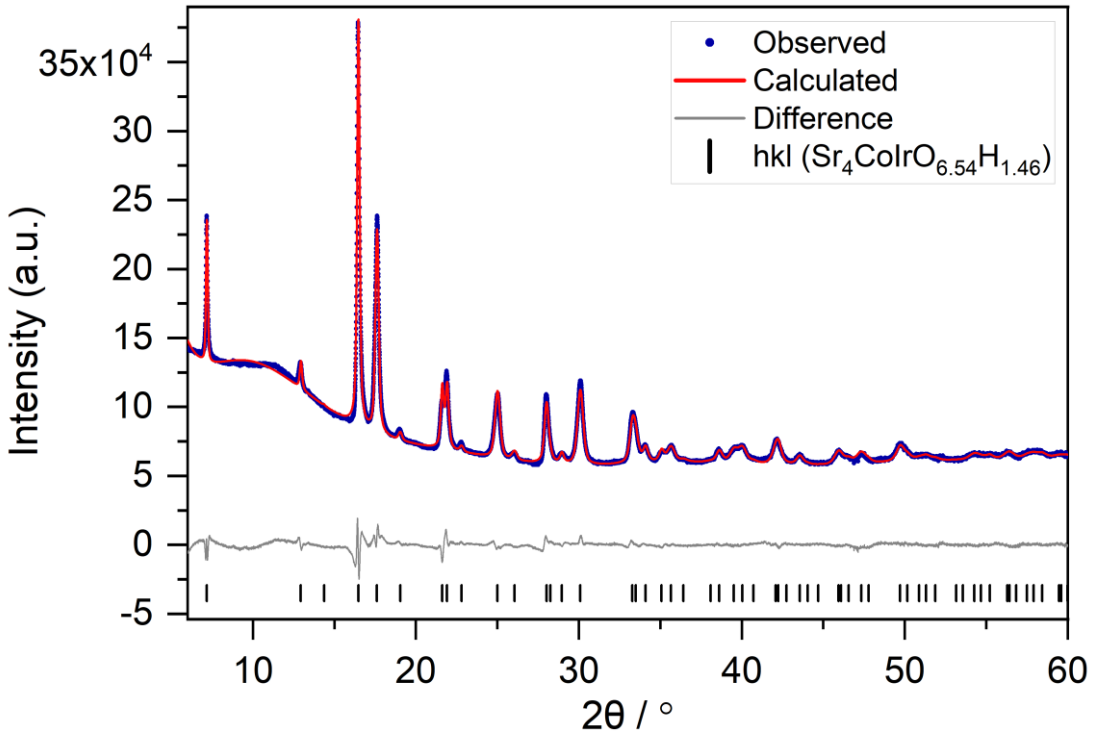

Figure A 6: Observed, calculated and difference plots from the structural refinement of $Sr_4CoIrO_{6.5}H_{1.5}$ against SXRD data collected at room temperature using a wavelength of 0.825 Å.

Table A 6: Parameters from the structural refinement of $Sr_4CoIrO_{6.5}H_{1.5}$ against SXRD data collected at room temperature. The oxide/hydride positions and occupancies were fixed using the values determined in Section 3.3.2.2.

$Sr_4CoIrO_{6.54}H_{1.46}$, space group *I4/mmm* (No. 139)						
		x	***y***	***z***	**Occ.**	**B_{iso} (Å^2)**
Sr(1)	4*e*	0	0	0.35465(6)	1	0.67(5)
Co(1)/Ir(1)	2*a*	0	0	0	0.5/0.5	0.55(4)
O(1)/H(1)	4*c*	0	½	0	0.635/0.365	1.2(1)
O(2)	4*e*	0	0	0.1629	1	1.2(1)
a = 3.8088(2) Å, c = 13.1949(8) Å						
V = 191.42(3) Å^3						
R_{wp} = 2.28%, R_p = 1.59%, *gof* = 6.42						

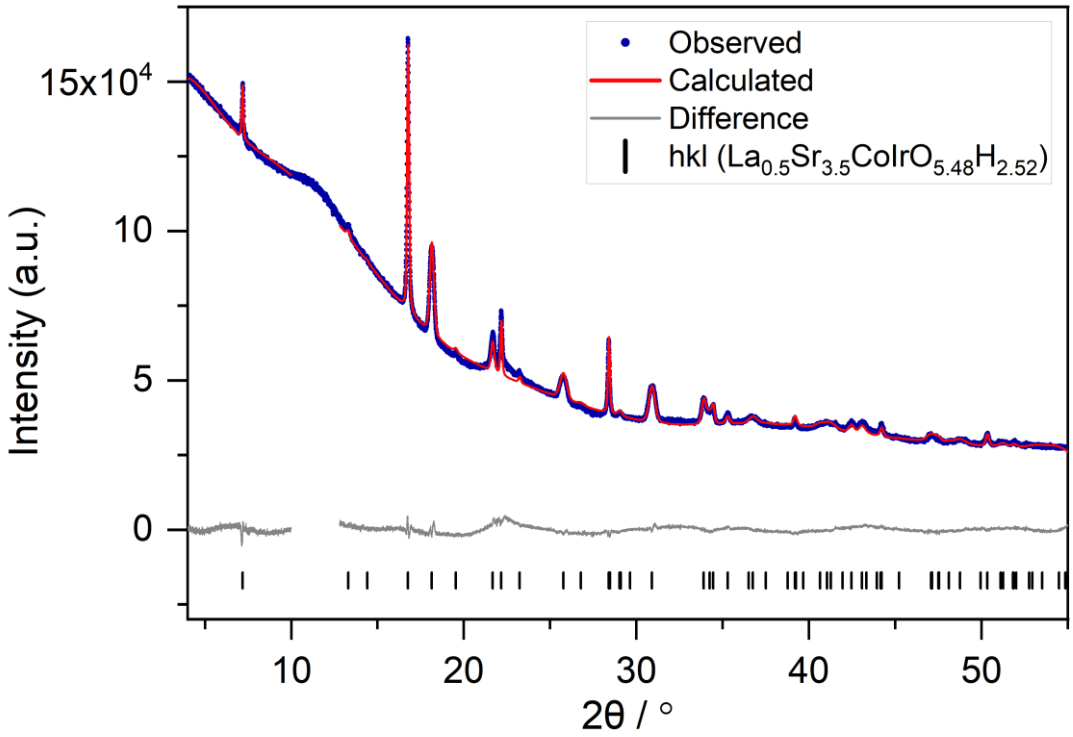

Figure A 7: Observed, calculated and difference plots from the structural refinement of $La_{0.5}Sr_{3.5}CoIrO_{5.5}H_{2.5}$ against SXRD data collected at room temperature using a wavelength of 0.825 Å. The 2θ region from 10° to 12.8° is excluded due to the presence of a broad background feature arising from silica used to dilute the sample to reduce X-ray absorption during the SXRD measurement.

Table A 7: Parameters from the structural refinement of $La_{0.5}Sr_{3.5}CoIrO_{5.5}H_{2.5}$ against SXRD data collected at room temperature. The oxide/hydride positions and occupancies were fixed using the values determined in Section 3.3.3.2.

$La_{0.5}Sr_{3.5}CoIrO_{5.48}H_{2.52}$, space group *I*4/*mmm* (No. 139)						
		x	***y***	***z***	**Occ.**	**B_{iso} (Å^2)**
La(1)/Sr(1)	4*e*	0	0	0.3537(1)	0.125/0.875	1.80(8)
Co(1)/Ir(1)	2*a*	0	0	0	0.5/0.5	2.07(8)
O(1)/H(1)	4*c*	0	½	0	0.369/0.631	0.7(2)
O(2)	4*e*	0	0	0.1624	1	0.7(2)
a = 3.6956(3) Å, c = 13.1509(9) Å						
V = 179.61(3) Å^3						
R_{wp} = 1.86%, R_p = 1.38%, *gof* = 4.40						

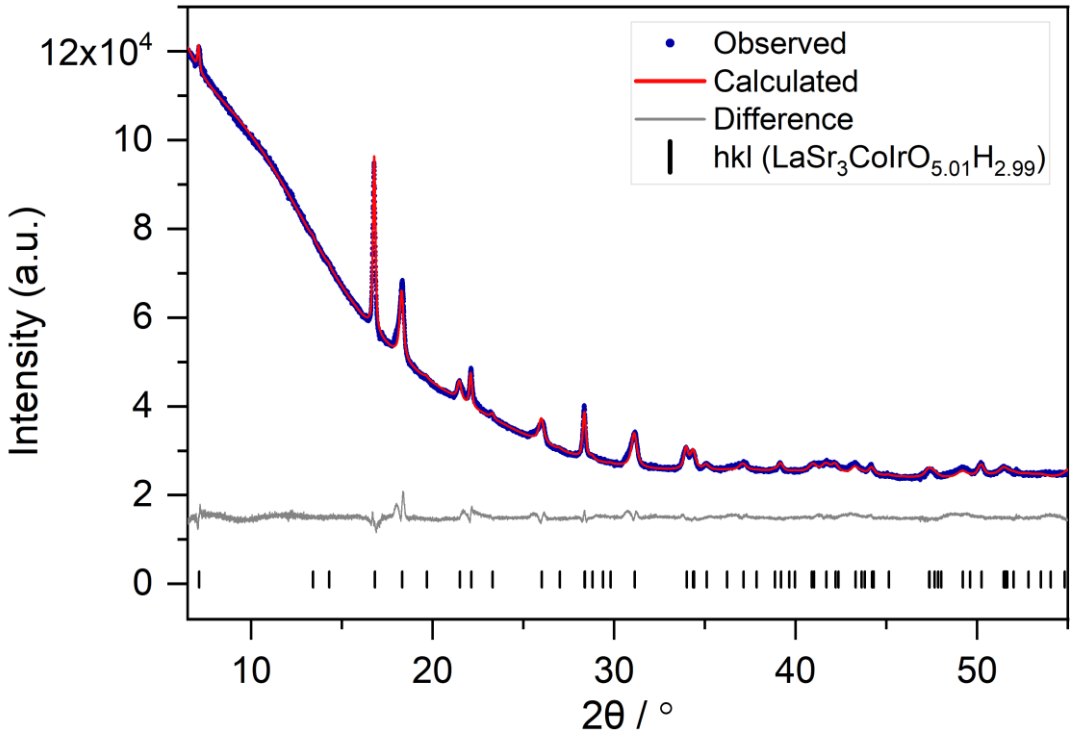

Figure A 8: Observed, calculated and difference plots from the structural refinement of $LaSr_3CoIrO_5H_3$ against SXRD data collected at room temperature using a wavelength of 0.825 Å.

Table A 8: Parameters from the structural refinement of $LaSr_3CoIrO_5H_3$ against SXRD data collected at room temperature. The oxide/hydride positions and occupancies were fixed using the values determined in Section 3.3.4.2.

$LaSr_3CoIrO_{5.01}H_{2.99}$, space group *I*4/*mmm* (No. 139)						
		x	***y***	***z***	**Occ.**	**B_{iso} (Å^2)**
La(1)/Sr(1)	4*e*	0	0	0.3544(1)	0.25/0.75	0.63(6)
Co(1)/Ir(1)	2*a*	0	0	0	0.5/0.5	1.64(7)
O(1)/H(1)	4*c*	0	½	0	0.253/0.747	0.9(2)
O(2)	4*e*	0	0	0.1656	1	0.9(2)
a = 3.6601(4) Å, c = 13.251(1) Å						
V = 177.52(4) Å^3						
R_{wp} = 1.25%, R_p = 0.86%, *gof* = 2.60						

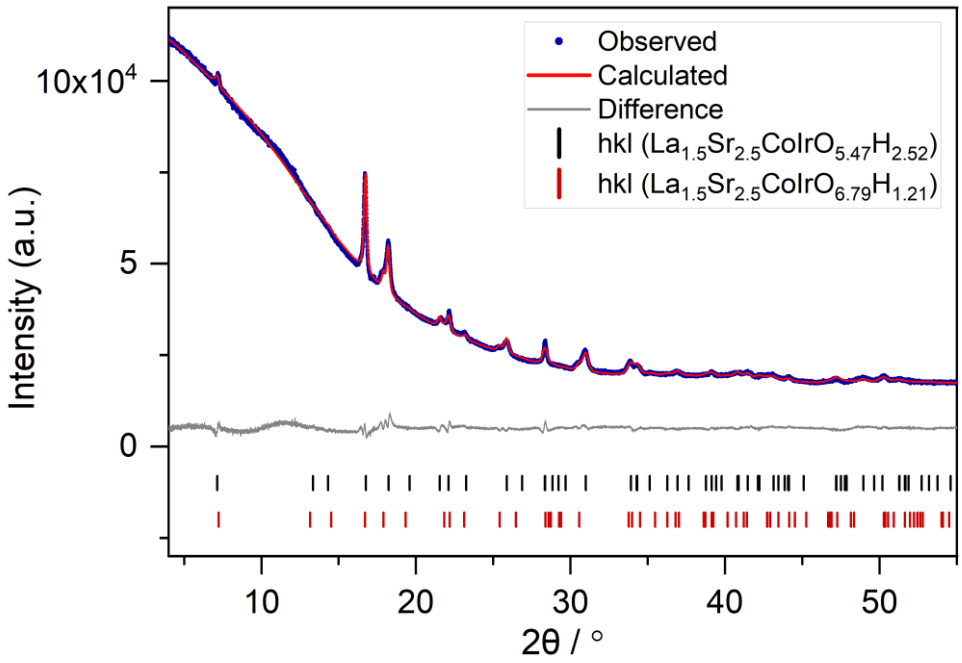

Figure A 9: Observed, calculated and difference plots from the two-phase structural refinement of $La_{1.5}Sr_{2.5}CoIrO_{8-y}H_y$ against SXRD data collected at room temperature using a wavelength of 0.825 Å.

Table A 9: Parameters from the two-phase structural refinement of $La_{1.5}Sr_{2.5}CoIrO_{8-y}H_y$ against SXRD data collected at room temperature. The oxide/hydride positions and occupancies were fixed using the values determined in Section 3.3.5.2. The isotropic thermal factors for $La_{1.5}Sr_{2.5}CoIrO_7H$ were constrained to be the same for all atoms.

$La_{1.5}Sr_{2.5}CoIrO_{5.47}H_{2.53}$, space group *I*4/*mmm* (No. 139), 75.0(5) wt%						
		x	***y***	***z***	**Occ.**	**B_{iso} (Å^2)**
La(1)/Sr(1)	4*e*	0	0	0.3563(1)	0.625/0.375	0.63(7)
Co(1)/Ir(1)	2*a*	0	0	0	0.5/0.5	2.9(1)
O(1)/H(1)	4*c*	0	½	0	0.367/0.633	0.8(3)
O(2)	4*e*	0	0	0.1692	1	0.8(3)
a = 3.6762(4) Å, *c* = 13.221(2) Å						
V = 178.68(5) Å^3						
$La_{1.5}Sr_{2.5}CoIrO_{6.79}H_{1.21}$, space group *I*4/*mmm* (No. 139), 25.9(5) wt%						
		x	***y***	***z***	**Occ.**	**B_{iso} (Å^2)**
La(1)/Sr(1)	4*e*	0	0	0.3562(1)	0.625/0.375	1.1(1)
Co(1)/Ir(1)	2*a*	0	0	0	0.5/0.5	1.1(1)
O(1)/H(1)	4*c*	0	½	0	0.76/0.24	1.1(1)
O(2)	4*e*	0	0	0.1687	1	1.1(1)
a = 3.7404(6) Å, *c* = 13.037(4) Å						
V = 182.40(9) Å^3						
R_{wp} = 1.32%, R_p = 0.97%, *gof* = 2.63						

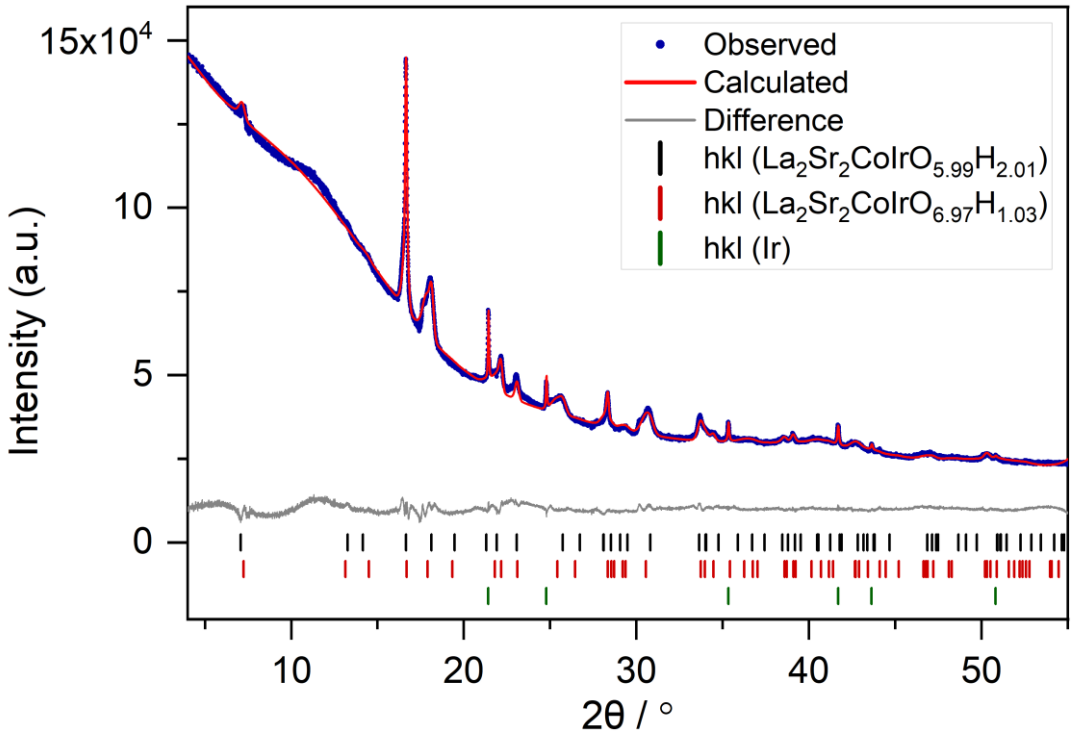

Figure A 10: Observed, calculated and difference plots from the structural refinement of $La_2Sr_2CoIrO_{8-y}H_y$ against SXRD data collected at room temperature using a wavelength of 0.825 Å.

Table A 10: Parameters from the structural refinement of $La_2Sr_2CoIrO_{8-y}H_y$ against SXRD data collected at room temperature. The oxide/hydride positions and occupancies were fixed using the values determined in Section 3.3.6.2.

$La_2Sr_2CoIrO_{5.99}H_{2.01}$, space group *I*4/*mmm* (No. 139), 33(1) wt%						
		x	***y***	***z***	**Occ.**	**B_{iso} (Å^2)**
La(1)/Sr(1)	4*e*	0	0	0.3539(6)	0.5/0.5	4.0(2)
Co(1)/Ir(1)	2*a*	0	0	0	0.5/0.5	9.1(6)
O(1)/H(1)	4*c*	0	½	0	0.50/0.50	1.9(9)
O(2)	4*e*	0	0	0.1696	1	1.9(9)
a = 3.6996(9) Å, c = 13.374(6) Å						
V = 183.1(1) Å^3						
$La_2Sr_2CoIrO_{6.97}H_{1.03}$, space group *I*4/*mmm* (No. 139), 64(1) wt%						
		x	***y***	***z***	**Occ.**	**B_{iso} (Å^2)**
La(1)/Sr(1)	4*e*	0	0	0.3601(2)	0.5/0.5	3.07(9)
Co(1)/Ir(1)	2*a*	0	0	0	0.5/0.5	6.2(2)
O(1)/H(1)	4*c*	0	½	0	0.74/0.26	1.8(4)
O(2)	4*e*	0	0	0.1719	1	1.8(4)
a = 3.745(1) Å, c = 13.068(3) Å						
V = 183.3(1) Å^3						
Ir, space group *Fm*$\bar{3}$*m*, (No. 225), 3.1(1) wt%						
		x	***y***	***z***	**Occ.**	**B_{iso} (Å^2)**
Ir(1)	4*a*	0	0	0	1	2.4(1)
a = 3.8397(3) Å						
V = 56.61(1) Å^3						
R_{wp} = 1.58%, R_p = 1.25%, *gof* = 3.73						

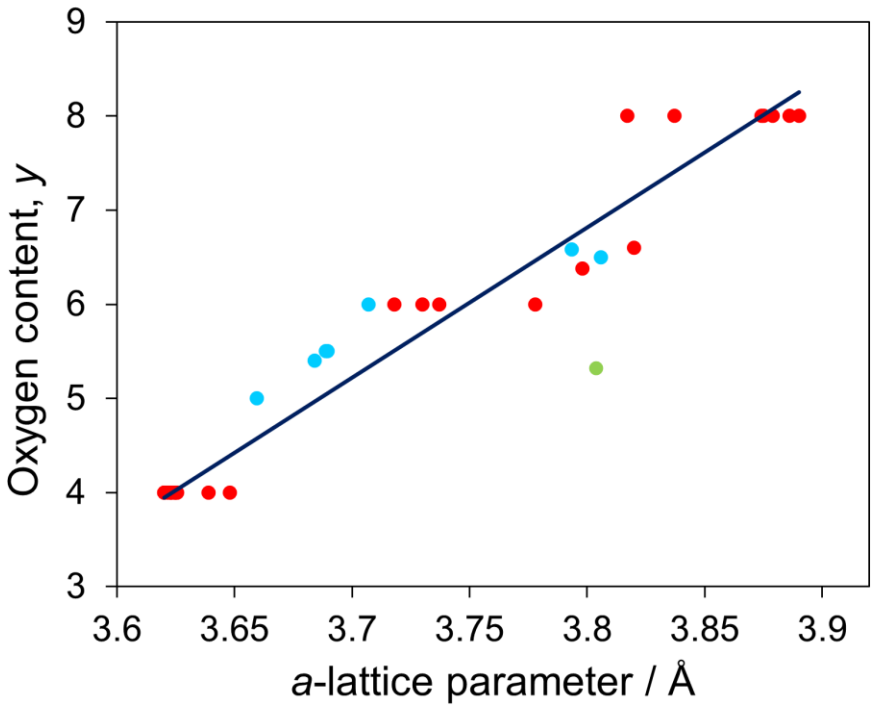

Figure A 11: Relationship between oxygen content and *a*-lattice parameter in $A_4B'B''O_{8-y}H_z$ oxyhydride phases with the n = 1 Ruddlesden-Popper structure. Only compounds in which the hydride ions are exclusively located in the equatorial positions are considered (apart from $Sr_4MnIrO_{5.32}H_{2.68}$, shown in green). Red markers represent reported compounds, blue markers represent compounds presented in this thesis and the blue line represents the line of best fit. Data from Refs [46–48,51–53,91,177].

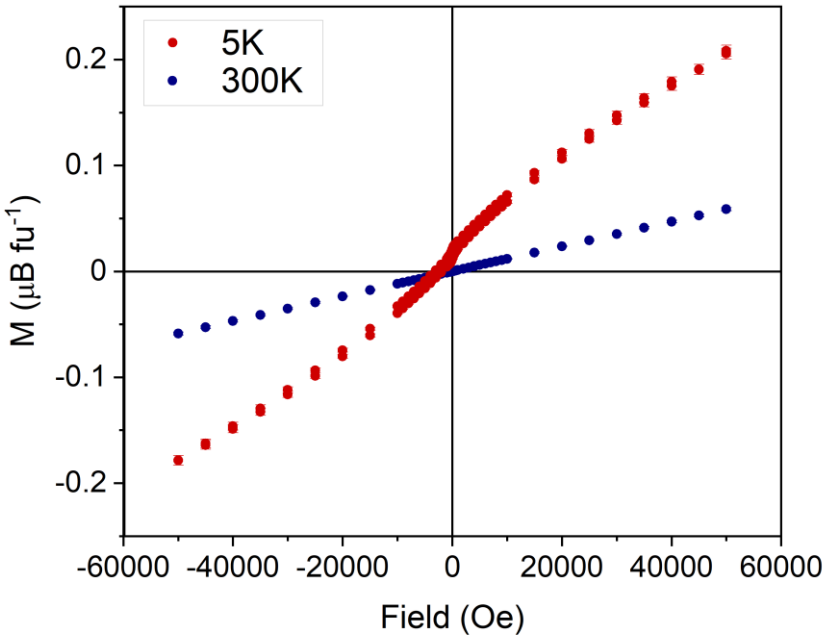

Figure A 12: Magnetisation-field isotherms for Sr_4CoIrO_8 measured at 5 K and 300 K.

A2 – Supplementary data for Chapter 4

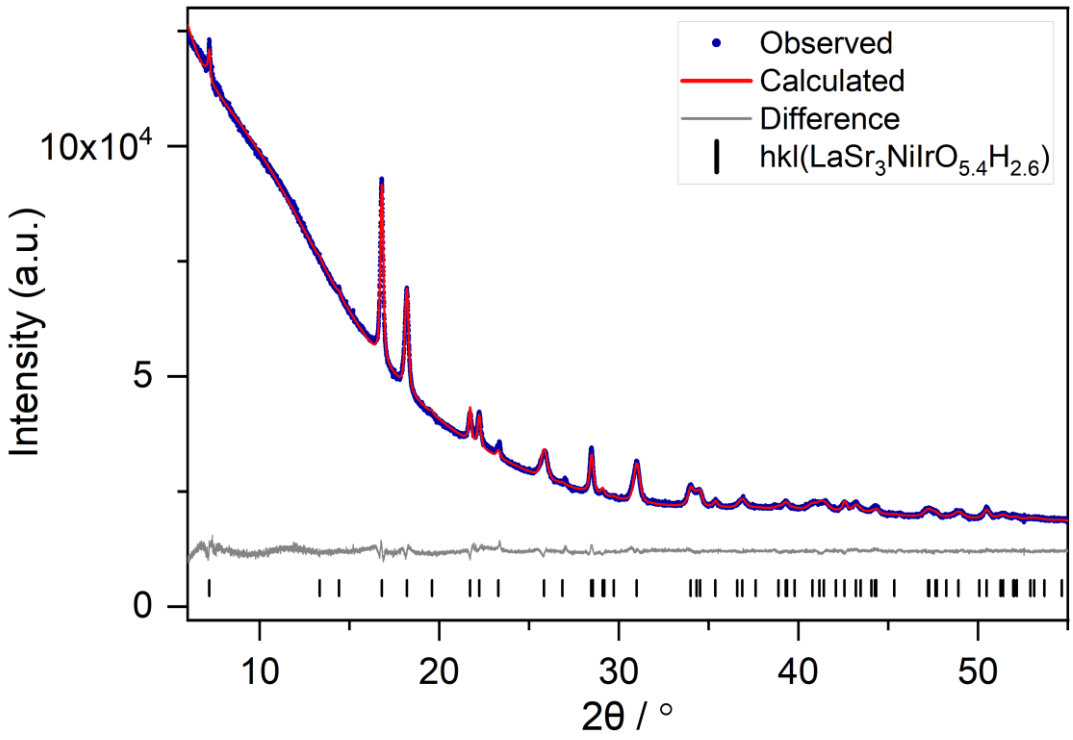

Figure A 13: Observed, calculated and difference plots from the structural refinement of $LaSr_3NiIrO_{5.4}H_{2.6}$ against SXRD data collected at room temperature using a wavelength of 0.825 Å.

Table A 11: Parameters from the structural refinement of $LaSr_3NiIrO_{5.4}H_{2.6}$ against SXRD data collected at room temperature. The occupancies and fractional coordinates of the anion sites were fixed at the values determined from the refinement against NPD data.

$LaSr_3NiIrO_{5.4}H_{2.6}$, space group *I*4/*mmm* (No. 139)						
		x	***y***	***z***	**Occ.**	**B_{iso} (Å^2)**
La(1)/Sr(1)	4*e*	0	0	0.35506(6)	0.25/0.75	1.14(4)
Ni(1)/Ir(1)	2*a*	0	0	0	0.5/0.5	2.84(5)
O(1)/H(1)	4*c*	0	½	0	0.351/0.649	0.8(1)
O(2)	4*e*	0	0	0.1677	1	0.8(1)
a = 3.6842(2) Å, c = 13.1185(6) Å						
V = 178.06(2) Å^3						
R_{wp} = 0.99%, R_p = 0.75%, *gof* = 1.98						

A3 – Supplementary data for Chapter 5

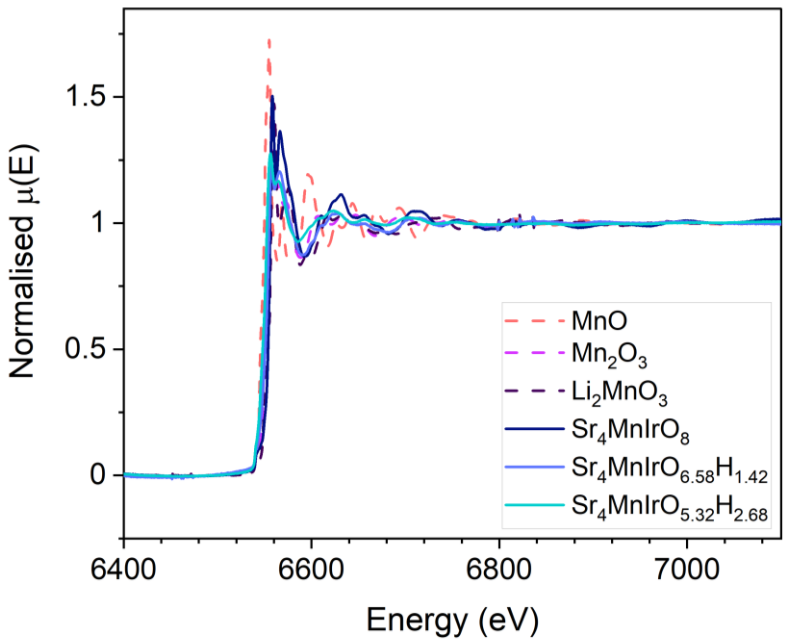

Figure A 14: Expanded view of XAS data collected from Sr_4MnIrO_8, $Sr_4MnIrO_{6.58}H_{1.42}$ and $Sr_4MnIrO_{5.32}H_{2.68}$ at the Mn K-edge, showing normalisation of the spectra.

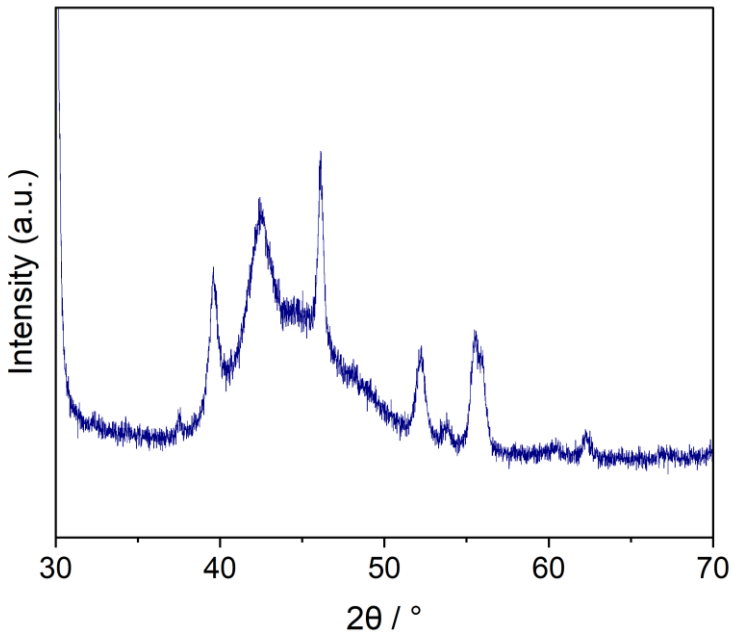

Figure A 15: PXRD data collected from the products of the reaction between $LaSr_3CoIrO_8$ and CaH_2 after washing with a 0.1 M solution of NH_4Cl in MeOH. Decomposition of the sample into finely divided Ir metal was observed, signalled by the appearance of a broad feature at $2\theta \sim 40{-}50°$.

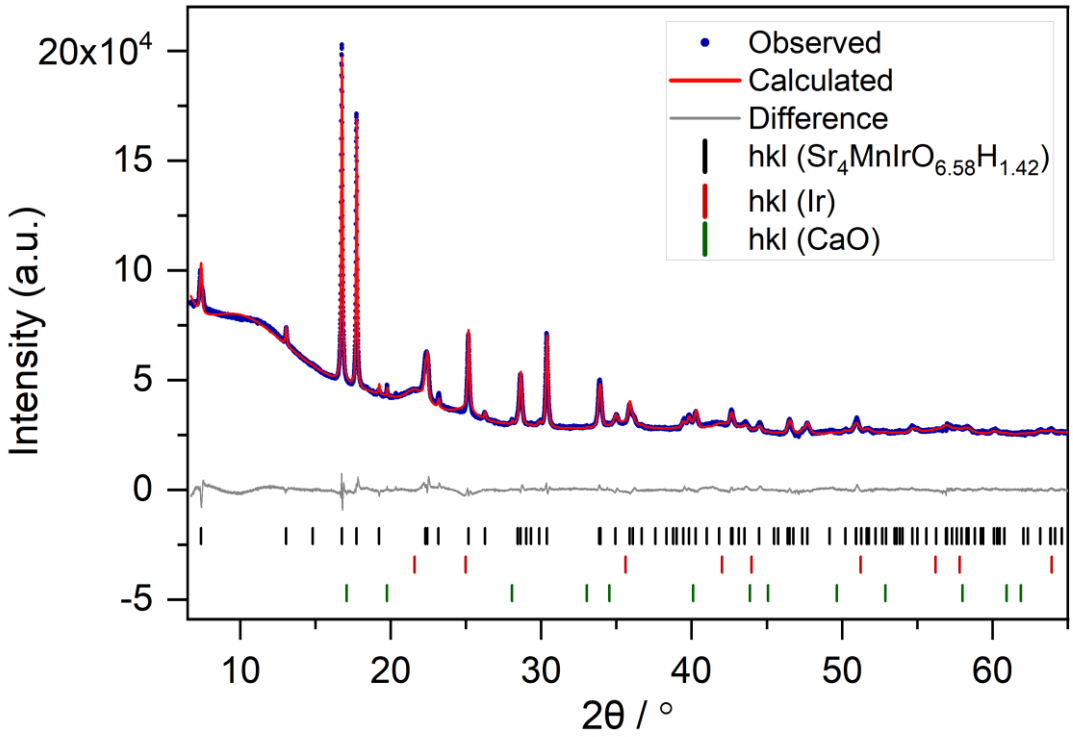

Figure A 16: Observed, calculated and difference plots from the structural refinement of $Sr_4MnIrO_{6.58}H_{1.42}$ against SXRD data collected at room temperature using a wavelength of 0.825 Å. A secondary phase of Ir metal is included in the refinement to account for the broad feature at 2θ ~ 22°, likely due to a small amount of decomposition during the reaction. A small impurity peak at 2θ ~ 20° is also observed, which is attributed to CaO remaining after the washing process, so this is included as a third phase in the refinement.

Table A 12: Parameters from the structural refinement of $Sr_4MnIrO_{6.58}H_{1.42}$ against SXRD data collected at room temperature. The oxide/hydride positions and occupancies were fixed using the values determined in Section 5.3.2.2.

$Sr_4MnIrO_{6.58}H_{1.42}$, space group *I*4/*mmm* (No. 139)						
		x	***y***	***z***	**Occ.**	**B_{iso} (Å^2)**
Sr(1)	4*e*	0	0	0.35307(8)	1	1.71(3)
Mn(1)/Ir(1)	2*a*	0	0	0	0.5/0.5	2.64(4)
O(1)/H(1)	4*c*	0	0.5	0	0.644/0.356	9.2(4)
O(2)	4*e*	0	0	0.1571	1	0.65(8)
a = 3.7890(1) Å, c = 12.8060(4) Å						
V = 91.4(3) Å^3						
R_{wp} = 2.00%, R_p = 1.48%, *gof* = 3.96						

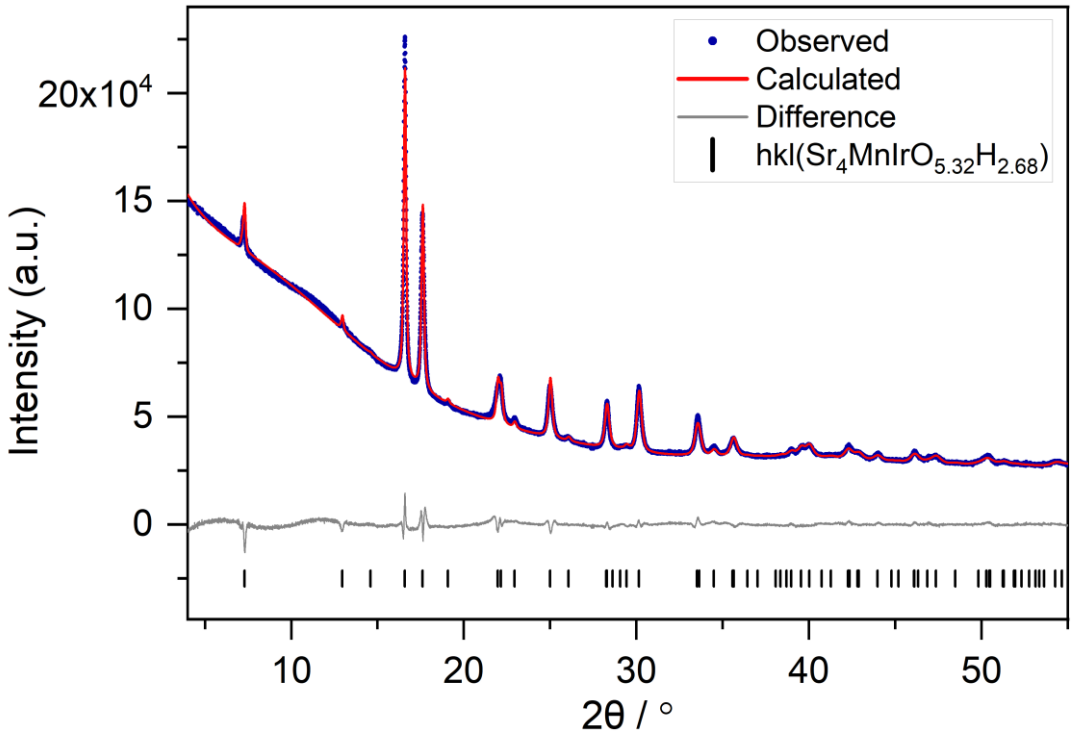

Figure A 17: Observed, calculated and difference plots from the structural refinement of $Sr_4MnIrO_{5.32}H_{2.68}$ against SXRD data collected at room temperature using a wavelength of 0.825 Å.

Table A 13: Parameters from the structural refinement of $Sr_4MnIrO_{5.32}H_{2.68}$ against SXRD data collected at room temperature. The oxide/hydride positions and occupancies were fixed using the values determined in Section 5.3.3.2.

$Sr_4MnIrO_{5.32}H_{2.68}$, space group *I*4/*mmm* (No. 139)						
		x	***y***	***z***	**Occ.**	**B_{iso} (Å^2)**
Sr(1)	4*e*	0	0	0.35144(8)	1	1.16(4)
Mn(1)/Ir(1)	2*a*	0	0	0	0.5/0.5	3.12(5)
O(1)/H(1)	4*c*	0	0.5	0	0.454/0.546	0.4(3)
O(2)/H(2)	4*e*	0	0	0.1640	0.877/0.122	1.3(1)
a = 3.8070(2) Å, c = 12.9772(7) Å						
V = 188.09(2) Å^3						
R_{wp} = 1.80%, R_p = 1.34%, *gof* = 4.28						

A4 – Supplementary data for Chapter 7

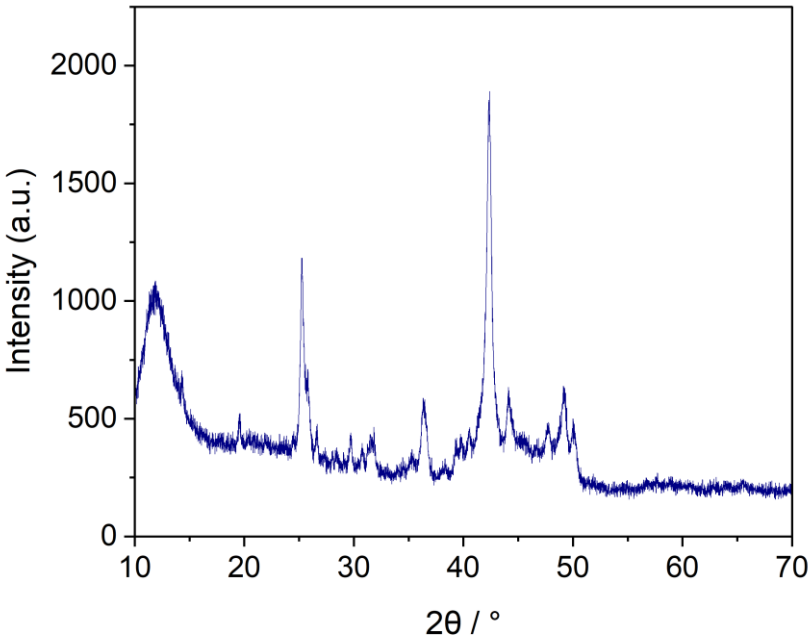

Figure A 18: PXRD data collected after the reductive TGA of $Sr_2CoIrO_{4.4}H_{1.6}$.

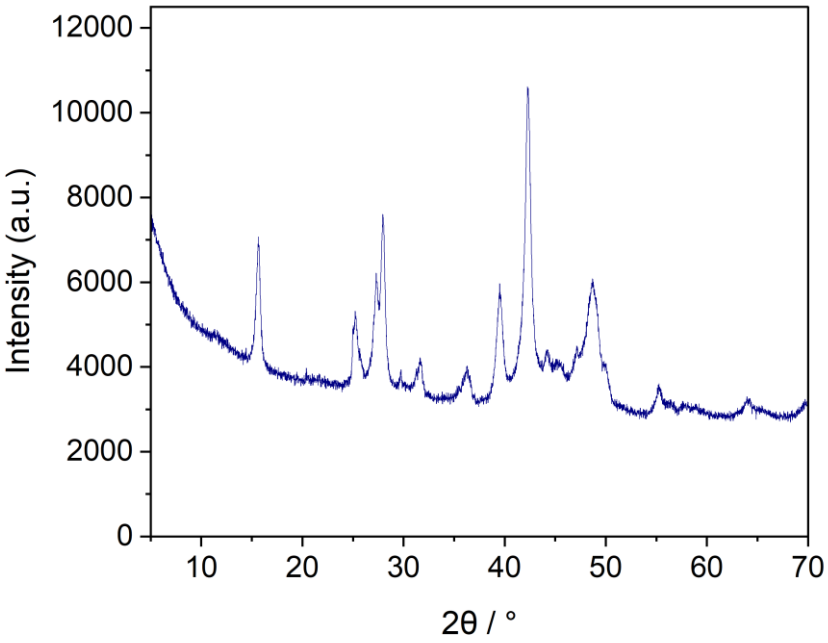

Figure A 19: PXRD data collected after the reductive TGA of $LaSrCoIrO_{4.4}H_{1.6}$.

A5 – Supplementary data for Chapter 10

A5.1 Synthesis and characterisation of $LaSrCoIrO_5$

An impure sample of $LaSrCoIrO_5$ was prepared by placing 1.2 g of $LaSrCoIrO_6$ in a glass thimble and sealing this in an evacuated Pyrex® ampoule with 1 g of finely-divided Zr metal, such that the $LaSrCoIrO_6$ sample was held approximately 5 cm from the Zr getter. The ampoule was then heated such that the temperature at the Zr getter was 400 °C. The sample was initially heated for 6 cycles of 4 days at 400 °C. The Zr getter was then removed and the sample was annealed in an empty, flame-dried Pyrex® tube at 375 °C for 4 days. 300 mg of $LaSrCoIrO_4$ (Chapter 10) was then mixed with the sample and the mixture was annealed at 375 °C for a further 4 days. The sample was then heated again with a Zr getter for two final cycles of 4 days at 390 °C. The sample was thoroughly reground between each heating cycle in an Ar-filled glovebox.

SXRD data collected from '$LaSrCoIrO_5$' appeared qualitatively similar to Sr_2CoIrO_5 and could be indexed using the *I*4/*mmm* space group. Therefore, a structural model based on Sr_2CoIrO_5 was constructed and refined against the data. A substantial impurity of $LaSrCoIrO_6$ was present in the sample, so this was added as a secondary phase. Furthermore, SrO and Ir metal were observed to be present in the sample, so these were added as additional phases. These models were then refined against the SXRD data, yielding lattice parameters of a = 5.4039(4) Å and c = 8.1834(7) Å for $LaSrCoIrO_5$, which corresponds to a contraction in the *xy*-plane and expansion in the *z*-direction relative to the parent $LaSrCoIrO_6$ phase (a = 5.58 Å, b = 5.59 Å, c = 7.91 Å). The fit to the SXRD data is shown in Figure A 20, with the refinement parameters detailed in Table A 14. Due to the substantial $LaSrCoIrO_6$ impurity, detailed structural characterisation of $LaSrCoIrO_5$ is not possible.

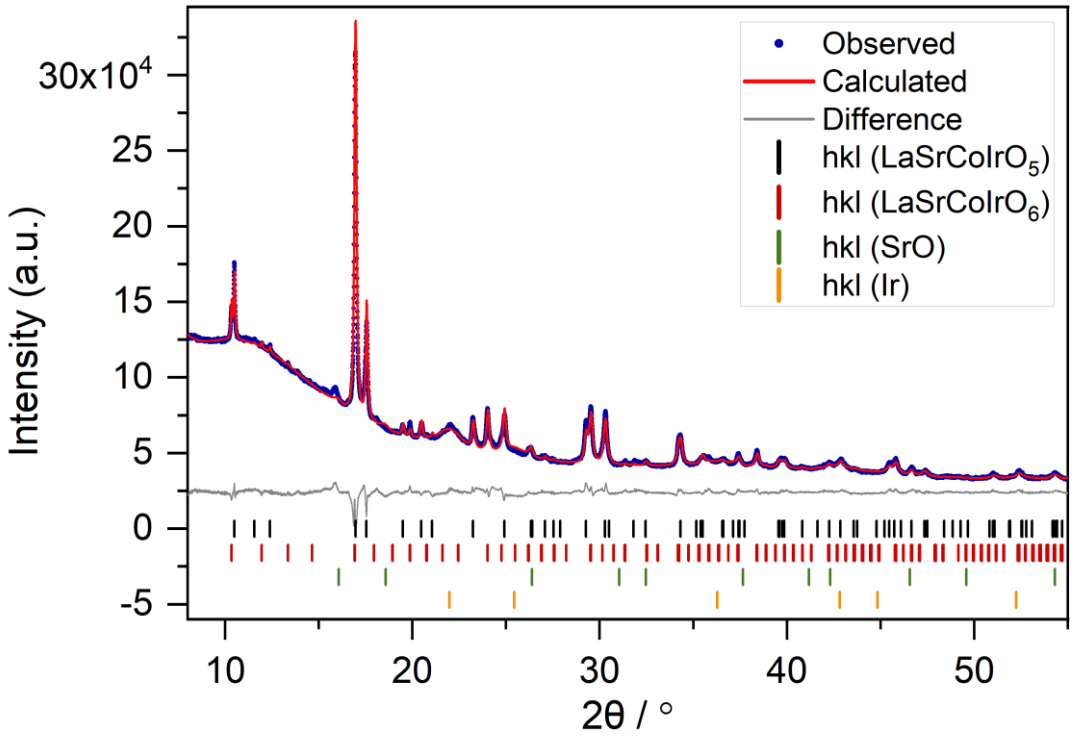

Figure A 20: Observed, calculated and difference plots from the structural refinement of $LaSrCoIrO_5$ against SXRD data collected at room temperature using a wavelength of 0.825 Å, with $LaSrCoIrO_6$, SrO and Ir metal included as secondary phases.

Table A 14: Parameters from the structural refinement of $LaSrCoIrO_5$ against SXRD data collected at room temperature. The occupancies at the transition metal sites were fixed at the values in the starting material. The atomic coordinates of $LaSrCoIrO_6$ were fixed at the values determined from the refinement of the parent oxide.

$LaSrCoIrO_5$, space group *I*4/*mmm* (No. 139), 48(2) wt%						
		x	***y***	***z***	**Occ.**	**B_{iso} (Å^2)**
Sr(1)/La(1)	4*d*	0	½	¼	0.5/0.5	2.38(8)
Co(1)/Ir(1)	2*a*	0	0	0	0.8985/0.1015	11.8(4)
Ir(2)/Co(2)	2*b*	½	½	0	0.8985/0.1015	4.3(1)
O(1)	8*h*	0.25	0.25	0	0.75	4.2(3)
O(2)	4*e*	0	0	0.25	1	4.2(3)
a = 5.4039(4) Å, c = 8.1834(7) Å						
V = 238.98(4) Å^3						
$LaSrCoIrO_6$, space group *P*2$_1$/*n* (No. 14), 28(1) wt%						
		x	***y***	***z***	**Occ.**	**B_{iso} (Å^2)**
Sr(1)/La(1)	4*e*	0.4996	0.5243	0.7383	0.5/0.5	1.6(1)
Co(1)/Ir(1)	2*c*	½	0	½	0.8985/0.1015	2.1(3)
Ir(2)/Co(2)	2*d*	½	0	0	0.8985/0.1015	6.6(3)
O(1)	4*e*	0.206	0.206	0.045	1	3.6(5)
O(2)	4*e*	0.738	0.225	0.015	1	3.6(5)
O(3)	*4e*	0.579	0.003	0.245	1	3.6(5)
a = 5.597(3) Å, b = 5.606(3) Å, c = 7.922(7) Å						
β = 90.0(1)°						
V = 248.6(3) Å^3						
Ir, space group *Fm*$\bar{3}$*m* (No. 225), 10.2(7) wt%						
		x	***y***	***z***	**Occ.**	**B_{iso} (Å^2)**
Ir(1)	4*a*	0	0	0	1	2.6(2)
a = 3.742(2) Å						
V = 52.4(1) Å^3						
SrO, space group *Fm*$\bar{3}$*m* (No. 225), 14(3) wt%						
		x	***y***	***z***	**Occ.**	**B_{iso} (Å^2)**
Sr(1)	4*a*	0	0	0	1	19(3)
O(1)	4*b*	½	½	½	1	19(3)
a = 5.105(4) Å						
V = 133.0(3) Å^3						
R_{wp} = 2.37%, R_p = 1.59%, *gof* = 5.82						

Magnetisation data collected from the impure sample of $LaSrCoIrO_5$ as a function of temperature are presented in Figure A 21, and magnetisation-field isotherms collected at 5 K and 300 K are presented in Figure A 22. NPD data collected at 10 K using the D20 diffractometer are shown in Figure A 23. Due to the presence of substantial amounts of $LaSrCoIrO_6$ in the sample, it is difficult to dissociate the magnetic behaviour of $LaSrCoIrO_5$ from that of $LaSrCoIrO_6$.

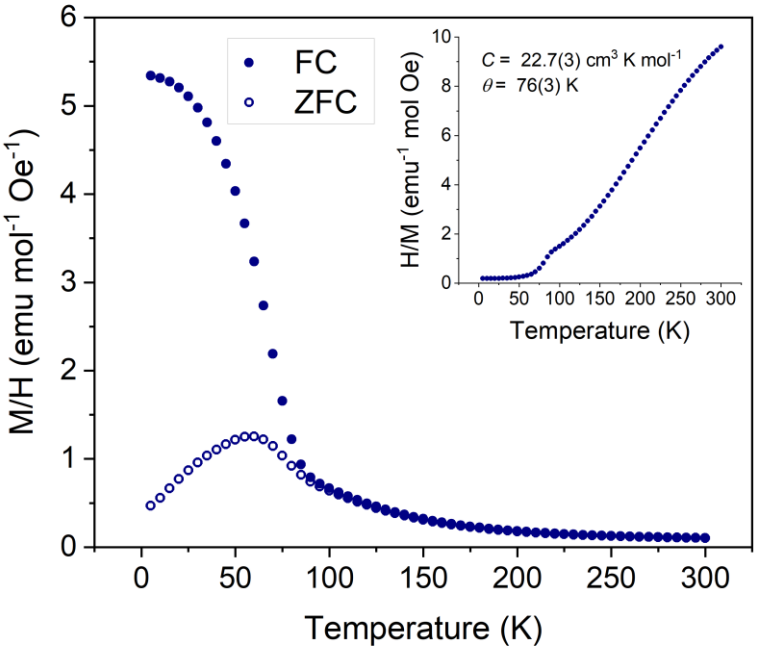

Figure A 21: Magnetisation data collected from $LaSrCoIrO_5$ as a function of temperature, measured in a field of 100 Oe under both ZFC and FC conditions.

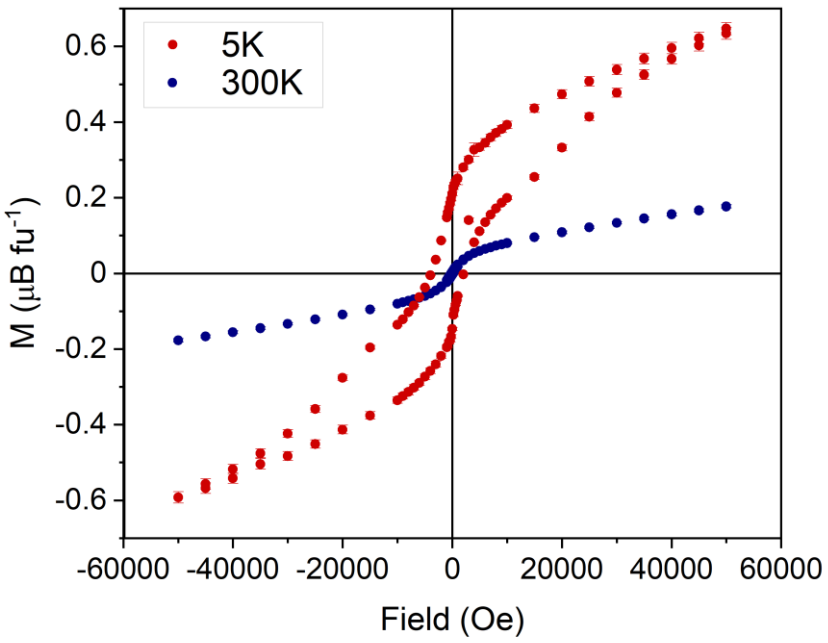

Figure A 22: Magnetisation-field isotherms for $LaSrCoIrO_5$ measured at 5 K and 300 K.

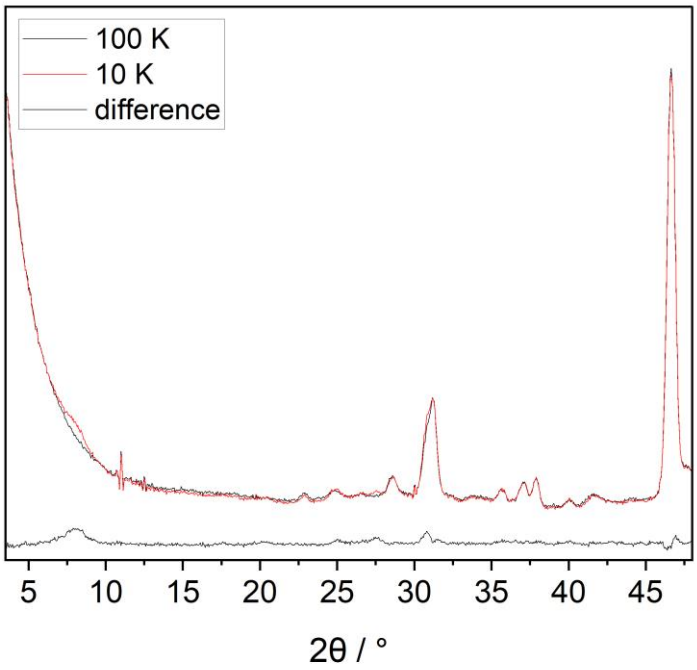

Figure A 23: NPD data collected from $LaSrCoIrO_5$ using the D20 diffractometer with a wavelength of 2.41 Å at 10 K and 100 K, and the difference between these patterns.

A5.2 Possible magnetic structure of $LaSrCoIrO_4$

The magnetic Bragg peaks observed at 10 K in $LaSrCoIrO_4$ can be indexed on the basis of a (3 × 3 × 1)-expansion of the nuclear unit cell. Following from this, the magnetic structure shown in Figure A 24 can be derived, which provides a good fit to the magnetic peaks observed in the NPD data, as shown in Figure A 25. The magnetic cell is defined as a [(−2, 0, 1), (1, 0, 1), (0, 1, 0)] transformation of the nuclear cell, and the ordering is described in magnetic space group 10.42. However, this magnetic ordering arrangement was deemed to be unlikely, due to the fact that equivalent nearest-neighbour Co−Ir coupling interactions would have different signs in the two layers of the structure.

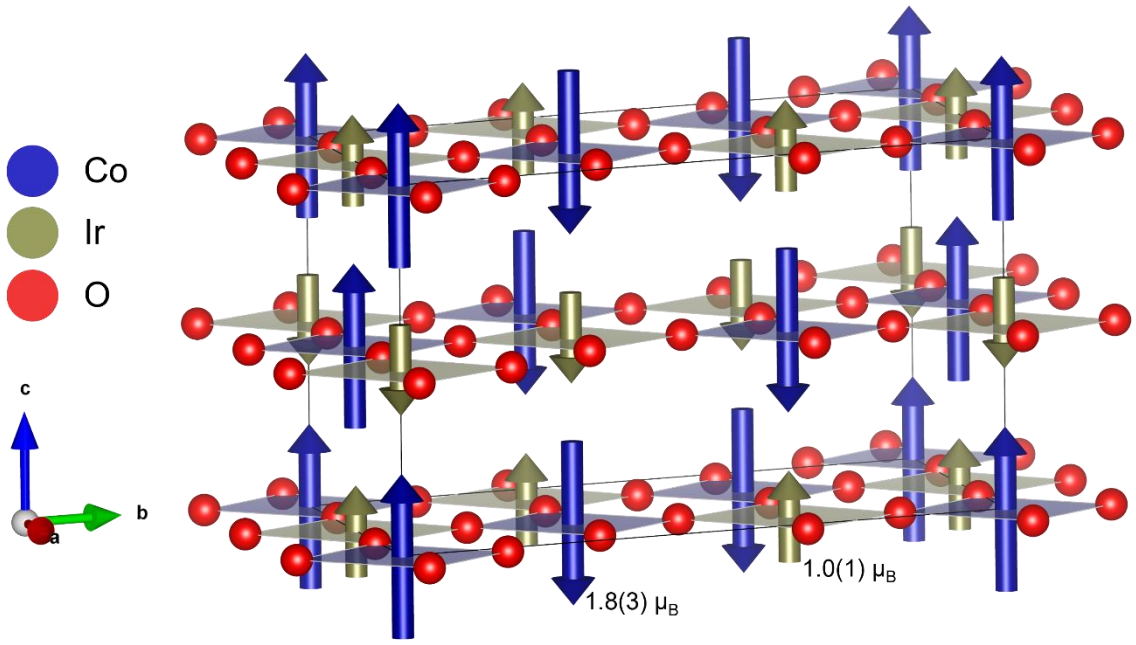

Figure A 24: Magnetic model based on a (3 × 3 × 1)-expansion of the nuclear unit cell that can account for the magnetic Bragg peaks observed in the NPD data collected from $LaSrCoIrO_4$ at 10 K. A refined magnetic moment of 1.8(3) μ_B is obtained at the Co sites and 1.0(1) μ_B at the Ir sites.

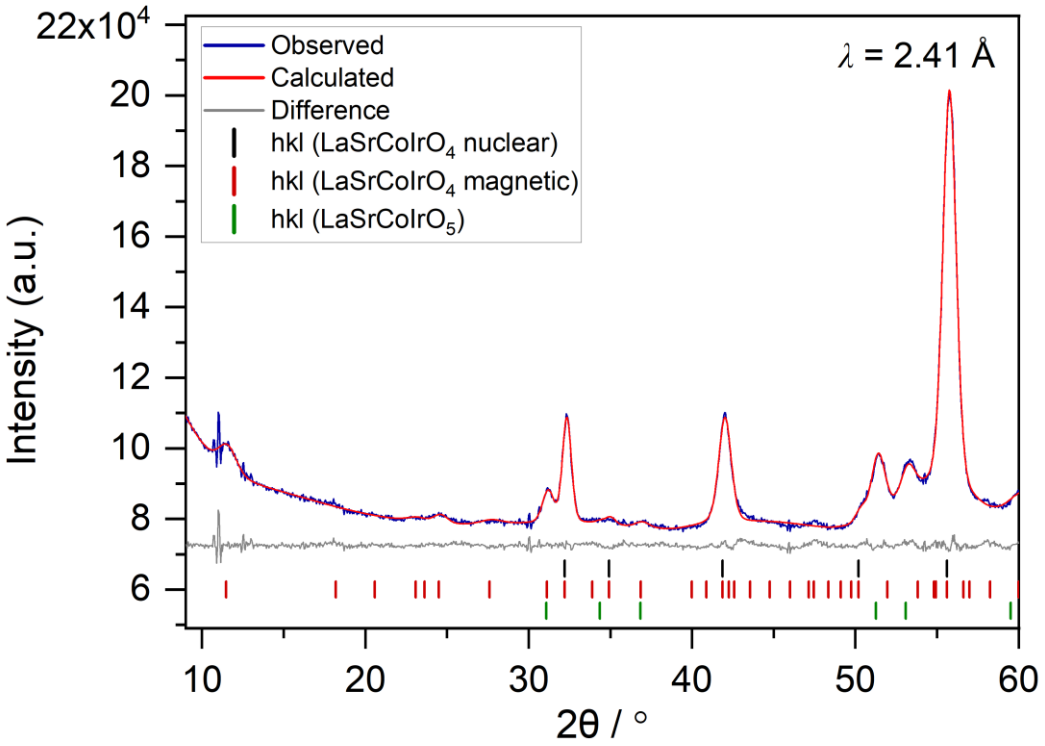

Figure A 25: Observed, calculated and difference plots from the magnetic refinement of $LaSrCoIrO_4$ against NPD data using the model shown in Figure A 24. The data were collected using the D20 diffractometer at 10 K with a wavelength of 2.41 Å.

Table of Figures

Figure 1.1: The cubic ABO_3 perovskite structure, where the grey sphere represents the A-cation, the blue spheres represent the B-cations and the red spheres represent the anions. 2
Figure 1.2: Possible ordering arrangements for B-site cations in the double perovskite structure.....4
Figure 1.3: Different polymorphs of $BaRuO_3$ with hexagonal perovskite structures.....6
Figure 1.4: Schematic illustrating paracrystalline ordering in $n = 1$ Ruddlesden-Popper phases. Although the B-site cations may be ordered within the perovskite sheets, there is very little ordering between the sheets. As such, the B-site cations appear disordered from diffraction methods. 7
Figure 1.5: Superexchange interactions between octahedrally coordinated transition metals via oxide ligands. 11
Figure 1.6: For a triangular arrangement of spins with antiferromagnetic coupling, the third spin must necessarily be aligned ferromagnetically to one spin and antiferromagnetically to the other, leading to magnetic frustration. 14
Figure 1.7: Schematic representing the crystal orbital energies as the number of interacting atomic orbitals increases. For an infinite periodic solid, the orbitals can be thought of as forming a continuous band, as shown on the right of the diagram. 16
Figure 1.8: Schematic illustrating how competition between on-site repulsion, U, and bandwidth, W, determines whether a material is a metal or a Mott-Hubbard insulator. 17
Figure 1.9: Schematic band diagrams for (a) $NaIrO_3$ ($5d^4$), in which the t_{2g} band is split into a $J_{eff} = 3/2$ band and a $J_{eff} = 1/2$ band by spin-orbit coupling, and (b) Sr_2IrO_4 ($5d^5$), in which the $J_{eff} = 1/2$ band is further split into two Hubbard bands by on-site repulsions, resulting in Mott insulating behaviour. 19
Figure 1.10: Reaction of $LaNiO_3$ with NaH to form the infinite-layer phase $LaNiO_2$. 20
Figure 1.11: Reaction of $(La/Sr)_4CoIrO_8$ with a Zr getter to form $(La/Sr)_4CoIrO_6$. 21
Figure 1.12: Crystal structure of (a) $SrVO_2H$ with an anion-ordered, tetragonal structure and (b) $SrV_{0.95}Ti_{0.05}O_{1.5}H_{1.5}$ with an anion-disordered, cubic structure. 22
Figure 1.13: Crystal field splitting for (a) a regular octahedral environment and (b) V^{3+} centres in which the hydride σ-donors are *trans* to each other. 23
Figure 2.1: Schematic representation of Zr getter reaction set-up. 28
Figure 2.2: Geometry used for derivation of the Bragg equation. 30
Figure 2.3: 2θ dependence of $1/\cos\theta_0$ and $\tan\theta_0$, highlighting that peak broadening due to crystallite size is significant at all angles, whereas broadening due to microstrain is more significant at high angles. 37
Figure 2.4: Schematic illustrating the superconducting ring in a DC SQUID magnetometer. 42
Figure 2.5: Schematic illustrating the principles of the ferrosubtraction technique. 43
Figure 2.6: Schematic illustrating varying the ω angle, whilst keeping 2θ constant to bring *hkl* planes that are not parallel with the sample surface into the Bragg plane. 47
Figure 3.1: Structural model for $La_xSr_{4-x}CoIrO_8$ ($0 \leq x \leq 2$) phases with the $n = 1$ Ruddlesden-Popper structure. 53
Figure 3.2: TGA trace (top panel) and H_2/H_2O contents of exhaust gas (bottom panel) when $Sr_4CoIrO_{6.5}H_{1.5}$ is heated under flowing oxygen. 54
Figure 3.3: Observed, calculated and difference plots from the structural refinement of $Sr_4CoIrO_{6.5}H_{1.5}$ against NPD data collected at room temperature from the 54° bank of the POLARIS diffractometer. 56

Figure 3.4: Observed, calculated and difference plots from the structural refinement of $Sr_4CoIrO_{6.5}H_{1.5}$ against NPD data collected at room temperature from the 94° bank of the POLARIS diffractometer. 57
Figure 3.5: Observed, calculated and difference plots from the structural refinement of $Sr_4CoIrO_{6.5}H_{1.5}$ against NPD data collected at room temperature from the 139° bank of the POLARIS diffractometer. 57
Figure 3.6: TGA trace (top panel) and H_2/H_2O contents of exhaust gas (bottom panel) when $La_{0.5}Sr_{3.5}CoIrO_{5.5}H_{2.5}$ is heated under flowing oxygen. 59
Figure 3.7: Observed, calculated and difference plots from the structural refinement of $La_{0.5}Sr_{3.5}CoIrO_{5.5}H_{2.5}$ against NPD data collected at room temperature from the 54° bank of the POLARIS diffractometer. 60
Figure 3.8: Observed, calculated and difference plots from the structural refinement of $La_{0.5}Sr_{3.5}CoIrO_{5.5}H_{2.5}$ against NPD data collected at room temperature from the 94° bank of the POLARIS diffractometer. 61
Figure 3.9: Observed, calculated and difference plots from the structural refinement of $La_{0.5}Sr_{3.5}CoIrO_{5.5}H_{2.5}$ against NPD data collected at room temperature from the 139° bank of the POLARIS diffractometer. 61
Figure 3.10: TGA trace (top panel) and H_2/H_2O contents of exhaust gas (bottom panel) when $LaSr_3CoIrO_5H_3$ is heated under flowing oxygen. 63
Figure 3.11: Observed, calculated and difference plots from the structural refinement of $LaSr_3CoIrO_5H_3$ against NPD data collected at room temperature from the 54° bank of the POLARIS diffractometer. 64
Figure 3.12: Observed, calculated and difference plots from the structural refinement of $LaSr_3CoIrO_5H_3$ against NPD data collected at room temperature from the 94° bank of the POLARIS diffractometer. 64
Figure 3.13: Observed, calculated and difference plots from the structural refinement of $LaSr_3CoIrO_5H_3$ against NPD data collected at room temperature from the 139° bank of the POLARIS diffractometer. 65
Figure 3.14: Observed, calculated and difference plots from the initial structural refinement of $La_{1.5}Sr_{2.5}CoIrO_{8-y}H_y$ against SXRD data. The additional feature close to the 110 reflection is highlighted. 66
Figure 3.15: TGA trace (top panel) and H_2/H_2O contents of exhaust gas (bottom panel) when $La_{1.5}Sr_{2.5}CoIrO_{8-y}H_y$ is heated under flowing oxygen. 67
Figure 3.16: Observed, calculated and difference plots from the initial structural refinement of $La_{1.5}Sr_{2.5}CoIrO_{5.5}H_{2.5}$ against NPD data collected at room temperature from the 54° bank of the POLARIS diffractometer. The region around 2.14 Å contains a peak from the vanadium sample can so is excluded from the refinement. The additional features observed close to the 200, 114 and 110 reflections are highlighted. 68
Figure 3.17: Observed, calculated and difference plots from the two-phase structural refinement of $La_{1.5}Sr_{2.5}CoIrO_{8-y}H_y$ against NPD data collected at room temperature from the 54° bank of the POLARIS diffractometer. Phase 1 has a refined composition of $La_{1.5}Sr_{2.5}CoIrO_{5.5}H_{2.5}$, whilst Phase 2 has a refined composition of $La_{1.5}Sr_{2.5}CoIrO_{6.8}H_{1.2.}$ The inset shows an expanded region from 1.5 to 2.9 Å to allow the fit to be compared to the initial one-phase refinement presented in Figure 3.16. 69
Figure 3.18: Observed, calculated and difference plots from the two-phase structural refinement of $La_{1.5}Sr_{2.5}CoIrO_{8-y}H_y$ against NPD data collected at room temperature from the 94° bank of the POLARIS diffractometer. 69
Figure 3.19: Observed, calculated and difference plots from the two-phase structural refinement of $La_{1.5}Sr_{2.5}CoIrO_{8-y}H_y$ against NPD data collected at room temperature from the 139° bank of the POLARIS diffractometer. 70

Figure 3.20: TGA trace (top panel) and H_2/H_2O contents of exhaust gas (bottom panel) when $La_2Sr_2CoIrO_{8-y}H_y$ is heated under flowing oxygen. 72
Figure 3.21: Observed, calculated and difference plots from the structural refinement of $La_2Sr_2CoIrO_{8-y}H_y$ against NPD data collected at room temperature from the 54° bank of the POLARIS diffractometer. Phase 1 has a refined composition of $La_2Sr_2CoIrO_6H_2$, whilst Phase 2 has a refined composition of $La_2Sr_2CoIrO_7H$. 73
Figure 3.22: Observed, calculated and difference plots from the structural refinement of $La_2Sr_2CoIrO_{8-y}H_y$ against NPD data collected at room temperature from the 94° bank of the POLARIS diffractometer. 74
Figure 3.23: Observed, calculated and difference plots from the structural refinement of $La_2Sr_2CoIrO_{8-y}H_y$ against NPD data collected at room temperature from the 139° bank of the POLARIS diffractometer. 74
Figure 3.24: Variation in *a*-lattice parameter and volume as a function of A-site cation composition in $La_xSr_{4-x}CoIrO_{8-y}H_y$ phases. 78
Figure 3.25: XANES Co K-edges for $Sr_4CoIrO_{6.5}H_{1.5}$, $LaSr_3CoIrO_5H_3$ and $La_2Sr_2CoIrO_6H_2$, with Sr_2CoIrO_6 (Co^{3+}) and $YBaCo_2O_5$ ($Co^{2.5+}$) acting as standards. 79
Figure 3.26: Composition space for the $La_xSr_{4-x}CoIrO_{8-y}H_y$ ($0 \leq x \leq 2$) series of oxyhydride phases as a function of anion composition and A-site cation composition. The blue, circular markers indicate the experimentally observed compositions. The pink, solid line connects the experimental compositions and is intended as a guide for the eye. The green, dashed lines represent the anion compositions corresponding to Co^{I}/Ir^{III} and Co^{II}/Ir^{III} transition metal oxidation state combinations. For a given A-site cation composition, transition metal oxidation state increases vertically, whilst, for a given anion composition, transition metal oxidation state increases towards the left of the diagram. 81
Figure 3.27: Schematic showing the anion ordering required to accommodate the *trans*-hydride coordination preference of Co^{II} and the *cis*-hydride coordination preference of Ir^{III} within the equatorial planes of the perovskite sheets in $La_xSr_{4-x}CoIrO_{5+x}H_{3-x}$, where $x = 1$. For $x < 1$, the oxide ions are partially replaced by hydride, whilst, for $x > 1$, the hydride ions are partially replaced by oxide. The green crosses represent hydride ions, whilst the red squares represent oxide ions. The dashed, orange line represents the simple, tetragonal unit cell of the all-oxide Ruddlesden-Popper phase. The dashed, purple line represents the $(2\sqrt{2} \times \sqrt{2} \times 1)$-expanded orthorhombic unit cell of the anion-ordered phase. 84
Figure 3.28: Magnetisation data collected from $Sr_4CoIrO_{6.5}H_{1.5}$ as a function of temperature, measured in a field of 100 Oe under both ZFC and FC conditions. 87
Figure 3.29: Magnetisation-field isotherms for $Sr_4CoIrO_{6.5}H_{1.5}$ measured at 5 K and 300 K. 88
Figure 3.30: AC susceptibility as a function of temperature for $Sr_4CoIrO_{6.5}H_{1.5}$, measured at frequencies between 5 Hz and 500 Hz. The measurements were performed using an AC field with amplitude of 2.5 Oe, and an applied DC field of 2 Oe. The inset shows the variation of T_f with ω for $Sr_4CoIrO_{6.5}H_{1.5}$. The red line shows the fit to the data using the power law shown in Equation 43. 88
Figure 3.31: Saturated ferromagnetic moment (top panel) and paramagnetic susceptibility (bottom panel) obtained from $Sr_4CoIrO_{6.5}H_{1.5}$ using the 'ferrosubtraction' technique described in Section 2.8.1. 89
Figure 3.32: Magnetisation data collected from $La_{0.5}Sr_{3.5}CoIrO_{5.5}H_{2.5}$ as a function of temperature, measured in a field of 100 Oe under both ZFC and FC conditions. 90
Figure 3.33: Magnetisation-field isotherms for $La_{0.5}Sr_{3.5}CoIrO_{5.5}H_{2.5}$ measured at 5 K and 300 K. 91
Figure 3.34: Magnetisation data collected from $LaSr_3CoIrO_5H_3$ as a function of temperature, measured in a field of 100 Oe under both ZFC and FC conditions. 92

Figure 3.35: Magnetisation-field isotherms for $LaSr_3CoIrO_5H_3$ measured at 5 K and 300 K. 92
Figure 3.36: Magnetisation data collected from $La_{1.5}Sr_{2.5}CoIrO_{8-y}H_y$ as a function of temperature, measured in a field of 100 Oe under both ZFC and FC conditions. 93
Figure 3.37: Magnetisation-field isotherms for $La_{1.5}Sr_{2.5}CoIrO_{8-y}H_y$ measured at 5 K and 300 K. 94
Figure 3.38: Magnetisation data collected from $La_2Sr_2CoIrO_{8-y}H_y$ as a function of temperature, measured in a field of 100 Oe under both ZFC and FC conditions 95
Figure 3.39: Magnetisation-field isotherms for $La_2Sr_2CoIrO_{8-y}H_y$ measured at 5 K and 300 K. 95
Figure 3.40: μ^+-SR data collected from $Sr_4CoIrO_{6.5}H_{1.5}$, $LaSr_3CoIrO_5H_3$ and $La_2Sr_2CoIrO_6H_2$ as a function of temperature. 97
Figure 3.41: (a) simplistic crystal field splitting diagrams for Co^{II}, Ir^{IV} and Ir^{V} in $Sr_4CoIrO_{6.5}H_{1.5}$, (b) schematics illustrating superexchange interactions between orbitals in $Sr_4CoIrO_{6.5}H_{1.5}$, whereby (i) and (ii) can be mediated by either oxide 2*p* or hydride 1*s* orbitals and (c) schematic illustrating next-nearest-neighbour Ir−Ir antiferromagnetic interactions, mediated by overlap between spatially diffuse $5d_{xy}$ orbitals. 99
Figure 3.42: Orbital diagrams illustrating the σ-superexchange pathway between Co^{I} ions via (a) hydride ions and (b) oxide ions. 100
Figure 3.43: Schematic illustrating the two independent magnetic lattices present within the perovskite sheets of $La_xSr_{4-x}CoIrO_{8-y}H_y$ phases. 101
Figure 4.1: Structural model of $LaSr_3NiIrO_8$ with the n = 1 Ruddlesden-Popper structure. 106
Figure 4.2: Observed, calculated and difference plots from the structural refinement of $LaSr_3NiIrO_8$ against SXRD data collected at room temperature using a wavelength of 0.825 Å. 107
Figure 4.3: TGA trace (top panel) and contents of exhaust gas (bottom panel) when $LaSr_3NiIrO_{5.4}H_{2.6}$ is heated under flowing oxygen. 108
Figure 4.4: Observed, calculated and difference plots from the structural refinement of $LaSr_3NiIrO_{5.4}H_{2.6}$ against NPD data collected at 200 K from the D20 diffractometer using a wavelength of 1.54 Å. 110
Figure 4.5: Refined structure of $LaSr_3NiIrO_{5.4}H_{2.6}$, showing hydride ions substituted into the equatorial positions. 111
Figure 4.6: Observed, calculated and difference plots from the structural refinement of $LaSr_3NiIrO_{6.4}$ against SXRD data collected at room temperature using a wavelength of 0.825 Å. 113
Figure 4.7: TGA trace when $LaSr_3NiIrO_{6.4}$ is heated under flowing oxygen. 114
Figure 4.8: Observed, calculated and difference plots from the structural refinement of $LaSr_3NiIrO_{6.4}$ against NPD data collected at room temperature from the D2B diffractometer using a wavelength of 1.594 Å. 115
Figure 4.9: Refined structure of $LaSr_3NiIrO_{6.4}$. 116
Figure 4.10: XANES Ni K-edges for NiO, $LaSr_3NiIrO_{5.4}H_{2.6}$ and $LaSr_3NiIrO_{6.4}$. 117
Figure 4.11: Electronic configurations of Ni^{I}, Ni^{II}, Ir^{I}, Ir^{II} and Ir^{III} in square-planar (D_{4h}) and square-pyramidal (C_{4v}) coordination environments. 119
Figure 4.12: Top: Illustration of electronic driving force for disproportionation of Ir^{II} into Ir^{I} (D_{4h}) and Ir^{III} (C_{4v}). Bottom: Illustration of coordination environments of Ni^{II}, Ir^{I} and Ir^{III} in disproportionated $LaSr_3NiIrO_{6.4}$. 120
Figure 4.13: Magnetisation data collected from $LaSr_3NiIrO_8$ as a function of temperature, measured in a field of 100 Oe under both ZFC and FC conditions. 121
Figure 4.14: Magnetisation-field isotherms for $LaSr_3NiIrO_8$ measured at 5 K and 300 K. .122

Figure 4.15: Magnetisation data collected from $LaSr_3NiIrO_{5.4}H_{2.6}$ as a function of temperature, measured in a field of 100 Oe under both ZFC and FC conditions. 123
Figure 4.16: Magnetisation-field isotherms for $LaSr_3NiIrO_{5.4}H_{2.6}$ measured at 5 K and 300 K. 124
Figure 4.17: Saturated ferromagnetic moment (top panel) and paramagnetic susceptibility (bottom panel) obtained from $LaSr_3NiIrO_{5.4}H_{2.6}$ using the 'ferrosubtraction' technique described in Section 2.8.1. 125
Figure 4.18: NPD data collected from $LaSr_3NiIrO_{5.4}H_{2.6}$ using the D20 diffractometer with a wavelength of 2.41 Å at 5 K and 100 K, and the difference between the patterns at these two temperatures. 126
Figure 4.19: Magnetisation data collected from $LaSr_3NiIrO_{6.4}$ as a function of temperature, measured in a field of 100 Oe under both ZFC and FC conditions. 127
Figure 4.20: Magnetisation-field isotherms for $LaSr_3NiIrO_{6.4}$ measured at 5 K and 300 K.127
Figure 4.21: Saturated ferromagnetic moment (top panel) and paramagnetic susceptibility (bottom panel) obtained from $LaSr_3NiIrO_{6.4}$ using the 'ferrosubtraction' technique described in Section 2.8.1. 128
Figure 4.22: NPD data collected from $LaSr_3NiIrO_{6.4}$ using the D20 diffractometer with a wavelength of 2.41 Å at 5 K and 100 K, and the difference between the patterns at these two temperatures. 129
Figure 4.23: Orbital diagrams illustrating the antiferromagnetic σ-superexchange pathway between Ni^{I} or Ni^{II} ions via diamagnetic Ir^{III} or Ir^{V} ions. 130
Figure 5.1: Structural model of Sr_4MnIrO_8 with the n = 1 Ruddlesden-Popper structure....136
Figure 5.2: Observed, calculated and difference plots from the structural refinement of Sr_4MnIrO_8 against SXRD data collected at room temperature using a wavelength of 0.825 Å. 136
Figure 5.3: TGA trace (top panel) and H_2/H_2O contents of exhaust gas (bottom panel) when $Sr_4MnIrO_{6.58}H_{1.42}$ is heated under flowing oxygen. 138
Figure 5.4: Observed, calculated and difference plots from the structural refinement of $Sr_4MnIrO_{6.58}H_{1.42}$ against NPD data collected at room temperature from the 35° bank of the GEM diffractometer. 140
Figure 5.5: Observed, calculated and difference plots from the structural refinement of $Sr_4MnIrO_{6.58}H_{1.42}$ against NPD data collected at room temperature from the 64° bank of the GEM diffractometer. 141
Figure 5.6: Observed, calculated and difference plots from the structural refinement of $Sr_4MnIrO_{6.58}H_{1.42}$ against NPD data collected at room temperature from the 91° bank of the GEM diffractometer. 141
Figure 5.7: Observed, calculated and difference plots from the structural refinement of $Sr_4MnIrO_{6.58}H_{1.42}$ against NPD data collected at room temperature from the 154° bank of the GEM diffractometer. 142
Figure 5.8: Refined structure of $Sr_4MnIrO_{6.58}H_{1.42}$ with hydride ions substituted into the equatorial positions. 143
Figure 5.9: TGA trace (top panel) and H_2/H_2O contents of exhaust gas (bottom panel) when $Sr_4MnIrO_{5.32}H_{2.68}$ is heated under flowing oxygen. 144
Figure 5.10: Observed, calculated and difference plots from the structural refinement of $Sr_4MnIrO_{5.32}H_{2.68}$ against NPD data collected at room temperature from the 35° bank of the GEM diffractometer. 146
Figure 5.11: Observed, calculated and difference plots from the structural refinement of $Sr_4MnIrO_{5.32}H_{2.68}$ against NPD data collected at room temperature from the 64° bank of the GEM diffractometer. 147

Figure 5.12: Observed, calculated and difference plots from the structural refinement of $Sr_4MnIrO_{5.32}H_{2.68}$ against NPD data collected at room temperature from the 91° bank of the GEM diffractometer. 147
Figure 5.13: Observed, calculated and difference plots from the structural refinement of $Sr_4MnIrO_{5.32}H_{2.68}$ against NPD data collected at room temperature from the 154° bank of the GEM diffractometer. 148
Figure 5.14: Refined structure of $Sr_4MnIrO_{5.32}H_{2.68}$ with hydride ions substituted into both the axial and the equatorial positions. 149
Figure 5.15: XANES Mn K-edges for Sr_4MnIrO_8, $Sr_4MnIrO_{6.58}H_{1.42}$ and $Sr_4MnIrO_{5.32}H_{2.68}$. A wide energy range is presented in Appendix A3 to show the normalisation of the spectra. .150
Figure 5.16: Fits of the magnitude of the Fourier-transform of k^3-weighted $\chi(k)$, extracted from EXAFS data collected at the Mn K-edge, performed in the *R*-range 1.0−4.3 Å (left) and corresponding fits of the real part of Fourier back-filtered $\chi(k)$ in the *R*-range 1.0−4.3 Å (right). The experimental data are shown as circles, with the fits represented by the solid lines. 151
Figure 5.17: Magnetisation data collected from Sr_4MnIrO_8 as a function of temperature, measured in a field of 100 Oe under both ZFC and FC conditions. 154
Figure 5.18: Magnetisation-field isotherms for Sr_4MnIrO_8 measured at 5 K and 300 K. 154
Figure 5.19: AC susceptibility as a function of temperature for Sr_4MnIrO_8, measured at frequencies between 5 Hz and 500 Hz. The measurements were performed using an AC field with amplitude of 2.5 Oe, and an applied DC field of 2 Oe. The inset shows the variation of T_f with ω for Sr_4MnIrO_8. The red line shows the fit to the data using the power law shown in Equation 43. 155
Figure 5.20: Magnetisation data collected from $Sr_4MnIrO_{6.58}H_{1.42}$ as a function of temperature, measured in a field of 100 Oe under both ZFC and FC conditions. 156
Figure 5.21: Magnetisation-field isotherms for $Sr_4MnIrO_{6.58}H_{1.42}$ measured at 5 K and 300 K. 157
Figure 5.22: AC susceptibility as a function of temperature for $Sr_4MnIrO_{6.58}H_{1.42}$, measured at frequencies between 5 Hz and 500 Hz. The measurements were performed using an AC field with amplitude of 2.5 Oe, and an applied DC field of 2 Oe. The inset shows the variation of T_f with ω for $Sr_4MnIrO_{6.58}H_{1.42}$. The red line shows the fit to the data using the power law shown in Equation 43. 157
Figure 5.23: Magnetisation data collected from $Sr_4MnIrO_{5.32}H_{2.68}$ as a function of temperature, measured in a field of 100 Oe under both ZFC and FC conditions. 158
Figure 5.24: Magnetisation-field isotherms for $Sr_4MnIrO_{5.32}H_{2.68}$ measured at 5 K and 300 K. 159
Figure 5.25: Hypothetical stages during the reaction of Sr_4MnIrO_8 with binary metal hydrides, highlighting the choice between axial and equatorial exchange when $Sr_4MnIrO_6H_2$ is converted to $Sr_4MnIrO_5H_3$. Axial exchange results in a *fac*-configuration, whilst equatorial exchange results in a *mer*-configuration. 163
Figure 5.26: (a) simplistic crystal field splitting diagrams for Mn^{IV} and Ir^{IV} in Sr_4MnIrO_8, (b) schematic illustrating nearest-neighbour antiferromagnetic interactions in Sr_4MnIrO_8 and (c) schematic illustrating next-nearest-neighbour Ir-Ir antiferromagnetic interactions, mediated by overlap between spatially diffuse $5d_{xy}$ orbitals. 165
Figure 6.1: Observed, calculated and difference plots from the structural refinement of $Ba_3CoIr_2O_9$ against SXRD data (λ = 0.825 Å) collected at room temperature using the undistorted $P6_3/mmc$ model and distorted models in the *Cmcm* and $C2/c$ space groups. 171
Figure 6.2: Structural model of $Ba_3CoIr_2O_9$ with an ortho-hexagonally distorted 6H-perovskite structure in the $C2/c$ space group. 172
Figure 6.3: TGA trace (top panel) and H_2/H_2O contents of exhaust gas (bottom panel) when $Ba_3CoIr_2O_{6.2}H_{2.8}$ is heated under flowing oxygen. 173

Figure 6.4: Observed, calculated and difference plots from the structural refinement of $Ba_3CoIr_2O_{6.2}H_{2.8}$ against SXRD data collected at room temperature using a wavelength of 0.825 Å. 175
Figure 6.5: Observed, calculated and difference plots from the structural refinement of $Ba_3CoIr_2O_{6.2}H_{2.8}$ against NPD data collected at 200 K from the D20 diffractometer using a wavelength of 1.54 Å. 175
Figure 6.6: Refined structures of (a) the $Ba_3CoIr_2O_9$ parent oxide and (b) the $Ba_3CoIr_2O_{6.2}H_{2.8}$ reduced phase in the *C*2/*c* space group. 176
Figure 6.7: Magnetisation data collected from $Ba_3CoIr_2O_{6.2}H_{2.8}$ as a function of temperature, measured in a field of 100 Oe under both ZFC and FC conditions. 177
Figure 6.8: Magnetisation-field isotherms for $Ba_3CoIr_2O_{6.2}H_{2.8}$ measured at 5 K and 300 K. 178
Figure 6.9: NPD data collected from $Ba_3CoIr_2O_{6.2}H_{2.8}$ using the D20 diffractometer with a wavelength of 2.41 Å at 5 K and 100 K, and the difference between the patterns at these two temperatures. 178
Figure 6.10: Top: Schematic illustrating ferromagnetic interactions between the Co^{II} ions in the Co layers, mediated by Ir^{IV} ions in the Ir_2O_9 dimers, with long-range magnetic ordering disrupted by the presence of diamagnetic Ir^{III}. Bottom: Proposed electronic configurations for the cobalt and iridium ions in $Ba_3CoIr_2O_{6.2}H_{2.8}$. 183
Figure 7.1: Observed, calculated and difference plots from the structural refinement of Sr_2CoIrO_6 against SXRD data collected at room temperature using a wavelength of 0.825 Å. 187
Figure 7.2: Observed, calculated and difference plots from the structural refinement of $LaSrCoIrO_6$ against SXRD data collected at room temperature using a wavelength of 0.825 Å. 188
Figure 7.3: Observed, calculated and difference plots from the Pawley refinement against SXRD data from $Sr_2CoIrO_{4.4}H_{1.6}$ using the *Fm*$\bar{3}$*m* space group using a wavelength of 0.825 Å. 189
Figure 7.4: TGA trace when $Sr_2CoIrO_{4.4}H_{1.6}$ is heated under a flow of 5%/95% H_2/N_2 190
Figure 7.5: Sample mass change and H_2/H_2O content of the exhaust gas when $Sr_2CoIrO_{4.4}H_{1.6}$ is heated under flowing oxygen. 191
Figure 7.6: NPD data collected from $Sr_2CoIrO_{4.4}H_{1.6}$ using the 94° and 139° detector banks of the POLARIS diffractometer. 192
Figure 7.7: Observed, calculated and difference plots from the structural refinement of $Sr_2CoIrO_{4.4}H_{1.6}$ against NPD data collected at room temperature from the 27° bank of the POLARIS diffractometer. 193
Figure 7.8: Observed, calculated and difference plots from the structural refinement of $Sr_2CoIrO_{4.4}H_{1.6}$ against NPD data collected at room temperature from the 54° bank of the POLARIS diffractometer. 194
Figure 7.9: Local Co−O coordination in $Sr_2CoIrO_{4.4}H_{1.6}$ using (a) isotropic thermal factors, (b) anisotropic thermal factors and (c) split anion sites. Possible octahedral tilting distortions are shown in (d). 195
Figure 7.10: Observed, calculated and difference plots from the Pawley refinement against SXRD data from $LaSrCoIrO_{4.4}H_{1.6}$ using the *Fm*$\bar{3}$*m* space group. 196
Figure 7.11: TGA trace when $LaSrCoIrO_{4.4}H_{1.6}$ is heated under a flow of 5%/95% H_2/N_2. 197
Figure 7.12: Sample mass change and H_2/H_2O content of the exhaust gas when $LaSrCoIrO_{4.4}H_{1.6}$ is heated under flowing oxygen. 198
Figure 7.13: Observed, calculated and difference plots from the structural refinement of $LaSrCoIrO_{4.4}H_{1.6}$ against NPD data collected at room temperature from the 27° bank of the POLARIS diffractometer. 199

Figure 7.14: Observed, calculated and difference plots from the structural refinement of $LaSrCoIrO_{4.4}H_{1.6}$ against NPD data collected at room temperature from the 54° bank of the POLARIS diffractometer. 200
Figure 7.15: Magnetisation data collected from $Sr_2CoIrO_{4.4}H_{1.6}$ as a function of temperature, measured in a field of 100 Oe under both ZFC and FC conditions. 202
Figure 7.16: Magnetisation-field isotherms for $Sr_2CoIrO_{4.4}H_{1.6}$ measured at 5 K and 300 K. 202
Figure 7.17: Magnetisation-field isotherms collected from $Sr_2CoIrO_{4.4}H_{1.6}$ at temperatures between 5 and 20 K, highlighting the change in coercivity as a function of temperature for the sample. 203
Figure 7.18: AC susceptibility data, χ' (top) and χ'' (bottom), collected as a function of temperature from $Sr_2CoIrO_{4.4}H_{1.6}$ at frequencies between 5 Hz and 500 Hz. The measurements were performed using an AC field with amplitude of 2.5 Oe, and an applied DC field of 2 Oe. 204
Figure 7.19: Magnetisation data collected from $LaSrCoIrO_{4.4}H_{1.6}$ as a function of temperature, measured in a field of 100 Oe under both ZFC and FC conditions. 205
Figure 7.20: Magnetisation-field isotherms for $LaSrCoIrO_{4.4}H_{1.6}$ measured at 5 K and 300 K. 206
Figure 7.21: Magnetisation-field isotherms collected from $LaSrCoIrO_{4.4}H_{1.6}$ at temperatures between 5 and 20 K, highlighting the change in coercivity as a function of temperature for the sample. 206
Figure 7.22: AC susceptibility data, χ' (top) and χ'' (bottom), collected as a function of temperature from $LaSrCoIrO_{4.4}H_{1.6}$ at frequencies between 5 Hz and 500 Hz. The measurements were performed using an AC field with amplitude of 2.5 Oe, and an applied DC field of 2 Oe. The inset shows an expanded region of χ' as a function of temperature to highlight the shift in susceptibility maximum as a function of frequency. 207
Figure 7.23: Proposed electronic configurations of cobalt and iridium in $Sr_2CoIrO_{4.4}H_{1.6}$ and $LaSrCoIrO_{4.4}H_{1.6}$. 208
Figure 8.1: Structural model of Sr_2CoIrO_5 based on the double perovskite structure with *I*4/*mmm* symmetry. The occupancy of the oxide ions at the O1 site was fixed to 0.75.....214
Figure 8.2: Observed, calculated and difference plots from the structural refinement of Sr_2CoIrO_5 against SXRD data (λ = 0.825 Å) collected at room temperature, with Sr_2CoIrO_4 included as a secondary phase. 214
Figure 8.3: Observed, calculated and difference plots from the structural refinement of Sr_2CoIrO_5 against NPD data collected at room temperature from the 54° bank of the POLARIS diffractometer. 216
Figure 8.4: Observed, calculated and difference plots from the structural refinement of Sr_2CoIrO_5 against NPD data collected at room temperature from the 94° bank of the POLARIS diffractometer. 217
Figure 8.5: Observed, calculated and difference plots from the structural refinement of Sr_2CoIrO_5 against NPD data collected at room temperature from the 139° bank of the POLARIS diffractometer. 217
Figure 8.6: TGA trace when Sr_2CoIrO_5 is heated under flowing oxygen. 219
Figure 8.7: XANES Co K-edge for Sr_2CoIrO_5, with Sr_2CoIrO_6 (Co^{3+}) and $YBaCo_2O_5$ ($Co^{2.5+}$) included as standards. 220
Figure 8.8: Magnetisation data collected from Sr_2CoIrO_5 as a function of temperature, measured in a field of 100 Oe under both ZFC and FC conditions. 222
Figure 8.9: Magnetisation-field isotherms for Sr_2CoIrO_5 measured at 5 K and 300 K. 222
Figure 8.10: AC susceptibility as a function of temperature for Sr_2CoIrO_5, measured at frequencies between 1 Hz and 500 Hz. The measurements were performed using an AC field

with amplitude of 2.5 Oe, and an applied DC field of 2 Oe. The inset shows the variation of T_f with ω for Sr_2CoIrO_5. The red line shows the fit to the data using the power law shown in Equation 43. 223
Figure 8.11: μ^+-SR data collected from Sr_2CoIrO_5 as a function of temperature. 224
Figure 8.12: Crystal structures of some perovskite-based $A_2B_2O_5$ compounds with different anion vacancy ordered arrangements. 226
Figure 8.13: Removal of an oxide ion from a $(Co/Ir)O_6$ octahedron, (a), to give $(Co/Ir)O_5$ in a square-based pyramidal coordination, (b), which imposes a specific coordination on the neighbouring $(Co/Ir)O_5$ species, resulting in the $(Co/Ir)_2O_{10}$ unit in (c). As such, the anion vacancy positions in Sr_2CoIrO_5 are likely to be constrained by the packing arrangements of $(Co/Ir)_2O_{10}$ units. 227
Figure 8.14: Proposed electronic configurations for the transition metals in Sr_2CoIrO_5 (a) and illustration of a possible source of magnetic frustration in Sr_2CoIrO_5 (b). 228
Figure 9.1: Observed, calculated and difference plots from the structural refinement of Sr_2CoIrO_4 against SXRD data collected at room temperature using a wavelength of 0.825 Å. 231
Figure 9.2: Comparison of the undistorted *I*4/*mmm* infinite-layer structure with the distorted *I*4/*m*, *I*112/*m* and $P12_11$ structures. The magnitudes of the distortions have been exaggerated for clarity. 233
Figure 9.3: Observed, calculated and difference plots from the structural refinement of Sr_2CoIrO_4 against NPD data collected at room temperature from the 54° bank of the POLARIS diffractometer using the undistorted *I*4/*mmm* structural model. The peaks denoted by asterisks are attributed to the cubic perovskite-type impurity identified in Section 9.3.1. 234
Figure 9.4: Observed, calculated and difference plots from the structural refinement of Sr_2CoIrO_4 against NPD data collected at room temperature from the 94° bank of the POLARIS diffractometer using the undistorted *I*4/*mmm* structural model. The peaks denoted by asterisks are attributed to the cubic perovskite-type impurity identified in Section 9.3.1. 234
Figure 9.5: Observed, calculated and difference plots from the structural refinement of Sr_2CoIrO_4 against NPD data collected at room temperature from the 54° bank of the POLARIS diffractometer using the undistorted *I*4/*mmm* structural model. The peaks denoted by asterisks are attributed to the cubic perovskite-type impurity identified in Section 9.3.1. 235
Figure 9.6: Refined structure of Sr_2CoIrO_4 with *I*4/*mmm* symmetry. 236
Figure 9.7: TGA trace when Sr_2CoIrO_4 is heated under flowing oxygen. 237
Figure 9.8: XANES Co K-edge for Sr_2CoIrO_4, with Sr_2CoIrO_6 (Co^{3+}) and $YBaCo_2O_5$ ($Co^{2.5+}$) included as standards. 238
Figure 9.9: Magnetisation data collected from Sr_2CoIrO_4 as a function of temperature, measured in a field of 100 Oe under both ZFC and FC conditions. 239
Figure 9.10: Magnetisation-field isotherms for Sr_2CoIrO_4 measured at 5 K and 300 K. 240
Figure 9.11: μ^+-SR data collected from Sr_2CoIrO_4 as a function of temperature. 241
Figure 9.12: Comparison of background-subtracted NPD data collected from Sr_2CoIrO_4 at 2 K and 298 K using the 27° bank of the POLARIS diffractometer. Additional peaks present at 2 K are highlighted by arrows. 242
Figure 9.13: Magnetic structures that arise from distortions described by the mX^{2+}, mX^{3+} and mX^{4+} irreducible representations of the *I*4/*mmm* space group. 243
Figure 9.14: Observed, calculated and difference plots from the magnetic refinement of Sr_2CoIrO_4 against NPD data collected at 2 K from the 27° bank of the POLARIS diffractometer. 243
Figure 9.15: Refined magnetic model for Sr_2CoIrO_4 at 2 K (a), and representation of Sr_2CoIrO_4 with a 'type I' antiferromagnetic structure (b), with the arrows representing the moments at the cobalt and iridium sites. The strontium ions have been omitted for clarity. 245

Figure 9.16: Comparison of 200 reflections in SXRD data collected from Sr_2CoIrO_4 at 300 K and 100 K. 246
Figure 9.17: Change in *a*-lattice parameter, *c*-lattice parameter and volume as a function of temperature obtained from refinements against SXRD data collected from Sr_2CoIrO_4 between 100 and 290 K. 247
Figure 9.18: Simple crystal field splitting diagram for Sr_2FeIrO_4 as determined by Page *et al.*[101] (left) and proposed crystal field splitting diagram for Sr_2CoIrO_4 (right). 248
Figure 9.19: Possible intralayer (J_1, J_2, J_3, J_4) and interlayer (J_5, J_6, J_7, J_8) coupling interactions in Sr_2CoIrO_4. The ● represents a moment coming out of the page, whilst the + represents a moment going into the page. 249
Figure 9.20: X-ray diffraction pattern (λ = 1.5406 Å) collected from Sr_2CoIrO_6 deposited onto (001)-oriented STO without annealing (top), after annealing in air at 500°C (middle) and after annealing in air at 700°C (bottom). The asterisk highlights the apparent presence of an amorphous Sr_2CoIrO_6 film after deposition. The miller indices labelling the Sr_2CoIrO_6 peaks correspond to the equivalent simple perovskite containing a single B-site cation. 252
Figure 9.21: RSM plot for the Sr_2CoIrO_6 film centred around the 103 peak, collected using an X-ray wavelength of 1.5406 Å. 253
Figure 9.22: X-ray diffraction pattern (λ = 1.5406 Å) from as-deposited Sr_2CoIrO_6 film (top) and after reaction with a Zr getter (bottom). The shift in 00*l* peaks to higher angle is consistent with the formation of Sr_2CoIrO_4. The peaks denoted by asterisks correspond to the STO 001 and 002 reflections. 254
Figure 9.23: RSM plot for the Sr_2CoIrO_4 film centred around the 103 peak, collected using an X-ray wavelength of 1.5406 Å. 255
Figure 9.24: Resistivity of Sr_2CoIrO_6 and Sr_2CoIrO_4 thin films measured as a function of temperature. The resistivity of Sr_2CoIrO_4 was measured in fields of 0 T and 7 T. 256
Figure 9.25: Magnetisation data collected from Sr_2CoIrO_4 as a function of temperature in a field of 100 Oe orientated parallel to the *ab*-plane (left) and parallel to the *c*-axis (right). 256
Figure 10.1: Observed, calculated and difference plots from the structural refinement of $LaSrCoIrO_4$ against SXRD data (λ = 0.825 Å) collected at room temperature, with $LaSrCoIrO_5$ included as a secondary phase. 260
Figure 10.2: Observed, calculated and difference plots from the structural refinement of $LaSrCoIrO_4$ against NPD data collected using the D20 diffractometer at 200 K with a wavelength of 1.54 Å, with $LaSrCoIrO_5$ included as a secondary phase. 262
Figure 10.3: Refined crystal structure of $LaSrCoIrO_4$. 263
Figure 10.4: TGA trace when $LaSrCoIrO_4$ is heated under flowing oxygen. 264
Figure 10.5: Magnetisation data collected from $LaSrCoIrO_4$ as a function of temperature, measured in a field of 100 Oe under both ZFC and FC conditions. 265
Figure 10.6: Magnetisation-field isotherms for $LaSrCoIrO_4$ measured at 5 K and 300 K. 266
Figure 10.7: Comparison between NPD data collected from $LaSrCoIrO_4$ at 10 K and 100 K using the D20 diffractometer with a wavelength of 2.41 Å, and the difference between the patterns at these two temperatures. The arrows highlight possible magnetic peaks. 267
Figure 10.8: (a) Fit to the NPD data collected from $LaSrCoIrO_4$ at 10 K when a magnetic distortion that transforms as the mM^{1+} irreducible representation is applied, corresponding to C-type antiferromagnetic order with the moments aligned along the *z*-axis. In this refinement, the value of the Co moment was constrained to be double that of the Ir moment. (b) Fit to the NPD data when a magnetic distortion that transforms as the $mM^{3+}M^{4+}$ irreducible representation is applied, corresponding to C-type antiferromagnetic order with the moments aligned in the *xy*-plane. 269
Figure 10.9: Proposed electronic structure of $LaSrCoIrO_4$, assuming the same transition metal oxidation states as those observed in $LaSr_3CoIrO_6$.[46] 271

Figure 11.1: Observed, calculated and difference plots from the structural refinement of pristine La_2CoRhO_6 against SXRD data (λ = 0.825 Å), with the isotropic crystallite size broadening and the isotropic microstrain broadening modelled using intermediate Gaussian-Lorentzian line shapes.....274
Figure 11.2: Plot of peak *fwhm* as a function of 2θ in SXRD data collected from pristine and ball-milled La_2CoRhO_6.....275
Figure 11.3: Observed, calculated and difference plots from the structural refinement of ball-milled La_2CoRhO_6 against SXRD data (λ = 0.825 Å), with the isotropic crystallite size broadening and the isotropic microstrain broadening modelled using intermediate Gaussian-Lorentzian line shapes.....276
Figure 11.4: Magnetisation data collected from pristine La_2CoRhO_6 as a function of temperature, measured in a field of 100 Oe under both ZFC and FC conditions.....278
Figure 11.5: Magnetisation-field isotherms for pristine La_2CoRhO_6 measured at 5 K and 300 K.....278
Figure 11.6: Magnetisation data collected from ball-milled La_2CoRhO_6 as a function of temperature, measured in a field of 100 Oe under both ZFC and FC conditions.....279
Figure 11.7: Magnetisation-field isotherms for ball-milled La_2CoRhO_6 measured at 5 K and 300 K.....280
Figure 11.8: Evolution of PXRD patterns (λ = 1.5406 Å) for the reaction between pristine La_2CoRhO_6 and NaH at several intervals when the reaction mixture is heated at temperatures of 170−190 °C.....281
Figure 11.9: Evolution of PXRD patterns (λ = 1.5406 Å) for the reaction between ball-milled La_2CoRhO_6 and NaH at several intervals when the reaction mixture is heated at temperatures of 170−190 °C.....281
Figure 11.10: TGA trace (top panel) and H_2/H_2O contents of exhaust gas (bottom panel) when the product from the reaction between pristine La_2CoRhO_6 and LiH is heated under flowing oxygen.....283
Figure 11.11: TGA trace (top panel) and H_2/H_2O contents of exhaust gas (bottom panel) when the product from the reaction between ball-milled La_2CoRhO_6 and LiH is heated under flowing oxygen.....284
Figure 11.12: Schematics of the reaction energy profiles for the reactions of pristine and ball-milled La_2CoRhO_6 with NaH (left) and LiH (right). For the NaH reaction, the activation energies for the topochemical reaction and for non-topochemical decomposition are decreased by roughly the same extent for both the ball-milled sample and the pristine sample, whereas for the LiH reaction, the activation energy for the topochemical reaction is decreased by a greater extent than that for non-topochemical decomposition.....286
Figure 11.13: Observed, calculated and difference plots from the structural refinement of $La_2CoRhO_4H_2$ against NPD data collected at room temperature from the 54° bank of the POLARIS diffractometer.....288
Figure 11.14: Observed, calculated and difference plots from the structural refinement of $La_2CoRhO_4H_2$ against NPD data collected at room temperature from the 94° bank of the POLARIS diffractometer.....288
Figure 11.15: Observed, calculated and difference plots from the structural refinement of $La_2CoRhO_4H_2$ against NPD data collected at room temperature from the 139° bank of the POLARIS diffractometer.....289
Figure 11.16: Refined structure of $La_2CoRhO_4H_2$.....290
Figure 11.17: Magnetisation data collected from $La_2CoRhO_4H_2$ as a function of temperature, measured in a field of 100 Oe under both ZFC and FC conditions.....292
Figure 11.18: Magnetisation-field isotherms for $La_2CoRhO_4H_2$ measured at 5 K and 350 K.....293

Figure 11.19: Saturated ferromagnetic moment (top panel) and paramagnetic susceptibility (bottom panel) obtained from $La_2CoRhO_4H_2$ using the 'ferrosubtraction' technique described in Section 2.8.1. 294
Figure 11.20: AC susceptibility data, χ' (top) and χ'' (bottom), collected as a function of temperature from $La_2CoRhO_4H_2$ at frequencies between 5 Hz and 500 Hz. The measurements were performed using an AC field with amplitude of 2.5 Oe, and an applied DC field of 2 Oe. 295
Figure 11.21: (a) the coupling regime for an ordered arrangement of Co^{I} and Rh^{III} ions and (b) a possible source of magnetic frustration arising from B-site cation disorder. 295
Figure 12.1: Magnetic structures and 3d transition metal electronic configurations in Sr_2FeIrO_4,[101] Sr_2CoIrO_4 and $LaSrCoIrO_4$. 302
Figure A 1: Observed, calculated and difference plots from the structural refinement of Sr_4CoIrO_8 against SXRD data collected at room temperature.....304
Figure A 2: Observed, calculated and difference plots from the structural refinement of $La_{0.5}Sr_{3.5}CoIrO_8$ against SXRD data collected at room temperature. 305
Figure A 3: Observed, calculated and difference plots from the structural refinement of $LaSr_3CoIrO_8$ against SXRD data collected at room temperature. 306
Figure A 4: Observed, calculated and difference plots from the structural refinement of $La_{1.5}Sr_{2.5}CoIrO_8$ against SXRD data collected at room temperature. 307
Figure A 5: Observed, calculated and difference plots from the structural refinement of $La_2Sr_2CoIrO_8$ against SXRD data collected at room temperature. 308
Figure A 6: Observed, calculated and difference plots from the structural refinement of $Sr_4CoIrO_{6.5}H_{1.5}$ against SXRD data collected at room temperature. 309
Figure A 7: Observed, calculated and difference plots from the structural refinement of $La_{0.5}Sr_{3.5}CoIrO_{5.5}H_{2.5}$ against SXRD data collected at room temperature. The 2θ region from 10° to 12.8° is excluded due to the presence of a broad background feature arising from silica used to dilute the sample to reduce X-ray absorption during the SXRD measurement. 310
Figure A 8: Observed, calculated and difference plots from the structural refinement of $LaSr_3CoIrO_5H_3$ against SXRD data collected at room temperature. 311
Figure A 9: Observed, calculated and difference plots from the two-phase structural refinement of $La_{1.5}Sr_{2.5}CoIrO_{8-y}H_y$ against SXRD data collected at room temperature. 312
Figure A 10: Observed, calculated and difference plots from the structural refinement of $La_2Sr_2CoIrO_{8-y}H_y$ against SXRD data collected at room temperature. 313
Figure A 11: Relationship between oxygen content and *a*-lattice parameter in $A_4B'B''O_{8-y}H_z$ oxyhydride phases with the $n = 1$ Ruddlesden-Popper structure. Only compounds in which the hydride ions are exclusively located in the equatorial positions are considered (apart from $Sr_4MnIrO_{5.32}H_{2.68}$, shown in green). Red markers represent reported compounds, blue markers represent compounds presented in this thesis and the blue line represents the line of best fit. Data from Refs [45–47,50–52,90,177]. 315
Figure A 12: Magnetisation-field isotherms for Sr_4CoIrO_8 measured at 5 K and 300 K. 315
Figure A 13: Observed, calculated and difference plots from the structural refinement of $LaSr_3NiIrO_{5.4}H_{2.6}$ against SXRD data collected at room temperature. 316
Figure A 14: Expanded view of XAS data collected from Sr_4MnIrO_8, $Sr_4MnIrO_{6.58}H_{1.42}$ and $Sr_4MnIrO_{5.32}H_{2.68}$, showing normalisation of the spectra. 317
Figure A 15: PXRD data collected from the products of the reaction between $LaSr_3CoIrO_8$ and CaH_2 after washing with a 0.1 M solution of NH_4Cl in MeOH. Decomposition of the sample into finely divided Ir metal was observed, signalled by the appearance of a broad feature at $2\theta \sim 40{-}50°$. 317
Figure A 16: Observed, calculated and difference plots from the structural refinement of $Sr_4MnIrO_{6.58}H_{1.42}$ against SXRD data collected at room temperature. A secondary phase of Ir

metal is included in the refinement to account for the broad feature at 2θ ~ 22°, likely due to a small amount of decomposition during the reaction. A small impurity peak at 2θ ~ 20° is also observed, which is attributed to CaO remaining after the washing process, so this is included as a third phase in the refinement. 318
Figure A 17: Observed, calculated and difference plots from the structural refinement of $Sr_4MnIrO_{5.32}H_{2.68}$ against SXRD data collected at room temperature. 319
Figure A 18: PXRD data collected after the reductive TGA of $Sr_2CoIrO_{4.4}H_{1.6}$. 320
Figure A 19: PXRD data collected after the reductive TGA of $LaSrCoIrO_{4.4}H_{1.6}$. 320
Figure A 20: Observed, calculated and difference plots from the structural refinement of $LaSrCoIrO_5$ against SXRD data collected at room temperature, with $LaSrCoIrO_6$, SrO and Ir metal included as secondary phases. 322
Figure A 21: Magnetisation data collected from $LaSrCoIrO_5$ as a function of temperature, measured in a field of 100 Oe under both ZFC and FC conditions. 324
Figure A 22: Magnetisation-field isotherms for $LaSrCoIrO_5$ measured at 5 K and 300 K. .325
Figure A 23: NPD data collected from $LaSrCoIrO_5$ using the D20 diffractometer with a wavelength of 2.41 Å at 10 K and 100 K, and the difference between these patterns. 325
Figure A 24: Magnetic model based on a (3 × 3 × 1)-expansion of the nuclear unit cell that can account for the magnetic Bragg peaks observed in the NPD data collected from $LaSrCoIrO_4$ at 10 K. A refined magnetic moment of 1.8(3) μ_B is obtained at the Co sites and 1.0(1) μ_B at the Ir sites. 326
Figure A 25: Observed, calculated and difference plots from the magnetic refinement of $LaSrCoIrO_4$ against NPD data using the model shown in Figure A 24. The data were collected using the D20 diffractometer at 10 K with a wavelength of 2.41 Å. 327

Bibliography

1 P. Schiffer, A. P. Ramirez, W. Bao and S.-W. Cheong, *Phys. Rev. Lett.*, 1995, **75**, 3336–3339.
2 J. B. Goodenough, *Nature*, 2000, **404**, 821–823.
3 J. B. Goodenough and M. Longo, in *Landolt-Börnstein Tabellen New Series III 4A*, eds. K.-H. Hellwege and A. M. Hellwege, Springer-Verlag, Berlin, 1970, pp. 126–129.
4 J. G. Bednorz and K. A. Müller, *Zeitschrift für Phys. B Condens. Matter*, 1986, **64**, 189–193.
5 V. M. Goldschmidt, *Naturwissenschaften*, 1926, **14**, 477–485.
6 A. M. Glazer, *Acta Crystallogr. Sect. B*, 1972, **28**, 3384–3392.
7 C. J. Howard and H. T. Stokes, *Acta Crystallogr. Sect. B*, 1998, **54**, 782–789.
8 Y. A. Abramov, V. G. Tsirelson, V. E. Zavodnik, S. A. Ivanov and B. I. D., *Acta Crystallogr. Sect. B*, 1995, **51**, 942–951.
9 G. Demazeau, A. Marbeuf, M. Pouchard and P. Hagenmuller, *J. Solid State Chem.*, 1971, **3**, 582–589.
10 M. Marezio and P. D. Dernier, *Mater. Res. Bull.*, 1971, **6**, 23–29.
11 M. T. Anderson, K. B. Greenwood, G. A. Taylor and K. R. Poeppelmeier, *Prog. Solid State Chem.*, 1993, **22**, 197–233.
12 G. King and P. M. Woodward, *J. Mater. Chem.*, 2010, **20**, 5785–5796.
13 C. J. Howard, B. J. Kennedy and P. M. Woodward, *Acta Crystallogr. Sect. B*, 2003, **59**, 463–471.
14 A. K. Azad, A. Mellergård, S.-G. Eriksson, S. A. Ivanov, S. M. Yunus, F. Lindberg, G. Svensson and R. Mathieu, *Mater. Res. Bull.*, 2005, **40**, 1633–1644.
15 D. Iwanaga, Y. Inaguma and M. Itoh, *Mater. Res. Bull.*, 2000, **35**, 449–457.
16 P. G. Radaelli, D. E. Cox, M. Marezio and S.-W. Cheong, *Phys. Rev. B*, 1997, **55**, 3015–3023.
17 M. T. Anderson and K. R. Poeppelmeier, *Chem. Mater.*, 1991, **3**, 476–482.
18 L. T. Nguyen and R. J. Cava, *Chem. Rev.*, 2021, **121**, 2935–2965.
19 H. Taguchi, Y. Takeda, F. Kanamaru, M. Shimada and M. Koizumi, *Acta Crystallogr. Sect. B*, 1977, **33**, 1298–1299.
20 P. C. Donohue, L. Katz and R. Ward, *Inorg. Chem.*, 1965, **4**, 306–310.
21 S.-T. Hong and A. W. Sleight, *J. Solid State Chem.*, 1997, **128**, 251–255.
22 J. G. Zhao, L. X. Yang, Y. Yu, F. Y. Li, R. C. Yu, Z. Fang, L. C. Chen and C. Q. Jin, *J. Solid State Chem.*, 2007, **180**, 2816–2823.
23 C.-Q. Jin, J.-S. Zhou, J. B. Goodenough, Q. Q. Liu, J. G. Zhao, L. X. Yang, Y. Yu, R. C. Yu, T. Katsura, A. Shatskiy and E. Ito, *Proc. Natl. Acad. Sci.*, 2008, **105**, 7115–7119.
24 B. V Beznosikov and K. S. Aleksandrov, *Crystallogr. Reports*, 2000, **45**, 792–798.
25 S. N. Ruddlesden and P. Popper, *Acta Crystallogr.*, 1957, **10**, 538–540.
26 S. N. Ruddlesden and P. Popper, *Acta Crystallogr.*, 1958, **11**, 54–55.
27 M. L. Robinson, E. Whitaker, L. Jin, M. A. Hayward and G. Laurita, *Inorg. Chem.*, 2020, **59**, 3026–3033.
28 S. Mugiraneza and A. M. Hallas, *Commun. Phys.*, 2022, **5**, 95.
29 J. Kanamori, *J. Phys. Chem. Solids*, 1959, **10**, 87–98.
30 J. B. Goodenough and A. L. Loeb, *Phys. Rev.*, 1955, **98**, 391–408.
31 R. I. Dass, J.-Q. Yan and J. B. Goodenough, *Phys. Rev. B*, 2004, **69**, 94416.
32 J.-W. G. Bos and J. P. Attfield, *J. Mater. Chem.*, 2005, **15**, 715–720.
33 A. K. Paul, M. Reehuis, V. Ksenofontov, B. Yan, A. Hoser, D. M. Többens, P. M. Abdala, P. Adler, M. Jansen and C. Felser, *Phys. Rev. Lett.*, 2013, **111**, 167205.

34 R. Morrow, J. W. Freeland and P. M. Woodward, *Inorg. Chem.*, 2014, **53**, 7983–7992.
35 N. A. Spaldin, *Magnetic Materials: Fundamentals and Applications*, Cambridge University Press, Cambridge, 2nd edn., 2010.
36 J. Hugel and M. Kamal, *Solid State Commun.*, 1996, **100**, 457–461.
37 T. M. Schuler, D. L. Ederer, S. Itza-Ortiz, G. T. Woods, T. A. Callcott and J. C. Woicik, *Phys. Rev. B*, 2005, **71**, 115113.
38 J. Hubbard and B. H. Flowers, *Proc. R. Soc. London. Ser. A. Math. Phys. Sci.*, 1997, **276**, 238–257.
39 A. J. Browne, A. Krajewska and A. S. Gibbs, *J. Mater. Chem. C*, 2021, **9**, 11640–11654.
40 M. Bremholm, S. E. Dutton, P. W. Stephens and R. J. Cava, *J. Solid State Chem.*, 2011, **184**, 601–607.
41 L. Du, X. Sheng, H. Weng and X. Dai, *Europhys. Lett.*, 2013, **101**, 27003.
42 B. J. Kim, H. Jin, S. J. Moon, J.-Y. Kim, B.-G. Park, C. S. Leem, J. Yu, T. W. Noh, C. Kim, S.-J. Oh, J.-H. Park, V. Durairaj, G. Cao and E. Rotenberg, *Phys. Rev. Lett.*, 2008, **101**, 76402.
43 F. Wang and T. Senthil, *Phys. Rev. Lett.*, 2011, **106**, 136402.
44 M. A. Hayward, M. A. Green, M. J. Rosseinsky and J. Sloan, *J. Am. Chem. Soc.*, 1999, **121**, 8843–8854.
45 Y. Tsujimoto, C. Tassel, N. Hayashi, T. Watanabe, H. Kageyama, K. Yoshimura, M. Takano, M. Ceretti, C. Ritter and W. Paulus, *Nature*, 2007, **450**, 1062–1065.
46 J. E. Page and M. A. Hayward, *Inorg. Chem.*, 2019, **58**, 6336–6343.
47 M. A. Hayward, E. J. Cussen, J. B. Claridge, M. Bieringer, M. J. Rosseinsky, C. J. Kiely, S. J. Blundell, I. M. Marshall and F. L. Pratt, *Science (80-.).*, 2002, **295**, 1882–1884.
48 F. Denis Romero, A. Leach, J. S. Möller, F. Foronda, S. J. Blundell and M. A. Hayward, *Angew. Chemie Int. Ed.*, 2014, **53**, 7556–7559.
49 M. Amano Patino, D. Zeng, S. J. Blundell, J. E. McGrady and M. A. Hayward, *Inorg. Chem.*, 2018, **57**, 2890–2898.
50 C. Tassel, Y. Goto, Y. Kuno, J. Hester, M. Green, Y. Kobayashi and H. Kageyama, *Angew. Chemie Int. Ed.*, 2014, **53**, 10377–10380.
51 L. Jin, M. Lane, D. Zeng, F. K. K. Kirschner, F. Lang, P. Manuel, S. J. Blundell, J. E. McGrady and M. A. Hayward, *Angew. Chemie Int. Ed.*, 2018, **57**, 5025–5028.
52 L. Jin and M. A. Hayward, *Chem. Commun.*, 2019, **55**, 4861–4864.
53 C. Tassel, Y. Goto, D. Watabe, Y. Tang, H. Lu, Y. Kuno, F. Takeiri, T. Yamamoto, C. M. Brown, J. Hester, Y. Kobayashi and H. Kageyama, *Angew. Chemie Int. Ed.*, 2016, **55**, 9667–9670.
54 J. Bang, S. Matsuishi, H. Hiraka, F. Fujisaki, T. Otomo, S. Maki, J. Yamaura, R. Kumai, Y. Murakami and H. Hosono, *J. Am. Chem. Soc.*, 2014, **136**, 7221–7224.
55 Y. Goto, C. Tassel, Y. Noda, O. Hernandez, C. J. Pickard, M. A. Green, H. Sakaebe, N. Taguchi, Y. Uchimoto, Y. Kobayashi and H. Kageyama, *Inorg. Chem.*, 2017, **56**, 4840–4845.
56 H. Nawaz, F. Takeiri, A. Kuwabara, M. Yonemura and G. Kobayashi, *Chem. Commun.*, 2020, **56**, 10373–10376.
57 T. Uchimura, F. Takeiri, K. Okamoto, T. Saito, T. Kamiyama and G. Kobayashi, *J. Mater. Chem. A*, 2021, **9**, 20371–20374.
58 Y. Sasahara, R. Terada, H. Ubukata, M. Asahi, D. Kato, T. Tsumori, M. Namba, Z. Wei, C. Tassel and H. Kageyama, *J. Am. Chem. Soc.*, 2024, **146**, 11694–11701.
59 W. M. Haynes, D. R. Lide and T. J. Bruno, Eds., *CRC Handbook of Chemistry and Physics*, CRC Press, 95th edn., 2014.
60 F. Denis Romero, S. J. Burr, J. E. McGrady, D. Gianolio, G. Cibin and M. A. Hayward, *J. Am. Chem. Soc.*, 2013, **135**, 1838–1844.

61 F. Denis Romero, D. Gianolio, G. Cibin, P. A. Bingham, J.-C. d'Hollander, S. D. Forder and M. A. Hayward, *Inorg. Chem.*, 2013, **52**, 10920–10928.
62 Y. Kobayashi, O. Hernandez, C. Tassel and H. Kageyama, *Sci. Technol. Adv. Mater.*, 2017, **18**, 905–918.
63 J. Hadermann, A. M. Abakumov, J. J. Adkin and M. A. Hayward, *J. Am. Chem. Soc.*, 2009, **131**, 10598–10604.
64 M. O'Malley, M. A. Lockett and M. A. Hayward, *J. Solid State Chem.*, 2007, **180**, 2851–2858.
65 Z. Liang, M. Batuk, F. Orlandi, P. Manuel, J. Hadermann and M. A. Hayward, *Inorg. Chem.*, 2024, **63**, 12691–13136.
66 M. A. Hayward, in *Comprehensive Inorganic Chemistry I I (Second Edition)*, eds. J. Reedijk and K. B. T. Poeppelmeier, Elsevier, Amsterdam, 2013, pp. 417–453.
67 R. E. Dinnebier, A. Leineweber and J. S. O. Evans, *Rietveld Refinement*, De Gruyter, Berlin, 2019.
68 W. H. Bragg and W. L. Bragg, *Proc. R. Soc. London. Ser. A, Contain. Pap. a Math. Phys. Character*, 1913, **88**, 428–438.
69 C. C. Tang, S. P. Thompson, T. P. Hill, G. R. Wilkin and U. H. Wagner, in *Geneva, September 1-4, 2006*, ed. Deutsche Gesellschaft für Kristallographie, Oldenbourg Wissenschaftsverlag, pp. 153–158.
70 N. Tartoni, S. P. Thompson, C. C. Tang, B. L. Willis, G. E. Derbyshire, A. G. Wright, S. C. Jaye, J. M. Homer, J. D. Pizzey and A. M. T. Bell, *J. Synchrotron Radiat.*, 2008, **15**, 43–49.
71 S. P. Thompson, J. E. Parker, J. Potter, T. P. Hill, A. Birt, T. M. Cobb, F. Yuan and C. C. Tang, *Rev. Sci. Instrum.*, 2009, **80**, 75107.
72 V. F. Sears, *Neutron News*, 1992, **3**, 26–37.
73 R. I. Smith, S. Hull, M. G. Tucker, H. Y. Playford, D. J. McPhail, S. P. Waller and S. T. Norberg, *Rev. Sci. Instrum.*, 2019, **90**, 115101.
74 P. Day, J. Enderby, W. Williams, L. Chapon, A. Hannon, P. Radaelli and A. Soper, *Neutron News*, 2004, **15**, 19–23.
75 T. C. Hansen, P. F. Henry, H. E. Fischer, J. Torregrossa and P. Convert, *Meas. Sci. Technol.*, 2008, **19**, 34001.
76 A. W. Hewat, *Mater. Sci. Forum*, 1986, **9**, 69–80.
77 H. M. Rietveld, *J. Appl. Crystallogr.*, 1969, **2**, 65–71.
78 A. A. Coelho, J. S. O. Evans, I. R. Evans, A. Kern and S. Parsons, *Powder Diffr.*, 2011, **26**, S22–S25.
79 P. Thompson, D. E. Cox and J. B. Hastings, *J. Appl. Crystallogr.*, 1987, **20**, 79–83.
80 K. Kobayashi, T. Nagao and M. Ito, *Acta Crystallogr. Sect. A*, 2011, **67**, 473–480.
81 V. da Cruz Pinha Barbosa, S. Das, T. Saha-Dasgupta and P. M. Woodward, *Inorg. Chem.*, 2023, **62**, 21353–21363.
82 G. S. Pawley, *J. Appl. Crystallogr.*, 1981, **14**, 357–361.
83 W. Grünert and K. Klementiev, *Phys. Sci. Rev.*, 2020, **5**, 20170181.
84 B. Ravel and M. Newville, *Phys. Scr.*, 2005, **2005**, 1007.
85 A J Dent, G Cibin, S Ramos, A D Smith, S M Scott, L Varandas, M R Pearson, N A Krumpa, C P Jones and P E Robbins, *J. Phys. Conf. Ser.*, 2009, **190**, 12039.
86 J. Clarke, *Sci. Am.*, 1994, **271**, 46–53.
87 A. D. Hillier, S. J. Blundell, I. McKenzie, I. Umegaki, L. Shu, J. A. Wright, T. Prokscha, F. Bert, K. Shimomura, A. Berlie, H. Alberto and I. Watanabe, *Nat. Rev. Methods Prim.*, 2022, **2**, 4.
88 S. J. Blundell, R. De Renzi, T. Lancaster and F. L. Pratt, *Muon Spectroscopy: An Introduction*, Oxford University Press, 2021.

89 G. F. Harrington and J. Santiso, *J. Electroceramics*, 2021, **47**, 141–163.
90 M. Yasaka, *Rigaku J.*, 2010, **26**, 1–9.
91 L. Jin, M. Batuk, F. K. K. Kirschner, F. Lang, S. J. Blundell, J. Hadermann and M. A. Hayward, *Inorg. Chem.*, 2019, **58**, 14863–14870.
92 D. Mikhailova, Z. Hu, C.-Y. Kuo, S. Oswald, K. M. Mogare, S. Agrestini, J.-F. Lee, C.-W. Pao, S.-A. Chen, J.-M. Lee, S.-C. Haw, J.-M. Chen, Y.-F. Liao, H. Ishii, K.-D. Tsuei, A. Senyshyn and H. Ehrenberg, *Eur. J. Inorg. Chem.*, 2017, **2017**, 587–595.
93 R. M. Helps, N. H. Rees and M. A. Hayward, *Inorg. Chem.*, 2010, **49**, 11062–11068.
94 M. A. Hayward, *Semicond. Sci. Technol.*, 2014, **29**, 64010.
95 K. Gunnarsson, P. Svedlindh, P. Nordblad, L. Lundgren, H. Aruga and A. Ito, *Phys. Rev. Lett.*, 1988, **61**, 754–757.
96 J. Souletie and J. L. Tholence, *Phys. Rev. B*, 1985, **32**, 516–519.
97 P. C. Hohenberg and B. I. Halperin, *Rev. Mod. Phys.*, 1977, **49**, 435–479.
98 X. Martínez de Irujo-Labalde, J. E. Page, H. W. T. Morgan, J. E. McGrady and M. A. Hayward, *J. Solid State Chem.*, 2022, **315**, 123477.
99 P. Stephens, *J. Appl. Crystallogr.*, 1999, **32**, 281–289.
100 Z. Xu, R. G. Palgrave and M. A. Hayward, *Inorg. Chem.*, 2020, **59**, 13767–13773.
101 J. E. Page, H. W. T. Morgan, D. Zeng, P. Manuel, J. E. McGrady and M. A. Hayward, *Inorg. Chem.*, 2018, **57**, 13577–13585.
102 K. Fujii and W. Kondo, *Zeitschrift für Anorg. und Allg. Chemie*, 1968, **359**, 296–304.
103 E. P. Serjeant and B. Dempsey, *Ionisation constants of organic acids in aqueous solution*, International Union of Pure and Applied Chemistry, Oxford, 1979.
104 J. Przewoznik, V. Paul-Boncour, M. Latroche and A. Percheron-Guégan, *J. Alloys Compd.*, 1995, **225**, 436–439.
105 B. C. Hernden, J. A. Lussier and M. Bieringer, *Inorg. Chem.*, 2015, **54**, 4249–4256.
106 H. J. Kitchen, I. Saratovsky and M. A. Hayward, *Dalt. Trans.*, 2010, **39**, 6098–6105.
107 O. J. Hernandez, G. Geneste, T. Yajima, Y. Kobayashi, M. Okura, K. Aidzu, C. Tassel, S. Paofai, D. Swain, C. Ritter and H. Kageyama, *Inorg. Chem.*, 2018, **57**, 11058–11067.
108 F. Takeiri, A. Watanabe, A. Kuwabara, H. Nawaz, N. I. P. Ayu, M. Yonemura, R. Kanno and G. Kobayashi, *Inorg. Chem.*, 2019, **58**, 4431–4436.
109 K. Okamoto, F. Takeiri, Y. Imai, M. Yonemura, T. Saito, K. Ikeda, T. Otomo, T. Kamiyama and G. Kobayashi, *Adv. Sci.*, 2023, **10**, 2203541.
110 G. Kobayashi, Y. Hinuma, S. Matsuoka, A. Watanabe, M. Iqbal, M. Hirayama, M. Yonemura, T. Kamiyama, I. Tanaka and R. Kanno, *Science (80-.).*, 2016, **351**, 1314–1317.
111 F. Takeiri, A. Watanabe, K. Okamoto, D. Bresser, S. Lyonnard, B. Frick, A. Ali, Y. Imai, M. Nishikawa, M. Yonemura, T. Saito, K. Ikeda, T. Otomo, T. Kamiyama, R. Kanno and G. Kobayashi, *Nat. Mater.*, 2022, **21**, 325–330.
112 J. E. Page, C. V Topping, A. Scrimshire, P. A. Bingham, S. J. Blundell and M. A. Hayward, *Inorg. Chem.*, 2018, **57**, 10303–10311.
113 X. Feng, Y. Deng and H. W. J. Blöte, *Phys. Rev. E*, 2008, **78**, 31136.
114 U. Treiber, S. Kemmler-Sack and A. Ehmann, *Zeitschrift für Anorg. und Allg. Chemie*, 1982, **487**, 189–198.
115 C. Garg, D. Roy, M. Lonsky, P. Manuel, A. Cervellino, J. Müller, M. Kabir and S. Nair, *Phys. Rev. B*, 2021, **103**, 14437.
116 C. Garg, A. Cervellino and S. Nair, *Phys. Rev. Mater.*, 2021, **5**, 44405.
117 C. D. Ling, B. J. Kennedy, Q. Zhou, J. R. Spencer and M. Avdeev, *J. Solid State Chem.*, 2010, **183**, 727–735.
118 Yoshihiro Doi and Yukio Hinatsu, *J. Phys. Condens. Matter*, 2004, **16**, 2849.
119 T. Yamamoto, K. Shitara, S. Kitagawa, A. Kuwabara, M. Kuroe, K. Ishida, M. Ochi, K.

Kuroki, K. Fujii, M. Yashima, C. M. Brown, H. Takatsu, C. Tassel and H. Kageyama, *Chem. Mater.*, 2018, **30**, 1566–1574.
120 K. Kageyama, Y. Yang, T. Kageyama, K. Murayama, K. Shitara, T. Saito, H. Ubukata, C. Tassel, A. Kuwabara and H. Kageyama, *Inorganics*, 2022, 10.
121 K. Higashi, M. Ochi, Y. Nambu, T. Yamamoto, T. Murakami, N. Yamashina, C. Tassel, Y. Matsumoto, H. Takatsu, C. M. Brown and H. Kageyama, *Inorg. Chem.*, 2021, **60**, 11957–11963.
122 M. Miyazaki, K. Ogasawara, T. Nakao, M. Sasase, M. Kitano and H. Hosono, *J. Am. Chem. Soc.*, 2022, **144**, 6453–6464.
123 D. C. Sinclair, J. M. S. Skakle, F. D. Morrison, R. I. Smith and T. P. Beales, *J. Mater. Chem.*, 1999, **9**, 1327–1331.
124 J. J. Adkin and M. A. Hayward, *J. Solid State Chem.*, 2006, **179**, 70–76.
125 K. Mori, T. Kamiyama, H. Kobayashi, K. Oikawa, T. Otomo and S. Ikeda, *J. Phys. Soc. Japan*, 2003, **72**, 2024–2028.
126 G. Liu and J. E. Greedan, *J. Solid State Chem.*, 1994, **110**, 274–289.
127 J. L. Delattre, A. M. Stacy and T. Siegrist, *J. Solid State Chem.*, 2004, **177**, 928–935.
128 A. M. Arévalo-López and J. P. Attfield, *J. Solid State Chem.*, 2015, **232**, 236–240.
129 J. J. Adkin and M. A. Hayward, *Chem. Mater.*, 2007, **19**, 755–762.
130 J. E. Auckett, K. L. Milton and I. R. Evans, *Chem. Mater.*, 2019, **31**, 1715–1719.
131 M. S. Chambers, K. S. McCombie, J. E. Auckett, A. C. McLaughlin, J. T. S. Irvine, P. A. Chater, J. S. O. Evans and I. R. Evans, *J. Mater. Chem. A*, 2019, **7**, 25503–25510.
132 M. Yashima, T. Tsujiguchi, Y. Sakuda, Y. Yasui, Y. Zhou, K. Fujii, S. Torii, T. Kamiyama and S. J. Skinner, *Nat. Commun.*, 2021, **12**, 556.
133 P. Kayser, J. A. Alonso, F. J. Mompeán, M. Retuerto, M. Croft, A. Ignatov and M. T. Fernández-Díaz, *Eur. J. Inorg. Chem.*, 2015, **2015**, 5027–5038.
134 D. Mikhailova, N. Narayanan, W. Gruner, A. Voss, A. Senyshyn, D. M. Trots, H. Fuess and H. Ehrenberg, *Inorg. Chem.*, 2010, **49**, 10348–10356.
135 N. Narayanan, D. Mikhailova, A. Senyshyn, D. M. Trots, R. Laskowski, P. Blaha, K. Schwarz, H. Fuess and H. Ehrenberg, *Phys. Rev. B*, 2010, **82**, 24403.
136 L. Wang, J. Ding, Y. Li, Y. P. Feng, N. X. Phuc and N. H. Dan, *J. Appl. Phys.*, 2001, **89**, 8046–8053.
137 L. Wang, J. Ding, Y. Li, H. Z. Kong, Y. P. Feng and X. Z. Wang, *J. Phys. Condens. Matter*, 2000, **12**, 4253.
138 M. Hagiwara, K. Nagata and K. Nagata, *J. Phys. Soc. Japan*, 1998, **67**, 3590–3600.
139 B. T. Shirk and W. R. Buessem, *J. Am. Ceram. Soc.*, 1970, **53**, 192–196.
140 L. A. Trusov, O. V Babarkina, E. O. Anokhin, A. E. Sleptsova, E. A. Gorbachev, A. A. Eliseev, T. V Filippova, A. V Vasiliev and P. E. Kazin, *J. Magn. Magn. Mater.*, 2019, **476**, 311–316.
141 R. C. Pullar, *Prog. Mater. Sci.*, 2012, **57**, 1191–1334.
142 C. V Topping and S. J. Blundell, *J. Phys. Condens. Matter*, 2019, **31**, 13001.
143 Z. Liang, M. Batuk, F. Orlandi, P. Manuel, J. Hadermann and M. A. Hayward, *Angew. Chemie Int. Ed.*, 2024, **63**, e202313067.
144 K. Vidyasagar, A. Reller, J. Gopalakrishnan and C. N. R. Rao, *J. Chem. Soc. Chem. Commun.*, 1985, 7–8.
145 V. Caignaert, N. Nguyen, M. Hervieu and B. Raveau, *Mater. Res. Bull.*, 1985, **20**, 479–484.
146 K. R. Poeppelmeier, M. E. Leonowicz and J. M. Longo, *J. Solid State Chem.*, 1982, **44**, 89–98.
147 K. R. Poeppelmeier, M. E. Leonowicz, J. C. Scanlon, J. M. Longo and W. B. Yelon, *J. Solid State Chem.*, 1982, **45**, 71–79.

148 J.-C. Grenier, S. Ghodbane, G. Demazeau, M. Pouchard and P. Hagenmuller, *Mater. Res. Bull.*, 1979, **14**, 831–839.
149 J. E. Auckett, W. T. Lee, K. C. Rule, A. Bosak and C. D. Ling, *Inorg. Chem.*, 2019, **58**, 12317–12324.
150 J. E. Page and M. A. Hayward, *Inorg. Chem.*, 2019, **58**, 8835–8840.
151 H. T. Stokes, D. M. Hatch and B. J. Campbell, ISODISTORT, ISOTROPY Software Suite, iso.byu.edu.
152 B. J. Campbell, H. T. Stokes, D. E. Tanner and D. M. Hatch, *J. Appl. Crystallogr.*, 2006, **39**, 607–614.
153 R. Morrow, J. Yan, M. A. McGuire, J. W. Freeland, D. Haskel and P. M. Woodward, *Phys. Rev. B*, 2015, **92**, 94435.
154 H. L. Feng, C.-J. Kang, P. Manuel, F. Orlandi, Y. Su, J. Chen, Y. Tsujimoto, J. Hadermann, G. Kotliar, K. Yamaura, E. E. McCabe and M. Greenblatt, *Chem. Mater.*, 2021, **33**, 4188–4195.
155 P. D. Battle and C. W. Jones, *J. Solid State Chem.*, 1989, **78**, 108–116.
156 J. M. Pruneda, J. Íñiguez, E. Canadell, H. Kageyama and M. Takano, *Phys. Rev. B*, 2008, **78**, 115101.
157 Z. Liang, *The topochemical reduction of Ru-containing double perovskite oxides*, University of Oxford, 2023.
158 M. A. Patino, D. Zeng, R. Bower, J. E. McGrady and M. A. Hayward, *Inorg. Chem.*, 2016, **55**, 9012–9016.
159 S. Esser, C. F. Chang, C.-Y. Kuo, S. Merten, V. Roddatis, T. D. Ha, A. Jesche, V. Moshnyaga, H.-J. Lin, A. Tanaka, C. T. Chen, L. H. Tjeng and P. Gegenwart, *Phys. Rev. B*, 2018, **97**, 205121.
160 R. Bower, *Topochemical Reduction of Ruthenium-containing Mixed Perovskites*, University of Oxford, 2014.
161 A. L. Patterson, *Phys. Rev.*, 1939, **56**, 978–982.
162 J. Li, A. E. Smith, K.-S. Kwong, C. Powell, A. W. Sleight and M. A. Subramanian, *J. Solid State Chem.*, 2010, **183**, 1388–1393.
163 K. Knížek, J. Hejtmánek, M. Maryško, Z. Jirák and J. Buršík, *Phys. Rev. B*, 2012, **85**, 134401.
164 S. V Streltsov, V. V Gapontsev and D. I. Khomskii, *J. Phys. Condens. Matter*, 2016, **28**, 86005.
165 Z. Xu, P. K. Thakur, T.-L. Lee, A. Regoutz, E. Suard, I. Puente-Orench and M. A. Hayward, *Inorg. Chem.*, 2022, **61**, 15686–15692.
166 K. Meadows, *Topochemical Reduction of some Complex Rhodium Oxide Phases*, University of Oxford, 2015.
167 S. Asai, N. Furuta, Y. Yasui and I. Terasaki, *J. Phys. Soc. Japan*, 2011, **80**, 104705.
168 X. G. Zheng, C. N. Xu, K. Nishikubo, K. Nishiyama, W. Higemoto, W. J. Moon, E. Tanaka and E. S. Otabe, *Phys. Rev. B*, 2005, **72**, 14464.
169 Y. J. Tang, D. J. Smith, B. L. Zink, F. Hellman and A. E. Berkowitz, *Phys. Rev. B*, 2003, **67**, 54408.
170 D. Tobia, E. Winkler, R. D. Zysler, M. Granada and H. E. Troiani, *Phys. Rev. B*, 2008, **78**, 104412.
171 S. Mørup, D. E. Madsen, C. Frandsen, C. R. H. Bahl and M. F. Hansen, *J. Phys. Condens. Matter*, 2007, **19**, 213202.
172 Z. Liang, M. Amano Patino, M. Hendrickx, J. Hadermann and M. A. Hayward, *ACS Org. Inorg. Au*, 2022, **2**, 75–82.
173 Z. Lu, V. Cherepakhin, I. Demianets, P. J. Lauridsen and T. J. Williams, *Chem. Commun.*, 2018, **54**, 7711–7724.

174 D. M. Heinekey, D. A. Fine, T. G. P. Harper and S. T. Michel, *Can. J. Chem.*, 1995, **73**, 1116–1125.
175 Y. Hu, L. Li, A. P. Shaw, J. R. Norton, W. Sattler and Y. Rong, *Organometallics*, 2012, **31**, 5058–5064.
176 H. Takaya, K. Yoshida, K. Isozaki, H. Terai and S.-I. Murahashi, *Angew. Chemie Int. Ed.*, 2003, **42**, 3302–3304.
177 L. Jin and M. A. Hayward, *Angew. Chemie Int. Ed.*, 2020, **59**, 2076–2079.